ΕΘΝΙΚΟ ΜΕΤΣΟΒΙΟ ΠΟΛΥΤΕΧΝΕΙΟ

ΣΧΟΛΗ ΜΗΧΑΝΟΛΟΓΩΝ ΜΗΧΑΝΙΚΩΝ

ΤΟΜΕΑΣ ΘΕΡΜΟΤΗΤΑΣ

ΕΡΓΑΣΤΗΡΙΟ ΑΤΜΟΚΙΝΗΤΗΡΩΝ & ΛΕΒΗΤΩΝ

<u>Διδακτορική Διατριβή</u>

ΑΡΙΘΜΗΤΙΚΗ ΠΡΟΣΟΜΟΙΩΣΗ ΚΑΙΝΟΤΟΜΩΝ ΣΥΣΤΗΜΑΤΩΝ ΑΠΟΘΗΚΕΥΣΗΣ ΕΝΕΡΓΕΙΑΣ ΒΑΣΙΖΟΜΕΝΩΝ ΣΕ ΠΟΛΥΦΑΣΙΚΕΣ ΡΟΕΣ

Numerical investigation of novel energy storage systems based on multi-phase flows

Μυρτώ Ζενέλη

Διπλ. Μηχανολόγος Μηχανικός Ε.Μ.Π.

Επιβλέπων Καθηγητής: Σωτήριος Καρέλλας

Στη μητέρα μου

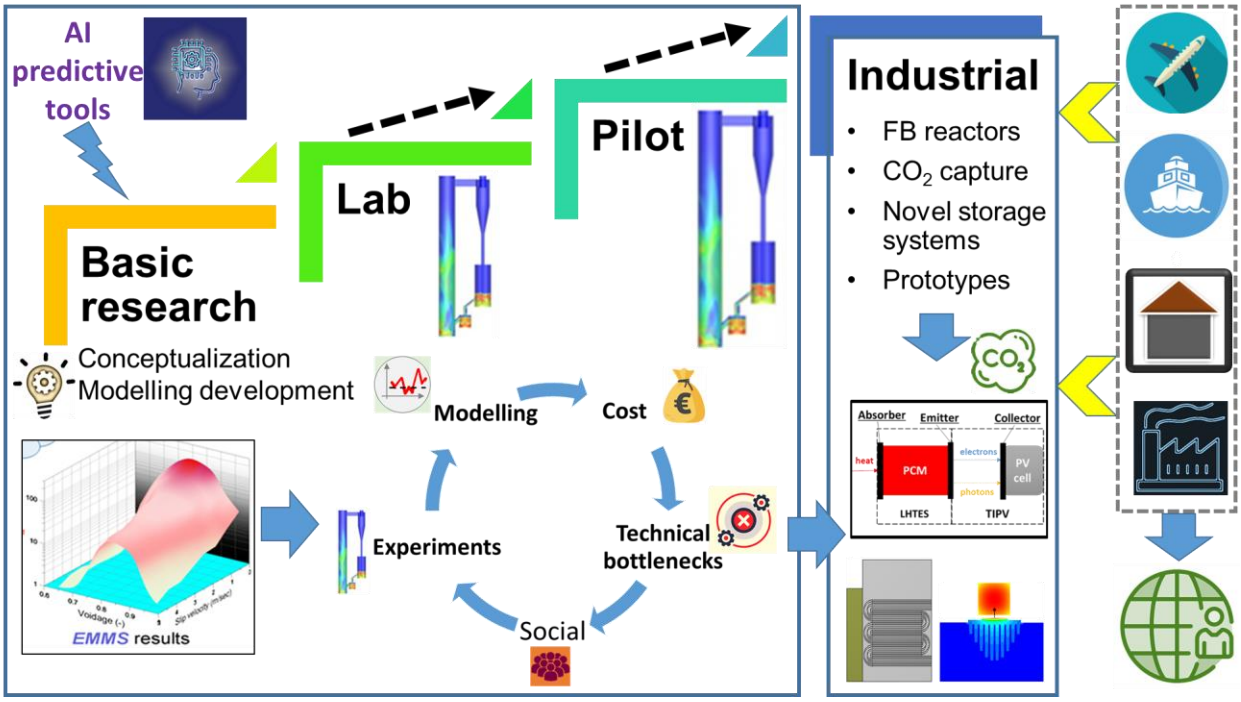

«Η επιστήμη και η τέχνη ανήκουν σε όλο τον κόσμο, και μπροστά τους εξαφανίζονται όλα τα σύνορα»

Βόλφγκανγκ Γκαίτε, 1749-1832, Γερμανός ποιητής & φιλόσοφος

Ευχαριστίες

Κατά τη διάρκεια όλου αυτού του ενδιαφέροντος ερευνητικού ταξιδιού θα ήθελα πρωτίστως να ευχαριστήσω των επιβλέποντα καθηγητή μου Σωτήριο Καρέλλα, ο οποίος μου έδωσε την ευκαιρία να εκπονήσω την παρούσα Διδακτορική Διατριβή, καθώς και την διπλωματική μου διατριβή. Η βοήθειά του υπήρξε πολύ σημαντική καθ' όλη τη διάρκεια της ερευνητικής μου πορείας. Επιπρόσθετα, θα ήθελα να ευχαριστήσω θερμά τους ερευνητές από το Εθνικό Κέντρο Έρευνας και Τεχνολογικής Ανάπτυξης για την αγαστή τους συνεργασία και υποστήριξη για δώδεκα συναπτά έτη. Πιο συγκεκριμένα, θα ήθελα να ευχαριστήσω τον ερευνητή Α' βαθμίδας Νικόλαο Νικολόπουλο που μου έδωσε την δυνατότητα να δουλέψω σε μια σειρά από ενδιαφέροντα ερευνητικά έργα, στο πλαίσιο των οποίων εκπόνησα την διδακτορική μου διατριβή. Η συνεισφορά του υπήρξε ύψιστης σημασίας για την ανάπτυξη της ερευνητικής και επαγγελματικής μου μου σκέψης. Φυσικά, πολύ κομβική και ουσιαστική υπήρξε η βοήθεια από τον επιβλέποντα μου επί μία δεκαετία Δρ. Αριστείδη Νικολόπουλο ο οποίος με βοήθησε σε κάθε στάδιο της εκπόνησης της διδακτορικής μου διατριβής, αλλά και εργασίας μου στα ερευνητικά έργα στο ΕΚΕΤΑ. Επιπρόσθετα, θα ήθελα να ευχαριστήσω θερμά τον Ερευνητή Α' βαθμίδας Παναγιώτη Γραμμέλη, ο οποίος μου έδωσε το κίνητρο να προχωρήσω και να ηγηθώ ενεργά ερευνητικών προγραμμάτων και συγγραφής προτάσεων, ενισχύοντάς μου την επαγγελματική μου αυτοπεποίθηση. Συνακολούθως, θα ήθελα να αναφερθώ στην πολύτιμη βοήθεια του φίλου και συναδέλφου Κωστή Ατσόνιου ο οποίος με έχει βοηθήσει σε όλα τα χρόνια της πορείας σε ηθικό, συναδελφικό και ερευνητικό επίπεδο. Τέλος, θα ήθελα να ευχαριστήσω θερμά τα λοιπά μέλη της 7μελούς επιτροπής (Καθηγητή Εμμανουήλ Κακαρά, Καθηγητή Κυριάκο Γιαννάκογλου, Καθηγητή Joergen Karl και Αναπληρωτή Καθηγητή Alejandro Datas) που δέχτηκαν να αξιολογήσουν τη διδακτορική μου διατριβή.

Δεν μπορώ να ξεχάσω από τις ευχαριστίες συναδέλφους και φίλους από την ομάδα υπολογιστικής ρευστοδυναμικής του ΕΚΕΤΑ με τους οποίους είχαμε πολύ καλή συνεργασία. Πιο συγκεκριμένα, τον συνάδελφο Δρ. Ηλία Μαλγαρινό, τον Δρ. Διονύσιο Στεφανίτση, τον Δρ. Σταύρο Φωστηρόπουλο, τον Παναγιώτη Δροσάτο, τον Πάνο Σταματόπουλο και τον Γιώργο Κανέλλη. Επιπρόσθετα, θέλω να ευχαριστήσω τους συναδέλφους και φίλους για την ηθική τους υποστήριξη όλα αυτά τα χρόνια τον Μιχάλη Κουγιουμτζή, την Βασιλική Γεμενή, τον Βασίλη Αποστολόπουλο, την Αγγελική Σαγάνη, την Χριστίνα Λουκά, τον Δρ. Χρήστο Χριστοδούλου, την Δρ. Εφηγιάννα Κουτσούμπα, τον Δημήτρη Κουρκούμπα, την Ιωάννα Καραίσκου, τον Μανώλη Καραμπίνη και τους λοιπούς συναδέλφους.

Επιπροσθέτως, θα ήθελα να ευχαριστήσω την ομάδα από το UPM για την δυνατότητα που μου έδωσαν να συνεχίσω την έρευνα μου στα υλικά αλλαγής φάσης, την ομάδα του TUDA για την πολυετή τους συνεργασία, τα πειράματα των οποίων ήταν κομβικά για να επιτελέσω την επικύρωση των μοντέλων των ρευστοποιημένων κλινών, την ομάδα του FAU για τη συνεργασία στο πλαίσιο του ANICA, καθώς και τους συναδέλφους από την Shi-FW οι οποίοι μοιράστηκαν τη βιομηχανική τους γνώση στο πλαίσιο του έργου FlexFlores, η οποία χρησιμοποιήθηκε στο πλαίσιο της παρούσας διδακτορικής διατριβής.

Τέλος, θα ήθελα να ευχαριστήσω θερμά τους φίλους μου Μαριάννα, Άννα, Δήμητρα, Βίβιαν, Άγγελο, Πάνο, Σοφία, Όλγα και Ελένη, καθώς και την μεγαλύτερη αδερφή μου Μαριάννα για την υποστήριξή τους σε προσωπικό, υλικό και ουσιαστικό επίπεδο. Πιο σημαντικό θα ήθελα να ευχαριστήσω και να αναγνωρίσω την πολυετή συνεισφορά της μητέρας μου Άννας σε όλα τα στάδια της ζωής μου από την εισαγωγή μου στο Πολυτεχνείο μέχρι και σήμερα, καθώς των εκλιπόντων παππούδων μου Κατερίνα και Λάζαρο Πετρίδη. Η υπερπλήρης αγάπη όλων αυτών των κοντινών μου προσώπων με βοήθησε στο να αντλήσω ψυχική δύναμη για να συνεχίσω στο απαιτητικό ερευνητικό ταξίδι.

Σύμφωνα με απόφαση της Γενικής Συνέλευσης της Σχολής Μηχανολόγων Μηχανικών του ΕΜΠ στις (20/03/2023) η παρούσα Διατριβή γίνεται αποδεκτή στην Αγγλική γλώσσα. Έχει επιπλέον προστεθεί ελληνική περίληψη με έκταση ίση περίπου με τον ένα τρίτο της έκτασης του αγγλικού κειμένου.

Η έγκριση της Διδακτορική Διατριβής από τη Σχολή Μηχανολόγων Μηχανικών του Εθνικού Μετσόβιου Πολυτεχνείου δεν υποδηλώνει αποδοχή των γνωμών του συγγραφέα (Ν. 5343/ 1932, Άρθρο 202).

Επιβλέπων Καθηγητής

Δρ. Σ. Καρέλλας
Καθηγητής ΕΜΠ

Τριμελής Συμβουλευτική Επιτροπή

Δρ. Σ. Καρέλλας
Καθηγητής ΕΜΠ

Δρ. Ν. Νικολόπουλος
Α' Ερευνητής ΕΚΕΤΑ

Δρ. Εμμ. Κακαράς
Καθηγητής ΕΜΠ

Επταμελής Εξεταστική Επιτροπή

Δρ. Σ. Καρέλας
Καθηγητής ΕΜΠ

Δρ. Ν. Νικολόπουλος
Ερευνητής Α΄ ΕΚΕΤΑ/ΙΔΕΠ

Δρ. Π. Γραμμέλης
Ερευνητής Α΄ ΕΚΕΤΑ/ΙΔΕΠ

Δρ. Εμμ. Κακαράς
Καθηγητής ΕΜΠ

Dr. Jürgen Karl
Καθηγητής FAU

Δρ. Κυριάκος Γιαννάκογλου
Καθηγητής ΕΜΠ

Dr Alejandro Datas
Αναπληρωτής καθηγητής, UPM

Summary

The scope of the present Doctoral Thesis is to model and optimize novel energy storage systems operating at high and ultra-high temperatures (>800-900 ºC) based on either (1) phase change materials (PCMs), or (2) granular materials. The latter can be part of sensible heat storage fluidized bed systems or thermochemical energy storage systems, such as the carbonate looping cycle. All three types of systems (latent heat, sensible and thermochemical) can be used in applications of various scales (from experimental facilities to industrial scale units) as stand-alone technological options or in conjunction with other conventional power generation units. In addition, they are aimed at temperatures above 500-600 ºC, without excluding their operation at medium or low temperatures. However, the use of such systems on a large scale requires in-depth knowledge of various heat transfer mechanisms and various complex fluid flow phenomena taking place during their operation. The use of computational fluid dynamics (CFD) tools can help to understand such mechanisms, as well as to optimize such systems, in terms of their operating conditions, but also of their design. In the framework of this Thesis, the development of several CFD based tools has been achieved by utilizing a commercial simulation platform (ANSYS Fluent™) and where it has been deemed necessary, in-house codes in C and FORTRAN programming language have been used, in order to improve the accuracy of the developed models. Validation of the numerical models has been done using experimental results, which have been retrieved either from the literature, or from cooperating universities carrying out the experimental campaigns of the studied systems in the context of the research projects, during which the doctoral thesis has been prepared. Verification of the CFD models against theoretical models has been also done in cases where there has been lack of experimental data. Seven chapters showcase the specific research effort that has been put during the PhD Thesis.

More specifically, in the First Chapter the general framework is set for the necessity of full decarbonization and clean energy transition by 2050, which increases the need of using renewable energy sources, advanced energy storage systems, as well as carbon capture systems. Reference is made to the energy storage technologies that are widely being used currently and, then, the innovative systems examined in this doctoral thesis are mentioned. These refer to a) a latent heat thermal energy storage system that contains silicon as a phase change material and operates at ultra-high temperatures (~1410 °C), b) the calcium looping cycle, which operates at high temperatures (~650-900 ºC) and can be used for energy storage in the form of chemical reaction and simultaneous capture of carbon dioxide and c) a sensible heat storage system based on gas-solid fluidized bed (~500-600 ºC) and can operate either for energy storage or as a heat exchanger in power plants.

The Second Chapter presents in detail the numerical methods and equations used in this PhD Thesis to model the under-studied innovative technologies. More specifically, in the case of PCMs, the heat transfer mechanisms through conduction and convection, the development of dendritic formations during the PCM solidification and their effect on system performance, as well as the PCM volume change during their phase change are taken into account. The enthalpy porosity approach combined with the Volume of fluid (VOF) method are used to simulate systems based on phase change materials. A critical parameter for the optimization of these systems is the heat losses from the crucible sidewalls, which increase inversely to their volume, while they also depend to a large extent on the shape of the storage container of the phase change material. In the case of fluidized bed units, two main approaches can be applied to simulate the multiphase flow (granular solid and gas), i.e. the Euler-Euler (Two fluid model - TFM), or the Euler-Lagrange (Dense discrete phase model - DDPM). In this doctoral thesis, the state-of-the-art Euler-Euler TFM method is used. Accurate modeling of the interaction between solid particles and fluid phase relies

heavily on the model used for the drag force, i.e. the force exerted on the solid particles by the gas phase. For this reason, an innovative drag model is applied which approximates the flow heterogeneity (e.g. particles clusters) at various scales. This model is called EMMS (Energy Minimization Multi-Scale Analysis) and tends to outperform conventional homogeneous drag models (such as that of Gidaspow). A new version of this model, with the new cluster correlation that takes into account the reactor diameter, has been validated for different reactors in the framework of this Thesis.

Chapter Three focuses on the latent heat energy storage system study and optimization. More specifically, a transient CFD model has been developed based on the principles mentioned in the Second Chapter for modeling the three-phase flow inside a container that contains a PCM that changes phase from solid to liquid and vice versa and an inert gas that is inside the same container over the material. Two types of PCMs are tested (i) paraffin wax, which changes phase at low temperatures (~40 °C) and (ii) new generation PCMs, such as boron/silicon alloys, which are characterized by a latent heat of the order of 2- 4 $MJ \cdot kg^{-1}$ (an order of magnitude greater than that of standard molten salts widely used today). Due to the high melting point of such materials (for example pure silicon melts at about 1400 °C), there are many technical problems in the system itself that need to be studied. A major problem is the high heat losses from the vessel sidewalls. The type of insulation (materials, thickness of materials), as well as the shape and volume of the container itself can play a high role in the amount of lateral losses. Other parameters investigated in such a storage system are its charging-discharging rate, as well as the storage time (the time before it loses all of its stored energy in the form of latent heat). Regarding the shapes, great emphasis has been placed on the optimization of the shape of the truncated cone, as it presents great flexibility in design in relation to, for example, the spherical shape. Finally, a parametric analysis has been made regarding the effect of the material properties (thermal conductivity, specific heat capacity, etc.) on the charging-discharging rate of the system.

Regarding the multi-phase flow simulations inside fluidized bed systems, several units have been modeled, which can be used in the calcium looping cycle (Chapter Four) or for energy storage in the form of sensible heat and in novel heat exchangers (Chapter Five). Modeling the multiphase flow using the developed EMMS model increases the accuracy of the results in terms of the overall pressure drop predictions, solids recirculation flux and predicted flow patterns. Finally, other elements investigated are the effect of radiative heat transfer (this particular phenomenon is worth studying in cases of (i) dilute flow fluidized beds, where the effect of radiative heat transfer can be significant in (ii) types of fluidized beds that store energy from the sun etc.). In the last case (i.e. solar particle receiver) the effect of radiation is very important, as the suspended particles absorb energy from the walls of the unit which are either permeable to solar radiation (direct energy absorption) or impermeable (indirect energy absorption). An important added value to the scientific community is that the developed models have been validated against experimental results from pilot units (300 kW_{th}-1 MW_{th}) which can provide a more realistic view of large-scale flow phenomena. More specifically the modeling carried out in Chapter Four includes, (a) Construction and validation of the EMMS model in a 1 MW_{th} circulating fluidized bed carbonator, (b) Modeling of the carbonator reactor at two scales (1 MW_{th} and 20 MW_{th}) and optimizing its design through the study of various scenarios (c) Modeling of a fluidized bed system that acts as calciner and receives heat either through the in-situ combustion of solid fuel (oxy-fired CaL) or through indirect heat transfer (Indirectly heated calcium looping). Chapter Five focuses on modeling a bubbling fluidized bed system that acts as a storage vessel/heat exchanger (2-phase flow) – In this unit, there is a series of tube buddles, in which steam flows and draws heat from the fluidized bed. Appropriate user defined functions (UDF – User Defined Functions) have been used to implicitly model the steam flow inside the pipelines. Added to this, a theoretical model

has been used to carry out extra parametric studies on the effect of several parameters (e.g. fluidizing agent type) on the overall heat transfer process inside the sensible heat storage system.

Finally, the Sixth Chapter sets a general framework for the application of the three main technologies studied (energy storage in solid granular particles in the form of sensible heat (a) and chemical reaction (b), as well as energy storage in the form of latent heat with change materials phase (c)). More specifically, a theoretical comparison is set by comparing the different types of heating and storing methods studied in this Thesis in terms of charging rates and charging time.

Finally, general conclusions from the individual chapters are summarized in the Seventh Chapter, whereas various themes are proposed for future development of the models based on the experience gained through this doctoral thesis.

Σύνοψη

Ο σκοπός της παρούσας διδακτορικής διατριβής είναι η μοντελοποίηση καινοτόμων συστημάτων αποθήκευσης ενέργειας βασιζόμενα, (1) σε υλικά αλλαγής φάσης υψηλής λανθάνουσας θερμότητας (latent heat thermal energy storage systems), ή (2) σε συστήματα κοκκώδους ροής (μονάδες ρευστοποιημένης κλίνης - fluidized beds). Τα τελευταία βασίζονται είτε στην αποθήκευση ενέργειας υπό τη μορφή λανθάνουσας θερμότητας, είτε σε κύκλους φόρτισης-εκφόρτισης μέσω χημικής αντίδρασης, χρησιμοποιώντας για παράδειγμα έναν κύκλο ενδόθερμης-εξώθερμης αντίδρασης, όπως ο κύκλος δέσμευσης διοξειδίου του άνθρακα ασβεστοποίησης-ενανθράκωσης (calcium-looping cycle). Αμφότερα συστήματα μπορούν να χρησιμοποιηθούν σε διάφορες εφαρμογές διαφόρων κλιμάκων (από πειραματικές εγκαταστάσεις, μέχρι μονάδες παραγωγής ηλεκτρισμού) και μπορούν να χρησιμοποιηθούν είτε αυτόνομα, είτε σε σύζευξη με άλλες συμβατικές μονάδες παραγωγής ενέργειας. Επιπρόσθετα οι θερμοκρασίες λειτουργίας τους στοχεύουν σε θερμοκρασίες άνω των 500-600 ^{o}C, χωρίς να αποκλείεται η λειτουργία τους και σε μεσαίες ή χαμηλές θερμοκρασίες. Ωστόσο η χρήση τέτοιων συστημάτων σε ευρεία κλίμακα απαιτεί εις βάθος γνώση διαφόρων μηχανισμών συναλλαγής θερμότητας και διαφόρων περίπλοκων ροϊκών φαινομένων. Η χρήση των εργαλείων υπολογιστικής ρευστοδυναμικής (Computational fluid dynamics - CFD tools) μπορεί να βοηθήσει στην κατανόηση τέτοιων μηχανισμών, καθώς και στη βελτιστοποίηση τέτοιων συστημάτων, όσον αφορά τις συνθήκες λειτουργίας τους, αλλά και τον σχεδιασμό τους. Η ανάπτυξη τέτοιων εργαλείων έγινε σε εμπορική πλατφόρμα προσομοίωσης (ANSYS Fluent^{TM}) και όπου κρίθηκε απαραίτητο χρησιμοποιήθηκαν διάφοροι κώδικες σε γλώσσα προγραμματισμού C και FORTRAN, ώστε να εμπλουτιστούν και να βελτιωθούν από άποψη ακρίβειας τα αναπτυγμένα μοντέλα. Επιβεβαίωση των αριθμητικών μοντέλων έγινε με τη χρήση πειραματικών αποτελεσμάτων, τα οποία ανακτήθηκαν είτε από τη βιβλιογραφία, είτε από συνεργαζόμενα πανεπιστήμια/φορείς στα πλαίσια των ερευνητικών έργων, κατά την διάρκεια των οποίων εκπονήθηκε η διδακτορική διατριβή. Η διδακτορική διαριβή χωρίζεται σε επτά επί μέρους κεφάλαια τα οποία παρουσιάζουν την συγκεκριμένη ερευνητική προσπάθεια.

Πιο συγκεκριμένα, στο Πρώτο Κεφάλαιο τίθεται το γενικό πλαίσιο για την αναγκαιότητα πλήρους απολιγνιτοποίησης μέχρι το 2050 η οποία αυξάνει την ανάγκη χρήσης ανανεώσιμων πηγών ενέργειας, προηγμένων συστημάτων αποθήκευσης ενέργειας, καθώς και συστημάτων δέσμευσης διοξειδίου του άνθρακα. Γίνεται αναφορά στις τεχνολογίες αποθήκευσης ενέργειας οι οποίες χρησιμοποιούνται ευρέως σήμερα και εν συνεχεία αναφέρονται τα καινοτόμα συστήματα που εξετάστηκαν στην παρούσα διδακτορική διατριβή. Αυτά αναφέρονται σε συστήματα αποθήκευσης θερμικής ενέργειας με τη χρήση α) ενός καινοτόμου συστήματος αποθήκευσης ενέργειας υπό τη μορφή λανθάνουσας θερμότητας το οποίο εμπεριέχει πυρίτιο σαν υλικό αλλαγής φάσης και λειτουργεί σε πολύ υψηλές θερμοκρασίες (~1410 ^{o}C), β) του κύκλου ασβεστοποίησης-ενανθράκωσης ο οποίος λειτουργεί σε υψηλές θερμοκρασίες (~650-900 ^{o}C) και μπορεί να χρησιμοποιηθεί για αποθήκευση ενέργειας υπό τη μορφή χημικής αντίδρασης και παράλληλη δέσμευση διοξειδίου του άνθρακα και γ) ενός συστήματος αποθήκευσης αισθητής θερμότητας (~500-600 ^{o}C) το οποίο βασίζεται στη ροή κοκκώδους ροής υπό την μορφή φυσαλίδων και μπορεί να λειτουργεί είτε για αποθήκευση ενέργειας αλλά και ως εναλλάκτης θερμότητας.

Το Δεύτερο Κεφάλαιο, παρουσιάζει αναλυτικά τις αριθμητικές μεθόδους και τις εξισώσεις που χρησιμοποιούνται στην παρούσα διδακτορική διατριβή για να μοντελοποιηθούν οι καινοτόμες τεχνολογίες που εξετάζονται. Πιο συγκεκριμένα, στη περίπτωση των υλικών αλλαγής φάσης (phase change materials - PCMs) λαμβάνονται υπόψη οι μηχανισμοί μεταφοράς θερμότητας μέσω αγωγής και συναγωγής, η ανάπτυξη δενδριτικών μορφών κατά την στερεοποίησή τους, καθώς και η αλλαγή του όγκου τους κατά την αλλαγή φάσης αυτών. Το μοντέλο enthalpy porosity approach σε συνδυασμό με τη μέθοδο Volume of fluid

(VOF) χρησιμοποιούνται για την προσομοίωση συστημάτων που βασίζονται σε υλικά αλλαγής φάσης. Κρίσιμη παράμετρος για την βελτιστοποίηση των συγκεκριμένων συστημάτων είναι οι απώλειες θερμότητας από τα τοιχώματά τους, οι οποίες αυξάνονται αντιστρόφως ανάλογα με τον όγκο τους, ενώ εξαρτώνται σε μεγάλο βαθμό και από το σχήμα που έχει το δοχείο αποθήκευσης του υλικού αλλαγής φάσης. Στην περίπτωση των μονάδων ρευστοποιημένης κλίνης εφαρμόζονται ειδικά μοντέλα που προσομοιώνουν την πολυφασική ροή (κοκκώδες στερεό και αέριο), είτε κατά Euler-Euler (Two fluid model – TFM), είτε κατά Euler-Lagrange (Dense discrete phase model - DDPM). Στην παρούσα διδακτορική διατριβή χρησιμοποιείται η μέθοδος κατά Euler-Euler TFM. Η ακριβής μοντελοποίηση της αλληλεπίδρασης μεταξύ στερεών σωματιδίων και ρευστού βασίζεται σε μεγάλο βαθμό στο μοντέλο που χρησιμοποιείται για την οπισθέλκουσα δύναμη, δηλαδή την δύναμη που ασκείται στα στερεά σωματίδια κατά την ροή τους μέσα στο ρευστό. Για το λόγο αυτό εφαρμόζεται ένα καινοτόμο μοντέλο οπισθέλκουσας το οποίο προσεγγίζει τη ροή υπό διάφορες κλίμακες. Το μοντέλο αυτό ονομάζεται EMMS (Energy Minimization Multi-Scale Analysis) και τείνει να υπερισχύσει έναντι των συμβατικών μοντέλων οπισθέλκουσας (όπως αυτό του Gidaspow).

Το Τρίτο Κεφάλαιο επικεντρώνεται στο σύστημα αποθήκευσης ενέργειας μέσω λανθάνουσας θερμότητας. Πιο συγκεκριμένα αναπτύσσεται ένα μοντέλο με τις αρχές που αναφέρονται στο Δεύτερο Κεφάλαιο για την μοντελοποίηση της τριφασικής ροής μέσα σε ένα δοχείο το οποίο εμπεριέχει ένα υλικό που αλλάζει φάση από στερεό σε υγρό και αντίστροφα και ένα αδρανές αέριο το οποίο εμπεριέχεται μέσα στο ίδιο δοχείο πάνω από το υλικό. Εξετάζονται δύο τύποι υλικών αλλαγής φάσεων (α) κερί παραφίνης το οποίο αλλάζει φάση σε χαμηλές θερμοκρασίες (~40 ^{o}C) και (β) υλικά αλλαγής φάσης νέας γενιάς, όπως τα κράματα βορίου/πυριτίου τα οποία χαρακτηρίζονται από λανθάνουσα θερμότητα της τάξεως των 2-4 $MJ \cdot kg^{-1}$ (μία τάξη μεγέθους μεγαλύτερη αυτής των τυπικών στηλών άλατος που χρησιμοποιούνται ευρέως σήμερα). Λόγω του υψηλού σημείου τήξεως τέτοιων υλικών (παραδείγματος χάριν το καθαρό πυρίτιο λιώνει περίπου στους 1400 ^{o}C) υπάρχουν πολλά τεχνικά προβλήματα στο ίδιο το σύστημα που πρέπει να μελετηθούν. Ένα σημαντικό πρόβλημα είναι οι μεγάλες θερμικές απώλειες από τα τοιχώματα του δοχείου. Ο τύπος μόνωσης (υλικά, πάχος υλικών), καθώς και το ίδιο το σχήμα και ο όγκος του δοχείου μπορούν να παίξουν ρόλο στο μέγεθος των απωλειών. Άλλες παράμετροι που διερευνήθηκαν σε ένα τέτοιο σύστημα αποθήκευσης είναι ο ρυθμός φόρτισης-εκφόρτισης του, καθώς και ο χρόνος αποθήκευσης (ο χρόνος πριν χάσει όλη την αποθηκευμένη ενέργεια υπό τη μορφή λανθάνουσας θερμότητας). Όσον αφορά τα σχήματα μεγάλη έμφαση δόθηκε στην βελτιστοποίηση του σχήματος του κόλουρου κώνου, καθώς παρουσιάζει μεγάλη ευελιξία στον σχεδιασμό σε σχέση παραδείγματος χάριν με το σφαιρικό σχήμα. Τέλος, έγινε μία παραμετρική ανάλυση όσον αφορά την επίδραση των ιδιοτήτων του υλικού (θερμική αγωγιμότητα, ειδική θερμοχωρητικότητα κλπ.) στον ρυθμό φόρτισης εκφόρτισης του συστήματος.

Όσον αφορά στις ρευστοποιημένες κυκλοφορίες ανακυκλοφορίας, έγινε μοντελοποίηση μονάδων οι οποίες μπορούν να χρησιμοποιηθούν σε έναν κύκλο ασβεστοποίησης ενανθράκωσης (Τέταρτο Κεφάλαιο) ή για αποθήκευση ενέργειας υπό τη μορφή αισθητής θερμότητας (Πέμπτο Κεφάλαιο). Η μοντελοποίηση της πολυφασικής ροής με τη χρήση του αναπτυγμένου μοντέλου EMMS αυξάνει την ακρίβεια των αποτελεσμάτων. Τέλος, άλλα στοιχεία που διερευνήθηκαν είναι η επίδραση της μεταφοράς θερμότητας μέσω ακτινοβολίας (το συγκεκριμένο φαινόμενο χρήζει αξίας να μελετηθεί σε περιπτώσεις (α) ρευστοποιημένων κλινών αραιής ροής όπου η επίδραση μεταφοράς θερμότητας μέσω ακτινοβολίας μπορεί να είναι σημαντική σε (β) τύπους ρευστοποιημένων κλινών που αποθηκεύουν ενέργεια από τον ήλιο κλπ.). Στην τελευταία περίπτωση η επίδραση της ακτινοβολίας είναι πολύ σημαντική, καθώς τα αιωρούμενα σωματίδια απορροφούν ενέργεια από τους τοίχους της μονάδας οι οποίοι είναι είτε διαπερατοί στην ηλιακή

ακτινοβολία (άμεση απορρόφηση ενέργειας) είτε αδιαπέραστοι (έμμεση απορρόφηση ενέργειας). Σημαντική προστιθέμενη αξία στην επιστημονική κοινότητα είναι ότι τα αναπτυγμένα μοντέλα έχουν επικυρωθεί έναντι πειραματικών αποτελεσμάτων από πιλοτικές μονάδες (300 kW_{th}-1 MW_{th}) οι οποίες μπορούν να προσφέρουν μία πιο ρεαλιστική εικόνα των ροικών φαινομένων σε μεγάλη κλίμακα. Πιο συγκεκριμένα οι μοντελοποιήσεις που διενεργήθηκαν στο Τέταρτο Κεφάλαιο περιλαμβάνουν, (α) Κατασκευή και επικύρωση του μοντέλου EMMS σε σύστημα ρευστοποιημένης κλίνης ανακυκλοφορίας 1 MWth, το οποίο λαμβάνει υπόψη τη διάμετρο του αντιδραστήρα (β) Μοντελοποίηση συστήματος ρευστοποιημένης κλίνης σε δύο κλίμακες (1 MW_{th} και 20 MW_{th}) το οποίο λειτουργεί ως εναναθρακωτής και βελτιστοποίηση του σχεδιασμού του μέσω της μελέτης διαφόρων σεναρίων (γ) Μοντελοποίηση συστήματος ρευστοποιημένης κλίνης το οποίο λειτουργεί ως ασβεστοποιητής και λαμβάνει θερμότητα είτε μέσω της εγγενούς καύσεως στερεού καυσίμου (oxy-fired CaL) είτε μέσω έμμεσης πρόσδοσης θερμότητας (Indirectly heated calcium looping). Το Πέμπτο Κεφάλαιο επικεντρώθηκε στη μοντελοποίηση συστήματος ρευστοποιημένης κλίνης με φυσαλίδες το οποίο λειτουργεί ως δοχείο αποθήκευσης/εναλλάκτης θερμότητας (2φασική ροή) – Στη συγκεκριμένη μονάδα υπάρχει μία σειρά από σωληνώσεις μέσα στις οποίες ρέει ατμός ο οποίος τραβάει θερμότητα από τη ρευστοποιημένη κλίνη. Για τη ροή του ατμού μέσα στις σωληνώσεις χρησιμοποιήθηκαν κατάλληλες συναρτήσεις διαμορφωμένες από το χρήστη (UDF – User Defined Functions).

Τέλος το Έκτο Κεφάλαιο, θέτει ένα γενικό πλαίσιο εφαρμογής των τριών βασικών τεχνολογιών που μελετήθηκαν (αποθήκευση ενέργειας σε στερεά κοκκώδη σωματίδια υπό τη μορφή αισθητής θερμότητας (α) και χημικής αντίδρασης (β), καθώς και αποθήκευση ενέργειας υπό τη μορφή λανθάνουσας θερμότητας σε υλικά αλλαγής φάσης (γ)). Πιο συγκεκριμένα, γίνεται μια θεωρητική σύγκριση για τους διαφορετικούς τύπους μεθόδων θέρμανσης και αποθήκευσης ενέργειας που μελετήθηκαν στην παρούσα διδακτορική διατριβή όσον αφορά τους ρυθμούς φόρτισης και το χρόνο φόρτισης τους.

Τέλος, στο Έβδομο Κεφάλαιο συνοψίζονται γενικά συμπεράσματα από τα επί μέρους κεφάλαια, ενώ παράλληλα προτείνονται διάφορες θεματικές για μελλοντική ανάπτυξη των μοντέλων με βάση την εμπειρία που αποκτήθηκε μέσω της παρούσας διδακτορικής διατριβής.

Preface

My name is Myrto Zeneli and I have studied Mechanical Engineering in the National Technical University of Athens (NTUA) during the period 2004-2011. Currently, I am a PhD candidate of NTUA. My major field of expertise is the modeling of laminar, turbulent, single- or multi-phase flows with heat transfer, phase change and/or chemical reaction.

My diploma thesis in National Technical University of Athens (NTUA) was undertaken in collaboration with CERTH (Centre for Research & Technology Hellas) and was focused on the gas-solid drag coefficients model investigation, which is necessary to be defined for the accurate simulation of a FB reactor.

In 2012, I started working as a research associate in the Centre for Research and Technology Hellas. More especially, I was involved in a FET-OPEN action H20H20 funded project for the proof-of-concept of a novel solid-state device with a silicon-based latent heat thermal energy storage (LHTES) system (AMADEUS Project).

Apart from this novel LHTES concept, I was also involved in several projects dealing with CO_2 capture calcium looping process (FP7 SCARLET and ACT2-ANICA Projects) and with fluidized bed type of heat exchangers (RFCS FLEXLFORES). Most of my research work on these projects was used for the writing of the 2nd and 3rd and 4th and 5th chapters of this PhD Thesis.

The scalability of the aforementioned concepts has been also addressed, whereas results of this model have been used to feed reduced order models (e.g. process models), which have been developed by my colleagues in CERTH involved in the aforementioned projects.

In short, this Thesis consists of the investigation of advanced energy systems that come forward as novel options for energy storage and GHG emissions minimization. At different stages of this work, results have been published in journals and conferences. A book chapter has been also published summarizing numerical methods of the LHTES systems. A list of publications, that are relevant with this thesis, is given below:

A. Publications in International Journals (3 first author)

1) Zeneli, M., Nikolopoulos, A., Nikolopoulos, N., Grammelis, P., Karellas, S., Kakaras, E. Simulation of the reacting flow within a pilot scale calciner by means of a three-phase TFM model. Fuel Processing Technology, 162, 2017, 105-125.
2) Nikolopoulos, A. Stroh, M. Zeneli, F. Alobaid, N. Nikolopoulos, J. Ströhle, S. Karellas, B. Epple, P. Grammelis. Numerical investigation and comparison of coarse grain CFD – DEM and TFM in the case of a 1 MW_{th} fluidized bed carbonator simulation. Chemical Engineering Science. 163, 2017, 189-205.
3) Zeneli, M., Malgarinos, I., Nikolopoulos, A., Nikolopoulos, N., Grammelis, P., Karellas, S., Kakaras E. "CFD modelling of silicon melting at ultra-high temperatures inside a novel Latent Heat Thermal Energy Storage system", Applied Energy
4) Zeneli, M., Bellucci, A., Sabbatella, G., Trucchi, D. M., Nikolopoulos, A., Nikolopoulos, N., Karellas, S., Kakaras, E. "Performance evaluation and optimization of the cooling system of a hybrid thermionic-photovoltaic converter". Energy Conversion and Management, 210 (2020),112717
5) Violidakis, I., Zeneli, M., Atsonios, K., Strotos, G., Nikolopoulos, N., Karellas, S. "Ultra-High Temperature PCM for heat storage with electricity production, at domestic buildings - Part I: Parametric investigation and calculation of domestic demand coverage". Energy and buildings, 222 (2020), 110067
6) Nikolopoulos, A., Samlis, C., Zeneli, M., Nikolopoulos, N., Karellas, S., Grammelis, P. "Introducing an artificial neural network energy minimization multi-scale drag scheme for fluidized particles". Chemical Engineering Science, 229 (2021),116013

B. Publications and plenary sessions in Conferences (3 first author)

1) Datas, M. Zeneli, C. del Cañizo, I. Malgarinos, A. Nikolopoulos, N. Nikolopoulos, S. Karellas, A. Martí, "Molten Silicon Storage of Concentrated Solar Power with Integrated Thermophotovoltaic Energy Conversion", SolarPaces, 2017, Chile
2) Zeneli M., Nikolopoulos A., Nikolopoulos N., Karellas S., Kakaras E. "Study of vessel shape effect on charge/discharge rates of a silicon-based LHTES system". ECOS 2019, Wroclaw, Poland
3) Zeneli M., Nikolopoulos A., Datas A., Nikolopoulos N., Karellas S., Kakaras E. "Study of heat losses during charge, discharge and storage period of a LHTES system operating at ultra-high temperatures". ECOS 2019, Wroclaw, Poland
4) Zeneli M., Nikolopoulos A., Nikolopoulos N., Karellas S., Kakaras E. "Numerical methods for fluid-dynamics and phase change". 1st International workshop on ultrahigh temperature thermal energy storage, transfer and conversion. UPM, Madrid, November, 2019
5) Kanellis, G., Zeneli M., Nikolopoulos, N.,, Hofmann, C., Ströhle, J., Karellas, S., Konttinen, J., "CFD modelling of an indirectly heated calciner reactor, utilized for CO2 capture, in an Eulerian framework", FBC24, Gothenburg, Sweden May 2022

C. Book Chapters (1 first author)

Zeneli M., Nikolopoulos A., Nikolopoulos N., Karellas S., "Numerical methods for phase change materials". Ultra-High Temperature Energy Storage, Transfer and Conversion, 2020, Elsevier Ltd. ISBN: 9780128199558

Table of contents

Nomenclature

Symbol	Explanation, units
a_c	acceleration of particles in dense phase, $m \cdot s^{-2}$
a_f	acceleration of particles in dilute phase, $m \cdot s^{-2}$
A_{mush}	mushy zone parameter [-]
A_r	pre-exponential factor in forward rate constant calculation, $kg \cdot m^{-3} \cdot s^{-1}$
Ar	Archimedes number, [-]
Ar_{cl}	Archimedes number for clusters, [-]
Bi	Biot number, [-]
c	adsorption constant, $Pa^{-0.5}$
c_0	adsorption constant pre-exponential factor, $Pa^{-0.5}$
C_{CO2}	concentration of CO_2 in the flue gas, $mol \cdot m^{-3}$
$C_{CO2,eq}$	CO_2 equilibrium concentration, $mol \cdot m^{-3}$
C_D	effective drag coefficient, [-]
C_{D0}	standard drag coefficient, [-]
c_p	specific heat capacity, $J \cdot kg^{-1} \cdot K^{-1}$
d_{cell}	equivalent cell size, m
d_{cl}	cluster diameter, m
D_e	effective ash diffusivity, $m^2 \cdot s^{-1}$
D_{O2}	Oxygen diffusivity, $m^2 \cdot s^{-1}$
d_p	particle diameter, m
d_p^*	dimensionless particle diameter, [-]
D_t	column diameter, m
D_v	void size, m
e_0	particle porosity, [-]
E_a	activation energy of adsorption constant c, $kJ \cdot mol^{-1}$
E_c	activation energy of chemical reaction rate constant, $kJ \cdot mol^{-1}$
E_r	activation energy of CO/volatiles oxidation, $J \cdot kmol^{-1}$
e_{ss}	restitution coefficient, [-]
E_v	activation energy of devolatilization, $kJ \cdot kmol^{-1}$
f	dense phase volume fraction, m^3 dense phase$\cdot m^{-3}$ cell
f_1	dimensionless factor in reaction rate of char combustion, [-]
f_i	factor that takes into account clusters permeability
F_{EMMS}	gas-solid drag force calculated with sub-grid EMMS scheme, N
F_{WenYu}	gas-solid drag force calculated with Wen & Yu model, N
F_c	drag force in the dense phase, N
F_f	drag force in the dilute phase, N
F_i	drag force in the inter-phase, N
Fo	Fourier number [-]
G	incident radiation, $W \cdot m^{-2}$
g	gravitational acceleration, $m \cdot s^{-2}$
g_0	radial distribution function, [-]

Gr	Grashof number [-]
ΔH	heat of reaction, $J \cdot kg^{-1}$
h	specific enthalpy, $J \cdot kg^{-1}$
H_d	heterogeneity index, [-]
I	unit tensor, [-]
II_{2D}	second invariant of the deviatoric stress tensor, $1 \cdot s^{-2}$
k_0	pre-exponential factor of chemical reaction rate constant, $kmol \cdot m^{-2} \cdot s^{-1}$
k_a	ash layer resistance, $s \cdot m^{-1}$
k_c	chemical reaction rate constant, $kmol \cdot m^{-2} \cdot s^{-1}$
k_{fl}	film resistance, $s \cdot m^{-1}$
$k_{f,r}$	forward rate constant in a homogeneous chemical reaction r, $kmol \cdot m^{-3}phase \cdot s^{-1}$
k_q	Thermal conductivity of phase q, $W \cdot K^{-1} \cdot m^{-1}$
k_r	surface reaction resistance, $s \cdot m^{-1}$
k_s	rate constant for surface carbonation, $m^4 \cdot mol^{-1} \cdot s^{-1}$
k_t	turbulent kinetic energy, $m^2 \cdot s^{-1}$
K_v	devolatilization rate pre-exponential factor, s^{-1}
L	latent heat of fusion, $J \cdot kg^{-1}$
m	mass, kg
MW	molecular weight, kg specie$\cdot kmol^{-1}$ specie
n	stoichiometric coefficient
N_{Ca}	number of moles of Ca, kmol
N_{st}	energy interchanged between flow phases, $W \cdot kg^{-1}$
Nu	Nusselt number, [-]
p_{CO2}	CO_2 partial pressure, Pa
p_{eq}	equilibrium CO_2 partial pressure, Pa
p_g	gas pressure, Pa
p_{O2}	O_2 partial pressure, Pa
Pr	Prandtl number of the fluid [-]
p_s	granular pressure, Pa
Q	heat stored in a storage medium, J
R	universal gas constant, $J \cdot kmol^{-1} \cdot K^{-1}$
Ra	Rayleigh number [-]
r_{cp}	ratio of core diameter to particle diameter, [-]
Re	Reynolds number, [-]
R_{O2}	O_2 individual gas constant, $J \cdot kg^{-1} \cdot K^{-1}$
r_{qq}	mass transfer rate per unit volume from one phase q to another, due to a phase change or a chemical reaction, $kg \cdot m^{-3} \cdot s^{-1}$
RR_{calc}	calcination rate, $kmol \cdot m^{-3} \cdot s^{-1}$
RR_{carb}	carbonation rate, $kmol \cdot m^{-3} \cdot s^{-1}$
RR_{CFD}	numerically calculated value of reaction rate, $kmol \cdot s^{-1}$
RR_{comb}	char combustion reaction rate, $kg \cdot m^{-3} \cdot s^{-1}$
RR_{dev}	devolatilization rate, kmol Vol$\cdot m^{-3} \cdot s^{-1}$
RR_{evap}	moisture evaporation rate, kmol $H_2O \cdot m^{-3} \cdot s^{-1}$

$RR_{Homogeneous}$	reaction rate for homogeneous conditions, kmol·s^{-1}
$RR_{vol(g)}$	kinetic rate of volatiles oxidation, kmol·m^{-3}gas·s^{-1}
R_{th}	thermal resistance, m^2·K·W^{-1}
S_0	initial surface area, m^2·m^{-3}
Sc	Schmidt number, [-]
S_e	specific surface area, m^2·m^{-3}
Sh	Sherwood number, [-]
S_i	Source term in momentum equation
Ste	Stephan number, [-]
T	temperature, K
T_{Calc}	operating temperature of calciner tor reactor, K
T_{Carb}	operating temperature of carbonator reactor, K
t	time, s
t_{aver}	time needed for averaging, s
u_q	actual velocity of qth phase, m·s^{-1}
u_{qq}	interphase velocity between two phases q, m·s^{-1}
U_c	superficial gas velocity in the dense phase, m·s^{-1}
U_f	superficial gas velocity in the dilute phase, m·s^{-1}
U_{mf}	minimum fluidization velocity, m·s^{-1}
U_s	superficial solids velocity, m·s^{-1}
U_{sc}	superficial slip velocity in dense phase, m·s^{-1}
U_{sf}	superficial slip velocity in dilute phase, m·s^{-1}
U_{si}	superficial slip velocity in inter-phase phase, m·s^{-1}
u_{sr}	slug velocity, m·s^{-1}
u_t	terminal velocity of a single particle, m·s^{-1}
u_t^*	dimensionless terminal velocity of a single particle, [-]
$v'_{i,r}$	stoichiometric coefficient for reactant i in reaction r
$v''_{j,r}$	stoichiometric coefficient for product j in reaction r
V	volume, m^3
Y_i^{specie}	mass fraction of a specie of the ith phase, kg specie·kg^{-1}ith phase
Y_{ash}	ash mass fraction, kg ash·kg^{-1} gas
Y_{ash}^0	Initial value of ash mass fraction, kg ash·kg^{-1} gas
Y_C	carbon mass fraction, kg C·kg^{-1} gas
Y_C^0	initial value of carbon mass fraction, kg C·kg^{-1} gas
Y_{CO2}	CO_2 mass fraction, kg CO_2·kg^{-1} gas
X_{CO2}	CO_2 mole fraction, mol CO_2/mol gas
X_{Carb}	actual carbonation conversion, mol $CaCO_3$·mol^{-1} Ca

Greek letters	
α	volume fraction, [-] (Used in VOF method)
β	liquid fraction, [-]
β_{qq}	momentum exchange coefficient between two phases, kg·m^{-3}·s^{-1}

β_{th}	volumetric thermal expansion coefficient [-]
$\gamma_{\Theta s}$	collisional dissipation of energy, $kg \cdot m^{-1} \cdot s^{-3}$
ε_q	volume fraction of q^{th} phase, m^3 phase$\cdot m^{-3}$cell
ε_{mf}	minimum fluidization voidage, [-]
$\varepsilon_{s,fr}$	friction limit, [-]
$\varepsilon_{s,max}$	particles packing limit, [-]
ε_t	rate of turbulent kinetic energy dissipation, $m^2 \cdot s^{-3}$
θ	temperature, ^oC
θ_{CO2}	fraction of active sites occupied by CO_2, [-]
Θ_s	granular temperature, $m^2 \cdot s^{-2}$
λ_s	granular bulk viscosity, Pa·s
μ_g	gas viscosity, $kg \cdot m^{-1} \cdot s^{-1}$
μ_s	granular shear viscosity of a solid phase, Pa·s
$\mu_{s,col}$	collisional viscosity, Pa·s
$\mu_{s,fr}$	frictional viscosity, Pa·s
$\mu_{s,kin}$	kinetic viscosity, Pa·s
μ_q^*	meso-scale viscosity of phase q, Pa·s
ρ_q	density of phase q, $kg \cdot m^{-3}$
ρ_q^*	meso-scale density of phase q, $kg \cdot m^{-3}$
σ	scattering coefficient, m^{-1}
σ_ε	dense phase voidage standard deviation, [-]
$\bar{\bar{\tau}}$	Stress tensor, Pa
φ	specularity coefficient, [-]
Φ_h	hydrodynamic factor, [-]
φ_{fr}	angle of internal friction, [-]
φ_s	sphericity, [-]

Indices

Symbol	Explanation, units
c	dense phase (for EMMS model)
cell	refers to computational cell
f	dilute phase (for EMMS model)
fl	film
g	gas
i	inter-phase (for EMMS model)
l	liquid
max	maximum
mf	minimum fluidization
min	minimum
p	particle
P	product
R	reactant

s	solid
w	wall
∞	ambient

Acronyms

Acronym	Explanation
ANN	Artificial Neural Network
BC	Boundary condition
BFB	Bubbling fluidized bed
CaL	Calcium looping
CCUS	Carbon capture utilization and storage
CFB	Circulating fluidized bed
CFD	Computational fluid dynamics
CGSM	Changing grain size model
COP26	UN Climate Change Conference
CPFD	Computational particle fluid dynamics
CPU	Central processing unit
CSP	Concentrated solar power
DAS	Dendrites arm spacing
DEM	Discrete elements method
DFB	Dual fluidized bed
DPM	Discrete phase method
EIIs	Energy intensive industries
EMMS	Energy minimization multi-scale scheme
FB	Fluidized bed
FBHE	Fluidized bed heat exchanger
FDM	Finite difference method
FEM	Finite element method
FSB	Fumed silica board
FT	Front tracking
FVM	Finite volume method
GFM	Graphite fiber
GHGs	Greenhouse gases
GPU	Graphics processing unit
HTC	Heat transfer coefficient
HTF	Heat transfer fluid
IHCaL	Indirectly heated calcium looping
INTREX™	Integrated recycle heat exchanger
ITP	Inverted truncated-pyramid
KPI	Key performance indicator

KTGF	Kinetic theory of granular flows
MFM	Multi-fluid model
MP-PIC	Multi-phase particle in cell
NZE	Net zero emissions
N-S	Navier-Stokes
LHTES	Latent heat thermal energy storage
P2H2P	Power-to-heat-to-power
PCM	Phase change material
PETE	Photon-enhanced thermionic emission
PF	Pulverized fuel
PSD	Particles size distribution
RBF	Radial basis function
RE/RES	Renewable energy/ Renewable energy sources
ROM	Reduced order model
S2H2P	Solar-to-heat-to-power
SCM	Shrinking core model
SHS	Sensible heat storage
SPSR	Solid particles solar receiver
STM	Source term method
TCES	Thermochemical energy storage
TES	Thermal energy storage
TFM	Two-fluid model
TIPV	Thermionic-photovoltaic
TPV	Thermo-photovoltaic
TR	Tapering ratio
UDF	User-defined function
UHT	Ultra-high temperature
URF	Under relaxation factor
VOF	Volume of fluid
1D	One-dimensional
2D	Two-dimensional
3D	Three-dimensional

CHAPTER 1
Introduction

1.1 Current status of energy mix

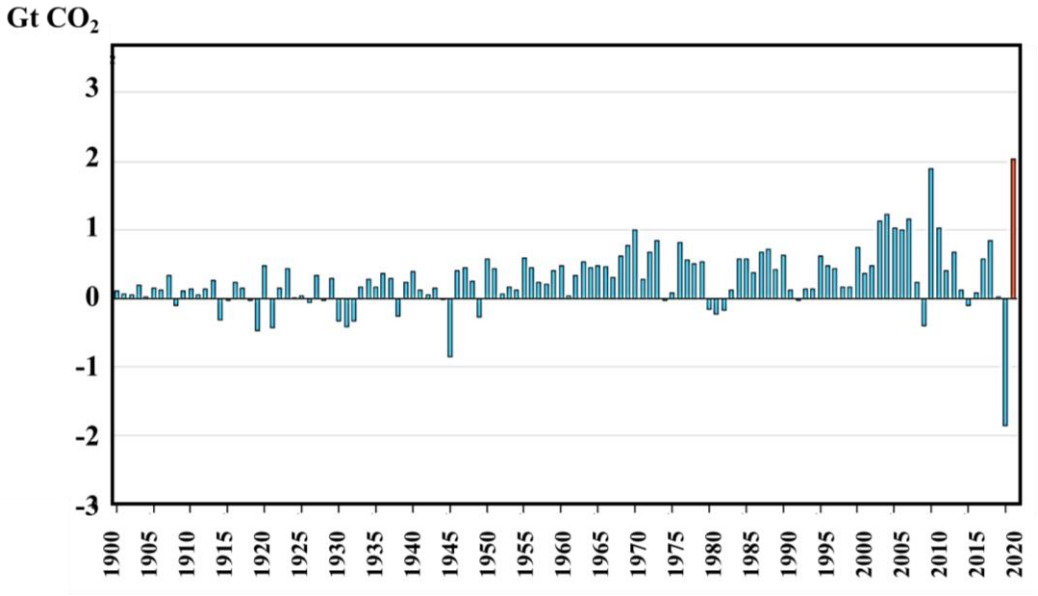

Figure 1. Annual change in CO_2 emissions from energy combustion and industrial processes, 1900-2021 [1].

Coal has been the largest source of electricity generation all over the world for several decades. In 2020 the share of coal-fired power generation reached a value of 35.2 % [2]. However, coal combustion results in the production of hazardous emissions for the environment and the human health, including sulfur dioxide (SO_2), nitrogen oxides (NO_x), particulate matter and carbon dioxide (CO_2).

Before, 2019 the "Net Zero Emissions by 2050" Scenario (NZE), i.e. the scenario of dropping related carbon dioxide emissions to net zero by 2050 by building an energy economy that relies on renewables instead of fossil fuels, required a worldwide plunge in coal consumption [2]. During the UN Climate Change Conference (COP26), 45 countries had signed the Global Coal to Clean Power Transition Statement [2, 3], a pact that includes a range of decisions, including coal utilization drop-off, to limit the global temperature rise of 1.5 degrees. The Covid-19 pandemic had a plasmatic negative impact on energy demand in 2020, and, thus, on fossil fuels consumption, reducing global CO_2 emissions by 5.2% (**Figure 1**). However, Post-Covid-19 era pushes the world economy to rely heavily on coal-combustion, due to an unprecedented increase in the energy demand, a situation leading once more to an increase in the GHG emissions.

More specifically, global energy-related CO_2 emissions from energy consumption and heavy industries (e.g. cement, lime, iron& steel) experienced an increase by 6% in 2021 to 36.3 gigatonnes (Gt), their highest ever level. CO_2 emissions in 2021 rose to around 180 megatons (Mt) above the pre-pandemic level of 2019. This amount is expected to increase, since the use of coal intensified owing to increasing natural gas prices in Europe and US and an increased energy consumption in China. Coal accounted for over 40% of the overall growth in global CO_2 emissions in 2021, reaching an all-time high of 15.3 billion tones [4]. This rebound of global CO_2 emissions largely driven by China's economic growth has led to an increase of CO_2 emissions by 750 Mt between 2019 and 2021. Finally, gas-to-coal switching pushed up global CO_2 emissions from electricity generation by well over 100 million tones, notably in the US and Europe where competition between gas and coal is tightest, especially after the breaking out of the Russo-Ukrainian war.

1.2 Decarbonization actions: RES and the role of energy storage

A thoroughgoing transformation of the energy system by applying decarbonization actions comes as a necessity to fulfill the EU ambitious target to be a carbon neutral economy by 2050 and comply with the current global situation. Such decarbonization actions should be applied across the whole spectrum of society and economic sectors. Energy intensive industries (EIIs) and the power sector are at the forefront in this long-term vision. The EIIs ecosystem includes a wide range of sectors, including non-ferrous metals, steel, aluminum, chemicals, ferilizers, cement, ceramics, lime, glass, and paper and pulp. These sectors are characterized by a high energy intensity and are responsible for a large share of greenhouse gas emissions (GHG) produced mainly due to the fuel combustion, the electricity production, and, the process emissions. The power sector is also a major GHG contributor. Several decarbonization actions can be applied for all these sectors, such as carbon capture utilization and storage (CCUS) of the inevitable process emissions, use of renewable energy sources (RES), such as wind, solar, hydropower, geothermal and biomass, for the production of electricity instead of fossil fuels, and, increase of carbon neutral fuels in the fuel mix. The zero-carbon transition of EIIs by embracing climate friendly practices will be beneficial for the environment, but also will ensure the individual companies' long-term competitiveness. Nevertheless, many sectors have already picked to their efforts of reducing their GHG emissions and improving their energy efficiency without fulfilling their targets. In this regard, innovative technological solutions are necessary to move towards a carbon-neutral future.

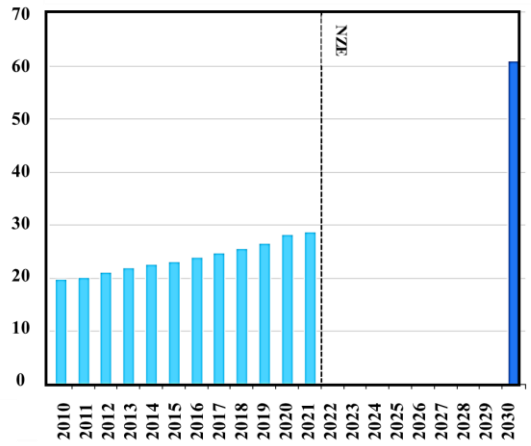

Figure 2. Renewables share of power generation in the Net Zero Scenario, 2010-2030 [5].

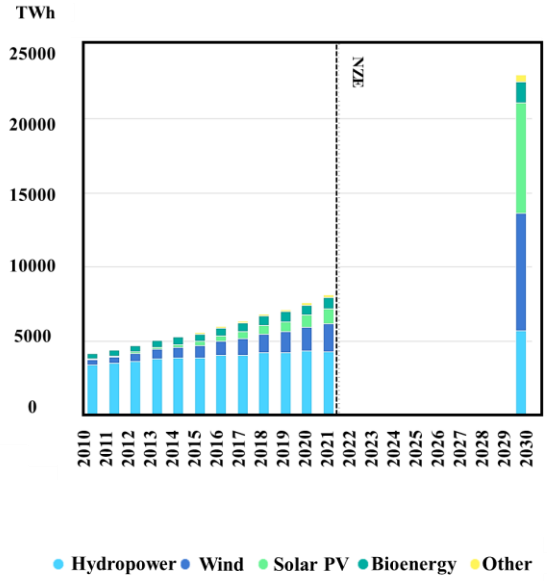

Figure 3. Renewable power generation by technology in the Net Zero Scenario, 2010-2030 [5].

Adoption of RES is a key point for a clean energy transition experiencing a rapid grown in recent years (**Figure 2**). The power sector is the frontrunner of renewables with a 28 % of the global electricity generation relying in RES in 2021 [6]. Nevertheless, electricity accounts for only a fifth of global energy consumption, and the role of renewables in other sectors as well remains critical to the energy transition. Among the prominent RES alternatives, solar and wind power are one of the few low-carbon technologies that can grow into large scale, exhibiting, thus, high potential to meet the global energy requirements [7]

(**Figure 3**) and promote a clean energy transition. Solar energy, in specific, seems as an attractive option, due to its low cost, and abundance compared to the other RES [8]. However, the energy that can be extracted from the sun varies in both space and time [9]. Most forms of RE must be transformed into electricity and consumed instantaneously. This makes the current economy be still dependent on fossil fuels.

1.3 State-of-the-art of thermal energy storage systems

Energy storage is a game changer technology, essential for optimizing the use of the scarce energetic resources in today's energy system. Many different energy storage solutions are currently under development covering all kinds of technological options (electrochemical, mechanical, electrical, chemical and thermal). Pumped-storage hydropower is the most widely applied storage technology (with a total installed capacity at around 160 GW in 2021) [10], whereas batteries as a form of electrochemical storage are the most scalable type of grid-scale storage with a growing market in recent years. Other alternatives include compressed air and gravity storage, but they play a comparatively small role in current power systems. Additionally, hydrogen (H_2) is an emerging technology that has potential for the seasonal storage of RE. While progress is being made, projected growth in grid-scale storage capacity is not currently on track with the NZE Scenario and requires greater efforts [10]. Thus, the development and use of efficient and innovative energy storage systems and devices are necessary to integrate RES to the electricity or the heating/cooling grids and eliminate discrepancies between supply and demand.

Among the abovementioned energy storage options, thermal energy storage (TES), i.e. the storage of excess thermal energy by heating or cooling a storage medium for later use, can play an important role to achieve these targets and eliminate the mismatch between supply and demand, mainly due to its modularity and the number of the different technological options available. Generally, TES systems can be classified into three categories: latent heat (LHTES), sensible heat (SHS), and thermochemical heat (TCES) storage systems [11]. Among these options, SHS is the most mature technological option due to its simple principle and low cost, followed by LHTES systems and then by TCES systems, both of which are characterized by higher storage densities than SHS. TES can be used in different possible applications, such as direct solar energy storage (in CSP -concentrated solar power- systems), electricity storage and cogeneration in domestic electrical/heating networks, and, energy storage in waste heat recovery systems etc.

TES systems differ in the amount of heat that can be stored per unit volume of storage medium. The key aspects in such systems is the energy density, the charging/discharging rate, the used storage media and, the operating temperature. In general terms, the storage media properties define the energy density, the charging/discharging rate and the overall performance of a system, whereas the higher the operating temperature the higher the storage potential. Regarding the storage media, a wide variety exists depending on the operating temperature range and the targeted application. Apart for the nature of storage type described above, TES are also classified according to the operating temperature into low-temperature (<100 °C), medium-temperature (100 °C≤θ≤300 °C), high-temperature TES (300 °C≤θ≤900 °C) and ultra-high temperature (>900 °C). A comparison of the different TES methods in general terms is reported in **Table 1**, whereas the state-of-the-art TES options are discussed below.

Table 1. Comparison of TES methods in terms of capacity, power, efficiency, storage and cost [12].

TES method	Capacity (kWh·ton^{-1})	Power (MW)	Efficiency (%)	Storage Time	Cost (€·kWh^{-1})
SHS	10–50	0.001–10	50–90	d/m	0.1–10
LHTES	50–150	0.001–1	75–90	h/m	10–50
TCES	120–250	0.01–1	75–100	h/d	8–100

1.3.1.1 Sensible heat storage (SHS)

A SHS system involves heating or cooling of a storage medium and, thus, changing its internal energy. The amount of heat stored (or rejected) in (or from) the system depends on the specific heat capacity (c_p) and mass (m) of the storage material, and, on its temperature difference (ΔT) with the heating/cooling medium.

$$Q = \int_{T1}^{T2} mc_p \Delta T \quad (1)$$

Additional, properties important for designing of a SHS system include, thermal conductivity and diffusivity, vapor pressure, compatibility among materials stability, heat loss coefficient as a function of the surface areas to volume ratio, and cost [13].

The storage medium in a SHS system can be solid (sand, packed beds, bricks) or liquid (water, molten salts, mineral oils and synthetic oils), but also gaseous, or on a supercritical state. Solid media are usually used in packed beds, requiring a fluid (e.g. air) to exchange with the storage medium. During the system charging, hot fluid passes through spaces between solid particles, causing their temperature to rise during the day. During the night (discharging loop) the quantity of sensible heat stored inside the tank is recovered. Examples of integrating SHS into a domestic application for cooling/heating are presented in **Figure 4**, whereas thermos-physical properties and average cost of several storage media can be found in [14].

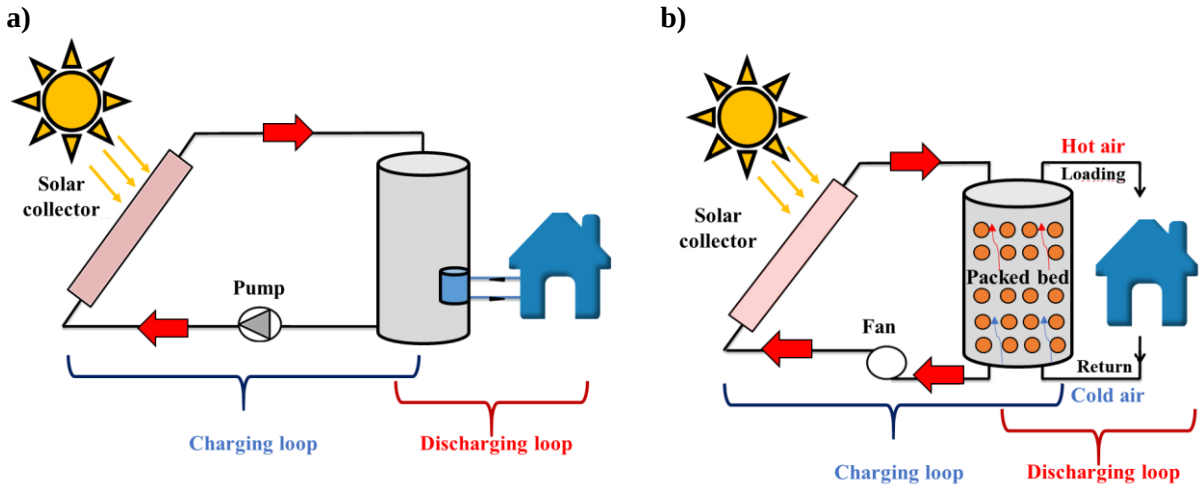

Figure 4. Examples of integrating SHS, such as (a) packed bed storage tank and (b) solar-based water heating device into domestic cooling/heating applications. Adapted from [13].

1.3.1.2 Latent heat thermal energy storage (LHTES)

Phase change materials (PCMs), which exploit latent heat are considered as an efficient option for energy storage that is emerging rapidly. Their principal advantage is that they can store significant amounts of energy, both as latent and sensible heat, within in a narrow temperature range [15], while requiring at the same time less energy volume or mass per stored energy compared to sensible heat systems [16]. The amount of heat stored in rejected in a LHTES system is the sum of sensible heat of the solid phase, latent heat of fusion (L), and sensible heat of the liquid phase:

$$Q = \int_{T1}^{T2} mc_p \Delta T\,(s) + \int_{T1}^{T2} mc_p \Delta T\,(l) + mL \qquad (2)$$

PCMs are used in a wide range of applications, from electronic devices cooling [17] to thermal storage in buildings [18], clothing/textile design [19] and for energy production in CSP plants (**Figure 5**), the latter being one the major applications of PCMs. However, their utilization has been restricted to low (20 °C-100 °C) [20], medium (100 °C-250 °C) [21] or high (250 °C-900 °C) [22] temperatures, so far. Added to this, most commercial PCMs are based on materials like salt hydrates, paraffin, and eutectic water-salt solutions [23], which have low thermal conductivities and, as a consequence, low charge/discharge rates [24]. This fact has limited so far their commercial application as an alternative to sensible heat transfer. This fact reveals the necessity of utilizing novel LHTES concepts that will unlock higher storage densities.

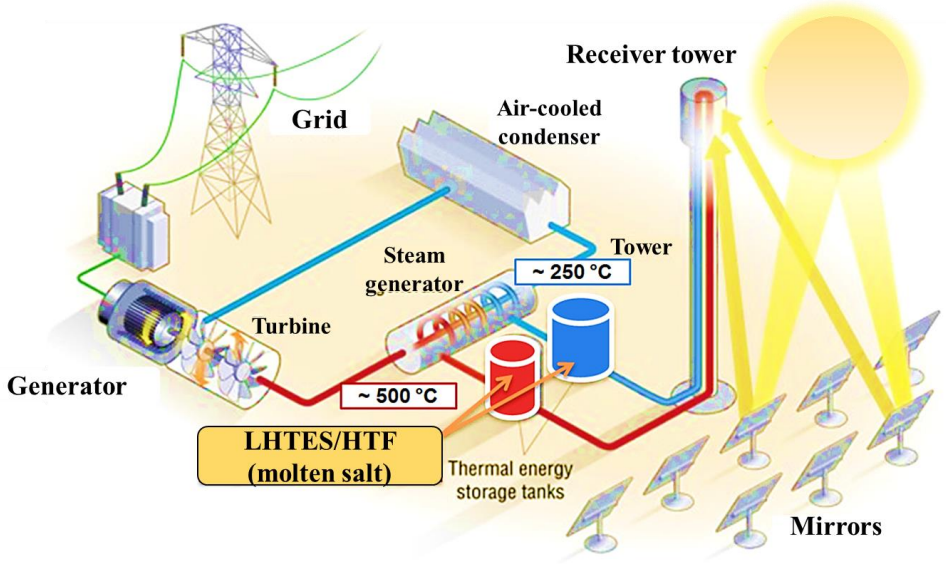

Figure 5. Integration of LHTES (two-storage tank) in a CSP plant. Taken from [25].

1.3.1.3 Thermochemical energy storage (TCES)

TCES involves the storing of energy through the simultaneous exploitation of reversible chemical or sorption reactions, being, thus, an analogous 'heat' battery. Among the available TES options, TCES is considered to have the highest heat density potential, but also the highest technical challenges, at the same time. The most basic TCES system is comprised of a working pair of two chemicals (A, B), a storage tank for each of these chemicals, and a chemical reactor. When energy is required from the system, these two chemicals react together, releasing energy in the form of heat. When energy is to be stored, external energy *Q* (again in the form of heat, due to solar, chemical reaction or waste heat) is added to the reacted chemicals to chemically or physically separate them.

$$n_{AB} \cdot AB_{(s)} + Q \leftrightarrow n_A \cdot A_{(s)} + n_B \cdot B_{(g)} \qquad (3)$$

, where *n* is the stoichiometric coefficient.

TCES has a wide range of applications at different temperatures (from 50 ºC up to 1000 ºC). Some of the most known chemical reactions involved in TCES include dehydration of salt hydrates, dehydration of metal hydroxides, dehydrogenation of metal hydrides, decarboxylation of metal carbonates and redox reactions of oxides enable a very wide range of applications at different temperatures.

Concluding, TES offers a strong potential for cross-sectoral decarbonization, especially for heating and cooling buildings, providing heat for industrial processes and other applications. Overall, current state-of-the-art TES systems are limited to temperatures below 500-600 ºC (e.g. molten salt based) due to high temperature thermal instability of currently available materials and devices. The benefit of working at high and ultra-high temperatures is particularly relevant for LHTES systems, where heat is stored or released during the phase change of a material by utilizing metallic PCMs. Novel SHS and TCES systems based on granular materials suspensions operating at high temperatures (900-1000 ºC) can also offer a high storage potential. However, no attention has been paid so far to this kind of systems due to lack of proper materials and devices able to operate at such high temperatures.

1.4 Beyond the state-of-the-art of thermal energy storage systems

Moving beyond the current TES storage solutions, several new trends for TES integration may be observed: (i) coupled TES technologies for possible higher operating temperature (e.g. SHS with TCES), (ii) TES systems with novel materials in compact tanks, and, (iii) circulation of granular particles. Design of such systems requires extensive research by using a combination of theoretical studies, experimental campaigns, and, simplified and advanced numerical models. Computational fluid dynamics (CFD) tools can help speed-up on the design process of such systems, especially when there is a need for a specific system's components design optimization and scale-up.

1.4.1 Use of latent heat thermal energy storage systems at ultra-high temperatures

In order to establish more efficient LHTES systems, than the current state-of-the-art molten-salt based, ultra-high temperature (UHT) storage comes as a necessity. Storage at ultra-high temperatures (>900 ºC) [26] with the utilization of metallic PCMs characterized by high thermal conductivities and heat of fusion, such as Si, Al, B, would unlock greater energy densities -more than 20-times higher- than the ones achieved in conventional molten-salt based systems [27]. Therefore, metallic PCMs have a high potential for increasing the energy and exergy efficiency in conventional steam Rankine cycles. Especially, silicon, one of the most abundant elements on Earth, has an energy density an order of magnitude larger and a thermal conductivity -at its phase transition temperature- two orders of magnitude higher than salt hydrates and paraffin [28]. On top of that, the silicon melting temperature (~1414 ºC) matches well the band gap of state-of-the-art thermophotovoltaic cells, allowing, thus, its integration into compact solar-to-heat-to-power (S2H2P) conversion technologies [29]. The same applies for boron, which has a melting temperature above 2000 ºC.

Figure 6 showcases the storage potential of silicon (1230 $kWh \cdot m^{-3}$) and boron (2680 $kWh \cdot m^{-3}$), having latent heats an order of magnitude greater than that of typical salts used in storage applications, such as $NaNO_3$ (110 $kWh \cdot m^{-3}$) and KNO_3 (156 $kWh \cdot m^{-3}$). In fact, silicon and boron PCMs provide higher storage energy densities than most forms of energy storage, including electrochemical batteries and pressurized H_2. Furthermore, **Figure 7** shows a novel concept of coupling a UHT-LHTES system with solid-state device in a compact design and how this concept can be integrated into a CSP plant for electricity production.

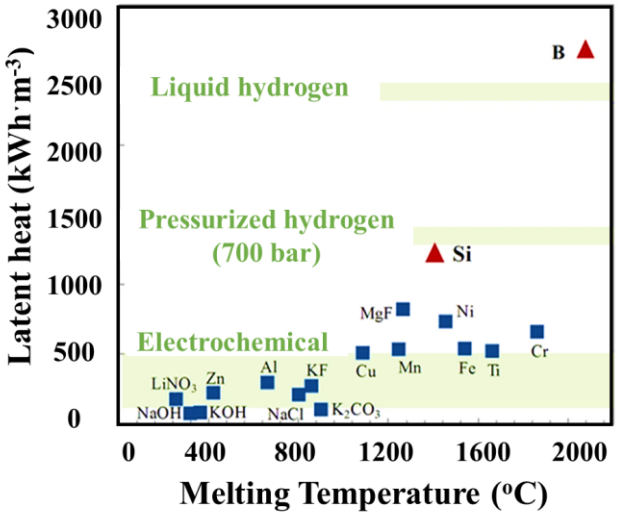

Figure 6. Latent heat of fusion of different materials as a function of melting temperature compared with the energy density of other storage technologies.

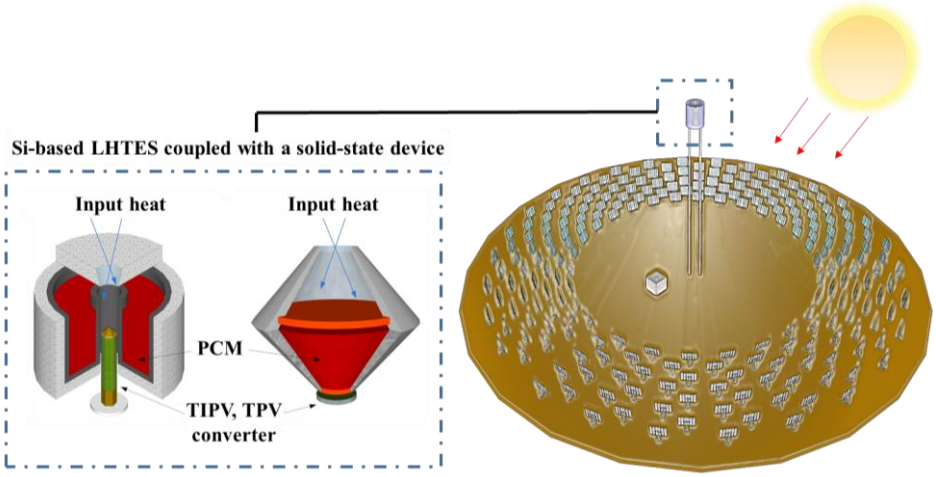

Figure 7. UHT-LHTES coupled with a solid-state-device in a compact design and its possible integration is a CSP plant [30].

Nevertheless, it is worth mentioning that there is a high necessity to deal with several challenges before moving towards UHT-TES systems. First, there is excessive heat loss from the vessel walls, due to ultra-high temperatures, which are difficult to eliminate. Additionally, radiation phenomena, which have not been explored yet, might occur inside possible gas voids in the solid PCM [31] affecting, thus, the thermal performance of such systems. Other challenges lay on how a commercial LHTES-system might be configured for different operating scenarios and which is the optimum vessel design that enables quick charge/ discharge rates. Finally, not all of the metallic materials are recommended for PCMs, because of some drawbacks of their thermo-chemical properties, such as high vapour pressure, chemical instability,

and high flammability [32]. This implies that such PCMs should be thoroughly explored, before being utilized in UHT-LHTES systems.

An in-depth research would allow developing effective methods of eliminating such problems and move towards more efficient LHTES systems. Many analytical, experimental and numerical researches have paid attention since the 80s to evaluate the thermal performance of PCMs, as that of paraffin wax, inside various geometric configurations, such as spherical, cylindrical or rectangular containers [33]. Concerning analytical models, the lubrication theory of viscous flow in thin films, which neglects natural convection in the liquid PCM, has been mostly used to solve unconstrained melting heat transfer in spherical capsules [34]. However, such a hypothesis induces severe errors. Melting experiments found in the literature have established that beyond conduction, buoyancy-driven natural convection in the liquid phase affects significantly the heat transfer process inside the PCM casing [35]. Apart from this, phenomena, such as a) the PCM volumetric change, b) the motion of the solid in the melt [36], and c) the motion of the liquid in the gap between the solid and the wall of the shell have been explored experimentally [31]. During recent years, numerical simulations of the PCM solidification/melting process have been used to gain a better understanding of the heat transfer process. The main advantage of CFD modelling compared to experiments is that the container size and shape, PCM thermophysical properties, PCM solidification/melting rate, lateral heat losses etc. can be easily quantified and optimized for various operating conditions and applications, without substantial research expenses [31].

Up to now, in recent literature, two basic numerical methods are usually followed, to model the conductive-convective heat transfer mechanisms controlling the PCM solidification/melting process; i.e. the moving (front tracking) [37] and fixed (front capturing) grid method [38]. The first one [39] gives more accurate results in the solid-liquid interface, however, it is more complicated for complex and three-dimensional (3D) domains or interface undergoing large deformations [38]. The second one, which includes both equivalent heat capacity and enthalpy methods, is a simpler one. The latter developed by Voller et al. [40] is more widely used, especially in commercial software packages, due to its advantage of describing the phase-change with a unique equation for the two phases saving, thus, computational cost [40]. This method has been used to simulate several different problems including melting in one and two-dimensional (2D) casings of various shapes, mostly in cylindrical [41], rectangular [42] and spherical [43] ones. However, numerical diffusion can be induced in the solid-liquid interface, which is strongly dependent on the grid size used. Therefore, application of a method capable of combining the advantages of both the fixed and moving grid method would be a real benefit for any type of solidification/melting simulation.

Another aspect that needs further attention and has not been explored yet thoroughly from a numerical point of view, is the PCM volume expansion/contraction during the phase change process. Such phenomenon occurs actually, due to the large density difference between the solid and liquid phases of the PCM. Moore and Bayazitoglu [36] were the first to explore the ‘‘unconstrained” melting, i.e. the solid floating (sinking) in the liquid phase, due to its higher (lower) density and the subsequent PCM volume increase. Lamberg et al. [44] studied numerically the solidification/melting process of paraffin at low temperatures by means of both the enthalpy-porosity and effective heat capacity methods. In his work he took in took account the PCM volume changes and proved that when the natural convection is not modelled there is a high numerical error. Sattari et al. [45] have investigated through CFD modelling a PCM melting inside a spherical capsule at low temperatures and the effect of different operating and design parameters, i.e. capsule size, parameters on the process evolution. However, in this Thesis the PCM volume change is not taken into account. Several similar works in which the density variations between the solid and liquid PCM are neglected, usually

referred to as constrained PCM melting, can be found in the literature [46]. However, taking into account such a phenomenon is of high importance for the accurate prediction of the melting process.

Nonetheless, as can be seen, during the last decades a considerable amount of numerical simulations has mainly focused on medium and low temperature PCMs, like paraffin wax. Very few reports are available for studies on PCMs with phase change temperature exceeding 100 ^{o}C. Archibold et al. [47] in their work analysed the melting and solidification processes of $NaNO_3$, in 306.8 ^{o}C, inside a spherical geometry. Elmozughi et al. [48] in their analysis used the enthalpy-porosity approach coupled with the volume of fluid (VOF) model to simulate the unconstructed $NaNO_3$ melting inside spherical and cylindrical shells up to 500 ^{o}C. Pirasaci et al. [49] worked on the same temperature range as Elmozughi et al. to study the melting process of an encapsulated Na_2SO_4 – KCl eutectic mixture. However, it is obvious that these studies centre on temperatures below 900 ^{o}C. Taking all into consideration, there still remains a gap of knowledge for a systematic attempt to explore high temperature PCMs and, in general, thermal energy storage processes [50], by means of an efficient and accurate numerical analysis that will take into account PCM volumetric change, buoyancy-driven natural convection and PCM structure. **Sub-section: Phase change problems** presents briefly the used methods adopted in LHTES systems and the applied methods in the current Thesis.

1.4.2 Use of SHS and TCES based on granular particles

Gas-solid fluidized bed (FB) systems, ranging from fixed bed to circulating fluidized beds (CFB) and downer reactors, have been used in a wide range of industrial applications, such as biomass gasification, pyrolysis, combustion and fluid catalytic cracking, just to name a few [51]. Moving beyond the-state-of-the-art, during recent years FB systems are being tested for energy storage in novel SHS and TCES storage concepts. Regarding operating principles, a gas-solid fluidized bed system obeys general rules, for the solid particles flow hydrodynamics (e.g. flow heterogeneity and flow regimes under specified operating conditions), heat transfer mechanisms etc. as described in Kunii and Levenspiel [52]. However, depending on the targeted application, the gas-solid-medium properties and the scale of the problem (lab, pilot or industrial), there are unique spatiotemporal flow characteristics that need to be explored by using advanced numerical tools. When validation of such models becomes available from both experimental results and industrial knowledge, design optimization and scale-up of novel FB-TES systems can be achieved.

1.4.2.1 SHS: FB with a diverse role of heat exchange and storage

FB systems are currently being studied for storage concepts in several applications from CSP plants to industrial processes. In CSP applications, solar particle solid receivers (SPSRs)/reactors are gaining interest as next-generation TES options, since solid particles can work as both heat transfer fluid (HTF) in the solar receiver, heat transfer and storage medium [53], [54] (**Figure 8**). The operating temperature of such systems can exceed 800-900 ^{o}C depending on the fluid particles and relevant operating conditions, opening, thus, the way of achieving conversion efficiencies greater than 50 %, with the supercritical carbon dioxide (sCO_2) Brayton cycle [55]. Finally, combined with fluidized bed technology, SPSRs can be used for H_2 production, coal/biomass gasification and CO_2 capture concepts [54], [56].

Most of the effort paid by the research community has focused on the structural designs and the overall thermal performance of various SPSRs, whereas other critical aspects, such as selection of appropriate solid particles, receiver system structures optimization, flow hydrodynamics, and heat transfer phenomena have not been meticulously studied. The use of advanced numerical models can help assist in such a process, however, numerical works dealing with SPSRs are quite limited.

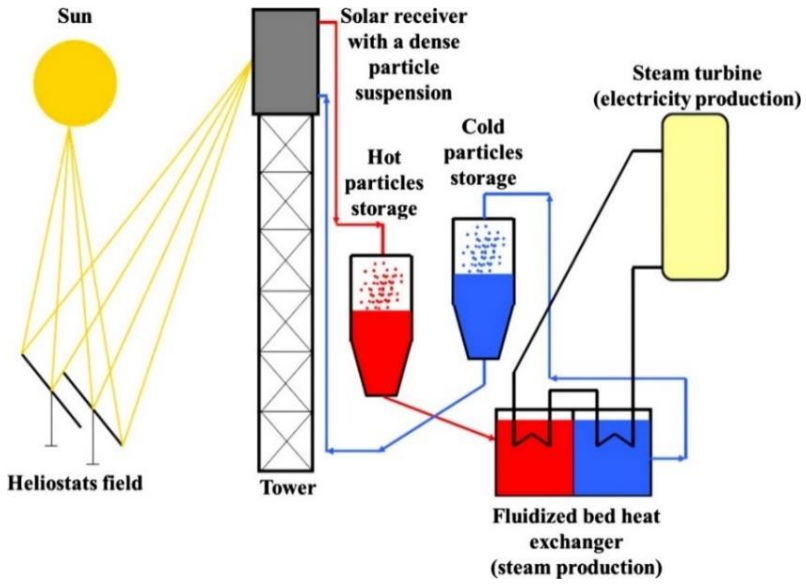

Figure 8. Thermal CSP plant concept with a receiver using particles as HTF and storage medium [57].

In industrial applications, external fluidized bed heat exchanger (FBHE) systems that comprise a bubbling fluidized bed (BFB) chamber and immersed tube bundles (horizontal or vertical) for heat recovery, are often employed, as superheaters or reheaters [58]. This is mainly done, because in traditional superheating/reheating systems that are placed at the upper part of the furnace, there is a difficulty in reaching the desirable steam temperatures (605/623 °C maximum design temperatures reached in ultra-supercritical CFB boiler in China [59]), especially under low load conditions. Such a difficulty arises from the low temperature operation (800-900 ºC) of a CFB boiler, in contrast to conventional pulverized fuel (PF) boilers [60]. Thus, based on the pioneering idea of Shi-FW, an Integrated Recycle Heat Exchanger (INTREX^{TM}) can be placed near the bottom part of the combustion chamber. By this way, heat can be recovered from both the recirculating solids from the cyclone and the hot solids from the combustion chamber (**Figure 9**). Due to the high heat transfer coefficient in the INTREX^{TM} heat exchanger, the heat transfer surfaces are considerably smaller than the superheaters or reheaters in conventional PF boilers. Such type of HE includes several advantages. First of all, the heat transfer surfaces are located away from the high-temperature flue gases that are highly corrosive for the involved materials, whilst air is used as a fluidizing medium. Secondly, installation of INTREX^{TM} allows extracting heat from the hot particles that are captured by the cyclone (external circulation) and, in addition, from solids that are derived from the bottom part of furnace (internal circulation). This internal solid circulation allows superheater heat absorption even at low loads when the external solids circulation is low. A continuous movement of granular material prevents formation of deposits and ensures high heat transfer rate. The level of heat transfer can be controlled by the rate of air flow that applied for returning solids to the lower furnace. In general, this leads to reduced maintenance needs and increased operational flexibility [61]. This novel type of heat exchanger can be used as well as an intermediate sensible type of storage system as it has been studied by using a dynamic process model in [62]. The solid particles in this type of storage system serve as well as both HTF and storage medium and they are indirectly heated by the heat pipes containing the gas medium (air or steam).

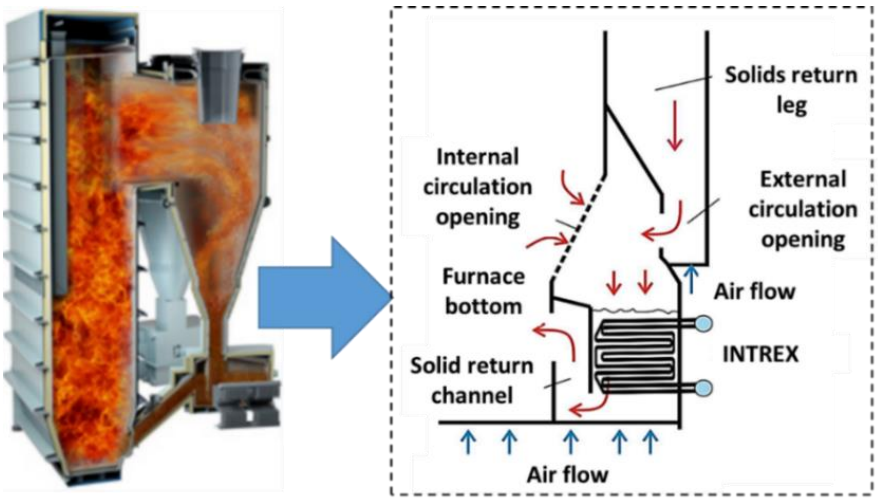

Figure 9. Use of Internal heat exchanger (INTREX^{TM}) for internal heat recovery and heat storage [63].

The knowledge about heat transfer process in BFBs is essential to properly design BFB heat exchangers. A BFB system is advantageous in a sense that it combines uniform temperature, high heat transfer rate between the gas/solids mixture and heat transfer surfaces, controlled steam temperature, continuous operation, excellent behavior even at the partial load, and enhancement of heat transfer capacity, due to the intensive mixing of bed material by the motion of gas bubbles. In this context, designers of BFB systems should consider the following [64]: (i) continuous recycling solid particles back to the main furnace, (ii) ensuring enough heat transfer exchange from the hot bed particles to the heat transfer medium (steam of water), (iii) elimination of corrosion and erosion related problems, (iv) protecting heat transfer surface from slagging and agglomerates of ashes that are contained in the circulating inventory, (v) controlling the solid mass flow rates to the HE or loop seal. Thus, design of a system as a BFB storage system/HE, especially at a large scale requires both an accurate numerical prediction, and operational experience.

There is wide number of studies concerning the heat transfer behavior in BFB systems targeted for heat exchange. However, most of these are limited to experimental investigations and theoretical models, especially for single horizontal tubes immersed in BFBs. Kim et al [65] have calculated experimentally the local and average heat transfer coefficient (HTC) between horizontal submerged tubes and a BFB heat exchanger with silica sand as fluidized particles. They also used theoretical models to describe the heat transfer process and they succeeded in getting similar results. Blaszczuk et al. [63] have followed the same approach of comparing measurements with theoretical models in an industrial-scale integrated heat exchanger. The most well-known heat transfer model for carrying out theoretical analysis in such type of systems it the mechanistic model of Mickley et al. [66]. However, theoretical models cannot capture in detail the spatio-temporal flow characteristics around complex heat transfer surfaces.

Advanced numerical models used to describe the heat transfer in gas-solid bubbling fluidized bed systems, especially the ones involving heat transfer with another medium through immersed tubes, have been scarce. The numerical cost of conducting simulations especially for large commercial-scale heat exchangers are the cause for such a lack of publications. However, carrying out detailed studies are important to set the grounds to establish the optimal heat exchange conditions and designs (e.g. tube buddles arrangement) in correlation with the bed hydrodynamics. This can lead subsequently to the optimization of such systems.

1.4.2.2 TCES: The CaL concept

The calcium looping concept (CaL), the second most mature post-combustion capture technology following amine scrubbing [67], comes at the forefront for TCES by ensuring at the same an effective CO_2 capture [68]. First proposed by [69] this process is performed through a dual fluidized bed facility (DFB), which comprises two reactors, named as calciner and carbonator. Inside these reactors multi-phase gas-solid heterogeneous reactions, one endothermic (calciner) and one exothermic (carbonator) are taking place. The carbonator, usually operating in a circulating mode, is the heart of the process; inside the reactor CO_2 is captured by calcium oxide particles (CaO) forming calcium carbonate ($CaCO_3$). The CaO particles are regenerated in the calciner, usually operating in a bubbling mode, and transported back to the carbonator, while a lean CO_2 stream is released almost ready for storage. The heat for the endothermic reaction can be provided by three options: (i) burning auxiliary fuel in the calciner in an oxy-firing mode (**Figure 10**) [70], (ii) providing the heat through heat pipes (**Figure 11**) [71] or the calciner sidewalls [72]or through direct heat transfer by means of heat carrier [73] and (iii) by exploiting solar energy during daytime from a heliostat field (**Figure 12**) [74].

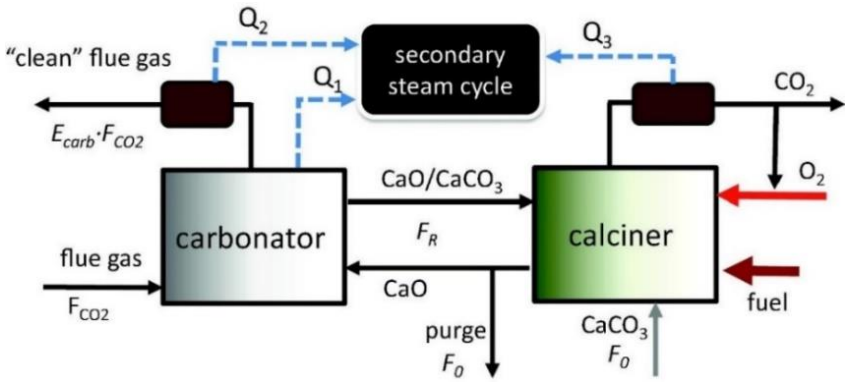

Figure 10. Schematic diagram of oxy-fired CaL process [75].

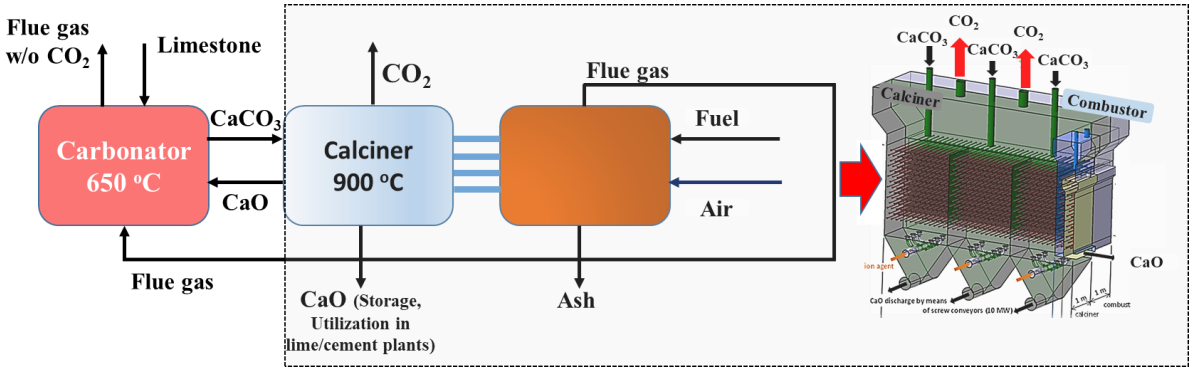

Figure 11. Indirectly heated CaL (IHCaL) process with heat pipes [76].

Over the last decades, the CaL concept has been tested successfully on the lab and pilot scale ranging from 3 kW_{th} up to 1.7 MW_{th} [77]. The lab-scale activities in facilities, such as the 30 kWth CFB-CFB at INCAR-CSIC [78], the 75 kW_{th} CFB-BFB at CANMET [79], and the 10 kW_{th} CFB-BFB at the University of Stuttgart [80], [81], have proven that the calcium looping could be feasible and achieve high CO_2 capture

efficiencies. In a European level three pilot scale CaL plants have been constructed; the 1.7 MW_{th} at La Pereda [82] in Spain, the 1 MW_{th} at TU Darmstadt [83], and the 200 kW_{th} at the University of Stuttgart [84]. Following these successful experimental campaigns, attempts are being made, during the recent years, to test the calcium looping concept on the large-scale [85], [86].

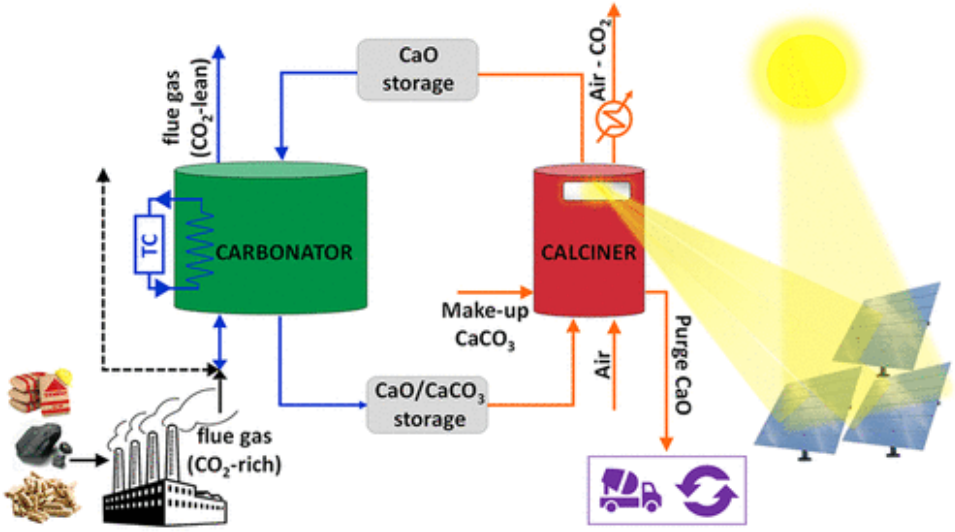

Figure 12. CaL-TCES concept coupled with CSP for carbon capture and energy storage [74].

During the recent years, the CaL concept has been proposed as a TCES option, especially for CSP heat storage, owing to its numerous advantages. This concept has a comparatively high efficiency and energy density (889 $kWh \cdot m^{-3}$), with respect to other TCES solutions (**Table 2**), whereas the storage medium can be purchased at a low cost being non-toxic at the same time. Added to this, the equilibrium calcination reaction is near to 900 °C (under a CO_2 partial pressure of 1 atm) that fits in the desirable range of high temperatures potentially attainable in CSP tower plants. This would allow for a more efficient electricity generation from stored energy, to overcome the current limitation of ~550 °C imposed by the degradation of molten salts employed as HTFs in state-of-the-art CSP plants [87].

Table 2. Comparison of CaL concept with other TCES systems in terms of energy density and turning temperature [88, 89].

TCES	Turning temperature (°C)	Energy density ($MJ \cdot m^{-3}$)
NH_3/N_2	195	131
CH_4/H_2O	688	223
SO_3/SO_2	782	459
CaO/H_2O	479	1967
Li_2O/H_2O	731	2216
NH_4HSO_4/NH_3	467	3082
CaO/CO_2	895	3226
SrO/CO_2	1108	3948

The concept of CaL-TCES storage dates back at the 70's [90]. However, up until recently it has turned out to be a promising technological option for heat storage at high temperatures to maximize the global plant

efficiency [91]. The CaL-TCES differs from the oxy-fired CaL process, where the heat from the endothermic reaction is provided through a clean type of energy (i.e. solar) in an either direct (volumetric heating) or indirect form (heat from the sidewalls) [92]. The latter concept resembles more to the indirectly heated calcium looping (IHCaL) concept, where heat provided as well indirectly through the reactor sidewalls or by immersed heat pipes. Both concepts may have an important effect on the multicycle CaO activity owing to the absence of a fossil fuel inside the reactor, as done in the oxy-fired CaL concept.

The CaL technology is close to its commercialization; however, the involved reactors still need to be optimized in terms of design and operation. Concerning its application for TCES with solar energy storage, ongoing projects are within TRL5 and will reach a demo scale within the next 2-3 years [93]. In the context of up-scaling, apart from the experience obtained through the operation of DFB systems on a bench or pilot scale, modelling tools can play a significant role, as well, towards their optimum and effective design. CFD models have a strong ability to deliver detailed information concerning the gas-solid flow hydrodynamics occurring inside a fluidized bed unit. Parameters, such as inert material distribution in the bed, particles residence time, reactants mixing efficiency and temperature distribution, can be more easily quantified at any point of the reactor, with a relatively lower cost [75], when compared to the experiments.

1.5 Scope of the current PhD thesis

In recent years, low/medium/high-temperature SHS, LHTES and TCES technologies have been a cutting-edge research topic, studied in detail from different perspectives, including suitable heat storage media, heat carriers, containers and overall system performance. Advanced numerical tools have stood at the core of collective actions that have aimed to bring forward novel TES concepts of optimized design and operating performance. In this regard, the main motivation of the present Thesis is to develop, validate and implement for design/operation optimization at a component level, advanced transient CFD models, accurate yet computationally efficient, to simulate novel sensible, chemical and latent heat thermal energy storage systems applicable in high and ultra-high temperatures. In this regard, three types of systems are mainly simulated and optimized: (i) a novel UHT-LHTES system that uses silicon as a PCM, (ii) a sensible gas-solid bubbling HE that can be used for sensible storage and (iii) the carbonate looping cycle that can be potentially used for TCES. Such concepts can be used as individual technical solutions (e.g. utilization of CaL cycle for post-combustion CO_2 capture), or a combination of them can be implemented towards an enhanced operation (e.g. TES and in-situ CO_2 capture).

As regards the novel UHT-LHTES system, the three-phase flow (gas-liquid-solid) and complex conductive-convective heat transfer mechanisms are studied inside a gas-PCM container operating at ultra-high temperatures. The applied model combines advantages of i) the fixed grid based enthalpy porosity method that implicitly models the solid/liquid PCM interface, ii) the Volume of fluid (VOF) method that models the gas-PCM flow and iii) an adaptive local grid refinement technique for enhanced numerical accuracy. The latter, which is based on the work of [94], is able track and smoothen a moving interface, between two immiscible fluids, offering the advantage of limiting interface numerical diffusion, without substantial increase in the computational cost. Initially, the developed model is validated against available experimental data and numerical results taken from the work of Assis et al. [43] for the case of paraffin wax melting at lower temperatures (~27 ^{o}C). During model validation, an insight is given on numerical parameters that affect the PCM melting rate, i.e. the mushy zone parameter, which is dependent on the secondary dendrites arm spacing (DAS) of the dendrites formed in the mushy zone during solidification process. This parameter is dependent on the PCM structure and affects, in essence, the PCM melting rate. Added to this, the

advantages of the local refinement technique compared to fixed mesh methods are unveiled. Later on, the CFD model is applied for the numerical simulation of the solidification/ melting process of pure silicon as a phase change material (PCM) inside a sealed container operating at ultra-high temperatures (~1410-2000 ^{o}C). The effect of different design and operating parameters, such as the container size/shape, and surface temperature, respectively, on the PCM melting rate are investigated. The effect of lateral heat losses on the system charging/discharging rates is also addressed, a parameter that is critical especially for such high operating temperatures. Finally, a sensitivity analysis on the PCM thermo-physical properties effect on the LHTES performance is carried out. The concept tested is a conceptual one for P2H2P (power-to-heat-to-power) applications and is based on the work of Datas et al. [27]. This concept can be alternatively implemented to S2H2P (solar-to-heat-to-power) applications. For the first time, an adaptive local grid refinement technique is coupled with the VOF/enthalpy-porosity method, to obtain a sharp solid-liquid, PCM-gas interface, by simultaneously taking into account density differences between the PCM solid and liquid phases. The work of the adaptive local refinement technique based on in-housing coding development has originated from the works of Nikolopoulos et al. [95, 96] and Malgarinos et al. [94, 97, 98] to track deformable interfaces, which was mainly focused in droplet dynamics (collision, break-up) applications. The whole research effort in this Thesis is going one step beyond to a different application of droplet dynamics to that of phase change problems and leads to the development of an effective and accurate CFD model that can be utilized for the simulation of low to ultra-high temperature LHTES systems.

As regards the gas-solid TCES-FB system, the novel concept of carbonate looping cycle for CO_2 capture that can be potentially utilized for TCES is investigated. Validation of sub-models is carried out by utilizing data from experimental campaigns in pilot scale units (i.e. a 1 MW_{th} carbonator, a 1 MW_{th} oxy-fired calciner and a 300 kW_{th} indirectly heated calciner, all units installed at the premises of TUDA). Both reactors obey in general terms in the same principles of gas-solid fluidization ranging from bubbling to circulating mode. The developed CFD model is based on the pure Eulerian-Eulerian approach. In specific, the state-of-the-art Two-Fluid Model (TFM) is utilized for the two-phase (gas-sorbent) flow of the carbonator and the indirectly heated calciner and the state-of-the-art Multi-Fluid (MFM) for the three-phase flow (gas-sorbent-fuel) of the oxy-fired calciner. However, several numerical advancements are utilized to enhance the individual models validity. These include development of the sub-grid drag coefficients Energy Minimization Multi-Scale scheme (EMMS), use of appropriate sub-models for the heat transfer among the gas-solid fluidized bed and heat pipes in the cases of the calciner, investigation of the turbulence effect on the overall heat transfer and application of appropriate reaction kinetics. The end-product from this analysis, is an advanced transient multi-phase model that can simulate gas-solid fluidized bed systems with and without heat transfer and with and without chemical reaction (the calcium-carbonate looping cycle in the specific Thesis). This model has been exploited in this Thesis, to optimize the involved reactors in terms of design and operating conditions and study up-scaling scenarios (up to 20 MW_{th} for the carbonator case) of their optimum designs.

Concerning the SHS-FB system, the advanced numerical model developed and validated for the TCES-FB system has been utilized to study an industrial-scale internal BFB heat exchanger that can be potentially used for sensible heat storage. An important add-on of this analysis is a reduced order model integrated into the CFD model that implicitly simulates the heat transfer from the fluidized bed towards a heat transfer medium (i.e. steam) flowing inside the tube buddles. Results of this model, e.g. solids volume fraction can be used to feed a theoretical heat transfer model, in order to carry out a multi-parametric analysis of several operating aspects (e.g. effect of temperature, fluidizing medium on the overall heat transfer coefficient).

This numerical approach can lead to cost-effective model that takes as well into account the flow hydrodynamics by utilizing a more advanced numerical model developed in this Thesis.

Finally, the different concepts studied in this Thesis, i.e. (i) Si-based LHTES, (ii) gas-solid SHS-BHB heated by means of steam filled tubes, (iii) TCES-FB with sodium filled tubes are compared in terms of several Key Performance Indicators (KPIs) for the same system scale. These include storage capacity, heating time, heating rate (technical aspects calculated by utilizing the CFD models developed in this Thesis) along with technical bottlenecks, maturity level, and solid medium properties (average cost, turning temperature and environmental effect).

The overall target of this Thesis, is to provide the research community with advanced transient CFD models that can be exploited for the numerical simulation and design/operation optimization of novel multi-phase systems (at a component level), targeted primarily for thermal energy storage, but also for heat exchange and oxy-combustion and CO_2 capture. Such models can act as stand-alone tools, but they can also feed with their results reduced order models (ROM), e.g. thermodynamic models for process engineering, to obtain calculations of a specific process with a higher level of accuracy.

1.6 Numerical modelling: general definitions, methodology, contribution

The most appropriate way to assess the potential scale-up, commercialization and erection of advanced heat exchanger and storage systems at a component level - based on either PCMs or granular flows- is by means of using advanced numerical tools. The scale-up process of advanced heat transfer systems is a complex procedure that involves various physical phenomena affected by the scale of the system, mainly the flow hydrodynamics, the heat and mass transfer and any possible reaction kinetics. There are four steps for the development and scale-up of a new process [99]: i) determination of the new process at lab scale, ii) selection of a mathematical model and determination of the hydrodynamics, kinetics etc., iii) construction of a continuous pilot plant, and, iv) construction of a demo or commercial plant.

Various modelling techniques can be used to simulate multi-phase flow processes and therefore assist in their scale-up process. The most important ones are the computational fluid dynamics (CFD) models, the artificial neural network (ANN) and the thermodynamic equilibrium models. The CFD and thermodynamic models are good candidates to be used as tools to derive guidelines for the scale up of the under-studied processes, especially when they are enhanced by sub-models or inter-linked for a higher level of accuracy.

The basic advantage of CFD tools in contrast to Thermodynamic models is that, in general terms, the calculated results can give insights on the underlying physics at a local level with a high level of accuracy. Another advantage is that challenging aspects, such as the design optimization and up-scaling at a component level, can be most appropriately addressed by means of CFD tools. Finally, CFD tools can be adjusted from more simplified to more advanced approaches depending on the studied domain, whereas they can deliver results that can feed from stress-strain analysis tools to ROMs, such as thermodynamic tools, being the core of a multi-level analysis approach (**Figure 13**).

The simulation tool that has been mainly used in this Thesis is ANSYS Fluent commercial platform and ANSYS Workbench. The main features of this CFD simulation software are summarized below:

- Design component for modification and clean-up of a studied geometry to be tailored for a CFD simulation.

- Meshing component with appropriate algorithms for constructing the computational grid. Use of custom-built codes in C programming language and/or built-in Fluent codes for local refinement, when necessary to improve accuracy and avoid diffusion related problems.
- Advanced numerical solver, by which transient calculations have been performed.
- Post-process capabilities of extracting of both local and global variables for further exploitation of results from ROMs, such as process models, or theoretical 0D models.

Apart from the main simulating software additional add-ons have been developed:

- Extensive coding in FORTRAN to extract in-house models (e.g. drag coefficient correction, (**Figure 14**) in order to increase the accuracy of the used model.
- Extensive coding in C programming language to include sub-models needed for the simulations, such as material properties, boundary conditions, reaction kinetics.

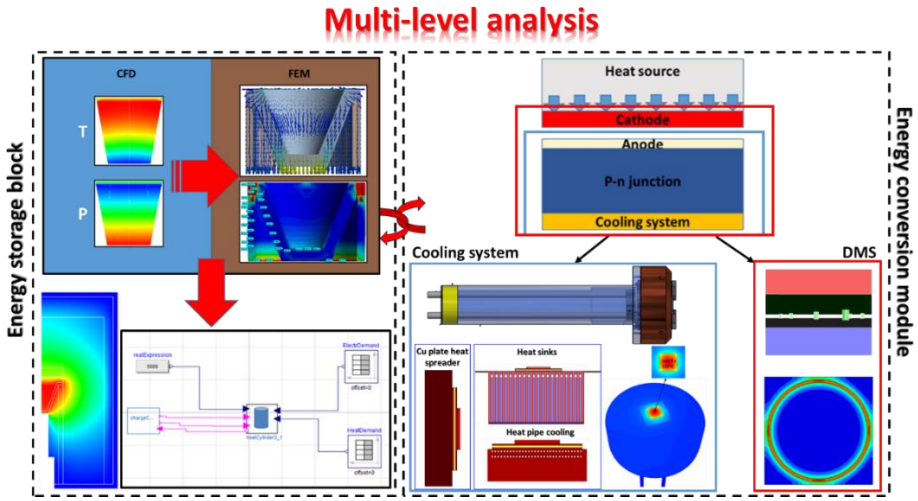

Figure 13. Example of numerical advancement in a LHTES system and possible coupling with other models.

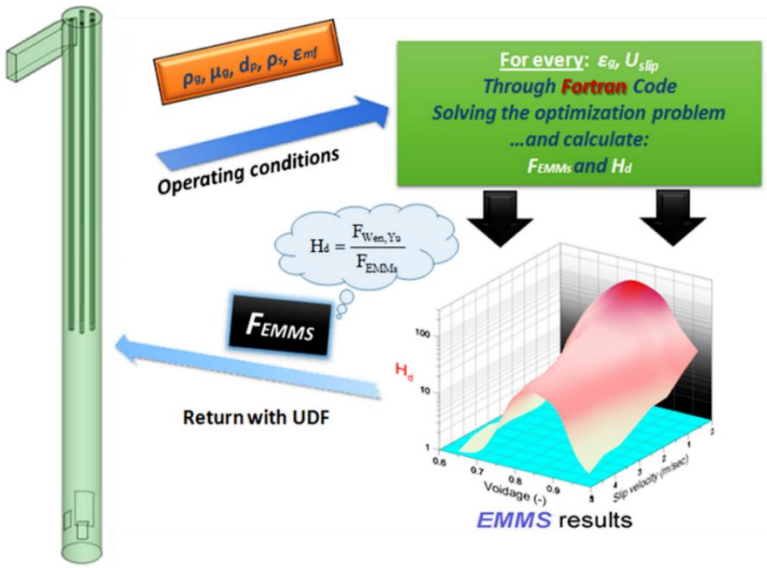

Figure 14. Example of numerical advancement in a FB system; The drag-coefficients EMMS scheme.

1.7 Summary of the used models

In all types of systems, it will be showcased that the developed numerical models are applicable for both two-phase and three-phase flow conditions and for a wide spectrum of operating conditions. A summary of the numerical advancements undertaken in this Thesis and their possible applications is given in **Table 3**.

Table 3. Summary of used models for each system studied in this Thesis, numerical advancements and possible applications.

System	Modelling approach	Advancements	Applications
LHTES	Eulerian VOF approach coupled with solidification melting model and adaptive local grid refinement for an enhanced accuracy; implicit inclusion of dendritic formation inside the PCM	Possible cracking of the PCM vessel, due to PCM volume change; excess heat losses due to ultra-high temperature operation **(Chapter 3)**	From low (paraffin wax) to ultra-high temperatures PCMs
CFB carbonator	Eulerian-Eulerian TFM coupled with in-house EMMS drag force model; inclusion of carbonation reaction; monosized approach	In-house code of the gas-solid drag force exerted on the solid particles; Design optimization of the carbonator reactor and CO_2 capture efficiency enhancement; study of carbonator in different scales from pilot (1 MW_{th}) to demo (20 MW_{th}) scale **(Chapter 4)**	CFB systems; carbonator reactors from pilot to demo scale; simulation of Geldart A/B particles with the EMMS model
Oxy-fired BGB calciner	Eulerian-Eulerian MFM (3 phase flow); inclusion of energy equation, turbulence effect; calcination reaction; recarbonation of CaO; inclusion of in-situ combustion of coal	Use of coal combustion along with calcination reaction. Modelling of the re-carbonation of CaO inside the reactor **(Chapter 4)**	Oxy-fired calciners; Oxy-fired FB systems
IHCaL calciner	Eulerian-Eulerian TFM; inclusion of heat transfer mechanisms (including radiation); calcination reaction; turbulence effect	Use of radiation model. Inclusion of turbulence effect in heat transfer process. Design optimization of the heat pipes arrangement **(Chapter 4)**	Solar TCES, BFB calciners. Granular systems including radiation heat transfer
SHS-BFB	Eulerian-Eulerian TFM/MFM coupled with in-house EMMS drag force model; heat transfer	In-house code in C language that implicitly simulates the steam fluid medium inside the tube buddles; explicit simulation of the demanding arrangement in an industrial BFB HE that can act a sensible heat storage system **(Chapter 5)**	HEs and TES including heat pipes/ tube buddles

CHAPTER 2
Numerical methods for multi-phase systems

2.1 Preface

Many industrial processes in chemical and metallurgical, environmental and power engineering employ multi-phase systems that are often designed to bring about heat and mass transfer and phase-change phenomena. A multiphase flow system is one characterized by the simultaneous presence of several phases, such as gas-solid, solid-liquid, and or gas-liquid, the two-phase system being the simplest case. From a design point of view, the development of general models, capable of predicting the flow fields of all involved phases and their presence rates in the studied domains is of great interest for the design, control and improvement of such multi-phase systems. From a scientific point of view, the study of multi-phase flows raises a number of challenging questions that still require theoretical advances and new experimental investigations. Operation/design optimization, multi-parametric analysis and construction of generalized scaling-up rules is also a necessity for such type of systems.

Multi-phase flows can be encountered in two main forms; the separated and the dispersed multi-phase flows. The former includes two or more phases separated by interfaces, such as slugging flows in FB systems, channeling flows or phase change materials. The latter consists of finite particles, solids or bubbles distributed within a continuous phase, such as in bubble columns, gas-solid fluidized bed reactors and cyclones.

For the design and optimization of such multi-phase systems, a detailed understanding of the interfacial transport phenomena is essential. For single-phase flows, CFD tools already have a long history and nowadays they stand out as the standard approach in the developments for aeronautical and automotive industries using different commercially available platforms. For multi-phase flows, the application of CFD tools is rather young (probably 30–40 years), owing to the complex physics involved in. Thus, there is room for development and further improvement of state-of-the-art CFD models for multi-phase flows across several applications. Currently there are two main approaches for the numerical calculation of multiphase flows: the Euler-Lagrange approach and the Euler-Euler approach. This Section goes through the most appropriate models to model multiphase flows, with a specific emphasis of Eulerian-Eulerian models applied for TES systems.

2.2 Granular flows

Fluidization has been widely used in industrial applications due to its continuous powder handling ability and its good heat and mass transfer characteristics. Quantitative understanding of the hydrodynamics of fluidization is needed for design and scale-up of efficient new reactors, novel energy storage systems and gas-solid or solid-solid heat exchangers that can be utilized in several energy intensive sectors, such as petroleum, cement, lime, chemical and electric power industries.

Many investigators worldwide have considered as a crucial issue the accurate and efficient simulation of FB reactors, aiming to their up-scaling for industrial uses. Concerning CFB regimes, in most of the cases the simulation only of the riser is preferred over the full loop [100, 101]. This strategy is in general preferred due to its lower computational cost [102] as long as the appropriate boundary conditions for the solids inlet and the riser exit are applied [103]. On the other hand, only few 3D studies are available in the literature for a full loop simulation, and these are mainly concentrated to lab-scale units in the range of 100 kW_{th}. This lies on the fact that even if such an approach is considered as the most accurate and valuable for an optimal fluidized bed design and operation [104], it is at the same time computationally very expensive. The most recent work is that of [105] who has applied the Computational Particle Fluid Dynamics (CPFD)

methodology in a CFB simulation with a loop seal. Previously [106] conducted a 3D CFB full loop simulation using the discrete particle method (DPM). [107] applied the Eulerian-Eulerian TFM approach combined with the EMMS scheme to study the hydrodynamics of a semi-industrial CFB reactor and two years later implemented their work in a 150 MW_{th} CFB boiler simulation [108]. Finally, [109, 110] used the coupled Eulerian approach with the EMMS model for the simulation of a CFB carbonator cold model.

In any case, the gas-solid flow characteristics inside a fluidized bed system are really complex and difficult to quantify. Nevertheless, due to parallel computing availability, and rapid upgrade of central processing unit (CPU) and graphics processing unit (GPU) hardware that allow for a considerable acceleration of the calculations, the numerical methods and algorithms of CFD have become a powerful tool towards achieving this target. In this context, two approaches have been proposed for the solution of the multiphase flow in a fluidized bed reactor; i.e. the Eulerian-Eulerian and ii) the Eulerian-Lagrangian approach. The Eulerian-Eulerian TFM approach, treats the gas and the solid phase as interpenetrating continua [111], [112]. This model has been extensively employed in many areas, especially in the fluidized bed simulations, due to its low computational cost compared to Eulerian-Lagrangian models that explicitly model the inter-particle interactions, such as that of Discrete Elements Method (DEM) [113-115]. Alternatively, multi-phase particle-in-cell (MP-PIC) methods [116-118], which implicitly simulate those interactions allows for a reduction of the associated CPU cost. This approach has gained popularity recently and seems promising. Some of its advantages are [119]: (a) the inclusion of particles size distribution (PSD) with a comparatively low computational cost, (b) the track of a great amount of particle parcels, and (c) the straightforward simulation of wall boundary conditions. Nonetheless, this approach has not been in depth investigated compared to the Eulerian TFM, which still remains to be the most mature methodology for the modeling of fluidized bed reactors. However, even in the case of the TFM, further research and numerical advancements are required, to accurately simulate the demanding multi-phase flows inside the FB reactors.

A parameter of crucial importance in TMF is the drag coefficient between the gas and the particulate phase. Up to present, several models that predict the inter-phase drag coefficient have been proposed in the literature. Conventional drag laws, as the ones given by Wen and Yu [120], Gidaspow [112] and Syamlal-O'Brien [121] over-predict the drag force induced on the solid particles by the gas phase, especially in cases where a coarse grid is used [122, 123]. This is because the solid particles inside a fluidized bed reactor are heterogeneously dispersed, forming dynamic meso-scale structures, such as clusters, bubbles, streamers [124] etc. These heterogeneous formations have a strong effect on the momentum, heat and mass transfer and the achievable conversion rates of a fluidized system [122], [125]. For their quantification and accurate prediction either an extremely fine grid, which would increase the computational cost considerably, or a proper sub-grid model that takes into account such meso-scale structures should be used ([126], [127]).
Several research groups have addressed the importance of sub-grid modelling. In Princeton group a filtered drag coefficient has been presented for Geldart A particles in a periodic domain [128]. Simonin's group has proposed a drag correlation similar to Princeton group with the main difference that the filter length is dimensionalised with the bed diameter instead of the terminal settling particle velocity [129, 130]. Kuiper's group presented a drag force model applicable to Geldart B and D particles in bubbling fluidized beds using coarse mesh [131]. Finally, a sub-grid model that has been implemented the last decades in fluidized bed simulations is the EMMS scheme.

The EMMS model is a sub-grid scale model that takes into account the effect of the heterogeneous formations on the determination of the momentum exchange coefficient, avoiding the application of a dense grid. This model was first introduced by [132] for the steady flow inside a CFB reactor. Several researchers

[102, 122] developed an improved version of the model taking into account particle acceleration and the effective inter-phase interaction. Researchers in [133] proposed an EMMS model for Geldart B particles in a cold dense CFB. All of the abovementioned studies use as a key parameter for the EMMS model, i.e. the cluster size. This is not always the case; some researchers, apply the EMMS theory by incorporating in the model the bubble size [134]. This is the so called bubble-based EMMS model, which was first proposed by [135]. The latter model is more theoretically sound for BFB reactors. For a CFB reactor though, the accurate quantification of the cluster size is considered as a key parameter for an accurate EMMS model.

The precise prediction of the cluster size has been a major issue that has not been solved yet. The main reason is that clusters are spatio-temporal structures that change size, effective density and shape constantly [136]. Several empirical and semi-empirical models have been proposed [122, 137-139], reflecting the necessity for its accurate prediction. A correlation proposed by [132], based on the work of [140], assumes that the cluster diameter is inversely proportional to the energy used for suspension and transportation. This approach has been widely used by many researchers [102, 141, 142]. However, in some cases those correlations result in an over-prediction of the cluster diameter. Gu and Chen correlation [138] has been implemented for the full loop simulation of a carbonator cold model unit in the work of [109]. All the aforementioned approaches share the important drawback that the riser diameter is not been taken into consideration. Nonetheless, this parameter should be incorporated in the EMMS model, so that the calculated cluster size should take values lower than the reactor diameter. A correlation introduced in the work of [143] takes into account the effect of the riser diameter, but it has not been extensively used and validated especially for CFB reactors.

Reaction kinetics is also a major aspect that should be cautiously selected, especially for multi-phase systems including chemical reaction, such as the calcium looping process studied in the current Thesis. Contrary to the flow hydrodynamics simulations, the understanding of the sorbent regeneration, has been the subject of many experimental studies [144]. Unfortunately quantification of the calcination kinetics is a really complicated issue, because the reaction itself is highly dependent on the CO_2 partial pressure and the particle size, whilst it can be inhibited by impurities, such as fly ash [145], [146]. Degradation of the sorbent material can be caused as well, due to consecutive carbonation – calcination cycles within the calciner in areas where the re-carbonation of CaO is favored. As regards the calcination kinetics, a series of reaction rates have been presented in the literature. The dominant models proposed regarding the specific surface area quantification are the Shrinking Core Model (SCM) [147], [148] and the Changing Grain Size Model (CGSM) [144]. Garcia- Labiano based on these models proposed a particle model for the most usual calcium based-sorbents for a wide range of operating conditions [144]. Apart from these models the homogeneous reaction rate model has been also proposed, which assumes a homogeneous reaction thought the sorbent, however, is applied mainly on particle sizes less than 90 μm.

Finally, achieving validation of the used models against experimental data –especially at a pilot scale- is a major asset in such type of developed tools, in a sense that the derived results become reliable enough to draw safe conclusions about a systems design and operation. By using such validated tools, the up-scaling of such systems at an industrial scale can be potentially achieved. The following sub-sections (2.1.1-2.1.5) present the numerical methodology that has been used for the simulation of the under-studied FB systems.

2.2.1 Multi-phase model

2.2.1.1 Multi-fluid model

The MFM approach is an expansion of the state-of-the-art TFM that was initially developed for the simulation of two-phase flows. The MFM uses a generalized form of the Navier-Stokes equations, with each phase having its own properties (velocity, temperature). In the MFM frame, the inclusion of closure equations for the solid phase is necessary in order to solve the model. These equations are based on the kinetic theory of granular flows (KTGF), which was first applied by [149] and later by [112], for the case of a two-phase flow, and concern the calculation of the granular stress tensor and pressure. The governing equations and constitutive closures of the MFM for a binary (fuel-sorbent) mixture are the following (the subscripts *g*, *s1*, and *s2* stand for gas, sorbent and fuel phase, respectively):

Mass conservation for gas phase

$$\frac{\partial}{\partial t}\left(\varepsilon_g \rho_g\right) + \nabla \cdot \left(\varepsilon_g \rho_g \vec{u}_g\right) = -r_{gs1} - r_{gs2} \tag{4}$$

Mass conservation for solid phase 1 (sorbent)

$$\frac{\partial}{\partial t}\left(\varepsilon_{s1} \rho_{s1}\right) + \nabla \cdot \left(\varepsilon_{s1} \rho_{s1} \vec{u}_{s1}\right) = -r_{s1g} - r_{s1s2} \tag{5}$$

Mass conservation for solid phase 2 (fuel)

$$\frac{\partial}{\partial t}\left(\varepsilon_{s2} \rho_{s2}\right) + \nabla \cdot \left(\varepsilon_{s2} \rho_{s2} \vec{u}_{s2}\right) = -r_{s2g} - r_{s2s1} \tag{6}$$

, where r_{qq} (kg·m^{-3}·s^{-1}) denotes for the mass transfer rate per unit volume from one phase to another, due to a phase change or a chemical reaction. Additionally, r_{gs1}=-r_{s1g}, r_{gs2}=-r_{s2g} and r_{s1s2}=-r_{s2s1}.

Gas phase momentum conservation equation

$$\begin{aligned}&\frac{\partial}{\partial t}\left(\varepsilon_g \rho_g \vec{u}_g\right) + \nabla \cdot \left(\varepsilon_g \rho_g \vec{u}_g \vec{u}_g\right) = -\varepsilon_g \nabla p_g + \nabla \cdot \overline{\overline{\tau_g}} + \varepsilon_g \rho_g g - \beta_{gs1}\left(\vec{u}_g - \vec{u}_{s1}\right)\\ &-\beta_{gs2}\left(\vec{u}_g - \vec{u}_{s2}\right) + r_{s1g}\vec{u}_{s1g} - r_{gs1}\vec{u}_{gs1} + r_{s2g}\vec{u}_{s2g} - r_{gs2}\vec{u}_{gs2}\end{aligned} \tag{7}$$

Solid phase 1 momentum conservation equation

$$\begin{aligned}&\frac{\partial}{\partial t}\left(\varepsilon_{s1} \rho_{s1} \vec{u}_{s1}\right) + \nabla \cdot \left(\varepsilon_{s1} \rho_{s1} \vec{u}_{s1} \vec{u}_{s1}\right) = -\varepsilon_{s1} \nabla p_g + \nabla p_{s1} + \nabla \cdot \overline{\overline{\tau_{s1}}} + \varepsilon_{s1} \rho_{s1} g\\ &-\beta_{gs1}\left(\vec{u}_{s1} - \vec{u}_g\right) - \beta_{s1s2}\left(\vec{u}_{s1} - \vec{u}_{s2}\right) - r_{s1g}\vec{u}_{s1g} + r_{gs1}\vec{u}_{gs1} + r_{s2s1}\vec{u}_{s2s1} - r_{s1s2}\vec{u}_{s1s2}\end{aligned} \tag{8}$$

Solid phase 2 momentum conservation equation

$$\begin{aligned}&\frac{\partial}{\partial t}\left(\varepsilon_{s2} \rho_{s2} \vec{u}_{s2}\right) + \nabla \cdot \left(\varepsilon_{s2} \rho_{s2} \vec{u}_{s2} \vec{u}_{s2}\right) = -\varepsilon_{s2} \nabla p_g + \nabla p_{s2} + \nabla \cdot \overline{\overline{\tau_{s2}}} + \varepsilon_{s2} \rho_{s2} g\\ &-\beta_{gs2}\left(\vec{u}_{s2} - \vec{u}_g\right) - \beta_{s2s1}\left(\vec{u}_{s2} - \vec{u}_{s1}\right) - r_{s2g}\vec{u}_{s2g} + r_{gs2}\vec{u}_{gs2} + r_{s1s2}\vec{u}_{s1s2} - r_{s2s1}\vec{u}_{s2s1}\end{aligned} \tag{9}$$

, where $\vec{u}_{gs}$, $\vec{u}_{sg}$, $\vec{u}_{gf}$, $\vec{u}_{fg}$, $\vec{u}_{fs}$ and $\vec{u}_{sf}$ are interphase velocities.

If, for instance r_{gs}>0 (mass from the gas phase is being tranferred to the sorbent phase), then $\vec{u}_{gs} = \vec{u}_g$; if r_{gs}<0 (mass from the sorbent phase is being tranferred to the gas phase), then $\vec{u}_{gs} = \vec{u}_s$. In a similar way, if r_{sg}>0, then $\vec{u}_{sg} = \vec{u}_s$ and if r_{sg}<0, then $\vec{u}_{sg} = \vec{u}_g$

Gas phase stress–strain tensor

$$\overline{\overline{\tau_g}} = \varepsilon_g \mu_g \left(\nabla \vec{u}_g + \nabla \vec{u}_g{}^T \right) + \varepsilon_g (\lambda_g - \frac{2}{3}\mu_g)(\nabla \cdot \vec{u}_g)\bar{\bar{I}} \quad (10)$$

Solid phase 1 stress–strain tensor

$$\overline{\overline{\tau_{s1}}} = \varepsilon_{s1} \mu_{s1} \left(\nabla \vec{u}_{s1} + \nabla \vec{u}_{s1}{}^T \right) + \varepsilon_{s1} (\lambda_{s1} - \frac{2}{3}\mu_{s1})(\nabla \cdot \vec{u}_{s1})\bar{\bar{I}} \quad (11)$$

Solid phase 2 stress–strain tensor

$$\overline{\overline{\tau_{s2}}} = \varepsilon_{s2} \mu_{s2} \left(\nabla \vec{u}_{s2} + \nabla \vec{u}_{s2}{}^T \right) + \varepsilon_{s2} (\lambda_s - \frac{2}{3}\mu_{s2})(\nabla \cdot \vec{u}_{s2})\bar{\bar{I}} \quad (12)$$

It should be noted that in the case of a single granular flow the above equations are solved by taking into account one solid phase, whereas the KTGF model for a single granular phase is applied. In the case of a bi-dispersed flow, the KTGF model for multiple granular phase is used.

2.2.1.2 KTGF for a single granular phase

Based on the KTGF theory the granular shear viscosity of a solid phase, μ_s, consists of three parts: the collisional, kinetic and frictional part:

$$\mu_s = \mu_{s,kin} + \mu_{s,col} + \mu_{s,fr} \quad (13)$$

Collisional viscosity [150], [151]

$$\mu_{s,col} = \frac{4}{5}\varepsilon_s \rho_s d_p g_0 (1 + e_{ss}) \sqrt{\frac{\Theta_s}{\pi}} \quad (14)$$

Kinetic viscosity [152]

$$\mu_{s,kin} = \frac{10 \rho_s d_p \sqrt{\Theta_s \pi}}{96 \varepsilon_s (1 + e_{ss}) g_0} \left[1 + \frac{4}{5} g_0 \varepsilon_s (1 + e_{ss}) \right]^2 \quad (15)$$

Frictional viscosity

The solids frictional viscosity is included in the model in cases where the solids volume fraction is higher than the friction limit ($\varepsilon_{s,fr}$>0.51). The correlation of Johnson and Jackson [153] is applied:

$$\mu_{s,fr} = \frac{p_{fr} sin\varphi_{fr}}{2\varepsilon_s \sqrt{II_{2D}}} \quad (16)$$

Frictional pressure [153]

(17)

$$p_{fr} = 0.1\varepsilon_s \frac{(\varepsilon_s - \varepsilon_{s,fr})^n}{(\varepsilon_{s,max} - \varepsilon_s)^p}$$

, where n=2 and p=5

Solids pressure [149]

$$p_s = \varepsilon_s \rho_s \Theta_s + 2\rho_s(1 + e_{ss})\varepsilon_s^2 g_0 \Theta_s \quad (18)$$

Granular bulk viscosity [149]

$$\lambda_s = \frac{4}{3}\varepsilon_s \rho_s d_p g_0 (1 + e_{ss}) \left(\frac{\Theta_s}{\pi}\right)^{1/2} \quad (19)$$

Granular temperature

The following algebraic form of the granular temperature transport equation is applied:

$$0 = \left(-p_s \bar{\bar{I}} + \bar{\bar{\tau}}_s\right) : \nabla \vec{u}_s - \gamma_{\Theta s} + \varphi_{gs} \quad (20)$$

, where $\gamma_{\Theta s}$ is the energy dissipation, due to inelastic particle-particle collisions, whilst the term φ_{gs} represents the kinetic energy exchange between the fluid or solid phase and the sth solid phase

Radial distribution function [154]:

$$g_0 = \frac{3}{5}\left[1 - \left(\frac{\varepsilon_s}{\varepsilon_{s,max}}\right)^{1/3}\right]^{-1} \quad (21)$$

All the above-mentioned equations are solved using the ANSYS Fluent platform. It should be underlined that the study of the solid stress tensor is an important issue for the TFM model. However, it is not the subject of the present Thesis, due to the fact that its effect on a FB reactor's hydrodynamics is less important than that induced by the inter-phase drag force [122].

2.2.1.3 KTGF for multiple granular phases

In the case of more than one solid phases, as in the case of the oxy-fired calciner simulated in this Thesis, there are complexities in the proper formulation of the stress tensor of multiple granular phases. The kinetic theory should be applied for particle - particle interactions for particles of different size and densities resulting in correlations for pressure, shear and bulk viscosity that sum the effect of all Eulerian solid phases. Mathiesen [155] developed such correlations for poly-dispersed systems in their novel work. A generic group of User Defined Functions (UDFs) that solves and extension of the KTGF model for poly-dispersed flows has been formulated from CERTH's research group [156] and is applied as well in this Thesis for the bi-dispersed flow of the oxy-fired calciner.

The granular pressure of a phase s1 is calculated using the next two correlations:

$$p_{s1} = \varepsilon_{s1}\rho_{s1}\Theta_{s1} + p_{c,s1s2} \quad (22)$$

$$p_{c,s1s2} = \frac{\pi}{3}(1 + e_{s1s2}) d_{ps1s2}^3 g_{0s1,s2} n_{s1} n_{s2} m_o \left\{\frac{\Theta_{s1}\Theta_{s2}}{\frac{m_{s1}}{m_{s2}}\Theta_{s1} + \frac{m_{s2}}{m_{s1}}\Theta_{s2}}\right\} x$$
$$\left\{\frac{(m_o/m_{s1})^2 \Theta_{s1}\Theta_{s2}}{[\Theta_{s1} + (m_{s2}/m_{s1})^2\Theta_{s2}] + (\Theta_{s1}+\Theta_{s2})}\right\}^{3/2} \quad (23)$$

, where the following scalar quantities are used for the calculation of the above equations:

$$d_{ps1s2} = \frac{1}{2}\left(d_{ps1} + d_{ps2}\right), m_o = m_{s1} + m_{s2}, n_{si} = \frac{6\varepsilon_{si}}{\pi d_{si}^3}, m_{si} = \frac{\pi d_{si}^3 \rho_{si}}{6}, i = 1{,}2 \tag{24}$$

The granular temperatures of the separate phases, Θ_{s1} and Θ_{s2} are calculated according to algebraic correlation (20). It should be underlined that e_{s1s2} is the restitution coefficient for collisions between particles of phases *s1* and *s2*, in contrast to e_{ss} which is the restitution coefficient for collisions between identical particles of phase *s* and is used in the KTGF approach for a single solid phase.

The radial distribution for two solid phases ($g_{o,s1s2}$) can be calculated by the following correlation reported by [155]. The radial distribution of the granular material (g_o) is calculated by the correlation developed by [149]. This correlation should encounter for all the granular material in a control volume and for this reason the total volume fraction of solids is used in it.

$$g_{0,s1s2} = \frac{1}{2}\frac{g_0}{1-\varepsilon_g}(\varepsilon_{s1} - \varepsilon_{s2}), g_0 = \left[1 - \left(\frac{1-\varepsilon_g}{\varepsilon_{s1,max}}\right)\right]^{-2.5\varepsilon_{s1,max}} \tag{25}$$

The frictional pressure is calculated based on equation (26) proposed by [156]:

$$p_{s1}^{fr} = \begin{bmatrix} 0 & ,for\ \varepsilon_{s2} < 0.5 \\ 0.1\varepsilon_{s1}\dfrac{\left(\varepsilon_{s2} - \varepsilon_{s1}^{fr}\right)^2}{(\varepsilon_{s1}^{max} - \varepsilon_{s2})^5} & ,for\ \varepsilon_{s2} \geq 0.5 \end{bmatrix} \tag{26}$$

As concerns the bulk and shear stresses based on the kinetic theory the following correlations are applied:

$$\lambda_{s1} = \frac{1}{\varepsilon_{s1}} p_{c,s1s2} \frac{d_{ps1s2}}{5}(\Theta_{s1} + \frac{m_{s2}}{m_{s1}}\Theta_{s2}) \sqrt{\frac{2}{\pi\Theta_{s1}\Theta_{s2}(\Theta_{s1} + \frac{m_{s2}}{m_{s1}}\Theta_{s2})}} \tag{27}$$

$$\mu_{col} = \frac{1}{\varepsilon_{s1}} p_{c,s1s2} \frac{d_{ps1s2}}{5}(\Theta_{s1} + \frac{m_{s2}}{m_{s1}}\Theta_{s2}) \sqrt{\frac{2}{\pi\Theta_{s1}\Theta_{s2}(\Theta_{s1} + (\frac{m_{s2}}{m_{s1}})^2\Theta_{s2})}} \tag{28}$$

$$\mu_{kin} = \frac{2\mu_{dil,s1}}{\varepsilon_{s1}(1+e_{s1s2})g_{s1s2}}\left\{1 + \frac{4}{5}g_{s1s2}\varepsilon_{s2}(1+e_{s1s2})\right\}^2 \tag{29}$$

The shear viscosity under dilute conditions and the average granular temperature are as follows:

$$\mu_{dil,s1} = \frac{5}{16 d_{s1}^2}\sqrt{\frac{m_{s1}\Theta_{s1,av}}{\pi}}$$

$$\Theta_{s1,av} = \frac{2m_{s1}\Theta_{s1}}{\left[\frac{n_{s2}}{n_{s1}}\left(\frac{d_{ps1s2}}{d_{ps1}}\right)^2\sqrt{\frac{(m_o/m_{s1})^2\Theta_{s2}}{(\Theta_{s1} + (m_{s2}/m_{s1})^2\Theta_{s2})}}\left(\frac{(m_o/m_{s1})^2\Theta_{s1}\Theta_{s2}}{(\Theta_{s1} + (m_{s2}/m_{s1})^2\Theta_{s2})(\Theta_{s1}+\Theta_{s2})}\right)^{3/2}\right]^2} \tag{30}$$

Finally, the respective frictional shear viscosity is calculated based on eq. (16).

2.2.2 Drag Force Model

This section presents drag force models used in multi-phase flows simulations, both homogeneous ones i.e. the Gidaspow model, and, heterogeneous ones as the sub-grid EMMS scheme. Such models are used for the calculation of the inter-phase drag coefficient between the gas-solid phases in equations (7) and (8).

Apart from the gas-solid drag force, in multi-phase flow systems that include more than one solid phases (e.g. oxy-fired calciner), there is a necessity to include as well the solid-solid drag force exchange coefficient that calculates the drag force between two distinct solid phases of different properties (e.g. density, particle size etc.). The most well-known model for calculating the solid-solid exchange coefficient is the Syamlal O'Brien symmetric model.

2.2.2.1 Gidaspow Model

The conventional drag law proposed by [112] is a combination of the Wen-Yu [120] and Ergun [157] equations and is formulated as follows:

Wen-Yu equation:

$$\beta_{gs} = \frac{3}{4d_p} C_{D0} \varepsilon_s \varepsilon_g \rho_g \left|\overrightarrow{u_g} - \overrightarrow{u_s}\right| \varepsilon_g^{-2.65} \quad \text{for } \varepsilon_g \geq 0.80 \tag{31}$$

Ergun equation:

$$\beta_{gs} = 150 \frac{\varepsilon_s^2 \mu_g}{\varepsilon_g d_p^2} + 1.75 \frac{\varepsilon_s \rho_g \left|\overrightarrow{u_g} - \overrightarrow{u_s}\right|}{d_p} \quad \text{for } \varepsilon_g < 0.80 \tag{32}$$

This model assumes homogeneous conditions in each computational cell, failing thus to predict correctly the heterogeneous formations inside a gas-solid fluidized bed reactor.

2.2.2.2 EMMS Model in-house development

Unlike the conventional Gidaspow model, the EMMS scheme, takes into account the meso-scale structural effect on the calculation of the drag coefficient in each computational cell [122]. It is based on the multi-scale modeling strategy, in which the phenomena occurring at higher scales (macro-scale) can be formulated by investigating the controlling mechanisms at smaller scales [158]. The fluid field is divided into three sub-domains that are homogeneous, i.e. the dilute, the dense and the interaction phase [132, 142], **Figure 15**. The dilute phase is controlled by a gas-dominated mechanism and the dense phase by a particle-controlled mechanism.

The flow heterogeneity induced by the cluster formation is taken into account through a dimensionless factor, which is called heterogeneity index, H_d, and is defined as:

$$H_d = \frac{F_{Wen\&Yu}}{F_{EMMS}} \tag{33}$$

The F_{EMMS} force calculated using the EMMS scheme and subsequently the H_d parameter are derived from the solution of the following set of analytical, empirical and semi-empirical equations. A stability criterion is introduced that minimizes the total energy consumed for suspension and transportation of the particles per unit mass of particles. Additionally, several closure terms for the dilute, dense and interaction phases are added to the non-linear system.

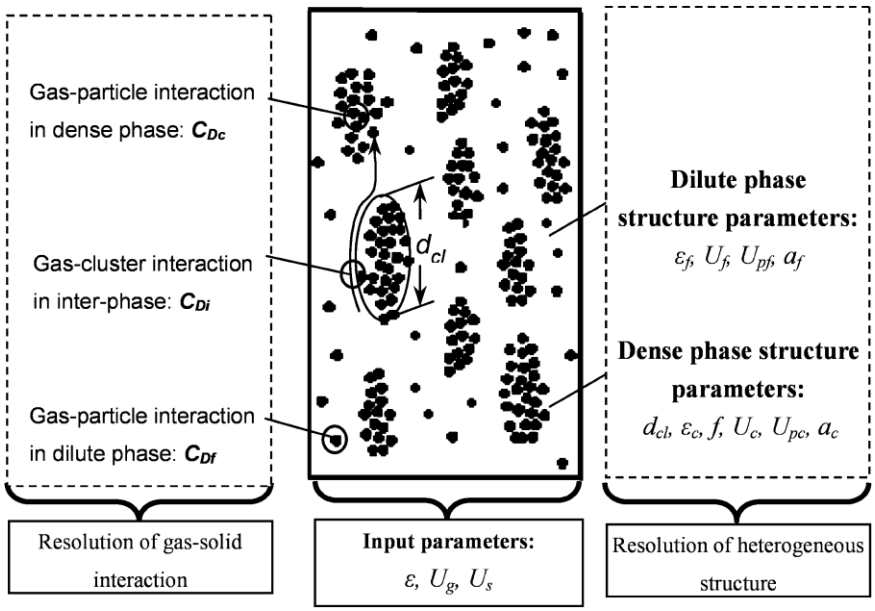

Figure 15. Multi-scale resolution of structure and gas-solid interaction in the EMMS model [159].

2.2.2.2.1 Analytical equations

Force balance for the dense phase:

$$\frac{3}{4}C_{dc}\frac{f(1-\varepsilon_c)}{d_p}\rho_g U_{sc}^2+\frac{3}{4}C_{di}\frac{f}{d_{cl}}\rho_g U_{si}^2=f(1-\varepsilon_c)(\rho_s-\rho_g)(g+a_c) \tag{34}$$

Force balance for the dilute phase:

$$\frac{3}{4}C_{df}\frac{(1-f)(1-\varepsilon_f)}{d_p}\rho_g U_{sf}^2=(1-f)(1-\varepsilon_f)(\rho_s-\rho_g)(g+a_f) \tag{35}$$

Pressure drop balance between the clusters and the dilute phase:

$$C_{df}\frac{(1-\varepsilon_f)}{d_p}\rho_g U_{sf}^2+\frac{f}{1-f}C_{di}\frac{\rho_g U_{si}^2}{d_{cl}}=C_{dc}\frac{(1-\varepsilon_c)}{d_p}\rho_g U_{sc}^2 \tag{36}$$

Fluid mass conservation equation:

$$U_g=fU_c+(1-f)U_f \tag{37}$$

Particle mass conservation equation:

$$U_s=fU_{pc}+(1-f)U_{pf} \tag{38}$$

Mean voidage definition:

$$\varepsilon_g=f\varepsilon_c+(1-f)\varepsilon_f \tag{39}$$

$$\varepsilon_g+\varepsilon_s=1 \tag{40}$$

2.2.2.2.2 Semi-empirical/empirical correlations

The cluster size is an important parameter in the EMMS model that strongly affects the value of the heterogeneity index H_d. However, it cannot be easily measured as clusters are spatio-temporal structures [122] that breakup, coalesce and behave differently in the core and annulus region [143]. According to the literature, near wall moving particles tend to coalesce and fall in wave-like patterns, which subsequently break up to form clusters of smaller size when entering the core region. The latter mechanism is enhanced, due to the high slip gas velocities exhibiting in the riser core zone. The variables involved in the EMMS model are expressed per control volume in the form of dimensionless variables, an issue that is very useful since the heterogeneity index should not depend on the size of the control volume. However, concerning the clusters diameter, most arithmetical correlations calculate this value either as an absolute dimensional number (m) or in best case as the ratio of clusters diameter to particle diameter. Additionally, such correlations neglect the effect of the macro-scale on the size of clusters. A good example of that is the neglect of a limitation that the riser diameter poses to the growth of the clusters.

In this light and to account for such type of limitations, the currently proposed EMMS model combines two cluster correlations, the one given by [143] and the other developed based on the work of [132]. The final cluster diameter, d_{cl}, is calculated as the smaller between the two expressions (41) and (42) given below.

The correlation for the cluster's diameter proposed by [132] is the following:

$$d_{cl,Li\&Kwauk} = \frac{d_p\left[U_s/(1-\varepsilon_{max}) - (U_{mf} + \varepsilon_{mf}U_s/(1-\varepsilon_{mf}))\right]g}{N_{st}\rho_s/(\rho_s-\rho_g) - \left(U_{mf} + \varepsilon_{mf}U_s/(1-\varepsilon_{mf})\right)g} \quad (41)$$

This expression incorporates important parameters that govern the flow, such as a) the energy which is consumed for the suspension and transport of the solid particles N_{st}, b) the superficial solids velocity U_s, $m \cdot s^{-1}$ and c) the minimum fluidization velocity U_{mf}, $m \cdot s^{-1}$. This has been used with success in many CFD simulations [142, 160]. However, its main drawback lies on the fact that it does not take into account the geometrical restriction that the riser diameter poses on the clusters size. Such a geometric restriction is considered in the following correlation.

Following the work of [143] a correlation for the cluster diameter is proposed:

$$d_{cl,Subbarao} = D_v\left(\frac{f}{1-f}\right)^{1/2} + d_p \quad (42)$$

, where f is the cluster volume fraction and d_p is the particle diameter. D_V is the void size in the bed. In this Thesis, the ratio of cluster to void surface in a cross section is preferred over the respective volumetric ratio. Therefore, the 1/2 and not the 1/3 exponent is used in the right hand side of equation (42). This reasoning is adopted since the limitation that the diameter of the riser poses to the cluster diameter is correlated with their area coverage at a cross-section, and not with their volume.

The void size in the bed, D_V, is expressed as:

$$D_V = \frac{2u_t^2}{g}\left(1 + \frac{u_t^2}{u_{sr}^2}\right)^{-1} \quad (43)$$

Equation (43) is the result of the combination of two asymptotic equations for the void size. The first equation takes into account the formation of voids with a rise velocity equal to the terminal velocity of a single particle and the second one is for cases where the void size expands so that it is almost equal to the column diameter (slugging flow), and the rise velocity is almost equal to the slug velocity. D_t is the column diameter and is related to the slug velocity as:

$$u_{sr} = 0.35(gD_t)^{1/2} \tag{44}$$

The terminal velocity of a single free-falling particle is taken from the work of [52], for particles with a sphericity in the range of $0.5<\varphi_s<1$:

$$u_t = u_t^* \left[\frac{\mu_g(\rho_s - \rho_g)g}{\rho_g^2}\right]^{1/3} \tag{45}$$

, where u_t^* is a dimensionless gas velocity and d_p^* is the dimensionless particle size given by the following correlations respectively:

$$u_t^* = \left[\frac{18}{(d_p^*)^2} + \frac{2.335 - 1.744\varphi_s}{(d_p^*)^{0.5}}\right]^{-1} \tag{46}$$

$$d_p^* = d_p \left[\frac{\rho_g(\rho_s - \rho_g)g}{\mu_g^2}\right]^{\frac{1}{3}} = Ar^{\frac{1}{3}} \tag{47}$$

Subbarao in his work follows the simplification that $1 - \varepsilon_g = f(\varepsilon_f - \varepsilon_c)$ taking $\varepsilon_f = 1$. However, the voidage in the dilute phase should not exceed the value of 0.9997, an assumption that has been followed in many works [136, 160, 161]. Thus, this Subbarao's simplification is not adopted in the present Thesis.

Concluding, the value of the modified cluster diameter is taken as:

$$d_{cl} = Min(d_{cl,Subbarao}, d_{cl,Li\&Kwauk}) \tag{48}$$

For the voidage in the dense phase, ε_c, a correlation proposed by [122] is adopted:

$$\varepsilon_c = \varepsilon_g - n\sigma_\varepsilon \tag{49}$$

, where n is taken equal to 3, as in the work of [162]. The latter parameter and subsequently ε_c affects the effective density of the dense phase, however there is not an analytical expression for its value. In other works a value of n=1 [163], [164], n=2 [165-167], or n=2.5 [138] is proposed.

The dense phase voidage standard deviation σ_ε used in equation (49) is calculated by adopting the Poisson distribution [122],

$$\sigma_\varepsilon = \varepsilon_s \sqrt{\frac{(1-\varepsilon_s)^4}{1 + 4\varepsilon_s + 4\varepsilon_s^2 - 4\varepsilon_s^3 + \varepsilon_s^4}} \tag{50}$$

Minimization of the energy needed for the solid particles suspension and transportation is used as a stability condition for the EMMS model. This energy is the sum of individual phases and their interface energies:

$$N_{st} = \frac{1}{(1-\varepsilon_g)\rho_s}\left[m_f F_f U_f + m_c F_c U_c + m_i F_i U_f (1-f)\right] \rightarrow min \quad (51)$$

2.2.2.2.3 Constraints and closure equations

The constraints for the acceleration and the gas voidage in both the dilute and the dense phase are:

$$a_{f,} a_c > 0 \quad (52)$$

$$\varepsilon_g < \varepsilon_f \leq \varepsilon_{max} \quad \text{and} \quad \varepsilon_{mf} \leq \varepsilon_c < \varepsilon_g \quad (53)$$

The constraints in (53) have been applied also in other works [160], [161], [168] and [136]. Constraints concerning the superficial slip velocity for the dilute, dense and inter-phase are as follows:

$$U_{sf}, U_{sc}, U_{si} > 0 \quad (54)$$

A constraint for the superficial velocity in the dilute phase is applied as in the work of [136]. This constraint is set to describe the fact that the velocity of a free-moving particle in the dilute phase cannot exceed the value of the particle's terminal velocity.

$$U_{sf}/\varepsilon_f > U_t \quad (55)$$

Finally, some closure equations for the dense, dilute and inter-phase, which are necessary for the solution of the model are summarized in **Table 4**. These closure terms, except for the effective-drag coefficient in the inter-phase, are the same as in the works of [122, 136].

Table 4. EMMS closure equations.

	Dense Phase	**Dilute Phase**	**Inter-phase**
Effective drag coefficient	$C_{dc} = C_{d0c}\varepsilon_c^{-4.8}$	$C_{df} = C_{d0f}\varepsilon_f^{-4.8}$	$C_{di} = C_{d0i}(1-f)^{-4.65}$
Standard drag coefficient	$C_{d0c} = \frac{24}{Re_c} + \frac{3.6}{Re_c^{0.313}}$	$C_{d0f} = \frac{24}{Re_f} + \frac{3.6}{Re_f^{0.313}}$	C_{d0i}: *Correlation* (56)
Characteristic Reynolds number	$Re_c = \frac{\rho_g d_p U_{sc}}{\mu_g}$	$Re_f = \frac{\rho_g d_p U_{sf}}{\mu_g}$	Re_{0i}: *Not used in this model*
Superficial slip velocity	$U_{sc} = U_c - \frac{\varepsilon_c U_{pc}}{1-\varepsilon_c}$	$U_{sf} = U_f - \frac{\varepsilon_f U_{pf}}{1-\varepsilon_f}$	$U_{si} = U_f - \frac{\varepsilon_f U_{pc}}{1-\varepsilon_c}(1-f)$
Drag force per particle/ cluster	$F_c = C_{dc}\frac{\pi d_p^2}{4}\frac{\rho_g}{2}U_{sc}^2$	$F_f = C_{df}\frac{\pi d_p^2}{4}\frac{\rho_g}{2}U_{sf}^2$	$F_i = C_{di}\frac{\pi d_{cl}^2}{4}\frac{\rho_g^*}{2}U_{si}^2$
Numbers of particles or clusters in unit volume	$m_c = \frac{f(1-\varepsilon_c)}{\pi\, d_p^3/6}$	$m_f = \frac{(1-f)(1-\varepsilon_f)}{\pi\, d_p^3/6}$	$m_i = \frac{f}{\pi\, d_{cl}^3/6}$

Regarding the inter-phase effective drag coefficient a correlation by the work of [143] is implemented:

$$C_{d0i} = f_i \frac{432}{Ar_{cl}} \quad \text{for } 0 < Ar_{cl} < 36$$
$$= f_i \frac{56.9}{Ar_{cl}^{0.4242}} \quad \text{for } 36 < Ar_{cl} < 83750 \tag{56}$$
$$= 0.44 f_i \quad \text{for } 83750 < Ar_{cl}$$

Ar_{cl} is the Archimedes number for clusters given by the following expression:

$$Ar_{cl} = \frac{d_{cl}^3 g(\rho_s^* - \rho_g^*)\rho_g^*}{{\mu_g^*}^2} \tag{57}$$

, where ρ_g^*, ρ_s^* and μ_g^* are the meso-scale fluid and solid densities and the gas viscosity that are given correspondingly by the following equations [160]:

$$\rho_g^* = \varepsilon_f \rho_g + (1 - \varepsilon_f)\rho_s \tag{58}$$

$$\rho_s^* = \varepsilon_c \rho_g + (1 - \varepsilon_c)\rho_s \tag{59}$$

$$\mu_g^* = \mu_g(1 + 2.5(1 - \varepsilon_f)) \tag{60}$$

Correlation (56) is considered as more suitable than the one proposed in the works of [122, 169], in as much as it takes into account both the permeability of clusters for the calculation of the drag coefficient and the effect of the Archimedes number. The permeability of clusters is incorporated in the model through the f_i parameter, which is chosen with a small degree of arbitrariness. In the work of Subbarao a value of 3 is chosen [143]. In the present study only the effect of Archimedes number is taken into consideration (f_i=1).

This set of equations is solved through a custom-built FORTRAN code for specific values of the gas-solid slip velocity u_{slip} (0.5, 1, 2, 3, 4, 5) and for discrete values of the gas volume fraction ε_g within the range of ε_{mf} to ε_{max}. The calculated heterogeneity index is interpolated using polynomials for three areas of ε_g; a) ε_g= [0.65, 0.82], b) ε_g= [0.82, 0.96], and c) ε_g= [0.96, ε_{max}]. The resulted polynomials are incorporated to the TFM model through UDFs and they have the following general form:

$$H_d = a_6\varepsilon_g^6 + a_5\varepsilon_g^5 + a_4\varepsilon_g^4 + a_3\varepsilon_g^3 + a_2\varepsilon_g^2 + a_1\varepsilon_g + a_0 \tag{61}$$

It is underlined that the interpolation procedure is only followed for the specific slip velocities that were chosen to solve the EMMS model. For other values of the slip velocity a linear interpolation method is adopted, using the expressions below:

$$H_d(u_{slip}) = (1 - x)H_d({u_{slip}}^+) + xH_d({u_{slip}}^-) \tag{62}$$

, where $x = \frac{{u_{slip}}^+ - u_{slip}}{{u_{slip}}^+ - {u_{slip}}^-}$ (63)

At this point, it should be noted that for a specific set of equations the value of the heterogeneity index is only dependent on the slip velocity, between the gas and the solid phase, and the gas voidage ε_g:

$$H_d = F(u_{slip}, \varepsilon_g) \tag{64}$$

This concept has also been adopted in the work of [136] and [107]. A detailed description of the custom-built FORTRAN code algorithm can be found in **Figure 16**. Finally, any additional information on the EMMS model can be found in [136], [122]. It should be underlined that the results of the EMMS scheme presented for each simulated case correspond to the operating conditions of the specific unit modeled.

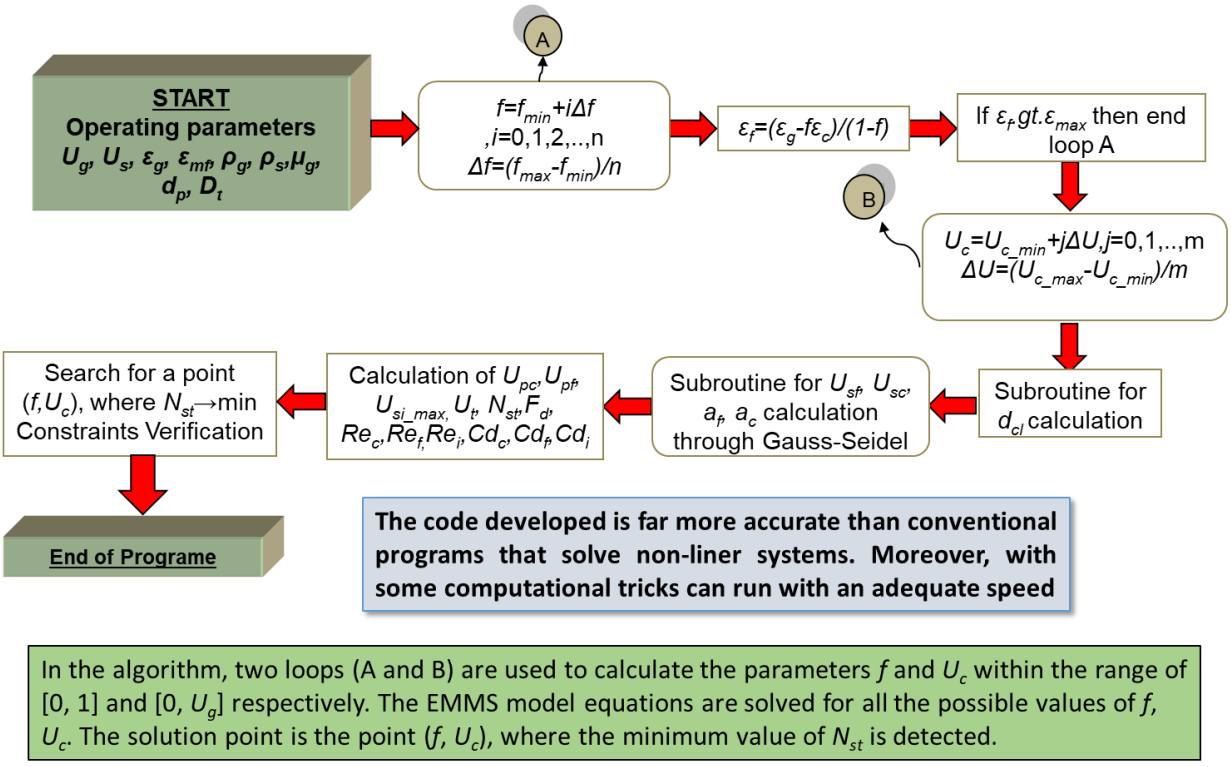

Figure 16. Solution algorithm of EMMS model.

2.2.2.3 Syamlal O'Brien symmetric model

If the number of solid phases simulated is more than one, as for instance in the cases of explicitly simulating the full PSD of a solid sample, or the bed inventory consists of more than one solid materials, then a solid-solid drag force model should be included into the CFD model. According to Syamlal Obrien symmetric model [170] the momentum exchange coefficient between two solid phases (denoted as *s1* and *s2* in the present Thesis) is given by the following expression**:**

$$\beta_{s1s2} = \frac{3(1+e_{s1s2})\frac{\pi}{2}\varepsilon_{s1}\rho_{s1}\varepsilon_{s2}\rho_{s2}(d_{ps1}+d_{ps2})^2 g_{0s1,s2}}{2\pi(\rho_{s1}d_{ps1}^3+\rho_{s2}d_{ps2}^3)}|\overrightarrow{u_{s1}}-\overrightarrow{u_{s2}}| \tag{65}$$

It is stressed out that the solid-solid exchange coefficient could have a meso-scale dependence likewise to the gas-sorbent momentum exchange coefficient, which is calculated according to the sub-grid EMMS scheme. To formulate such a model, one should calculate the percentage of the different solid phases within the dilute and the dense phase and the respective interaction, at sub-grid level. However, it is neglected in this Thesis, as there is not a suitable model for that in the literature to the best of the author's knowledge.

2.2.3 Reactive multi-phase flows

The reactors modelled in the present Thesis are a CFB carbonator, an indirectly heated BFB calciner and a BFB oxy-fired calciner. It the first two reactors, carbonation of the regenerated lime and calcination of limestone occur, respectively. In the case of the oxy-fired calciner, where the heat for the limestone calcination is provided through the oxy-combustion of a solid fuel (coal in the specific case studied), a series of homogeneous and heterogeneous reactions occur simultaneously.

For the accurate simulation of the coal conversion mechanisms, three heterogeneous reactions, i.e., evaporation, devolatilization, char combustion, and two homogeneous reactions, i.e. volatiles and CO combustion, are modelled. The heterogeneous reaction rates are incorporated into ANSYS through custom-built UDFs, while the homogeneous reactions are already available in the ANSYS Fluent Platform.

The heat (ΔH) of each chemical reaction described below is calculated as:

$$\Delta H^o_{reaction} = \sum \Delta H^o_f(products) - \sum \Delta H^o_f(reactants) \quad (66)$$

, where $\Delta H^o_f(products)$ is the sum of the standard state enthalpies of the products in a chemical reaction and $\Delta H^o_f(reactants)$ the sum of the standard state enthalpies of the reactants. The standard state enthalpies of the different species that take part in the simulated chemical reactions are presented in **Table 5**.

Table 5. Species Standard State enthalpies.

Specie	ΔH^o_f (kJ·kmol^{-1})		Specie	ΔH^o_f (kJ·kmol^{-1})
CaO	-6.351003e+05		***O_2***	0
$CaCO_3$	-1.206934e+06		***CO***	-1.105396e+05
Char	-0.10127		***CO_2***	-3.935324e+05
Vol$_{(f)}$	-5.165e+05		***Vol$_{(g)}$***	-5.165e+05
Ash	-0.10127		***N_2***	0
$H_2O_{(f)}$	-2.858412e+05		***SO_2***	-2.968612e+05
$H_2O_{(g)}$	-2.418379e+05			

2.2.3.1 Sorbent reactions

2.2.3.1.1 Carbonation

The carbonation of calcium oxide (CaO) to calcium carbonate ($CaCO_3$) is an exothermic heterogeneous reaction occurring approximately at a temperature 600-700 ^oC and is described by the following equation:

$$CaO_{(s)} + CO_{2(g)} \rightarrow CaCO_{3(s)} \quad (67)$$

The rate of this reaction equals to [171], [172]:

$$RR_{carb} = N_{Ca} \frac{k_s S_0}{1 - e_0} (X_{max} - X_{carb})^{2/3} \left(C_{CO_2} - C_{CO_2,eq}\right) \quad (68)$$

, where k_s (m^4·mol^{-1}·s^{-1}) is the rate constant for surface carbonation, S_0 (m^2/m^3) is the initial surface area of CaO per unit volume of solid CaO and e_0 (-) is the particle porosity. These three parameters depend on the type of the limestone. The constants values are retrieved from the work of [173]. The value of the maximum

conversion X_{max} (mol %) is taken equal to 0.1 and is based on the measured sorbent activity in the DFB loop [174]. The X_{carb} (mol $CaCO_3$·mol^{-1} Ca) is the actual carbonation conversion and is calculated for each computational cell of the discretized domain. Concerning the last term in the right hand side of equation (68), C_{CO2} (mol·m^{-3}) is the concentration of CO_2 in the flue gas and is calculated locally in each cell as X_{carb}, while $C_{CO2,\,eq}$ is the equilibrium CO_2 concentration at the specific operating temperature of the reactor (T_{carb}). According to [171] the $C_{CO2,eq}$ is equal to:

$$C_{CO_2,eq} = \frac{1.462x10^{11}}{T_{carb}} \exp(\frac{-19130}{T_{carb}}) \quad (69)$$

2.2.3.1.2 Calcination

The calcination of $CaCO_3$ to CaO is an endothermic heterogeneous reaction described as:

$$CaCO_{3(s)} \rightarrow CaO_{(s)} + CO_{2(g)} \quad (70)$$

The model applied for the calculation of the calcination rate is based on Garcia-Labiano's approach [144]:

$$RR_{calc} = k_c S_e (1 - \theta_{CO_2})(1 - \frac{p_{CO_2}}{p_{eq}}) \quad (71)$$

In the above expression the assumption that S_e=S_0 has been followed for reasons of simplicity [75]. The parameter θ_{CO2} represents the fraction of active sites occupied by CO_2 given by an adsorption isotherm:

$$\theta_{CO_2} = c p_{CO_2}{}^{\frac{1}{2}} \quad \text{and} \quad c = c_0 e^{\frac{-E_a}{RT}} \quad (72)$$

The kinetic rate constant, k_c, and the isotherm adsorption constant, c, are calculated as follows:

$$k_c = k_0 e^{\frac{-E_c}{RT}} \quad (73)$$

The equilibrium decomposition pressure p_{eq} is calculated as:

$$p_{eq} = 4.137 \cdot 10^{12} e^{\frac{-20474}{T}} \quad (74)$$

The partial pressure of p_{CO_2} is calculated in each cell of the computational grid.

Table 6. Values for the calcination reaction parameters [144].

Parameter	**Value**	**Units**
k_0	$254 \cdot 10^{-3}$	kmol·m^{-2}·s^{-1}
E_c	131	kJ·mol^{-1}
c_0	$3.7 \cdot 10^{-7}$	Pa$^{-0.5}$
E_a	-90	kJ·mol^{-1}
S_0	$0.5 \cdot 10^{6}$	m^{-1}

The supplementary variables used for the calculation of the calcination rate are dependent on the sorbent material used. Their values presented in **Table 6** are retrieved through the literature [144], since there are no data available for the specific limestone used from any of the experimental campaigns used for validation of the CFD models of the current Thesis.

2.2.3.2 Coal combustion

2.2.3.2.1 Evaporation

The moisture evaporation is a heterogeneous reaction described by the following equation:

$$H_2O_{(f)} \rightarrow H_2O_{(g)} \tag{75}$$

When the fuel phase contains moisture and reaches the evaporation point, i.e. 100 °C, an evaporation rate is applied based on the classic model of a boiling droplet, for which the moisture content is supposed to form a liquid film around the particle itself, [175]. The rate is described by the following equation [176]:

$$RR_{evap} = \left(\frac{6m_{s2}}{\pi\rho_{s2}d_{ps2}^2}\right)\left(-\frac{\pi d_{ps2}^2}{MW_{H_2O}V_{cell}}Nu_{s2}\frac{k_{s2}}{c_{ps2}}ln\left(1+\frac{c_{ps2}(T_g-T_{s2})}{1-L_{H_2O}}\right)\right) \tag{76}$$

, where m_{s2} is the mass of fuel in a computational cell. Thus, the first term within brackets in the right hand side of the equation represents the number of fuel particles in the control volume.

The Nusselt number of fuel phase (denoted as s2) applied in the above equation is equal to:

$$Nu_{s2} = 2 + 0.5Re_{s2}{}^{0.5} \tag{77}$$

2.2.3.2.2 Devolatilization

Devolatilization is a non-reversible intermediate process of combustion given by the following equation:

$$Vol_{(f)} \rightarrow Vol_{(g)} \tag{78}$$

The characteristics of the devolatilization process are dependent on the type of fuel and operating conditions (temperature, heating rate and devolatilization atmosphere). However, due to lack of experimental data a reaction rate retrieved from the recent literature is applied [177]. One of the simplest approaches is the use of Arrhenius type expressions that correlate the rates of weight loss with temperature, i.e.

$$RR_{dev} = \frac{Y_{vol}\varepsilon_{s2}\rho_{s2}}{MW_{vol}}K_v e^{-E_v/(RT_{s2})} \tag{79}$$

, where K_v is the pre-exponential factor, E_v the activation energy and Y_{vol} and MW_{vol} the mass fraction and molecular weight of the volatiles in the fuel phase (denoted as s2), respectively. The values of the above parameters are retrieved from the work of [177] and are summarized in **Table 7**:

Table 7. Kinetic values for the devolatilization reaction rate.

Parameter	Value	Units
K_v	4.68e+10	s^{-1}
E_v	155.9e+3	$kJ \cdot kmol^{-1}$

2.2.3.2.3 Char combustion

Char oxidation is the slowest step of the combustion process, which includes a series of heterogeneous gas-solid reactions that lead to the production of both CO and CO_2 [178]. At high temperatures (>1100 °C) and

high O_2 percentage in the air, CO_2 is the most dominant product, whilst in low temperatures (600 ºC) CO is the dominant one. For the specific conditions simulated, where temperature lies in-between, one should calculate the ratio of CO/CO_2 produced as a function of temperature and set that using a more sophisticated model. However, in order to save computational cost, and for reasons of simplicity the char combustion is assumed to follow a shrinking core mechanism and take place in two steps, which are i) combustion of char into CO and ii) further oxidation of the CO into CO_2. Additionally, the water-gas-shift reaction is not of high importance for the specific oxy-fired conditions [179] and, thus, is not taken into account.

The char combustion towards CO is described by the following equation:

$$2C_{(f)} + O_{2(g)} \rightarrow 2CO_{(g)} \tag{80}$$

The reaction rate of char combustion into CO is taken by the work of [180], [181], [182]:

$$RR_{comb} = \frac{-6\varepsilon_{s2} p_{O_2} f_1}{d_{ps2}\left[\frac{1}{k_{fl}} + \frac{1}{k_a} + \frac{1}{k_r}\right]} \tag{81}$$

, where p_{O2} is the partial pressure of oxygen and f_1 is a factor calculated as:

$$f_1 = \frac{Y_C}{Y_C + 10^{-6}} \tag{82}$$

The latter factor is used in line with the work of [181], to allow for the rate equation to behave linearly for small values of the carbon mass fraction value Y_C. This allows to eliminate numerical instabilities that arise, when reactants mass fractions approach to zero. As a consequence, at values of Y_C equal to 10^{-4} a numerical error is introduced in the rate equal to 1%, which decreases for higher values of Y_C.

The shrinking core mechanism considers in physical terms, three resistances; i) external film diffusion, ii) diffusion through the ash layer and iii) reaction at the surface of the unreacted core.

The film resistance is given by:

$$k_{fl} = \frac{D_{O_2} Sh_{s2}}{d_{ps2} R_{O_2} T_{fl}} \tag{83}$$

, where D_{O2} is the O_2 diffusivity:

$$D_{O_2} = 4.26 \cdot 10^{-4} \left(\frac{T_g}{1800}\right)^{1.75} / P_g \tag{84}$$

, with P_g the absolute gas pressure in atm.

R_{O2} is the individual gas constant for oxygen:

$$R_{O_2} = \frac{R}{MW_{O_2}} \tag{85}$$

T_{fl} is the average film temperature, which is equal to:

$$T_{fl} = \frac{T_g + T_{s2}}{2} \tag{86}$$

The Sherwood number, Sh_{s2}, is taken as [183]:

$$Sh_{s2} = \left(7 - 10\varepsilon_g + 5\varepsilon_g^2\right)\left(1 + 0.7Re_{s2}^{0.2}Sc^{1/3}\right) + (1.33 - 2.4\varepsilon_g + 1.2\varepsilon_g^2)Re_{s2}^{0.7}Sc^{1/3} \tag{87}$$

The Schmidt number is defined as:

$$Sc = \frac{\mu_g}{\rho_g D_{O_2}} \tag{88}$$

The ash layer resistance is calculated as:

$$k_a = \frac{2r_{df}D_e}{(1-r_{df})d_{pf}R_{O_2}T_f} \tag{89}$$

, where r_{cp} is the ratio of core to particle diameter

$$r_{cp} = \frac{d_c}{d_{ps2}} \tag{90}$$

According to the work of [182] this ratio can be related to the carbon and ass mass fractions as:

$$r_{cp} = \left(\frac{Y_C Y_{ash}^0}{Y_C^0 Y_{ash}}\right)^{1/3} \tag{91}$$

, where Y_{ash}^0 and Y_C^0 are the initial value of the ash and carbon mass fractions.

D_e is an effective ash diffusivity given:

$$D_e = D_{O_2}\varepsilon_{ash}^{2.5} \tag{92}$$

The ash porosity is equal to [184]:

$$\varepsilon_{ash} = 0.25 + 0.75(1 - Y_{ash}^0) \tag{93}$$

Finally, the surface reaction resistance equal to [185]:

$$k_r = 23227r_{cp}^2 exp(-\frac{27000}{1.987T_{s2}}) \tag{94}$$

2.2.3.2.4 CO oxidation

The CO oxidation to CO_2 is a homogeneous volumetric reaction and is described by the following equation:

$$CO_{(g)} + 0.5O_{2(g)} + H_2O_{(g)} \rightarrow CO_{2(g)} + H_2O_{(g)} \quad (95)$$

The rate of the reaction is calculated according to the Finite-Rate/Eddy-Dissipation model [186], which is dependent both on an Arrhenius kinetic rate and on the turbulence fluctuations. More specifically, in each cell of the discretized domain both the kinetic rate and the turbulent (mixing) rate are calculated, taking as rate of the reaction the minimum of them.

The turbulent kinetic rate is proportional to the ratio of the turbulent dissipation rate ε_t to the turbulent kinetic energy k_t and is calculated according as the minimum of the following two values:

$$RR_{i,r} = v'_{i,r} MW_i A \rho_g \frac{\varepsilon_t}{k_t} min_R \left[\frac{Y_R}{v'_{R,r} MW_R} \right] \quad (96)$$

$$RR_{i,r} = v'_{i,r} MW_i AB \rho_g \frac{\varepsilon_t}{k_t} \frac{\sum_P Y_P}{\sum_j^N v''_{j,r} MW_j} \quad (97)$$

, where *A* and *B* are empirical constants equal to 4.0 and 0.5, respectively [186].

Y_P and Y_R is the mass fraction of any product species and reactant respectively, $M_{W,R}$ the molecular weight of a particular reactant R, $M_{W,i}$ the molecular weight of any product species i and $M_{W,j}$ the molecular weight of any product species j. Finally, $v'_{i,r}$is the stoichiometric coefficient for species i in reaction (equal to 1 for CO and 0.5 for O_2) and $v''_{j,r}$ the stoichiometric coefficient for product j in reaction (equal to 1 for CO_2).

The kinetic rate of CO oxidation, is calculated according to the following expression:

$$RR_{CO} = k_{f,r} [C_{CO}] \cdot [C_{O_2}]^{0.25} \cdot [C_{H_2O}]^{0.5} \quad (98)$$

It should be noted that the catalytic effect of steam is taken into account in CO oxidation by applying a rate exponent for the steam specie equal to 0.5 [187].

The forward rate constant $k_{f,r}$ for a reaction r is calculated according to Arrhenius law:

$$k_{f,r} = A_r e^{-E_r/RT} \quad (99)$$

, where A_r is pre-exponential factor and E_r the activation energy. Their values are presented in **Table 8**:

Table 8. Kinetic values for the reaction rate of CO oxidation [187].

Parameter	Value	Units
$\boldsymbol{A_r}$	2.239e+12	$kg \cdot m^{-3} \cdot s^{-1}$
$\boldsymbol{E_r}$	1.7e+08	$J \cdot kmol^{-1}$

2.2.3.2.5 Volatiles combustion

The volatiles combustion is a homogeneous non-reversible reaction. The volatiles ($Vol_{(g)}$) in the specific Thesis are described by the $C_mH_nS_pO_qN_r$ chemical formula and are oxidized by the general form:

$$C_m H_n S_p O_q N_r + \left(\frac{m}{2} + \frac{n}{4} + p = \frac{q}{2}\right) O_2 \rightarrow mCO + \left(\frac{n}{2}\right) H_2 O + \left(\frac{r}{2}\right) N_2 + pSO_2 \quad (100)$$

The stoichiometric coefficients in the above equation are derived by following some simple calculations based on the ultimate and proximate analysis of the specific fuel given and assuming that char represents the actual pure carbon content of the fuel. Any chemical bond of carbon with additional species as those of N, S, H and/or O are represented by the chemical composition of volatiles introduced in the numerical model. More specifically, the *m, n, p, q, r* fractions of the C, H, S, O, N chemical components can be easily defined by calculating the weight percentage of each chemical component in the volatiles matter and dividing it with its atomic mass.

It should be stressed out that according to experiments the devolatilized gases contain a large proportion of CO_2, as well [188], and the simulation approach undertaken maybe underestimates locally the CO_2 gas content since volatiles in the models should be firstly oxidized to produce CO_2. However, this oxidation is quite fast and the simplified approach follower in order to save computational cost is assumed to have negligible effect on results accuracy.

The rate of the reaction is calculated according to the Finite-Rate/Eddy-Dissipation model [186], already presented in the CO oxidation section. The rate exponent of gas-volatiles and O_2 are set to 0.2 and 1.3, respectively. The rate exponent of the product species are set all equal to zero.

Thus, the kinetic rate of volatiles combustion is set equal to:

$$RR_{vol(g)} = k_{f,r} \left[C_{vol(g)}\right]^{0.2} \cdot [C_{O_2}]^{1.3} \quad (101)$$

Finally, the values of the pre-exponential factor and activation energy of the volatiles combustion kinetic rate are presented in **Table Table 9**.

Table 9. Kinetic values for the reaction rate of volatiles combustion [187].

Parameter	Value	Units
A_r	2.119e+11	$kg \cdot m^{-3} \cdot s^{-1}$
E_r	2.027e+08	$J \cdot kmol^{-1}$

2.2.4 Heat transfer at high-temperatures (radiation phenomena)

The heat transfer mechanisms in a fluidized bed system –operating at high/ultra-high temperatures- are radiation (particle-wall, particle-particle, and fluid-particle), convective (particle- fluid), and conduction (particle-particle or particle-wall).

2.2.4.1 Conservation equation

Conservation of energy

For each phase included into the model a separate enthalpy equation is solved. The general case of solving a three-phase flow is presented in this Sub-section. However, in the case of a two-phase flow only the equation for the gas and solid phase 1 are included into the model.

Gas phase

$$\frac{\partial}{\partial t}\left(\varepsilon_g \rho_g h_g\right) + \nabla \cdot \left(\varepsilon_g \rho_g \overrightarrow{u_g} h_g\right) = \varepsilon_g \frac{dp_g}{dt} + \overline{\overline{\tau_g}} : \nabla \overrightarrow{u_g} - \nabla \cdot \overrightarrow{q_g} + S_g + \dot{Q}_{s1g} + \dot{Q}_{s2g} \quad (102)$$

Solid phase 1

$$\frac{\partial}{\partial t}\left(\varepsilon_{s1} \rho_{s1} h_{s1}\right) + \nabla \cdot \left(\varepsilon_{s1} \rho_{s1} \overrightarrow{u_{s1}} h_{s1}\right) = \varepsilon_{s1} \frac{dp_{s1}}{dt} + \overline{\overline{\tau_{s1}}} : \nabla \overrightarrow{u_{s1}} - \nabla \cdot \overrightarrow{q_{s1}} + S_{s1} - \dot{Q}_{s1g} - \dot{Q}_{s1s2} \quad (103)$$

Solid phase 2

$$\frac{\partial}{\partial t}\left(\varepsilon_{s2} \rho_{s2} h_{s2}\right) + \nabla \cdot \left(\varepsilon_{s2} \rho_{s2} \overrightarrow{u_{s2}} h_{s2}\right) = \varepsilon_{s2} \frac{dp_{s2}}{dt} + \overline{\overline{\tau_{s2}}} : \nabla \overrightarrow{u_{s2}} - \nabla \cdot \overrightarrow{q_{s2}} + S_{s2} - \dot{Q}_{s2g} - \dot{Q}_{s2s1} \quad (104)$$

, where h_g, h_{s1} and h_{s2} are the enthalpies of gas, sorbent and fuel phase, respectively, and S_g, S_{s1} and S_{s2} are source terms that include sources of enthalpy, due to the homogeneous and heterogeneous reactions, and, radiative sources. Thus, each heat source term of the q^{th} phase is equal to:

, where $\Delta H_{Homogeneous}$ is the heat due to a homogeneous reaction and $\Delta H_{Heterogeneous}$ the heat, due to a heterogeneous reaction. The negative sign in front of $\Delta H_{Homogeneous}$ is inserted, because the homogeneous reactions taking part in the specific rector are exothermic.

The volumetric rate of energy transfer between two phases,$\dot{Q}$, is calculated as a function of the temperature difference between the two phases and the interfacial area, A_i.

As concerns the energy transfer between the gas and each solid phase the parameter $\dot{Q}$ is calculated as being equal to:

$$\dot{Q}_{gq} = h_{gq}^{e}\left(T_g - T_q\right), q = s1, s2 \quad (105)$$

, where h_{gq}^{e} is the volumetric heat exchange coefficient between the gas and the q^{th} solid phase. The heat exchange coefficient is given by the following expression:

$$h_{gi}^{e} = A_i h_{gi}^{q}\ h_{gq}^{e} = A_i h_{gq}^{q} \quad (106)$$

, where A_i is the specific interfacial exchange area and h_{gq}^{q} is the heat transfer coefficient between the two phases equal to:

$$h_{gq}^{q} = \frac{k_g Nu_{pq}}{d_{pq}} \quad (107)$$

Thus, the heat exchange coefficient is equal to:

$$h_{gq}^{e} = \frac{6 k_g \varepsilon_g \varepsilon_q Nu_{pq}}{d^2{}_{pq}} \quad (108)$$

, where k_g is the thermal conductivity of the gas phase and Nu_{pq} is the Nusselt number of the qth solid phase.

For the calculation of the Nusselt number, a model developed by Gunn [183] is applied. This model is already available in the Ansys Fluent platform for the sorbent-gas interaction.

$$Nu_{pq} = \left(7 - 10\,\varepsilon_g + 5\,\varepsilon_g^2\right)\left(1 + 0.7Re_q^{0.2}Pr^{1/3}\right) + (1.33 - 2.4\varepsilon_g + 1.2\varepsilon_g^2)Re_q^{0.7}Pr^{1/3} \quad (109)$$

2.2.4.2 Inclusion of radiation model

In the current Thesis, the P1 model [189, 190] is used for the simulation of radiative heat transfer inside the FB reactors. The following equation is solved when the P1 model is enabled in Fluent solver to calculate the local radiation intensity:

$$-\nabla \cdot q_r = aG - 4an^2\sigma T^4 \quad (110)$$

, where G is the incident radiation, T the temperature at each computational cell, σ the Stefan-Boltzmann constant, α the absorption coefficient of the cell and n the cell refractive index.
The transport equation of the incident radiation is:

$$\nabla \cdot (\Gamma \nabla G) - aG + 4an^2\sigma T^4 = 0 \quad (111)$$

In the above equation the parameter, Γ is defined as follows:

$$\Gamma = \frac{1}{3(\alpha + \sigma_s)} \quad (112)$$

The absorption a and scattering coefficient σ_s of the particles can be calculated as follows [191, 192]:

$$a = \varepsilon_s \frac{3}{2}\frac{e_p}{d_p} \quad (113)$$

$$\sigma = \varepsilon_s \frac{3}{2}\frac{(1 - e_p)}{d_p}. \quad (114)$$

, where ε_s is the volume fraction of particles at each computational cell and e_p the particles emissivity.

In the absence of measured data concerning the radiative properties of the particles, e_p is set at 0.9 (approximate values for sand and limestone particles particles).

Regarding the gaseous mixture, the absorption coefficient is given from the weighted-sum-of-gray-gases model (WSGGM), applying a cell-based computation of the mean beam length, while the scattering is neglected, since gases in general do not scatter much radiation [143], especially for the applications simulated in the current Thesis.

2.2.4.3 Heat transfer between fluidized bed and a surface

The overall heat transfer coefficient, h [$W \cdot m^{-2} \cdot K^{-1}$] between a fluidized bed of particles and a surface (i.e. wall, immersed tubes etc.) is defined as [52]:

$$q = A_w h \Delta T \quad 115)$$

, where q is the heat transfer rate [W], A_W is the heat exchange area and ΔT is the temperature difference between the bed and heat transfer area.

The heat transfer between a surface, such as heat pipes, and a gas-solid fluidized bed is a complex phenomenon dependent on several design and operating variables. Some of these can be summarized in the following **Table 10**.

Table 10. Summary of operating properties/design specifications needed in a heat transfer process involving a FB with heat pipes [193].

Operating properties	
Properties of the fluid	ρ, μ, cp, k, α, σ
Properties of the granular solid material	d_p, ρ_s, c_p, k_s, φ_s, α, e_p
Fluidization conditions	U0, ε
Bed properties	H_{bed}, m_{solids}
Design specifications	
Geometric variables of the FB	D_t, L_t
Geometric variables of the heat transfer surface	*D, A, arrangement*

2.3 Phase change problems

Advanced numerical tools capable of modelling UHT-LHTES systems are necessary to move beyond the state-of-the-art LHTES systems, which are limited to 767 ^{o}C [194]. Before UHT-LHTES systems are considered as a solution for commercial-scale CSP plants and other solar technologies, further research is required to understand the complex heat transfer mechanisms occurring at such demanding temperatures.

Solidification-melting problems are part of a wide category of heat transfer problems involving phase-change, such as casting processes, production of alloys of improved properties and energy storage [195]. Such problems are accompanied by a phase transformation of a medium and by either absorption or release of thermal energy in an interface area (phase-change front). The dominant mechanism of energy absorption or release is usually conduction or convection, whilst at high or ultra-high temperatures, radiation can also play a significant role. Systems undergoing solid-liquid phase-change share a common feature: two phases of different thermophysical properties separated by the interface area, which is moving as the phase-change proceeds. This moving front results in a generation of a local flow near the interface and a negligible flow in the bulk of the melt, away from the boundary. Due to this moving boundary not known a priori, such problems are generally non-linear and, thus, more difficult to solve with respect to single-phase problems [196]. This poses significant theoretical difficulties that generally requires a numerical solution.

During phase change, there are different phenomena that affect the PCM melting/solidification rate and subsequently the methodology that should be followed. These are 1) buoyancy-driven natural convection, 2) PCM volumetric change, 3) dendrites formation, 4) moving solid-liquid front and 5) effect of radiation at high temperatures. Furthermore, several additional factors must be taken into account, such as lateral heat losses, container shape, and mechanical properties and reactivity between the involved materials. These factors can become more or less important depending on the scale of the system. PCM are either packaged in specially designed containers, such as shell-in-tube or radial-finned tubes, with or without a presence of a HTF, or encapsulated as capsules at macro (size>1 mm) [197, 198], micro (size ~1–1000 μm) [199, 200] and nano scale [201, 202]. Evidently, solid–liquid phase change problems vary over multiple scales, but for UHT-LHTES systems, a macro-level modelling is adequate.

A successful study of the fluid flow in a two-phase heat transfer problem depends upon the capability of the developed models to accurately and efficiently represent the flow mechanisms for each phase and their interactions. In three-phase systems, e.g. PCM (solid/liquid) and inert gas inside a vessel, the complexity of the used algorithms increases dramatically. Analytical solutions of phase change problems can be subject to several simplifications. They are usually based on one-dimensional (1D) analysis, they do not include convection mechanisms, and consider constant PCM thermophysical properties. Such simplifications make any attempt for a thorough analysis incomplete; however, they are usually unavoidable. On the other hand, numerical models can simulate complex phenomena occurring during phase-change at different scales. This has resulted in an increasing interest for numerical models to describe a LHTES system behavior.

In terms of numerical modelling, there is a wide variety of methodologies able to study solid-liquid phase change. Those include approaches based on enthalpy, effective heat capacity, front tracking, adaptive grid etc. However, to accurately study a system in question, the specific numerical approach should be chosen carefully. This requires a solid knowledge about the different phenomena occurring during phase-change. The aim of this Section is to provide a comprehensive overview of the numerical models that have been developed so far for the simulation of the solidification-melting process, address the challenges that are involved at ultra-high temperatures, and, give a briefing on the models used in the current Thesis.

2.3.1 Moving boundary problem: Stefan problem

A Stefan problem is a moving boundary problem. In the context of solidification/melting problems, other terminologies for the moving boundary are the free boundary, phase-change boundary, melting front, freezing front or phase-change front [203], [204]. In its simplest formulation, a Stefan problem is a linear 1D problem, where conduction is the predominant heat transfer mechanism. Since convection is neglected, there is no need to solve Navier-Stokes (N-S) equations for the fluid flow motion.

The governing energy equation, which is solved separately for the solid and liquid phases, is the following:

$$\rho_i c_{p_i} \frac{\partial T_i}{\partial t} = \nabla \cdot (k_i \nabla T_i) \qquad i\text{=liquid, solid phase} \tag{116}$$

In eq. (116) the specific heat capacity, c_p, the thermal conductivity, k, and the density ρ, are assumed constant during the phase-change.

The general form of the heat balance on the solid-liquid interface, i.e. the Stefan condition, is as follows:

$$k_s \nabla T_s \cdot \boldsymbol{n} - k_l \nabla T_l \cdot \boldsymbol{n} = \rho L \boldsymbol{v} \cdot \boldsymbol{n} \tag{117}$$

, where n and v are the unit normal and velocity vector of the moving interface and L the latent heat per unit mass. This equation assumes that no additional heat sources/sinks are present at the interface.

In 1D form, the Stefan condition is defined as follows:

$$k_s \frac{\partial T_s}{\partial x} - k_l \frac{\partial T_l}{\partial x} = \rho L v \tag{118}$$

2.3.1.1 Non-linear conditions in a Stefan problem

Several phenomena induce non-linear characteristics in the Stefan problem: (i) variation of the PCM thermophysical properties with temperature and space, (ii) presence of a heat source/sink on the moving front and (iii) spatial and temporal temperature variation at the front [204]. The second condition entails that there will not be a sharp change between solid-liquid phases, but rather a temperature range, a "mushy region". Numerical treatment of this case will be analyzed in the following sub-sections.

2.3.1.2 Density variation and natural convection

The assumption of a conduction-dominated problem is a rough simplification. In reality, natural convection in the molten PCM effects the propagation and the shape of the moving boundary, especially during melting process [205] [40, 206-209]. Gau and Viskanta [210], have proven through experiments that natural convection affects the heat transfer process, even in the case of a metallic PCM (gallium) that has high thermal conductivity. Convection in the melt and in the solid-liquid boundary influences the phase-changing process in two different contradictory ways. During melting, convection acts as a beneficial mechanism, by increasing the growth rate of the liquid phase. During solidification, convection decreases the growth of the solid phase and affects the morphology of the solid-liquid interface adversely [210].

In terms of solidification/melting rates solely, convection affects more the PCM melting with respect to solidification phase. Muhammad et al. [211] confirmed this argument, whilst they pointed out that convection plays a small role at the first stages of the system discharging. This rather small effect of the convective motion during solidification has been also highlighted by Formanelli et al. [212]. Finally,

Kroeger et al. [196] noticed that during solidification, the effect of natural convection is strong for Grashof numbers within the range of 10^5-10^6. It is noted that in order to the take into account the natural convection effect, the NS equations should be solved and a convection term should be included in the energy equation (116). The Stefan problem has attracted large interest for an analytical/numerical prediction and has been mostly solved by means of 1D or 2D approaches, **Figure 17**. An overview of different approaches, can be found in the works of Gupta [203] and Crank [204]. Some of them will be briefly discussed below. Prior to this, some parameters of interest and dimensionless numbers involved in such problems are presented.

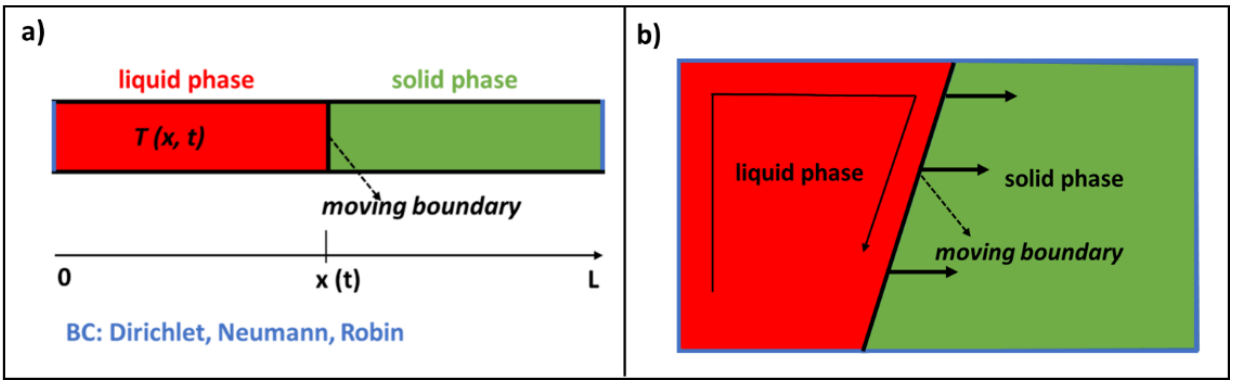

Figure 17. Schematic representation of the a) 1D and b) 2D Stefan problem.

The most important parameters to study in a LHTES are the following:

i. Charge/discharge rates: This is key parameter in a solidification/melting problem to evaluate the thermal performance of a LHTES.
ii. Dendritic formation (crystal growth) during solidification that might affect the thermal performance of a LHTES system.
iii. PCM properties, which effect on charging/discharging rates is important and has been widely studied in [16, 213-215].
iv. Wetting phenomena during melting of PCM. Some researchers have studied this issue [216, 217], however, it is out of scope of this Thesis.
v. Vessel geometry: The vessel design has a high effect on the phase-change rate [202, 218]. Various designs have been suggested for LHTES systems, **Table 11**, **Figure 18**. Amongst them, the inversed truncated cone (or trapezoidal cavity) is a good choice for a LHTES system, due to its high flexibility – its height can be easily modified, to improve charging/discharging rates [218].

Table 11. Studies on different enclosure designs found in the recent literature.

Geometry	References
Spherical	[43, 219], [220]
Cylindrical	[221], [222], [223], [224], [225]
Shell-and-tube	[226], [227], [228]
Cubic	[202]
Rectangular	[210], [229], [227], [230]
Inversed truncated cone	[231], [202, 218], [232]
Cut-off sphere	[202]
Fins	[159], [220]

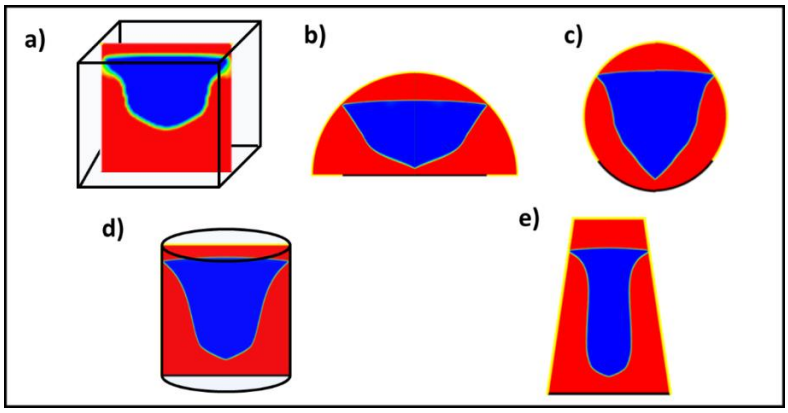

Figure 18. Shapes tested in moving boundary problems a) cube [202], b) cut-off sphere [202], c) sphere [202], d) cylinder [202] and e) truncated cone [202].

2.3.1.3 Characteristic (dimensionless) numbers

Rayleigh number (*Ra*): The Rayleigh number is defined as the product of the Grashof number and determines whether the buoyancy-driven natural convection plays an important role in the heat transfer:

$$Ra = \frac{g\beta_{th}(T_w - T_\infty){L_c}^3\rho^2 c_p}{k\mu} \quad 119)$$

Prandtl number: The Prandlt number (*Pr*) is the ratio of momentum diffusivity to thermal diffusivity:

$$Pr = \frac{c_p\mu}{k} \quad 120)$$

Stefan number: The Stefan number (*Ste*) is the ratio of sensible to latent heat:

$$Ste = \frac{c_p(T_w - T_m)}{L}, \text{ with } T_m = \frac{T_{solidus} - T_{liquidus}}{2} \quad 121)$$

Biot number: The Biot number (*Bi*) is the ratio of heat transfer resistance in the interior of the system to the resistance between the surroundings and the system surface:

$$B_i = \frac{L_c h_c}{k} \quad 122)$$

, where L_c is the characteristic length of the body ($L_c = V_{body}/A_{surface}$).

Grashof number (*Gr*): It is the ration of buoyant to viscous forces within a fluid:

$$Gr = \frac{g\beta_{th}(T_w - T_\infty){L_c}^3\rho^2}{\mu^2} \quad 123)$$

Fourier number (*Fo*): It is the ratio of diffusive or conductive transport to thermal energy storage rate:

$$Fo = \frac{diffusive\ transport\ rate}{storage\ rate} = \frac{kt}{c_p\rho{L_c}^2} \quad 124)$$

2.3.2 Numerical methods of LHTES systems

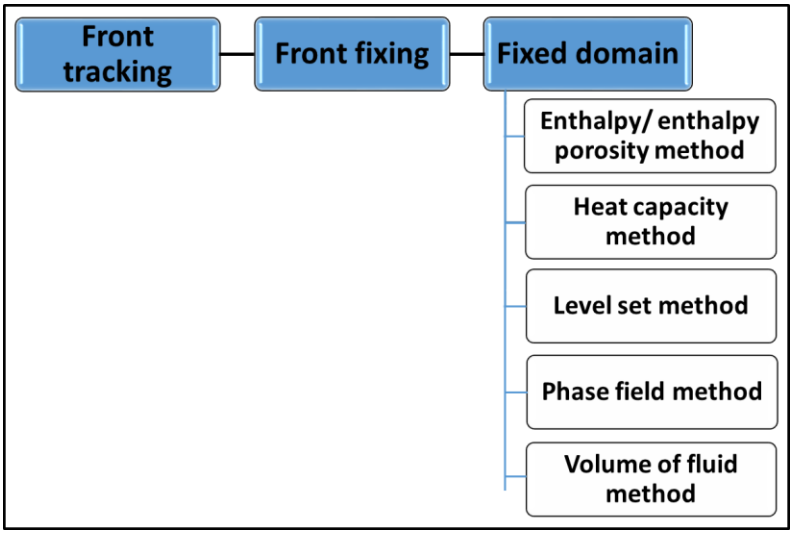

Figure 19. Common methods to simulate a phase change problem.

The possible strategies to simulate a Stefan problem with solidification-melting include the moving (front tracking) method with fixed or adaptive grid [37] and the fixed domain method [38], **Figure 19**. The first one [39] produces more accurate results in the solid-liquid interface, however, it is more complicated for complex and 3D domains or for solid-liquid interfaces subjected to large deformations [38]. The second one is a simpler one, since a single energy equation is solved for both phases and the melting front position is tracked implicitly. The front capturing method includes the heat capacity and the enthalpy method. Among these two the enthalpy method developed by Voller et al. [40] is the most popular in phase change simulations, especially in commercial software packages, such as ANSYS Fluent, and will be mostly analyzed in this Section, since it is adopted in the current Thesis.

2.3.2.1 Front-tracking methods

Front tracking (FT) methods, track the moving boundary in an explicit manner [233], i.e. they compute at the beginning of each time step the location of the phase change boundary. This induces a complexity in their programming and solution. Other problems arise from the interaction of the interface grid with the stationary grid, or with other moving fronts present in the domain. Usually such problems are overcome with a numerical model that dynamically reconstructs the interface grid as the phase-change proceeds and merges double interfaces into a single interface [234]. Numerical solution of FT methods can be achieved with finite difference method (FDM) [235-239], finite element method (FEM) [228, 240, 241], finite volume method (FVM) [242, 243], boundary element method [195, 244], [245], [246] [247], [248] and mesh free method [249], [250].

2.3.2.2 Front fixing Methods

Front fixing (or interface fitting) methods fix the moving front by introducing a new space variable, by changing the coordinates of the problem. Along with front tracking methods, they track the moving boundary explicitly. The difference from them is that the moving boundary is dynamically tracked at each time step and the mesh boundary is setup to be attached to the moving front and to follow its movement. This method is recommended for simple geometries, due to its complexity. As regards spatial discretization, current schemes for moving boundary problems employ FEM, FDM, Chebyshev and Legendre spectral

collocation mesh-based methods or radial basis function (RBF) collocation technique as high order meshless method. The difference of collocation methods from FE and FD methods is that they yield the approximate solution of a boundary value problem in the form of a function, and not with a set of discrete points. The Chebyshev and Legendre are high order mesh-based techniques [249]. More specifically, with the Legendre method the computational domain is divided into (curved) quadrilateral elements and is more applicable to multi-dimensional moving boundary problems. The numerical solution, data and geometry are expanded within each macroelement by means of tensor-product Lagrangian interpolants [251].

2.3.2.3 Fixed Domain methods

Fixed domain methods are simple and user-friendly for numerical simulations of Stefan problems. The enthalpy/enthalpy porosity (EM) approach, the heat capacity, level set (LSM), volume of fluid (VOF) and phase-field methods (PFM) are the main fixed domain methods.

Table 12 summarizes these methods used for the simulation of phase change problems. Among them, the enthalpy porosity approach is a simple and effective method that can be used for the simulation of an UHT-LHTES system. This method has been used to simulate different problems including melting in one and 2D casings of various shapes [36, 43, 252]. However, numerical diffusion can be induced in the solid-liquid interface, which is strongly dependent on the grid size used. Application of a hybrid method capable of combining the advantages of both the fixed and moving grid method would be a real benefit for any type of solidification/melting simulation. Such a hybrid method is followed in the current Thesis.

Table 12. Summary of numerical methods used for the solution of different types of Stefan problems.
Additional references: PFM [253, 254], EM [220] [211] [212, 225, 255], LSM [256, 257] and FTM [258, 259]

Numerical Method	Phenomenon	Domain	Reference
VOF	Solidification	2D	[260]
VOF	Solidification	3D	[261]
PFM	Solidification	2D	[262]
EM	Melting	2D axisymmetric	[226]
LSM	Melting, Solidification	2D, axisymmetric	[263]

2.3.2.3.1 Enthalpy method

A simple and widely applicable fixed-domain method for solving the convection/diffusion phase change problem is the enthalpy method proposed by Voller and Cross [264]. The essential feature of this formulation is that it tracks the moving front in an implicit manner, by isolating the latent heat effects in a source/sink term. Therefore, a difficulty arises in accounting for mass and heat transfer conditions near the interface. A common approach to overcome this is to define appropriate volume source terms in the governing equations [229]. More specifically, in the energy equation the latent heat is taken into account, by assigning a latent heat value to each computational cell according to the temperature of the cell. The governing energy equation of the enthalpy method is the following:

$$\frac{\partial}{\partial t}\rho H + \frac{\partial}{\partial x_i}(\rho u_i H) = \frac{\partial}{\partial x_i}\left(k\frac{\partial T}{\partial x_i}\right) \quad 125)$$

, where H is the specific enthalpy, which is defined in each control volume as the sum of the sensible enthalpy (h) and the latent heat (ΔH):

$$H = h + \Delta H \quad (126)$$

The sensible enthalpy h is equal to:

$$h = h_{ref} + \int_{T_{ref}}^{T} c_p dT \quad (127)$$

, where h_{ref} *is* the enthalpy at the reference temperature (T_{ref} = 25 ºC).

Eq. (125) contains the source term S_h used in the basic formulation of enthalpy method defined as:

$$S_h = \frac{\partial(\rho \Delta H)}{\partial t} + \frac{\partial}{\partial x_i}(\rho u_i \Delta H) \quad (128)$$

In the enthalpy method, the latent heat is a function of temperature:

$$\Delta H = f(T) \quad (129)$$

This method includes several advantages: (1) it is valid for a wide range of cases where the PCM melts, either in a single temperature point or over a temperature range, (2) the enthalpy formulation and velocity correction schemes are independent of the used numerical technique (FEM, FDM, FVM), (3) the governing energy equation is similar to the single-phase equation, and (4) there is no condition to be satisfied at the solid–liquid interface as it automatically obeys the interface condition. On top of that, it is a simple and accurate method; it has been validated by many researchers against experimental data [43, 219, 225]. Due to its numerous advantages, it is one of the most popular methods for solidification/melting problems. Solution of the flow field is done by either using the N-S equations or by means of the Lattice Boltzmann method. As concerns the first approach, the following equations are solved:

Continuity equation

$$\frac{\partial u_i}{\partial x_i} = 0 \quad (130)$$

Momentum equation

$$\frac{\partial}{\partial t}(\rho u_i) + \frac{\partial}{\partial x_j}(\rho u_j u_i) = -\frac{\partial p}{\partial x_i} + \mu \frac{\partial^2 u_i}{\partial x_j x_j} + \rho g_i \quad (131)$$

Regarding the solution of the flow field with Lattice Boltzmann method, and its coupling with enthalpy method details can be found in the work of Fuentes et al. [265].

2.3.2.3.2 Enthalpy-porosity method

The enthalpy-porosity method has been widely used to investigate the solidification/meting process inside containers, in which natural convection is significant. The main advantages of this method include fast convergence and high accuracy. It is one of the leading tools today for modeling solid-liquid phase change processes. Assis et al. [43, 219] successfully validated this method against experimental predictions.

Analytical equations

In the enthalpy-porosity model, the governing energy equation is taken as in the enthalpy method, whereas the latent heat is given as $\Delta H=\beta L$

, where β is the liquid fraction defined as:

$$\begin{aligned} &\beta = 0 && if\ T<T_s \\ &\beta = \frac{T-T_s}{T_l-T_s} && if\ T_s<T<T_l \\ &\beta = 1 && if\ T>T_l \end{aligned} \qquad 132)$$

Thus, the latent heat varies between zero (solid phase) and L (liquid phase). Two important issues that need special attention in this method is the density variation and solids velocity handling. Additionally, depending on the grid resolution, numerical diffusion can occur in the solid-liquid interface. Such a problem can be overcome, by coupling this methodology with more advanced numerical techniques, such as adaptive grid refinement techniques.

PCM density variation and natural convection

The presence of density changes between phases might affect the PCM structure, but not so much the heat transfer process [31]. Situations where density differences are present between phases or where density variations occur in the liquid are handled in this Thesis by the two different approaches described below.

Boussinesq approximation: With the Boussinesq approximation, the density change in the PCM is considered only in the buoyancy term of the momentum equation (131).

$$\rho = \rho_0(1-\beta_{th}\Delta T) \qquad 133)$$

, where ΔT is the difference between the cell temperature and the reference temperature, T_0, at which the reference density (usually 25 ºC), ρ_0, is measured.

The Boussinesq approximation with the enthalpy porosity approach has been widely used in the literature to simulate the effect of natural convection in the thermal performance of various PCMs [40], [229].

Density change during phase change: Most of the numerical methods found in the literature for solving solid–liquid phase change assume a constant density upon melting or solidification, or in best cases, a density variation with Boussinesq approximation. However, those methods are not efficient when applied to phase change with volume expansion or shrinkage. A more accurate approach is to consider the density change amongst the two different phases, and a linear interpolation in the mushy zone to avoid numerical instabilities.

$$\rho_{pcm} = \begin{cases} \rho_s & T < T_s \\ linear\ variation & T_s < T < T_l \\ \rho_l & T > T_l \end{cases} \qquad 134)$$

This approach has been followed by different researchers, such as [220], [43], [202, 218]

Dumping of velocity at the solid region

In a solidification-melting problem with a fixed-domain method, solution of the momentum equation requires a modification in order to consider the transition from liquid to solid phase and ensure zero velocity

values. A common approach is the Source term method (STM). The STM uses a high source term (S_i) to the momentum equation to set the solid velocities equal to zero, when the material is solid. In its original form this method suffers from discontinuity at the phase-change boundary. A variation of STM developed by Voller et al. [264] and Brent et al. [229] is the Darcy-STM, used in this Thesis.

With the Darcy-STM method, a source term is added to the momentum equation (131):

$$\frac{\partial}{\partial t}(\rho u_i) + \frac{\partial}{\partial x_j}(\rho u_j u_i) = -\frac{\partial p}{\partial x_i} + \mu \frac{\partial^2 u_i}{\partial x_j x_j} + \rho g_i + S_i \quad (135)$$

The source term S_i is derived from Darcy's law [40]. It is defined so that the momentum equations are forced to mimic Carman-Kozeny equations for flow in a porous media:

$$S_i = -A_{mush} \frac{(1-\beta)^2}{\beta^3 + \varepsilon_1} u_i \quad (136)$$

, where ε_1 is a small constant (ε_1=0.001) used to avoid division by zero. A_{mush} is the mushy zone parameter, a sink term that takes into account the damping effect within the mushy region and is dependent on the dendrites formed during solidification process, the material density and viscosity, parameters that reflect in turn the PCM permeability. This parameter takes values from 10^3–10^9 and in most studies available [43, 266] a default value of 10^5 is used. In the work of [202, 267] the following equation has been used:

$$A_{mush} = 180 \frac{\mu}{\rho DAS^2} \quad (137)$$

The validity of equation (136) in describing the flow in a dendritic mushy region has been proven experimentally [268] and has a physical meaning for substances, such as metal alloys. When the heat transfer direction is parallel to the primary dendrite arms, the phase-change rate is affected by the liquid volume fraction and the primary dendrite arm spacing. When the flow is normal to them, the rate depends upon the primary and secondary dendrite arms spacing and the volume fraction. Combination of equation (136) and (137) can correlate the *DAS* and β with the melting rate, however, there is not available an equation that correlates all three variables in common numerical methodologies.

In an isothermal phase change system, the flow inside computational cells that experience solidification or melting cannot follow the classical Carman-Kozeny equation. In this case, a linear function can be used:

$$S_i = -A_{mush}(1-\beta)u_i \quad (138)$$

Another possible approach is to consider a small temperature integral, without a physical meaning, especially for pure metals, but necessary from a numerical point of view, in which the phase change occurs.

Numerical solution

The numerical solution of this problem entails selection of a suitable discretization scheme of the governing equations. Finite-element, finite-difference schemes or a mesh-free method can be applied [269, 270]. The most usual approach in PCM simulations is the control volume-based formulation [242], [229].

2.3.3 Challenges in phase change simulations

2.3.3.1 Inclusion of radiation

Inclusion of radiation in a UHT-LHTES is a necessity especially for ultra-high temperature devices, where radiation absorption can be one of the dominant mechanisms in the liquid PCM. However, the literature is limited as regards the inclusion of rigorous radiation models, coupled with the abovementioned numerical methods. Such a difficulty arises from the fact that common radiation models found in commercial solvers, such as P1 or Discrete ordinates (DO), use a series of settings and simplifications that for the specific application of a LHTES need further improvement. Additionally, due to lack of experimental data it is difficult to validate their accuracy. Some information can be found in [265, 271, 272], where solidification/melting models are coupled with DO method to model natural convection and radiation inside the PCM.

2.3.3.2 PCM volume change

Generally, during the phase change of the majority of materials found in the nature there is a change of their volume, due to their density change, **Figure 20**. Most metals and alloys have a lower density in the liquid than in the solid phase (e.g. aluminum, nickel, tin, boron and titanium). This provokes the PCM compression during solidification that leads, in turn, the melt to move upwards. This flow can lead to formation of cavities and change the shape of the final product, cause porosity, change the species concentrations in alloys, and consequently lead to poor mechanical properties [261]. On the other hand, in cases where the PCM has lower density in the solid phase and therefore, expands during solidification process (e.g. silicon, gallium and bismuth) the melt has a downward movement. Moreover, in this case mechanical stresses induced by the volume expansion during solidification can harm the vessel/container. In both cases, density variations occur in both phases due to changes in temperature, known as solid or liquid contraction. Liquid contraction can also drive convective motion in the melt, while solid contraction can induce thermal strain in the solid phase, leading to high stresses in the PCM container.

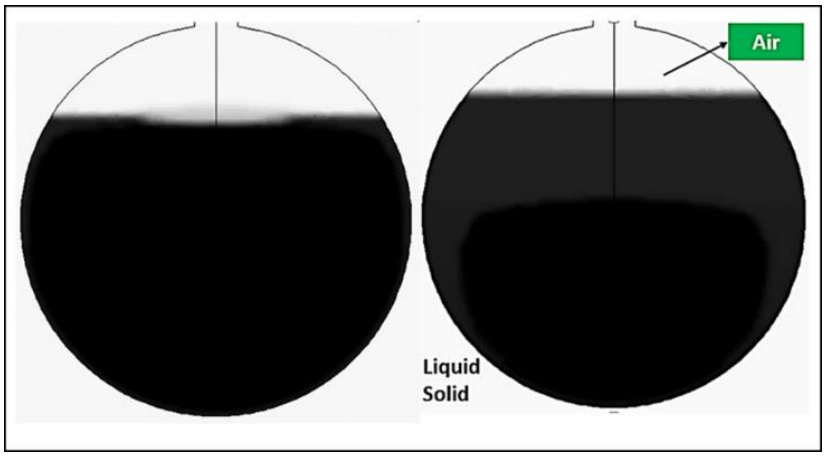

Figure 20. Paraffin wax volume increase during its melting.

This PCM density change accompanied by its volume change needs a special numerical treatment. First of all the density change should be explicitly taken into account. Secondly, if the PCM shrinks/expands inside a sealed rigid shell during its phase change, another material –inert gas, in specific- should be included in the computational domain, in order to avoid the exertion of high pressure values and as a consequence divergence of the numerical solution. Such a practice has been followed in the work of [202, 218].

2.3.3.3 Presence of air/inert gas in the vessel

Assis et al. [43] modeled the melting of a PCM in a spherical shell, by the presence of air in the upper part. They used the enthalpy-porosity approach to account for the solid-liquid phase change and the volume of fluid (VOF) method to account for the two immiscible fluids (PCM, air). They evaluated their methodology for the case of paraffin wax melting [43] and solidification [219].

In this gas-PCM system, the continuity equation is reformulated as:

$$\frac{\partial a_n}{\partial t} + u_i \frac{\partial a_n}{\partial x_i} = 0 \qquad 139)$$

, where the air is the primary phase and PCM the secondary phase. Following Assis at al. [43] other researchers [220, 221] have followed this approach to take into account compressibility effects.

2.3.3.4 Crystal growth (dendritic formation) during solidification

The simulation of crystal growth in the mushy region, during the PCM solidification, is of importance in terms of the thermal performance of the LHTES system, because it determines the PCM permeability, which in turn effects the PCM melting rate. Smooth solidification fronts are often unstable and develop a wide variety of microstructures (dendrites) that modify the material properties of the solid PCM. Simulation of such demanding flows has been performed with front-tracking methods [235], BEM methods [273], LSM and Phase-field methods, briefly described in previous sub-sections.

2.3.3.5 Constrained vs. unconstrained melting

There are two types of solidification/melting process inside a container; the constrained and unconstrained problem [274]. In the first one, the solid PCM is fixed and the effect of natural convection should be considered, whilst in the second one the solid PCM is free to move inside the melt, and thus, this movement should be also taken into account. The main disadvantage of implicit methods, such as the enthalpy method, is that the PCM solid velocities are set to zero. This means that any solid motion inside the liquid PCM is not explicitly modelled. In the numerical context, the solid phase shape and position inside the PCM are implicitly shaped as a result of the liquid motion. When the liquid phase is lighter (heavier) than the solid one, it moves upwards (downwards) enhancing the heat transfer process from the PCM upper (lower) part, **Figure 21**. There are several works found in the recent literature that implicitly take into account the solid movement through the movement of the liquid phase [43, 202, 218-220].

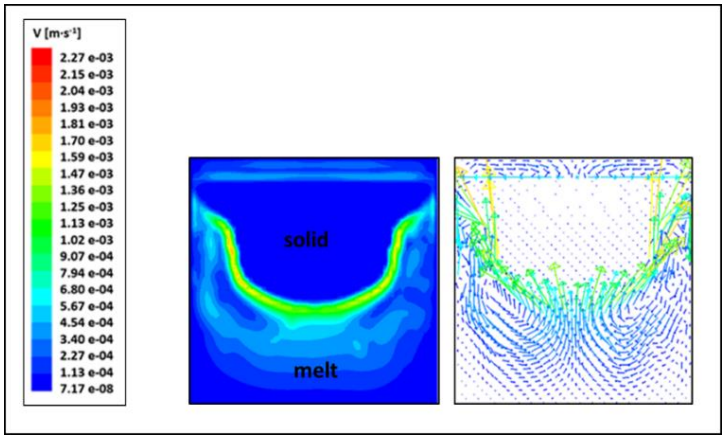

Figure 21. Velocity field of the flow motion in unconstrained melting of silicon inside a cubic cavity [202].

2.3.3.6 Need for a sharp interface at the phase change front

The state-of the art CFD models utilizing the enthalpy-porosity approach are tracking the solid-liquid interface using fixed grid methods [40, 264]. This results in cases, where the grid density should be cautiously selected in order to avoid numerical diffusion that might affect the accuracy of the derived results. More specifically, in coarse grid cases, the solid-liquid front (i.e. mushy zone region) is represented by an artificially larger area than what occurs in reality (**Figure 25**). This consequently leads to an overestimation of the solidification/melting time. On the other hand applying of a dense grid that should lead to a sharper interface and, thus, more accurate numerical predictions, might increase considerably the induced computational cost. An effective grid method that combines advantages of both coarse (efficiency) and denser grids (sharp interface) is the adaptive local refinement technique. This technique has been mostly utilized in droplet dynamics simulations by [94-96, 98]. The current Thesis uses this technique to model phase change problems by achieving a sharp liquid-solid interface.

CHAPTER 3
Modelling of storage applications using PCMs

3.1 Preface

The aim of this section is to present the numerical methodology and results of the full cycle of an UHT-LHTES system, part of a novel electric-TES concept [27]. Overall, this concept couples in a single compact device the UHT-LHTES block with a thermal-to-electric energy hybrid thermionic-photovoltaic (TIPV) converter [275]. The first one, i.e. the TES storage block, during the system charging period, can store any kind of energy (heat, electricity, or solar) in the form of latent heat. The second one, during discharging period, converts the stored thermal energy into electricity.

More specifically, the TIPV converter includes two parts, i.e. a metallic cathode (referred to as emitter), which is in direct contact with the PCM vessel bottom part and emits photons-electrons, when is heated, and a GaAs anode coupled with a photovoltaic (PV) cell. Its operation is similar to a photon-enhanced thermionic emission (PETE) device [276], with the main difference that the semiconductor used for electricity production is placed in the anode and not in the cathode as usually done is such devices. At the rear side on the TIPV converter, i.e. the PV cell, a cooling system is patched for any excess heat collection. The PCM container, depicted in **Figure 22**, during the charge phase, is heated either from the sidewalls and/or the top in a P2H2P (power-to-heat-to-power) application or only from the top in a S2H2P (solar-to-heat-to-power) application, reaching ultra-high temperatures (above 900 ^{o}C). If the temperature inside the vessel exceeds the PCM melting point, i.e. 1414 ^{o}C for pure silicon, the material starts to melt. During this stage, i.e. melting of the contained PCM, the TIPV anode is disconnected from the system and the LHTES is insulated from the emitter side to prevent excess heat losses. During the system discharging, the TIPV anode is connected to the system, and converts the emitted from the cathode photon –electron flux into electricity.

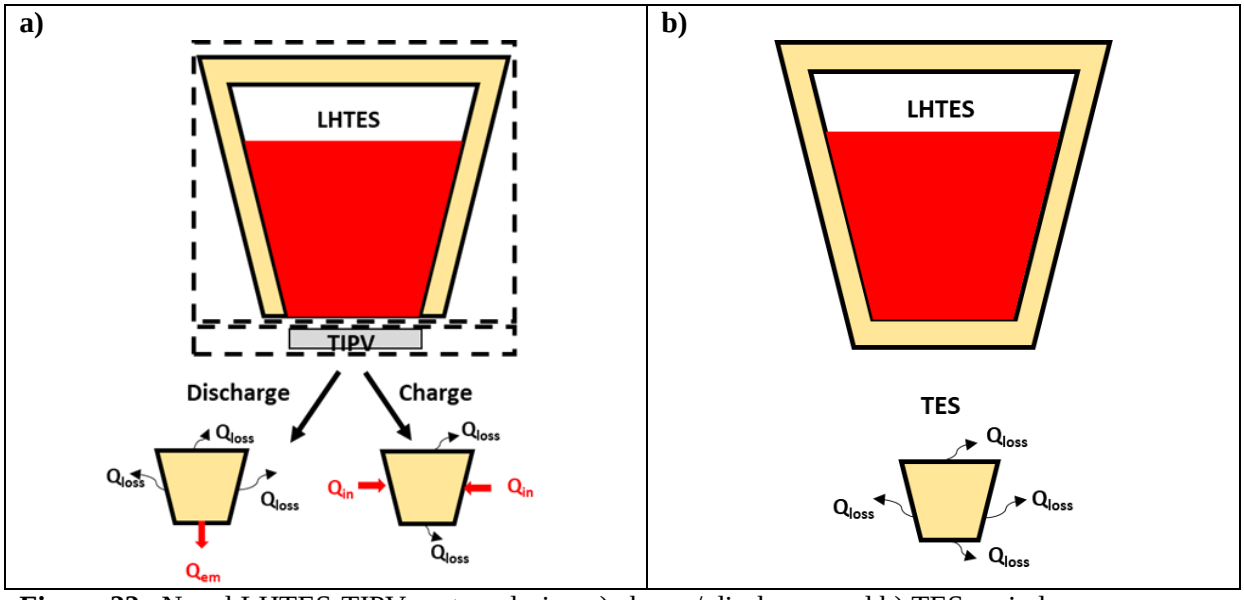

Figure 22. Novel LHTES-TIPV system during a) charge/ discharge and b) TES period.

This novel LHTES-TIPV concept, has been described theoretically in the work of [275] and a prototype has been constructed in the framework of AMADEUS Project [277]. Part of the numerical work done in this Thesis, has been used for the design study and optimization of this novel system. Its novelty as aforementioned, lies in its operation at ultra-high temperatures that can potentially unlock storage energy densities as high as 1230 kWh·m^{-3}, which are considerably higher than the state-of-the-art molten salt based

TES systems. This increase in the storage density plus the high electrical power density of the TIPV converter (several 10's of $kW \cdot m^{-2}$) can potentially enable the fabrication of compact S2H2P or P2H2P systems that integrate thermal energy storage and power generation in the same unit [232]. Nevertheless, proper design and optimization of the LHTES device and better understanding of the PCM phase change at such unprecedented temperatures are key aspects that need to be in-depth analysed, before this complex system being manufactured and tested in a lab-scale.

For the study and optimization of the LHTES system, an advanced axisymmetric 2D CFD model is implemented in ANSYS Fluent platform (v17.1) [278]. The CFD model is based on the enthalpy-porosity approach [264], which is presented in **Sub-section 2.3.2.3.2: Enthalpy-porosity method**, coupled with the Volume of fluid (VOF) model [279]. Initially, the model is validated against experimental data found in the literature [43, 219] for paraffin wax solidification/melting at low temperatures (~30 ºC). Then, the model is verified against a 1D analytical model for silicon solidification inside a sealed crucible at ultra-high temperatures (>1000 ºC) [232]. Model validation at such temperatures is not possible, owing to a lack of experimental data. The effect of complex phenomena are incorporated, as those of natural convection in the PCM liquid phase and volumetric expansion/compression, due to PCM solidification/melting process. In this system, the PCM occupies part of the vessel, and, above the PCM a non-reacting gas fills the rest of the domain. For a more accurate representation of the gas-PCM and solid-liquid PCM interfaces, an adaptive local grid refinement technique [94] is applied by using codes in C programing language, at both the PCM-gas and solid-liquid interfaces. This technique is used to enhance the numerical accuracy and the efficiency of the model in terms of CPU cost. As a further step, design optimization of the silicon-based storage tank is carried out by taking into account lateral thermal losses. The overall system performance is assessed during its charging, discharging and storage periods. Finally, a sensitivity analysis is presented to investigate the effect of the PCM thermal properties on the system charging/discharging rates. An outline of the modelling activities is presented in **Figure 23**.

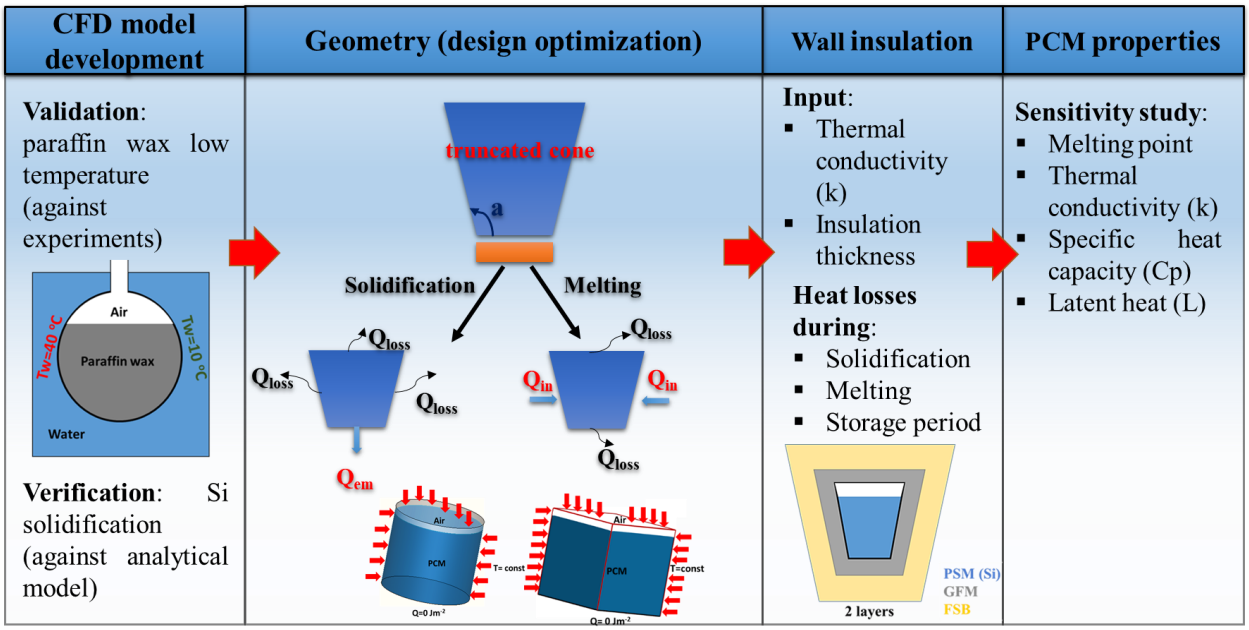

Figure 23. UHT-LHTES system studied during a) charge/ discharge and b) TES period [27].

3.2 Numerical methodology

The current numerical model, is based on the enthalpy-porosity method by Voller [40], already incorporated in Fluent, to model the PCM transition from solid to liquid phase. In this method, the PCM liquid fraction is calculated based on the energy equation (125). Thus, the melting front (phase change transition) is almost linearly dependent on the temperature distribution. A mushy zone is defined, which represents the liquid-solid transition and is treated as a 'pseudo' porous medium. In this zone, the liquid fraction increases gradually from 0 (solid) to 1 (liquid) as the PCM melts and vice versa during its solidification, as described in equation (132). In reality, the mushy zone is a porous layer of partially solidified regions, usually resembling to dendritic crystals, with liquid among their interstices. Such structures are formed during the PCM solidification and are oriented along the direction of the strongest thermal gradient [280].

Apart from the enthalpy-porosity method, the multiphase VOF approach [279] is applied for the simulation of the PCM-air moving interface tracking, without inter-penetration of the two media. The conservation equation of mass is calculated as follows:

$$\frac{\partial a_n}{\partial t} + \frac{\partial a_n \mathrm{u}_i}{\partial x_i} = 0 \qquad 140)$$

, whereas the momentum equation contains the Darcy STM method (refer to eq. (135)-(137)).

In this model, the volume fraction α_n of the primary phase –gas in the specific case studied- is equal to unity if the computational cell is occupied only by it, and the value of zero if the cell is completely occupied by the secondary phase (PCM). If $0 < \alpha_n < 1$ the cell contains the 'interface' region between the two phases. Thus, the physical properties in any given computational cell are either corresponding to one of the phases, or are calculated based on the media mixture in the interface region, depending upon the α_n values.

Finally, the VOF model includes compressibility effects of the inert gas, enclosed inside the PCM casing. The latter can be either compressed (expanded) inside a sealed rigid shell, or exit (enter) the container through a small opening, during the PCM expansion (contraction), in order to avoid the exertion of high stresses in the PCM casing.The main assumptions adopted in the modelling activities are as follows [232]:

1. **Transient fluid flow** and heat transfer mechanisms;
2. 2D axisymmetric domain;
3. Inclusion of **gravitational force**;
4. The flow is **laminar, due to low Reynolds numbers;**
5. The **molten PCM** is an **incompressible Newtonian fluid**;
6. Both solid and melt are **homogeneous** and **isotropic**;
7. The **PCM thermophysical properties and insulation/vessel materials thermal properties** are dependent on temperature variations;
8. The **PCM density changes** during its transition from solid to liquid phase and vice versa;
9. The inert gas is treated as a compressible fluid [278];
10. **Radiative** heat transfer within the vessel is neglected, when the PCM is heated from the sidewalls;
11. **Contact thermal resistances** between solid/liquid PCM and walls are considered **negligible;**
12. The PCM crucible walls and insulation layers can be either modelled as thin walls, by solving an 1D heat conduction equation [278], or implicitly modelled for a more accurate description of the temperature field. If the heat losses are not modelled, the sidewalls are considered adiabatic;
13. **Surface tension** effect between the different phases is neglected; and.

14. An implicit formulation is adopted for the VOF solution with a sharp gas-PCM interface modelling.

3.2.1 Domain discretization

In order to increase accuracy in the solid-liquid and gas-PCM interfaces an adaptive local grid refinement technique is applied, based on the work of [94]. This results in a coarse static grid and a dense adaptive grid at the moving fronts. The dense mesh is created by refining the coarse grid –two or more levels of refinement- in ANSYS Fluent platform through the adapt region tool [281]. Then, the refined grid follows the position of the moving interfaces, by means of proper UDFs.

3.2.2 Boundary conditions

The most common wall boundary condition, which is usually imposed in the classical formulation of the Stefan problem, is a constant heating or cooling temperature (Dirichlet BC). Such a condition is considered during the solidification/melting phase of paraffin wax at low temperatures and the melting phase of silicon. During the solidification of silicon, where there is a heat extraction from the container bottom by the TIPV converter, it is more realistic to impose a heat flux boundary condition (Neumann BC).

3.2.3 Under-relaxation factors

The under relaxation factors (URFs) values should be chosen carefully in terms of model robustness and CPU efficiency. The used URFs to run the numerical cases are presented in **Table 13**.

Table 13. URFs used in a solidification-melting problem based on the enthalpy porosity approach.

Pressure	**0.3**
Momentum	0.1-0.3
Density	0.7
Volume fraction	0.5
Liquid fraction	0.95
Energy	0.95

3.2.4 Numerical solution

3.2.4.1 Discretization schemes

Time and spatial discretization schemes should be used to obtain numerical solution of this problem. Some of the recommended schemes are presented in **Table 14**.

Table 14. Discretization schemes used in solidification-melting simulations.

Transient formulation	**Bounded second order implicit**
Pressure-velocity coupling	PISO/ Coupled
Spatial discretization	
Gradient	Least squares cell based
Pressure	PRESTO!
Density	QUICK
Momentum	QUICK
Volume fraction	Compressive
Energy	QUICK

3.2.4.2 Time step

A variable time step with a courant number equal to 0.2 is used, contrary to the constant time step methods adopted in other works utilizing the enthalpy porosity method [43, 219]. However, further research is needed to impose a variable time-step size depending on parameters, such as the thermal diffusivity, derivative of the temperature in space etc.

3.3 Model validation (Paraffin wax solidification/melting: Low temperatures)

Initially, the CFD model is validated against experimental data for the solidification/ melting process of paraffin wax, RT27, at low temperatures, i.e. ~30 ^{o}C, inside a spherical casing open from the top. Such data along with the appropriate boundary and operating conditions are obtained from the work of Assis et al. [43], [282]. During melting (solidification) process, the vessel is heated (cooled) from its walls, almost 10 ^{o}C above (20 ^{o}C below) its melting point.

During model validation, a parametric study is conducted as concerns the A_{mush} parameter effect on the PCM solidification/ melting rate. A set of A_{mush} values equal to [10^5, $5 \cdot 10^5$ and $2 \cdot 10^6$] and [10^5, 10^6 and 10^9] are tested during melting and solidification phase, respectively. Additionally, the effect of the grid density on the numerical results is also investigated by taking as a reference the PCM melting process. The decided applied grid methodology follows the local grid refinement method with two refinement levels. This results in a maximum number of quadrilateral cells equal to 11,133 and a minimum cell size equal to $1.07 \cdot 10^{-4}$ m.

3.3.1 Geometry and Mesh layout

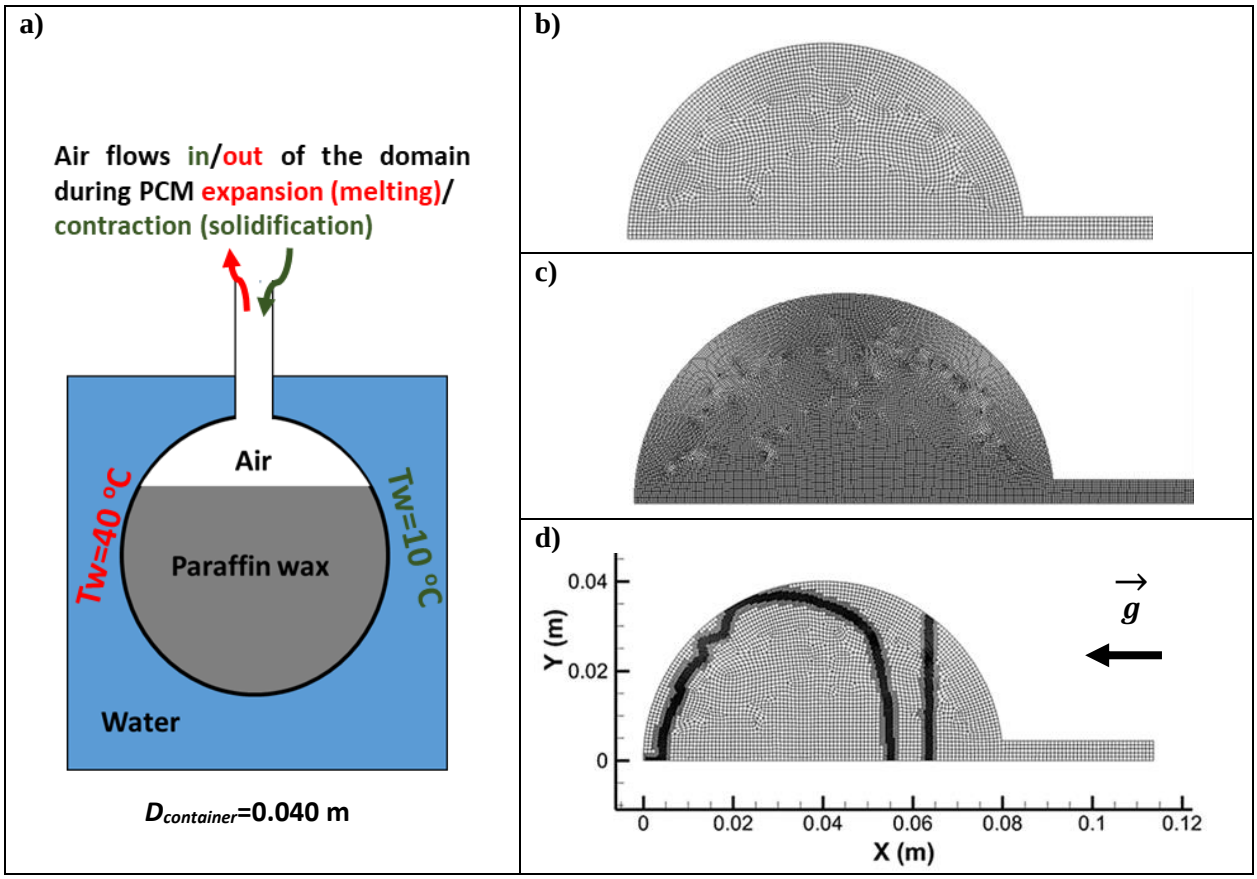

Figure 24. a) 2D scheme of the PCM container and discretized domain using the b) coarse and c) medium fixed grid density method and d) the adaptive local grid refinement technique (2 Levels of refinement).

The spherical container, depicted in **Figure 24a**, is made of glass and has an inner diameter equal to 0.040 m. Initially, the PCM fills 85% of the container for the melting study and 96 % of the domain for the solidification study. At the top of it, a non-reactive gas –air in the specific case studied- fills the rest of the domain and can flow in and out of it through a small opening, during the PCM expansion/contraction. A

uniform temperature is set at the walls, equal to 40 ºC (10 degrees above paraffin wax melting point) for the melting study and to 10 ºC for the solidification study (20 degrees below paraffin wax solidification point). This is because the container is submerged inside water, whose temperature is kept at a constant level inside the tank with an electric heater.

For the CFD model validation, a fixed coarse grid, consisting of 3,858 quadrilateral cells, is used. Then, a grid independence study is performed -using a medium and a dense sized grid density, comprising 15,432 (4 times the coarse grid) and 61,728 quadrilateral cells (16 times the coarse grid), respectively. The coarse mesh is constructed in ANSYS Meshing component, whilst the medium and dense meshes are created by refining the coarse grid –with one and two levels of refinement, respectively- in ANSYS Fluent v17.0 through the adapt region tool [278]. Such type of analysis is of high importance in CFD modelling to ensure that the numerical results do not depend on the grid used.

Finally, for a sharp representation of the gas-PCM and solid-liquid PCM interfaces, the adaptive local grid refinement technique with two refinement levels (referred to as 2Lev. ref.) is applied, by means of several in-house UDFs in C programming language, based on the work of [94]. In this technique, the coarse mesh is used as the basis and is dynamically refined at a prescribed distance from the gas-PCM and solid-liquid interfaces throughout the melting process, **Figure 24d**. The adaptive local grid refinement method is applied to enhance the numerical results accuracy without substantial increase of the associated computational cost.

3.3.2 Boundary and operating conditions

In order to solve the CFD problem several boundary conditions are applied. For the melting process, boundary conditions are taken by the work of [43], **Table 15**. Initially, the temperature of the whole system is set equal to 23 ºC, i.e. the PCM is slightly sub-cooled.

Table 15. Air-paraffin wax problem boundary conditions (melting process).

	BC type	**Parameters**	**Units**	**Values**
Wall	Wall	T_W	ºC	40
		b_W	m	0.002
		k_W	W m^{-1} K^{-1}	0.81
	Shear condition: No slip			
Outlet	Pressure Outlet	P_o	bar	1.013*
		T_o	ºC	40
Axis	Symmetry			

* Parameter of typical ambient conditions

For the solidification process, boundary conditions are taken from [282], **Table 16**:

Table 16. Air-paraffin wax problem boundary conditions (solidification process).

	BC type	**Parameters**	**Units**	**Values**
Wall	Wall	T_W	ºC	10
		b_W	m	0.002
		k_W	W m^{-1} K^{-1}	0.81
	Shear condition: No slip			
Outlet	Pressure Outlet	P_o	bar	1.013
		T_o	ºC	10
Axis	Symmetry			

The most important thermophysical properties of the air and the PCM (paraffin wax) are summarized in **Table 17**. It should be noted that the PCM properties (density, thermal conductivity, specific heat) are assumed to vary linearly within the "mushy zone".

Table 17. Gas-solid properties (gas: air, PCM: paraffin wax) [43].

Property	**Gas**	**PCM-solid**	**PCM-liquid**
ρ, **kg·m^{-3}**	$\rho = 1.2 \cdot 10^5 T - 0.01134T + 3.4978$	870	730-760*
k, **W·m^{-1}·K^{-1}**	0.0242	0.24	0.15
C_p, **J·kg^{-1}·K^{-1}**	1006.43	2400	1800
μ, **kg·m^{-1}·s^{-1}**	$1.789 \cdot 10^{-5}$	-	$3.42 \cdot 10^{-3}$
$T_{solidus}$, **ºC**		28	
$T_{liquidus}$, **ºC**		30	
L, **J·kg^{-1}**		$1.79 \cdot 10^5$	

* A temperature dependent density relation is used for the PCM liquid phase:

$$\rho_l = \frac{760}{5E-04(T - T_{liquidus)} + 1}$$

3.3.3 Studied cases

Several cases (Case 1-4) are simulated in order to validate the model and test the effect of the grid density on the numerical results, by taking as a reference the PCM melting process. The melting fraction values obtained by the CFD model are compared against the ones presented in Assis et al. [43] work –both numerical results and experimental data. In this initial set of studied cases, the mushy zone parameter has the same value, i.e. 10^5. As a further step, a parametric study for the effect of the mushy zone parameter on the melting/solidification process is conducted (Cases 4-9). The parametric study is carried out by using one of the four grid densities tested in Cases 1-4, which is chosen as the most accurate and efficient.

Transient calculations are performed in Fluent v.170 solver. A variable time step Δt is used with a courant number equal to 0.2, **Table 18**. The time and discretization schemes used during numerical calculations are the ones mentioned in **Table 14**. For the pressure-velocity coupling, the Coupled Scheme is used.

Table 18 summarizes the simulated cases, during model validation.

Table 18. List of cases simulated, during model validation.

Case	**Grid**	***Process***	A_{mush} **[-]**	**DAS [m]**	**Δt, max [s]**	**Δt, min [s]**	**Courant [-]**
Case 1	Coarse	Melting	10^5	$9 \cdot 10^{-7}$	$\sim 2 \cdot 10^{-2}$	$\sim 1.4 \cdot 10^{-2}$	0.2
Case 2	Medium	Melting	10^5	$9 \cdot 10^{-7}$	$\sim 5 \cdot 10^{-3}$	$\sim 2 \cdot 10^{-3}$	
Case 3	Dense	Melting	10^5	$9 \cdot 10^{-7}$	$\sim 1 \cdot 10^{-3}$	$\sim 5 \cdot 10^{-4}$	
Case 4	2 Lev. ref.	Melting	10^5	$9 \cdot 10^{-7}$	$\sim 6 \cdot 10^{-3}$	$\sim 3.5 \cdot 10^{-3}$	
Case 5	2 Lev. ref.	Melting	$5 \cdot 10^5$	$4 \cdot 10^{-7}$			
Case 6	2 Lev. ref.	Melting	$2 \cdot 10^6$	$2 \cdot 10^{-7}$			
Case 7	2 Lev. ref.	Solidification	10^5	$9 \cdot 10^{-7}$			
Case 8	2 Lev. ref.	Solidification	10^6	$3 \cdot 10^{-7}$			
Case 9	2 Lev. ref.	Solidification	10^9	$9 \cdot 10^{-9}$			

3.3.4 Results

Figure 25a compares the melting fraction results as a function of time of the CFD model with the ones obtained from Assis et al. [43], both numerical model and experiments. The model of Assis, which is based on the VOF method with the enthalpy porosity approach, utilizes a grid of 3,520 cells and a constant time step size equal to Δt=0.002 s. The melting fraction parameter used for comparison is calculated as the ratio between the liquid PCM mass over the total PCM mass ($MFR = m_{liquid}/m_{PCM}$), at a given moment.

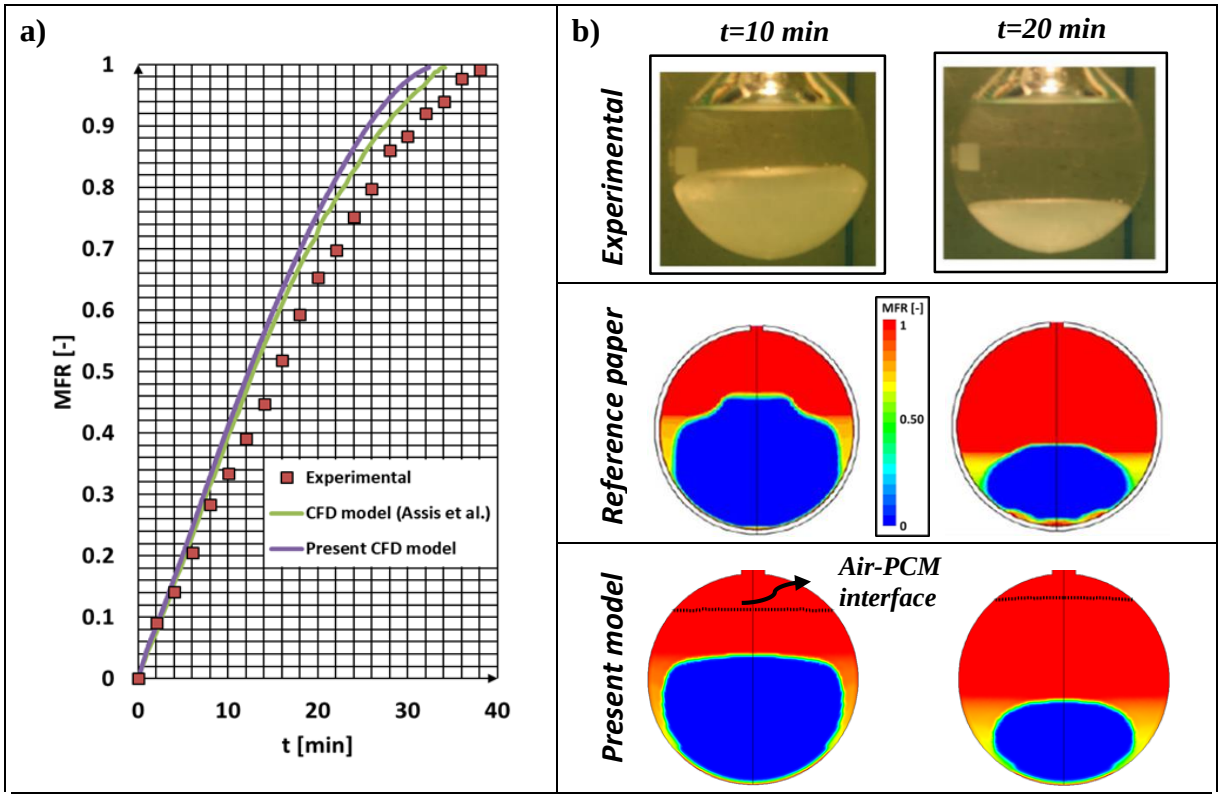

Figure 25. Comparison of the experimental, reference paper CFD model and developed CFD model a) melt fraction values at different time instants and b) melt fraction contours at t=10 and 20 min.

From the graph, it is proven that for most of the simulation time, the results of the present model virtually coincide with that of the reference paper and are close enough to the experimental data. A small deviation of approximately equal to 6 %, between the two models noticed, can be primarily, attributed to the time-step size method followed; in this Thesis a variable time step with a courant number equal to 0.2 is used, contrary to the constant time step method adopted in Assis et al. [43] model. Furthermore, in the reference paper, there are not any details available concerning the spatial and time discretization schemes and VOF formulation (implicit or explicit), the selection of which can affect the numerical results.

Additionally, a qualitative comparison is conducted, based on simple observations, by comparing liquid fraction contours for two time instants, t = 10 and 20 min, of the present Thesis, with the experimental and numerical results of Assis et al. [43]. As can be noticed from **Figure 25b**, similar liquid fraction patterns are obtained between the present model and the reference paper. Over and above that, with the currently applied CFD model, a limited numerical diffusion is achieved, whilst the melting fraction patterns bear a

greater resemblance to the experimental visualizations than Assis et al. [43] model. This can be evidently noticed, from the melting front shape, at a time instant equal to *t*=10 min, depicted in **Figure 25b**.

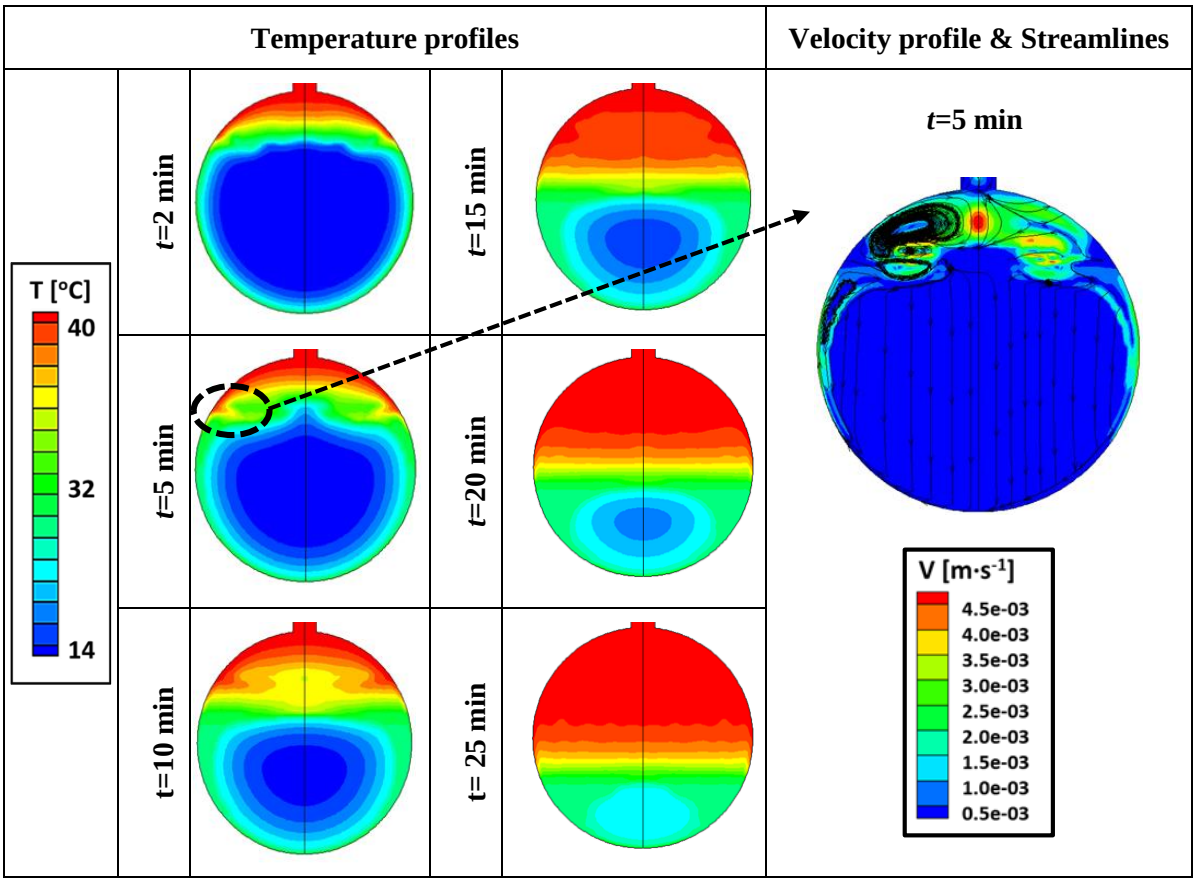

Figure 26. Temperature and velocity contours at different time instants.

Figure 26 illustrates the temperature and velocity profiles obtained at various time instants by the numerical problem. As can be clearly seen, a few minutes after the beginning of the melting process a thin layer of molten PCM forms around the solid phase. During this period of time the PCM melting occurs faster at the proximity of the PCM-gas interface, near the walls, due to the induced gas-liquid vortex. This is because, there are two fluid motions occurring simultaneously inside the container that accelerate the heat transfer through convection. On the one hand, the molten paraffin wax is lighter than its solid phase and, for this reason, moves upwards due to buoyancy-driven natural convection, enhancing thus, the melting process near the gas-PCM interface. On the other hand, there is the hot air movement, which promotes as well the heat transfer near that area. Similar observations can be found in [43].

The heat transfer rate Q [$W \cdot m^{-2}$] at the sphere wall determines the energy transferred to the container interior over time. Results of Q as a function of φ (angle measured with its vertex placed at the centre of the circle –x=0.04 m- and its beginning at x=0.08 m) obtained through the CFD model for two time instants (*t*=2, 10 min), are shown in **Figure 27**. Based on the numerical results it is proven that in the mushy zone the PCM absorbs the highest amounts of heat. For instance, at a time instant equal to *t*=2 min, the highest amounts of heat absorbed can be noticed in the sphere circumferential area for a φ range in-between 60-90 deg. This area, based on graph (c) is the mushy region. Thus, it is clearly understood that the 'overestimation' of the

mushy zone region, due to numerical diffusion, might cause overestimation of the amounts of heat absorbed by the PCM and, as a consequence, lead to inaccurate numerical results.

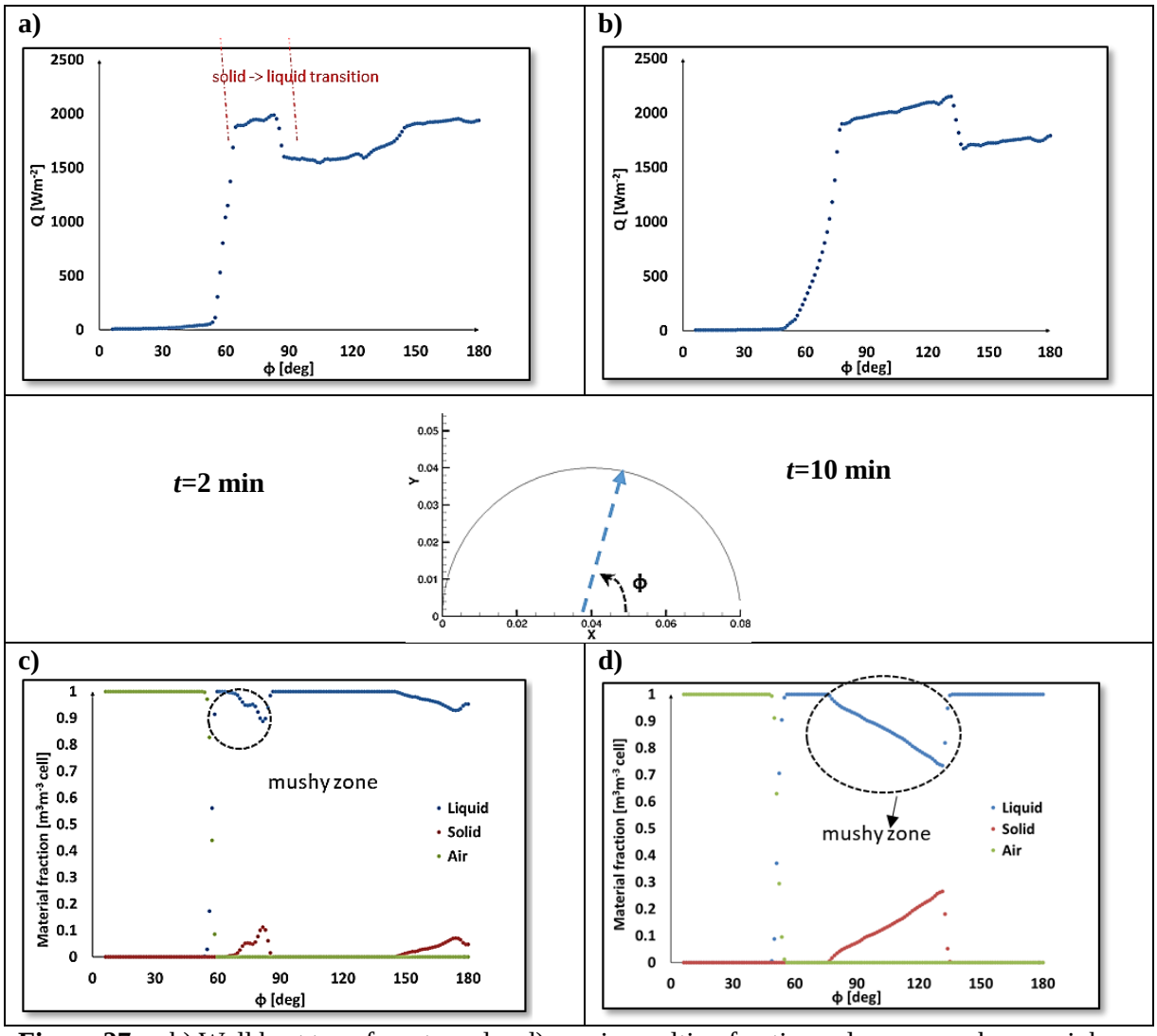

Figure 27. a, b) Wall heat transfer rate and c, d) species melting fraction values over sphere periphery for *t*=2, 10 min, respectively.

3.3.5 Grid independence study

This section presents numerical results derived from the grid independence study, during which four grid resolutions have been tested, i.e. three fixed grids of coarse, medium and dense resolution and a dynamically refined grid, with two levels of refinement. A key parameter important for the objective of this analysis is the PCM liquid fraction as a function of time, which in turn reflects the PCM melting rate.

From **Figure 28a** it is evident that the medium, dense and refined grid almost coincide in their numerical results, revealing that a grid independency has been achieved. On the other hand, the coarse grid results in a slower PCM melting process –almost two minutes slower- compared to the rest of the cases studied. Such a difference does not seem of high importance for the specific vessel design and operation. However, for other vessel designs and operating conditions, which could lead to lower PCM melting rates, this difference in the PCM melting rates might be more apparent.

Another conclusion drawn from this analysis is that the dynamically refined grid gives results of almost the same accuracy as the medium and dense grids. This fact can be attributed to the limited numerical diffusion induced, due to the sharp gas-PCM and solid-liquid PCM interface treatment achieved by the adaptive grid refinement method, as if a dense grid was applied. The medium grid leads to a sharper interface compared to the coarse, eliminating numerical diffusion, but not on the desirable level, as the one achieved with the refined or dense grid, **Figure 28b**.

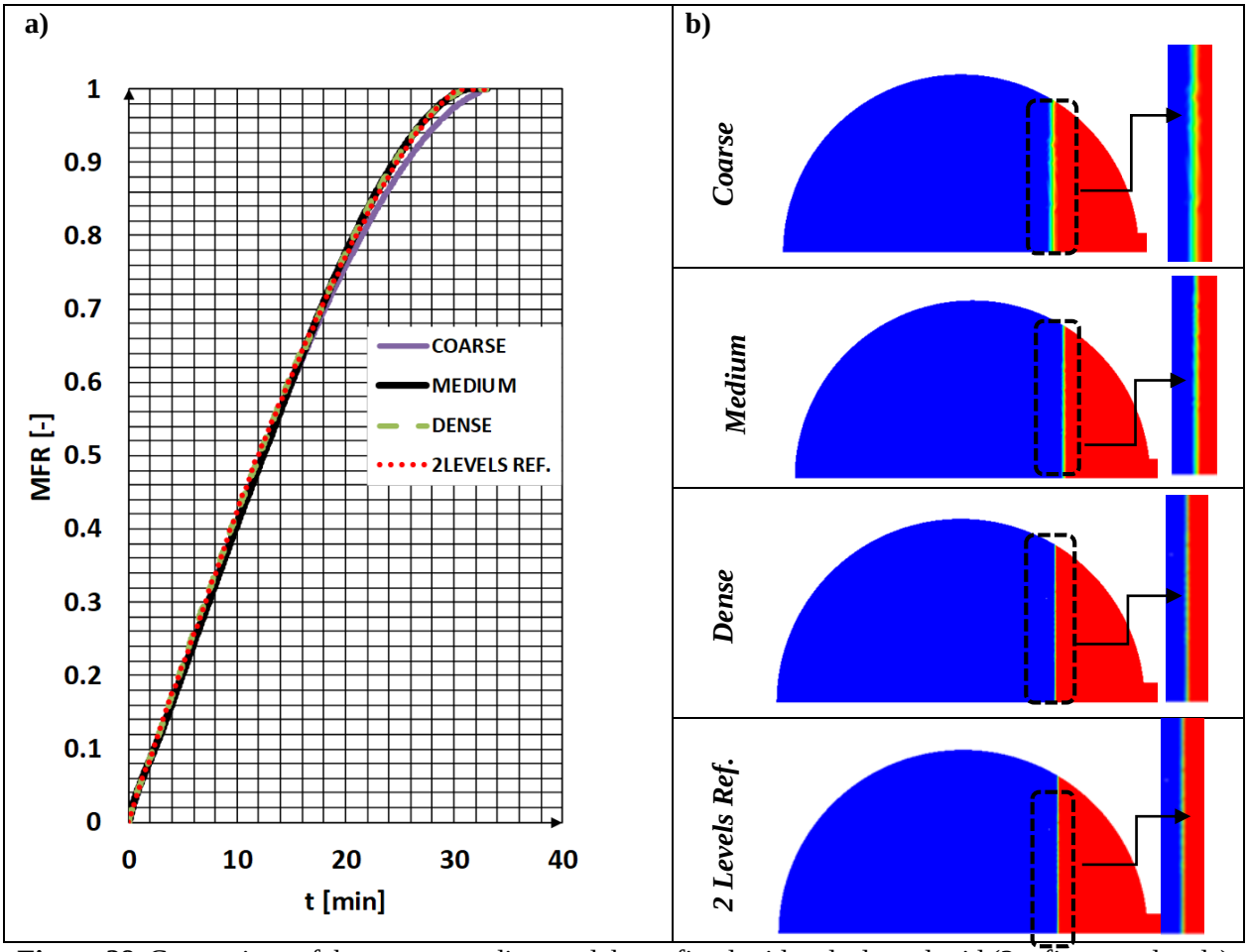

Figure 28. Comparison of the coarse, medium and dense fixed grid and adapted grid (2 refinement levels) a) melt fraction values at different time instants and b) and gas-PCM volume fraction contours at *t*=0 min.

Table 19 gives insight into the numerical cost needed to reach 30 minutes of simulation time for the four grid resolutions tested. It should be noted that in order to calculate the computational cost on a fair basis, additional tests were run in serial processing –of a 64-bit operating system with a 16 GB installed RAM memory- and with the same fixed time step equal to 0.002 s. Additionally, details are presented concerning the number of computational cells and grid resolution, i.e. minimum cell size, for each grid used. It is obvious that Case 1 (Coarse grid) is the least computational expensive, while being the one that introduces the highest numerical diffusion. On the other hand, Case 3 (Dense grid) is the most accurate, but the least efficient. Finally, Case 4 (2 Levels. Ref.) requires a relative low computational cost, considerably lower than Case 3 –almost 85%- and it is far more accurate than Case 1, in terms of numerical diffusion.

Taking all into account, the grid refined with the adaptive local refinement technique (Case 4) should be preferred over the rest, as it presents the advantages of both the medium and dense fixed mesh, in terms of

efficiency and accuracy, respectively (**Table 19** and **Figure 28**). Therefore, the latter has been used in the CFD analysis of the silicon solidification/melting process at ultra-high temperatures.

Table 19. Computational cost required to simulate the paraffin wax melting process (t=30 min simulation time) for the four grid densities investigated.

***** *Varying from 5,664 (number of cells at the beginning of the calculation) to 11,133 (maximum number of cells which is reached during the calculation)*

Case	Grid	Actual time (using 1 CPU core) (d)	Number of cells	Minimum cell size (m)
Case 1	Coarse	2.55	3,858	$5.54 \cdot 10^{-4}$
Case 2	Medium	12.5	15,432	$2.39 \cdot 10^{-4}$
Case 3	Dense	62.5	61,728	$1.07 \cdot 10^{-4}$
Case 4	2 Levels Ref	9.61	*	$1.07 \cdot 10^{-4}$

3.3.6 Mushy zone parameter effect

Figure 29a compares the melting fraction results as a function of time of the applied CFD model with the ones obtained from Assis et al. [43], both numerical model and experiments. The model of Assis, utilizes a grid of 3,520 cells– in contrast to the current model that uses the adaptive local grid refinement method. The graph shows that for most of the simulation time, the numerical results of the CFD model virtually coincide with that of the reference paper and are close enough to the experimental data. A small deviation, almost equal to 6 %, between the two models, can be primarily attributed to the different meshing methods used –coarse fixed grid in the reference paper and an adaptive local grid refinement method in the current model. Furthermore, in the reference paper, there are not any details available concerning the spatial and time discretization schemes and VOF formulation (implicit or explicit), the selection of which can affect the numerical results.

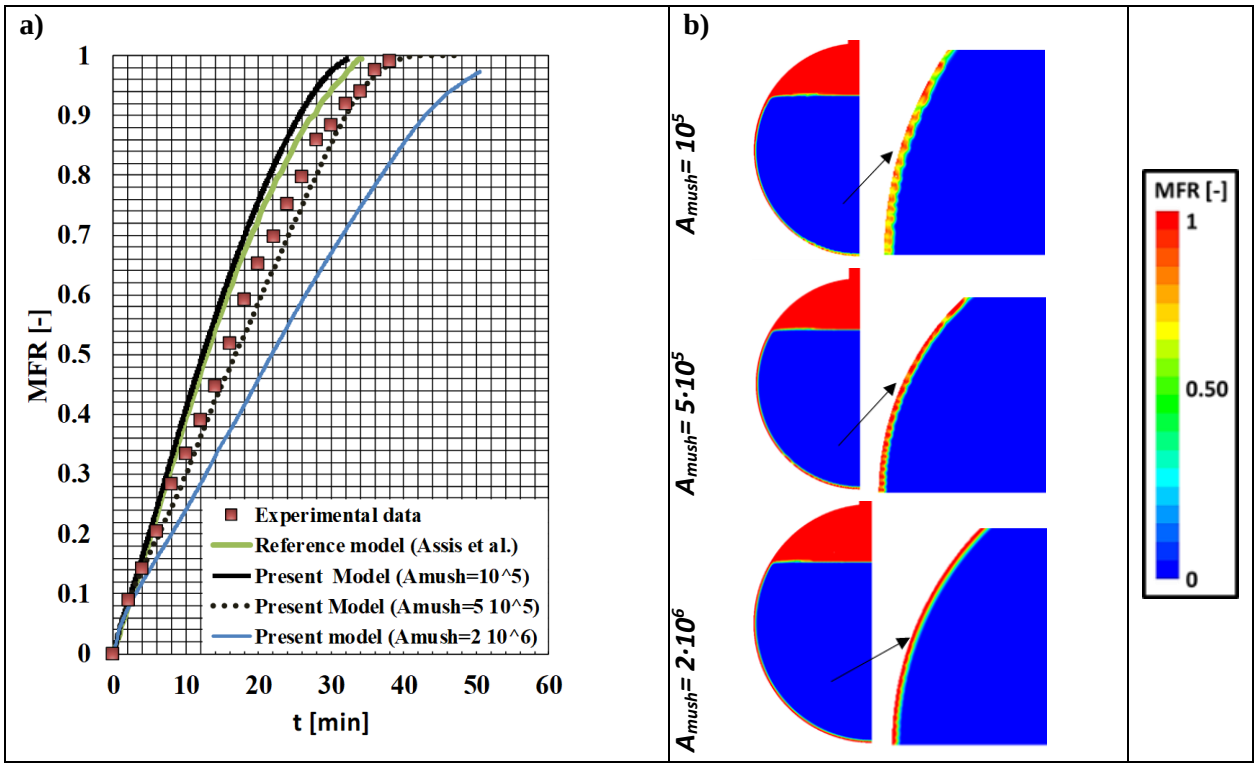

Figure 29. a) Paraffin melt fraction values versus time and b) liquid fraction contours at t= 1 min.

In the same graph, quantitate results of the A_{mush} parameter versus time are depicted. It can be deduced that this parameter affects significantly the PCM melting rate. An A_{mush} value equal to $5 \cdot 10^5$, which corresponds to a DAS=0.4 μm, gives the most accurate results for the melting performance of the specific PCM studied, i.e. paraffin wax. Thus, the values of this parameter should not be chosen arbitrarily, since A_{mush} is dependent on the solid PCM morphology, which in turn is highly affected by the imposed cooling rate [283]. Numerically, the dendrites presence in the solid PCM and subsequently the PCM permeability are modelled implicitly. Decrease in the A_{mush} parameter, which considers higher DAS values and, subsequently, higher permeability, increases the velocity values in the mushy zone, allowing significant flow motion in that region. This in turn accelerates the heat transfer, through convection, at the vicinity of that area.

As can be noticed in **Figure 29b**, visualization of 'structures' resembling to dendrites can be roughly obtained through the dynamically refined grid, with two levels of refinement (the cell size at the area of refinement is almost equal to 200 μm). Since the DAS for $A_{mush}=10^5$ is approximately 1 μm, it is expected that the dendrites representation can be possibly achieved explicitly, if a quite higher local grid resolution is adopted. This is an important outcome, since for the first time it is suggested that the enthalpy porosity approach coupled with an adaptive local grid method can potentially reproduce the mushy structure.

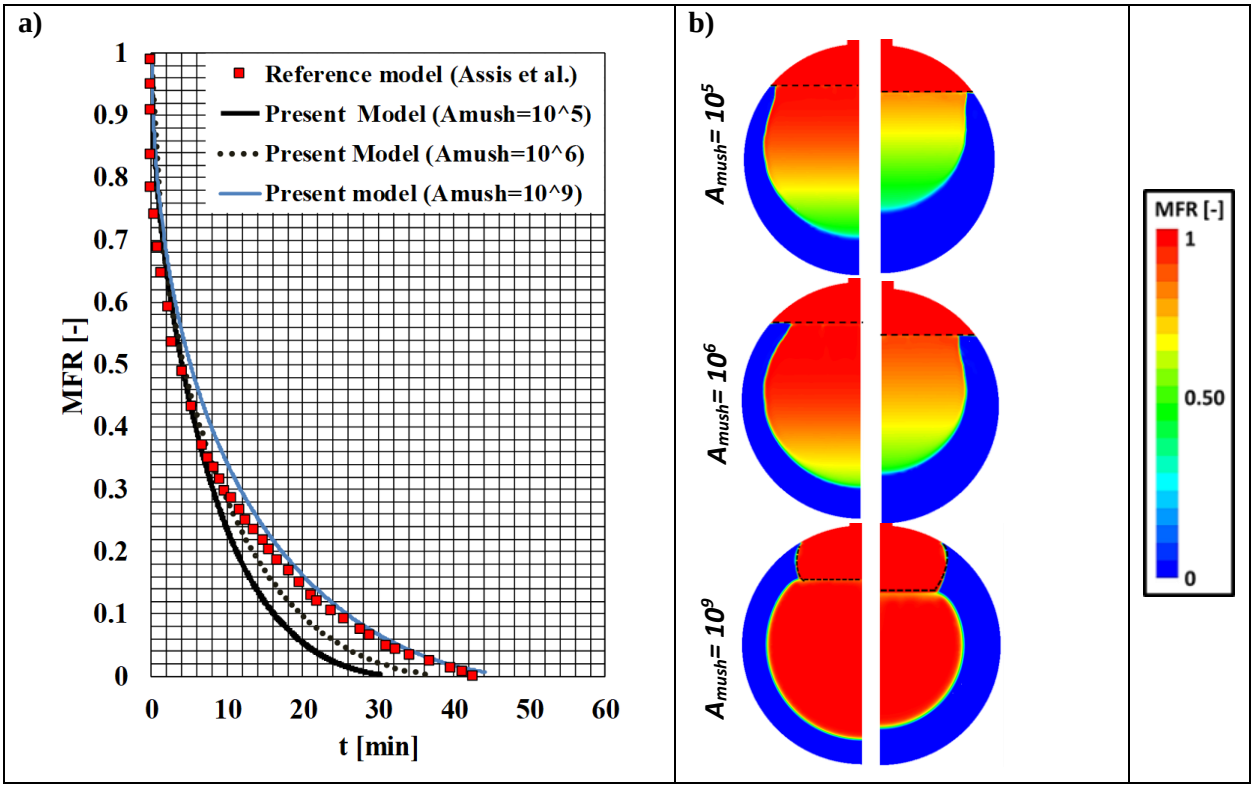

Figure 30. a) Paraffin melt fraction values vs. time and b) liquid fraction contours at t= 5, 10 min.

Figure 30a shows numerical results of the PCM melt fraction as a function of time obtained for different values of the A_{mush} parameter. Those results are compared with the ones of Assis et al. model [282]. As can be noticed, numerical results of the current CFD model agree well with the reference paper, as long as high values of the A_{mush} parameter (~10^9) are used. Over and above that, for this case, a limited numerical diffusion is achieved, whilst the melting fraction patterns bear a greater resemblance to the experimental visualizations of Assis et al. [282], than the cases with $A_{mush}=10^5$ and $A_{mush}=10^6$, **Figure 30b**. Therefore, in order to avoid excess numerical diffusion, during solidification phase, such high values are recommended.

It should be stressed out that with such a high value of the A_{mush} the solid phase velocities are set equal to zero artificially and thus, the floating of the solid in the liquid silicon cannot be represented, because the solid PCM does not move. Additionally, in contrast to melting phase, the A_{mush} parameter value does not play such a significant role on the PCM solidification times – since during solidification phase, heat transfer through conduction is the dominant mechanism- but mostly on the induced numerical diffusion.

3.4 Model verification (Silicon solidification: Ultra-high temperatures)

As a further step, the advanced CFD solidification/melting model developed in the framework of this Thesis is verified against other models –CFD in another solver and 1D analytical ones- for the solidification process of pure silicon. The studied vessel, inside which the PCM is contained, has the shape of an inverted truncated-pyramid (ITP). The ITP is sealed at the top, instead of the open spherical vessel previously used during validation process, and, it operates at ultra-high temperatures. Such a case study is more representative of the final prototype design and operation that will contain silicon-boron alloys, solidifying and melting at ultra-high temperatures. It should be noted that validation against experimental data would be preferable, however, is not attainable, due to lack of such a set of data for ultra-high temperatures. Additionally, by modelling the pure silicon as a PCM the volume expansion phenomena that occur during the silicon solidification phase are taken into account that subsequently cause high pressure values inside the vessel and a possible cracking. This comes into contrast with a silicon-boron alloy behaviour that is expected not to expand, at least to that extend of silicon. For safety reasons, and due to the fact that the vessel will be sealed, an inert gas is placed above the PCM to accommodate the PCM expansion –even for the case of silicon-boron alloy where a small expansion is expected.

In the current subsection, the results of a simplified version of the currently applied rigorous CFD model, which does not include the PCM expansion/contraction–designated as Fluent1Phase model- are compared against the ones obtained from the respective simplified model developed by [284] in OpenFoam (meltFoam) solver [285] – called as OpenFoam model. Comparison between the Fluent1Phase and OpenFoam models is undertaken in order to assess the enthalpy-porosity model validity against different solvers, i.e. Fluent vs. OpenFoam. Both models use similar settings (mesh, PCM properties, and operating conditions). Finally, the advanced CFD model developed in this Thesis, designated as Fluent2Phase, is applied and results of all models are compared. Finally, all 3-D models, i.e. Fluent2Phase, Fluent1Phase and OpenFoam model, are compared against an 1D analytical model developed by Datas et al. [286] in terms of temperature profiles and the dimensionless solid-liquid PCM interface at different time instants.

3.4.1 Geometry and mesh layout

The geometry and mesh layout used in the Fluent1Phase and Fluent2Phase models are depicted in **Figure 31a** and **Figure 31b**, respectively. In both models, the ITP geometry is placed vertically. Additionally, the emitter, which is fixed at the lowest part of the vessel, radiates heat during the discharge process, causing the PCM solidification. The radiated heat is more or less dependent on the emitter temperature according to a study conducted by Datas et al. [286]. For this reason, a custom-UDF is applied to calculate iteratively for each time step the temperature dependent heat flux $Q=Q_e\ (T)$, equation (141), at the emitter surface. Finally, the upper and sidewalls of the tank are considered adiabatic during the model verification process. However, in real conditions, heat losses through the container walls must be assessed in order to determine the validity of these idealistic results. Such an analysis is presented below.

Apart from the similarities, some small differences are traced between Fluent1Phase and Fluent2Phase models as regards the geometry and mesh layout. First of all, in the Fluent1Phase model the sealed crucible contains only the PCM and has a height equal to 0.1 m, whilst in the Fluent2Phase model, the molten PCM fills 85% of the vessel and the rest of the domain is filled with an inert gas. For this reason, in the latter model the crucible is extended up to a height of 0.021 m to contain the inert gas, as well. Finally, in the Fluent1Phase model a uniform 3D coarse grid of 4356 hexahedral cells is used, as in the OpenFoam model. In the Fluent2Phase model, the problem is solved as axisymmetric and the adaptive local refinement technique -2 levels of refinement- is implemented, which results in a maximum grid size of almost 7000 cells. Based on preliminary calculations conducted the axisymmetric problem leads to almost equal results as the 3D, in terms of solidification/melting rates. Therefore, in order to save computational cost the axisymmetric problem is preferred over the 3D for the specific heat transfer problem.

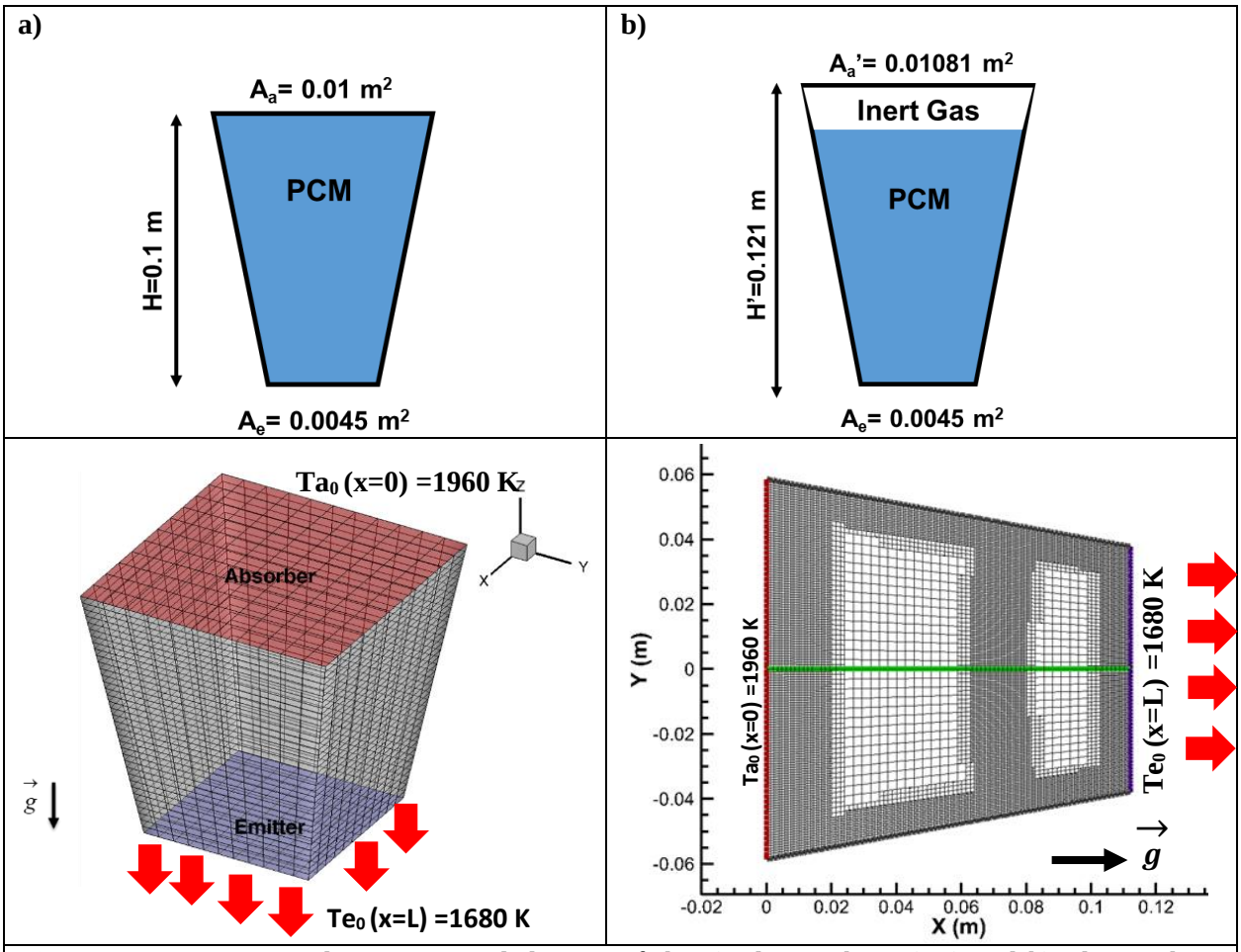

Figure 31. Geometry and computational domain of the a) Fluent1Phase (3D) and b) Fluent2Phase (axisymmetric) models. Purple: emitter surface, green: axis, red: absorber, black: walls.

It should be stressed out that in all of the applied models, the floating of the solid in the liquid silicon cannot be represented, because the solid PCM does not move. In a future model formulation the natural phenomenon of floating or sinking of the solid material inside the liquid PCM due to buoyancy forces, should be also taken into account, for an even more realistic representation.

3.4.2 Boundary and operating conditions

The boundary conditions assigned for both the Fluent1Phase and Fluent2Phase problems are presented in **Table 20**. The equation of the heat flux at the emitter surface is the following:

$$Q_e = -(3.17 - 04 \cdot T_{em}^3 - 0.7616 \cdot T_{em}^2 + 6.438E02 \cdot T_{em} - 1.8385E05 \quad 141)$$

, where T_{em} is the emitter temperature.

It should be noted that this equation is a 3rd order fit to a more complex radiative model that describes the radiative exchange, between an emitting surface and a TPV cell [27].

Table 20. CFD verification problem boundary conditions used in Fluent1Phase and Fluent2Phase models.

	BC type	**Parameters**	**Units**	**Values**
Wall	Wall	Q	$W \cdot m^{-2}$	0
Absorber	Wall	Q	$W \cdot m^{-2}$	0
Emitter	Wall	Q	$W \cdot m^{-2}$	$Q_e\ (T)$
	Shear condition: No slip			

The PCM-gas thermophysical properties are listed in **Table 21**. The silicon properties are retrieved from the literature [287]. In the Fluent2Phase model, a melting interval of 1679-1681 K is used, for numerical reasons, in order to avoid the sharp transition of the PCM properties, between its solid-liquid phases. In reality, in pure metals, like pure silicon, there exists no 'mushy' zone [288]. Additionally, in the 1Phase model the silicon thermal conductivity has a sharp transition around its melting point, whilst in the Fluent 2Phase model there is a small transition owing to the presence of the mushy zone.

Initially, the temperature is set equal to 1680 K at the emitter and equal to 1960 K at the upper part of the tank. For the rest of the domain a linear interpolation of these two values is used to patch the temperature profile. Transient calculations are performed, with a fixed time step set equal to Δt=0.05 s in the Fluent 1Phase model and a variable time step (Courant number=0.2, max. Δt=0.01 s) in the Fluent 2Phase model.

Table 21. Gas-solid properties (gas: air, PCM: silicon) used in Fluent1Phase and Fluent2Phase model.

Model	**Fluent 1Phase**		**Fluent 2Phase**		
Property	**PCM-solid**	**PCM-liquid**	**Gas**	**PCM-solid**	**PCM-liquid**
ρ, $kg \cdot m^{-3}$	2520	2520	Compressible (Tait equation)	2330	2570
k, $W \cdot m^{-1} \cdot K^{-1}$	20	60	0.0573	20	60
C_p, $J \cdot kg^{-1} \cdot K^{-1}$	1040	1040	1189	1040	1040
μ, $kg \cdot m^{-1} \cdot s^{-1}$	-	$0.7484 \cdot 10^{-3}$	4.96-05	-	$0.7484 \cdot 10^{-3}$
$T_{solidus}$, K	1680		-	1679	
$T_{liquidus}$, K			-	1681	
L, $J \cdot kg^{-1}$	$1.8 \cdot 10^6$		-	$1.8 \cdot 10^6$	
β_{th}, K^{-1}	0.000143		-	-	

3.4.3 Results

The model verification process has proven the accuracy of the Fluent2Phase model, for the simulation of LHTES systems operating at ultra-high temperatures. More specifically, from the CFD analysis it was revealed that for most of the simulation time results of the advanced Fluent2Phase model virtually coincide with that of the Fluent 1Phase, OpenFoam and 1D model in terms of solidification rates (**Figure 32**) and melt fraction contours (**Figure 33**). At approximately 2 hours of simulation time, the temperature results indicate that the solidification is terminated and afterwards the temperature decreases rapidly. Such a good agreement enhances the applied models validity. More specifically, it is proven that during the silicon solidification inside the closed shell, the dominant heat transfer mechanism is thermal conduction. A small deviation, of almost 4%, between the 1Phase and 2Phase model is tracked as concerns the prediction of the overall discharge time. Such discrepancy is mainly attributed to the fact that the solidification process in the 2Phase model lasts more than in the 1Phase one, due to PCM expansion. Actually, the PCM solidification lasts ~2 hours based on the 2Phase model results, whilst in the 1Phase model lasts ~1.9 hours.

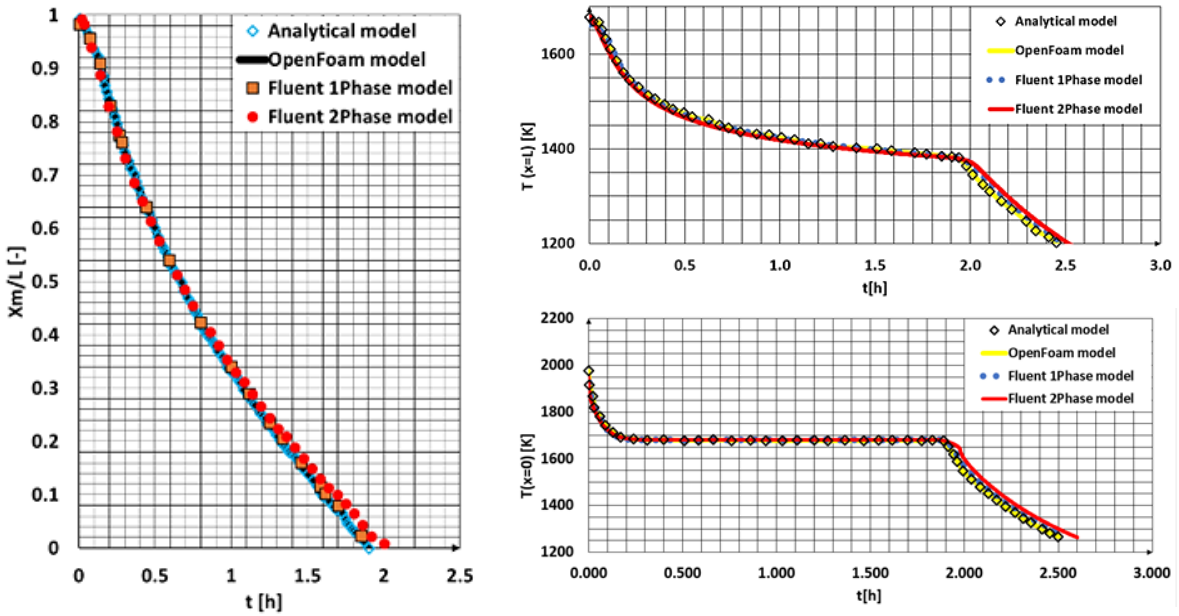

Figure 32. Comparison of the four models in terms of (a) the dimensionless solid-liquid interface location (X_m/L) and b) the PCM temperature at x=0 (upper part) and x=L (lower part) as a function of time.

It is worth noticing that with the 1D and 1Phase CFD models any PCM volume changes and possible dendrites formation effect on the phenomenon temporal evolution are not considered; the PCM volume change during solidification is approximately 7%. Contrary to that, the Fluent 2Phase model predicts the PCM solidification process in a more realistic manner, since volume expansion is considered. By this way the induced pressure field is also predicted more realistically, **Figure 34**, since in the case of Fluent1Phase model, where volume expansion is not taken into account, minor increase in the induced pressure is predicted. In a pure heat transfer problem, such an assumption is of minor importance, however, if the stress-strain field should be modelled with high accuracy, volume expansion should be taken into account, especially when density variations between solid and liquid phases are high enough (>15%).

Another conclusion is that in the specific problem, the silicon is contained in a rigid casing in a shape of truncated cone, where the direction of the smallest resistance to expansion is the axial. During the PCM solidification a slightly higher expansion can be observed near the PCM centreline than the one noticed

near the walls (**Figure 33**). This is reasonable since the distance between the lateral walls of the vessel increase with height and therefore in these areas both axial and radial expansion is observed. This observation cannot be predicted with the 1Phase model, where the PCM volume change is not modelled.

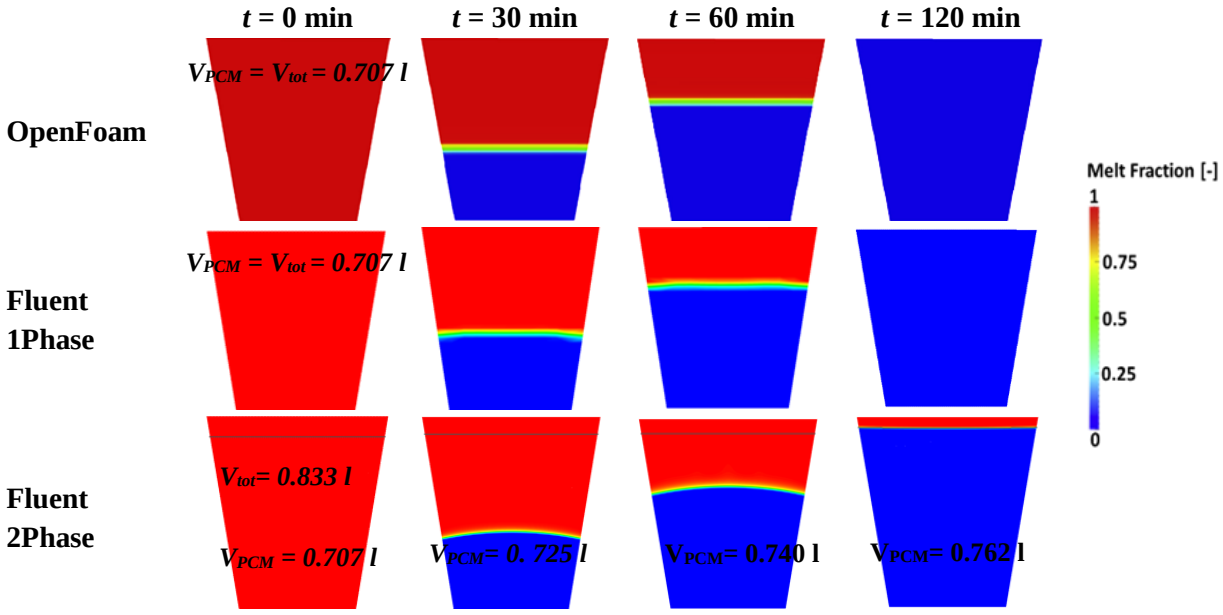

Figure 33. Contours of the a) OpenFoam b) Fluent1Phase and c) Fluent2Phase CFD model melt fractions (*t*=0, 30, 60 and 120 min). (Blue: solid phase, red: liquid PCM+ inert gas (In the 2-phase model these two phases are distinguished through a line at the interface between gas-PCM).

Finally, it is observed in **Figure 34** that in the closed PCM shell case the pressure profile is almost homogeneous at each time instant. The induced pressure values increase as the PCM volume increases during solidification process, almost up to 5-6 bar**.** Therefore, it is suggested that apart from the inert gas above the PCM, a release valve should be also added in the final prototype design to ensure that no high pressures are induced inside the vessel. Such pressures can be even higher in case of an uncontrollable reaction of the PCM with the crucible, due to ultra-high temperatures. Similar observation for the pressure increase during silicon solidification can be also found in [289].

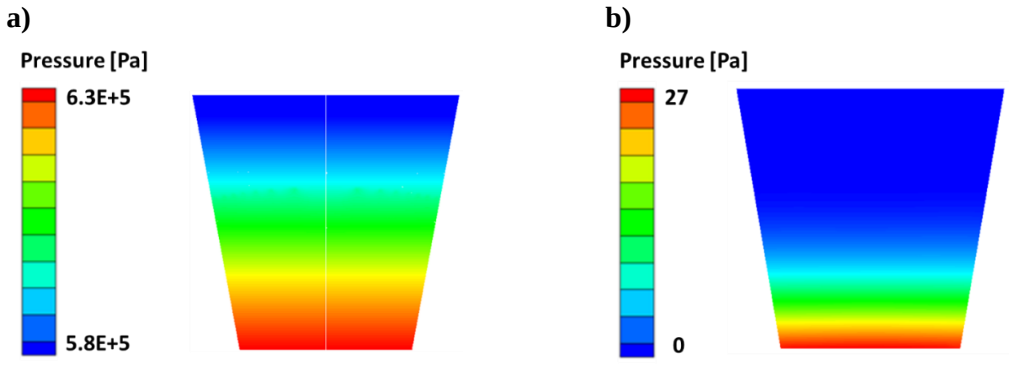

Figure 34. Pressure field predicted inside the sealed vessel by a) the Fluent2Phase model (volume expansion of almost 7%), and b) the Fluent1Phase model (volume expansion is neglected).

Concluding, many aspects of the real phenomenon are neglected in the 1D and 1Phase CFD models. The 1-D model can be considered a valuable tool for the PCM casing design, especially during the earlier design

stages, as it can quantify very fast important design parameters, without high error. On the other hand, the advanced CFD 2Phase model should be applied for more complicated applications, characterized by high gradients of different properties, and for the more realistic representation of the solidification process in the case of more complex and promising designs. In addition, operating parameters that cannot be easily predicted from 1D models, such as pressure distribution, thermal stresses, thermal losses etc., can be described in a more detailed manner. Thus, the 3D numerical solution of the transient PCM phase change process is more accurate than the 1D solution and can be used in different engineering conditions.

3.5 Parametric study A: Vessel shape/size effect

3.5.1 Geometry and mesh layout

Following its validation the CFD model is applied for the numerical study of Si solidification/ melting process at ultra-high temperatures (~1400 °C) inside a novel electric-TES system, described in [27]. Five different TES design concepts are studied (**Figure 35**), i.e. sphere, cut-off sphere, cylinder, truncated cone and cube, with the same volume (V_{vessel} = 3.75·10^{-3} m^3) and emitter surface (A_{Em}=2.25·10^{-2} m^2)–vessel bottom area where the heat extraction occurs during discharging. All the tested geometries are created in ANSYS DesignModeller and they are sealed from the top.

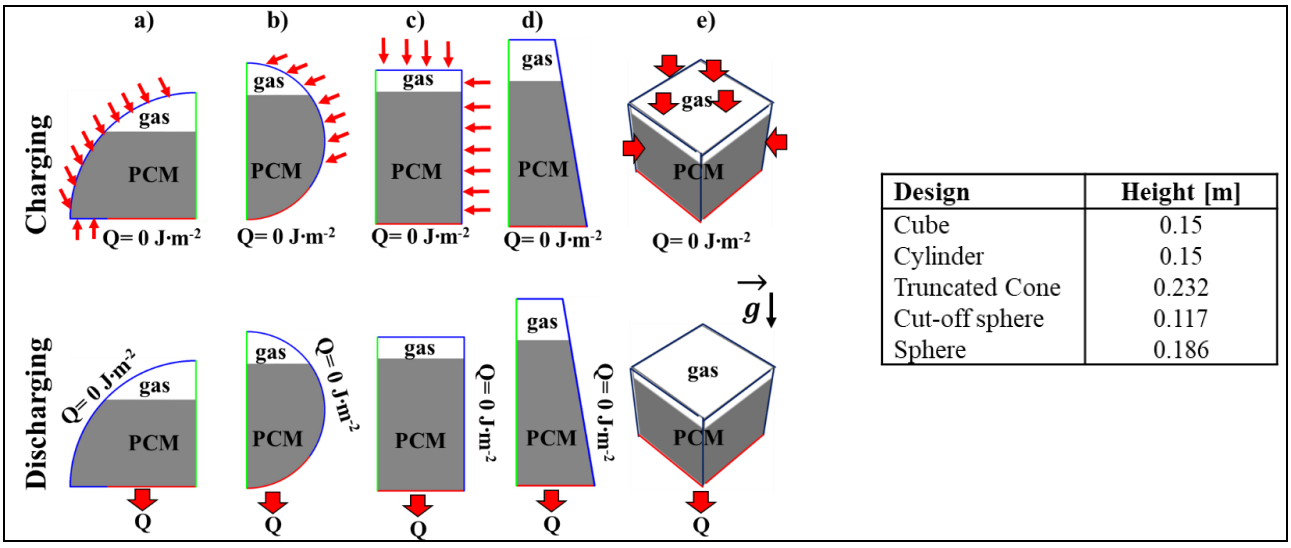

Design	Height [m]
Cube	0.15
Cylinder	0.15
Truncated Cone	0.232
Cut-off sphere	0.117
Sphere	0.186

Figure 35. Physical models of the studied geometries: (a) cut-off sphere, (b) sphere, (c) cylinder, (d) truncated cone and (e) cube. Red: emitter, green: axis, Blue: sidewalls.

The applied grid methodology follows the local grid refinement method with two refinement levels, as in the model validation case. **Table 22** provides information on the number of cells required to achieve the sharp gas-PCM and solid (PCM)–liquid (PCM) interface by using either the local grid refinement technique or an equivalent uniform dense grid of the same grid resolution near the interfaces.

Table 22. Mesh details for the different geometries tested.

Design	Grid	# Cells	# Cells of equivalent dense grid	Problem
Cube	2 Lev. ref.	~7.5·10^5	~3·10^6	3D
Cylinder	2 Lev. ref.	~1.6·10^4	~7·10^4	Axisymmetric
Cone	2 Lev. ref.	~1.1·10^4	~4·10^4	Axisymmetric
Cut-off sphere	2 Lev. ref.	~1·10^4	~4.9·10^4	Axisymmetric
Sphere	2 Lev. ref.	~1.1·10^4	~5.9·10^4	Axisymmetric

3.5.2 Boundary/Operating conditions

The problem boundary conditions imposed on the five tested geometries during Si melting are presented in **Table 23**. More specifically, the container sidewalls are heated at a uniform temperature equal to 1707 ^{o}C. The emitter is insulated during melting, as the device is in "charging" mode, thus, no heat loss conditions are considered there. Additionally, the contact resistance R_c is set equal to zero, following the assumption that there is not an additional air gap between the walls and the PCM and a no slip boundary condition is set at the solid boundaries, as in the work of Assis et al. [43]. The wall thermal resistance, $R_{th,w}$, is considered equal to the one used in the model validation case. However, in ultra-high temperature LHTES systems, crucibles of lower R_w (such as ceramic materials) are used.

Initially, the PCM occupies the 92% of the domain, which is sub-cooled with a temperature 10 degrees lower than the PCM melting point, i.e. 1413 ^{o}C.

Table 23. Boundary conditions imposed during the study of vessel shape effect on Si melting.

	BC type	**Parameters**	**Units**	**Values**
Sidewalls	Wall	T_W	^{o}C	1707
		$R_{th,W}$	$m^2 \cdot K \cdot W^{-1}$	0.0025
		$R_{th,c}$	$m^2 \cdot K \cdot W^{-1}$	0
Emitter	Wall	Q_{Em}	$W \cdot m^{-2}$	0
	Shear condition at walls: No slip			
Axis	Symmetry			

The PCM solidification process is simulated shortly after its melting phase. In this case, heat is extracted from the vessel bottom part, making the dominant heat transfer direction the vessel axis. A uniform temperature is set at this surface equal to 1097 ^{o}C, whilst zero heat losses are considered at the sidewalls, **Table 24**. Initially, the molten PCM fills 86.2 % of the domain, due to its contraction after melting. Additionally, the whole domain is patched with temperature 5 degrees greater than the PCM melting point. In both phases, transient calculations are performed, with a variable time step size (courant number =0.2). Information on the discretization schemes and the gas-silicon properties can be found in [232] and in **Sub-section:** Model verification (Silicon solidification: Ultra-high temperatures)**.**

Table 24. Boundary conditions imposed during the study of vessel shape effect on Si solidification.

	BC type	**Parameters**	**Units**	**Values**
Emitter	Wall	T_W	^{o}C	1097
		$R_{th,W}$	$m^2 \cdot K \cdot W^{-1}$	0.0025
		$R_{th,c}$	$m^2 \cdot K \cdot W^{-1}$	0
Sidewalls	Wall	Q_W	$W \cdot m^{-2}$	0
	Shear condition at walls: No slip			
Axis	Symmetry			

3.5.3 Results

Figure 36 shows contours of silicon liquid fraction for the five geometries tested. As can be noticed, a gradual melting of the PCM occurs from the side to the bottom region at each case. Additionally, the solid material is free to float in the PCM-air interface, thus forcing the liquid silicon aside to a downward movement and in return producing a more rapid melting due to natural convection. This phenomenon

observed is the opposite of paraffin wax, which sinks during melting process, whilst its melting is mainly favored in its upper region, due to the molten PCM upward movement.

More specifically, in the beginning of the melting process, the solid silicon is in direct contact with the container walls. During the first seconds of the PCM melting at t=1 min, a thin liquid region of homogeneous shape –a shape similar to that of the heated sidewalls- is formed around the solid phase. This indicates that the dominant mechanism during the initial stages of the melting process is the heat transfer via conduction. Later on, as the liquid region grows more and more over time, natural convection becomes more pronounced, influencing the melting shape of the PCM.

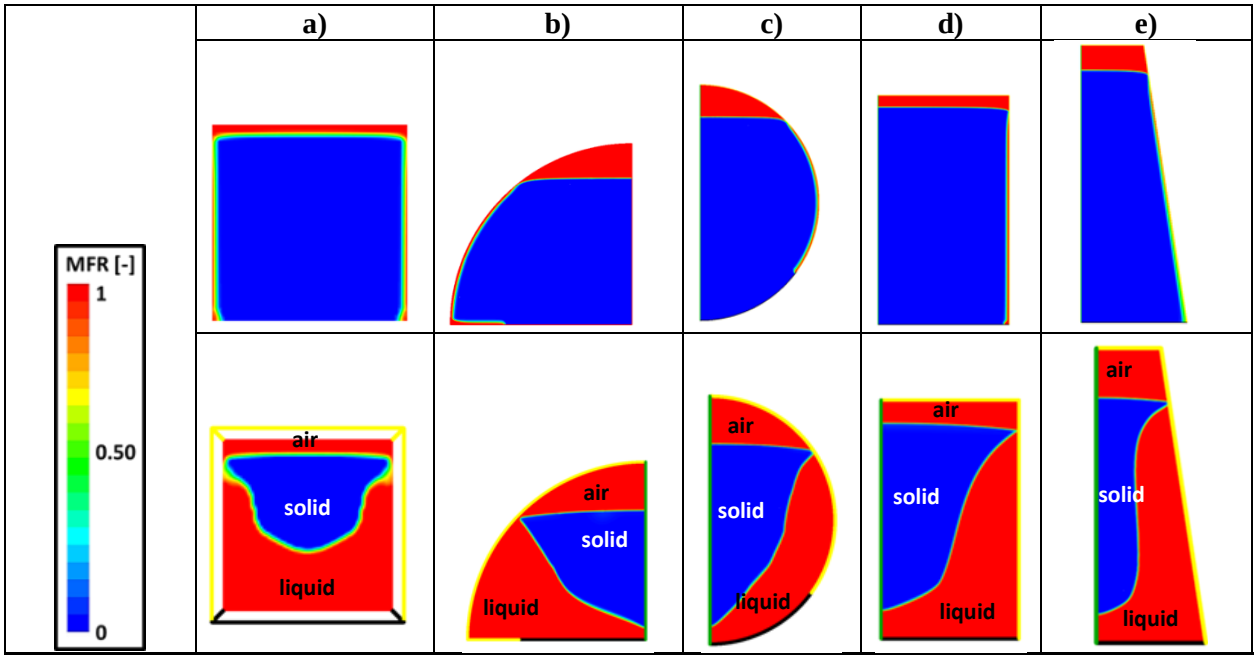

Figure 36. Melt fractions contours at *t*=1, 20 min for the: a) cube, b) cut-off sphere, c) sphere, d) cylinder, and e) truncated-cone. (Green: axis, yellow: sidewalls and black: emitter).

The quantified evolution of the melting fraction with time for all designs tested is presented in **Figure 37a**. It can be inferred that the melting process is the slowest in the sphere (~40 minutes) and the fastest in the cube and truncated cone (~ 26-28 min), due to the smaller or larger heated surface, which undermines or enhances the heat transfer process, respectively. Actually, cube and cone are 25 % and 21 % quicker than the sphere, respectively. It is highlighted that even if the cubic shape seems advantageous, it should be noted that during solidification and storage processes the PCM is expected to experience the highest thermal losses, since it has the highest surface area per unit volume.

Figure 37b, shows the Si solidification rates for the five studied geometries. The solidification process is the slowest in the cone (~280 minutes) and the fastest in the cut-off sphere (~ 140 min), due to its smaller or higher height, **Figure 35**, which undermines or enhances the heat transfer process, accordingly. The vessel height plays an important role in this heat transfer problem in a sense that the heat is extracted from the bottom of the vessel, making the dominant direction of the heat transfer the vessel axis. Actually, a maximum difference of almost 50% can be observed in the solidification times, between the cut-off sphere and the truncated-cone –the truncated-cone height is almost two times higher than that of cut-off sphere. In between these two geometries, lie the cube, sphere and cylinder, which almost have the same height.

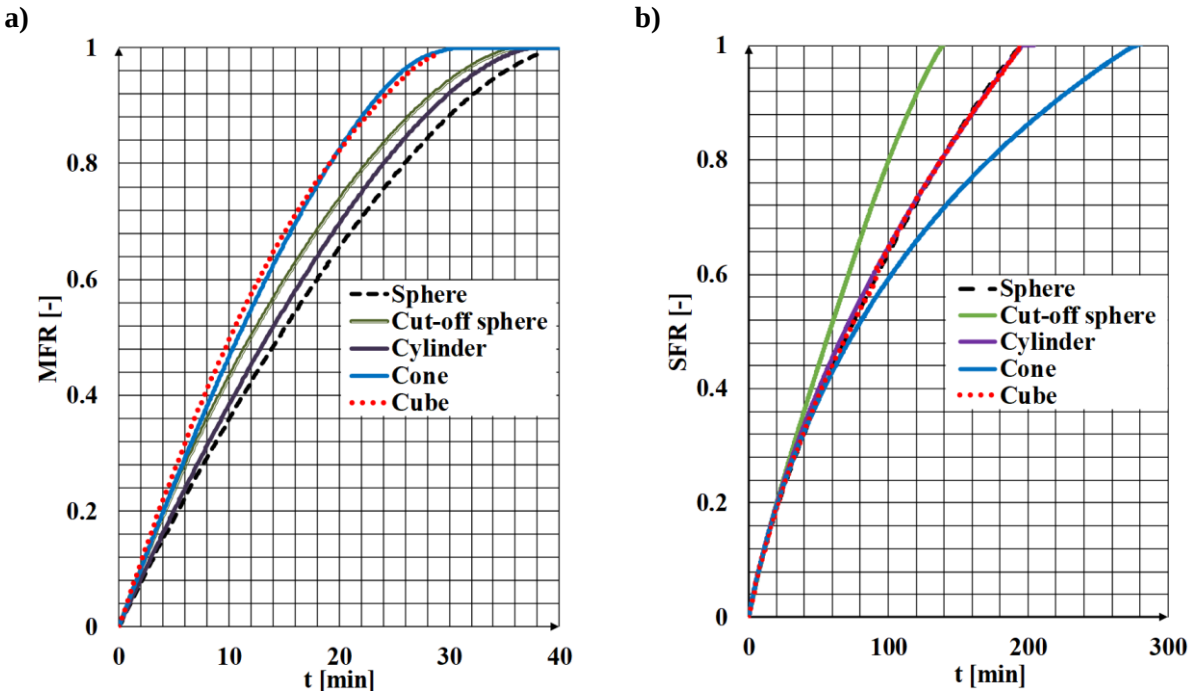

Figure 37. a) Melt and b) solid fraction values versus time for the different geometries tested.

Indicative values of the lateral heat losses during thermal energy storage period of the studied geometries are also reported. In all cases ambient temperature conditions are considered, whilst insulation of small thermal resistance ≈0.002 m^2 K W^{-1} is considered. At t=0 s all geometries are patched with a temperature equal to 2000 ºC. As can be noticed in **Table 25** the dominant parameter that affects system heat losses during storage period –for a specific insulation method- is its exterior surface to volume ratio. Therefore, the spherical design, with the lowest surface to volume ratio, is the most favourable in terms of heat losses and is followed by the cylinder and the truncated cone. The cubic design is the worst case, since it has the highest lateral surface to volume ratio, resulting in the highest lateral heat losses, accordingly.

Table 25. Indicative heat losses for the different shapes tested during storage period.

Design	Outer Surface (m^2)	Lateral heat losses* (kW)	Q_{loss} (kJ)*
Cube	0.135	~ 86.5	~ 5868
Cylinder	0.1248	~ 80	~ 5517
Truncated Cone	0.1296	~ 84	~ 5720
Cut-off sphere	0.1296	~ 85	~ 5756
Sphere	0.1088	~ 73	~ 4891

* At t=60 s after the start of simulation

Taking all into account, the cut-off sphere is the optimum shape among the ones tested, as concerns thermal losses, and charge/discharge rates, **Table 26**. Apart from this, such a design eliminates the structural tension as it redirects the gravity force or compression forces, downwards in multiple directions. Additionally, its lateral surface, from where heat losses are expected is rather moderate, compared to the rest of the cases tested. The most advantageous, considering stresses and thermal losses, but not so much as regards charge rates, is the sphere. Both geometries would be interesting to construct and test their performance in a compact P2H2P concept; however, the vessel integration in the whole system might be difficult. An alternative option to these and easier and more flexible to construct for such an application is the truncated

cone, which also results in high melting rates and moderate heat losses. Its solidification rates even though they are the lowest compared to the rest of the designs tested can be further reduced by altering its tapering ratio (bottom to upper surface ratio).

Table 26. Classification of the different designs tested from the most to the least optimum in terms of a) solidification and b) melting rate and c) heat losses during thermal energy storage period.

Selection criteria	**Solidification rate**	**Melting rate**	**Minimum Q_{loss} during TES**
	Cut-off sphere	Cube Truncated Cone	Sphere
	Sphere Cylinder Cube		Cylinder
		Cut-off sphere	Truncated Cone Cut-off sphere
		Cylinder	
	Truncated Cone	Sphere	Cube

3.6 Parametric study B: Heat losses effect

Following the study on the vessel shape effect on the PCM solidification/melting process, under the assumption of adiabatic conditions, the Fluent2Phase model is applied to study in a more detail –and with the more realistic scenario of including heat losses- the ITC design. The reason for such a choice is that the truncated-cone can be fabricated more easily compared to other novel designs suggested in this Thesis, such as sphere and cut-off sphere. Another advantage of the ITC compared to similar ones, such as the inversed truncated pyramid, is that it does not have sharp corners, reducing, thus, the local stresses and any possible risks of mechanical failure in these areas. An alternative solution to ITC is the cylindrical design, which will be also studied briefly. Several vessel geometries, volumes and insulating materials are investigated.

3.6.1 Numerical cases examined

Regarding the vessel insulation, two methods have been tested, **Figure 38**. In the first one, only graphite fiber mat- GFM (Case 1A, **Table 27**) is used. In the second one, GFM is utilized as an inner layer and fumed silica board-FSB as an outer layer (Case 2A-4A, **Table 27**). Data concerning materials thermal properties are retrieved by [290]. Their values have been calculated by taking into account both thermal conduction and radiation through the insulating materials. The geometry used in this set of cases studied is the ITC design with a tapering ratio (*TR*) –emitter to absorber surface ratio- equal to 0.45 and a reference volume *V* equal to 8.326e-04 m^3 (Case 1B, **Table 28**). The cases simulated are presented in **Table 27**.

Table 27. List of cases studied regarding the container insulating layers effect on system heat losses.

* Insulating materials thermal resistance at a temperature *T*=1680 K.

Case	**# Layers**	**b_{GFM} [m]**	**b_{FSB} [m]**	**$R_{th,total,1680}$* [m^2 K·W^{-1}]**	**Phase studied**
Case 1A	1	0.03	-	0.1179	Charge/ Discharge
Case 2A	**2**	0.03	0.06	1.88	Charge/ Discharge
Case 3A	2	0.06	0.09	2.88	Discharge
Case 4A	2	0.1	0.15	4.80	Discharge

As concerns the vessel geometry, the following cases have been investigated:

A. <u>During system charge/discharge</u>, **Table 28**:

I. Different vessel volumes *V* (Case 1B), *V*/2 (Case 2B) and *V*/4 (Case 3B);

II. Different vessel tapering ratios [*TR*=1 (Case 5B-6B), 0.45 (Case 1B), 0.225 (Case 4B)], by keeping the latent heat storage system volume constant equal to *V*.

Table 28. List of cases studied regarding the container design effect on LHTES system performance.

Case	V [m^3]	A_{em} [m^2]	A_{abs} [m^2]	A_{wall} [m^2]	H [m]	Shape	Phase studied
Case 1B	0.0008326	0.0045	0.01081	0.03456	0.1121	ITC	Charge/ Discharge
Case 2B	**0.0004163**	0.0045	0.01081	0.01813	0.0560	ITC	Charge/ Discharge
Case 3B	**0.0002081**	0.0045	0.01081	0.01058	0.0280	ITC	Charge/ Discharge
Case 4B	0.0008326	0.0045	**0.02054**	0.03130	0.0721	ITC	Charge/ Discharge
Case 5B	0.0008326	0.0045	**0.0045**	**0.0440**	0.185	Cylinder	Charge/ Discharge
Case 6B	0.0008326	**0.01081**	0.01081	0.02839	0.077	Cylinder	Charge/ Discharge

B. <u>During storage period</u>:

I. Different ITC volumes (V, V/2, V/4, 2V and 4V), **Table 30**. In this set of cases tested **(Table 28)**, insulating method of two layers (Case 2A, **Table 27**) has been used.

3.6.2 Geometry and mesh layout

The vessel geometry –volume V and TR ratio equal to 0.45- and discretised domain used during insulating layers parametric study are depicted in Figure **38a** and **Figure 38b**, respectively. The ITC geometry is placed vertically and contains silicon as a PCM. At its bottom, the emitter of the TIPV converter is fixed, coming into direct contact with the molten silicon. During system discharge, the TIPV anode, which comprises a thermionic and a photovoltaic cell, is patched to the system and is irradiated by the emitter, producing electricity. This radiated heat, which is more or less dependent on the emitter temperature - $Q=Q_{em}(T)$, eq. (141) - causes the PCM solidification. During charge or TES period, the TIPV converter anode is dispatched from the system, insulating materials are placed on the vessel bottom part and, as a result, the emitter stops radiating heat. Other surfaces in the vessel include lateral and upper walls, designated in this analysis as walls and absorber, respectively.

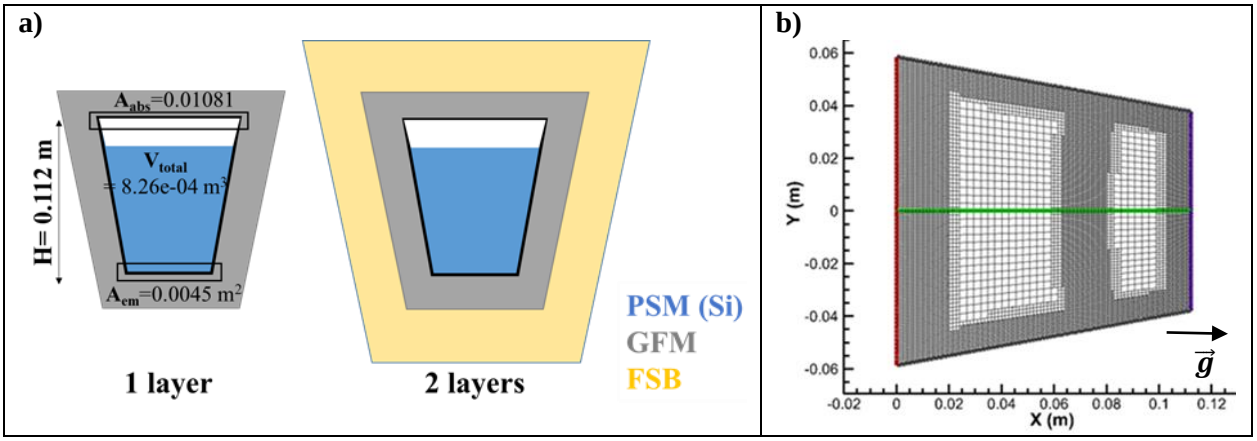

Figure 38. a) Cases investigated during the insulating layers parametric study and b) computational domain (**purple**: emitter surface, **green**: axis, **red**: absorber, **black**: walls).

Figure 39 depicts the mesh layouts of the different geometries tested. The adaptive grid local refinement technique [94] is applied in order to capture the sharp gas–PCM and solid-liquid interfaces. This technique results in a maximum grid size of almost 20,000 quadrilateral cells, in all cases. The refined grid comprises elements of maximum and minimum cell volume equal to $3\cdot10^{-7}$ m^3 and 10^{-11} m^3, respectively.

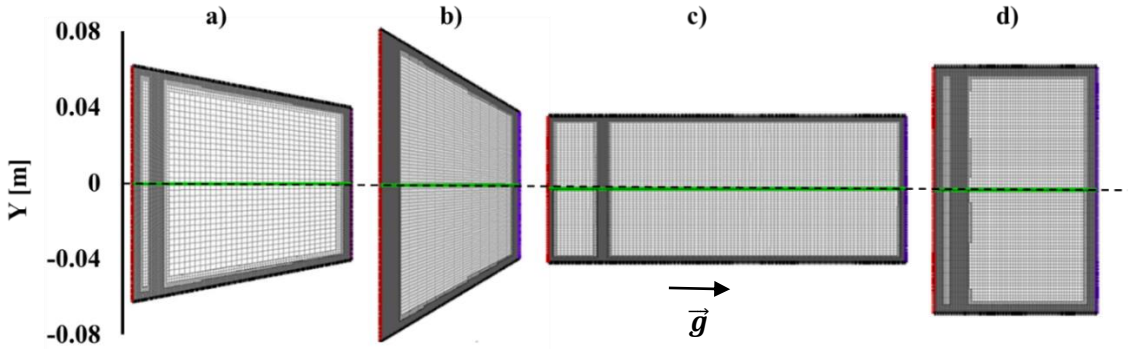

Figure 39. Mesh layout of the studied geometries: a) Case1B, b) Case4B, c) Case5B and d) Case6B.

3.6.3 Boundary and operating conditions

Solidification/ melting process

In **Table 29** are presented the boundary conditions assigned during the system charge/discharge. More specifically, during discharging, the heat flux at the emitter surface follows the temperature dependent equation (1). The rest of the surfaces (wall, absorber) are insulated, whilst a temperature equal to 300 K is considered at the system exterior surface, assuming that the temperature there tends to homogenize to the ambient one (study of worst case scenario). During system charge, the temperature at the lateral walls, where the heater is placed, is defined equal to T_{wall}=2000 K. At the rest of the surfaces (emitter, absorber), a temperature equal to 300 K is considered at the system exterior surface.

The PCM-gas thermo-physical properties are retrieved from [232]. Its melting and solidification points are equal to 1681 K and 1679 K, respectively. During system discharge, the temperature is initially (t=0) set equal to 1680 K at the emitter and equal to 1960 K at the absorber. For the rest of the domain a linear interpolation of these two values is used to patch the temperature profile. The PCM melting process is simulated shortly after its solidification phase. Initially, the solid PCM fills 92 % of the vessel, to avoid any problems due to its expansion after melting. In this phase, the PCM subdomain is patched with a temperature 140 degrees lower than its melting point.

Table 29. CFD problem boundary conditions used during system charge/ discharge phase.

		BC type	Parameters	Units	Values
Solidification	***Wall/ Absorber***	Wall	T	K	300
			$R_{insulation}$	$m^2 K \cdot W^{-1}$	Varying, (**Table 27**)
			b_{vessel}	m	0.01
			k_{vessel}	$W \cdot m^{-1} \cdot K^{-1}$	12.5
	Emitter	Wall	Q	$W \cdot m^{-2}$	Q_{em} (T), eq. (141)
Melting	***Emitter/ Absorber***	Wall	T	K	300
			$R_{insulation}$	$m^2 K \cdot W^{-1}$	Varying, (**Table 27**)
	Wall	Wall	T_{wall}	K	2000
			b_{vessel}	m	0.01
			k_{vessel}	$W \cdot m^{-1} \cdot K^{-1}$	12.5

Storage period

In order to study and estimate how much time will pass until the vessel loses completely its contained energy in the form of latent heat during storage period the different concepts tested are patched at 2000 K.

All the walls (including at the emitter) are insulated following the insulating method presented in **Table 27** (Case 2A). Since the storage period lasts more time than charge/discharge phase, more realistic boundary conditions have been imposed at the system outer surface. Therefore, an ambient temperature of 300 K has been considered, whilst both convective and radiative heat losses to the environment are calculated. A value of a convective heat transfer coefficient equal to 20 $W \cdot m^{-2} \cdot K^{-1}$ and external emissivity equal to 0.3 are set to the system exterior surfaces.

3.6.4 Results

3.6.4.1 Insulating layers effect

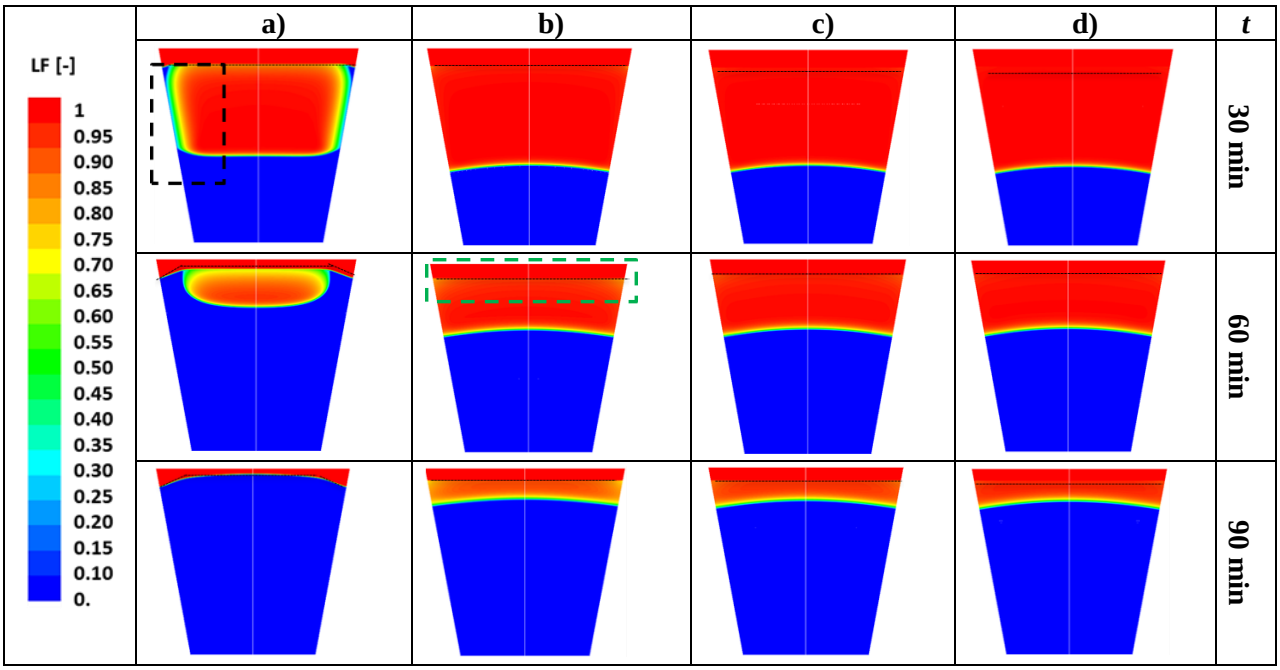

Figure 40. Comparison of the melt fraction contours at t=30, 60 and 90 min for a) Case 1A, b) Case 2A, c) Case 3A and d) Case 4A (**Red**: gas-PCM liquid phase, **blue**: PCM solid phase, **dashed black line**: gas-PCM interface).

In **Figure 40**, are depicted contours of the silicon melting fraction inside the crucible for the different insulating layers tested. As can be noticed, in all cases a gradual solidification of the PCM occurs from the bottom to the upper region of the vessel, owing to heat release from the emitter. What differentiates each case is the heat losses from the vessel sidewalls and upper part, due to different insulating materials/thicknesses applied, which can affect the system performance. More specifically, it has been revealed that, for the specific operating conditions examined, in order to have an optimum system performance, an insulation of a total mean thermal resistance R_{th} at least equal to 2 $m^2 \cdot K \cdot W^{-1}$ is needed to avoid excess heat losses. In any other case, it has been observed that the heat losses from the sidewalls are considerably high, almost comparable to the heat flux coming out from the emitter Q_{em} (from $Q_{loss}/Q_{em} \approx 6.5$ % for $R \approx 2$ $m^2 \cdot K \cdot W^{-1}$, up to $Q_{loss}/Q_{em} \approx 65$ % for $R \approx 0.1$ $m^2 \cdot K \cdot W^{-1}$). In this case, a discrete solid phase is formed near the sidewalls, and a thin crust at the upper part of the PCM, near the PCM-inert gas interface. Due to these formations, there is high risk of entrapping liquid PCM inside the solid PCM that can potentially cause high pressure values inside the crucible. This tendency can be observed in **Figure 40a**, 30 minutes after the initiation of solidification process. In any other case, i.e. $Q_{loss} << Q_{em}$, such formations are not

observed, but rather a “crust like” mushy region of the PCM at the sidewalls and the PCM upper part, and only during the final stages of silicon solidification -almost 1 h after the initiation of solidification process (**Figure 40b,c** and **d**).

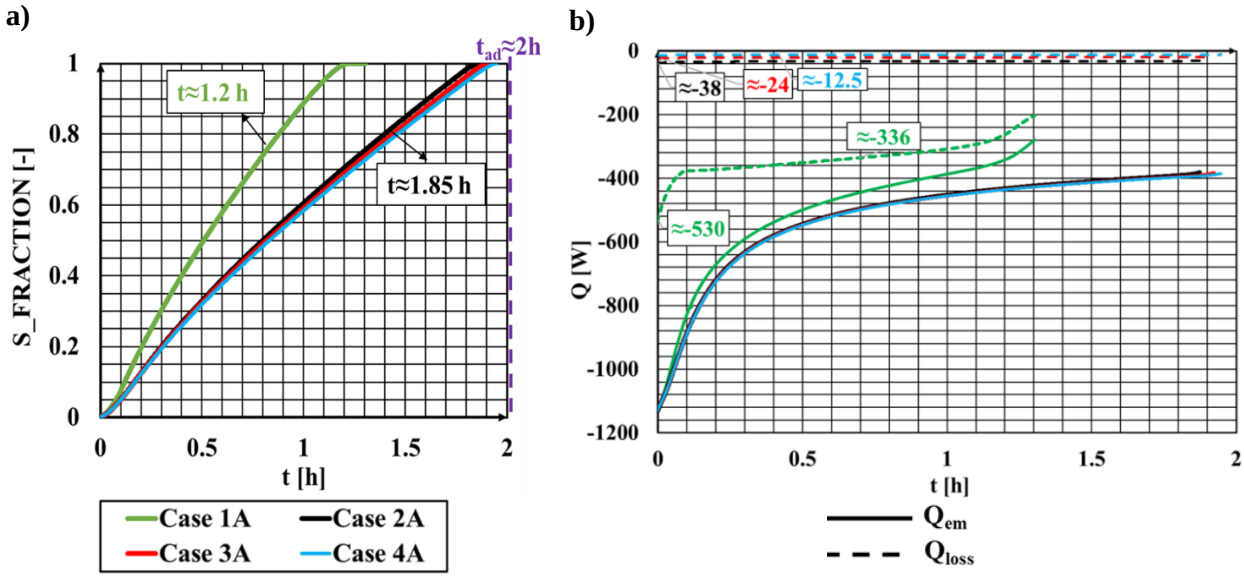

Figure 41. a) Solid fraction values and b) heat losses vs. time for the different insulating layers tested.

Finally, the high lateral heat losses, can affect negatively the total power output. This fact is proven in Case 1A, where the power output is lower than in the rest of the cases studied. Therefore, the total heat released during system discharge is considerably lower in Case 1A than in Cases 2A-4A (Q_{em}≈-2.3E+03 kJ in Case 1A, whilst Q_{em}~-3.5E+03 kJ for the rest of the cases studied). Nevertheless, due to the decreasing temperature difference between the PCM and the environment, as the PCM solidifies, and the increasing values for *R* as the temperature drops, the heat loss reduces as the time goes by, **Figure 41b**. Such a fact is more evident for Case 1A, **Figure 41b**.

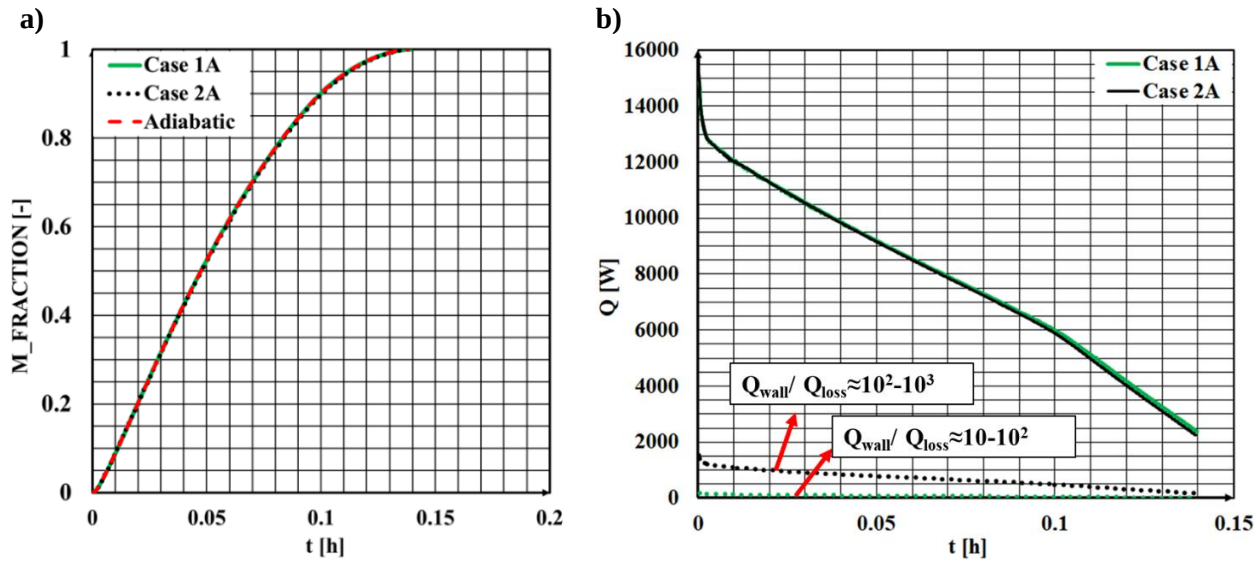

Figure 42. a) Melt fraction values and b) heat losses vs. time for the different insulating layers tested.

During system charge, a proper insulation must ensure quick melting rates, as the ones obtained under adiabatic conditions, since in any other case the excess heat losses from the sidewalls might slow down the melting process. During this phase, a minor effect on the system heat losses has been observed for values of R equal or higher than 0.1 $m^2 \cdot K \cdot W^{-1}$. The main reason behind that is that in this case the incoming heat from the sidewalls, Q_{wall}, is considerably higher than Q_{loss}, **Figure 45b**, maintaining the high charging rates that would be achieved under adiabatic conditions, **Figure 45a**. More specifically, in Case 2A the Q_{wall}/Q_{loss} ratio is almost equal to 10^3 at the beginning of the process and drops down to 10^2 at the end of it. Similarly in Case 1A, the the Q_{wall}/Q_{loss} ratio takes values within the range of 10^1 -10^2. However, it is expected that for lower Q_{wall} values, comparable to the lateral heat losses, the melting rate will decrease.

3.6.4.2 Vessel tapering ratio/ size effect

3.6.4.2.1 Charge/ discharge phase

From the analysis, it has been revealed that the system performance during charge/ discharge phase highly depends on key parameters, such as the vessel volume/ storage capacity, tapering ratio and emitter surface. More specifically, for geometries of the same volume (Cases 1B, 4B-6B), the solidification time increases, when their height increases accordingly, since during discharging the dominant direction of heat transfer is the vessel axis. For this reason, the quickest solidification is observed in Case 6B ($t_{discharge}$=0.72 h) and the slowest in Case 5B ($t_{discharge}$=2.56 h), which have the lowest and highest height, respectively, of all geometries tested, **Table 28**. In particular, in Case 6B the solidification time is almost 70 % quicker than in Case 5B. Moderate solidification rates are noticed in Cases 1B and 4B (ITC with a TR=0.45 and 0.225). By comparing these two, it is observed that the ITC with a TR equal to 0.225 (Case 4B) solidifies almost 17 % quicker than that with a TR=0.45.

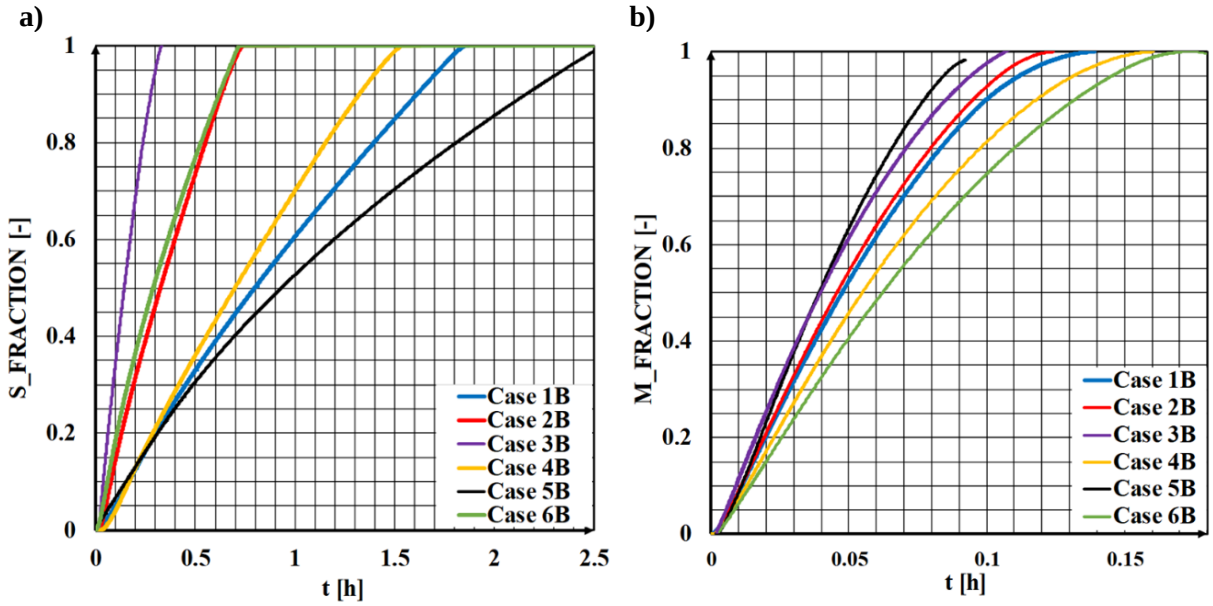

Figure 43. a) Solid fraction and b) melt fraction values for the different geometries tested.

The opposite trend is expected during the PCM melting period, **Figure 43b**, since the heat in this concept comes from the sidewalls. In this case, for the same vessel volume, the higher the height, and therefore the larger the sidewall surface, the quicker the PCM melts. This is the reason why Case 5B -cylinder with a side wall surface equal to 0.044 m^2, almost 1.3 times bigger than the reference case (Case 1B)- melts quicker than all cases tested. On the other hand, the slowest melting rate can be noticed in Case 6B, where the vessel

has the smallest heated wall, equal to 0.0284 m^2. Concerning the ITC tapering ratio, the vessel with a *TR*=0.45 melts quicker, due to its bigger surface wall compared to that with a *TR*=0.225. A trade-off between the system charge and discharge rate leads to the conclusion that the truncated-cone with the tapering ratio, between 0.225-0.45 is the optimum solution to be constructed among the geometries tested.

Concerning lateral losses during charge/ discharge phase, the tapering ratio has a rather not severe effect, when a proper insulation is imposed at the vessel walls. The total amount of losses during the PCM solidification phase are equal to ~223 kJ and ~ 158.2 kJ for the truncated-cone with a tapering ratio equal to 0.45 and 0.225, respectively. Such values correspond to a ~ 3.7 % and ~2.6 % ratio of the total losses to the initial energy stored (~6 MJ) of the system, whilst the Q_{loss}/Q_{em} ratio is almost equal to 6.4% and 4.5 %, for the two geometries compared. The importance of the insulation should be highlighted, since as aforementioned such losses can be almost an order of magnitude higher, when an insulation of a thermal resistance of an order of magnitude lower than the reference case (Case 2A) is used. During charge period, the same small effect of the *TR* on the system losses has been noticed – the ratio of Q_{losses}/ Q_{wall} is less than 1 % for all cases studied. Nevertheless, it should be noted that for the same vessel capacity (Case1B and Cases4B-6B) and for the specific concept studied, the heat loss decreases with the tapering ratio increasing.

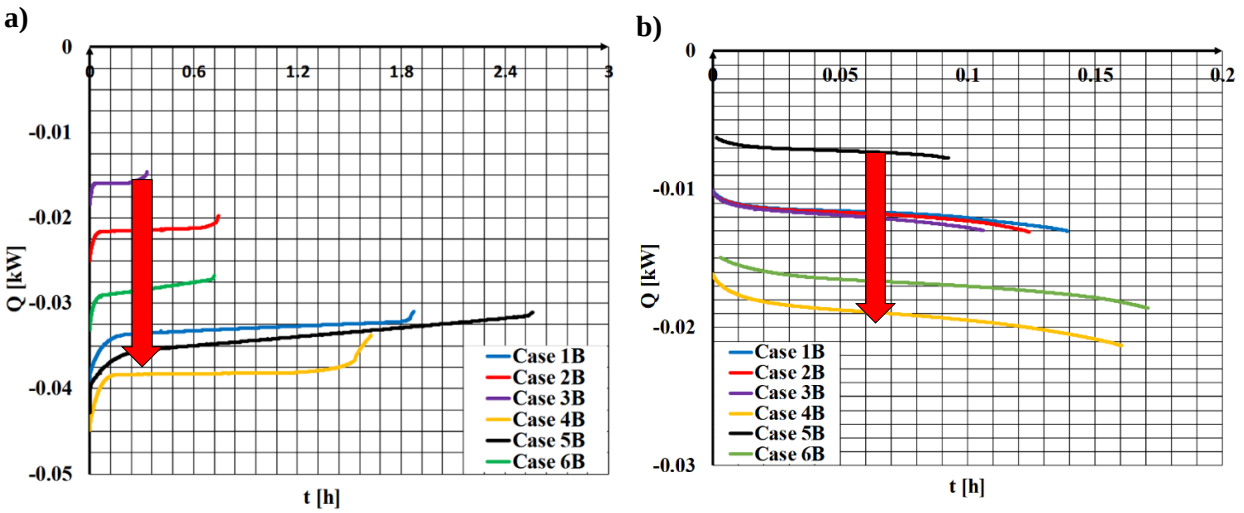

Figure 44. System heat losses during a) solidification, b) melting for the different geometries tested.

On the other hand, the vessel volume plays an important role on both heat losses and power output. Even though the total system heat losses are almost equal for the three volumes tested, **Figure 43b**, the total heat losses per stored energy increases with reducing the volume. Specifically, the Q_{losses}/E_{in} ratio is equal to 0.1 in Case 1B, whilst in Case 3B ($V'=V/4$, $E_{in}'=E_{in}/4$) this ratio is equal to 0.3. For the same cases the total amount of released heat during system discharge is ranges from -3.5E+03 kJ for Case 1B (of volume *V*) to -9.3E+02 kJ for Case 3B (of volume *V*/4).

Another conclusion is that the possible risk of entrapping of molten PCM inside the solid one, which is related to the imposed insulating method, is not increased when the vessel tapering ratio changes. However, such an observation is valid, as long as an efficient insulating method is imposed at the sidewalls. Finally, in the case of the shape of truncated cone, a slightly higher expansion can be observed near the PCM centerline than the one noticed near the walls, than in the case of the cylinder, **Figure 45**.

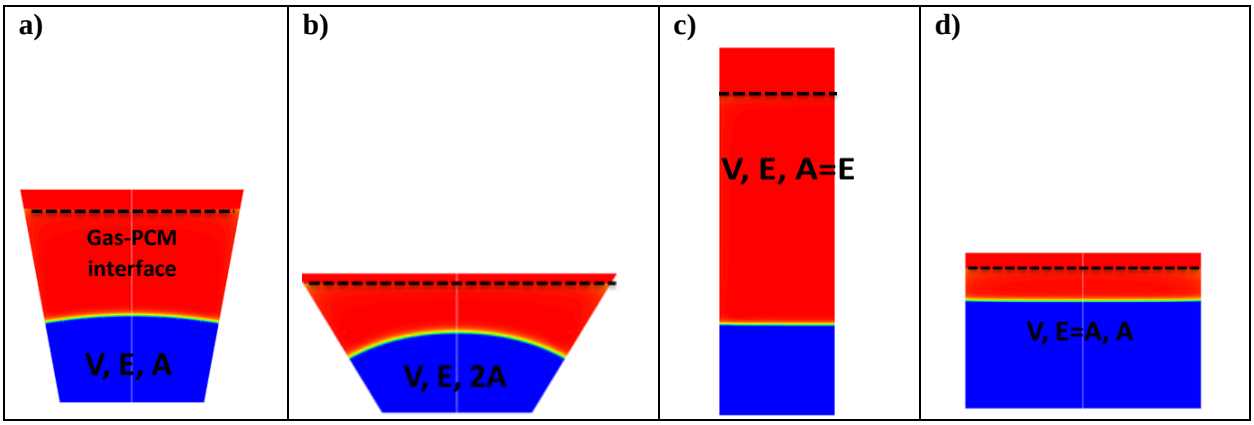

Figure 45. Comparison of the melt fraction contours at *t*=30 min, after the initiation of discharge phase for: a) Case 1B, b) Case 4B, c) Case 5B, and d) Case 6B.

3.6.4.2.2 Storage period

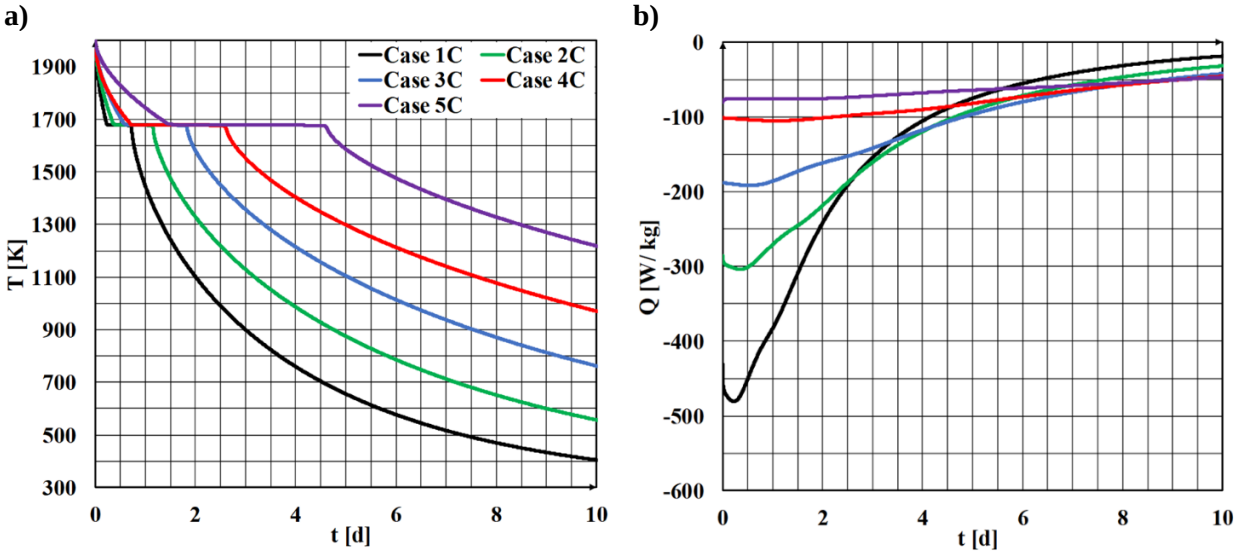

Figure 46. a) Temperature variation and b) heat losses per unit mass of the system during TES.

In this section is discussed the potential of the LHTES to store large quantities of energy –in the form of sensible and latent heat- for several days. A key aspect during this period is to identify whether the insulating method imposed is sufficient to eliminate lateral heat losses and keep the PCM temperature close to its melting point, as much as possible. Additionally, different vessel volumes, apart from that of the reference case are investigated, **Table 28**.

Table 30. Storage time for each vessel (ITC) before it loses its contained latent heat ($t_{discharge,\ latent}$).

Case	V_{vessel} [m^3]	A_{vessel} [m^2]	V_{vessel}/ A_{vessel} [m]	$V_{insulation}$ [m^3]	$R_{total,1680}^{*}$ [m^2 K·W^{-1}]	$t_{discharge,\ latent}$ [d]
Case 1C	0.0002081	0.02589	0.0080	0.00420	1.18	~0.7
Case 2C	**0.0004163**	0.03344	0.0124	0.00839	1.49	~1.2
Case 3C	**0.0008326**	0.04987	0.0167	0.01678	1.88	~1.8
Case 4C	**0.0016652**	0.07917	0.02103	0.03356	2.37	~2.6
Case 5C	**0.0033303**	0.12567	0.02650	0.06712	2.98	~4.6

Based on the results, the under-investigation system can maintain its stored energy in the form of latent heat for almost two days at least partially. However, within one-week storage period the vessel loses considerable amounts of its stored energy and, thus, its temperature drops down to 900 K. Longer-term storage can be achieved, but with vessels of higher capacity, i.e. Case 5C. Added to this it should be noted that the system heat losses per mass decrease with the increasing tank volume. The highest are traced for Cases 1C and 2C; such cases seem impractical for storage even for one day, since they have high lateral heat loses –higher than 200 $W \cdot kg^{-1}$- within the first two days of storage.

3.7 Sensitivity analysis

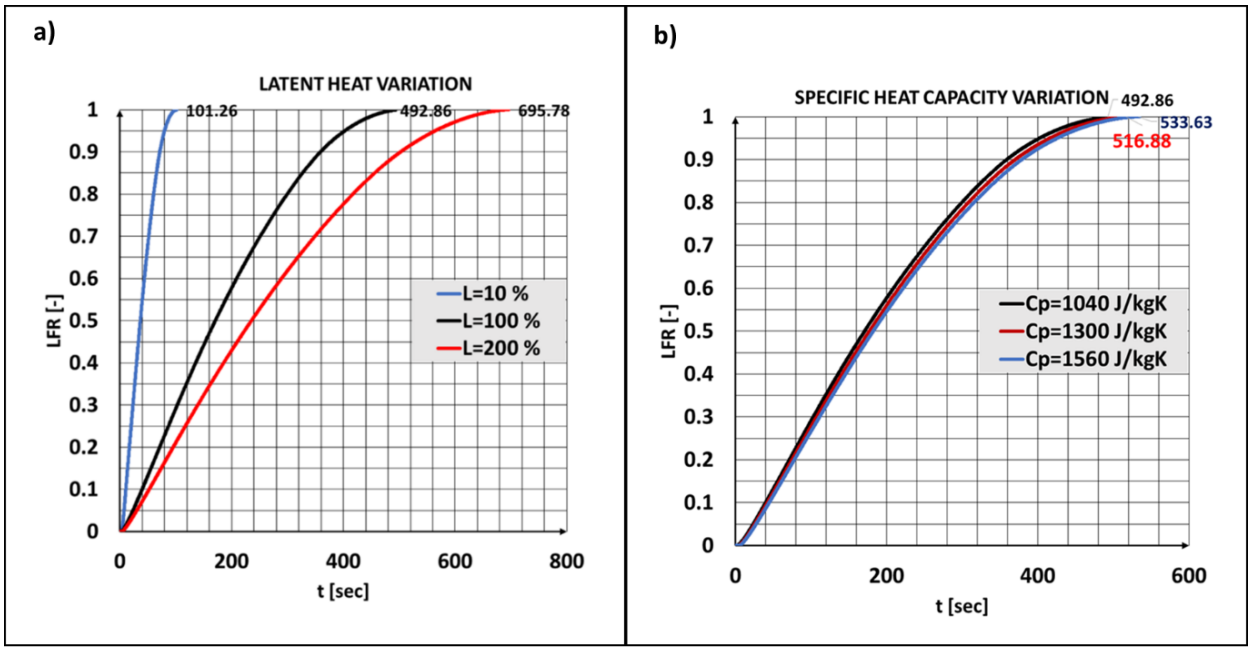

Figure 47. Melt fraction values at different time instants for the different a) Latent heat of fusion and b) Specific heat capacity values (L= $1.8 \cdot 10^6$ $J \cdot kg^{-1}$).

The PCM material properties can affect the LHTES system thermal performance in various ways. Briefly, a sensitivity analysis for the latent heat of fusion, specific heat capacity, mushy zone variation and thermal conductivity effect on the heat storage block charging time are presented. The PCM reference properties correspond to that of silicon. As regards the first two parameters, it can be noticed that by increasing the latent heat by a factor of two the heat storage block charging time increases almost 30 %, **Figure 47**. This fact demonstrates the high effect of the PCM latent heat on its melting time. On the contrary, a small effect of the specific heat capacity on the numerical results is observed. An increase in the specific heat by almost 50 % results in a small increase in the heat storage block charging time, i.e. 7 %.

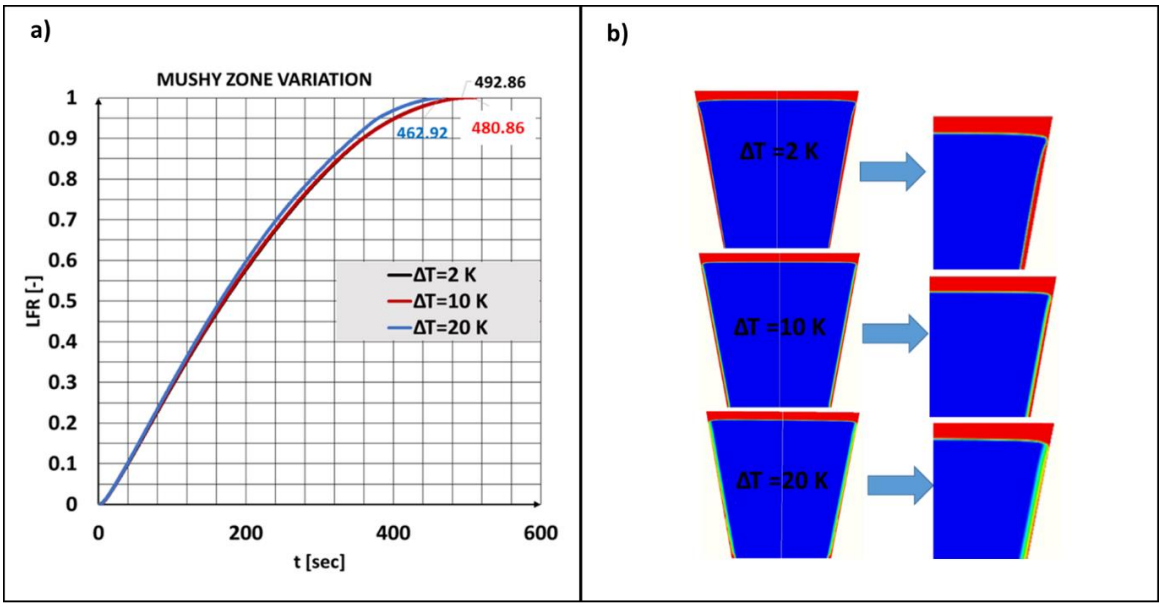

Figure 48. a) Melt fraction values at different time instants for three different mushy zone ranges and b) melt fraction contours at t=30 sec.

A small effect of the mushy zone range on the numerical results is also observed, **Figure 48**. More specifically, increase of ΔT from 2 to 20 K results in a change in the melting time less than 10 %. In general, increase of the mushy region promotes the melting of the PCM.

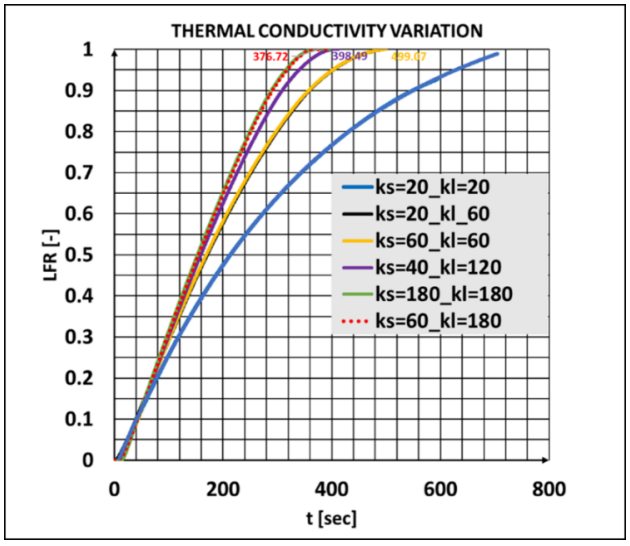

Figure 49. Melt fraction vs. time for various thermal conductivity values.

Finally, the sensitivity analysis shows a great influence on the charging time with the thermal conductivity k, **Figure 49**. More specifically, a study case with k_s, k_l=20 $W \cdot m^{-2} \cdot K^{-1}$ requires almost double the time for the PCM to melt in comparison to cases k_s, k_l=180 $W \cdot m^{-2} \cdot K^{-1}$ and k_s=60, k_l=180 $W \cdot m^{-2} \cdot K^{-1}$. A reduction by 25 %, when the k is increased from 20 $W \cdot m^{-2} \cdot K^{-1}$ to 60 $W \cdot m^{-2} \cdot K^{-1}$ (66% increase), is also noticed. Another conclusion drawn is that during melting process the thermal conductivity of PCM liquid phase influences more the charging time than the thermal conductivity of solid phase, especially after melting starts to occur.

3.8 Main conclusions

In this Thesis, an advanced CFD model has been developed in Fluent v17.0 platform to investigate the silicon solidification/melting behavior at ultra-high temperatures (~1410-2000 ^{o}C) inside a novel LHTES system. This system is part of a compact heat-to-electricity device that is recently under development. The applied methodology combines an adaptive local grid refinement technique with both the enthalpy porosity approach and the VOF method. In contrast to other models available in the literature this one simultaneously takes into account the a) PCM volume change, b) buoyancy driven natural convection and c) possible dendrites formation effect on the PCM melting, aspects that should be taken into account for an accurate simulation of LHTES systems. Several activities have been undertaken in the framework of this Chapter.

Model validation against experiments (low temperatures): The model has been validated against numerical and experimental data retrieved from the literature, for paraffin wax solidification/melting at low temperatures (~27 ^{o}C). From a numerical point of view, several valuable results have been extracted. First of all, the superiority of the local grid refinement over fixed grids, both in terms of efficiency and accuracy, has been unveiled. A reduction in simulation time of almost 85 % is achieved when the refined grid is applied in comparison to the dense fixed one; both grids have the same resolution near the solid-liquid and gas-PCM interfaces and eliminate numerical diffusion, in contrast to the coarse grid. Secondly, the strong effect of the mushy zone parameter, which is dependent on the PCM structure, on the melting rate has been highlighted. The physical interpretation of this result is that the highest this parameter the smallest the secondary DAS formed inside the PCM and therefore the lowest its melting rate. Furthermore, it has been possible to implicitly represent the effect of the dendritic formation within the mushy zone, through the dynamically refined grid. Finally, it has been revealed that with the enthalpy porosity method, the floating/sinking of the solid PCM inside its molten phase is represented indirectly–and not directly as widely misunderstood - through the liquid motion, which depending on its upward or downward motion forms accordingly the melting front shape. In a future model reformulation, this natural phenomenon of floating/sinking should be modelled explicitly, by taking into account the solid motion, for a more realistic representation. During PCM solidification, a moderate effect of the A_{mush} parameter on the solidification time is traced. However, high values of this parameter should be used to avoid numerical diffusion.

Model verification against other models (ultra-high temperatures): The advanced 3D CFD solidification model has been also applied to study a novel Si-based LHTES system operating at ultra-high temperatures. Owing to the absence of experimental data for the Si solidification /melting at ultra-high temperatures, the model has been verified against an analytical model. Simulation results indicate that the CFD model results agree very well with a 1D-analytical for most of the PCM simulation time verifying, thus, the validity of the derived results. This model has been used extensively in this Thesis to carry out a multi-parametric analysis of the LHTES system at its charging, discharging and storage period.

Design optimization: From a design perspective, one of the key challenges of this storage system lies on the identification of the optimum size/shape and operating conditions that can enable high charge/discharge cycles. For this reason, different container sizes and shapes, i.e. cube, sphere, cut-off sphere, truncated cone and cube, and heating conditions at the walls (for a Stefan number equal to 0.26) have been tested. It has been revealed that during melting process, if the heating of the container is from its sidewalls, as in a P2H2P concept, the heated surface area plays an important role on the PCM melting rate. Specifically, the cubic shape results in the highest melting rate, approximately 25 % higher than the one achieved in the spherical design, due to its biggest heated surface. On the other hand, the spherical shape is expected to have the

lowest lateral thermal losses and thermal stresses during solidification and storage period, but is not a practical solution to be integrated into a compact heat-to-electricity device. The most practical solution in terms of melting rates, heat losses and design flexibility is the truncated cone. Finally, it has been observed, that the silicon melting time is further reduced by 31 %, when the Stefan number increases by 35 %.

Heat losses study: As a further step, the validated CFD model has been used to evaluate the performance of the silicon-based UHT-LHTES system during its charging/ discharging and storage periods. The storage tank of this system has a volume equal to V= 8.33e-04 m^3. In order to optimize its operation, i.e. eliminate lateral heat losses, maximize power output and achieve high charge/ discharge rates, different insulating materials of a R_{th}=[0.11, 4.8] $m^2 \cdot K \cdot W^{-1}$ have been tested. Two types of geometries (truncated cone and cylinder) of different volumes and heights have been tested; in the case of the truncated cone, its height has been modified by altering its lower to upper surface (tapering) ratio. From the numerical analysis it has been revealed that the vessel *TR* parameter and height have a low to moderate effect on the system heat losses, if a sufficient insulation is imposed at the system walls, i.e. R_{th} ~2 $m^2 \cdot K \cdot W^{-1}$. Specifically, the total amount of losses during the PCM solidification phase inside the truncated cone correspond to a ~ 3.7% (*TR*: 0.45) and ~2.6% (*TR*: 0.225) ratio of the total losses to the initial energy stored (~ 6 MJ) of the system. During charging, a small effect of the *TR* on the system losses has been noticed – the ratio of total losses to incoming energy is less than 1% for all cases studied. As regards charging / discharging rates, an important effect of the *TR* has been noticed. More specifically, when the TR of the vessel increases then the solidification, time increases, respectively, whilst the opposite trend is observed during charging phase. A geometry with the same volume, but lower *TR* (0.225), solidifies quicker than that with *TR*=0.45; the solidification time in the first case is almost 17 % lower than in the second case. A trade-off between the system charging and discharging rates leads to the conclusion that the truncated-cone with the *TR*, between 0.225-0.45 is the optimum solution to be constructed among the geometries tested. Last and foremost, the tank volume significantly influences its total energy storage capacity; the specific vessel can be used for storage for up to two days, before it loses its contained energy in the form of latent heat. In summary, building a highly efficient heat storage block aimed to be integrated in a P2H2P system means considering a vessel with short length, low lateral surface area to volume ratio, proper insulating method (of R_{th} ≈2 $m^2 \cdot K \cdot W^{-1}$) and a *TR* within 0.225-0.45. It should be noticed that the conclusions drawn in this analysis are for the specific designs tested, volume, or volumes close to the one examined and for the specific insulating materials used. For scaled-up geometries, there is a room in the future to carry out a muti-parametric study to deliver general conclusions, i.e. dimensionless correlations applicable from large to small-scale systems.

3.9 Milestones achieved

The milestones achieved during this research study include:

- ✓ Development of an efficient and accurate CFD model able of simulating PCMs from low to ultra-high temperatures. This model can be utilized to simulate and scale-up of a PCM container;
- ✓ Proof that the enthalpy-porosity approach coupled with an adaptive local refinement technique can implicitly capture the dendritic structure effect on the solidification/melting front; future room for development is to explicitly model such structure by using the adaptive local refinement technique;
- ✓ Model validation against experiments (low temperatures) for paraffin wax solidification/ melting
- ✓ Model verification against other models (ultra-high temperatures) for silicon solidification;
- ✓ Design optimization of a novel silicon-based LHTES system; results of this work where used as input to fabricate the LHTES prototype in UPM.

CHAPTER 4
Modelling of storage applications using FB systems (TCES)

4.1 Preface

The aim of this section is to present the development and validation of advanced numerical models and sub-models, which can be used for the simulation of the flow hydrodynamics, heat transfer mechanisms and reaction kinetics –if available- of a gas-solid FB system. The main CFD approach is based on the Eulerian-Eulerian TFM or MFM for a two-phase or a three-phase flow, respectively, and is coupled with a new version of the drag coefficients sub-grid EMMS model –developed in the framework of this Thesis. Additional advancements of the current model that are validated in the present Section include the simulation of all heat transfer mechanisms (convection, conduction and radiation) in FB systems.

The developed models/sub-models are built by using operating data and boundary conditions of a calcium looping system and are applicable for FB systems of both bubbling and circulating regime and for Geldart A/B particles. They can also be used for the simulation of FB systems under both cold flow and hot flow conditions. For the sake of this analysis ANSYS Fluent platform (v19.1 and v21.1) is used. The model is validated against experimental data of a 1 MW_{th} DFB facility located at TUDA for both the oxy-calciner calcium-looping concept and a novel IHCaL concept. In the latter concept, the effect of complex phenomena are incorporated as those of radiation and turbulence effect on heat transfer process. In this section is also highlighted the importance of CFD modelling tools in the design optimization and scale-up of such novel reactors.

The basic concept of calcium looping technology uses two interconnected fluidized bed reactors, usually a bubbling calciner and a CFB carbonator (**Figure 50**). Simulation of fluidized beds is done in a transient 3D manner to capture with a high level of accuracy the heterogeneous formations (e.g. bubbles, clusters etc.) The calcium looping cycle can be eventually used for both thermochemical heat storage and CO_2 capture, actions that are essential towards a carbon-neutral future transition.

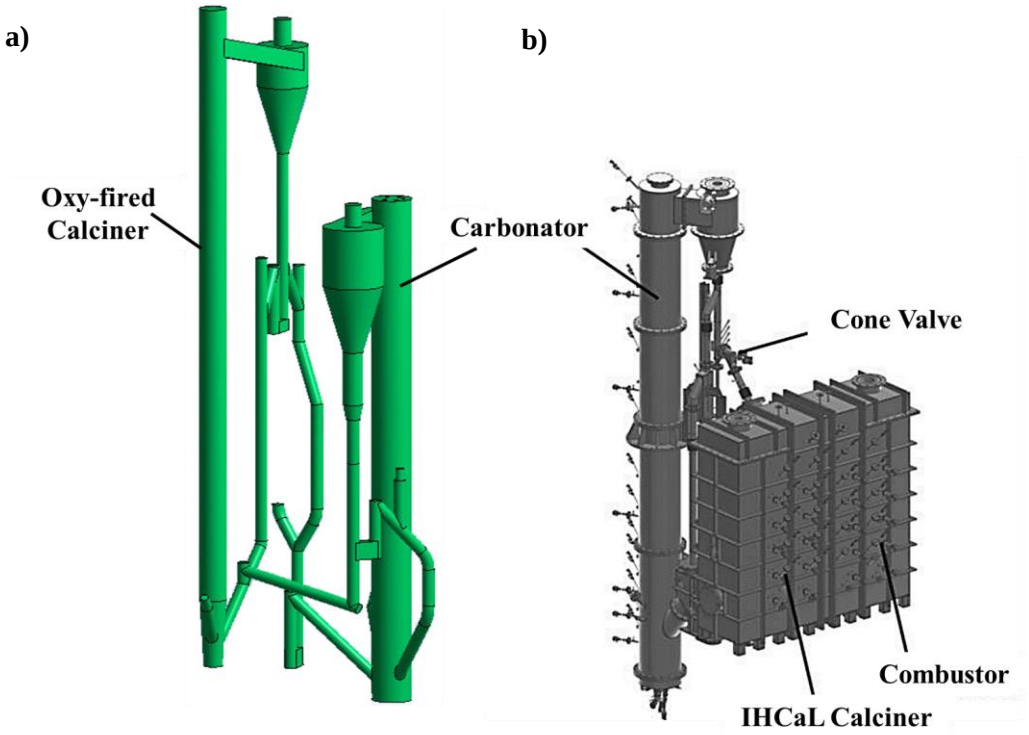

Figure 50. 3D scheme of the 1 MW_{th} DFB facility with a) the oxy-fired and b) the IHCaL calciner [291].

4.2 Model validation (EMMS, carbonation reaction validation 1 MW_{th} unit)

The sub-grid EMMS model developed in this Thesis is a follow-up of the research work developed by Nikolopoulos et al. [136], who acted as forerunner for the EMMS formulation in Europe, taking as reference the work of Wang et al. [160]. In this previous work of [136], the non-linear problem of EMMS model was solved in the commercial software of GAMS and a cluster correlation based on [143] was used. This old version of the EMMS model along with the interpolation methodology was used as a basis for the currently developed EMMS model. Specific advancements of this new sub-grid model with regard to [136] and [160] include the utilization of a cost-effective code in FORTRAN that can be easily modified to include additional sub-models (e.g. new cluster correlations, additional regimes etc.). Additionally, a new cluster correlation based on the work of Subbarao et al. [143], which takes into account as a bounding parameter the reactor diameter has been utilized. In this sense, the size of the reactor affects the model results and provides more realistic H_d values. Finally, this model can be easily used to run consecutively several data sets and has been used as the basis for the construction of an artificial intelligence based EMMS model [292], which is out of the scope of the current Thesis. In order to test the EMMS model validity the 1 MW_{th} carbonator reactor of TUDA DFB system is used as a reference, by using experimental data for comparison and validation. Validating the model at a pilot-scale – which lies in-between the lab and the demo scale- can help develop models that will derive as close as possible realistic to and industrial scale results.

4.2.1 Numerical methodology

In this section, some of the common assumptions adopted in such type of modelling tools are presented:

- Transient flow with a Courant number lower than 0.75;
- A 3D domain is used in all of the simulated cases;
- Multi-phase method: Eulerian-Eulerian Two-fluid model with two phases (solid-gas);
- The particle-particle forces are modelled implicitly by using the KTGF theory;
- The used drag force model is the custom-built EMMS model. Additionally, the homogeneous Gidaspow model has been used during model validation to compare it with the EMMS model;
- The unit is simulated to operate under isothermal conditions, as the experimental campaigns indicate. Thus, the solution of the energy equation is not included in the simulated case. The temperature of the domain is set to 908 K for the 1 MW_{th} unit;
- The flow is considered as laminar, due to the fact that the turbulence effect on the cold flow hydrodynamics is considered of minor importance [293];
- The carbonation reaction is incorporated into the model. The heterogeneous reaction rate (Ref. equation (68)) is validated against experimental data for the mass fraction of CO_2 at the riser exit. As comparison data, the mass weighted time-averaged mean mass fraction of CO_2, Y_{CO2}, is used;
- The same rate is used for any other simulation runs (e.g. design optimization, up-scaling concept);
- The solids inventory is kept constant, by monitoring the solids flux at the carbonator outlet and re-injecting the particles at the domain by a return inlet;
- Solids pressure model: Lun et al. [149];
- Radial distribution model: Arastoopour [154];
- Fictional viscosity model: Johnson et al. [153];
- Granular viscosity model: Gidaspow [152];
- Granular bulk viscosity model: Lun et al. [149];

- Features of the CFD model that are not supported by the CFD platform, such as the EMMS model and the heterogeneous reaction rate are incorporated through UDFs.

4.2.2 Geometry and mesh layout

Figure 51 depicts the actual carbonator geometry, which is presented in detail in the paper of [294]. During the simulation process, only the riser section is modelled, whereas the cyclone, the two loop seals (1 and 2) and the auxiliary burner section are excluded from the model. However, the intersections of the excluded parts with the riser are used as boundary conditions for the gas and solid phase. The height and the inner diameter of the riser are 8.661 m and 0.59 m, respectively. As a further step, a 3D computational domain is constructed with full respect to the riser geometry. Two different grid resolutions, one coarse and one dense, consisting of 31,207 and 285,369 hexahedral elements respectively, are tested in order to identify to which extend the numerical results are grid dependent. The d_{cell}/d_p ratio is equal to 465.64 for the coarse grid, **Figure 51**, and 222.67 for the dense grid respectively.

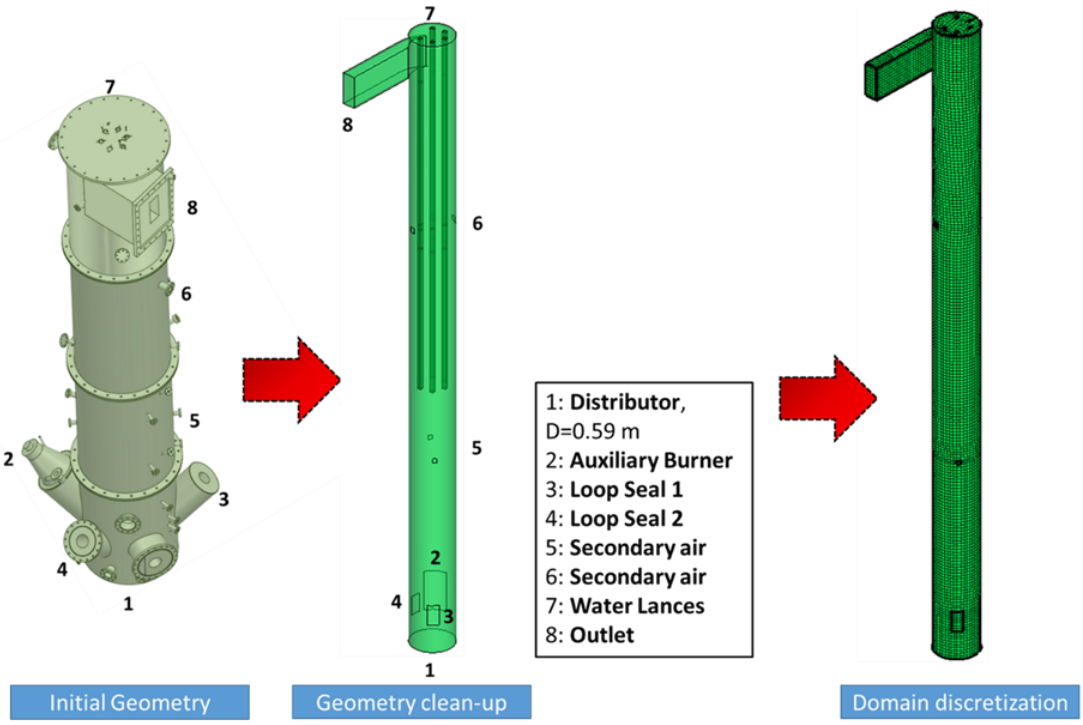

Figure 51. 3D scheme of the carbonator riser and domain discretization.

4.2.3 Boundary and operating conditions

In order to solve the CFD problem several boundary conditions are applied. The distributor is treated as a velocity inlet, while the two loop seals and the auxiliary burner as mass-flow inlets. The outlet boundary zone is defined as a pressure-outlet, with an operating pressure set equal to the atmospheric. Finally, the water lances used for any excess heat extraction in the real problem (temperature is considered to be around to 635ºC for the whole domain) and the remaining boundary zones are defined as walls.

More specifically, loop seal 2 performs the transportation of the regenerated limestone from the calciner to the carbonator. Thus, fresh material enters the riser through the intersection of loop seal 2 with the riser. The recirculation rate between the two units is equal to 1.0158 $kg \cdot s^{-1}$. Moreover, loop seal 1 is used for the internal recirculation of the solid particles in the CFB unit. In order to keep the solids inventory constant,

the solid particles are entering the riser with a mass flow rate equal to the one predicted at the outlet for each time instant by using a custom-made user defined function. The same numerical technique has been used in other works as well [125, 142, 295]. A flue gas consisting of CO_2, O_2 and N_2 enters the carbonator from the distributor. Additional air enters the riser from the two loops seals and the auxiliary burner.

A no-slip boundary condition is considered for the gas phase at the walls. For the solid phase the Johnson and Jackson [153] wall boundary condition is adopted. Finally, a constant temperature is defined, i.e. 908 K, as the experimental campaign suggests. The boundary and operating conditions used for the solution of the model are presented in **Table 31.**

Table 31. Boundary conditions (Carbonator reactor).

Section	BC type	Parameters	Units	Values
Distributor	Velocity-Inlet	$\dot{m}_{gas}$	$kg \cdot s^{-1}$	0.2146
		V_{gas}	$m \cdot s^{-1}$	1.9304
		Y_{O2}	$kg \cdot kg^{-1}$	0.187
		Y_{CO2}	$kg \cdot kg^{-1}$	0.188
		Y_{N2}	$kg \cdot kg^{-1}$	0.627
		V_{solid}	$m \cdot s^{-1}$	0
Loop Seal 1	Mass flow Inlet	$\dot{m}_{gas}$	$kg \cdot s^{-1}$	0.01153
		Y_{O2} / Y_{N2}	$kg \cdot kg^{-1}$	0.23/ 0.77
Loop Seal 2	Mass flow Inlet	$\dot{m}_{gas}$	$kg \cdot s^{-1}$	0.00759
		Y_{O2} / Y_{N2}	$kg \cdot kg^{-1}$	0.23/ 0.77
		$\dot{m}_{solid}$	$kg \cdot s^{-1}$	1.0158
		Y_{CaCO3} / Y_{CaO}	$kg \cdot kg^{-1}$	0.09/ 0.91
Burner	Mass Flow Inlet	$\dot{m}_{gas}$	$kg \cdot s^{-1}$	0.03589
		Y_{O2} / Y_{N2}	$kg \cdot kg^{-1}$	0.23/ 0.77
		$\dot{m}_{solid}$	$kg \cdot s^{-1}$	0
Outlet	Pressure Outlet	P	bar	1
Walls	Gas phase: No slip condition		Solid phase: φ^{1}=0.01	

Table 32. PSD of the limestone (**Geldart A particles**).

Interval	Mean diameter in interval	Interval weight percentage	Accumulated weight percentage
[μm]	**[μm]**	**[%]**	**[%]**
0-25	12.5	2.20%	2.20%
25-42	33.5	2.35%	4.55%
42-72	57	10.84%	15.39%
72-102	87	19.66%	35.05%
102-122	112	14.35%	49.40%
122-146	134	15.76%	65.16%
146-174	160	14.58%	79.74%
174-206	190	11.02%	90.76%
206-294	250	9.24%	100.00%

[1] *This value is set only for the four preliminary cases simulated*

Initially, the solid phase is evenly patched all over the 3D domain with ε_s=0.067 corresponding to a solids inventory equal to 282 kg, as suggested by the experimental data. Moreover, an initial value of 0.16 is given to the $CaCO_3$ mass fraction, in order to speed-up the simulation, a value close to the respective limiting value of 0.1655 that corresponds to X_{max}=0.1.The initial velocities of both phases were set to zero. Following the Geldart classification, the particles are of type A with a mean particle diameter 91.39 μm. The particle size distribution (PSD), presented in **Table 32** is not taken into account as it increases considerably the computational cost [296]. The same monosized approach has been followed in other works [107, 122]. The mean diameter is calculated according to the expression given by [52]:

$$d_p = \frac{1}{\sum \frac{f_k}{d_{pk}}} \tag{142}$$

, where f_p is the fraction of particles with diameter d_{pk}. The gas-solid properties that are setup in the model are presented in **Table 33**.

Table 33.Properties of the gas and solid phase.

Parameter	Value	Parameter	Value
$\boldsymbol{\rho_s}$, kg·m^{-3}	1650	$\boldsymbol{\mu_g}$, kg·m-1·s^{-1}	3.91085 ·10^{-5}
$\boldsymbol{d_p}$, μm	91.39 (Geldart A)	$\boldsymbol{\varepsilon_{mf}}$, (-)	0.55
$\boldsymbol{U_g}$, m·s^{-1}	1.930375	$\boldsymbol{\varepsilon_{max}}$, (-)	0.9997
$\boldsymbol{U_{mf}}$, m·s^{-1}	2.9495 ·10^{-3}	$\boldsymbol{\varepsilon_{s,max}}$ (-)	0.65
$\boldsymbol{u_t}$, m·s^{-1}	0.175746	$\boldsymbol{e_{ss}}$, (-)	0.9
$\boldsymbol{\rho_g}$, kg·m^{-3}	0.389		

4.2.4 Numerical model

The TFM approach, which has been presented in detail in Section 2.1, is incorporated into the ANSYS/Fluent commercial package. For the drag force exerted on the solid particles the EMMS scheme and the conventional Gidaspow model are implemented and their results are compared and evaluated against experimental data. Four preliminary cases are simulated in order to test the effect of i) the grid density and ii) the drag force model on the pressure profile. Initially, for the specularity coefficient the same value is used, i.e. 0.01. The four preliminary cases are presented in **Table 34**.

Table 34. Preliminary Cases Simulated (carbonator model validation).

Test Case	Grid	Drag Force Model	Specularity Coefficient
Case 1	Coarse	Gidaspow	0.01
Case 2	Coarse	EMMS	0.01
Case 3	Dense	Gidaspow	0.01
Case 4	Dense	EMMS	0.01

As a further step, a parametric study for the effect of the specularity coefficient φ (0.01, 0.1, 0.6 and 0.99) on the bed hydrodynamics is conducted. The parametric study is carried out to the one of the four preliminary cases, which is chosen as the most accurate and less computational expensive.

Transient calculations are performed with a time step size of 10^{-4} s is for Cases2-4, while for Case 1 a double time step (2·10^{-4} s) is adopted. As concerns the spatial discretization of the equations, the QUICK scheme is applied for the solution of the momentum, volume fraction and species equations, while for the time

discretization a bounded second order implicit scheme is adopted [297]. Moreover, the phase-coupled SIMPLE algorithm is applied for the velocity-pressure coupling. For the accurate prediction of the pressure profile, the overall simulation time for each numerical simulation is approximately 20 seconds, while the last 15 being are used for time averaging. It is predicted that 5 seconds after the initialization in every case, an equilibrium state is almost reached concerning the flow hydrodynamics. For the prediction of the CO_2 at the outlet of the riser reactor longer simulation times are needed, that is almost 200 seconds, and a time averaging of approximately 65 seconds is done. This is due to the fact that for the specific reaction rate used, the solid species, i.e. CaO and $CaCO_3$ cannot reach fast enough equilibrium. However, it should be noted that the effect of CO_2 capturing mechanisms on the hydrodynamics is negligible.

4.2.5 Results: Validation

4.2.5.1 EMMS model results (pre-CFD)

Figure 52 depicts the heterogeneity index variation for different values of the gas voidage ε_g and slip velocity u_{slip}. For each slip velocity, H_d reaches its maximum value, when ε_g takes a value of 0.82. For -values of ε_g within the range of [0.82, ε_{max}], clusters diameter and density increases as ε_g decreases leading to an enhancement in the clusters mass and a subsequent increment of H_d. However, for ε_g=0.82 the void fraction in the cluster ε_c takes the value of ε_{mf}. Moreover, when ε_g takes values below 0.82, ε_c becomes less than ε_{mf}. In order to avoid that, a constraint was set to the model so that when ε_c is lower than ε_{mf}, ε_c can have a threshold (ε_c=ε_{mf}). Thus, for ε_g<0.82 the clusters mass increases only because of the cluster diameter increase. For all these reasons, the heterogeneity index takes its higher value for ε_g=0.82. These observations are in a good agreement with the work of [109, 136]. Moreover, as the slip velocity increases the H_d decreases approaching unity. This is due to the fact that the high slip between the gas and the solid phase hampers the cluster formation. The latter observation is also verified in the work of [126]. Finally, **Figure 53** shows the variation of some important parameters of the EMMS model, i.e. the cluster size and the dilute and dense phase accelerations for different values of ε_g and for a specific gas-solid slip velocity (u_{slip}=1). It should be noted that the term a_f is the inertial term in dilute phase and represents in a sense the acceleration of the particles in this phase. Correspondingly, the term a_c is the dense particulate phase inertial term and represents the acceleration of the particles in the dense phase [126, 298].

From **Figure 53a** and **Figure 53b** it is evident that the correlation of Li and Kwauk gives an over-prediction of the cluster size since it predicts the cluster characteristic length bigger than that of Subbarao's correlation and almost equal to the riser diameter for ε_g<0.7. On the other hand, the correlation given by Subbarao predicts clusters of smaller size and acts as a limiter for the cluster diameter for mostly all gas voidage values. Only, near the dilute area, which is for ε_g>0.98, the expression by Li and Kwauk predicts clusters of smaller size than the ones predicted by Subbarao. As it concerns the acceleration terms **Figure 53c** it is depicted that both a_f and a_c take values near the gravitational acceleration for most of the range of ε_g values. Near the dense (ε_g<0.7) area the acceleration in the dense phase a_c takes considerably higher values than that of the gravitational acceleration. This is owed to the fact that in these areas the clusters tend to collapse resulting in the acceleration of both phases. Moreover, for higher slip velocities clusters are more unstable and easier to break-up compared to lower slip velocities. The gas accelerations both of the dilute and the dense phases, as well as the slip velocities (U_{sf}, U_{sc}, U_{si}) near $\varepsilon_g = 0.7$ (and as ε_g approaches the packing limit) get considerably higher values for high slip velocities than for the low slip velocities. Correspondingly, the same trend stands for the Reynolds number in dilute, dense and inter-phase. This fact affects considerably the monotonic behavior of H_d trend near the value of ε_g=0.7.

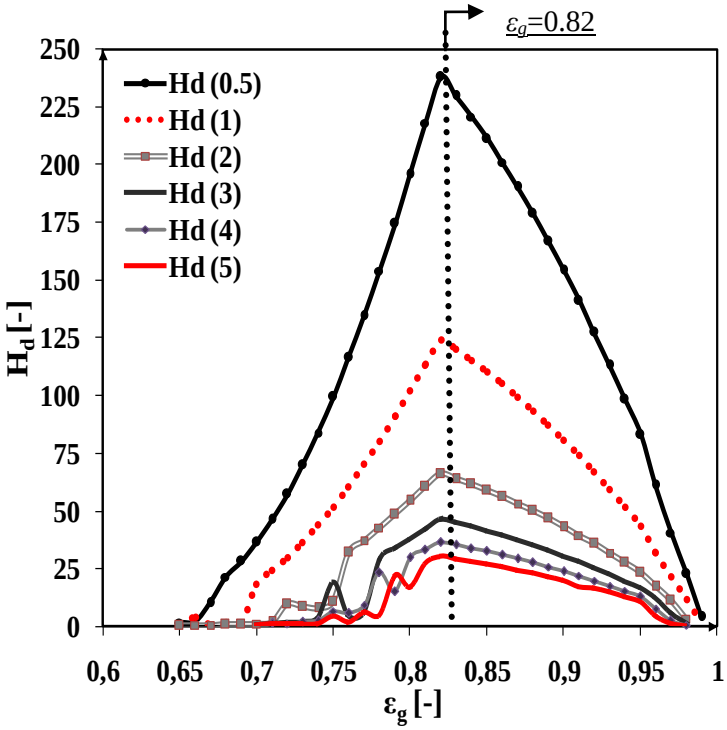

Figure 52. H_d index for different values of ε_g and u_{slip} (u_{slip}=0.5, 1, 2, 3, 4 and 5 m·s^{-1}).

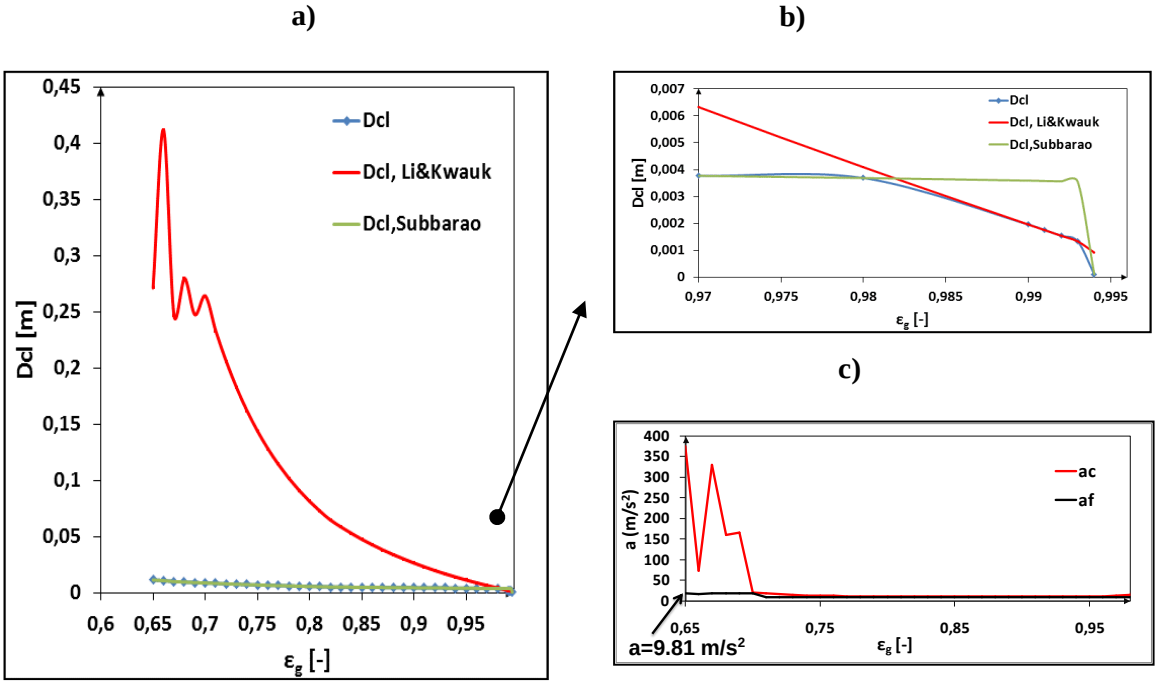

Figure 53. Variation of (a), (b) cluster diameter and (c) acceleration with ε_g (u_{slip}=1).

4.2.5.2 Static Pressure Distribution

Figure 54 depicts the numerical results of the time averaged mean static pressure along the riser axis for the preliminary cases tested along with the corresponding experimental data. As evident, the Gidaspow model over-predicts the static pressure almost all over the riser height. This fact has been observed in other

works as well [299]. On the contrary, the EMMS model reproduces results of significantly higher accuracy, especially at the riser dense bottom zone. The deviations from the experimental data near the height of 1m, are related to the fact that the recirculated solid particles enter the riser close to this height and due to the fact that in the present study only the riser is simulated, any pulsing behavior of the recirculation system is not taken into consideration. Thus, such an effect on the local hydrodynamics, especially at the proximity of this height, is ignored. It is expected that if a full loop simulation is applied for this system, any discrepancies in this area will be reduced.

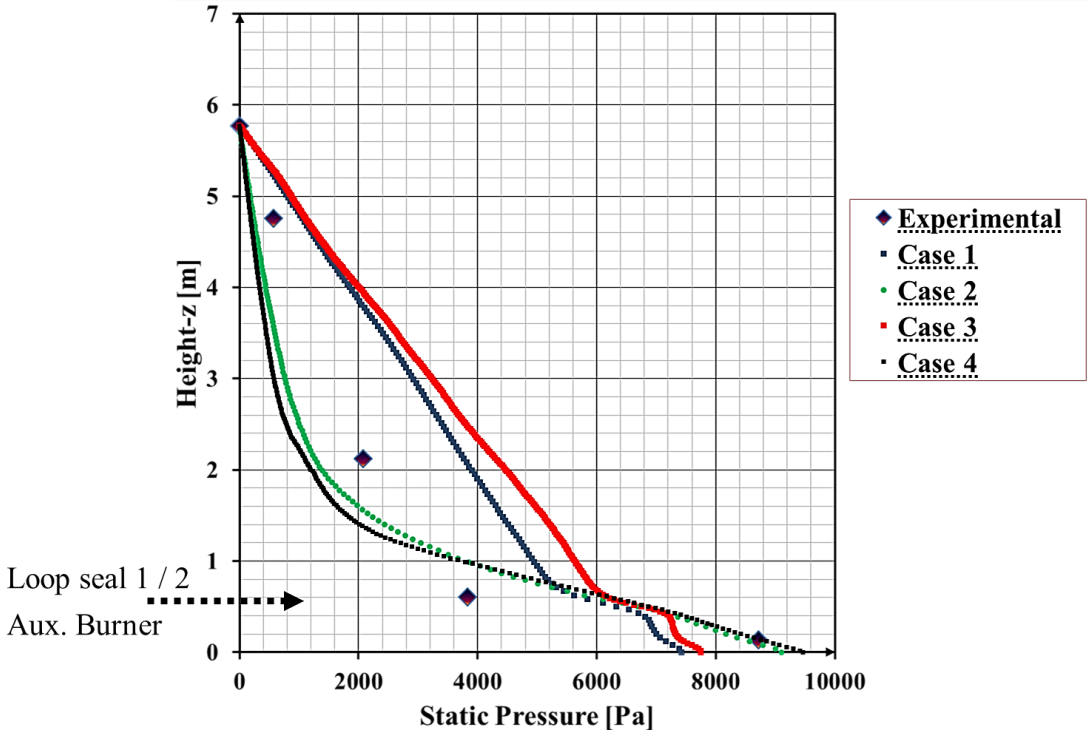

Figure 54. Time averaged mean static pressure along the riser axis.

Considering the grid density effect, the deviation of the calculated pressure drop along the riser axis between the results of the two grids tested for the EMMS drag model is less than 10%. More specifically, the L2 norm error is calculated between the axial pressure results for the coarse and dense grid cases in order to check the grid independency. The calculated dependency on the grid for the EMMS model is approximately 6.5 %. This value is considered low enough for this kind of simulations (almost grid independent). The same is not observed for the Gidaspow case, where the calculated L2 norm error is around 11%.The latter fact verifies similar observations referred in the work of [126]. This is an important outcome of the present investigation, especially of large scale CFD investigations, in which the application of an EMMS scheme may speed-up considerably the computational speed.

Figure 55 depicts instantaneous snapshots of the solid phase volume fraction at the plane Y=0 and for a riser height within the range of [0, 3.5] m. The prediction of cluster formation is evident for the case of the EMMS model even if the coarse grid is implemented. On the contrary, the conventional Gidaspow model induces significant errors in the prediction of the flow patterns and the macro-scale structures. The solid particles are distributed quite uniformly throughout the riser and there is not a clear distinction between the dense bottom bed and the freeboard. Thus, the Gidaspow model fails to predict accurately the high solid volume fraction near the bottom zone of the bed even if a finer grid is implemented.

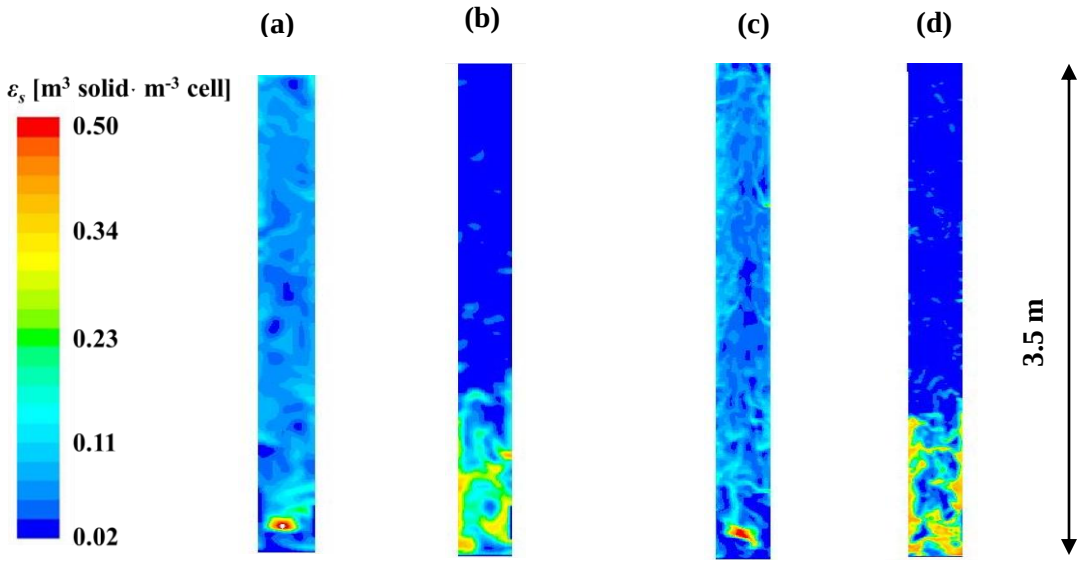

Figure 55. Time instants of solid volume fraction at t=20 s after the initialization of the case, at a plane Y=0 for: (a) Case 1, (b) Case 2, (c) Case 3 and (d) Case 4.

Figure 56 depicts the time dependent solid mass flow rate at the riser exit for a time interval equal to 10s. The negative sign stands for the solid particles mass exiting the reactor. As it is evidenced, 5 seconds after the initialization of each case the mass flow rate reaches equilibrium. Moreover, it is proven that the homogeneous Gidaspow model gives a higher value of the carryover, i.e. around 182.89 kg·m^{-2}·s^{-1}, compared to the EMMS scheme that gives a value around 25.6 kg·m^{-2}·s^{-1}. The corresponding mass flow rate is equal to around 50 kg·s^{-1} for the Gidaspow case and around to 10 kg·s^{-1} (5 times lower than the Gidaspow) for the EMMs case. The prediction of the Gidaspow model seems unrealistic, since high recirculation rates are typical for high-density CFBs [300].

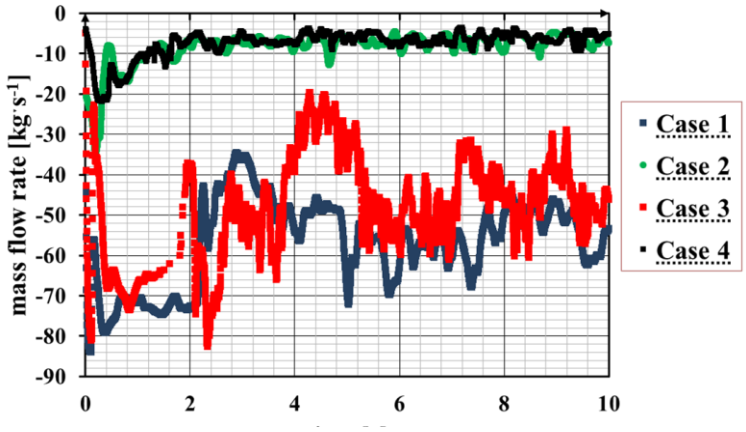

Figure 56. Time-dependent solid mass flow rate at the riser exit.

Finally, additional numerical tests were carried out in order to compare the four preliminary cases in terms of computational cost. For this reason the actual time required to achieve 20 seconds of simulation time was calculated. All additional tests were run in serial processing. It should be noted, that all preliminary cases (Case1, Case 2, Case 3 and Case 4), as well as the parametric study cases for the specularity coefficient were run in parallel processing. From **Table 35**, it is obvious that Case 1 is the least computational expensive, while being the most inaccurate. On the contrary, Case 2 requires a relative low computational cost and it is far more accurate than Cases 1 and 3.

Table 35. Computational cost needed for the preliminary cases studied.

Case	Actual time (using 1 CPU core)
Case 1	15.4 d
Case 2	23.15 d
Case 3	238.1 d
Case 4	333.35 d

Concluding, the coarse grid d_{cell}/d_p ~465 and the EMMS drag model are considered as the best combination of accuracy and CPU cost. This case has been used in the specularity coefficient parametric analysis.

4.2.5.3 Slip Velocity Distribution

To further address the validity of the numerical model on the accurate description of the flow patterns inside the CFB reactor, the effect of the drag force model and grid density on the axial gas-slip velocity is studied. Generally, the slip velocity is influenced by the solid distribution. At higher solid concentrations the slip velocity takes higher values and vice versa. A dimensionless factor of $U_{slip,z}/U_t$ that accounts for the existence of particles aggregates is used to study this effect. If this factor takes values near unity then the particles are at the dilute phase and are moving freely, with their movement mainly influenced by the gravity and drag force. On the other hand, higher values of this factor imply the existence of a dense phase, where the motion of a particle is influenced by gravitational and drag forces, but also by the neighboring particles.

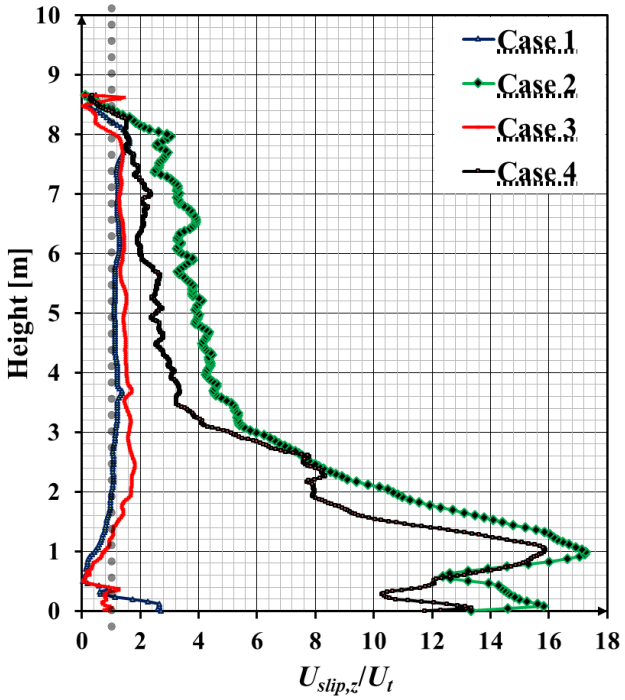

Figure 57. Time-averaged axial gas-solid slip velocity at z direction for t_{aver}=15 s.

Based on the analysis, the $U_{slip,z}/U_t$ factor takes higher values for the EMMS case than for the Gidaspow case near the dense bottom bed zone (**Figure 57)**. Near the freeboard, where the flow is quite dilute, its value approaches unity for all studied cases. The dense grid does not affect significantly the slip velocity parameter especially in the Gidaspow case. Values of the slip velocity close to the terminal velocity near the bottom zone of the riser reflect the weakness of the Gidaspow model to properly predict the dense flow occurring in this area. Finally, it should be noted that for the EMMS model even in the dilute phase the

dimensionless factor $U_{slip,z}/U_t$ takes values approximately around 3 for the dense grid and 4 for the coarse grid. This result is in contrast with the work of [136], where the factor takes values almost close to unity in the dilute phase. Such differences may attributed to the fact that in the present model the simulated particles are Geldart A and, thus, the clustering formation is enhanced even at higher parts of the reactor. On the contrary, in the work of [136] the simulated particles are of type B, where the clustering formation is not so important. Another reason for this phenomenon is the present of the water lances at the freeboard that might lead to the accumulation of particles even at this area.

4.2.5.4 Specularity Coefficient

Figure 58 shows the effect of the specularity coefficient on the solid volume fraction distribution along the riser for a time averaging equal to t_{aver}=15 sec. As can be noticed, the solid volume fraction near the walls is strongly affected by this value. As φ approaches zero the volume fraction near the walls increases. This is more evident at heights above z=2. Near the riser bootom zone the specularity coefficient does affect the flow significantly. On the contrary, at heights z=4 and 6 m the accumulation of solid particles near the walls, and especially near the area of the water lances is better represented if a value of φ=0.01 is adopted. Thus, the core annulus flow occurring inside the FB reactor can be better represented for an φ value equal to 0.01 than 0.99. It should be noted, that the results of this parametric study are qualitative, because there are not any available experimental data for validation.

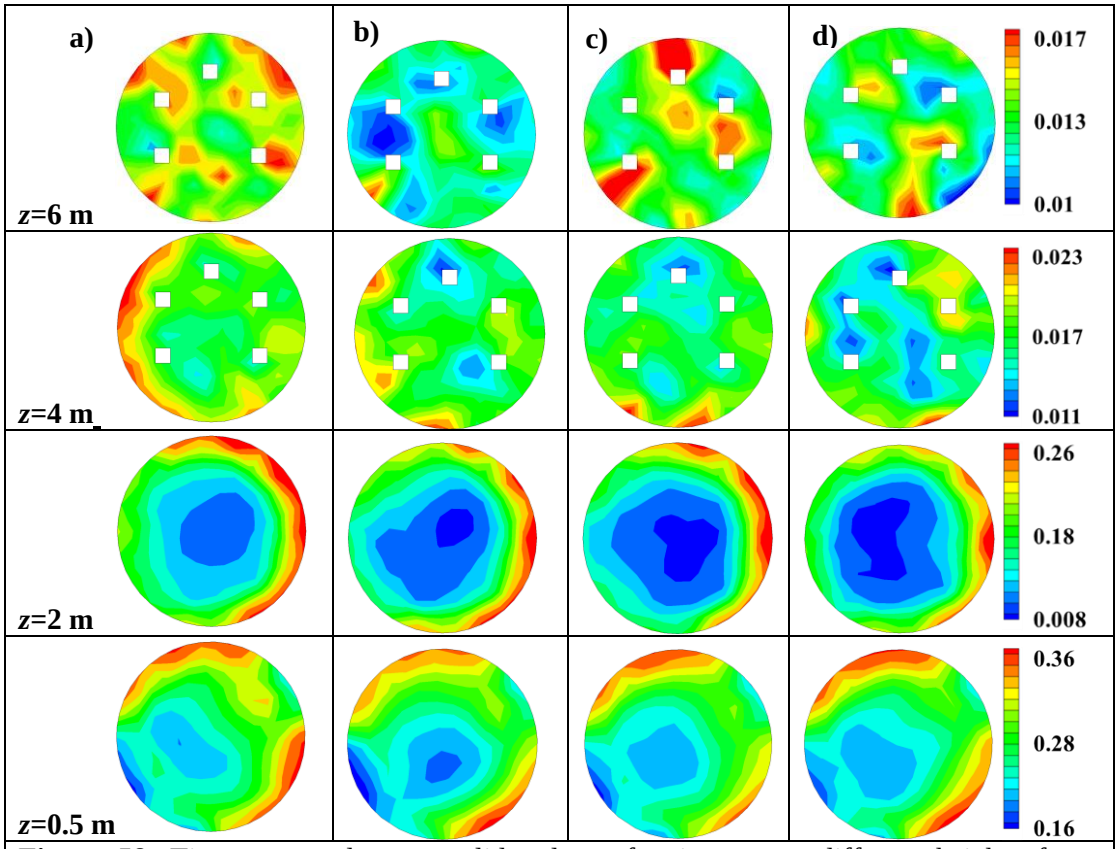

Figure 58. Time averaged mean solid volume fraction, ε_s, at different heights for a specularity coefficient equal to (a) 0.01, (b) 0.1, (c) 0.6 and (d) 0.99.

Regarding the pressure distribution along the riser axis the numerical results are slightly affected by the specularity coefficient (**Figure 59a**). For a value of φ=0.01 and a height range z= [1.5, 3] m the time-

averaged mean static pressure results are slightly closer to the experimental data, than using a value of 0.99. The latter observation is more evident in **Figure 59b**. For other areas inside the reactor, for example near the dense bottom bed zone or near the riser exit, the numerical results almost coincide for all four cases tested. As a conclusion, taking into account the numerical results for the axial static pressure and the solid volume fraction at different heights the value of φ=0.01 can be considered as the most appropriate for a more accurate modeling approach, always in the sense of qualitative results.

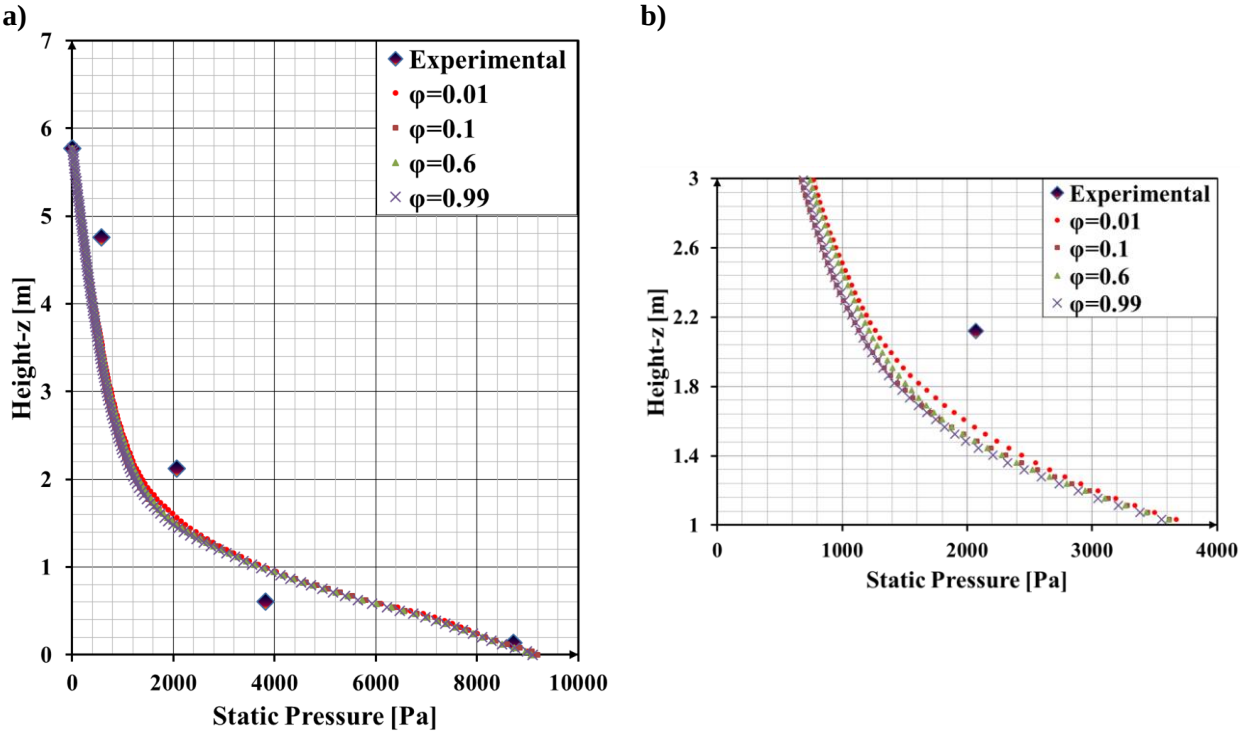

Figure 59. Time averaged mean static pressure, a) along the riser axis and b) for a height range z=1÷3 m, for different values of the specularity coefficient: i) φ=0.01, ii) φ=0.1, iii) φ=0.6 and iv) φ=0.99.

4.2.5.5 Reaction Rate Results

Figure 60 and **Figure 61a** depict the spatial distributions of the time-averaged mean mass fraction of CO_2, Y_{CO2}, for a period of t_{aver}= 65 s. For this analysis, the EMMS scheme with a coarse grid is used (Case 2). The numerically calculated value and the corresponding experimental data are 0.025518 kg $CO_2 \cdot kg^{-1}$ gas and 0.027505 kg $CO_2 \cdot kg^{-1}$ gas respectively. The relative error is 7.22 %. This underestimation may be attributed to the fact that particle clustering may hinder the carbonation reaction and the assumption of homogeneous conditions for the calculation of the reaction rate in each cell overestimates the reaction rate. Moreover, as it is deduced from **Figure 61b**, the root mean square (RMS) of the mass fraction especially in the dense zone of the riser takes values up to 0.04 kg $CO_2 \cdot kg^{-1}$ gas. This indicates that as moving upwards the riser height the fluctuations of the instantaneous Y_{CO2} mass fraction around the time averaged-mean mass fraction are decreasing, with the maximum values traced near the bottom bed zone area (~27%).

Figure 62a shows contours of i) the time averaged CO_2 and $CaCO_3$ mass fractions for a time averaging equal to t_{aver}= 65s and of ii) the reaction rate at a time instant equal to t=270 s at different planar slices along the riser. As it can be seen the CO_2 capture is realized mostly near the center axis of the reactor. At this area the CO_2 mass fraction and thus the heterogeneous reaction rate take high values. On the contrary, the area

near the riser walls is mostly occupied by the solid $CaCO_3$ species due to the induced lower gas velocity, a fact which is not tracked near the core area that is quite dilute (core-annulus flow pattern) [293]. As a result, close to the riser walls the carbon dioxide capture is negligible. It should be noted that the lowest values of the $CaCO_3$ mass fraction are tracked near the bottom zone, **Figure 62b**, owed to the fact that near this area limestone consisting of 9% CaO/ 91% $CaCO_3$ enters the carbonator from the loop seal 2.

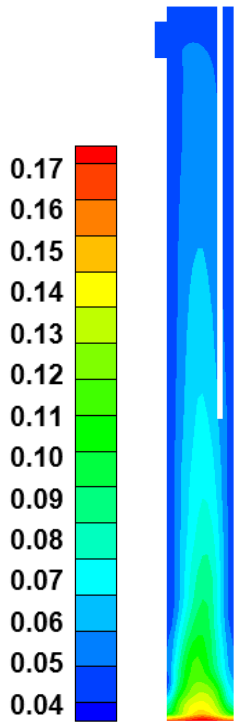

Figure 60. Mass weighted CO_2 mean mass fraction at plane X=0, for t_{aver}= 65 s.

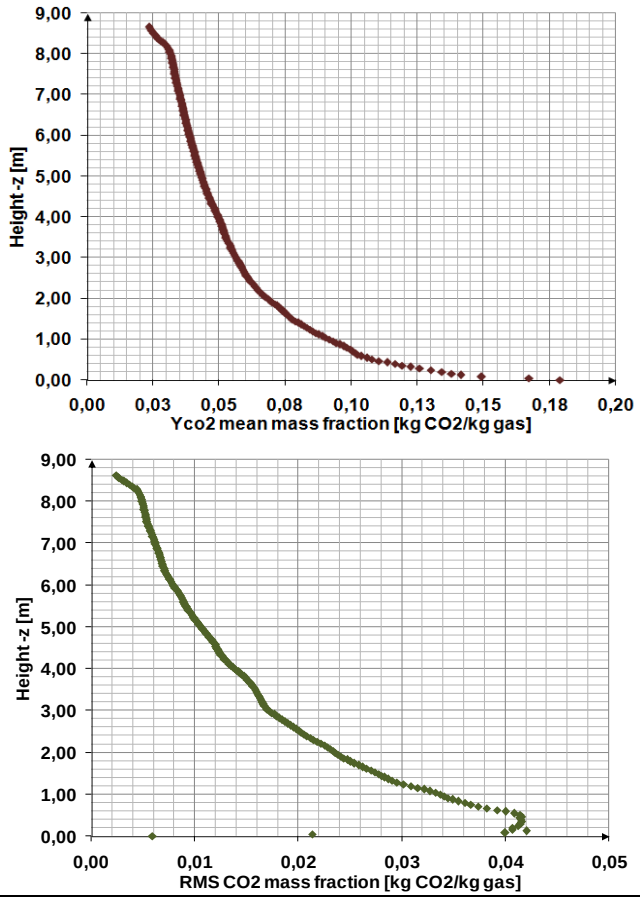

Figure 61. (a) Mean and (b) RMS, Y_{CO2} mass fraction along the riser axis for t_{aver}= 65 s.

The value of the numerically calculated reaction rate (RR_{CFD}) is strongly affected by the flow hydrodynamics and the heterogeneous conditions in each computational cell. In reality, heterogeneity is induced to the flow due to lack of perfect mixing between the two phases, while under ideal conditions, i.e. perfect mixing, homogeneous conditions occur inside the FB. In the case of perfect mixing the numerically calculated variables (mole fraction, volume fraction etc.) should be represented by their average values. For this reason, the numerical results of the reaction rate (RR_{CFD}) at different heights along the riser at a time instant t=270 s are compared against the values of the homogeneous reaction rate ($RR_{Homogeneous}$). The latter is calculated by assuming that at the corresponding heights the radial CaO and CO_2 distribution is homogeneous. Following this, the $RR_{Homogeneous}$ is calculated using the following expression:

$$RR_{Homogeneous} = \overline{Na_{Ca}} \frac{k_s S_0}{1-e_0} (X_{max} - \overline{X_{carb}})^{2/3} (\overline{C_{CO_2}} - C_{CO_2,eq}) [kmol \cdot s^{-1}] \quad (143)$$

, where $\overline{Na_{Ca}}$, $\overline{X_{carb}}$ and $\overline{C_{CO_2}}$ are the area weighted values at the respective heights.

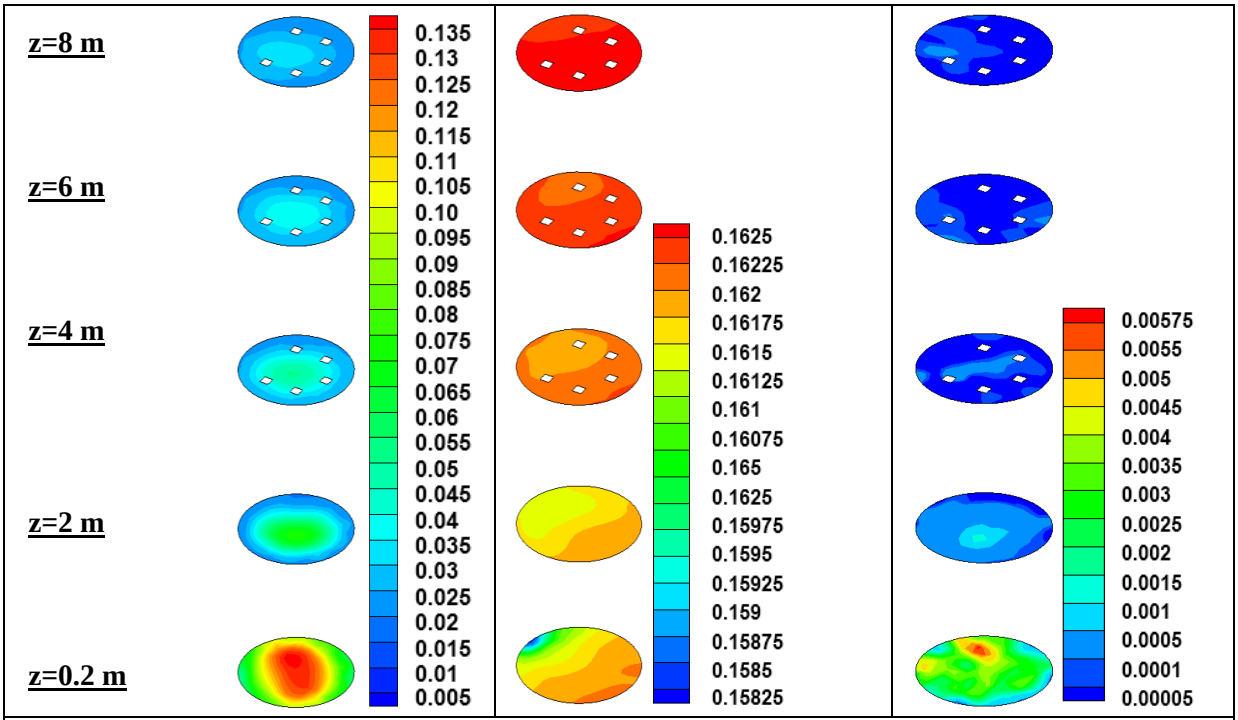

Figure 62. Contours of time-averaged (a) CO_2 and (b) $CaCO_3$ mass fraction and (c) instantaneous reaction rate at different riser heights.

As a further step, a dimensionless hydrodynamic factor Φ_h ($\Phi_h = RR_{CFD}/RR_{Homogeneous}$) is introduced that should take values between [0, 1]. Under ideal conditions, this factor (total mixing between the two phases) should take a value of unity. It is underlined that the $RR_{Homogeneous}$ should always take values greater than the RR_{CFD}, because the CO_2 capture is enhanced under homogeneous conditions.

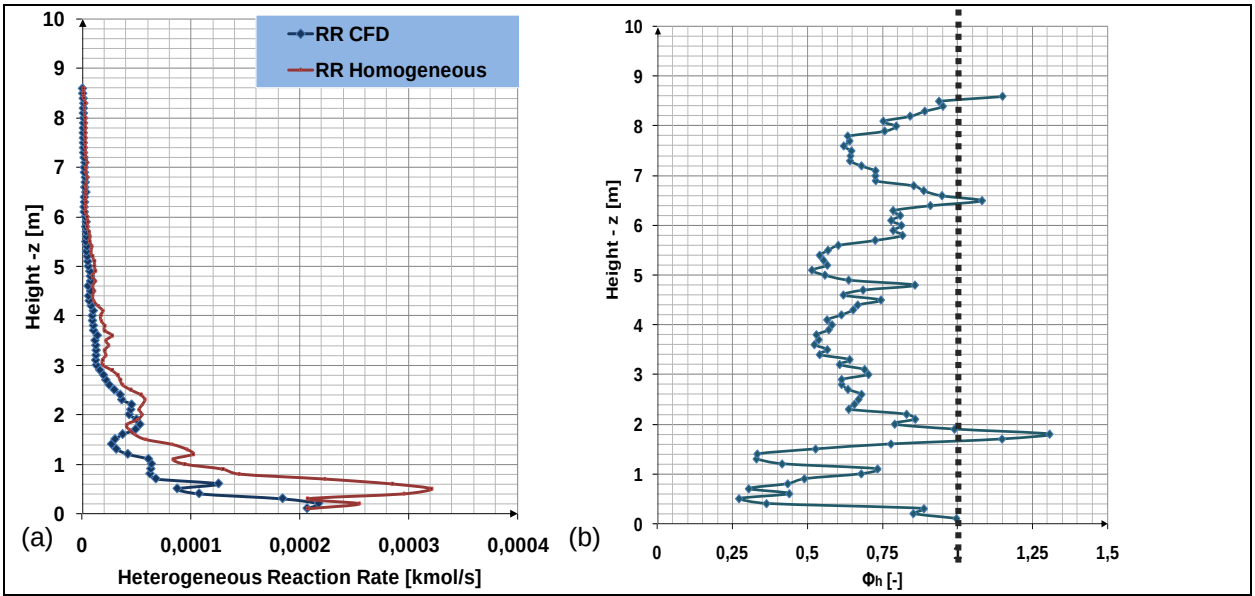

Figure 63. (a) RR_{CFD} vs. $RR_{Homogeneous}$, and (b) hydrodynamic factor Φ_h along the riser for t=270 s.

As it is depicted in **Figure 63** this factor takes values within the range [0.25, 0.5] close the dense bottom zone of the riser. These values are considerably lower that the unity revealing the strong effect of the

heterogeneity on the carbonation reaction. Respectively, the value of the RR_{CFD} in this area deviates significantly from the corresponding theoretical value of $RR_{Homogeneous}$. On the other hand, near the freeboard area where the flow is quite dilute the hydrodynamic factor takes value almost equal to unity.

Figure 64 shows the time series of the mass weighted average of CO_2 mass fraction at different heights along the riser axis (z= 0.2, 2, 4, 6, 8 m) and near the riser exit. The oscillations of CO_2 are demonstrated for all heights and are stronger near the dense bottom zone area. These observations are in accordance with **Figure 61**. Additionally, it is proven that the averaging period of 65 seconds is enough to accurately predict the CO_2 mean mass fraction.

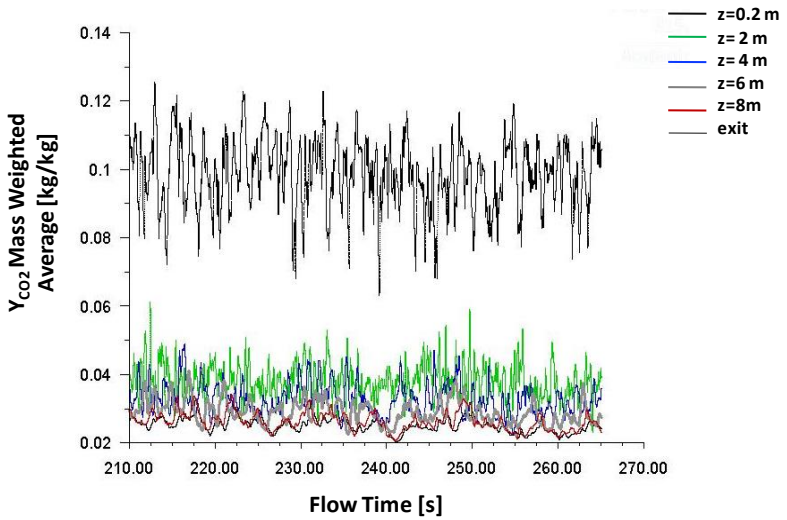

Figure 64.Time series of the numerically calculated Y_{CO2} mass weighted average at different height along the riser axis.

Finally, **Figure 65** presents an FFT (Fast Fourier Transformation) analysis of the oscillating cross sectional mass weighted average of CO_2 concentrations at two different heights, i.e. at the outlet and close to the distributor. This post-processing reveals that CO_2 gas species concentration varies more close to the bottom than the freeboard zone and can be calculated that at low frequencies the oscillations are higher near the dense bottom zone than near the outlet.

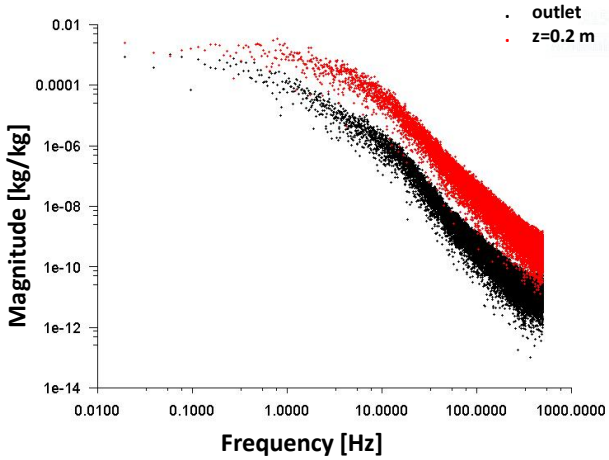

Figure 65. Comparison between the magnitude of CO_2 oscillations at the outlet and at a cross-sectional area near the bottom zone of the riser, using the FFT.

4.2.6 Parametric runs (Design optimization)

The CaL process is a post-combustion CO_2 capture technology that has been tested successfully up to present on a bench and pilot scale, ranging from 3 kW_{th} up to 1.7 MW_{th} [77-79, 82]. Recently, attempts are being made towards its up-scaling to an industrial scale [85, 86]. For the implementation of this technology on a large scale, modeling work is essential to eliminate any financial risks that might arise during the construction of such units [301]. In this frame, computational fluid dynamic (CFD) models can be valuable cost-efficient tools for the optimum design and up-scaling of CaL systems.

In a calcium looping system the carbonator reactor is a critical component. Its optimal design and operation can increase considerably the CO_2 capture efficiency. Thus, a meticulous study of its performance under varying operating conditions and design parameters should be undertaken prior to constructing large-scale units. However, even though the study of the carbonator design effect on the CO_2 capture efficiency is an essential work, there are not any available published works in the recent literature; most of the research is focused on matters relative to the carbonation reaction itself, such as the sorbent maximum activity (X_{max}) [302], the effect of sulphur[303]/ hydration[304] on reaction kinetics etc. Some other available works only deal with the pilot plant operation under different carbonator operation regimes, but design effects have not been studied yet [305, 306]. However, the importance of a CFB reactor design on its performance is an undeniable fact that has been addressed in [307], as well.

In general, in reactor design the main target is the search of the appropriate size and operating method of a reactor for a specific process [308]. An optimum carbonator design for a CaL system should enable high solid particles residence times and good gas-solid mixing resulting, thus, in an efficient carbonation reaction. An idea, quite easy and flexible, is to provide the carbonator riser with more than one sorbent feeding lines, a concept that has been introduced in CFBC boilers [307] where solid fuels that are needed to react with gaseous species are injected in the boiler through various inlets. Another alternative is to modify the riser bottom bed design and introduce a varying riser diameter, rather than a constant value of this design parameter. Such concepts are quite innovative and have not been tested yet in a CaL system.

In the present study, five different carbonator design concepts are tested and compared, regarding static pressure profiles and CO_2 capture efficiency. These concepts include a reference carbonator design, part of the Dual Fluidized Bed facility of TUDA, with a riser height and diameter equal to 8.661 m and 590 mm, respectively, and four retrofitting concepts of the reference design, i.e. Fat Bottom Design (FBD) with two different solids inventories, Sorbent Staging Design (SbS) and Sorbent in Splash Zone Design (SZD). In the FBD case the riser diameter is modified and taken equal to 759 mm up to a height of 1 m from the distributor, whilst for a height range equal to [1, 8.661] m the riser diameter remains the same as in the initial geometry, i.e. 590 mm. In the SbS case, 10% of the regenerated material that comes from the calciner unit, is injected in the carbonator through a section (staging inlet) designed approximately 1 meter above the existing loop seal opening that connects the two reactors, whereas 90% of it keeps entering the unit from the existing loop seal section; in the reference design the regenerated sorbent enters the carbonator exclusively through the loop seal. Finally, in the sorbent in splash zone design (SZD) 100% of the regenerated material is injected from the staging inlet and 0% from the existing loop seal section. 3D CFD simulations of the CFB carbonator riser are carried out in each case in order to evaluate those scenarios effectiveness. The TFM Eulerian approach coupled with the sub-grid EMMS drag scheme is incorporated into the ANSYS FLUENT^{TM} commercial software. The model applied has been already tested and validated for the reference carbonator design [174], using experimental data provided by TUDA.

4.2.6.1 Numerical model

In the present work a 3D numerical model based on the Eulerian approach is applied for the simulation and comparison of four different carbonator design/operation concepts. The riser of the carbonator unit, depicted in **Figure 66a**, is used as a reference design for the four retrofitting concepts, summarized in **Table 36**. The first retrofitting concept includes the construction of the TUDA carbonator riser with a fat bottom design (FBD). In the FBD concept the new riser diameter is equal to 759 mm, greater than that of the 590 mm of the reference design, and extends upwards, up to 1 m from the distributor section. For a height range equal to [1, 8.661] m the riser diameter remains equal to that of the initial geometry. The cyclone, the two loop-seals and the auxiliary burner section are not included in the simulation process likewise in the initial geometry. However, in their intersections with the riser proper boundary conditions are applied for the gas and solid phase, the same as the ones applied in the reference design. Loop Seal 1 is used for the recirculation of the solid particles inside the carbonator, whilst Loop Seal 2 performs the transportation of the regenerated limestone from the calciner to the carbonator unit. The solids inventory is set equal to 282 kg, as in the initial geometry. However, the new riser diameter taken for a height range equal to [0, 1] m, results in a lower pressure drop at this area compared to the reference design. In the second concept, the same fat bottom design is tested, without changing the boundary and operating conditions, except for the solids inventory, which is set equal to 340 kg. This value gives almost the same pressure drop with the one obtained for the reference design. It should be noted that from a designer point of view the approach of comparing cases characterized by the same pressure drop makes a technical sense, since the pressure drop and not the mass in the reactor affects the energy self-consumption of such a unit.

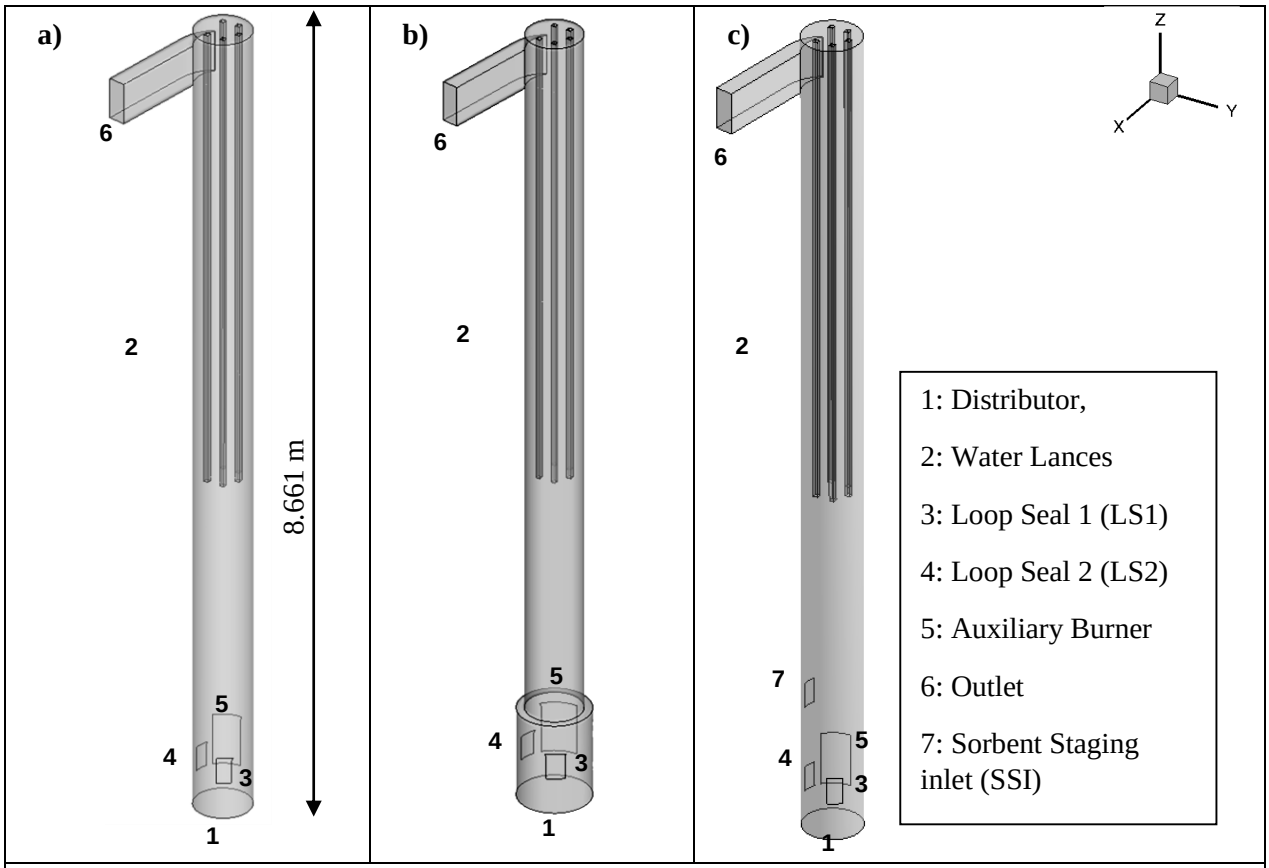

Figure 66. Geometry layout of the a) Reference design, b) FBD and c) SbS/ SZD.

In the third concept, i.e. the sorbent staging design (SbS) concept, 10% of the regenerated sorbent, coming from the calciner unit, is injected from a higher height, approximately 1 meter from Loop Seal 2, whilst the rest of it keeps entering the reactor from Loop Seal 2. The geometrical configuration is the same as in the reference design, with the exception that an additional face is inserted, used as a mass flow inlet of the sorbent injection staging. The sorbent staging inlet has the same dimensions, with the intersection of the Loop Seal 2 section with the carbonator riser. In the fourth concept, i.e. the sorbent in splash zone design (SZD), 100% of the regenerated sorbent is injected exclusively from the sorbent staging inlet and a wall boundary condition is assigned to Loop Seal 2 face.

For the numerical simulations 3D structured grids are constructed with ANSYS Meshing component fully respecting the modified geometries of the carbonator riser. The discretized domain consists of 35,870 hexahedral elements for the FBD case and of 31,346 hexahedral elements for the SbS and SZD cases. Both numerical grids correspond to a d_{cell} *to* d_p ratio equal to 465.64. A grid independency test has been already conducted for the reference geometry case [174].

The CFD model is incorporated into the ANSYS Fluent 17.1 platform. Transient calculations are performed, with a time step size equal to 10^{-4} s. Parallel computing is used, with 12 parallel cores, in order to enhance the CFD model computational efficiency. A time interval equal to 65 seconds is taken for the time averaging of the numerical results. It should be noted that 5 s after the initialization in all cases, an equilibrium state is almost reached as concerns the pressure profile. However, the solid species, i.e. CaO and $CaCO_3$, delay in reaching equilibrium requiring thus longer simulation times of almost 200 s in order to predict them correctly. The $CaCO_3$ mass fraction is initialized with a value of 0.16 close to the value of 0.1655 that corresponds to X_{max}=0.1, in order to speed-up the simulation. The phase-coupled SIMPLE scheme is applied for the pressure-velocity coupling. As concerns the spatial discretization of the main governing equations, i.e. momentum, volume fraction and species equations, the QUICK scheme is applied. The time discretization is conducted by a bounded second order implicit scheme [297]. A detailed description of the governing equations used can be found in [297]. For the drag force exerted on the solid particles the sub-grid EMMS scheme developed in this Thesis is applied. The limestone particles are of type Geldart A, with a density equal to 1650 kg/m^3 and a mean particle diameter 91.39 μm. The carbonation of CaO particles to $CaCO_3$ is taken into account by incorporating into the CFD model the reaction rate of Hawthorne et al. [172]. The boundary and operating conditions, except for some modifications analysed above, are presented in [174].

Table 36. Compared cases simulated.

Case Number	Test Case	Solids Inventory	Superficial gas velocity (U_g)
Case 1	Reference design (100%-0%)	282 kg	1.93 m·s^{-1}
Case 2	FBD-282	282 kg	1.162 m·s^{-1}
Case 3	FBD-340	340 kg	1.162 m·s^{-1}
Case 4	SbS (90% - 10%)	282 kg	1.93 m·s^{-1}
Case 5	SZD (0-100%)	282 kg	1.93 m·s^{-1}

4.2.6.2 Results

Figure 67 depicts the numerical results of the four proposed technical concepts tested, as regards the time-averaged static pressure profile, in comparison with the corresponding numerical results of the reference design case. It is evident that near the dense bottom zone the predicted pressure in the FBD-282 test case is lower compared to one calculated for the reference design. In the second fat bottom design test case, i.e.

FBD-340 kg, the static pressure profile is virtually the same as in the reference design. Additionally, concerning the SbS and SZD test cases compared to the reference design, it can be seen that all three static pressure-height curves almost coincide for a height range [0, 1] m. Above that height, a higher pressure drop is observed in the reference design than in the SbS and SZD test cases indicating the presence of higher amounts of solid particles in the freeboard.

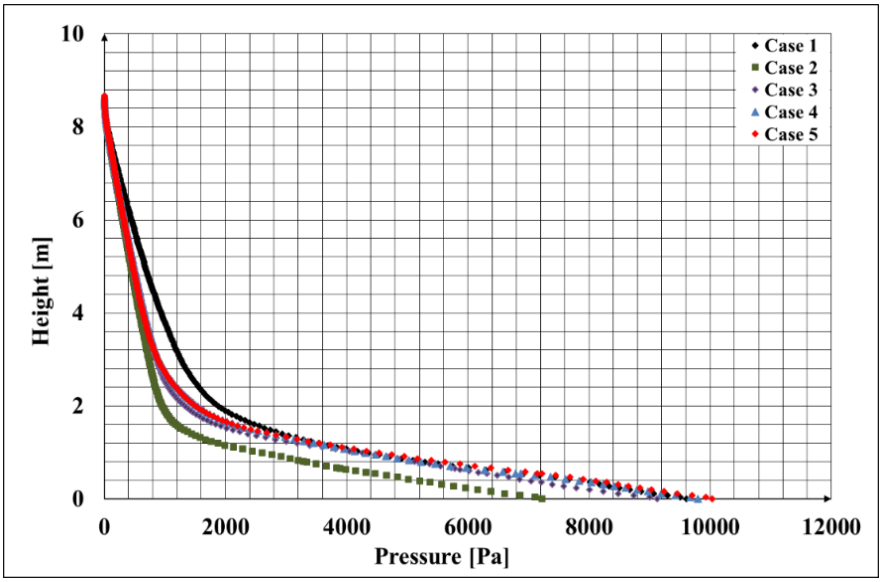

Figure 67. Time-averaged mean static pressure along the riser axis for a time averaging equal to *t*=15 sec.

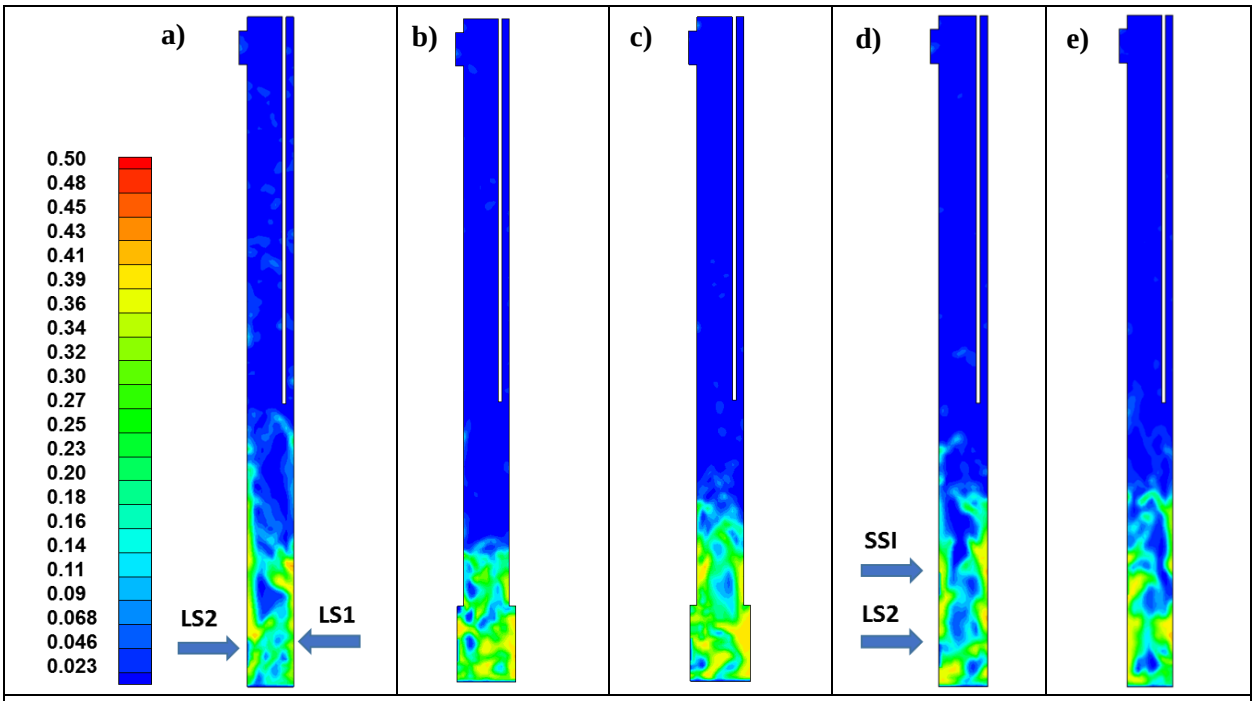

Figure 68. Instantaneous solids volume fraction at *X*=0 (the medium *X* of the reactor) for a) the Reference design b) the FBD-282 kg, c) the FBD-340 kg, d) SbS and e) SZD.

This fact is also evident in **Figure 68**, where the contours of the instantaneous solids volume fraction at a plane X=0 for all the compared cases is presented. As can be seen, in the reference design higher values of

the solid volume fraction can be observed in the freeboard, when compared with the other cases. This is the reason why in the reference design case the mean static pressure drop is slightly higher compared to the other cases. Another important conclusion to be drawn is that the core-annulus flow pattern exhibited in CFB risers, is less intense in the FBD concept –especially in the FBD-282 case- than in the other design concepts. In this case, low values of the solid volume fraction are observed for heights greater than 2 meters.

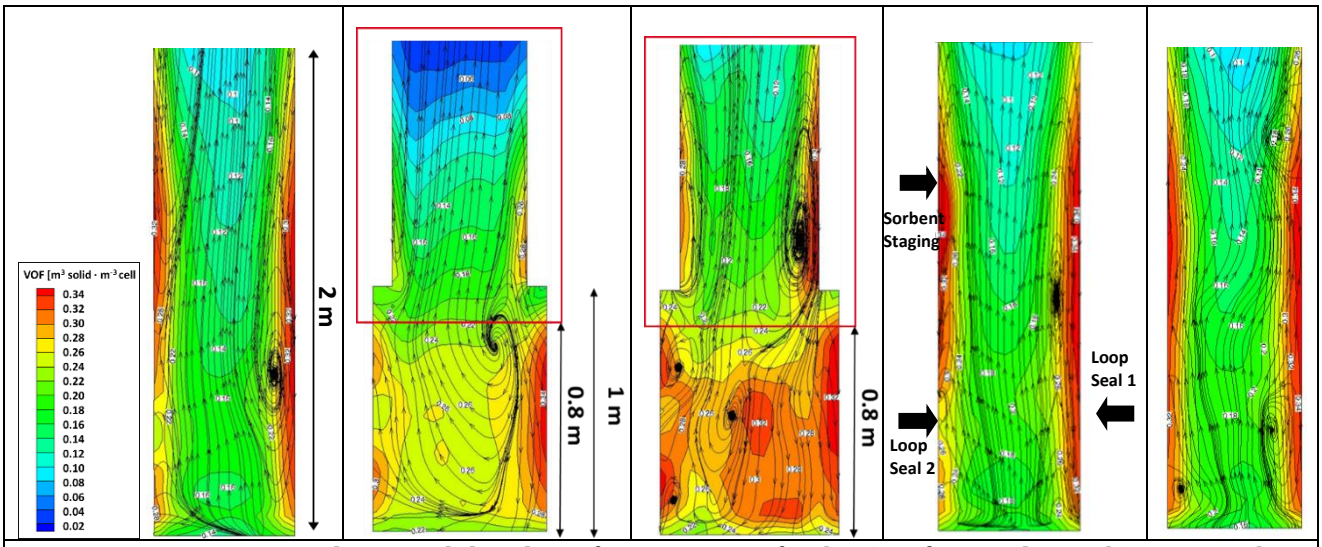

Figure 69. Time-averaged mean solids volume fraction at *X*=0 for the a) Reference design, b) FBD-282 kg, c) FBD-340 kg, d) SbS and e) SZD concept.

Figure 69 presents the contours of the time-averaged mean solids volume fraction at a plane X=0 for the studied cases. Generally, in the fat bottom design the solid volume fraction near the bottom zone is higher than the one observed in the reference design. Additionally, in the FBD-282 kg case, the flow tends to be homogeneous, for heights greater than 0.8 meters, resulting in a better gas-solid mixing. On the other hand in the FBD-340 kg test case, higher heterogeneity is observed, even if this case should be compared with the reference design, owing to the higher solids inventory. However, in the latter case a quite high CO_2 capture is achieved; the highest among all cases examined. This is attributed to the fact that high back flow mixing of the solid phase occur in the fat bottom bed, keeping thus more sorbent mass in this area. In the SbS and SZD concepts the gas-solid flow pattern is quite similar as in the reference design case.

Figure 70 depicts the time-averaged spatial distribution of mass weighted CO_2 mean mass fraction at a plane X=0 for the cases tested. It is evident that in the reference design, SbS and SZD most of the CO_2 capture occurs near the center axis of the reactor and continues up to a height of approximately 1-2 meters. In the FBD, in both cases tested, most of the CO_2 capture occurs at the fat bottom area of the riser.

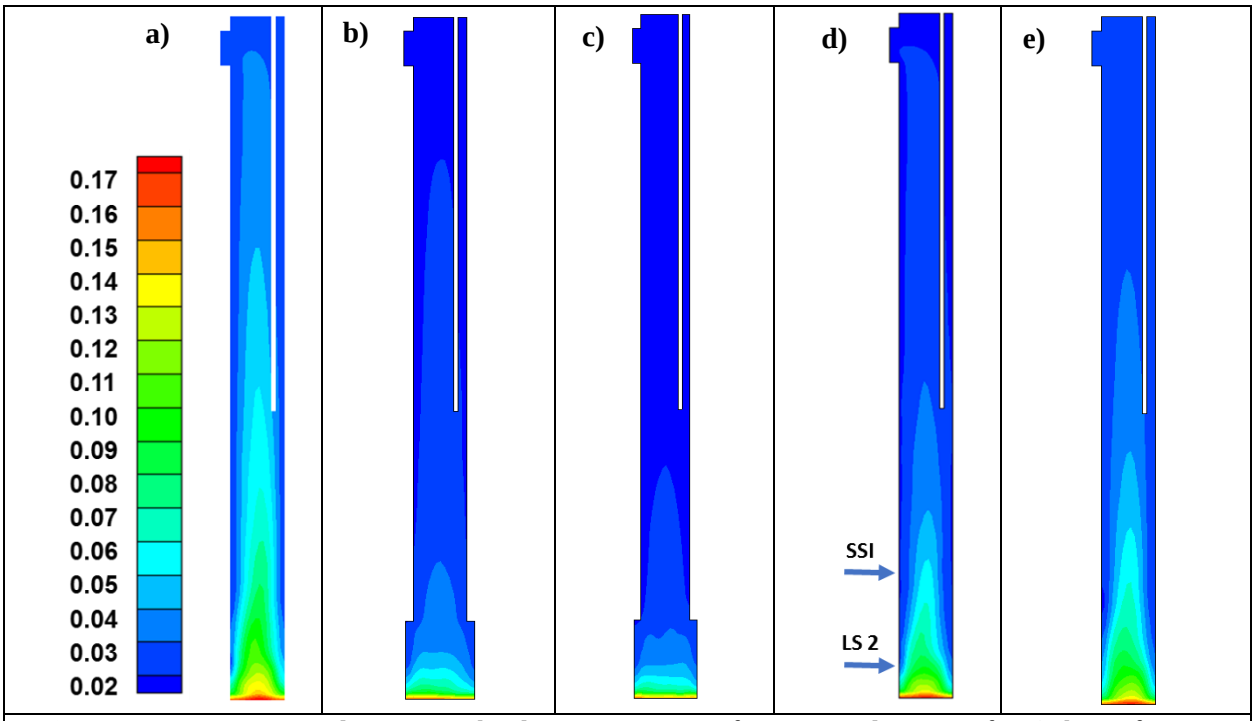

Figure 70. Time-averaged mass weighted CO_2 mean mass fraction at plane X=0 for a) the Reference design b) the FBD-282 kg, c) the FBD-340 kg, d) SbS and e) SZD.

Finally, the numerical results indicate that a better CO_2 capture efficiency is achieved in all retrofit cases compared to the reference design. More specifically, the capture efficiency is equal to 90.36% and 91.91%, in the FBD-282 and FBD-340 concepts, respectively, as can be seen in **Table 37**; such values are close enough to the CO_2 equilibrium capture efficiency (93.33%). In the SbS design concept a CO_2 capture efficiency equal to 89.64% can be achieved, whilst the efficiency is lower (88.70%) when 100% of the sorbent phase is injected from the sorbent staging inlet. This confirms the advantages of staging the sorbent injection, since injecting all of the regenerated material to the bottom or to the splash zone leads to lower capture efficiency.

Table 37. Comparison of the capture efficiency achieved in the reference design and FBD concepts.

Case Studied	Capture Efficiency
Case 1	87.03 %
Case 2	90.36 %
Case 3	91.91 %
Case 4	89.64 %
Case 5	88.70 %

Such fact is proven in **Figure 71**, as well, where numerical results of the CO_2 mean mass fraction at different riser heights of all the retrofit cases are presented. More specifically, it can be seen that higher capture efficiency can be achieved when part of the regenerated sorbent is split and introduced to the reactor at different heights than being introduced completely from the same height. A simple interpretation to such fact is that when the regenerated sorbent is introduced from the same section, the solids volume fraction and subsequently the flow heterogeneity increases locally, a fact that hinders the effective gas-solid mixing.

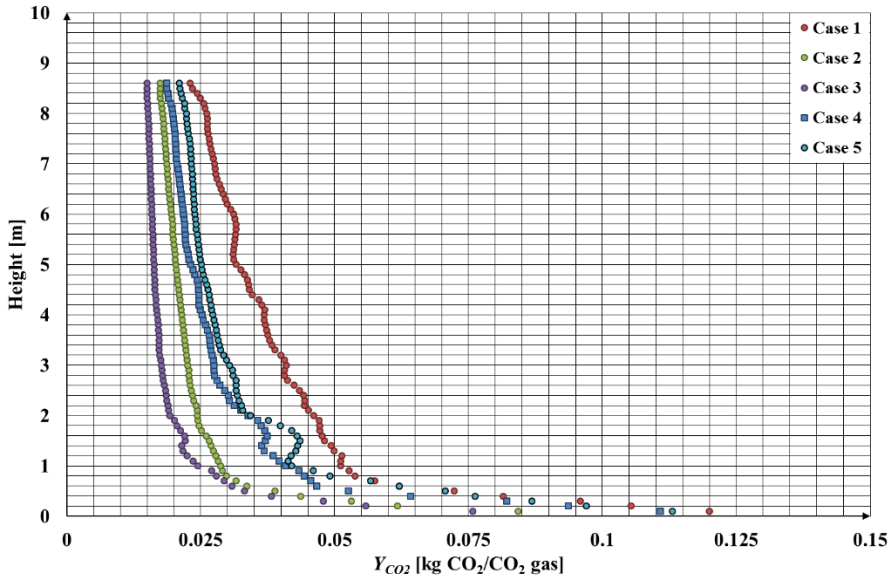

Figure 71. Time-averaged mean Y_{CO2} along riser center line for the a) Reference design, b) FBD-282 kg, c) FBD-340 kg, d) SbS and e) SZD.

The advantages of the four retrofitting concepts over the reference design in terms of CO_2 capture efficiency are reflected, as well, by the values of the effective material to CO_2 ratio. The contours of this molar ratio at different horizontal slices near the bottom bed area are depicted in **Figure 72**. In all retrofitting cases, better mixing is achieved and the regions of the reactor with low ratios are minimized. In such areas although there is CO_2 in the gaseous phase, the amount of the active CaO is not that high.

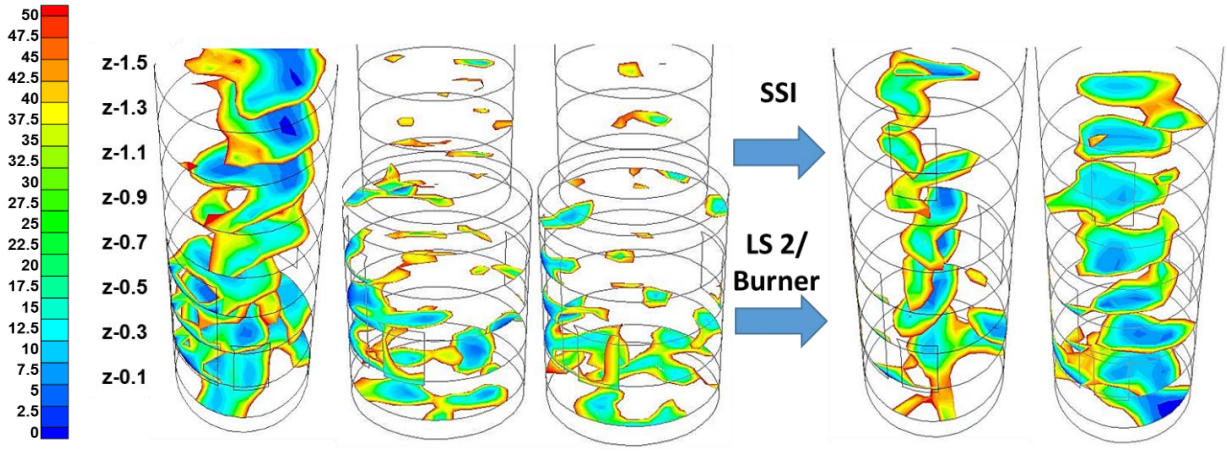

Figure 72. Effective material to CO_2 ratio (kmol CaO (active) / kmol CO_2) for the a) Reference design, b) FBD-282 kg, c) FBD-340 kg, d) SbS and e) SZD. (Values greater than 50 have been cut-off).

It should be underlined that in terms of CO_2 capture efficiency the FBD concept seems the most promising among all, however the SbS design concept is the most preferable solution, because apart from the high capture efficiency, it can be more easily modified to the initial design concept by simply opening or closing the sorbent staging inlet.

4.2.7 Up-scaling assessment (towards 20 MW_{th})

Moving forward, the validated CFD model is utilized for the simulation of a 20 MW_{th} carbonator, which is a scaled-up unit of the 1 MW_{th} carbonator unit [309]. More specifically, the TFM model coupled with a the new updated version of the sub-grid EMMS scheme developed in this Thesis [174], and a proper carbonator reaction rate based on the work of Hawthorne et al. [172] are integrated into the ANSYS Fluent platform.. The challenging, in terms of CPU cost, lasted approximately five months. Parallel simulation runs have been conducted in order to increase the CFD model computational efficiency and decrease the associated actual time of running. Apart from the initial design (Standard design concept), the Sorbent Staging (SbS) concept have been also tested, as previously done for the 1 MW_{th} unit [310]. In this concept, 10 % of the regenerated material coming from the calciner unit is injected from a higher height than the loop seal that interconnects the two reactors.

4.2.7.1 Geometry/Mesh layout and Boundary conditions

The reactor of the 20 MW_{th} unit has a height equal to 20 m and its cross sectional area is square with dimensions equal to 1.5x1.5 m. The given geometry, **Figure 73a** includes the distributor from which the flue gas is inserted upwards to the unit, the outlet section and two Loop Seal sections; the first one (LS_recirculation) is used for the internal circulation of the sorbent particles inside the carbonator, whilst the second one (LS_from_calciner) serves for the transportation of the regenerated material from the calciner to the carbonator unit. According to the technical document received by TUDA, in the design of the 20 MW_{th} pilot plant, LS_recirculation is fluidized by air and not by steam, due to operational cost reasons. However, in real conditions both loop seals are fluidized with steam in order to avoid contamination of CO_2 by N_2 and O_2. For this reason, the numerical model was set up with the condition of using steam, as fluidization gas for the two loop seals. Apart from the two loop seals and the distributor section, two additional faces were added, by TUDA to the geometry design, i.e. Stage 1, Stage 2, which can be potentially used as mass flow inlets of the regenerated sorbent particles for the Sorbent Staging (SbS) Design concept [310]. Both of them are placed above LS_from_calciner, with the first of them, i.e. Stage 1, being placed at the same height with LS_recirculation, which is around 2 m above the distributor section. The second one, Stage 2, is placed 1 m above Stage 1.

The 3D grid consists of 296,464 hexahedral elements, with a mean cell volume equal to 0.00016 m^3. According to the given PSD and following the Geldart classification the sorbent particles are of type A and have a mean diameter equal to 108.43 μm. Thus, the grid resolution tested corresponds to a d_{cell} to d_p ratio equal to 500.73, close to the value of 466.64, which is the grid resolution of the coarse mesh of the 1 MW_{th} carbonator unit case. It is noted that the particle size distribution (PSD), provided by TUDA is not taken into account in this set of simulations as it increases considerably the computational cost [296]. **Figure 73b** depicts the full 3D coarse mesh of the carbonator riser and some zoom areas.

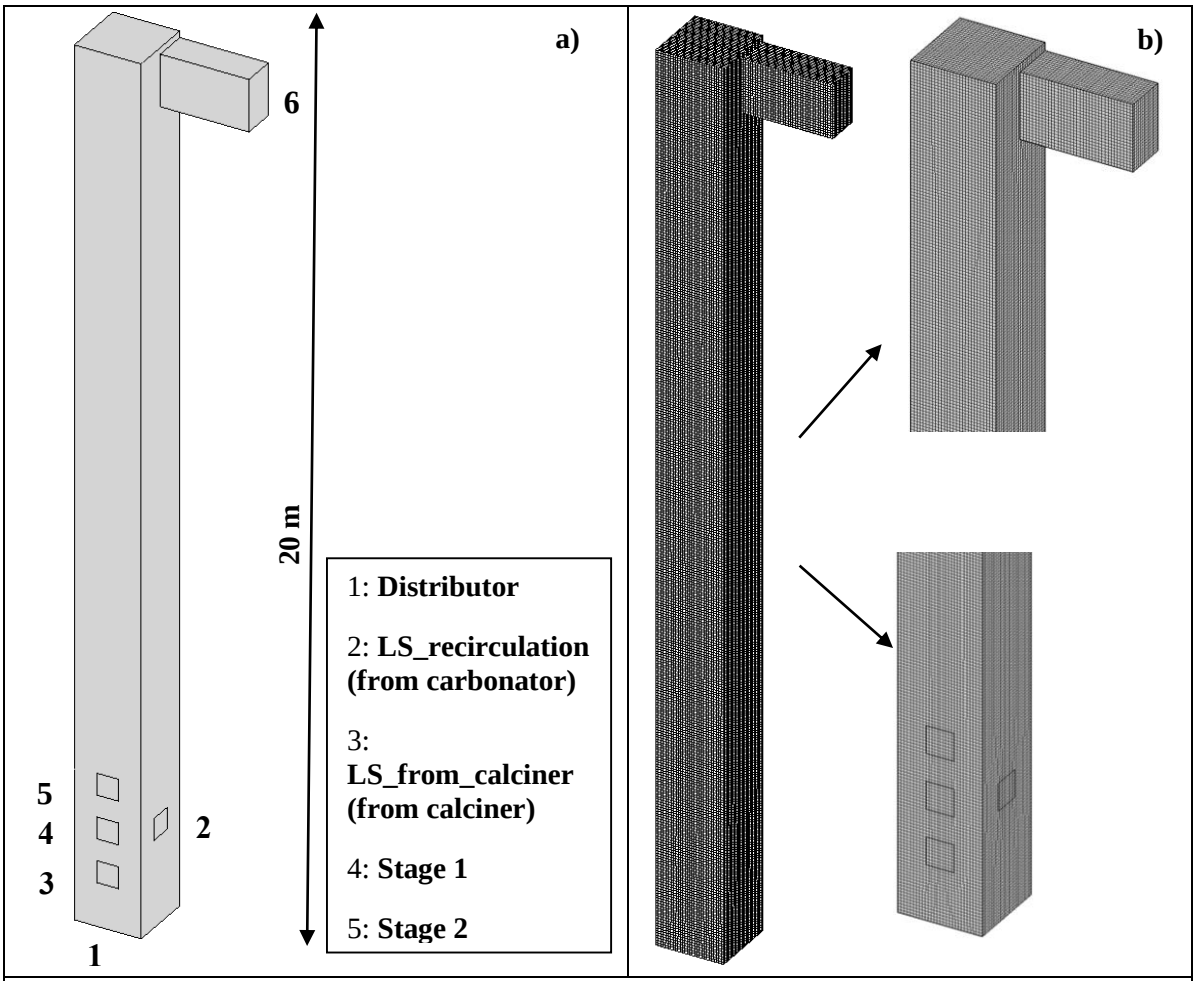

Figure 73. a) 3D scheme and b) 3D domain with zoom areas of the carbonator riser.

Table 38 summarizes the physical/chemical properties of the two interacting phases (gas and solid phase). It is noted that the values for the minimum fluidization voidage, coefficient etc. are kept the same as in the CFD model setup of the 1 MW_{th} unit.

Table 38. Gas-solid properties.

Parameter	Value	Units
d_p	108.4327	μm
ρ_s	1923.276	$kg \cdot m^{-3}$
ρ_g	0.3567	$kg \cdot m^{-3}$
μ_g	3.9515E-05	$kg \cdot m^{-1} \cdot s^{-1}$
ε_{mf}	0.55	(-)
ε_{max}	0.9997	(-)
$\varepsilon_{s,max}$	0.65	(-)
e_{ss}	0.9	(-)

4.2.7.2 Cases simulated

Two design concepts were tested, corresponding to two of the test cases simulated for the 1 MW_{th} carbonator unit [310]. The first one corresponds to the reference design case (Standard design), in which the regenerated material coming from the calciner is injected exclusively through LS_from_calciner to the carbonator riser. In the second one, i.e. the Sorbent Staging design concept (SbS), 10% of the regenerated material is injected from a higher height than LS_from_calciner (from Stage 2), whilst 90% of it is injected through LS_from_calciner. Thus, in the SbS concept simulated in this section, only Stage 2 was set up as mass flow inlet, whilst Stage 1 was treated as wall. The outlet boundary zone is defined as a pressure-outlet, with an operating pressure set equal to the atmospheric. In both cases, the solids inventory was kept the same as given by TUDA, i.e. 2270 kg. No slip boundary condition is considered for the gas phase at the walls. For the solid phase the Johnson and Jackson [153] wall boundary condition is applied, with a specularity coefficient equal to 0.01. Finally, a constant temperature is defined, i.e. 923 K, because the unit is simulated to operate under almost isothermal conditions

Transient calculations were performed with a fixed time step size equal to $5 \cdot 10^{-4}$ s. The Eulerian TFM coupled with the sub-grid EMMS scheme with a new cluster correlation already been validated for the operating conditions of the 1 MW_{th} carbonator unit was incorporated into the ANSYS Fluent 17 platform. This new version of the EMMS model has proven to give more accurate results than conventional models, i.e. the homogeneous Gidaspow model. The map of the EMMS scheme implemented for different slip velocities is depicted in **Figure 74**. Apart from the flow hydrodynamics, the carbonation reaction kinetics were also modelled and a reaction rate based on the work of Hawthorne et al. [172], with an X_{max} value equal to 0.1 was incorporated into the CFD model. The CFB operates under almost isothermal and a steady temperature equal to 923 K was considered throughout the whole domain. Both the EMMS model and the carbonation reaction rate were incorporated through custom-built UDFs into the ANSYS Fluent platform.

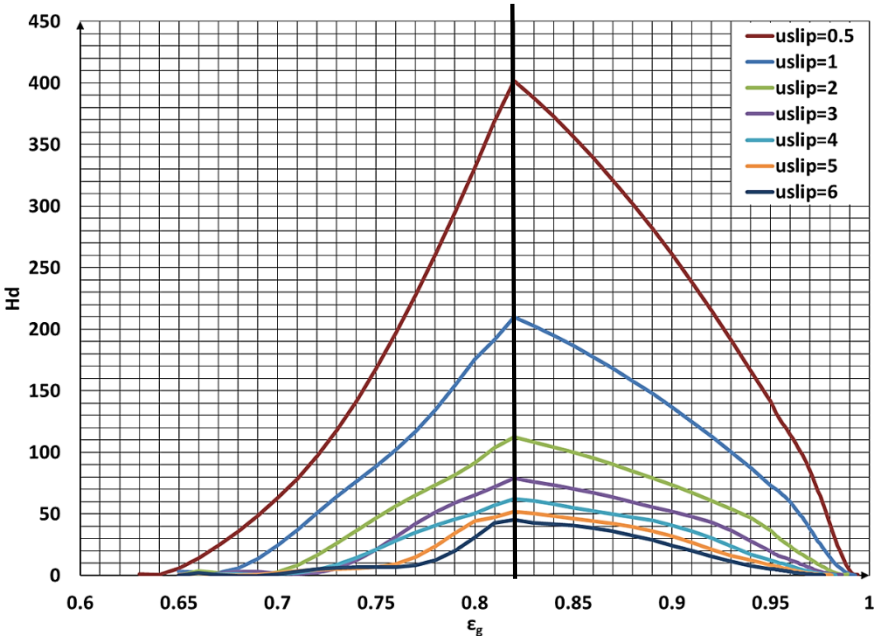

Figure 74. EMMS map implemented in the 20 MW_{th} case.

As concerns the spatial discretization of the main governing equations, the QUICK scheme was applied for the solution of the momentum, volume fraction and species equations, whilst for the time discretization a

bounded second order implicit scheme was adopted [297]. Moreover, the phase-coupled SIMPLE algorithm was applied for the velocity-pressure coupling. For the accurate prediction of the numerical results, a time averaging of approximately 100 seconds was applied, almost the double of the one used for the time averaging of the numerical results of the 1 MW_{th} unit test cases. Such high time averaging is because the $CaCO_3$ mass fraction could not reach fast enough an equilibrium state. More details on the governing equations can be found in [174, 311]. **Table 39** presents the boundary/operating conditions of the simulated cases.

Table 39. Boundary/operating conditions for the carbonator model.

	BC type	**Parameters**	**Units**	**Values**
Distributor	Mass flow Inlet	$\dot{m}_{gas}$	$kg \cdot s^{-1}$	4.44125
		Y_{O2} /Y_{CO2}	$kg \cdot kg^{-1}$	0.0739/0.161397
		Y_{H2O} /Y_{N2}	$kg \cdot kg^{-1}$	0.07120/0.69350
LS_recirculation	Mass flow Inlet	$\dot{m}_{gas}$	$kg \cdot s^{-1}$	0.004680556
		Y_{H2O}	$kg \cdot kg^{-1}$	1
LS_from_calciner*	Mass flow Inlet	$\dot{m}_{gas}$/ $\dot{m}_{solid}$	$kg \cdot s^{-1}$	0.00354167/12.6
		Y_{H2O}	$kg \cdot kg^{-1}$	1
		Y_{CaSO4}/$Y_{coal[ash]}$ /Y_{CaO}	$kg \cdot kg^{-1}$	0.03966/0.027896/0.9324
Stage 2**	Mass flow Inlet	$\dot{m}_{gas}$/ $\dot{m}_{solid}$	$kg \cdot s^{-1}$	0/ 1.26 (10 % of the regenerated sorbent)
		Y_{CaSO4}/$Y_{coal[ash]}$ /Y_{CaO}	$kg \cdot kg^{-1}$	0.03966/0.027896/0.9324
Outlet	Pressure Outlet	P	bar	1
Walls	Gas phase: No slip condition Solid phase: φ=0.01			

** The value of $\dot{m}_{solid}$=12.6 $kg \cdot s^{-1}$ is applied in the Standard design. In the SbS 90 % of this value is applied in the boundary*

*** This boundary condition is applied for the SbS concept. In the Standard design Stage 2 is treated as wall*

4.2.7.3 Numerical results

Figure 75 depicts the time-averaged mean solids volume fraction at planes X=0 and Y=0 for both cases simulated. As it can be seen the dense fluidized bed is extended up to a height of approximately 2.5 m, which is near the height where LS_recirculation is placed and 0.5 meter approximately upwards Stage 2. In both concepts tested, LS_recirculation serves for the internal recirculation of the carbonator unit. For this reason at the proximity of this area the velocity field is highly affected, whilst there is accumulation of solid particles, a fact that is affecting subsequently the capture efficiency. Additionally, some solid particles are moving downwards, especially in the SbS concept, a trend that is depicted in **Figure 76**.

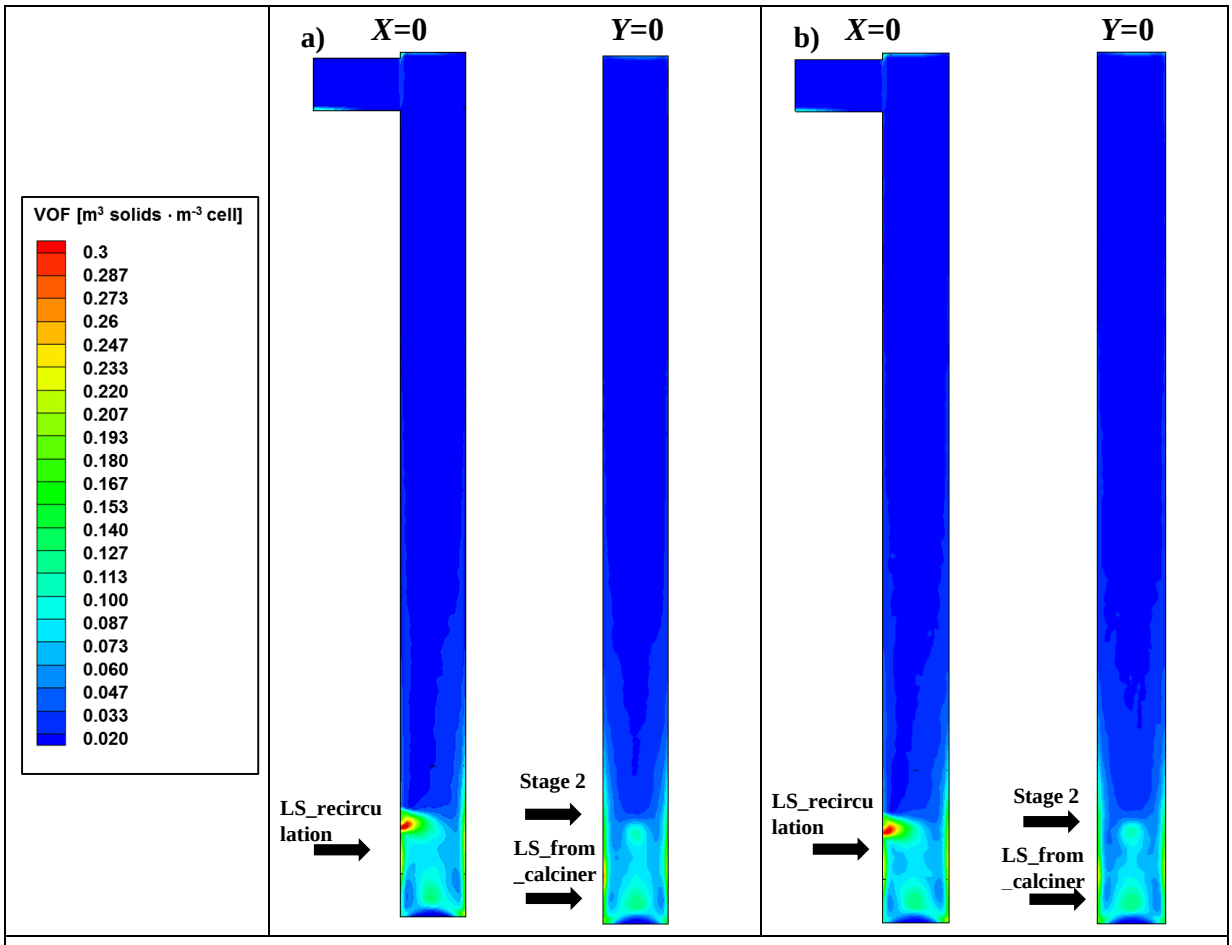

Figure 75. Mean solids volume fraction for a) Reference design, b) SbS at *X*=0 and *Y*=0 respectively.

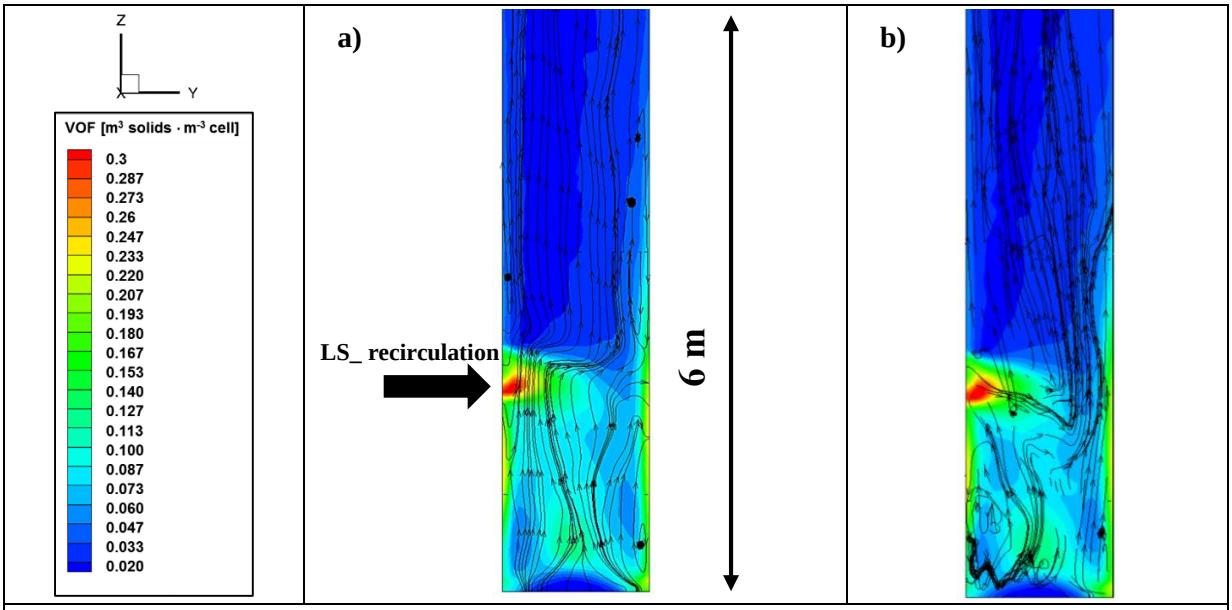

Figure 76. Mean solids volume fraction at *X*=0 for the a) Reference design, b) SbS near the bottom area.

In **Figure 77** the contours of the time-averaged mean CO_2 mass fraction for the two examined cases are depicted. In both cases tested, the core-annulus flow is evident. Moreover, it is observed that in both concepts most of the CO_2 capture occurs near the bottom bed and continues up to a height of approximately 4 meters. The same core-annulus flow pattern was also observed in the 1 MW_{th} carbonator case.

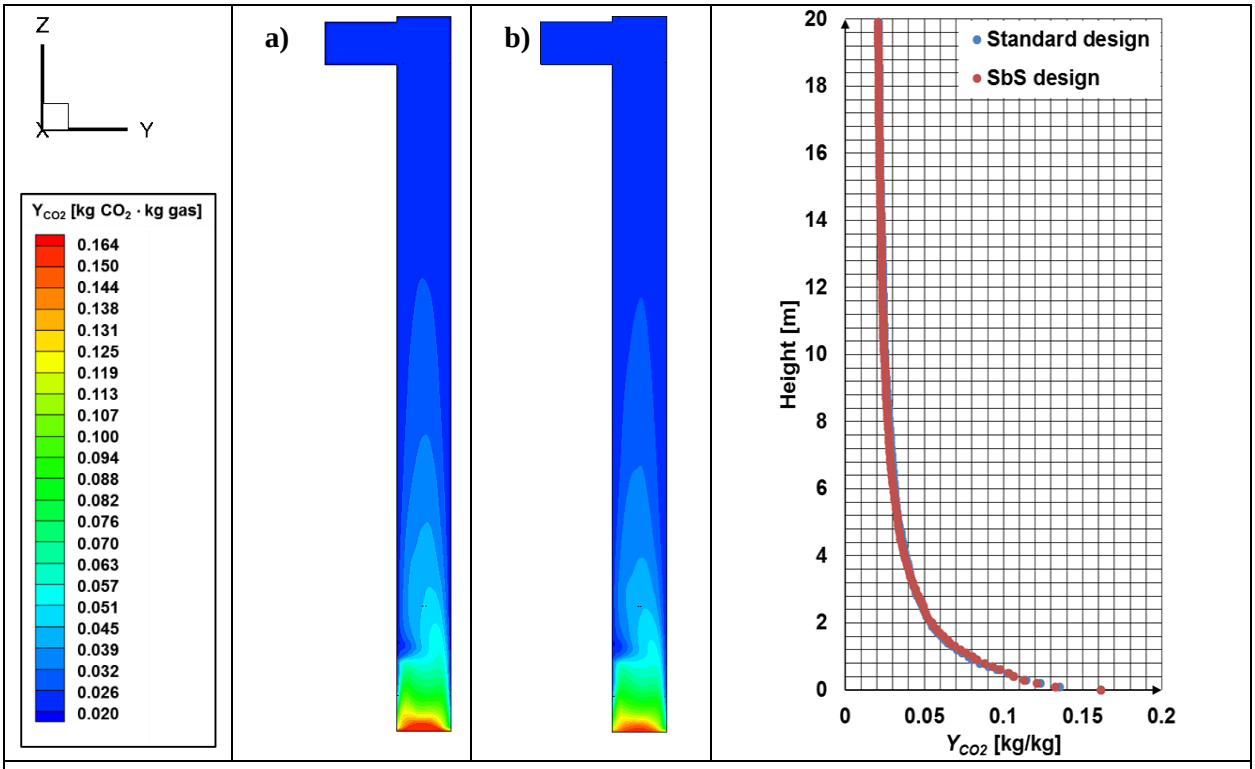

Figure 77. Contours of the time-averaged mean Y_{CO2} at X=0, for t_{aver}= 100 s for the a) Initial design and b) SbS concept.

Table 40. CO_2 capture efficiency (1 MW_{th} and 20 MW_{th} unit).

Case Studied	Capture Efficiency
Standard design (20 MW_{th})	86.95 %
SbS design (20 MW_{th})	**87.13** %
Standard design (1 MW_{th})	87.03 %
SbS design (1 MW_{th})	89.64 %

Finally, in **Table 40** the CO_2 capture efficiencies achieved for the two concepts tested both on the 1 MW_{th} and 20 MW_{th} units, are presented. The research has shown so far that in the pilot scale 1 MW_{th} carbonator unit the SbS concept has proven to give a higher CO_2 capture efficiency than the baseline case design. Added to this the pressure drop achieved in the SbS concept is virtually the same with the base case, a fact that implies that the operating cost in both concepts is almost the same. However, in the scaled-up 20 MW_{th} carbonator unit the capture efficiency for the SbS design is nearly equal –less than 1% higher- to the baseline design. One possible explanation to this is that Stage 2 is quite close to LS_from_calciner. This fact intervenes to the flow pattern we want to create in a sense that the regenerated material is not effectively split as it was previously achieved in the 1 MW_{th} carbonator unit. Thus, this concept should be further examined for the scaled-up unit; however, in the 1 MW_{th} unit it has been revealed that the idea of SbS concept seems to be very promising in terms of optimization.

4.2.8 Main Conclusions

- **Validation:** In this Thesis the 3-D CFD TFM simulation of the second biggest pilot-scale CFB carbonator, located at the premises of TUDA, is performed and the results are compared and evaluated against available experimental data for i) the pressure distribution along the riser and, ii) the carbon dioxide concentration at the carbonator exit. Two drag force models were tested; i) the homogeneous Gidaspow model and ii) EMMS scheme with a modified cluster size correlation that takes into account the riser diameter. The advanced EMMS model coupled with the TFM proposed in this work reproduced results of higher accuracy, when compared to the corresponding one by the conventional Gidaspow one. Moreover, unlike the Gidaspow model with the EMMS model a relative low grid dependency in the range of L2 norm error 6.5% is achieved, thus boosting the application of such a model for industrial-scale reactors. The value of the specularity coefficient has a negligible effect on the axial static pressure, but a value of 0.01 seems to qualitatively reproduce better the core-annular flow. Concerning the reaction kinetics, the value of the carbonation reaction rate is affected by the heterogeneous conditions in each computational cell, especially close the dense bottom zone of the riser. The reaction rate implemented based on the work of Hawthorne et al. gives results of high accuracy concerning the CO_2 concentration with a relative error of 7.22 %, while the assumption of homogeneous conditions inside each control volume for the calculation of the carbonation reaction rate may limit the accuracy of the model. It should be noted, that in future simulations it would be of great scientific interest to compare the sub-grid EMMS model, with other advanced models, as for instance the filtered two-fluid model or the DNS-derived drag model.

- **Design optimization:** The effect of the carbonator riser geometry on the gas-solid flow hydrodynamics and CO2 capture efficiency is an important issue that is investigated in the present work. For this purpose, a validated 3D Eulerian CFD model is implemented for different design/operation concepts. All the test cases simulated are retrofitting concepts of a reference design. This design corresponds to the TU Darmstadt (TUD) carbonator, which is part of the 1 MW_{th} DFB installation, and has been used in a previous research activity to validate the CFD model. The retrofitting concepts are a fat bottom design (FBD) with two different setups of the solids inventory, i.e. 282 kg and 340 kg, a sorbent staging design (SbS) and a sorbent in splash zone design (SZD). The drag force model implemented in all cases is the sub-grid EMMS scheme that takes into account the clustering formation inside such units. The numerical results indicate that a better CO_2 capture efficiency is achieved in all retrofit cases compared to the reference design. More specifically, the highest capture is achieved in the FBD concept for both solid inventories used; in the FBD-282 kg and FBD-340 kg cases the capture efficiency is equal to 90.36 % and 91.91 %, respectively, close enough to the CO_2 equilibrium capture efficiency (93.33 %). In the SbS and SZD cases the capture efficiencies are 89.94 % and 87.03 %, higher than the reference design, mainly because a better mixing is achieved in the lower part of the reactor, i.e. bottom and splash zone. As concerns the gas-solid flow patterns, in the FBD-282 kg case the flow tends to be homogeneous for heights greater than 0.8 m (the fat bottom extends up to a height equal to 1 meter). In the SbS and SZD cases the gas-solid flow pattern is quite similar to the reference design. Even if the FBD case seems the most promising among all, in terms of CO_2 capture efficiency, the SbS design is the most attractive solution, because apart from the high capture efficiency, it can be more easily incorporated into retrofit units. Among, the improvements investigated through the

aforementioned numerical tools the sorbent staging idea could be implemented with not many technical complications in larger scale units to boost the efficiency of the carbonator.

- **Up scaling concept of the 1 MW_{th} unit:** The up-scaling on the 1 MW_{th} carbonator unit to the scale of 20 MW_{th} unit has been also assessed by means of the developed CFD tool. Two design concepts were tested; a base case in which the regenerated material is inserted into the unit exclusively from the loop seal that is used for the interconnection of the calciner and carbonator reactors, namely LS_from_calciner, and a SbS design concept, in which 10% of the regenerated material is injected from a higher height than the LS_from_calciner and 90% is injected from the LS_from_calciner. The numerical results have shown that in the scaled-up 20 MW_{th} carbonator unit the capture efficiency for the SbS design is nearly equal –less than 1% higher- to the baseline design, contrary to the results of the pilot scale 1 MW_{th} carbonator unit, in which a higher capture efficiency is achieved in the SbS design than the baseline case. One possible explanation to this is that the height from which 10% of the regenerated material is injected into the unit is quite close to LS_from_calciner. This fact intervenes to the flow pattern we want to create in a sense that the regenerated material is not effectively split as it was previously achieved in the 1 MW_{th} carbonator unit. Thus, the SbS concept should be further examined for the 20 MW_{th} unit as for the 1 MW_{th} unit it has been revealed that it seems to be a very promising concept in terms of CO_2 capture optimization.

4.2.9 Milestones achieved

Numerical advancements:

- ✓ Validation of a transient hydrodynamic model based on the pure Eulerian-Eulerian approach able of simulating gas-solid circulating fluidized bed reactors for both Geldart A and Geldart B particles;
- ✓ Development and validation of the sub-grid EMMS scheme;
- ✓ Proof of the superiority of the in-house EMMS model with respect to homogeneous ones (e.g. Gidaspow) already found in commercial platforms;
- ✓ Sensitivity analysis on the specularity coefficient effect on the flow patterns and suggestion of the most realistic value for such type of flows;
- ✓ Application of carbonation reaction based on the literature with X_{max} based on experimental data and validation against experiments;

Design advancements:

- ✓ Design optimization of carbonator reactor;
- ✓ Study of several designs of interest, such as fat bottom design and carbonator design with a sorbent staging;
- ✓ The proposed designs, especially the sorbent staging concept, have proved to increase the CO_2 capture efficiency. This outcome is really valuable for FB reactor designers targeted for CO_2 capture and similar reactive flows;
- ✓ Study of the carbonator reactor at two different scales: 1MW_{th} (pilot) and 20 MW_{th} (demo).

4.3 Model of Oxy-fired calciner (calcination model validation, 1 MW_{th} unit)

4.3.1 Preface

The aim of the present work is the 3-D CFD simulation of the reacting flow inside a pilot-scale calciner, which is part of the 1 MW_{th} DFB installation located at TU Darmstadt (TUD). The riser of the fluidized-bed calciner is a cylindrical tube with a height of 11.365 m and a varying inner diameter equal to 0.28 m near the bottom area and 0.3967 m at the freeboard. The energy required for the endothermic reaction is provided by the coal combustion inside the same reactor. The gas-sorbent-fuel flow is simulated by means of the pure Eulerian-Eulerian MFM, which is incorporated into the ANSYS Fluent commercial platform, with the implementation of numerous user-defined functions. Owing to the presence of two solid phases a modified version of the KTFG model for the bi-dispersed flow proposed by [156] is applied. The advanced EMMS scheme with a new cluster correlation and the homogeneous Gidaspow model are applied for the calculation of the gas-sorbent and gas-fuel momentum exchange coefficients, respectively. Additionally, the Syamlal-Obrien symmetric model is used for the calculation of the sorbent-fuel momentum exchange coefficient. Proper reaction rates retrieved from the literature are applied for the simulation of the heterogeneous and homogeneous reactions occurring inside the reactor. The effect of turbulence is taken into account with the application of the standard k-ε model. For the first time, following a suggestion from Professor Abanades [312], [313] the carbonation reaction rate is also added to a CFD model for a calciner simulation, in order to test to which extent the reverse reaction takes place, when the temperature inside the reactor is below calcining conditions. This is of high interest, because unintentional carbonation inside the calciner increases the sorbent carbonation / calcination cycles. Due to the fact that inside a Fluidized Bed back-mixing of the solid particles might occur, if there are areas within the calciner where carbonation is favored, some Ca particles could be carbonized and calcined a lot of times before eventually exiting the reactor. This is not desirable, as such a pattern would decrease the overall activity of the sorbent ($X_{max,ave}$).. A monosized approach is followed for reasons of computational cost, and the solid particles diameter is calculated by applying the Sauter mean diameter correlation [52]. The innovative character of this work relies on the fact that very few similar numerical works, especially for pilot-scale calciner reactors, are available in the literature. CFD model is validated against available experimental data regarding the pressure and temperature distribution along the riser and O_2/CO_2 concentrations at the calciner exit.

4.3.2 Geometry and mesh layout

The 3D computational domain is constructed by means of the Meshing component of ANSYS commercial software with full respect to TUDA calciner reactor, the riser of which is depicted in **Figure 78**. The reactor is part of the DFB facility, presented in [294], and serves for the calcination of CaO particles. The riser of the fluidized bed calciner is a cylindrical tube with a height of 11.365 m and a varying inner diameter of 0.28 m near the bottom area up until a height of 1.14 m above the distributor section. From this height approximately until the height near its exit, the diameter is constant with a value of 0.3967 m. Compared to the actual designed FB, only the riser section is modelled, **Figure 78**. The structured numerical grid consists of 18,698 hexahedral elements, with a d_{cell} / d_p ratio equal to 466.52. A denser grid is not investigated in the present work as it might increase considerably the computational cost. **Figure 79** depicts the applied 3D domain.

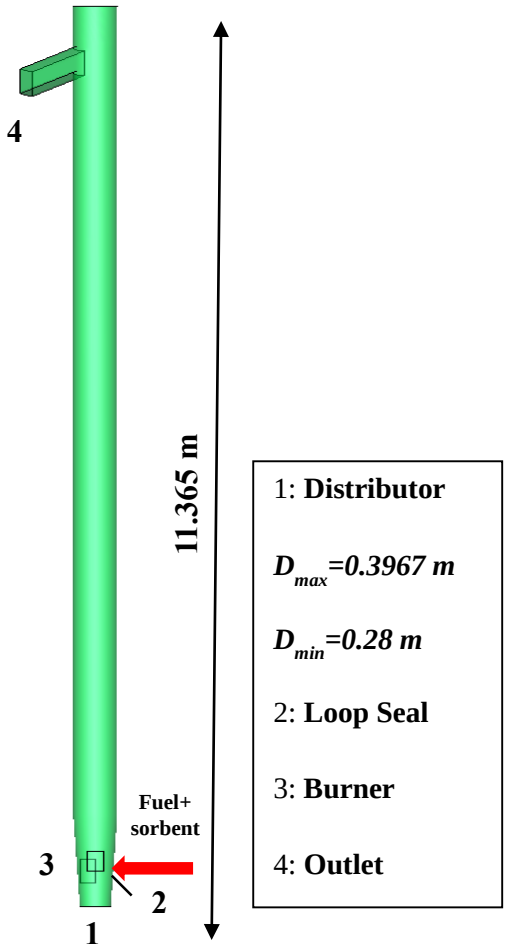

Figure 78. 3D scheme of the falconer riser.

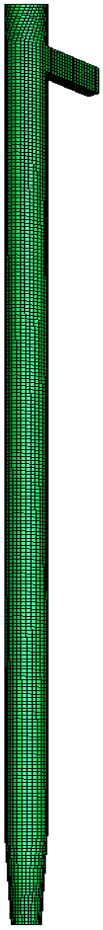

Figure 79. 3D coarse grid of the calciner.

4.3.3 Boundary and operating conditions

The gas / solid fluxes and other boundary conditions of the problem are determined experimentally by TUDA. It should be noted that during the operation of the 1 MW_{th} calciner the burner section is not used for burning any additional fuel; only a small amount of false air is being introduced to the reactor through this section. Additionally, the CO_2 entering the pilot-scale unit is lower compared to what would be expected in an actual unit. This is because O_2 enriched air is introduced to the unit from the distributor, instead of a O_2/CO_2 mixture, due to operational reasons [294].

From a numerical point of view, the distributor, the loop seal and the auxiliary burner are treated as mass-flow inlets, **Table 41**. The outlet boundary zone is defined as a pressure-outlet, with an operating pressure equal to the atmospheric. Finally, concerning the shear condition at the walls, the no slip boundary condition is considered for the gas phase. For the solid phases the Johnson and Jackson [153] wall boundary condition is adopted, with a specularity coefficient equal to 0.01. Moreover, the heat flux at the walls is set equal to zero, since data for the heat losses through reactor walls has not been available; an approximation, which may affect slightly the calculated temperature profiles, especially at the vicinity of the riser wall surfaces. The solids inventory is equal to 13.5 kg and in order to keep this value constant, the sorbent particles are entering the riser from the loop seal section with a mass flow rate equal to the one calculated at the outlet for each time instant. In the actual unit there is not internal recirculation of the solid particles.

Table 41. Boundary conditions.

Section	BC type	Parameter	Value	Units	Parameter	Value	Units
Burner	***Mass flow inlet***						
		Y_{N2}	0.77	$kg \cdot kg^{-1}$	Y_{O2}	0.23	$kg \cdot kg^{-1}$
		m_g	0.02498	$kg \cdot s^{-1}$	T_g	297.23	K
		m_{s1}	0	$kg \cdot s^{-1}$	T_{s1}	1113	K
		m_{s2}	0	$kg \cdot s^{-1}$	T_{s2}	1113	K
Distributor	***Mass flow inlet***						
		Y_{N2}	0.41886	$kg \cdot kg^{-1}$	Y_{O2}	0.581	$kg \cdot kg^{-1}$
		m_g	0.09222	$kg \cdot s^{-1}$	T_g	623.1	K
		m_{s1}	0	$kg \cdot s^{-1}$	T_{s1}	623.1	K
		m_{s2}	0	$kg \cdot s^{-1}$	T_{s2}	623.1	K
Loop Seal	***Mass flow inlet***						
		Y_{O2}	0.58	$kg \cdot kg^{-1}$	Y_{CO2}	0.118	$kg \cdot kg^{-1}$
		Y_{N2}	0.21553	$kg \cdot kg^{-1}$	Y_{H2O}	0.086	$kg \cdot kg^{-1}$
		Y_{CaO}	0.92	$kg \cdot kg^{-1}$	Y_{CaCO3}	0.08	$kg \cdot kg^{-1}$
		m_g	0.00018	$kg \cdot s^{-1}$	T_g	293	K
		m_{s1}	(defined by the outlet)	$kg \cdot s^{-1}$	T_{s1}	908	K
		m_{s2}	0.02836	$kg \cdot s^{-1}$	T_{s2}	306.39	K
		Y_{ash}	0.0785	$kg \cdot kg^{-1}$	Y_{H2O}	0.118	$kg \cdot kg^{-1}$
		Y_{char}	0.49392	$kg \cdot kg^{-1}$	$Y_{volatiles}$	0.3096	$kg \cdot kg^{-1}$

In **Table 42** the properties of the gas and solid phases are presented. Following the Geldart classification both solid particles are of type A. The PSD distribution of each solid phase is not taken into account, an approach that has been followed in the works of [174], [107], as well. Thus, the Sauter mean diameter [52] is applied for the calculation of the mean particles diameter (Refer eq. 147). Added to this, an assumption that has been followed in the specific study, is that the size of the fuel and sorbent particles does not change with time or due to physical mechanisms as that of attrition. Generally, the chemical reactions inside FB reactors constantly affect the sizes of the particles [314]. However, in Eulerian simulations it is computationally expensive to take into account such an effect, as additional sub-models should be added to the main model. Moreover, as regards the gas viscosity a constant value has been set, **Table 42**, because the temperature variation was small for the specific case conditions simulated. This value is representative of the average temperature exhibited, without introducing any significant errors in the numerical calculations.

Table 42. Particle-gas properties (Particles: **Geldart A particles**).

Parameter	Value	Units	Parameter	Value	Units
ρ_s	1650	$kg \cdot m^{-3}$	ε_{mf}	0.55	-
d_{ps}	91.39	μm	ε_{max}	0.9997	-
d_{pf}	34.67	μm	$\varepsilon_{s,max}$	0.65	-
ρ_g	0.3434	$kg \cdot m^{-3}$	e_{ss}	0.9	-
μ_g	$4.45 \cdot 10^{-5}$	$kg\ m^{-1}s^{-1}$			

4.3.4 Numerical model setup

Transient calculations are performed, with a fixed time step size equal to $5 \cdot 10^{-5}$ s. As concerns the spatial discretization of the equations, the QUICK scheme is applied for the solution of the momentum, volume fraction and species equations, whilst for the time discretization a bounded second order implicit scheme is adopted [297]. Moreover, the phase-coupled SIMPLE algorithm is applied for the velocity-pressure coupling. For the accurate prediction of the flow variables, the overall averaging time for each simulation is approximately 15 seconds, for a time range of $5 \leq t \leq 20$s.

The energy required for the endothermic reaction is provided by the coal combustion inside the reactor. Due to the non-homogeneous temperature field, which is attributed mainly to the fuel combustion, the energy equation is solved, as well. The thermal conductivity of all three phases is set equal to 0.0454 $W \cdot K^{-1} \cdot m^{-1}$. As concerns the specific heat capacity of each phase the mixing-law has been applied, whilst for the species of each phase the piecewise-polynomial (PP), polynomial law (PL) or a constant value has been selected with coefficients taken as the ones given by ANSYS Fluent software [297]. Finally, the effect of turbulence is taken into account by a proper viscous model. In the present work the standard k-ε model is solved. The specific heat capacity coefficients implemented in the CFD model, are presented in the Appendix section.

4.3.5 Results

Figure 80 depicts the numerical results of the time averaged mean static pressure along the riser axis compared to the corresponding experimental data. From the graph it can be inferred that the pressure profile is predicted with a moderate level of accuracy. It should be noted that based on previous similar numerical studies tracked in the open literature [133, 136, 174], mostly as concerns the validity of EMMS scheme, the present study can confirm its better validity as a drag model over the corresponding of Gidaspow, even for complex numerical conditions, where a series of many and complex physical mechanisms take place simultaneously, as in the case of a calciner. The maximum deviation form experimental data is tracked at the bottom zone of the reactor, where the second pressure point measured is almost two times higher than the actual pressure calculated. For the rest of the points, the agreement of the numerical model with the corresponding experimental data is better; thus justifying that the proposed EMMS model, behaves quite good, even under complex physical conditions and under coarse grid conditions. With respect to this, the particle distribution and the respective pressure drop is fairly-well predicted.

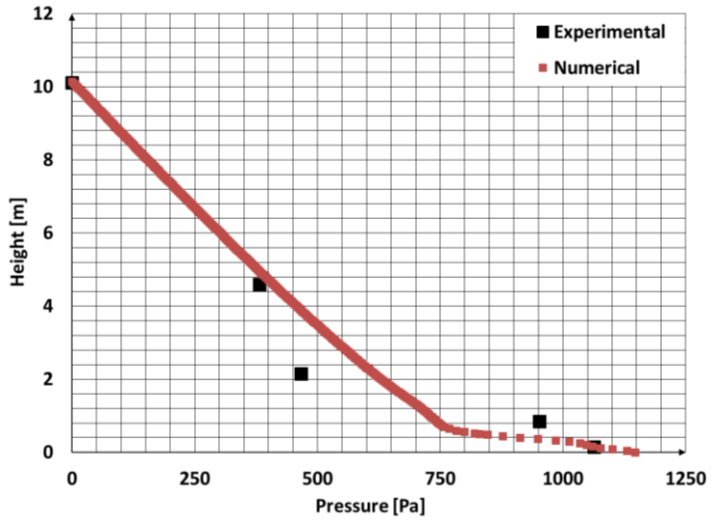

Figure 80. Time averaged mean static pressure across the riser axis for t_{aver} =15 sec.

In **Figure 81** contours of the time-averaged mean solid volume fractions of the sorbent and fuel phases are depicted. It is worth-mentioning that the particle loading is rather low and the fuel particle size is rather small, when a reference to a typical CFB is made. These operating conditions minimize the solids backflow within the calciner and the produced fly ash will be of very low particle size and therefore will not be captured by the cyclone of the calciner. This has as an effect, which is the recirculation of this inert mass between the two reactors of the Dual Fluidized Bed system, a fact that should be avoided. However, carbon slip to the carbonator and combustion there is minimized, due to the very fine particle size of the fuel.

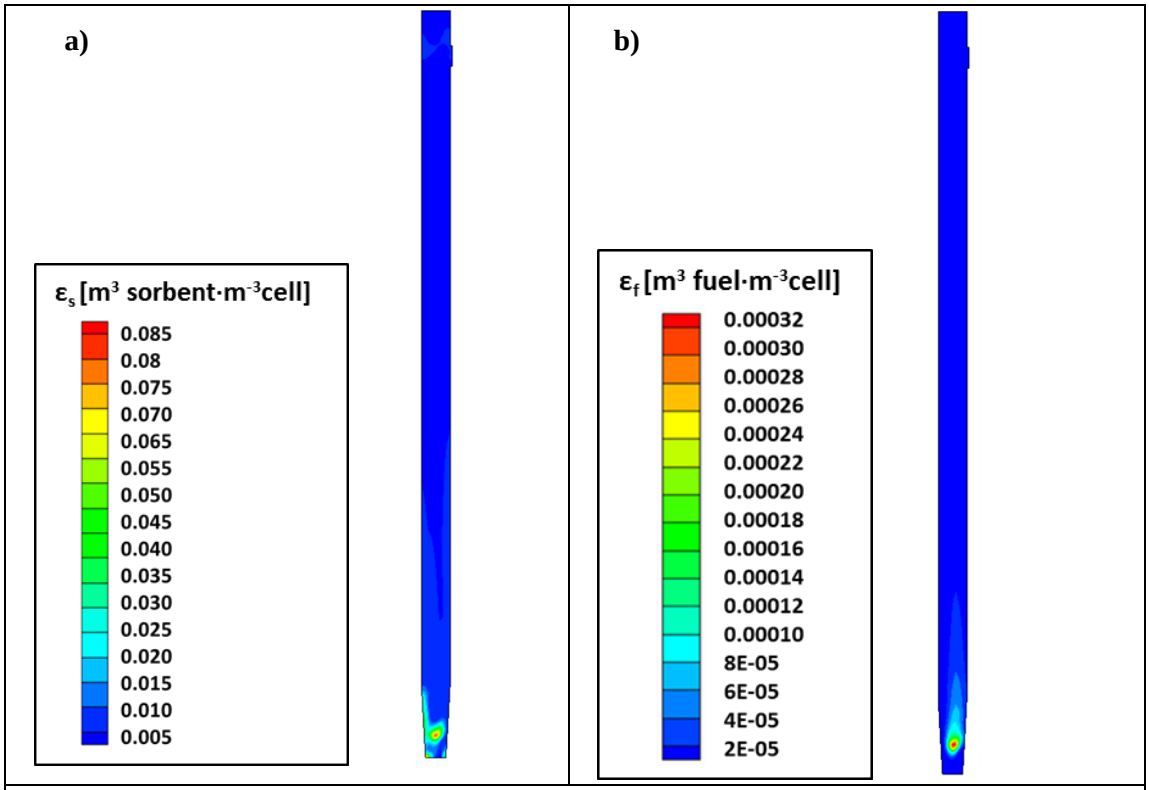

Figure 81. Contours of the time averaged mean volume fractions of the a) sorbent and b) fuel phase at a plane X=0 for a time averaging equal to t_{aver} =15 sec.

Figure 82a depicts the time-averaged mean gas temperature numerical values along the riser axis for a time averaging equal to t_{aver} =15 sec. As can been seen, the temperature curve delivered from the CFD model follows almost the same trend with the experimental data. A small under prediction of the temperature profile results is attributed to the fact that the reaction rate constants implemented in the present work have been retrieved from the literature and may not absolutely describe the behavior of the specific fuel and sorbent used in the experiments. A more or less reactive fuel and / or sorbent would affect the temperature distribution along the riser. Moreover, the gas temperature under prediction can be further corrected by applying more accurate polynomial coefficients for a more realistic specific heat capacity dependence on the temperature. The strong effect of the heat capacity values on the temperature results have been addressed in other works as well [315], [316].

Apart from this, any heat losses through the walls have not been taken into account in the specific case studied. In addition, the mathematical expressions based on which the heat transfer coefficients are calculated may have an inherent error, when trying to express/calculate the exhibited heat transfer coefficient –*h*- under so complex conditions, where particulate and gas phases co-exist and inter-react. In this light, it is proposed the validity of the current existing arithmetical expressions for the calculation of heat transfer coefficients to be examined in detail by simple and well controlled experimental conditions.

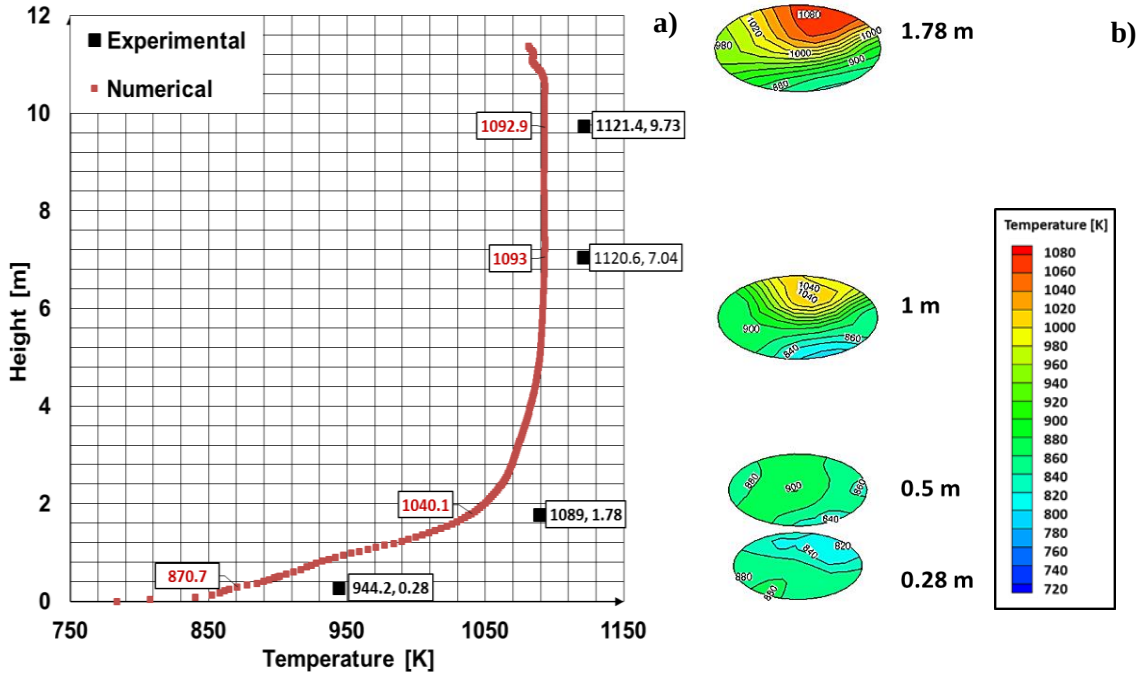

Figure 82. a) Time-averaged mean gas temperature along the riser axis. b) Time-averaged temperature contours at different riser heights.

Additionally, the measurement uncertainties may be another source for the significant temperature under-prediction, since two of the four measuring probes are located near the bottom area –at heights equal to 0.28 m and 1.78 m- where the flow is strongly inhomogeneous, **Figure 82b**. On the other hand, the numerical values plotted are the mass-weighted average values of the temperature in different heights. Thus, a more accurate comparison would include the numerical values of the temperature at the points where the measuring probes are exactly located in each cross-sectional area. However, such an information is not available (e.x. if the probes are placed either near the walls, or inside the unit near the reactor axis) and only the height in which the measuring probes are placed is known.

Another important conclusion to be drawn is that, for a height range approximately [0-0.9] meters the gas temperature is less than the required one for calcination. For this reason, at the vicinity of this area, the reverse reaction, i.e. carbonation, takes place. This fact, which is observed as well in **Figure 83**, is attributed to the flow of the primary air and O_2 that enter the unit from the distributor section, with a temperature equal to 623.1 K, as well as to the auxiliary air that comes from the loop seal and burner sections, with a temperature approximately equal to 300 K. Over the height of the burner section, where the fuel enters the reactor, the temperature rises quickly to the calcining conditions.

Regarding instantaneous temperature values, the fuel phase generally has a slightly higher temperature than the sorbent phase of around 5 K maximum in the splash zone, up to a height of 4 m where the temperature difference approaches zero. Near the area, where the char combustion occurs, the maximum difference observed is around 15 K. On the contrary, near the bottom bed the sorbent has higher temperatures than the fuel phase, whilst such difference approaches its maximum, i.e. 600 K near the loop seal section. This high temperature difference is attributed to the fact that the fuel phase enters the reactor with a low temperature equal to 306.39 K (set as a boundary condition) and has not yet been heated up.

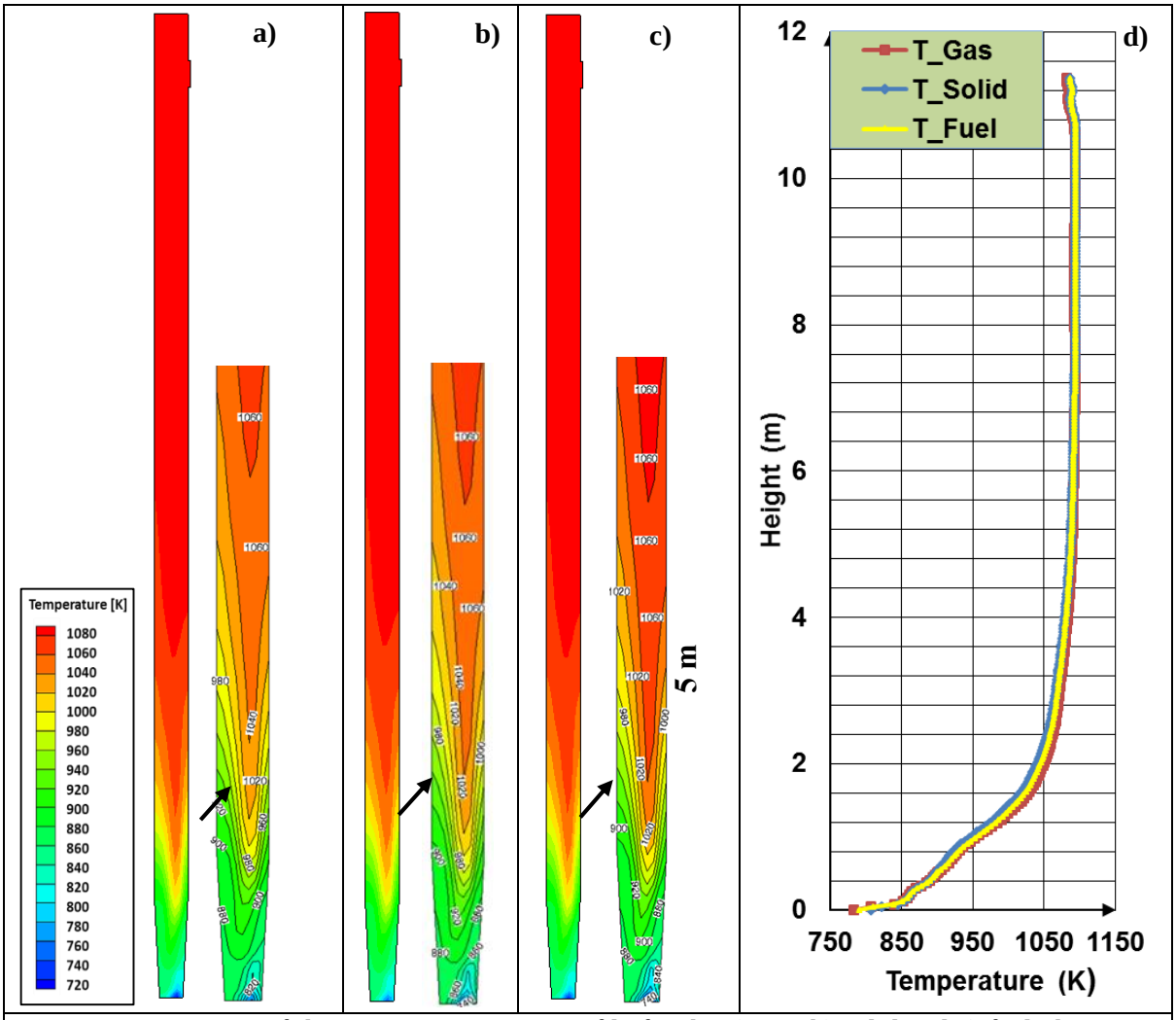

Figure 83. Contours of the mean temperature profile for the a) gas, b) solid and c) fuel phase at a plane X=0 and d) mass-weighted time averaged temperature profile at different slices across the reactor (time averaging equal to t_{aver} =15 sec).

Figure 83 illustrates the contours of the time-averaged mean static gas, solid and fuel temperature at a plane X=0. It is evident that the temperature field is unbalanced owing to the presence of the fuel phase. This is also reflected by the unbalanced velocity field of both solid phases, as can be seen in **Figure 84**.

Another important conclusion drawn (**Figure 84**, **Figure 85**) is that the solid particles of the sorbent phase move upwards and no back-mixing is observed except for a height approximately equal to 0.4 meters where some solid particles move downwards. However, in this area up until a height of approximately 1 meter the temperature is below calcining conditions and only the carbonation reaction is favored. Thus, based on the current model assumptions and the range of expressions validity of the particular unit modelled, the sorbent particles that enter this area most probably will not undergo multiple carbonation-calcination cycles. However, since the validity of the current model should be examined in more detail, in terms of the assumptions followed, this argument should be considered with second thoughts. It should be stressed out that a possible entrapping of sorbent particles to areas with multiple carbonation-calcination cycles might decrease the overall sorbent activity and should be examined more thoroughly in future simulations.

Additionally, from **Figure 83** it can be inferred that all three phases –gas, solid and fuel- undergo the same temperature profile, as expected, owing to the mixing mechanism of all phases. This in reality proves the reasonable calculation of any heat transfer rates among the interacting three -and more- individual phases. This in turn implies that an effective heat transfer is achieved among them, based on the numerical models applied. This fact is also proven by the high values of the axial time-averaged heat exchange coefficient presented in Figure 86.

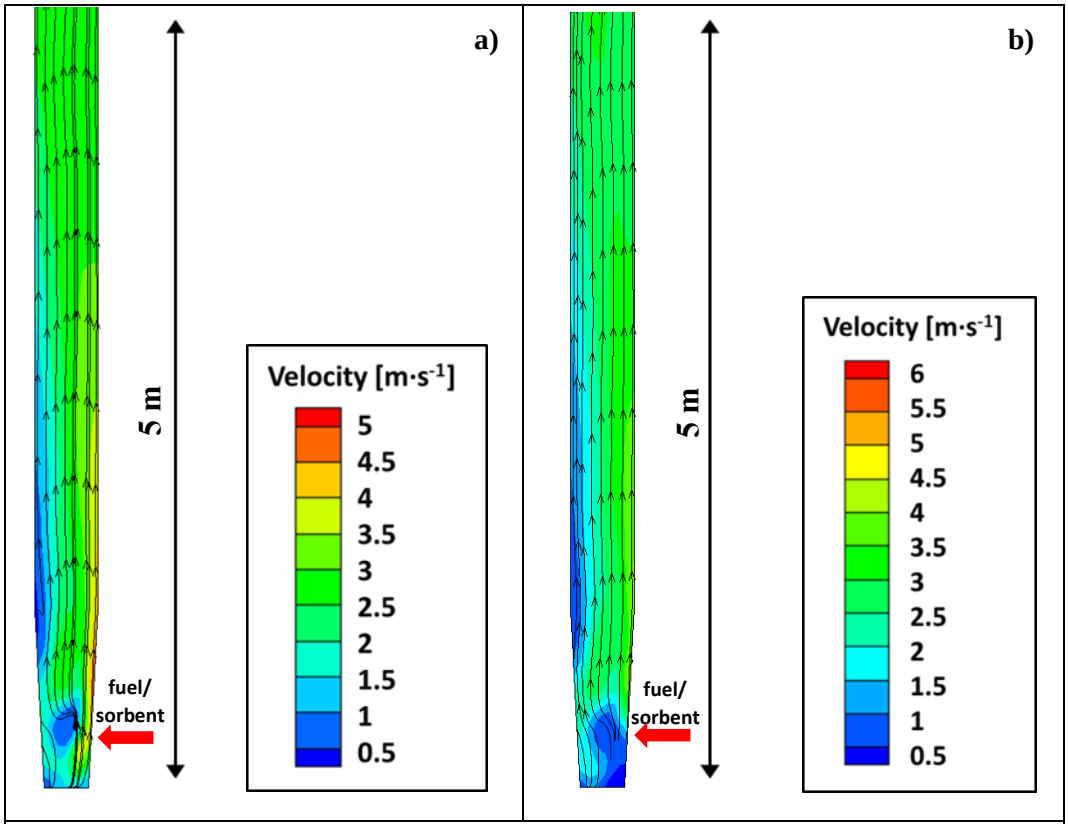

Figure 84. Contours of the mean velocity profile for the a) sorbent and b) fuel phase at a plane X=0 for a time averaging equal to t_{aver} =15 sec.

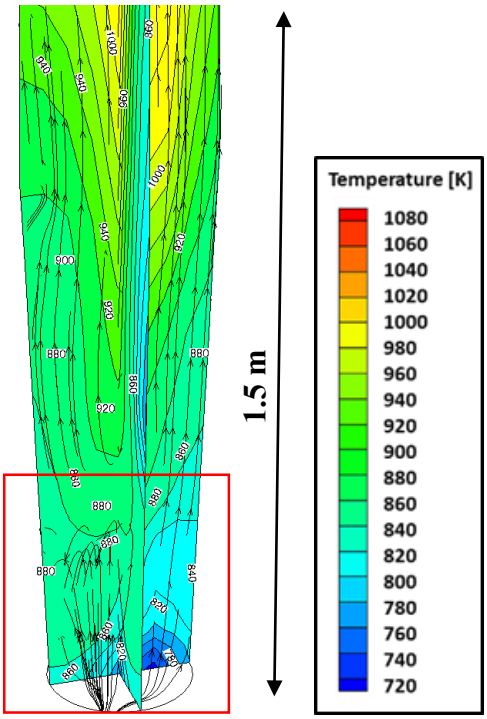

Figure 85. Contours of the mean gas temperature profile with sorbent streamlines for t_{aver} =15 sec.

More specifically, from **Figure 86** it is evident that in both solid phases the gas-solid heat exchange coefficient takes its maximum value near the bottom bed and then decreases, as the flow becomes more dilute. The same fact is also observed for the sorbent-fuel heat exchange coefficient. Thus, there is a strong dependence between the convective exchange coefficient and the particulate volume fraction. The dependence of this parameter on the solid volume fraction has been also observed in the work of [317]. Another important outcome is that the particle-particle heat transfer is negligible compared to the overall gas-solid heat transfer. This has been also demonstrated in the works of [317], [318], [319].

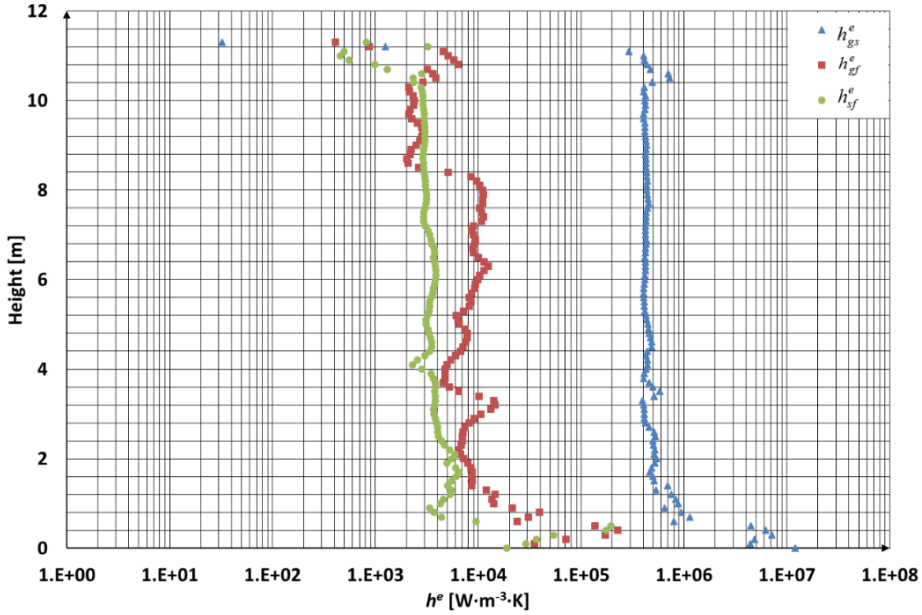

Figure 86. Convective HTC across the reactor between the gas-sorbent, gas-fuel and sorbent-fuel phase.

Figure 87 shows contours of the CO_2, O_2, CO and gas volatiles mean mass fractions at X=0 for a time averaging equal to 15 seconds. As it can be observed most of the char combustion occurs at the bottom zone of the riser, near where the fuel enters the reactor. For this reason, the O_2 concentration is higher near the distributor area and decreases as the flue gas approaches the calciner exit; a fact that can be also observed in **Figure 88**. However, some amount of the O_2 remains in the flue gas stream, which implies that full char conversion is not achieved. On the contrary the CO formed during the char combustion and the gas volatiles react quickly with the oxygen and, thus, only a small amount of them remains in the flue gas.

From the development of the CO_2 profile, it can be concluded that the calcination reaction is slower and occurs at greater heights than the char combustion. The low values of CO_2 near the distributor are attributed to the fact that O_2 enriched air is introduced to the unit instead of a recirculating CO_2 mixture. For this reason and owing to the low temperature values at this area that are below calcining conditions, the reverse reaction, i.e. carbonation reaction occurs, whilst the calcination reaction is negligible. This can be also seen from **Figure 89** where a plot of the instantaneous values of the calcination/carbonation reaction rates at different slices across the reactor are presented. From this plot, it can be inferred that for heights up until 4 meters the carbonation reaction can be faster than regeneration of the limestone, a fact that is mainly attributed to the low temperature values and low CO_2 concentration inside the reactor.

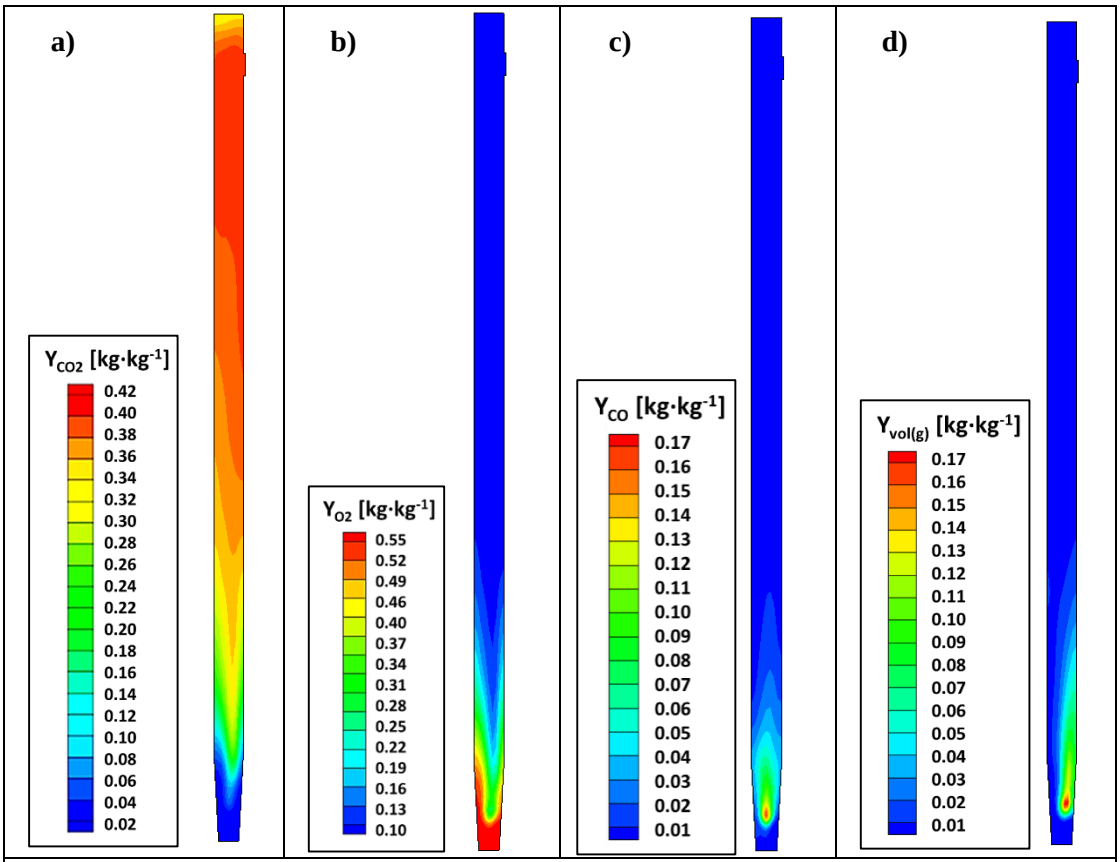

Figure 87. Contours of the time-averaged a) Y_{CO2}, b) Y_{O2}, c) Y_{CO}, and d) $Y_{vol(g)}$ at a plane X=0 for a time averaging equal to t_{aver} =15 sec.

Overall, the volume-averaged carbonation reaction rate ($1.877 \cdot 10^{-4}$ kmol·m^{-3}·s^{-1}) is 1.239 times greater than the volume averaged calcination reaction rate ($1.516 \cdot 10^{-4}$ kmol·m^{-3}·s^{-1}). The proposed CFD model can be potentially used in future simulations to investigate even further how much the CO_2 concentration and the

temperature profile inside the reactor can affect the effective regeneration of the limestone and the activity loss due to carbonation in the calciner.

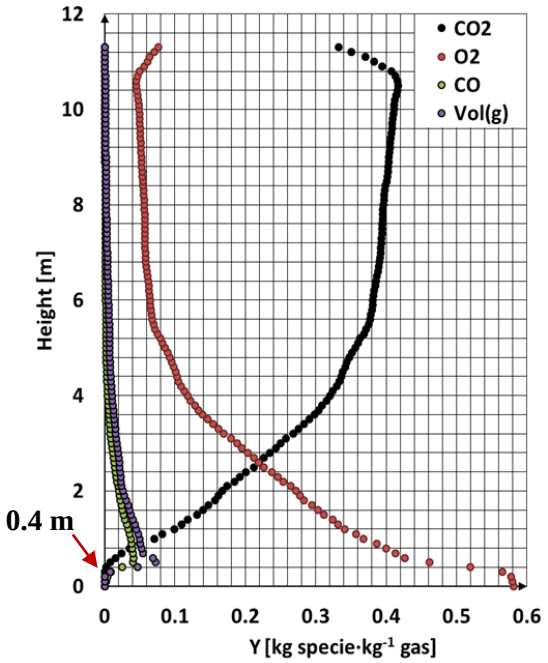

Figure 88. Mass-weighted time-averaged Y_{CO2}, Y_{O2}, Y_{CO}, and $Y_{vol(g)}$ at different slices across the reactor for a time averaging equal to t_{aver} =15 sec.

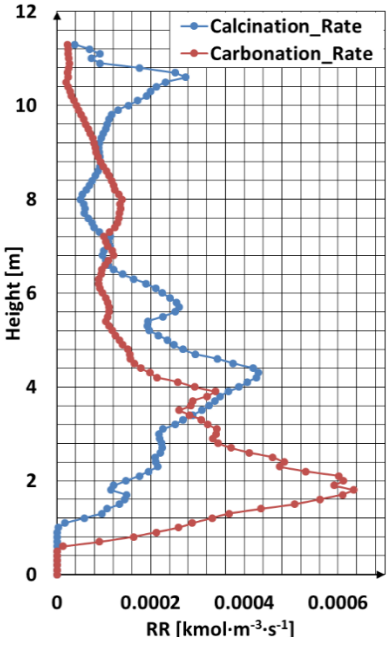

Figure 89. Instantaneous carbonation, calcination rates at different slices across the reactor.

In **Table 43** are presented the numerically calculated mass-weighted time-averaged CO_2, O_2 concentrations (on a dry basis) at the riser exit compared with the given experimental data. The high numerical errors for specific areas of calciner (close to its bottom) and variables monitored, reported in the present work can mainly be attributed to the fact that the developed complicated numerical model has not been extensively examined in validity terms. One reason may be the possible invalidity of heat transfer coefficients or the neglect of any heat transfer losses from the calciner. However, given the fact that similar numerical studies are very rare in the open literature and that the governing physical mechanisms, this approach tries to model are very complex, this study is a good step forward, to what is already available; though it should be critically examined in all its aspects in the future, before being considered as totally valid. The reaction rates -for the heterogeneous reactions- applied are retrieved from the open literature affecting, thus, the CFD model accuracy, as discussed above, as they should be tuned for different coals. Thus, if a slower combustion reaction rate was applied, the calculated O_2 concentration at the reactor exit might be higher than the one predicted by this model. Due to the fact that the heat released during char combustion is proportional to the amount of oxygen consumed for complete combustion [320], in such a case, the calcination of CaO to $CaCO_3$, which is an endothermic reaction, might be affected, as well. As a result, the CO_2 concentration, predicted by the CFD model, at the outlet would decrease and the respective error would increase. It should be underlined though, that the CFD model applied in the present study is of high complexity and, other factors, such as the applied drag models, might potentially affect the species reaction. Thus, such speculation should be further investigated in future works.

Apart from this, the coarse mesh used in the specific case simulation might be the source of some of the tracked numerical inaccuracies compared to corresponding experimental data, especially as concerns the

species concentrations imposed by the not perfect solution/representation of the actual reaction rates taking place. Nevertheless, preliminary numerical tests have been performed for examining the grid density effect on pressure profiles for the simpler case of not considering energy or species solutions (isothermal conditions). From the numerical tests, it was derived that the grid density is good enough to reproduce the correct hydrodynamics for at least an isothermal case, which however should be extended to examine the extent up to which the reaction rates calculated are correctly reproducing the actual phenomenon.

Table 43. CO_2 and O_2 mole fractions at the calciner exit.

Species	Numerical value	Experimental value	Relative Error
CO_2 outlet dry			
	(38.55±6.79)%	(44.2±2.4)%	12.79%
O_2 outlet dry			
	(4.11±3.722)%	(6±2.04)%	31.52%

Regarding the numerically calculated O_2 concentration at the calciner exit another fact that should be drawn attention to, is the high oscillations observed, as can be seen in **Figure 90**. Such oscillations could affect the accuracy of the measured O_2. Oscillations were observed as well in the pilot scale unit [294], [321], but not as high as the ones in the numerical model. A possible explanation is that the flow in the reactor is not that dense, when compared to a typical Fluidized bed unit. Such fact is affecting the flow field causing instabilities, especially near the exit. However, the reason behind such oscillations in the numerical model needs further investigation in future simulations.

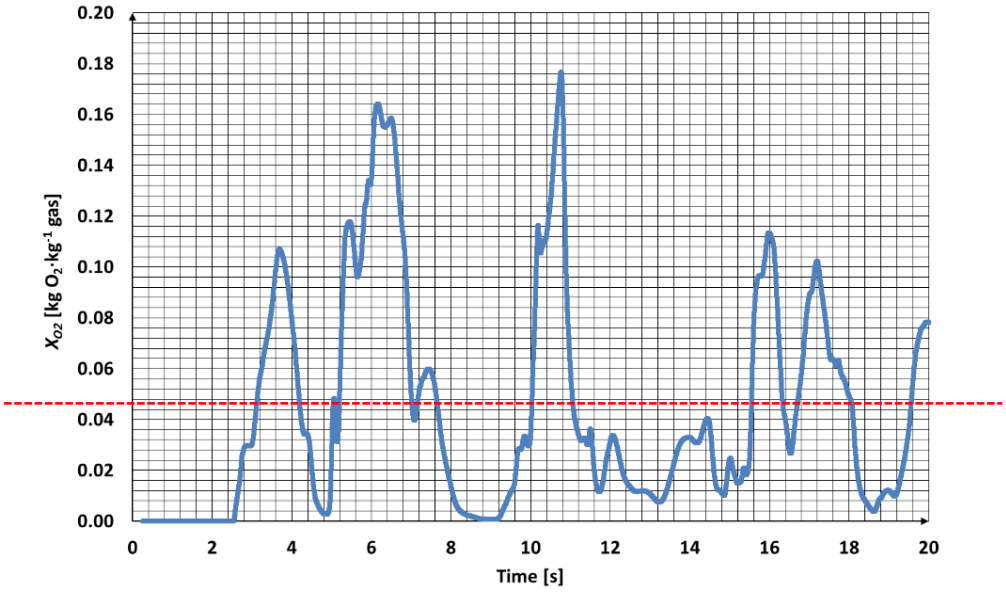

Figure 90. Time dependent X_{O2} (on a dry basis) at the riser exit.

Finally, the research have shown that the computational cost required to reach 20 seconds of simulation for the three-phase flow inside the calciner unit is high, especially if it to be compared with a simpler case of a two-phase flow inside the carbonator unit of the same DFB facility presented in [174]. For both cases a simulation with 1 CPU core is used as a reference. In the calciner case it would be needed 864.2 days to simulate the flow and reach 20 seconds of simulation, whilst in the carbonator unit only 23.2 days. Such fact proves that the flow inside the calciner reactor is characterized by high physics complexity, owing mainly to the presence and the combustion of the fuel phase. Thus, for this reason, a series of assumptions

have been followed regarding the applied CFD model. It should be noted that parallel processing can help overcome problems related to high computational costs.

4.3.6 Main Conclusions

In the present Thesis, the 3-D CFD simulation of the three-phase flow inside the TUDA pilot-scale oxy-fired calciner is performed by means of the TFM methodology. The numerical results are compared and evaluated against available experimental data for i) the pressure and temperature distribution along the reactor and, ii) the O_2 and CO_2 concentrations at the calciner exit, all provided by TUDA. A modified version of the KTGF with a generic C code is applied for more than one solid phases, whilst the advanced EMMS scheme with a new cluster correlation, already validated in the carbonator unit of the same DFB facility, is incorporated into the CFD model. Both the char and calcination mechanisms are investigated, whilst the carbonation reaction is also applied in order to evaluate if the reverse reaction takes place inside the reactor, affecting the maximum carbonation conversion of the sorbent. Simulation results indicate that the applied CFD model is of moderate accuracy, but it can be further enhanced if more realistic kinetic parameters are used for the specific sorbent and fuel modelled. Added to this, the EMMS model for binary mixtures can increase the model accuracy, especially if a denser flow is simulated. Thus, in future three-phase flow simulations such drag model will be implemented into the CFD model. Regarding the calcination of calcium carbonate, results indicate that the reaction occurs at heights over the area where the fuel is burnt. For lower heights, i.e. near the bottom bed the reverse reaction is favoured owing to the low temperature values, mainly because of the cold gas stream that enters the reactor from the distributor and auxiliary burner section. Finally, from the velocity streams it can be inferred that no back-mixing of the sorbent phase is observed except for a small area, where only carbonation occurs. Thus, in the particular reactor modelled, the sorbent particles might not be trapped in areas where both carbonation and calcination reactions are favoured. Such possible patterns of multiple carbonation-calcination cycles might decrease the overall sorbent activity and should be examined in detail in future simulations.

4.3.7 Milestones achieved

The milestones achieved during this research study include:

- ✓ Development of an efficient and accurate 3D CFD model able of simulating the multi-phase flow inside an oxy-fired calciner;
- ✓ In this reactor a three phase flow is simulated (one gas phase and two solid phases);
- ✓ This model takes into account heat transfer mechanisms, effect of turbulence and reaction kinetics (calcination reaction);
- ✓ An important aspect in this model is that for the first time the CaO recarbonation is also taken into account;
- ✓ Model validation has been achieved with experiments from the operation of the 1 MW_{th} unit.

4.4 Model of IHCaL calciner with heat pipes (heat transfer model, 300 kW_{th} unit)

4.4.1 Preface

In the previous Subsection, the in-house sub-grid EMMS scheme was validated against experiments by taking as a reference a pilot scale unit, i.e. the 1 MW_{th} carbonator located in TUDA. Furthermore, the calcination reaction inside an oxy-fired 1MW_{th} calciner was simulated and results of the CO_2 mass fraction compared well with experimental data. Following the sub-grid EMMS model validation and the successful representation of the flow hydrodynamics under iso-thermal conditions in the carbonator, along with the successful reactive model development in the oxy-fired calciner, this sub-section presents the model development and validation of a 300 kW_{th} indirectly heated calciner located at the premises of TUDA. This model, takes into account, apart from the flow hydrodynamics, all the involved heat transfer mechanisms (conduction, convection, radiation) inside the gas-solid domain. The effect of turbulence is also taken into account, along with the calcination reaction kinetics. The end-product, which is an efficient and accurate CFD model, can be further exploited to study different scenarios of gas-solid suspensions that are targeted for both sensible and thermochemical heat storage.

The studied calciner forms part of the novel IHCaL system depicted in **Figure 11**. The whole system consists of a FB carbonator and a heat pipes heat exchanger, which is the core of this novel concept. The heat pipes heat exchanger is, in turn, split into the combustor and the bubbling calciner, which are separated by a sealed middle wall. The combustor is propane fired and provides indirectly heat to the calciner by means of heat pipes. The heat pipes are placed inside the calciner/combustor system in a form of a staggered horizontal arrangement (in the reference design). Inside the heat pipes a working fluid flows that is an alkali metal, either sodium or potassium, for a working temperature range within 750-1050 ^oC [322]. Concerning calcination reaction, an operating temperature around 900 ^oC is needed and, thus, sodium is selected with a working temperature within 890-950 ^oC. The heat pipes are designed for a heat transfer capacity of about 300 kW_{th} at 950°C [323]. Besides, sodium with respect to potassium, is the best option for this unit, due to its low working pressure at the highest operating temperatures which reduces the induced stresses and its lower hazard potential.

4.4.2 Numerical methodology

In this section, some of the common assumptions adopted in such type of modelling tools are presented:

- Transient flow with a Courant number lower than 0.75;
- A quasi-2D domain (3D domain with a with<<height, depth) is used in all of the simulated cases to speed-up calculations;
- Multi-phase method used: Eulerian-Eulerian TFM approach;
- Number of simulated phases: 2 (one solid and one gaseous);
- The particle-particle forces are modelled implicitly by using the KTGF theory, with the same sub-models as in the carbonator model;
- The used drag force model is the custom-built EMMS model;
- The solution of energy equation is included in the simulated case by modelling all involved heat transfer mechanisms (i.e. conduction, convection and radiation);
- The flow is considered as turbulent, due to the fact that the turbulence effect should be taken into account for heat transfer problems. The *k-ε* dispersed model is used with an enhance wall treatment to more accurately predict the thermal boundary layer near the heat pipes;

- The calcination reaction is incorporated into the CFD model. The heterogeneous reaction rate given by equation (71) is validated against available experimental data for the mass fraction of CO_2 at the riser exit. This model has been also validated for the case of oxy-fired calciner presented in [324]. As comparison data, the mass weighted time-averaged mean mass fraction of CO_2, Y_{CO2}, is used. Then, the same rate is used for any other simulation runs (design and operation optimization);
- The solids inventory is kept constant, i.e. 18 kg, by monitoring the solids flux at the calciner outlet and re-injecting the particles at the domain by the bottom of the reactor. This is a simplification, as in the real geometry the solid particles flow enter the reactor from a return inlet, **Figure 91**.
- Make-up flow and spent sorbent comes from the carbonator. This extra material is inserted in the domain as well from the bottom of the reactor by using a UDF.
- Features of the CFD model that are not supported by the CFD platform, such as the EMMS model, the calcination reaction rate and the solid particles radiation properties (scattering, absorption coefficient) are incorporated through UDFs.
- The working fluid inside the heat pipes is sodium with a mean temperature equal to 895 ºC.

4.4.3 Model validation

4.4.3.1 Geometry and mesh layout

The simplified geometry of the BFB calciner is depicted in **Figure 91**. Only one slice of the 3D domain is modelled in order to study several scenarios of the heat pipes arrangements. Concerning the numerical mesh, a pure hexahedral grid is used and three mesh densities are tested a Coarse consisting of 6600 cells, a medium consisting of 28115 cells and a dense one consisting of 224600 cells. Each one of the grid density corresponds to a d_{cell}/d_p ratio equal to ~220, ~110, and ~55, respectively. The coarser grid density corresponds to one of Case 4 (**Table 34**) studied and validated for the carbonator reactor. However, denser grids are also used in this setup (i.e. Medium and Dense grid) in order to capture with a higher level of accuracy the heat transfer near the heat pipes.

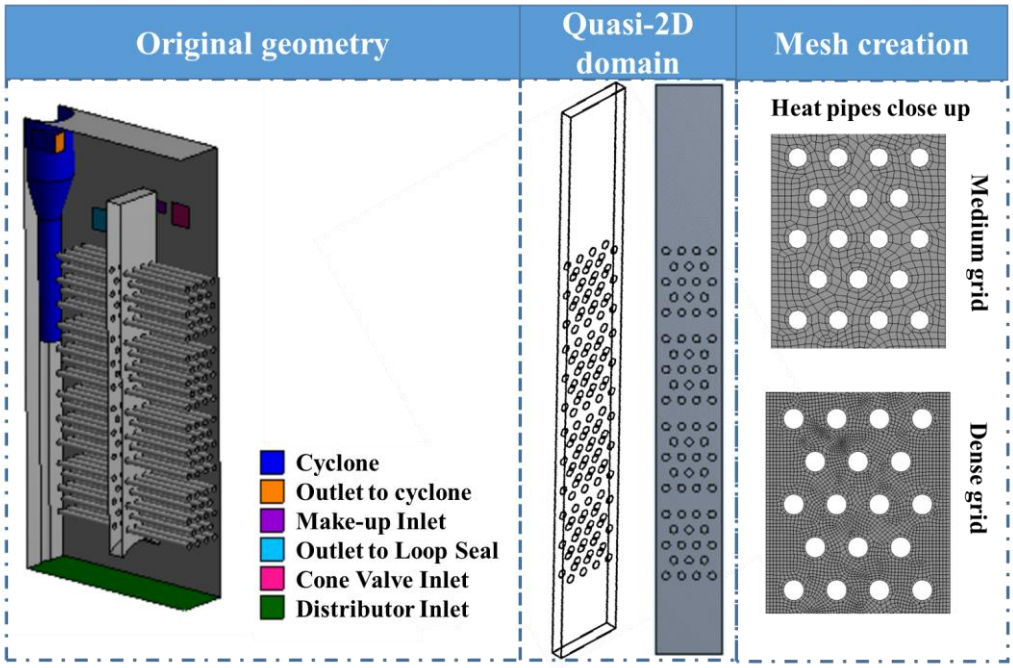

Figure 91. 3D scheme of the calciner riser, quasi-2D domain, and, domain discretization.

4.4.3.2 Boundary and operating conditions

Appropriate boundary conditions are applied in order to study the flow inside the IHCaL calciner. The applied boundary conditions are listed in **Table 44**:

Table 44. Boundary conditions (Indirectly heated calciner).

** A UDF is used to recirculate the solid particles back to the reactor and include any additional solid steam (from the cone valve, make-up flow).*

*** A UDF is used to take into account the solid streams coming inside the reactor consist of recirculating material and fresh material with T_{solid}=950 K. Then, the overall temperature is a mass weighted average sum of all streams.*

Section	BC type	Parameters	Units	Values
Distributor	Mass flow Inlet	$\dot{m}_{gas}$	$kg \cdot s^{-1}$	0.00106
		V_{gas}	$m \cdot s^{-1}$	0.16
		Y_{O2}	$kg \cdot kg^{-1}$	0.23
		Y_{CO2}	$kg \cdot kg^{-1}$	0
		Y_{N2}	$kg \cdot kg^{-1}$	0.77
		V_{solid}	$m \cdot s^{-1}$	* Use of UDF
		T_{gas}	K	825.15
		T_{solid}	K	** Temperature averaging based on UDF
		Y_{CACO3}	$kg \cdot kg^{-1}$	* Based on UDF
Outlet	Pressure Outlet	P	bar	1
Tube Walls	Wall	T_w	K	1163.15
		b_w	m	0.0036
		k_w	$W \cdot m^{-1} \cdot K^{-1}$	26.6
	Gas phase: No slip condition Solid phase: φ=0.01			

Table 45. Operating conditions (inlet streams from carbonator reactor for quasi-2D domain).

Parameters	Units	Values
$\dot{m}_{solids,cone,valve}$	$kg \cdot s^{-1}$	0.013066719
Y_{CaCO3}	$kg \cdot kg^{-1}$	0.1138
$T_{solids,cone,valve}$	K	950

The gas-solid properties used in the model and the inlet streams from the carbonator reactor are listed in **Table 46** and **Table 45**, respectively. Thermal properties of $CaCO_3$ and CaO are retrieved from [325].

Table 46. Gas-solid properties.

Parameter	Units	Value	Parameter	Units	Value
ρ_s	$kg \cdot m^{-3}$	1657	U_0	$m \cdot s^{-1}$	~0.16
d_p	μm	99	ρ_g	$kg \cdot m^{-3}$	0.42
$k_{s,CaCo3}$	$W \cdot m^{-1} \cdot K^{-1}$	~2.259	μ_g	$kg \cdot m^{-1} \cdot s^{-1}$	$4.7 \cdot 10^{-5}$
$k_{s,CaO}$	$W \cdot m^{-1} \cdot K^{-1}$	~0.318			

As concerns the applied boundary/operating conditions, it should be noted that they correspond to the initial domain (full operating conditions as suggested by the experimental data). The different values of the input parameters in the initial and simplified domain are listed in **Table 47**.

Table 47. Operating/ boundary conditions (Initial and quasi-2D domain).

Parameter	Initial Domain	Simplified Unit*
Inventory [kg]	370	~18
Reactor volume [m^3]	0.724	0.036
Heat pipes total surface area [m^2]	6.45	0.375
Distributor surface [m^2]	0.345	0.015
Primary velocity [m/s]	~0.16	~0.16
Primary gas flow rate [kg/s]	0.0244	0.00106
Solid mass coming from carbonator (cone valve) [$kg \cdot s^{-1}$]	0.263	0.013
**** The values are calculated by setting a scalability factor ~20***		

4.4.3.3 Simulated cases matrix

During model validation, several cases are simulated to test (i) the effect of grid and (ii) the effect of used near wall treatment on the numerical model results. The compared cases are listed in **Table 48**. The sensitivity analysis for the near-wall treatment has been carried out in order to test its effect on the overall heat transfer, when the grid density changes. This has come as a necessity since in a previous work [326] it has been revealed that the overall heat transfer from the heat pipes is grid dependent, when the thermal boundary layer is not taken in to account (e.g. with a laminar flow).

Table 48. Compared cases simulated (model validation).

Case Number	Grid	Turbulence model	Near-wall treatment
Case 1	Coarse-Medium-Dense	*k-ε* Dispersed	Enhanced wall treatment
Case 2	Coarse-Medium	*k-ε* Dispersed	Standard wall functions
Case 3	Coarse-Medium	*k-ε* Dispersed	Non-equilibrium wall functions
Case 4	Coarse-Medium	*k-ε* Dispersed	Scalable wall functions
Case 5	Coarse-Medium	Laminar	N/A

4.4.3.4 Results

Numerical results indicate that the used CFD model compares well with the experimental results concerning the CO_2 mass fraction at the outlet of the reactor (**Table 49**). As regards the heat from the heat pipes, the numerical model results in a small over prediction, a fact that can be attributed to the uncertainties imposed by the materials properties set (e.g. heat pipes emissivity). It should be noted that in the actual geometry the heat from the heat pipes arrangement is equal to 116–132.9 kW, which results in a 17.98-20.60 $kW \cdot m^{-2}$ (the total heat transfer area in the actual geometry is A_{HP}=6.45 m^2). Furthermore, it can be noticed that a grid independency can be achieved with a medium grid density, as results of the medium and the dense grid virtually coincide. Thus, it can be noted that the model with the medium grid density (d_{cell}/d_p ~110) gives results of acceptable accuracy and can be used for the numerical simulation of several scenarios (e.g. heat pipes arrangement optimization, operating conditions study etc.).

Table 49. CFD model numerical results for Case 1 (model validation) (t_{aver}=10 sec).

	Experiment	**CFD (Coarse grid)**	**Error (%)**	**CFD (Medium grid)**	**Error (%)**	**CFD (Dense grid)**	**Error (%)**
CO_2 outlet ($kg \cdot kg^{-1}$)	0.32–0.33	~0.348	~5.45	~0.35	~6.00	~0.35	~6.00
Heat from HPHE ($kW \cdot m^{-2}$)	17.98-20.60	~21.67	5.23	~25.46	23.62	~24.79	20.4

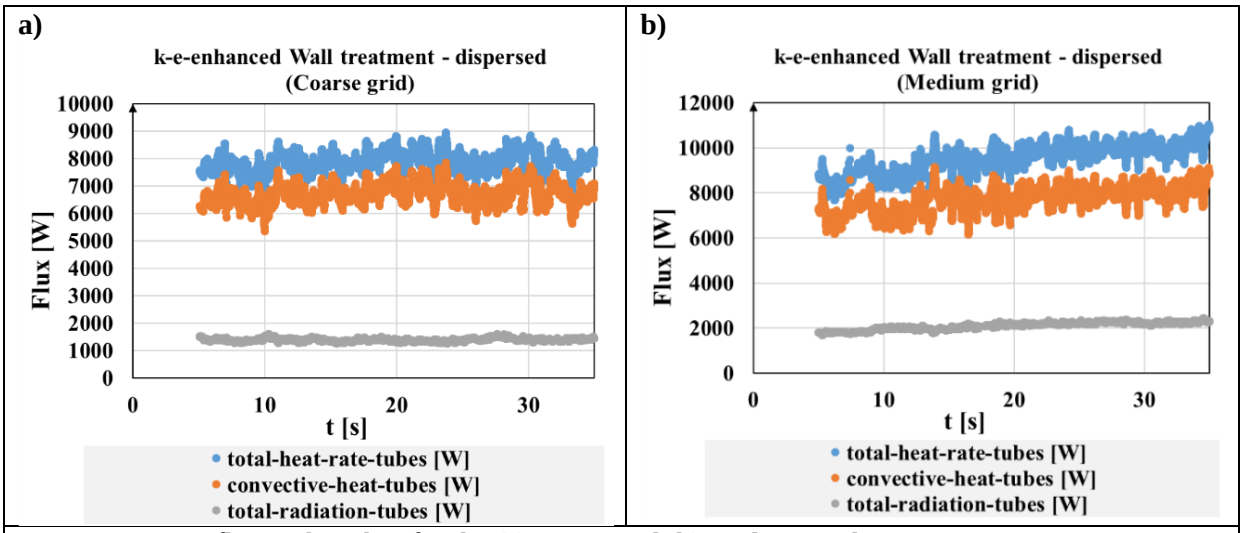

Figure 92. Heat flux at the tubes for the (a) coarse and (b) medium grid.

Another conclusion drawn from this analysis is that the share of the radiative heat flux to the overal heat transfer rate is 15 % to 19 % for the coarse and medium grid, respectively. Most of the heat transfer, thus, arises from the convective term. This is a result quite resonable proven as well by [326] where the full reactor has been simulated and results of the heat transfer rate have been compared with theoretical models as that of Kunii and Levenspiel [52]. It is expected that in more dilute flows the share of the radiative term will increase in the overal heat transfer rate.

Table 50. Comparison of Case 1-Case 5 in terms of heat flux. (C: Coarse Grid, M: Medium Grid).

Turbulence model/Wall treatment (Grid)	**Calculated heat rate at the heat pipes based on the CFD model**				
	Convective heat rate [W]	**Radiative heat rate [W]**	**Total heat rate [W]**	**Total heat flux [W·m^{-2}]**	**Rel. diff from experimental**
***k-ε*/ Enhanced (C)**	6728.84	1392.28	7888.35	21673.67	5.23%
***k-ε*/ Enhanced (M)**	7742.58	2112.41	9544.82	25462.44	23.62%
Relative diff.	**13.09%**	**34.09%**	**17.35%**	**14.88%**	
***k-ε*/ Standard (C)**	6267.42	1348.94	7371.17	20252.69	-1.67%
***k-ε*/ Standard (M)**	7410.59	2040.44	9110.75	24304.47	18.00%
Relative diff.	**15.43%**	**33.89%**	**19.09%**	**16.67%**	
***k-ε*/ Non-equilibrium (C)**	6300.12	1276.95	7329.33	20137.73	-2.23%
***k-ε*/ Non-equilibrium (M)**	7532.39	1989.79	9164.09	24446.76	18.69%
Relative diff.	**16.36%**	**35.82%**	**20.02%**	**17.63%**	
***k-ε*/Scalable (C)**	6444.84	1338.24	7521.22	20664.97	0.33%
***k-ε*/Scalable (M)**	7410.59	2040.44	9110.75	24304.47	18.00%
Relative diff.	**13.03%**	**34.41%**	**17.45%**	**14.97%**	
Laminar (C)	645.17	1696.11	2008.17	5517.57	-73.21 %
Laminar (M)	1039.84	1999.59	2630.00	7015.98	-65.94 %
Relative diff.	37.95%	15.18%	23.64%	21.36%	

As regards the effect of the near-wall treatment, it can be seen that the *k-ε* model with the enhanced wall treatment has the smallest difference (14.88 %), in the overall heat flux, when moving from the coarse grid to the medium grid (**Table 50**). The highest difference (17.63 %) is noticed when the non-equilibrium wall function is used. Concerning the inclusion of the turbulent model it can be seen that when a laminar flow is consifered the overall difference in the heat transfer flux values is almost 21 % when moving from the coarse to the medium grid. However, future room for development is needed to apply a more rigorous model grid independent (e.g. use of a model that includes the thermal boundary layer by improving the imposed boundary condition at the walls). The time evolution of the heat flux rate (overall, radiative and convective) at the heat pipes for the different cases studied can be found in the **Appendix Section**.

Figure 95 compares the two grid densities tested (Case 1 – Coarse and Medium Grid) with the experimental data. As observed, the calculated pressure drop along the riser axis almost coincides with the experimental measurements for both grid densities. A slight difference between the medium and the coarse grid is observed concerning the flow patterns. More specifically, the medium grid predicts denser areas in the bubbling reactor and more discrete bubbling formations, a fact which is more representative of the real case.

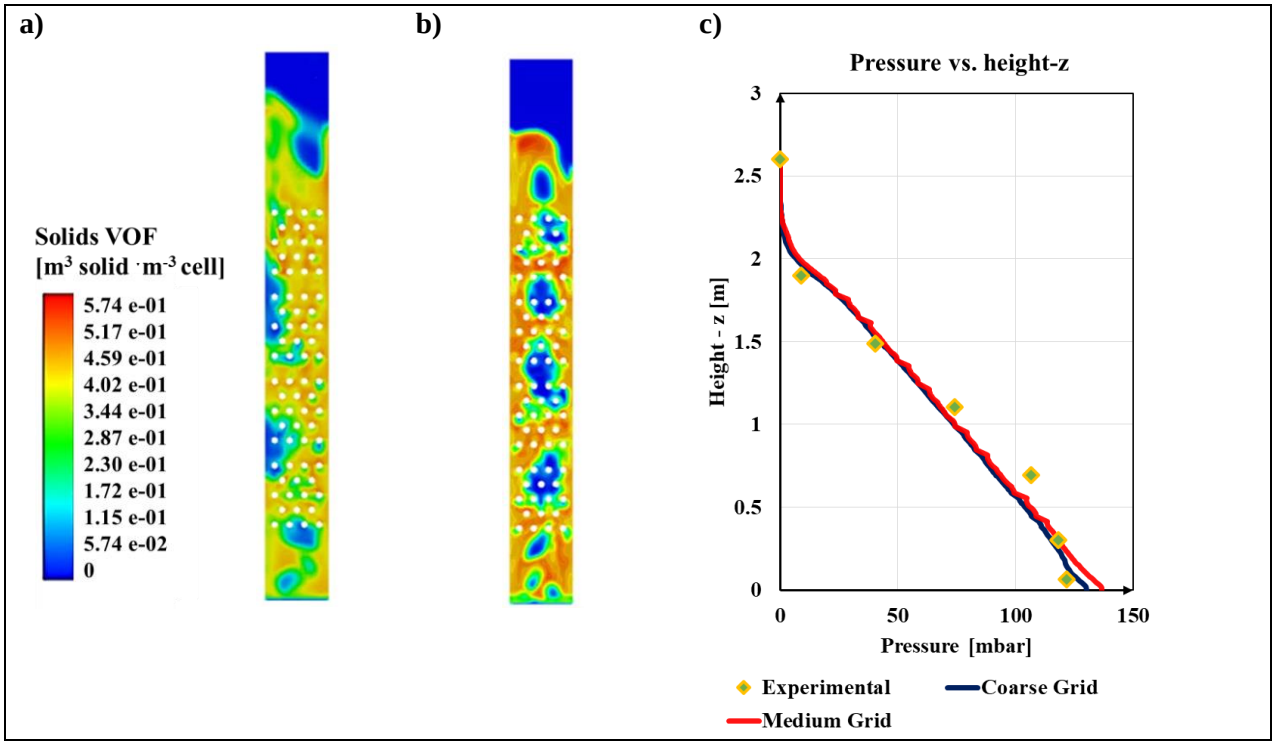

Figure 93. Instantaneous solids volume fraction at t=20 s for (a) Coarse grid, and (b) Medium grid, and (c) axial pressure profile of the instantaneous volume fraction at *t*=40 sec.

4.4.4 Design optimization

This sub-section presents results of the design optimization of the heat pipes arrangement inside the novel calciner by using the validated CFD model. During this study, several heat pipes arrangements have been investigated by (i) varying their lateral distance (ii) by comparing in-line vs. staggered arrangements. It should be noted that the vertical distance has been kept the same (equal to 2d) and no further investigation has been made since its effect in the overall heat transfer and local flow hydrodynamics is considered negligible [327]. In all studied cases, the same number (i.e. 72) and diameter of heat pipes has been kept

the same as well as the d_{cell}/d_p ratio (~110) to keep the same grid density. As concerns, the boundary and operating conditions, the same as in **Table 44**, **Table 45** and **Table 47** are setup in the model.

4.4.4.1 Simulated cases studied

The list of the simulated cases for the heat pipes design optimization is presented in **Table 51**. As a distance x is taken the distance from the heat pipes center line, **Figure 94**.

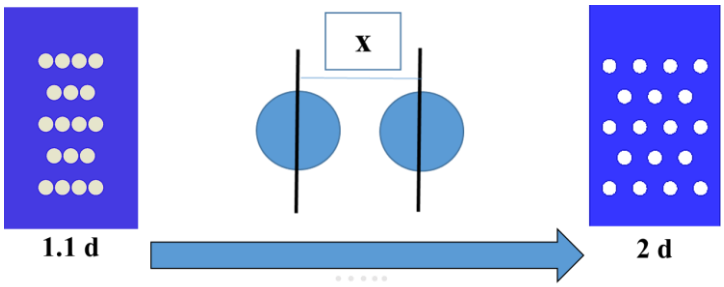

Figure 94. Heat pipes arrangements studied (example of x= 1.1d, x=2 d).

Table 51. Compared cases simulated.

Case Number	Arrangement	Heat pipes distance (x)
Case 1	Staggered	1.1d
Case 2	Staggered	1.5d
Case 3	Staggered (Reference case)	2d
Case 4	In-line	2d

Transient calculations are performed with a time step size equal to 0.005 sec, whereas after 30 seconds of simulation time, after the case initialization, a time averaging equal to 10 seconds is obtained.

4.4.4.2 Results

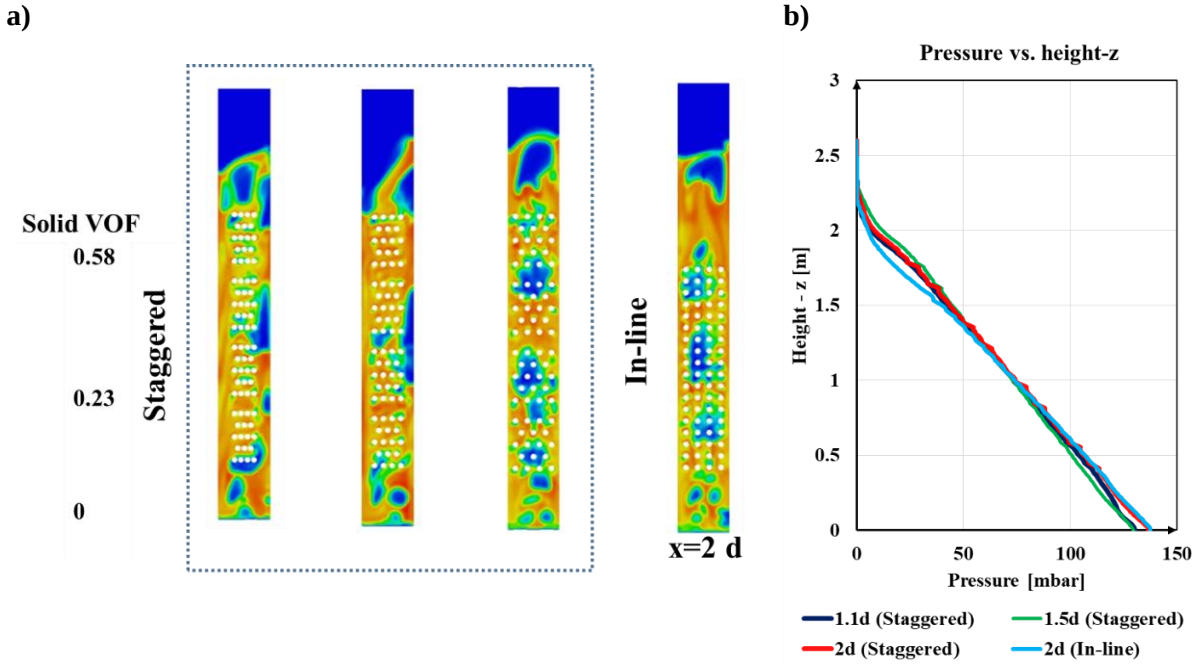

Figure 95. a) Instantaneous solids volume fraction at t=30 sec and b) time averaged pressure profile (comparison of different staggered arrangements and staggered vs. inline arrangement).

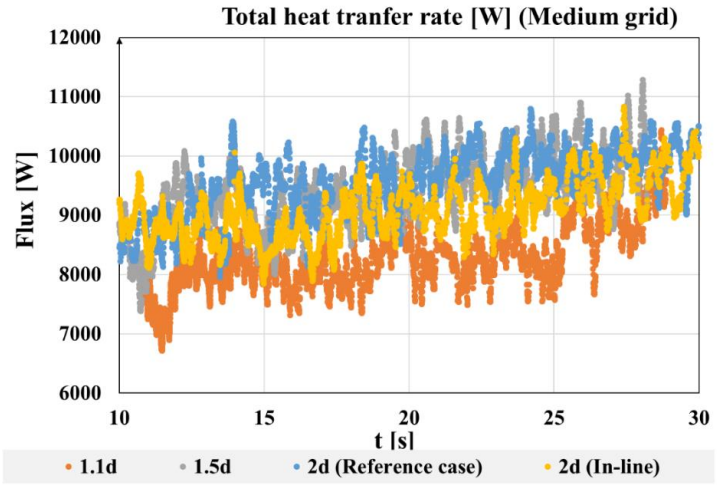

Figure 96. (a) Overall heat flux on the heat pipe heat exchanger wall evolution with time.

Hydrodynamic results of this analysis indicate that the heat pipes arrangement does not affect significantly the overall pressure drop of the system **Figure 95**. A small difference on the overall pressure drop, with the reference case (staggered arrangement 2d), can be traced for the in-line arrangement at the upper section of the fluidized bed. Locally it is observed that in the case of staggered arrangement with the heat pipes being at a close distance of 1.1 d, the gas bubbles flow at the sides of the tubes close to the sidewalls. A good mixing of gas-solids is better achieved when moving to higher heat pipes distances, such as 2d, promoting, thus, the overall heat transfer rate, **Figure 96**. For instance, in Case 1 the overall heat transfer rate is equal to 7943.29 W and in Case 3 the overall heat transfer rate increases by 20 % to a value of 9544.82 W.

Table 52. Results of different arrangements.

Case Number	Arrangement	Overall heat transfer Q [W]	Radiation/ Overall heat transfer %	CO2 outlet ($kg \cdot kg^{-1}$)
Case 1	Staggered 1.1d	7943.29	~21.80	~ 0.328
Case 2	Staggered 1.5d	9262.50	~22.01	~ 0.345
Case 3	Staggered 2d	9544.82	~23.62	~ 0.35
Case 4	In-line 2d	8929.34	~21.80	~ 0.34

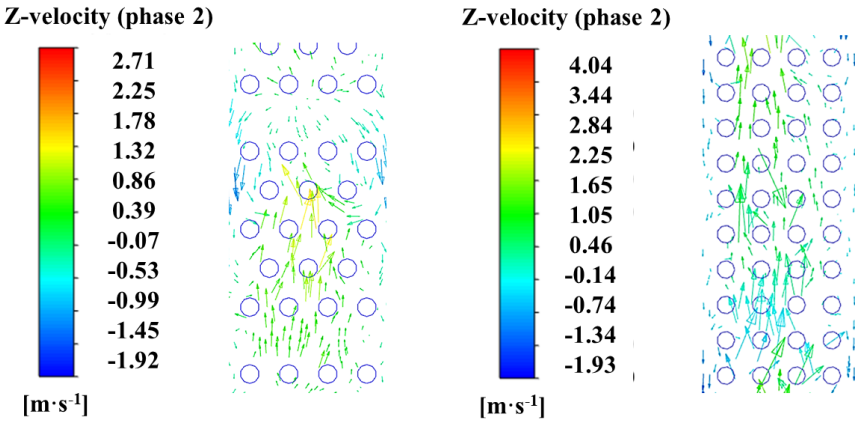

Figure 97. Instantaneous solids velocity profile at *t*=30 sec for a) staggered and b) in-line arrangement.

Figure 97 shows a comparison of the instantaneous solids velocity profile for the staggered and in-line arrangements. As can be noticed with the staggered arrangement a strong mixing (back mixing is observed) of the gas-solid particles is obtained with particles forming recirculation areas around the heat pipes, increasing, thus, the convective heat transfer term and the overall heat transfer rate. Slightly higher velocities are also observed in the staggered arrangement close to the heat pipes section (i.e. 0.8-1.5 $m \cdot s^{-1}$) compared to in-line arrangement (i.e. 0.5-1 $m \cdot s^{-1}$). All in all, the overall heat transfer rate increases by ~7 % in the staggered arrangement with regard the inline arrangement (**Table 52**). Finally, a slight effect is also observed in the calcination efficiency, for the specific operating point studied. At higher heat transfer rates there might be a higher effect on the overall calcination efficiency of the different studied designs.

4.4.5 Main conclusions

A transient 3D CFD model using a quasi-2D domain of an indirectly heated 300 kW_{th} calciner has been developed in the framework of this section. Validation of the used model has been achieved against experimental data concerning the CO_2 mass fraction at the reactor exit and overall heat transfer rate from the sodium filled pipes to the BFB. A sensitivity analysis on the effect of the near wall treatment and use of turbulence model has been carried out. It has been revealed that the k-ε model with an enhanced wall treatment can lead to an almost grid independent solution for a d_{cell}/d_p~110; this grid density is almost 4 times higher than the grid density needed to reach grid independency for the flow hydrodynamics in a CFB riser simulation (Refer to Sub-Section: Model validation (EMMS, carbonation reaction validation 1 MWth unit). The analysis has revealed that the lateral inter-tube space affects the overall heat transfer rate. Generally, use of a lateral distance between the heat pipes in the range of 1.5-2 d is a good option for an enhanced heat transfer. A higher distance (2.5d) for the specific design results is expected to give the highest heat transfer between the FB and the heat pipes. However, for the specific calciner width there are concerns regarding this arrangement, in the long-term operation of the unit, i.e. possible failure of heat pipes close to the walls, due to their expansion at such high operating temperatures. Thus, the reference case with a heat pipes distance of 2d is recommended for construction. Concerning the comparison of the in-line with the staggered arrangement, it can be observed that the staggered arrangement results in a higher heat transfer rate (by 7 % higher) than the in-line arrangement. The developed model is efficient and accurate and can help to study similar TCES/SHS novel systems as the one studied in the present Thesis.

4.4.6 Milestones achieved

The milestones achieved during this research study include:

- ✓ Development of an efficient and accurate 3D CFD model able of simulating the multi-phase flow inside an indirectly heated calciner - This model takes into account radiation phenomena, effect of turbulence and reaction kinetics (calcination reaction);
- ✓ Once more it has proved that the EMMS multi-scale scheme should be used in the numerical simulations, in order to capture with a high level of accuracy the flow patterns and pressure-profile;
- ✓ It has been showcased that even with a quasi-2D domain– domain with a small width-a high level of accuracy can be achieved for such demanding geometries. This quasi 2D domain can capture to some small extend the 3D solid clusters/gas bubbles evolution, but also speed-up calculations in order to facilitate the multi-parametric studies;
- ✓ Model validation has been achieved with experiments from the operation of the 300kW_{th} unit;
- ✓ A multi-parametric study has been carried out by testing various heat pipes arrangements.

CHAPTER 5
Modelling of an industrial sensible FB-TES

5.1 Preface

The large-scale BFB heat exchanger –integrated recycle heat exchanger (INTREX™) used in the setup of the CFD model has been developed by SFW. **Figure 98** shows the layout of the INTREX™ heat exchanger. In this exchanger, hot solids coming from the cyclone enter the main HE chamber through the downcomer. The heat transfer surfaces (tube bundles), where steam or water flows in, are located in this chamber and come into contact with the suspended particles. The solids flow rate around the tube bundles is controlled by controlling the velocity of fluidizing air to the chamber bottom part. Apart from this, by controlling the solids flow rate through the chamber of the INTREX™ superheater, the heat absorption can be varied giving operational flexibility to control furnace and/or superheat steam temperature. In the specific case, the heat exchanger is operated in the bubbling regime. Changing fluidization of the solids in the INTREX™ chamber can be used as well to adjust the heat transfer coefficient from solids to the tubes. The cooled solids return to the lower furnace via the solids return channel. With internal solid circulation, additional hot bed materials are taken from the furnace to the INTREX™ through openings in the furnace rear/common wall. Finally, any excess solid particles inside the main INTREX™ chamber return to the furnace via overflow openings.

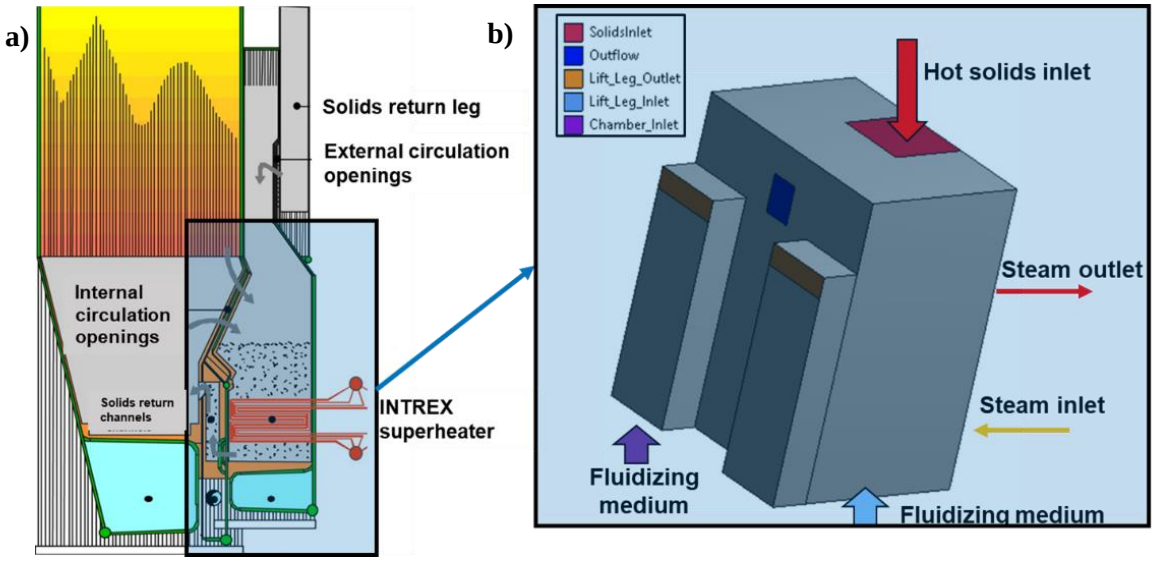

Figure 98. a) SFW's INTREX™ heat exchanger, b) geometrical configuration used in model setup.

5.2 Numerical methodology

To achieve the accurate modelling of the internal heat exchanger (INTREX™), a 3D transient CFD model is developed in ANSYS Fluent v17.1 platform. This model explicitly models the tube bundles enclosed inside the heat exchanger chamber, in contrast to available models in the recent literature that implicitly model the HE section through porous media. The model is similar as the one used for the bubbling 300kW_{th} calciner of TUDA described in **Section 4.4,** however it does not take into account the calcination reaction, but it includes extra coding development for the heat transfer inside the heat pipes. Even though there are not any available experimental data to validate the model, it is considered reliable enough and the results of adequate accuracy. The development of this model was based on design specifications and boundary/operating conditions delivered by SFW for a specific INTREX unit that serves as superheater.

Heat transfer from the core of the bubbling fluidized bed to the horizontal tube bundles involves several mechanisms, **Figure 99**. More specifically, heat is transferred from bed inventory to tube walls (i) by particle convection and (ii) by gas convection (A), through conduction within the tube (B) and through convection inside the tube (C). Heat transfer by radiation from clusters and the dispersed phase are not included in this model. Application of the heat transfer mechanisms B and C are included in the CFD model through proper UDFs in C programming language. In this algorithm in each iteration, the total heat transfer in watts (total Q) in each tube bundle is retrieved from the solver. Based on the steam properties (c_p), mass flow rate and inlet temperature, the outlet temperature can be estimated. Then, the temperature along the tubes in calculated based on a linear interpolation between (inlet temperature) T_{in} and (outlet temperature) T_{out}. The solution proceeds until it reaches equilibrium. **Figure 100** presents a schematic diagram of the heat transfer model algorithm that has been developed in this Thesis.

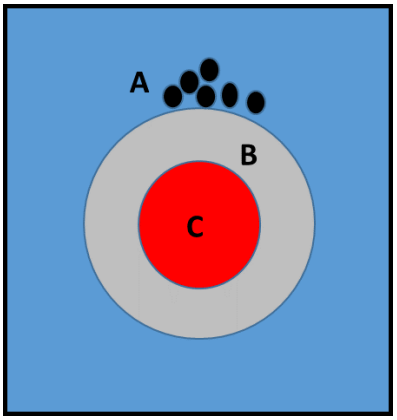

Figure 99. Heat transfer mechanisms involved in a BFB HE.

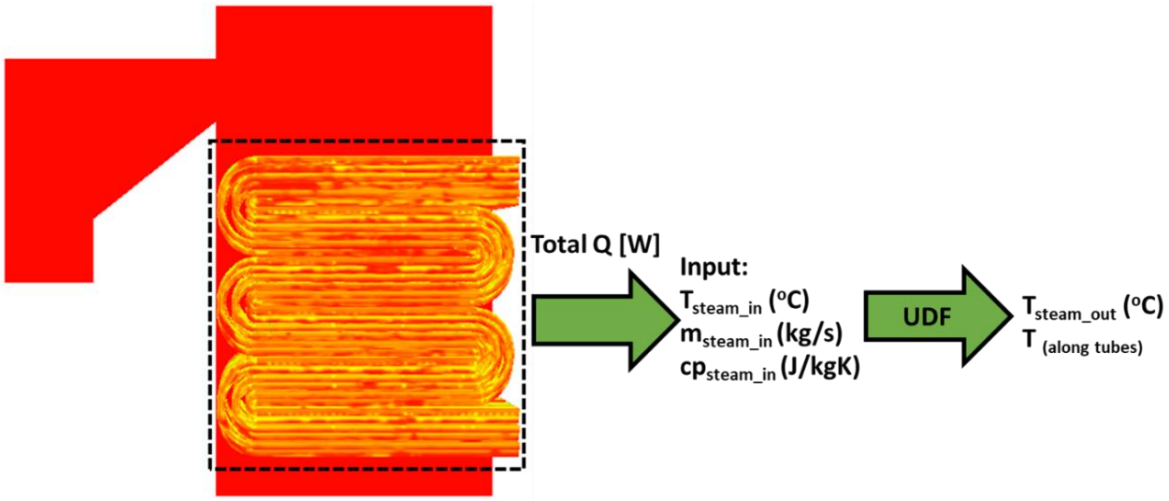

Figure 100. Heat transfer model algorithm, applied in this Thesis.

5.3 Geometry and mesh layout

The CAD geometry is created in ANSYS Design Modeler, **Figure 101**. In contrast to other models available in the literature, in the current model applied the tube bundles are modelled explicitly. This gives the advantage of calculating more accurately the heat transfer coefficient between the bubbling bed and the tubes. However, the design of tube bundles of staggered arrangement is quite demanding. Since the whole chamber along with the tubes presents a symmetry across a plane **Figure 101b**, only half of the chamber is modelled. This is mainly done to reduce the high computational cost, arising from the high number of grid elements that are needed to accurately capture the geometry. The design specifications of the modelled HE design are similar to those of the industrial HE presented in [63].

Some design and operating data are not presented in this Thesis because of confidential information for the studied industrial-scale FBHE system. However, it should be noted that the specific operational parameters

of the external heat exchanger (including fluidizing medium temperature and flow rate, bed temperature, pressure drop, properties of the working fluid inside the heat pipes) comply with the typical range of values of operating parameters for FBHEs in industrial CFB boilers. Dimensionless heat transfer properties are presented to set a baseline of the studied system, so that it can be easily comparable with other similar systems.

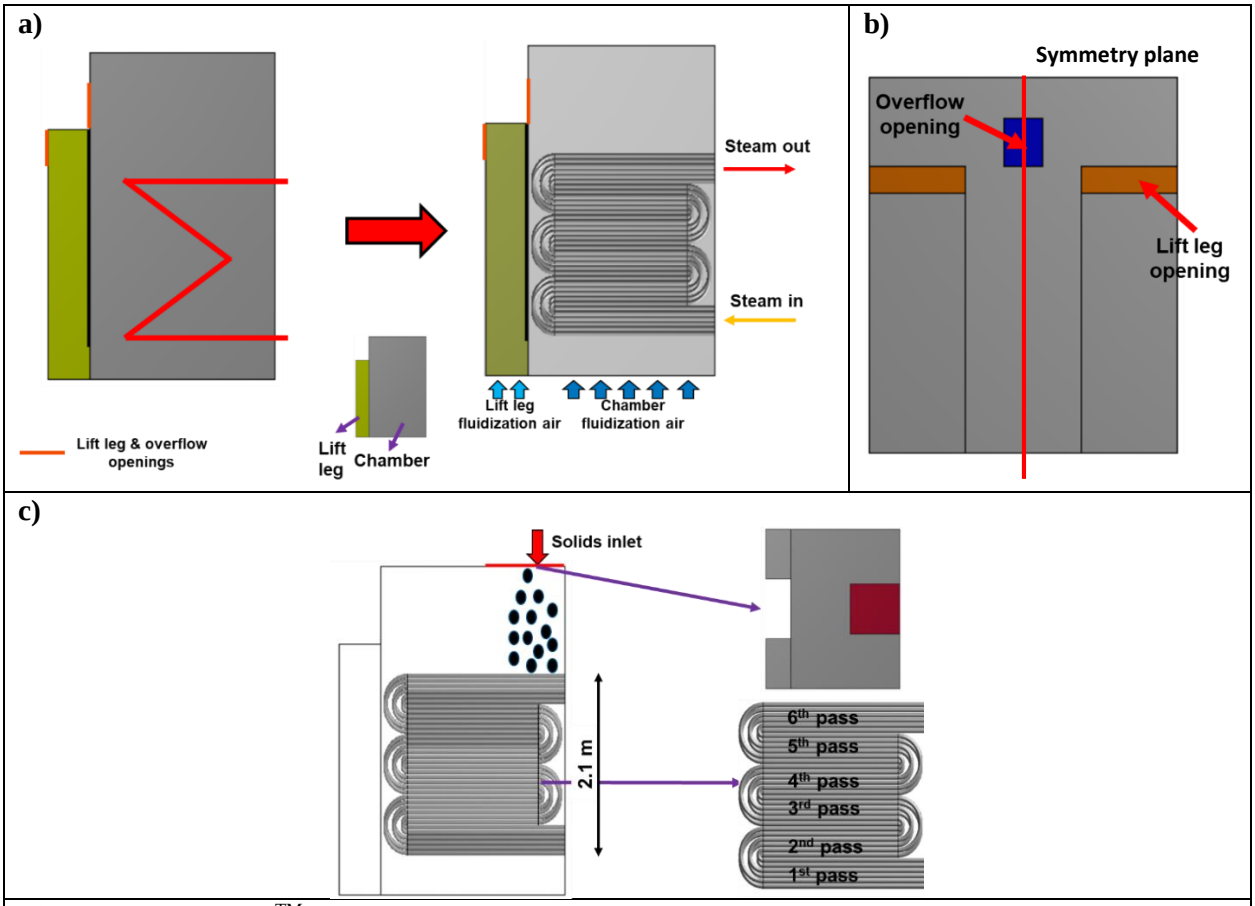

Figure 101. INTREX™ geometry creation in ANSYS DM.

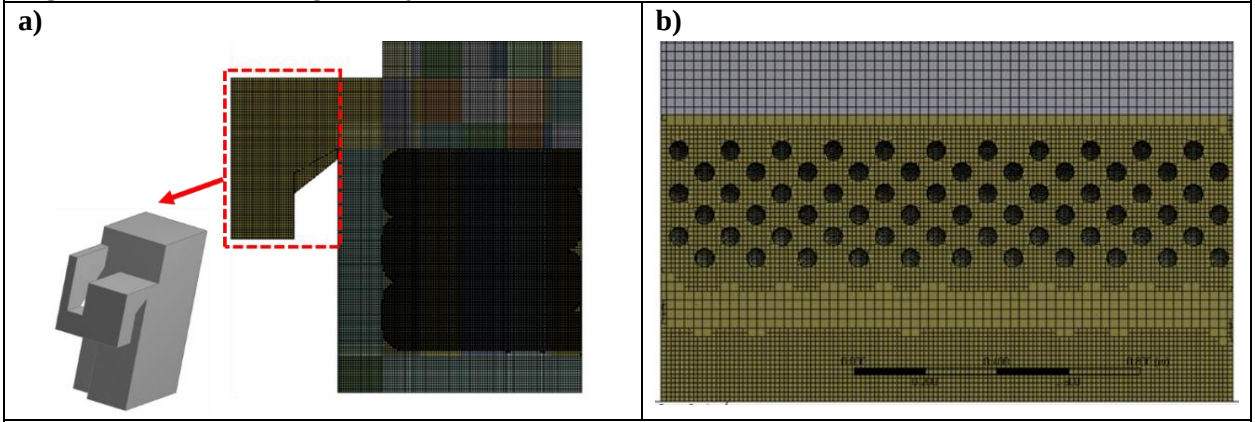

Figure 102. Numerical grid created with Cut cell method: a) side and b) front view.

A 3D numerical grid consisting of 3.7 million hexahedral elements is constructed in AM Component. Due to geometry complexity and the presence of tube bundles, the CutCell method is used (**Figure 102)**,

available in AM platform. The CutCell mesher converts a volume mesh into a predominantly Cartesian mesh (i.e. the mesh consists of mostly hexahedral elements, with faces that are aligned with the coordinate axes). This method has the advantage of automatically creating –with a rather easy way- hexahedral based elements with inflation layers at the wall boundaries. This is of high importance for the specific geometrical configuration that comprises of a series of tubes and an accurate estimation of the heat transfer rate is needed there. Implementation of a tetrahedral based grid might cause severe numerical instabilities –as it has been observed in preliminary runs conducted. Good grid quality is not so easy to achieve especially at such a close proximity of the tubes (longitudinal pitch is equal to 0.060m).

5.4 Results

5.4.1 Hydrodynamics results

After some 10 seconds, the inventory reaches an equilibrium value close to 9750 kg –averaging is obtained from within a time interval of 20 seconds. This is virtually equal to the inventory value predicted by the industrial partner. From this point on, solution of the heat transfer process is initiated. The time averaged mass flow rate of solid particles coming out of the chamber through the lift leg and overflow is equal to approximately 293.5 kg·s^{-1} and 3.35 kg·s^{-1}. The ratio of those two fluxes is quite indicative for the proportion of the solids leaving the BFB through the lift leg and the overflow.

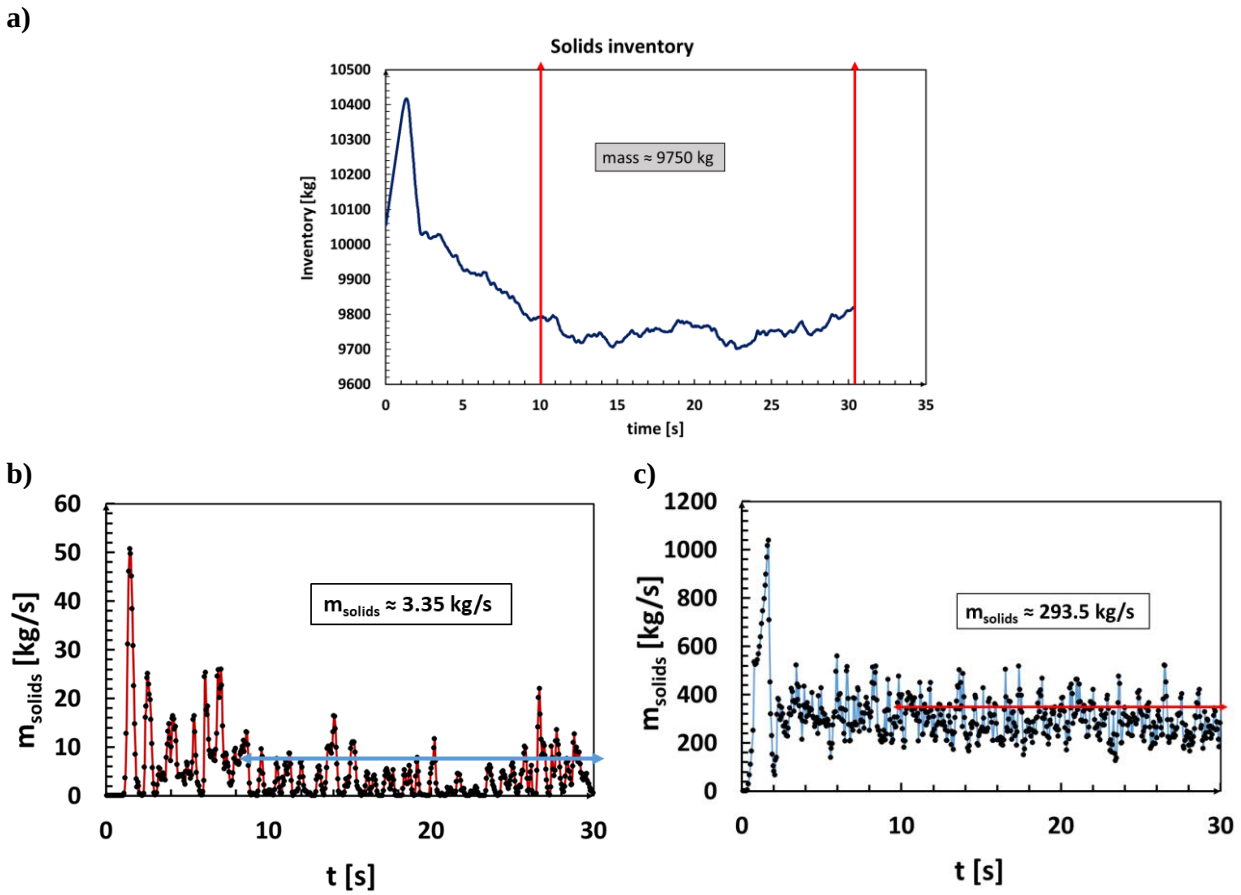

Figure 103. Time variation of solids a) inventory, b) mass flow rate at the overflow and c) mass flow rate at the lift leg outlet.

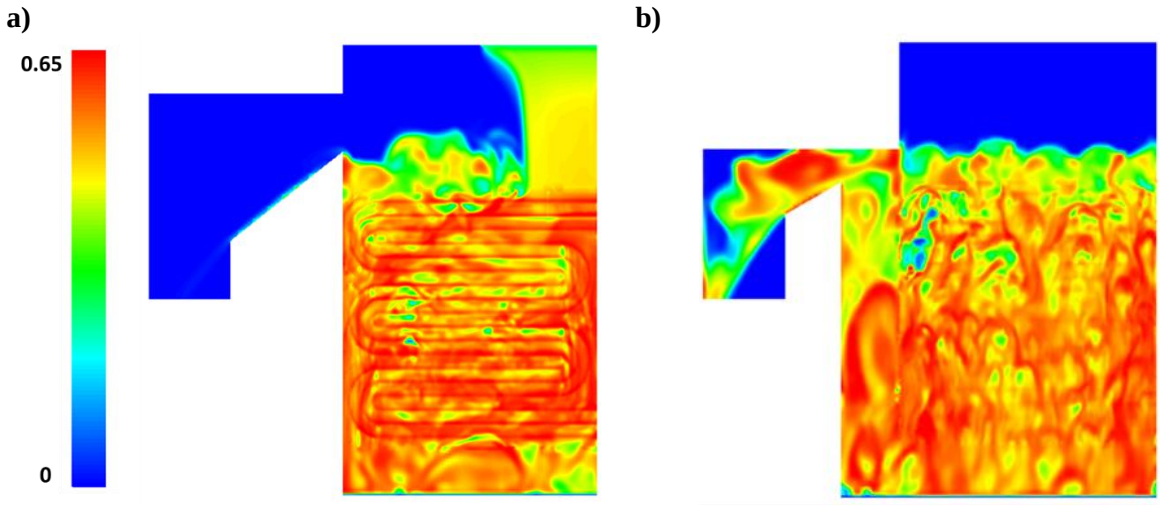

Figure 104. Instantaneous solids volume fraction at *t*=10 sec at a) symmetry plane (located at the middle of the overflow) and at) *z*=0.75 (located at the middle of the lift leg).

Figure 104 presents contours of the instantaneous volume fraction of solid particles at *t*=10 sec at a symmetry plane and at a plane at *z*=0.75 m (located in the middle of one of the lift legs). As can be noticed with the currently applied models there is a good representation of the flow patterns (bubbling formation) of the FB. The height of the bubbling bed is 3 meters, which is higher than the height of the last passes of the tubes bundles. Nonetheless, near the last pass of the tube bundles (sixth pass) the fluid flow is more dilute than near the bottom, a fact that might affect the heat transfer coefficient at this area, **Figure 105**.

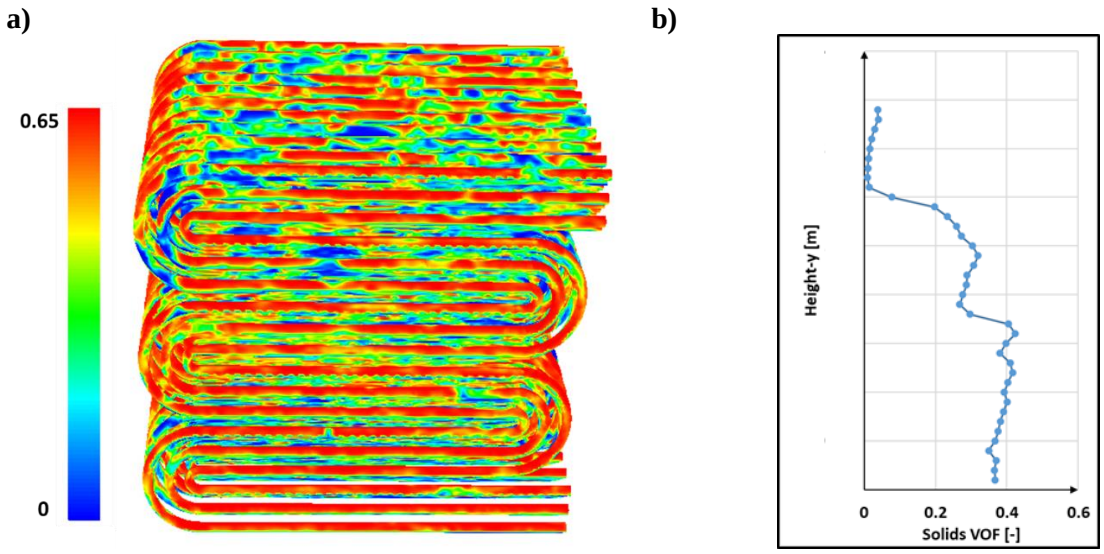

Figure 105. a) Contours of instantaneous solids volume fraction at *t*=10 sec and b) area weighted average of solids volume fraction at different heights of the BFB.

5.4.2 Heat transfer results

In this type of bubbling bed heat exchanger that utilizes Geldart B type of particles, two different heat exchange regions are formed. A dense region, where the fluidization regime is in the transition zone from bubbling to turbulent, depends upon the superficial gas velocity, and the heat transfer rate at this area is high and a dilute region, above the bubbling bed, where the upper part of tube bundles are exposed to rather low solids suspension density conditions, **Figure 105**. The total heat transfer rate based on the CFD analysis (time averaging 20 seconds after the inventory has reached equilibrium) is equal to 1.35 MW_{th} for the volume simulated (½). Those heat transfer rate values are the result of the analytical model applied by the heat transfer algorithm developed in this Thesis. In a more simplified approach (a mean steam temperature is imposed at the boundaries and no temperature variation of the steam is considered inside the tubes) the results of the CFD analysis give a total heat transfer rate equal to 1.15 MW_{th} (15 % lower than the one predicted with the more "detailed" approach). This analysis proves the importance of: 1) explicitly modelling the heat transfer surfaces and 2) using an analytical model that calculates the temperature of the working fluid inside the tube bundles. Therefore, the developed CFD model is an important tool that can be used to study with high accuracy this and similar heat exchangers as that of INTREX.

5.4.3 Comparison with theoretical model

By using a theoretical model, we can assess if the developed CFD model gives accurate results. The calculated variables of the several parameters of the model are based in the model of Subbarao and Basu [328] with additional equations taken from Kunii and Levenspiel [52]. Additionally, as an extra add-on the CFD model can feed such theoretical models with several input data (e.g. gas/solid voidage near the heat pipes) to increase the theoretical model predictions. This is an important aspect of the CFD model, so that it will help study several parameters of interest of such FB systems involving heat transfer, without the need of experimental data. Moreover, for a more analytical calculation of the heat transfer coefficient, solid VOF values can be retrieved at different sections of the tube bubbles (e.g. near the bottom bed or at the upper section). As it can been observed from **Table 53** the overall heat transfer coefficient values differ by 14 % when feeding the numerical model with values from the CFD with respect to the theoretical calculations. For another operating point of lower fluidizing velocity (**Table 54**) it can be seen that such discrepancies increase. This fact proves that such theoretical models should be fed with input data from advanced ones in order to deliver results of high accuracy.

Table 53. Summary of heat transfer properties based on [328] (indicative values of air-sand system) (for a velocity U_0=17.5 U_{mf}).

Parameter	Theoretical Value	Based on CFD model (time averaged VOF values, t_{aver}=10 sec)	Relative difference %
ε_e, [-]	0.67	0.62	7.46
k_ε, [$W \cdot m^{-1} \cdot K^{-1}$]	0.098	0.112	-14.29
c_{pe}, [$J \cdot kg^{-1} \cdot K^{-1}$]	944	933	1.17%
ρ_e, [$kg \cdot m^{-3}$]	819	975	-19.05
A, [-]	0.80	0.8	0.00
Fr, [-]	0.01	0.01	0.00
t_e, [s]	0.083	0.083	0.00
HTC, [$W \cdot m^{-2} \cdot K^{-1}$]	538	614	-14.13
h_r, [$W \cdot m^{-2} \cdot K^{-1}$]	52.64	52.64	0.00

Finally, based on both the theoretical and the CFD model the overall heat transfer coefficient is higher by 7-12 % (based on the theoretical and the CFD model, respectively) when using a fluidizing velocity equal to *8.75* U_{mf} with respect the operating point with U_0*=17.5* U_{mf}.

Table 54. Summary of heat transfer properties based on [328] (indicative values of air-sand system) (for a velocity U_0=8.75 U_{mf}).

Parameter	Theoretical Value	Based on CFD model (time averaged VOF values, t_{aver}=10 sec)	Relative difference %
ε_e, [-]	0.67	0.58	13.43
k_e, [W·m^{-1}·K^{-1}]	0.098	0.119	-21.43
c_{pe}, [J·kg^{-1}·K^{-1}]	944.27	928	1.72
ρ_e, [kg·m^{-3}]	819.60	1050	-28.11
A, [-]	0.80	0.80	0.00
Fr, [-]	0.04	0.04	0.00
t_e, [s]	0.13	0.13	0.00
HTC, [W·m^{-2}·K^{-1}]	579	702	-21.24
h_r, [W·m^{-2}·K^{-1}]	52.65	52.65	0.00

Based on the coupling of the theoretical model with the CFD results a sensitivity analysis is carried out to test the effect of the *A* factor, temperature values and fluidizing type of medium (air vs. CO_2) in the overall HTC (**Figure 106**). As it can be noticed, the overall heat transfer is slightly favored at temperatures above 700 K, when CO_2 is used as a fluidizing medium. Concerning the area coverage it can be seen that there is an almost linear dependence of the HTC with the heat pipes surface coverage at the BFB cross section.

a)

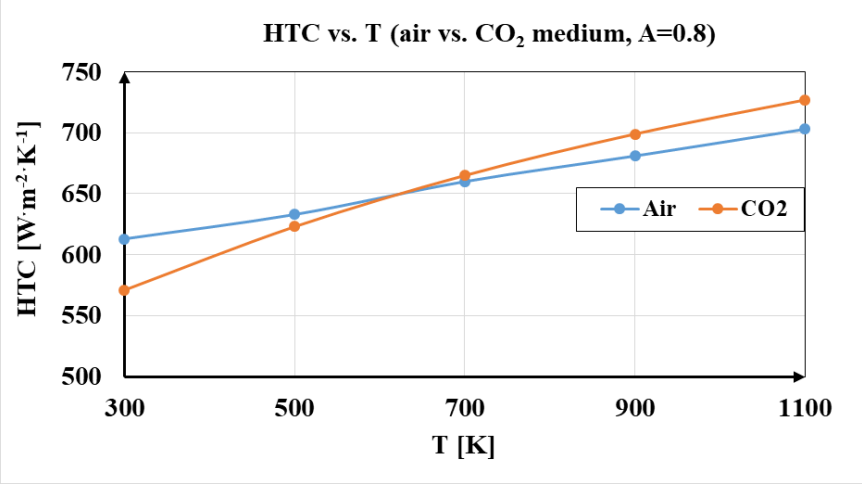

b)

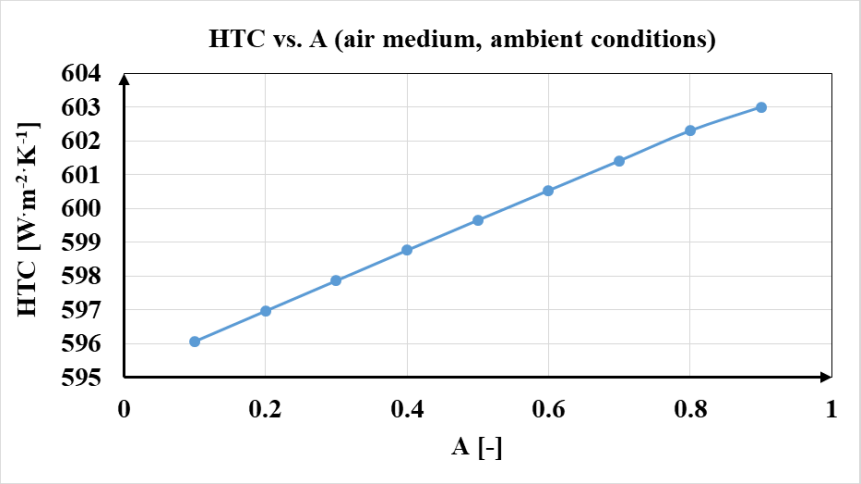

Figure 106. HTC results by altering (a) the temperature and fluidizing medium and (b) tubes coverage at the BHB cross-sectional area *(U_0=17.5 U_{mf}).*

5.5 Main conclusions

A transient 3D CFD model of the integrated HE of an industrial CFB boiler has been developed in the framework of this Thesis. The model is based on the pure Eulerian-Eulerian TFM and has been utilized to perform transient simulations of the heat transfer process from the bubbling bed to the tube buddles. This HE serves as a superheater, but can be used as well as an internal storage system. Simulation of such an exchanger is demanding, due to its complex geometry. The applied model explicitly takes into account the tube bundles arrangement –instead of using simplified approaches, such as flow in porous media- whereas a UDF is integrated into the model to implicitly model the fluid medium flow inside the tube buddles and, thus, better predicts the heat transfer instead of imposing a simplified boundary condition (e.g. temperature boundary condition). Both aspects are of high importance to increase the model predictions accuracy. Based on the results the flow hydrodynamics are represented with an acceptable accuracy, i.e. the typical flow patterns of a BFB. In this regard, use of the Cutcell grid method can be applied in order to construct the demanding computational grid. This is of high importance to accurately predict the heat transfer rate near the tubes. Based on a preliminary analysis (with a mean steam temperature imposed at the HE wall boundaries, equal to 538 ^{o}C) the total heat transfer rate is almost equal to 2.3 MW_{th}. By imposing a more appropriate boundary condition and using the heat transfer model constructed in this Thesis the total heat transfer rate is equal to 2.7 MW_{th}, which is closer to what is expected based on know-how from an industrial company's feedback. Results of this model, mostly concerning flow hydrodynamics, can feed theoretical models, such as that of Kunii and Levenspiel, in order to carry out a sensitivity analysis of several parameters effect on the overall heat transfer coefficient by saving up computational time.

CHAPTER 6

Comparative assessment of novel TES systems and methods

6.1 Overview

In order to set a comparison between the different TES concepts and make an informed decision on the possible TES solutions to be applied for high/ultra-high temperature storage, specific KPIs are required to be determined, both quantitative and qualitative. Concerning the qualitative aspects, some of these include design specs, such as design flexibility, maturity level, scaling-up potential and type of storage use. Other aspects include the environmental impact of the TES system (e.g. environmental friendliness of the storage medium). Some of the main quantitative aspects as defined by [329] are the following:

- Storage capacity [MWh]: It is the energy stored in the system and depends on the storage method, medium, and the system size/design.
- Power [MW or $J \cdot s^{-1}$]: defines the charging rate of a specific system.
- Charge and discharge times [h]: it the total time needed to charge or discharge a TES system.
- Efficiency [%]: it is the ratio of the discharging energy to the system charging energy that takes into account the energy loss during the storage period and the charging/discharging cycle. This factor is more critical for ultra-high temperature LHTES systems (Chapter Three). In FB systems, latter heat losses are not so important.
- Cost [$€ \cdot kW^{-1}$ for capacity or $€ \cdot kWh^{-1}$ for power]: It is the thermal or electric cost, and it commonly includes the storage medium $€ \cdot kg^{-1}$, the heat exchanger for charging/discharging the system, and the cost of the space and/or vessel for the TES.

A comparison of the different types of storage technologies studied in this Thesis in terms of several design specs is presented in **Table 55**.

Table 55. Comparison of SHS, LHTES and TCES with CaL in terms of design flexibility, maturity level and their relative advantages and disadvantages.

HE/storage system	Advantages	Disadvantages	Design flexibility	Maturity level; Scaling-up potential
SHS-FB	Efficient heat transfer; excellent gas-solid mixing; solid medium flexibility;	Particle entrainment; by-pass of gas in bubbles; particles attrition; extra energy consumption for fluidization	It can vary from CFB/BFB and fixed bed to free-falling particles	Already applied at industrial scale (e.g. INTREX technology) and pilot scale projects are ongoing for SPSR in CSP plants [330]
TCES with CaL	CO_2 capture; includes advantages of SHS-FB	Includes disadvantages of SHS-FB, including CaO/CO_3 reactivity decrease after several cycles (> 20)	It requires a DFB system with in-between connecting systems (e.g. loop seals, drop tubes)	Demo scale projects are under-development for oxy-fired CaL [331], indirectly heated CaL [332]. Pilot project of CSP-CaL at TRL 5 [333]
UHT-LHTES (Si-based)	Compact design; small heat storage volume, which reduces the involved cost	Possible cracking of the PCM vessel, due to PCM volume change; excess heat losses due to ultra-high temperatures	Yes, especially if a truncated cone is used	Studied up until now at a low TRL<3 (proof-of-concept) [277] and ongoing pilot demonstrator.

Some additional aspects that need to be determined in a TES are the type of storage medium in terms of its energy density, turning temperature (temperature for phase change, chemical reaction or agglomeration for

the LHTES, TCES and SHS systems, respectively), cost and environmental impact. A summary of the different storage medium studied in this Thesis is give in **Table 56**.

Table 56. Comparison of storage medium in terms of energy density, turning temperature, cost (Ref. year 2018-2021) and environmental aspects.

** Refers to agglomeration temperature for sand/quartz, temperature of chemical reaction for calcination reaction*

*** It can be oxidized if inside the LHTES there is presence of oxygen*

Type of storage medium	Type of storage use	Energy density ($MJ \cdot m^{-3}$)	Turning temperature (ºC)*	Cost (€·kg^{-1})	Environmental aspects
Molten salts (e.g. carbonate salt, chloride salt)	LHTES	800	~700 (for carbonate salt) [334]	0.9-1	Strongly corrosive
Sodium salt	SHS	~1300	~800	0.2-0.5	Strongly corrosive
Silicon	LHTES	4660-9320	1410	2-3 [335, 336]	Environmentally benign**
Sand	SHS	2.48	800-900	0.07 [337]	Environmentally benign
Quartz	SHS	2.48	1327	0.14 [337]	Environmentally benign
CaO/CO_2	TCES	3226	895	0.1-0.5 [338]	Environmentally benign

It's worth noting that the price/kg of some of the abovementioned medium, such as sodium, can fluctuate due to a number of factors such as supply and demand, market conditions, and production costs. Some technical aspects for the specific designs still to be determined. This include charging time, charging discharging rates and capacity for specific case studies. The added value of the current CFD models developed in that they can assist in the quantification of such KPIs. An example of this is presented in the following Sub-section, where the charging time and rates are compared for the some of the studied concepts in this Thesis.

6.2 Comparative assessment of novel TES systems in terms of system performance (Case A)

6.2.1 Studied cases

The different types of storage methods –mostly targeting on the storage medium providing heat- are compared in terms of charging rates (T_{solid} versus time) by using as a reference the simplified geometry of the 300-kW_{th} unit in TUDA described in Sub-section 4.4. For the sake of this analysis, a multi-parametric analysis is carried out by using ANSYS Fluent. The simulation cases matrix is presented in **Table 57**. In all of the above studied cases, the solids inventory is set equal to around 18 kg. The gas-solid temperature at t=0 sec is set equal to 300 K. For Cases 1A and Case 2A the simple case of heating the storage medium through a fluidizing gas of a higher temperature (890 ºC) coming from the riser bottom has been simulated. The scope of this comparison is to test the effect of the primary air velocity effect on the system charging rate. The maximum mass flow rate tested is equal to 0.0053 $kg \cdot s^{-1}$, which corresponds to a small incoming heat rate of ~ 5.1kW. A higher velocity has not been studied as this will lead to a change in the FB operating regime **Figure 107**, which is out of scope of the current assessment.

In Cases 3A and 4A the indirect heating of the granular material by using sodium and steam filled heat pipes, respectively, is undertaken. The incoming heat rate from these two cases are equal to approximately 12 and 28.5 kW. In order to reach such high incoming heat rates the simple case of heating the granular material through a gas medium studied in Case1A and Case 2A the fluidizing gas should enter the domain with a mass flow rate higher than 0.01 $kg \cdot s^{-1}$. This will affect as already mentioned the FB operating regime. Finally, in Case 5A, a TCES with calcination reaction is explored with similar settings as in Case 3A (heating from the sodium filled heat pipes with the same incoming heat rate) to directly compare the TCES with the SHS in granular material. In all cases studied, the FB system operates under pure bubbling conditions, except for the Case 5A, where owing to the CO_2 release extra fluidization is observed leading to a small circulation of particles around 0.001-0.003 $kg \cdot s^{-1}$.

Table 57. List of compared cases of SHS and TCES in a domain heated through heat pipes.

TES type	HT medium inside HPs	T_{medium} [ºC] inside HPs	Fluidized medium	Fluidizing agent [type, m-$kg \cdot s^{-1}$, T-K]	Regime
FB-SHS (Case 1A)	N/A	N/A	Sand	Air, 0.00106 $kg \cdot s^{-1}$, 1163 K	BFB
FB-SHS (Case 2A)	N/A	N/A	Sand	Air, 0.0053 $kg \cdot s^{-1}$, 1163 K	BFB
FB-SHS (Case 3A)	Sodium	890	Sand	Air, 0.00106 kg/s, 300 K	BFB
FB-SHS (Case 4A)	Steam	488	Sand	Air, 0.00106 kg/s, 300 K	BFB
FB-TCES (Case 5A)	Sodium	890	CaO	Air, 0.00106 kg/s, 300 K	BFB

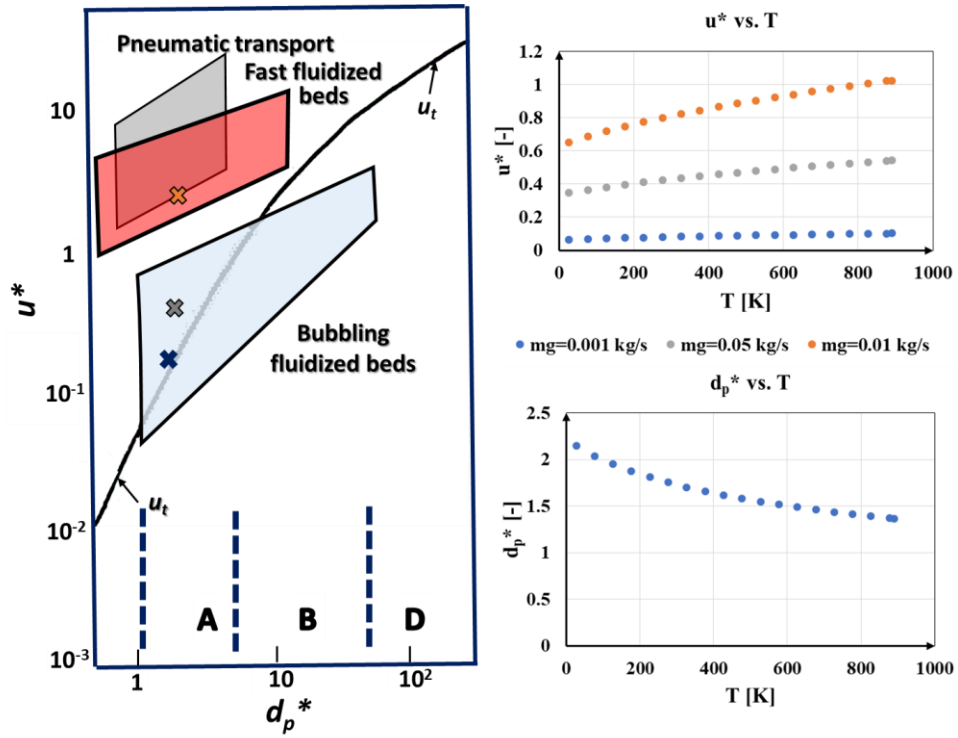

Figure 107. Fluidization regime of the modelled particles for different operating points (Graph is based on [52, 300].

6.2.2 Results

Indicative results of this parametric analysis are presented in **Table 58**, where the charging rates and charging times are presented along with the incoming heat at the beginning of the simulation, in order to define the scale of the problem. As it can be observed the most effective method with the highest charging rate and lowest simulation time is Case 3A (heating of the FB with sodium filled pipes). Additional, add-on in this method is the inclusion of $CaCO_3$ for an in-situ CaO (CO_2) production. For specific applications where the FB system is targeted for medium to high operating conditions, heating the FB through steam filled tubes or another medium operating around this temperature will be effective enough. However, further assessment is needed in the future to constract an operating map of the FB systems under various operating conditions (including particle properties, fluidization velocities and heating methods).

Table 58. Comparison of the different test cases in terms of charging rates and charging times.

** This refers to the time before the TCES system enters calcination reaction*

Case	TES type	$Q_{in,\ 300K}$ [kW]	CO_2 production [kg/s]	Charging rate ΔT/dt [K/min]	Charging time [s] from 300 K to 600 K
Case 1A	**FB-SHS**	~ 1.1	NO	**~8**	**~6200**
Case 2A	**FB-SHS**	~ 5.1	NO	**~45**	**~ 400**
Case 3A	**FB-SHS**	~ 28.5	NO	**~330**	**~53**
Case 4A	**FB-SHS**	~ 12.14	NO	**~166**	**~136**
Case 5A	**FB-TCES**	~ 28.5	YES	**~330***	**~53**

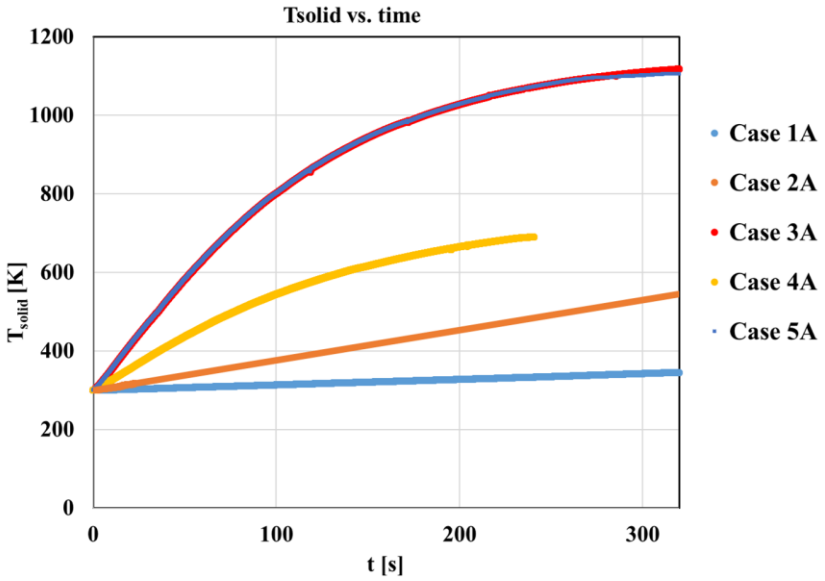

Figure 108. Time evolution of the mass weighted average of solids temperature, T_{solid}, of the different cases studied.

6.3 Comparative assessment of novel TES systems in terms of system performance (Case B)

6.3.1 Studied cases

Finally, this sub-section presents a comparison between a FB system and a LHTES for thermal heat storage at high/ultra-high temperatures (>650 ºC). Two types of systems are tested and compared; a gas-sand FB system and a silicon based LHTES. Both systems have the same container size (of height of 2.6 m and volume of ~0.036 m^3) and shape (i.e. cylindrical), and, they are heated at the sidewalls at a high temperature of almost 1773 K. It should be noted that the scale of the problem is similar to that of Case 3A. In both systems, the validated models presented in the previous sections have been utilized. More specifically, in the FB system the TFM-EMMS model, which includes the turbulence effect and the heat transfer through radiation has been utilized as the same in Sub-Section: **Model of IHCaL calciner with heat pipes (heat transfer model, 300 kWth unit**). In the LHTES, the VOF model coupled with the solidification-melting model (Refer to Sub-Section: **Modelling of storage applications using PCMs: Numerical methodology**) has been used. In both systems the same grid density has been utilized with a mean cell size equal to 0.015 m (this corresponds to a d_{cell}/d_p~150 for the FB system). The main difference between the two cases tested is that a 3D domain has been used in the FB system in order to better capture the transient heterogeneous formations and an axisymmetric domain for the LHTES system, **Figure 109**. This results in a number of cells equal to 27318 (hexahedral) and 1776 (quadrilateral), respectively.

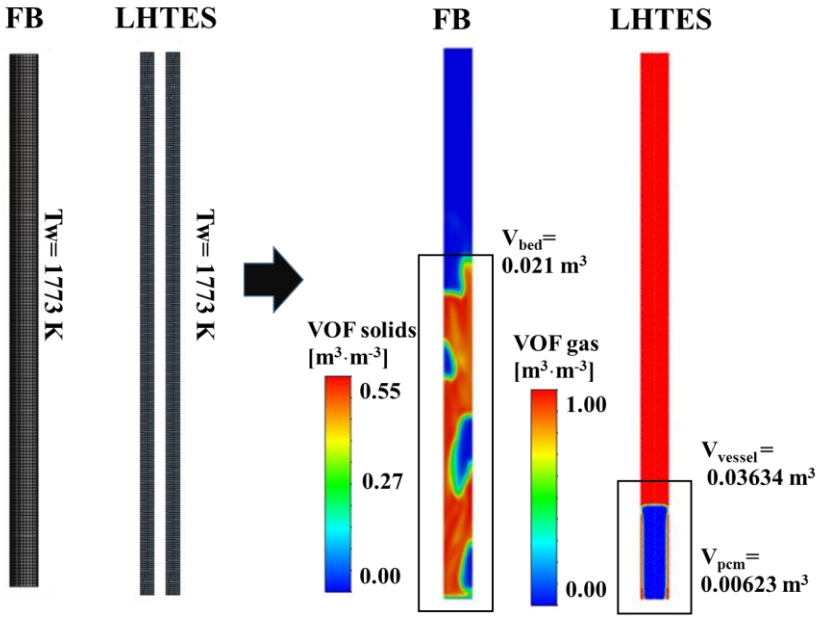

Figure 109. Compared cases mesh and reproduced flow patterns: gas-sand FB vs. Silicon based LHTES

Some of the operating data used in this analysis are listed in the **Table 59**.

Table 59. List of operating data used in the comparative assessment of the FB-SHS vs. LHTES systems.

TES type	Storage medium	mass [kg]	C_p [J·kg^{-1}· K^{-1}]	k_s [W m^{-1}· K^{-1}]	V_{vessel}/V_{medium} [-]
FB-SHS	Sand	~15	940	0.4	1.7
LHTES	Silicon	~15	1040	25 (solid) – 50 (liquid)	5.8

6.3.2 Results

Figure 110 presents results of the numerical analysis in terms of mass-weighted average solids temperature and incoming heat rate per surface area evolution with time. As it can be noticed the overall heat transfer rate at the beginning of the storage process is almost the same and both systems present similar charging rates (**Table 60**). However, as soon as the LHTES systems enters the phase change mode (at approximately 20 seconds after the beginning of the heating phase) its charging rate starts to slow down. This effects the overall charging time of the LHTES system with respect to the granular SHS system. For the full charging time, it takes almost 100 seconds for the SHS system and almost 1600 seconds for the LHTES to reach their full charging condition. However, it should be noted that even if the SHS system seems advantageous in terms of charging rates, on the other hand it occupies almost 3.3 times the volume (under bubbling fluidized bed conditions) with regard to the LHTES system, a fact that will increase the total investment cost. Another, benefit of the Si-based LHTES system is its considerably higher storage capacity with respect to other systems, **Table 56**. Thus, it should be stressed out that a multi-criteria analysis taking into account all these aspects should be undertaken in the future in order to make a decision of which type of system should be used depending on the application. The currently developed CFD tool can feed such model with input data concerning several technical parameters of interest, such as charging/ discharging time, charging/discharging rates, heat losses etc.

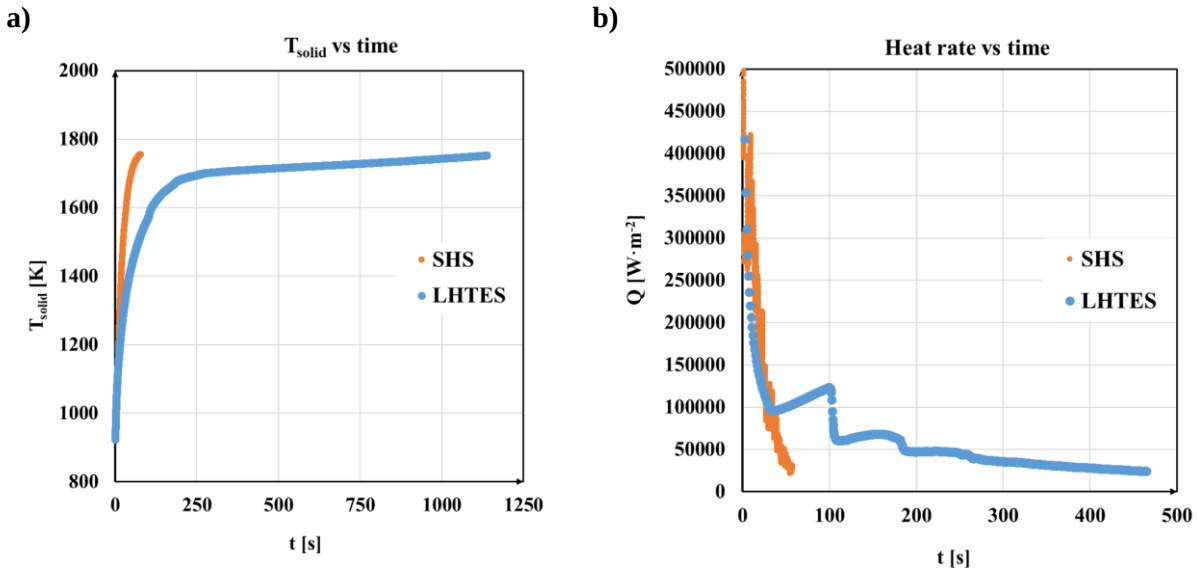

Figure 110. a) T_{solid} vs. time and b) Heat rate per surface area Q vs. time for the two compared TES systems: gas-sand FB vs. Silicon based LHTES

Table 60. Comparison of two types of storage systems in terms of power per surface area, charging rate, and charging time.

Case	TES type	Charging time [s] from 923 K to 1173 K	Charging time [s] from 923 K to 1770 K
Case 1B	**FB-SHS**	**~9.2**	**~100**
Case 2B	**LHTES**	**~11**	**~1640**

6.4 Main conclusions

Chapter Six has presented a summary of the studied systems (FB-SHS, TCES-CaL and Si-based LHTES) in terms of general design aspects (i.e. design flexibility, maturity level, advantages and disadvantages), storage medium used (storage capacity, average cost/kg, environmental friendliness). Additionally, two test cases have been simulated in order to set a theoretical comparison between the different systems studied in terms of heating rates and total charging times, when they are heated up with different heating methods (e.g. heating through steam filled or sodium filled heat pipes of a FB system for either SHS of TCES) or when they are heated up with the same method (i.e. heating from the side walls of a LHTES and a FB-SHS by assuming the same wall temperature).

Criterion	**TES type**		
	1st option	**2nd option**	**3rd option**
Storage capacity	Si-based LHTES	TCES-CaL	FB-SHS
Storage medium cost	FB-SHS	TCES-CaL	Si-based LHTES
System volume	Si-based LHTES	FB-SHS	TCES-CaL
Maturity level (TRL)	FB-SHS	TCES-CaL	Si-based LHTES
Design flexibility	Si-based LHTES	FB-SHS	TCES-CaL
Investment cost	Si-based LHTES	FB-SHS	TCES-CaL

For the same type of storage medium and system (e.g. granular material inside a FB system) the heating through sodium filled heat pipes (at ~900 ^{o}C) results in the highest heating rates with regard to the heating methods through steam filled heat pipes or with simpler FB systems, where the granular material is heated up directly by a heat transfer fluid (e.g. air). The SHS with TCES methods in the same FB reactor present similar behavior in terms of heating rates, with the latter being slightly slower, due to the fact that part of the incoming heat is used for the calcination reaction. The TCES method presents the advantage of producing CaO that can be further used for CO_2 capture in a calcium-looping concept, however, the $CaO/CaCO_3$ material suffers from loss in reactivity after some cycles (approximately 20 cycles), requiring, thus, a fresh make-up material.

Concerning the comparison of the heat storage in granular materials with the storage in a LHTES system it should be noted that the FB-SHS presents higher heating rates than the LHTES system. Initially, both systems have similar heating rates when they are at the sensible heat storage mode (owing to the materials similar specific heat capacities), but when the PCM starts to melt the heating rate of the LHTES slows down up until the PCM melts completely. In terms of maturity level, the gas-sand FB-SHS is at a higher TRL than the Si-based LHTES, which is still at a lab scale and several aspects need to be explored before this is used at a large scale (e.g. possible cracking of the storage medium, reactivity of the PCM with the presence of a gaseous medium inside the vessel, excessive lateral heat losses etc.). On the other hand, the Si-based LHTES system presents a higher potential in terms of storage capacity, design flexibility and cost effectiveness (it requires less than half of the volume of a typical BFB system to store a storage medium of the same mass, without the need of additional components needed in FB systems, such as cyclones, loop seals, downers etc.) than the granular based storage systems. Owing to its compact design the LHTES system is expected to require the least investment cost with regard to granular based TES systems.

All in all, all of the TES systems studied in the current Thesis, present several advantages and seem promising for thermal energy storage at high/ ultra-high temperatures. Their selection for thermal storage needs further investigation by a rigorous decision making tool that should deliver a multi-criteria analysis covering both technical and non-technical (environmental, social, economic) aspects for a targeted

application. The numerical models developed in the specific Thesis, can be utilized in the future to deliver several technical parameters of interest for the different types of technologies. Such parameters, including charging/discharging rates, storage capacity, storage efficiency and charging time can be used as input data for such a decision making tool. The CFD model results can also feed other types of reduced order models (e.g. feed process models with species concentrations, temperature/pressure profiles, particle loadings) to enhance their predictions accuracy, or they can be coupled with stress-strain models (2D/3D pressure/temperature distribution) to verify if possible cracking of the studied systems might occur.

CHAPTER 7
Conclusions and future work

7.1 Conclusions

In this Thesis, advanced CFD models based on Eulerian approaches have been developed into ANSYS Fluent platform, to investigate several novel multi-phase flow concepts mainly targeted for TES applications (SHS, TCES-CaL and LHTES). A series of models and sub-models have been developed in order to accurately and efficiently simulate the different applications. The main conclusions of the applied models and modelling activities are summarized in the present Chapter.

7.1.1 LHTES systems

In Chapter 3, the silicon solidification/melting behavior at ultra-high temperatures (~1410-2000 ^{o}C) inside a LHTES system has been studied by covering several aspects from a design and operational perspective. This system is part of a compact heat-to-electricity device that is recently under development. The applied methodology combines an adaptive local grid refinement technique with the enthalpy porosity approach and the volume of fluid method in order to model the three-phase flow (molten/solid PCM and inert gas) inside the novel LHTES. The model takes into account the a) PCM volume change – important to identify any pressure increase inside the vessel, b) buoyancy driven natural convection, c) possible dendrites formation effect on the PCM melting and d) heat losses from the vessel sidewalls. The model has been validated against numerical and experimental data retrieved from the literature, for paraffin wax melting at low temperatures (~27 ^{o}C) and then verified against a theoretic model for silicon solidification at ultra-high temperatures (~1410 ^{o}C).

From a numerical point of view, several valuable results have been extracted. First of all, the superiority of the local grid refinement over fixed grids, both in terms of efficiency and accuracy, has been unveiled. A reduction in simulation time of almost 85 % is achieved when the refined grid is applied in comparison to the dense fixed one; both grids have the same resolution near the solid-liquid and gas-PCM interfaces and eliminate numerical diffusion, in contrast to the coarse grid. Secondly, the strong effect of the mushy zone parameter, which is dependent on the PCM structure, on the melting rate has been highlighted. The physical interpretation of this result is that the highest this parameter the smallest the secondary dendrites arm spacing formed inside the PCM and therefore the lowest it's melting rate. On top of that, it has been possible to implicitly represent the effect of the dendritic structured formation within the mushy zone, through the dynamically refined grid. Finally, it has been revealed that with the enthalpy porosity method, the floating/sinking of the solid PCM inside its molten phase is represented indirectly–and not directly as widely misunderstood - through the liquid motion, which depending on its upward or downward motion forms accordingly the melting front shape. In a future model reformulation, this natural phenomenon of floating/sinking should be modelled explicitly, by taking into account the solid motion, for its more realistic representation of the phenomenon evolution.

From a design perspective, one of the key challenges of this storage system lies on the identification of the optimum size/shape and operating conditions that can enable high charge/discharge cycles. For this reason, different container sizes and shapes, i.e. cube, sphere, cut-off sphere, truncated cone and cube, and heating/ cooling conditions at the walls have been tested. It has been revealed that during melting process, if the heating of the container is from its sidewalls, as for instance in a P2H2P (power-to-heat-to-power) concept, the heated surface plays an important role on the PCM melting rate. Specifically, the cubic shape results in the highest melting rate, approximately 25 % higher than the one achieved in the sphere, due to its biggest heated surface. On the other hand, the spherical shape is expected to have the lowest lateral thermal losses and thermal stresses during solidification and storage period, but is not a practical solution to be integrated

into a compact heat-to-electricity device. The most practical solution in terms of melting rates, heat losses and design flexibility is the truncated cone. Finally, it has been observed, that the silicon melting time is further reduced by 31 %, when the Stefan number increases by 35 %.

As a further step, the validated CFD model has been used to evaluate the performance of the silicon-based UHT-LHTES system during its charging/ discharging and storage period by taking into account the thermal losses effect. The storage tank of this system has a volume equal to V= 8.33e-04 m^3. In order to optimize its operation, i.e. eliminate lateral heat losses, maximize power output and achieve high charge/ discharge rates, different insulating materials of a thermal resistance within the range R_{th}=0.11-4.8 $m^2 \cdot K \cdot W^{-1}$ have been tested. Apart from this, different geometries (truncated cone and cylinder) of different volumes and heights have been tested, as well; in the case of the truncated cone, its height has been modified by altering its tapering ratio. From the numerical analysis it has been revealed that the vessel TR parameter and height have a low to moderate effect on the system heat losses, as long as a sufficient insulation is imposed at the system walls, i.e. R_{th} ~2 $m^2 \cdot K \cdot W^{-1}$. Specifically, the total amount of losses during the PCM solidification phase are equal to ~223 kJ and ~ 158.2 kJ for the truncated-cone with a tapering ratio equal to 0.45 and 0.225, respectively. Such values correspond to a ~ 3.7% and ~2.6% ratio of the total losses to the initial energy stored (~ 6 MJ) of the system. During charging, a small effect of the TR on the system losses has been noticed – the ratio of total losses to incoming energy is less than 1% for all cases studied. As regards charge/ discharge rates, an important effect of the TR has been noticed. More specifically, when the tapering ratio of the vessel increases then the solidification, time increases, respectively, whilst the opposite trend is observed during charge phase. A geometry with the same volume, but lower TR (0.225), solidifies quicker than that with TR=0.45; the solidification time in the first case is almost 17 % lower than in the second case. A trade-off between the system charge and discharge rates leads to the conclusion that the truncated-cone with the TR, between 0.225-0.45 is the optimum solution to be constructed among the geometries tested. Last and foremost, the tank volume significantly influences its total energy storage capacity; the specific vessel can be used for storage for up to two days, before it loses its contained energy in the form of latent heat. In summary, building a highly efficient heat storage block aimed to be integrated in a power-to-heat-to-power system means considering a vessel with short length, low lateral surface area to volume ratio, proper insulating method (of $R \approx 2$ $m^2 \cdot K \cdot W^{-1}$) and a tapering ratio, between 0.225-0.45.

Finally a sensitivity analysis on the PCM (silicon) material properties (i.e. latent heat of fusion, specific heat capacity, mushy zone variation and thermal conductivity) effect on the heat storage block charging time have been presented. Results have revealed that by increasing the latent heat by a factor of two the heat storage block charging time increases almost 30 %. This fact demonstrates the high effect of the PCM latent heat on its melting time. On the contrary, a small effect of the specific heat capacity on the numerical results has been observed. An increase in the specific heat by almost 50 % results in a small increase in the heat storage block charging time, i.e. 7 %. A small effect of the mushy zone range on the numerical results has been also observed. More specifically, increase of ΔT from 2 to 20 K results in a change in the melting time less than 10 %. In general, increase of the mushy region promotes the melting of the PCM. Finally, the sensitivity analysis has shown a great influence on the charging time with the thermal conductivity k. More specifically, a study case with k_s, k_l=20 $W \cdot m^{-2} \cdot K^{-1}$ requires almost double the time for the PCM to melt in comparison to cases k_s, k_l=180 $W \cdot m^{-2} \cdot K^{-1}$ and k_s=60, k_l=180 $W \cdot m^{-2} \cdot K^{-1}$. A reduction by 25 %, when the k is increased from 20 $W \cdot m^{-2} \cdot K^{-1}$ to 60 $W \cdot m^{-2} \cdot K^{-1}$ (66% increase), is also noticed. Another conclusion drawn is that during melting process the thermal conductivity of PCM liquid phase influences more the charging time than the thermal conductivity of solid phase, especially after melting starts to occur.

It should be noticed that the conclusions drawn in this analysis are for the specific designs tested, volume, or volumes close to the one examined and for the specific insulating materials used. For scaled-up geometries, there is a room in the future to carry out a series of parametric studies to deliver general conclusions, i.e. dimensionless correlations applicable for both large and small-scale systems.

7.1.2 TCES-CaL and SHS in FB systems

In this Thesis, 3-D transient CFD tools based on the Eulerian-Eulerian MFM/TFM approach have been developed to simulate gas-solid fluidized bed systems from bubbling to circulating regimes.

7.1.2.1 1 MW_{th} CFB carbonator

More specifically, Chapter Four describes the simulation activities for a 1 MW_{th} pilot-scale CFB carbonator (of a total height of around 8.6 meters), located at the premises of TUDA. Numerical results of the developed CFD model have been compared and evaluated against available experimental data for i) the axial pressure distribution along the riser and, ii) the carbon dioxide concentration at the carbonator exit. The reproduced flow patterns at several slices in the reactor have been also assessed and cross-verified based on experimental observations. In essence, this pilot unit operating under isothermal conditions has been used as a reference to primarily validate the in-house EMMS scheme for the operating conditions of a typical circulating fluidized bed. Without loss of generality the developed model can be used for the simulation of CFB reactors operating with or without any chemical reaction at several scales (from lab to industrial scale). The added value of validating the developed models with experimental data based on pilot scale units is highlighted.

More specifically, the carbonator simulation process has revealed that the advanced EMMS model coupled with the TFM reproduced results of higher accuracy, when compared to the corresponding one by the homogeneous Gidaspow for a CFB reactor. Moreover, unlike the Gidaspow model with the EMMS model a relative low grid dependency in the range of norm error 6.5% is achieved. This fact can boost the application of such a model for industrial-scale reactors with a relatively coarse mesh of up to d_{cell}/d_p~500. The value of the specularity coefficient φ at the walls - 0 for perfect specular collisions to 1 for perfectly diffuse collisions- has a negligible effect on the overall pressure drop, but a value of 0.01 seems to qualitatively reproduce better the core-annular flow, which implies a more dilute flow in the reactor core and higher volume fractions near the reactor walls. Concerning the reaction kinetics, the value of the carbonation reaction rate is affected by the heterogeneous conditions in each computational cell, especially close the dense bottom zone of the riser. The reaction rate implemented based on the work of Hawthorne et al. gives results of high accuracy concerning the CO_2 concentration with a relative error of 7.22 %, while the assumption of homogeneous conditions inside each control volume for the calculation of the carbonation reaction rate may limit the accuracy of the model. This shows once more the importance of reproducing the heterogeneous formations with a high level of accuracy, by applying an appropriate drag force model as the EMMS model utilized in this Thesis. In essence, the drag-force model is at the core of the CFD simulations of FB systems, since it subsequently affects heat transfer and reaction kinetics.

Supplementary to the TFM-EMMS model development and validation, but with a critical impact for the research community is the optimization of the CFB carbonator design, general principles of which can be applicable to other types of reactive flows inside FB reactors, such as oxy-combustion, chemical looping etc. For the purpose of this analysis, the validated 3D TFM-KTG model has been implemented for different design/ operation concepts of the CFB reactor. All the test cases simulated are retrofitting concepts of a reference design, i.e. the original 1 MW_{th} carbonator reactor located at TUDA, which mainly includes in

the riser section two inlet ports for the solid streams, i.e. one from the an internal loop and another for the regenerated material coming from the calciner unit. This reactor riser has a uniform diameter across its height and all of the solids inlets are close to its bottom bed section. The retrofitting concepts studied are a fat bottom design (FBD) with two different setups of the solids inventory, i.e. 282 kg (reference value) and 340 kg, a sorbent staging design (SbS) and a sorbent in splash zone design (SZD). The numerical results have shown that with all the retrofit cases a better CO_2 capture efficiency is achieved compared to the reference design. More specifically, the highest capture is achieved in the FBD concept for both solid inventories used; in the FBD-282 kg and FBD-340 kg cases the capture efficiency is equal to 90.36 % and 91.91 %, respectively, close enough to the CO_2 equilibrium capture efficiency (93.33 %). In the SbS and SZD cases the capture efficiencies are 89.94 % and 88.7 %, values higher than the reference design (87.03 %), mainly because a better mixing is achieved in the lower part of the reactor, i.e. bottom and splash zone. As concerns the flow hydrodynamics, in the FBD-282 kg case the flow tends to be homogeneous for heights greater than 0.8 m (the fat bottom extends up to a height equal to 1 meter). In the SbS and SZD cases the gas-solid flow pattern is quite similar to the reference design. Even if the FBD case seems the most promising among all, in terms of CO_2 capture efficiency, the SbS design is the most attractive solution, because apart from the higher capture efficiency achieved with regard the reference design, it can be more easily considered as a retrofit concept. Among, the improvements investigated the sorbent staging idea could be implemented without serious technical complications in larger scale units to boost the efficiency of the carbonator. Based on this analysis, it is highlighted once more as in the LHTES study that the system design flexibility is an important aspect that should be seriously taken into account during a design optimization process.

7.1.2.2 20 MW_{th} CFB carbonator

The up-scaling on the 1 MW_{th} carbonator unit to the scale of 20 MW_{th} unit has been also assessed by means of the developed CFD tool. Two design concepts have been tested; a base case in which the regenerated material is inserted into the unit exclusively from the loop seal that is used for the interconnection of the calciner and carbonator reactors, namely LS_from_calciner, and a SbS design concept, in which 10% of the regenerated material is injected from a higher height than the LS_from_calciner and 90% is injected from the LS_from_calciner. The numerical results have shown that in the scaled-up 20 MW_{th} carbonator unit the capture efficiency for the SbS design is nearly equal –less than 1% higher- to the baseline design, contrary to the results of the pilot scale 1 MW_{th} carbonator unit, in which a higher capture efficiency is achieved in the SbS design than the baseline case. One possible explanation to this is that the height from which 10% of the regenerated material is injected into the unit is quite close to LS_from_calciner. This fact intervenes to the flow pattern we want to create in a sense that the regenerated material is not effectively split as it was previously achieved in the 1 MW_{th} carbonator unit. Thus, the SbS concept should be further examined for the 20 MW_{th} –and of similar scale- unit as for the 1 MW_{th} unit it has been revealed that it seems to be a very promising concept in terms of CO_2 capture optimization.

7.1.2.3 1 MW_{th} oxy-fired calciner

Concerning the three-phase flow (gas-sorbent-fuel) inside the oxy-fired 1 MW_{th} pilot scale calciner (of total height of around 11 meters), a 3D CFD model based on the MFM approach has been utilized to perform numerical calculations. The numerical results have been compared and evaluated against available experimental data for i) the pressure and temperature distribution along the reactor and, ii) the O_2 and CO_2 concentrations at the calciner exit, all provided by experimental campaigns carried out in the same reactor. A modified version of the KTGF with a generic C code has been applied for more than one solid phases,

whilst the advanced EMMS scheme with a new cluster correlation, already validated in the carbonator unit of the same DFB facility, has been incorporated into the CFD model. Both the char and calcination mechanisms have been investigated, whilst the calcium oxide re-carbonation reaction has been also applied in order to evaluate if the reverse reaction takes place inside the reactor, affecting the maximum carbonation conversion of the sorbent. The latter mechanism that has been included into the model, is of critical importance for such a type of reactor not previously explored by means of an advanced numerical model. Simulation results indicate that the applied CFD model is of moderate accuracy, especially concerning the predicted O_2 values (with an error of almost 31 %) and a relatively good accuracy concerning the CO_2 values (with an error of around 12 %). Numerical predictions of the currently applied model can be further enhanced if more realistic kinetic parameters are used for the specific sorbent and fuel modelled in the future. Added to this, the EMMS model for the binary mixtures can be developed in the future to increase the model accuracy, especially if a denser flow is simulated. Regarding the calcination of calcium carbonate, results indicate that the reaction occurs at heights over the area where the fuel is burnt. For lower heights, i.e. near the bottom bed and up until a height of 4 meters re-carbonation of the produced calcium oxide is favoured owing to the low temperature values, mainly because of the cold gas stream entering the reactor from the distributor and auxiliary burner section. Finally, from the velocity streams it can be inferred that no back-mixing of the sorbent phase is observed except for a small area (up until a height of 0.4), where only carbonation occurs. Thus, in the particular reactor modelled, there is no propensity of entrapping the solid particles in multiple carbonation-calcination cycles. However, under different operating conditions/reactor designs the sorbent particles might be trapped in areas where both carbonation and calcination reactions are favoured. Such patterns of multiple carbonation-calcination cycles will eventually decrease the overall sorbent activity before this re-enters back to the carbonator and should be seriously taken into account in similar reactors.

7.1.2.4 300 kW_{th} indirectly heated BFB calciner

Following the calcination model validation in the oxy-fired 1MW_{th} calciner and the EMMS model validation in the 1 MW_{th} carbonator, a transient 3D CFD is applied for the simulation of an indirectly heated 300 kW_{th} calciner located, as well, at the premises of TUDA. The indirectly heated calciner absorbs heat by sodium filled heat pipes in a staggered arrangement. The used model includes the TFM-KTGF-EMMS modelling approach for the simulation of the two-phase flow (gas-sorbent) inside the calciner, as well as the effect of turbulence on the overall heat transfer process and flow hydrodynamics. An add-on of this model with regard the previous ones used to simulate the DFB 1 MW_{th} facility, is the inclusion of radiative heat transfer from the heat pipes to the bubbling bed and inside the reactor. A quasi-2D domain has been also used to speed-up the numerical simulation and facilitate a sensitivity/multi-parametric analysis owing to the high computational grid required to capture the demanding geometry of the indirectly heated calciner. Validation of the used model has been achieved against experimental data by acquiring a good prediction accuracy of the CO_2 mass fraction (relative error ~6.00 %) at the reactor exit and a moderate prediction accuracy of the overall heat transfer rate from the sodium filled pipes to the BFB (relative error ~23.00 %). A sensitivity analysis has been carried out to assess the effect of the near wall treatment, and thus the prediction of the thermal boundary layer, (i.e. standard wall functions, enhanced wall treatment, non-equilibrium and scalable wall functions) and the use or not of turbulence model on the overall heat transfer rate from the heat pipes to the bubbling bed. Three grid densities – with a d_{cell}/d_p ratio equal to ~220, ~110, and ~55, respectively- have been tested for a reference case where k-ε model was used with an enhanced

wall treatment. It has been revealed that the k-ε model with an enhanced wall-treatment can lead to an almost grid independent solution for a d_{cell}/d_p~110.
Following the model validation, a parametric study on the heat pipes arrangement effect on the overall heat transfer rate has been carried out. The analysis has revealed that both the lateral inter-tube space and the heat pipes arrangement (staggered vs. in-line) affects the overall heat transfer rate. Generally, use of a lateral distance between the heat pipes in the range of 1.5-2 d is a good option for an enhanced heat transfer. Concerning the comparison of the in-line with the staggered arrangement, it can be concluded that the staggered arrangement results in a higher heat transfer rate (by 7 % higher) than the in-line arrangement. The developed model is efficient and accurate and can help to study similar granular based TCES/SHS systems.

7.1.2.5 Industrial BFB HE

In Chapter Five, the transient 3D CFD model based on the TFM model has been utilized to simulate an integrated BFB heat exchanger of an industrial CFB boiler. The model has been utilized to model the heat transfer process from the bubbling bed to the steam filled tube buddles, which are in a staggered arrangement. This HE serves as a superheater, but can be used as well as an internal storage system that can give or take heat from heat pipes. Simulation of such an exchanger is demanding, due to its complex geometry, owing to the presence of the heat pipes, which are modelled explicitly in the present Thesis to increase the model accuracy. Based on the results the flow hydrodynamics are represented with an acceptable accuracy. In this regard, use of the Cutcell grid method can be applied in order to construct the demanding computational grid. This is of high importance to accurately predict the heat transfer rate near the tubes. Based on a preliminary analysis (with a mean steam temperature imposed at the HE wall boundaries, equal to 538 ^{o}C) the total heat transfer rate is almost equal to 2.3 MW_{th}. By imposing a more appropriate boundary condition and using the heat transfer model constructed in this Thesis the total heat transfer rate is equal to 2.7 MW_{th}, which is closer to what is expected. Results of this model, mostly concerning flow hydrodynamics, can feed theoretical models in order to carry out a sensitivity analysis of several parameters effect on the overall heat transfer coefficient by saving up computational time.

7.1.3 Comparison of TES systems

Finally, Chapter Six has given a summary of the studied systems (FB-SHS, TCES-CaL and Si-based LHTES) in terms of design aspects, storage medium used and charging potential. All in all, all of the TES systems studied in the current Thesis, present several advantages and seem promising for thermal energy storage at high/ ultra-high temperatures (> 800-900 ^{o}C) and can be chosen depending on the targeted application. Such systems will help unlock higher energy densities and storage efficiencies with respect to state-of-the-art molten salt based systems. The numerical models developed in turn in the specific Thesis, can be utilized to deliver several technical parameters of interest (charging/discharging rates, storage capacity, storage efficiency and charging time etc.) for the different types of technologies –these and similar ones. Optimization of such systems in terms of design and operation can be also achieved by utilizing the advanced numerical tools currently presented. Finally, the CFD model results can feed other types of reduced order models (e.g. feed process models with species concentrations, temperature/pressure profiles, particle loadings) to enhance their predictions accuracy, they can be coupled with stress-strain models (2D/3D pressure/temperature distribution) to verify if possible cracking of the studied systems might occur or even feed advanced decision making multi-criteria analysis tools.

7.2 Numerical advancements

In the present Thesis, several numerical advancements has been achieved concerning the sensible/TCES granular based storage, latent heat storage and heat exchange systems simulation.

Concerning the granular based systems the numerical advancements are summarized as follows:

- An improved version of the drag-coefficients EMMS scheme has been integrated into the MFM/TFM model, by using an interpolation procedure. The model can be applied for the transient simulation of several FB systems from circulating to bubbling mode, for both Geldart A and Geldart B particles. In this new version of the EMMS model, a new correlation for the prediction of the cluster size has been proposed that takes into account the limitation that the riser diameter poses to the clusters size. This sub-grid model has been solved by using an in-house code in FORTRAN.
- The developed CFD model simulates flow hydrodynamics inside the multi-phase flow systems, but also reaction kinetics and the transient evolution of the heat transfer, not widely addressed in common FB simulations.
- Several applications (reactive, non-reative) have been studied and validation of the models has been achieved based on experimental data from pilot scale campaigns (in the scale of 300 kW_{th}-1 MW_{th}).
- Regarding the carbonation reaction of calcium looping process, a reaction rate correlation drawn from the literature has been implemented. The strong dependence of the reaction rate and subsequently of the carbon dioxide capture on the hydrodynamics of the flow has been investigated. The gas-solid contacting effect on the CO_2 capture efficiency is an important criterion, whose importance has also been revealed in other works [339].
- Regarding the calciner reactor, CFD models for both oxy-fired and indirectly heated conditions have been applied. The model of the indirectly heated calciner, can be also applied in the future for calciners heated with solar energy.
- For the oxy-fired calciner, an important aspect modelled in this Thesis is the recarbonation of CaO, not done in other works, when the temperature inside the reactor favors such reaction. Several important outcomes can be extracted for the simulation of such phenomenon (e.g. possible entrapping of the solid particles in areas inside the reactor where multiple carbonation-calination cycles are done).
- In the indirectly heated calciner, the heat transfer through radiation has been included into the model, whereas the effect of turbulence has been assessed. The flow around the heat pipes has been studied, whereas a scaled-up HE has been also studied.

The novelties addressed concerning the LHTES are as follows:

- ✓ A transient axisymmetric CFD model has been developed in ANSYS Fluent platform to simulate the solidification/melting process of PCMs covering a wide spectrum of temperature values (from low to ultra-high temperatures).
- ✓ The applied model combines advantages of i) the fixed grid based enthalpy porosity method that implicitly models the solid/liquid PCM interface, ii) the VOF method that models the gas-PCM flow (if the PCM vessel contains apart from the PCM a gas medium at the top) and iii) an adaptive local grid refinement technique.
- ✓ The developed CFD model takes into account the PCM volume/expansion contraction during its solidification/melting process for a more realistic flow field (usually neglected in similar CFD

models in the literature), the thermo-physical properties variation from the liquid to solid phase and vice versa and vessel lateral heat losses.

- ✓ The CFD model can implicitly model the dendritic formations in a PCM near the "mushy" region. High accuracy in the resresentation of this area is achieved by applying the adaptive local refinement technique.
- ✓ The developed model has been proven to be of high accuracy and efficiency –based on several numerical tests- and can act as a valuable tool towards the design and operation optimization of this and similar latent heat storage systems operating at ultra-high temperatures.

7.3 Future work

Future numerical advancements in by taking as a reference this Thesis include:

As regards the granular material:

- Development of CFD models for the simulation of novel fluidized encapsulated PCMs that combine the advantages of both the granular material and PCMs.
- Application of artificial based intelligence models for scale-up of the studied systems, as for instance ANN-EMMS model.
- Extension of the numerical work with the EMMS in other regimes, such as dilute/dense downer reactors. Development and validation of a generalized version of the EMMS model for poly-dispersed systems.
- Development of a sub-grid heat transfer model and coupling with the EMMs model. This proposed advancement is of high importance for FB systems simulations, since the state-of-the-art heat transfer models include indirectly the flow heterogeneity into their predictions and are highly dependent on the CFD model results at each time step and partially on the grid density. A sub-grid heat transfer model that is solved in conjuction with the EMMS model (e.g. evolution of Kunii and Levenspiel model and integration into EMMS model) will lead to a grid indepented numerical model that can be applied for the simulation of large scale systems.
- Development of hybrid numerical models for the simulation of FBs, apart from the state-of-the-art Eulerian-Eulerian model, such as the DDPM model. The latter approach requires extra coding development and validation against experiments.

As regards the LHTES systems a follow-up of this numerical work can include:

- Explicit simulation of dendrites formation in LHTES systems including alloys.
- Explicit simulation of the natural phenomenon of floating/sinking, by taking into account the solid motion, for a more realistic representation of the flow patterns inside the LHTES system. Development in 2D domains can be a starting point for such type of advancement.
- Inclusion of surface tension effect between the inert gas and the PCM inside the LHTES system.
- Inclusion of radiation phenomena and validation with experimental measurements for ultra-high temperatures, inside the PCM.
- Inclusion of possible reactivity of the PCM with any gas at the top.

Εκτεταμένη Περίληψη της Διδακτορικής Διατριβής στην Ελληνική Γλώσσα

ΚΕΦΑΛΑΙΟ 1 Εισαγωγή

1.1 Υπάρχουσα κατάσταση του ενεργειακού μίγματος

Ο άνθρακας έχει αποτελέσει τη μεγαλύτερη πηγή παραγωγής ηλεκτρικής ενέργειας για αρκετές δεκαετίες. Το 2020, το ποσοστό παραγωγής ηλεκτρικής ενέργειας με καύση άνθρακα έφτασε το 35,2 % [2]. Ωστόσο, η καύση άνθρακα έχει ως αποτέλεσμα την παραγωγή επικίνδυνων ρύπων για το περιβάλλον. Πριν από το 2019, το σενάριο «Καθαρές Μηδενικές Εκπομπές έως το 2050» (NZE) απαιτούσε μια παγκόσμια μείωση στην κατανάλωση άνθρακα [2]. Η πανδημία Covid-19 είχε πλασματικό αρνητικό αντίκτυπο στη ζήτηση ενέργειας το 2020 και, ως εκ τούτου, στην κατανάλωση ορυκτών καυσίμων, μειώνοντας τις παγκόσμιες εκπομπές CO_2 κατά 5,2% (**Εικόνα 1**). Η μετά Covid-19 εποχή ωθεί την παγκόσμια οικονομία να βασίζεται σε μεγάλο βαθμό στην καύση άνθρακα, λόγω της σημαντικής αύξησης της ζήτησης ενέργειας, γεγονός που οδηγεί σε αύξηση των εκπομπών αερίων του θερμοκηπίου. Πιο συγκεκριμένα, οι παγκόσμιες εκπομπές CO_2 που σχετίζονται με την κατανάλωση ενέργειας και τις βαριές βιομηχανίες αυξήθηκαν κατά 6% το 2021 σε 36,3 γιγατόνους (Gt). Οι εκπομπές CO2 το 2021 αυξήθηκαν σε περίπου 180 μεγατόνους (Mt) πάνω από το προπανδημικό επίπεδο του 2019. Η ποσότητα αυτή αναμένεται να αυξηθεί, καθώς η χρήση του άνθρακα εντάθηκε λόγω της αύξησης των τιμών του φυσικού αερίου στην Ευρώπη και τις ΗΠΑ.

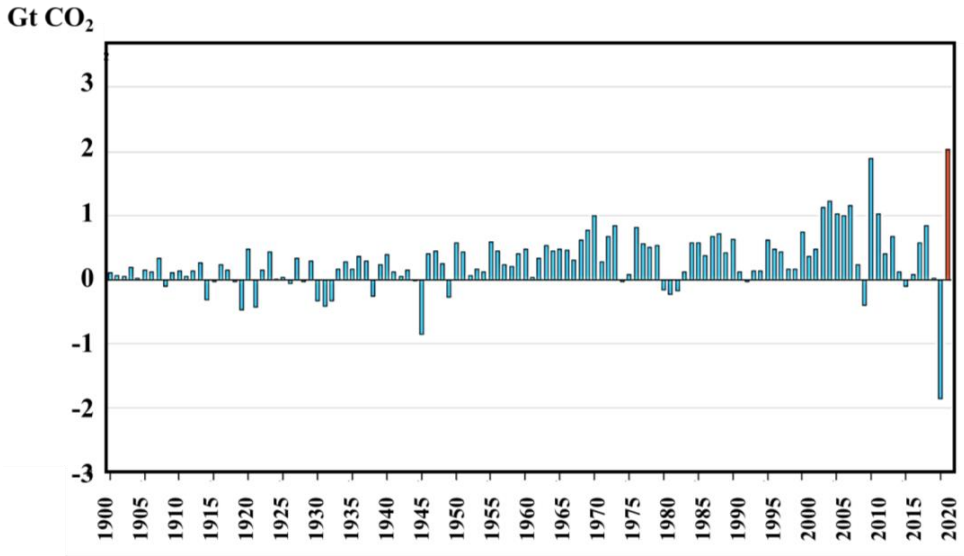

Εικόνα 1. Ετήσια αλλαγή εκπομπών διοξειδίου από την καύση ενέργειας και βιομηχανικές διεργασίες [1].

1.2 Δράσεις απανθρακοποίησης: ΑΠΕ και ο ρόλος της αποθήκευσης ενέργειας

Ο ουσιαστικός μετασχηματισμός του ενεργειακού συστήματος με την εφαρμογή δράσεων απαλλαγής από τις ανθρακούχες εκπομπές αποτελεί αναγκαιότητα για την εκπλήρωση του στόχου της ΕΕ να καταστεί μια οικονομία ουδέτερη ως προς τις ανθρακούχες εκπομπές μέχρι το 2050. Οι ενεργοβόρες βιομηχανίες και ο τομέας της ενέργειας βρίσκονται στην πρώτη γραμμή αυτού του μακροπρόθεσμου οράματος. Οι συγκεκριμένοι τομείς χαρακτηρίζονται από υψηλή ενεργειακή ένταση και ευθύνονται για μεγάλο μερίδιο των εκπομπών αερίων του θερμοκηπίου που παράγονται κυρίως λόγω της καύσης καυσίμων, της παραγωγής ηλεκτρικής ενέργειας και των εκπομπών από διεργασίες. Για όλους αυτούς τους τομείς μπορούν να εφαρμοστούν διάφορες δράσεις απαλλαγής από τον άνθρακα, όπως η δέσμευση, αξιοποίηση

και αποθήκευση του διοξειδίου του άνθρακα (CCUS), η χρήση ανανεώσιμων πηγών ενέργειας (ΑΠΕ) για την παραγωγή ηλεκτρικής ενέργειας αντί των ορυκτών καυσίμων και η αύξηση των ουδέτερων από άνθρακα καυσίμων στο μείγμα καυσίμων. Παρ' όλα αυτά, πολλοί τομείς έχουν εξαντλήσει τις προσπάθειές τους για τη μείωση των εκπομπών αερίων του θερμοκηπίου και τη βελτίωση της ενεργειακής τους απόδοσης, χωρίς να εκπληρώσουν τους στόχους τους. Από την άποψη αυτή, απαιτούνται καινοτόμες τεχνολογικές λύσεις για να προχωρήσουμε προς ένα μέλλον χωρίς εκπομπές διοξειδίου του άνθρακα.

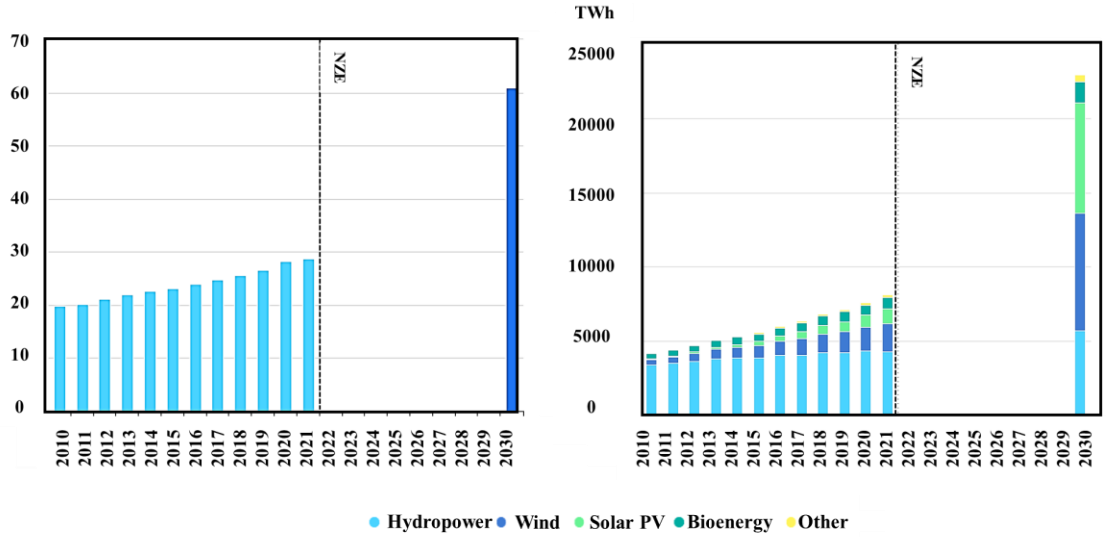

Εικόνα 2. Μερίδιο των ΑΠΕ στην ηλεκτροπαραγωγή στο σενάριο Net Zero α) συνολικά και β) ανά τεχνολογία, 2010-2030 [5].

Η υιοθέτηση των ΑΠΕ αποτελεί σημείο-κλειδί για τη μετάβαση στην καθαρή ενέργεια, η οποία αναπτύσσεται ραγδαία τα τελευταία χρόνια (**Εικόνα 2α**). Ο τομέας της ηλεκτρικής ενέργειας είναι ο πρωτοπόρος των ΑΠΕ, με το 28 % της παγκόσμιας παραγωγής ηλεκτρικής ενέργειας να βασίζεται σε ΑΠΕ το 2021 [6]. Ωστόσο, η ηλεκτρική ενέργεια αντιπροσωπεύει μόνο το ένα πέμπτο της παγκόσμιας κατανάλωσης ενέργειας και ο ρόλος των ανανεώσιμων πηγών ενέργειας και σε άλλους τομείς παραμένει κρίσιμος για την ενεργειακή μετάβαση. Μεταξύ των σημαντικών εναλλακτικών λύσεων ΑΠΕ, η ηλιακή και η αιολική ενέργεια είναι μία από τις λίγες τεχνολογίες χαμηλών εκπομπών άνθρακα που μπορούν να αναπτυχθούν σε μεγάλη κλίμακα, παρουσιάζοντας, ως εκ τούτου, υψηλό δυναμικό για την κάλυψη των παγκόσμιων ενεργειακών απαιτήσεων [7] (**Εικόνα 2β**). Η ηλιακή ενέργεια, συγκεκριμένα, φαίνεται ως ελκυστική επιλογή, λόγω του χαμηλού κόστους και της αφθονίας της σε σύγκριση με τις άλλες ΑΠΕ [8]. Ωστόσο, η ενέργεια που μπορεί να εξαχθεί από τον ήλιο ποικίλλει τόσο στο χώρο όσο και στο χρόνο [9]. Οι περισσότερες μορφές ΑΠΕ πρέπει να μετατρέπονται σε ηλεκτρική ενέργεια και να καταναλώνονται άμεσα. Αυτό κάνει την τρέχουσα οικονομία να εξακολουθεί να εξαρτάται από τα ορυκτά καύσιμα.

1.3 Σύγχρονα συστήματα αποθήκευσης θερμικής ενέργειας

Η αποθήκευση ενέργειας είναι απαραίτητη για τη βελτιστοποίηση της χρήσης των ΑΠΕ στο σημερινό ενεργειακό σύστημα. Πολλές διαφορετικές λύσεις αποθήκευσης ενέργειας βρίσκονται επί του παρόντος υπό ανάπτυξη και καλύπτουν όλα τα είδη τεχνολογικών επιλογών (ηλεκτροχημικές, μηχανικές, ηλεκτρικές, χημικές και θερμικές). Μεταξύ των διαφορετικών επιλογών αποθήκευσης ενέργειας, η αποθήκευση θερμικής ενέργειας (TES), δηλαδή η αποθήκευση της περίσσειας θερμικής ενέργειας με θέρμανση ή ψύξη ενός αποθηκευτικού μέσου για μεταγενέστερη χρήση, μπορεί να διαδραματίσει σημαντικό ρόλο στην

επίτευξη αυτών των στόχων και στην εξάλειψη της αναντιστοιχίας μεταξύ προσφοράς και ζήτησης της ενέργειας. Γενικά, τα συστήματα TES μπορούν να ταξινομηθούν σε τρεις κατηγορίες: συστήματα αποθήκευσης λανθάνουσας θερμότητας (LHTES), αισθητής θερμότητας (SHS) και θερμοχημικής θερμότητας (TCES) [11]. Μεταξύ αυτών των επιλογών, η SHS είναι η πιο ώριμη τεχνολογική επιλογή λόγω της απλής αρχής και του χαμηλού κόστους της, ακολουθούμενη από τα συστήματα LHTES και στη συνέχεια από τα συστήματα TCES, τα οποία χαρακτηρίζονται από υψηλότερες πυκνότητες αποθήκευσης ενέργειας από την SHS. Οι TES μπορούν να χρησιμοποιηθούν σε διάφορες πιθανές εφαρμογές, όπως η άμεση αποθήκευση ηλιακής ενέργειας (σε συστήματα CSP - συγκεντρωμένης ηλιακής ενέργειας-), η αποθήκευση ηλεκτρικής ενέργειας και η συμπαραγωγή σε οικιακά δίκτυα ηλεκτρισμού/θέρμανσης και η αποθήκευση ενέργειας σε συστήματα ανάκτησης θερμότητας κ.λπ.

Τα συστήματα TES διαφέρουν ως προς την ποσότητα θερμότητας που μπορεί να αποθηκευτεί ανά μονάδα όγκου αποθηκευτικού μέσου. Οι βασικές πτυχές σε αυτά τα συστήματα είναι η ενεργειακή πυκνότητα, ο ρυθμός φόρτισης/εκφόρτισης, το χρησιμοποιούμενο μέσο αποθήκευσης και η θερμοκρασία λειτουργίας. Όσον αφορά τα μέσα αποθήκευσης, υπάρχει μεγάλη ποικιλία ανάλογα με το εύρος της θερμοκρασίας λειτουργίας και τη στοχευόμενη εφαρμογή. Εκτός από τη φύση του τύπου αποθήκευσης που περιγράφηκε παραπάνω, οι TES ταξινομούνται επίσης ανάλογα με τη θερμοκρασία λειτουργίας σε TES χαμηλής θερμοκρασίας (<100 °C), μεσαίας θερμοκρασίας (100 °C≤θ≤300 °C), TES υψηλής θερμοκρασίας (300 °C≤θ≤900 °C) και πολύ υψηλής θερμοκρασίας (>900 °C). Ο **Πίνακας 1** παρουσιάζει μία σύγκριση των συστημάτων αποθήκευσης θερμικής ενέργειας.

Πίνακας 1. Σύγκριση συστημάτων αποθήκευσης θερμικής ενέργειας [12].

Μέθοδος αποθήκευσης	**Αποθηκευτική ικανότητα (kWh·ton^{-1})**	**Ισχύς (MW)**	**Απόδοση (%)**	**Χρόνος αποθήκευσης**	**Κόστος (€·kWh^{-1})**
Αισθητής	10–50	0.001–10	50–90	μέρες/μήνες	0.1–10
Λανθάνουσας	50–150	0.001–1	75–90	ώρες/μήνες	10–50
Θερμοχημική	120–250	0.01–1	75–100	ώρες/μέρες	8–100

1.4 Καινοτόμα συστήματα αποθήκευσης θερμικής ενέργειας

Πέρα από τις τρέχουσες λύσεις αποθήκευσης TES, μπορούν να παρατηρηθούν διάφορες νέες τάσεις για την ενσωμάτωση TES: (i) συζευγμένες τεχνολογίες TES για επίτευξη υψηλότερων θερμοκρασιών λειτουργίας (π.χ. SHS με TCES), (ii) συστήματα TES με νέα υλικά σε συμπαγή συστήματα, όπως παραδείγματος χάρην μεταλλικά υλικά αλλαγής φάσεως και (iii) συστήματα αποθήκευσης βασιζόμενα σε κοκκώδεις ροές. Ο σχεδιασμός τέτοιων συστημάτων απαιτεί εκτεταμένη έρευνα με τη χρήση συνδυασμού θεωρητικών μελετών, πειραματικών εκστρατειών και, απλουστευμένων και προηγμένων αριθμητικών μοντέλων. Τα εργαλεία υπολογιστικής ρευστοδυναμικής (CFD) μπορούν να συμβάλουν στην επιτάχυνση της διαδικασίας σχεδιασμού τέτοιων συστημάτων, ιδίως όταν υπάρχει ανάγκη βελτιστοποίησης του σχεδιασμού των εξαρτημάτων ενός συγκεκριμένου συστήματος και μελέτη των συστημάτων σε μεγαλύτερες κλίμακες (π.χ. βιομηχανικές).

1.5 Σκοπός της Διδακτορικής Διατριβής

Τα τελευταία χρόνια, οι τεχνολογίες αποθήκευσης αισθητής (SHS), λανθάνουσας (LHTES) και θερμοχημικής (TCES) θερμότητας χαμηλής/μέσης/υψηλής θερμοκρασίας αποτελούν ένα ερευνητικό θέμα αιχμής, το οποίο μελετήθηκε λεπτομερώς από διαφορετικές οπτικές γωνίες, συμπεριλαμβανομένων των κατάλληλων μέσων αποθήκευσης θερμότητας, των μέσων μεταφοράς θερμότητας, των δοχείων και της

συνολικής απόδοσης του συστήματος. Τα προηγμένα αριθμητικά εργαλεία βρίσκονται στον πυρήνα συλλογικών ενεργειών (συμπεριλαμβανομένων και πειραμάτων, τεχνοοικονομικών αναλύσεων, αναλύσεων κύκλου ζωής κλπ.) που αποσκοπούν στην προώθηση νέων τεχνολογικών λύσεων TES με βελτιστοποιημένο σχεδιασμό και απόδοση λειτουργίας. Στο πλαίσιο αυτό, το κύριο κίνητρο της παρούσας διατριβής είναι η ανάπτυξη, επικύρωση και εφαρμογή προηγμένων χρονικά μεταβλητών μοντέλων CFD, για την προσομοίωση καινοτόμων συστημάτων αποθήκευσης θερμικής ενέργειας με αισθητή, χημική και λανθάνουσα θερμότητα που εφαρμόζονται σε υψηλές και πολύ υψηλές θερμοκρασίες.

Τα συστήματα που εξετάζονται στην παρούσα διδακτορική διατριβή αποτελούν α) ένα καινοτόμο σύστημα αποθήκευσης ενέργειας υπό τη μορφή λανθάνουσας θερμότητας το οποίο εμπεριέχει πυρίτιο σαν υλικό αλλαγής φάσης και λειτουργεί σε πολύ υψηλές θερμοκρασίες (~1410 ^{o}C), β) ο κύκλος ασβεστοποίησης-ενανθράκωσης ο οποίος λειτουργεί σε υψηλές θερμοκρασίες (~650-900 ^{o}C) και μπορεί να χρησιμοποιηθεί για αποθήκευση ενέργειας υπό τη μορφή χημικής αντίδρασης και παράλληλη δέσμευση διοξειδίου του άνθρακα και γ) ένα σύστημα αποθήκευσης ενέργειας υπό τη μορφή αισθητής θερμότητας (~500-600 ^{o}C) το οποίο βασίζεται στη ροή κοκκώδους ροής υπό την μορφή φυσαλίδων και μπορεί να λειτουργεί είτε για αποθήκευση ενέργειας αλλά και ως εναλλάκτης θερμότητας. Ωστόσο η χρήση τέτοιων συστημάτων σε ευρεία κλίμακα απαιτεί εις βάθος γνώση διαφόρων μηχανισμών συναλλαγής θερμότητας και διαφόρων περίπλοκων ροϊκών φαινομένων. Η χρήση των εργαλείων υπολογιστικής ρευστοδυναμικής (computational fluid dynamics - CFD tools) μπορεί να βοηθήσει στην κατανόηση τέτοιων μηχανισμών, καθώς και στη βελτιστοποίηση τέτοιων συστημάτων, όσον αφορά τις συνθήκες λειτουργίας τους, αλλά και τον σχεδιασμό τους. Η ανάπτυξη των διαφόρων υπολογιστικών εργαλείων γίνεται στη παρούσα διατριβή σε εμπορική πλατφόρμα προσομοίωσης (ANSYS Fluent^{TM}) και όπου κρίνεται απαραίτητο χρησιμοποιούνται διάφοροι κώδικες σε γλώσσα προγραμματισμού C και FORTRAN, ώστε να εμπλουτιστούν και να βελτιωθούν από άποψη ακρίβειας. Επιβεβαίωση των αριθμητικών μοντέλων γίνεται με τη χρήση πειραματικών αποτελεσμάτων, τα οποία ανακτήθηκαν είτε από τη βιβλιογραφία, είτε από συνεργαζόμενα πανεπιστήμια/φορείς στα πλαίσια των ερευνητικών έργων, κατά την διάρκεια των οποίων εκπονήθηκε η διδακτορική διατριβή.

ΚΕΦΑΛΑΙΟ 2 Αριθμητικές μέθοδοι για συστήματα πολυφασικών ροών

2.1 Συστήματα κοκκώδους ροής

Στην περίπτωση των μονάδων ρευστοποιημένης κλίνης εφαρμόζονται ειδικά μοντέλα που προσομοιώνουν την πολυφασική ροή (κοκκώδες στερεό και αέριο), είτε κατά Euler-Euler (Two fluid model – TFM), είτε κατά Euler-Lagrange (Dense discrete phase model - DDPM). Στην παρούσα διδακτορική διατριβή χρησιμοποιείται η μέθοδος κατά Euler-Euler TFM. Η ακριβής μοντελοποίηση της αλληλεπίδρασης μεταξύ στερεών σωματιδίων και ρευστού βασίζεται σε μεγάλο βαθμό στο μοντέλο που χρησιμοποιείται για την οπισθέλκουσα δύναμη, δηλαδή την δύναμη που ασκείται στα στερεά σωματίδια κατά την ροή τους μέσα στο ρευστό. Για το λόγο αυτό εφαρμόζεται ένα καινοτόμο μοντέλο οπισθέλκουσας το οποίο προσεγγίζει τη ροή υπό διάφορες κλίμακες. Το μοντέλο αυτό ονομάζεται EMMS (Energy Minimization Multi-Scale Analysis) και τείνει να υπερισχύσει έναντι των συμβατικών μοντέλων οπισθέλκουσας (όπως αυτό του Gidaspow).

2.2 Υλικά αλλαγής φάσης

Στην περίπτωση των υλικών αλλαγής φάσης (phase change materials - PCMs) λαμβάνονται υπόψη οι μηχανισμοί μεταφοράς θερμότητας μέσω αγωγής και συναγωγής, η ανάπτυξη δενδριτικών μορφών κατά την στερεοποίησή τους, καθώς και η αλλαγή του όγκου τους κατά την αλλαγή φάσης αυτών. Το μοντέλο enthalpy porosity approach σε συνδυασμό με τη μέθοδο Volume of fluid (VOF) χρησιμοποιούνται για την προσομοίωση συστημάτων που βασίζονται σε υλικά αλλαγής φάσης. Κρίσιμη παράμετρος για την βελτιστοποίηση των συγκεκριμένων συστημάτων είναι οι απώλειες θερμότητας από τα τοιχώματά τους, οι οποίες αυξάνονται αντιστρόφως ανάλογα με τον όγκο τους, ενώ εξαρτώνται σε μεγάλο βαθμό και από το σχήμα που έχει το δοχείο αποθήκευσης του υλικού αλλαγής φάσης. Η χρήση μεθόδου τοπικής πύκνωσης του πλέγματος στην διεπιφάνεια αλλαγής φάσης μπορεί να οδηγήσει στην αύξηση της ακρίβειας των αποτελεσμάτων.). Επιπρόσθετα, άλλα στοιχεία που εξετάζονται είναι η επίδραση της μεταφοράς θερμότητας μέσω ακτινοβολίας (το συγκεκριμένο φαινόμενο χρήζει αξίας να μελετηθεί σε περιπτώσεις (α) ρευστοποιημένων κλινών αραιής ροής όπου η επίδραση μεταφοράς θερμότητας μέσω ακτινοβολίας μπορεί να είναι σημαντική, αλλά και σε (β) τύπους ρευστοποιημένων κλινών που αποθηκεύουν ενέργεια από τον ήλιο κλπ.). Στην τελευταία περίπτωση η επίδραση της ακτινοβολίας είναι πολύ σημαντική, καθώς τα αιωρούμενα σωματίδια απορροφούν ενέργεια από τους τοίχους της μονάδας οι οποίοι είναι είτε διαπερατοί στην ηλιακή ακτινοβολία (άμεση απορρόφηση ενέργειας) είτε αδιαπέραστοι (έμμεση απορρόφηση ενέργειας).

ΚΕΦΑΛΑΙΟ 3 Μοντελοποίηση υλικών αλλαγής φάσης

3.1 Πρόλογος

Ο στόχος της παρούσας ενότητας είναι να παρουσιάσει την αριθμητική μεθοδολογία και τα αποτελέσματα προσομοίωσης του πλήρους κύκλου φόρτισης-εκφόρτισης ενός καινοτόμου συστήματος αποθήκευσης ενέργειας υπό τη μορφή λανθάνουσας θερμότητας (UHT-LHTES) [27]. Συνολικά, το σύστημα αυτό αποτελεί μέρος ενός συνολικού συστήματος που εμπεριέχει επιπρόσθετα έναν υβριδικό θερμιονικό-φωτοβολταϊκό μετατροπέα (TIPV) για την μετατροπή της αποθηκευμένης θερμικής ενέργειας σε ηλεκτρική [275]. Το δοχείο αποθήκευσης ενέργειας που απεικονίζεται στην **Εικόνα 3**, εμπεριέχει καθαρό πυρίτιο ως υλικό αλλαγής φάσης (PCM) το οποίο κατά τη φάση φόρτισης, θερμαίνεται είτε από τα πλευρικά τοιχώματα και/ή από το πάνω μέρος φτάνοντας σε θερμοκρασίες πάνω από 900 ^{o}C. Εάν η θερμοκρασία στο εσωτερικό του δοχείου υπερβεί το σημείο τήξης του πυριτίου, δηλαδή τους1414 ^{o}C, το υλικό αρχίζει να λιώνει. Κατά τη διάρκεια αυτού του σταδίου, η άνοδος του υβριδικού μετατροπέα αποσυνδέεται από το σύστημα και το δοχείο αποθήκευσης ενέργειας είναι μονωμένο από την πλευρά του εκπομπού για την αποφυγή υπερβολικών απωλειών θερμότητας. Κατά την εκφόρτιση του συστήματος, η άνοδος του υβριδικού μετατροπέα συνδέεται με το σύστημα αποθήκευσης ενέργειας και μετατρέπει την εκπεμπόμενη ροή φωτονίων-ηλεκτρονίων σε ηλεκτρική ενέργεια.

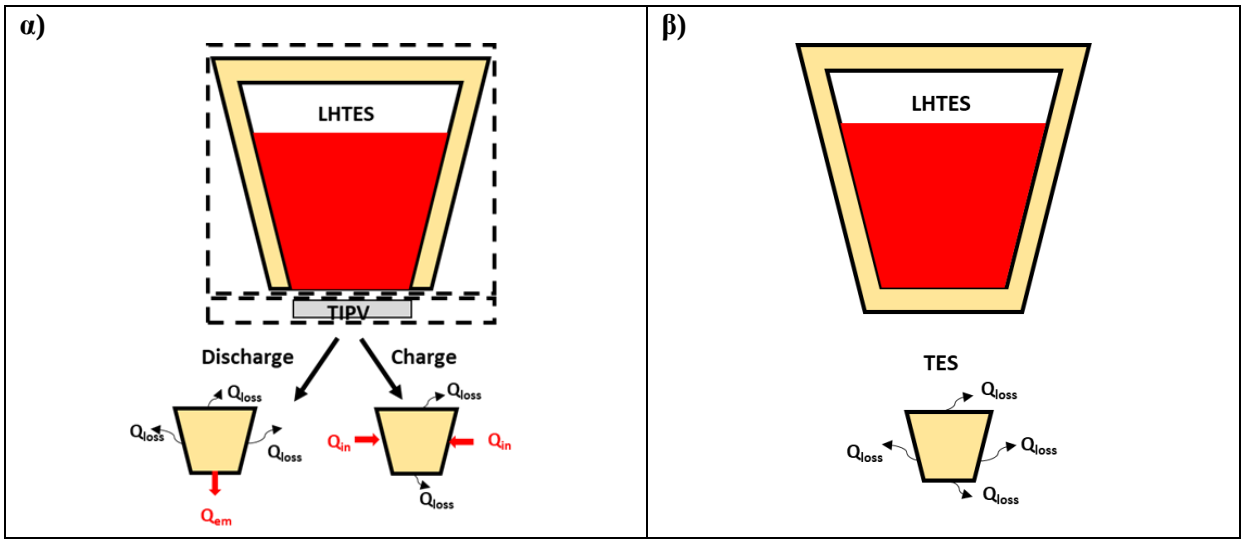

Εικόνα 3. Σύστημα LHTES-TIPV κατά τη διάρκεια a) φόρτισης/εκφόρτισης, β) αποθήκευσης.

Το καινοτόμο σύστημα LHTES-TIPV έχει περιγραφεί θεωρητικά στην εργασία των Datas et al. [275] και απόδειξη της ιδέας έγινε στο πλαίσιο του έργου AMADEUS [277]. Μέρος της αριθμητικής μελέτης που έγινε σε αυτή τη Διατριβή, έχει χρησιμοποιηθεί για τη μελέτη σχεδιασμού και βελτιστοποίηση αυτού του νέου συστήματος. Για τη μελέτη και τη βελτιστοποίηση του συστήματος αποθήκευσης ενέργειας, ένα προηγμένο αξονοσυμμετρικό μοντέλο υπολογιστικής ρευστοδυναμικής (CFD) εφαρμόζεται στην πλατφόρμα ANSYS Fluent (v17.1) [278]. Το μοντέλο CFD βασίζεται στην προσέγγιση ενθαλπίας-πορώδους [279] συνδυασμένης με το πολυφασικό μοντέλο VOF. Αρχικά, το μοντέλο επικυρώνεται με πειραματικά δεδομένα που βρίσκονται στη βιβλιογραφία [43, 219] για τη στερεοποίηση/τήξη κεριού παραφίνης σε χαμηλές θερμοκρασίες (~30 ^{o}C). Στη συνέχεια, το μοντέλο επαληθεύεται σε σχέση με ένα

1Δ αναλυτικό μοντέλο για τη στερεοποίηση πυριτίου μέσα σε ένα σφραγισμένο δοχείο σε πολύ υψηλές θερμοκρασίες (>1000 ºC) [232]. Η επίδραση πολύπλοκων φαινομένων λαμβάνονται υπόψην, όπως αυτά της μεταφοράς θερμότητας λόγω συναγωγής στο υγρό PCM και της ογκομετρικής διαστολής/συμπίεσης του PCM. Σε αυτό το σύστημα, το PCM καταλαμβάνει μέρος του δοχείου και, πάνω από το PCM, αέριο γεμίζει την υπόλοιπη περιοχή. Ως περαιτέρω βήμα, πραγματοποιήθηκε η βελτιστοποίηση σχεδιασμού του δοχείου αποθήκευσης με βάση το πυρίτιο λαμβάνοντας υπόψη τις πλευρικές θερμικές απώλειες. Η συνολική απόδοση του συστήματος αξιολογείται κατά τις περιόδους φόρτισης, εκφόρτισης και αποθήκευσης. Τέλος, παρουσιάζεται μια ανάλυση ευαισθησίας για τη διερεύνηση της επίδρασης των θερμικών ιδιοτήτων PCM στους ρυθμούς φόρτισης/εκφόρτισης του συστήματος.

3.2 Αριθμητική μέθοδος

Το τρέχον αριθμητικό μοντέλο βασίζεται στη μέθοδο ενθαλπίας-πορώδους (enthalpy-porosity approach) [40] για τη μοντελοποίηση της μετάβασης του PCM από την στερεά στην υγρή φάση και αντίστροφα. Με το συγκεκριμένο μοντέλο, ορίζεται μία ενδιάμεση περιοχή, η οποία αντιπροσωπεύει τη μετάβαση υγρού-στερεού και αντιμετωπίζεται ως «ψευδοπορώδες». Σε αυτή τη ζώνη, το ποσοστό της υγρής φάσης αυξάνεται σταδιακά από 0 (στερεό) σε 1 (υγρό) καθώς το υλικό λιώνει και αντίστροφα κατά τη στερεοποίησή του. Τέλος, η πολυφασική μέθοδος VOF [279] εφαρμόζεται για την προσομοίωση της κινούμενης διεπαφής PCM-αερίου. Οι κύριες παραδοχές που υιοθετήθηκαν είναι οι εξής [232]:

1. **Χρονικά μεταβαλόμενη** προσομοίωση **σε διδιάστατο αξονοσυμμετρικό** πεδίο;
2. Συμπερίληψη της **βαρυτικής δύναμης**;
3. Η ροή είναι **στρωτή, λόγω των χαμηλών αριθμών Reynolds;**
4. Η υγρή φάση του **PCM** αντιμετωπίζεται ως **ασυμπίεστο Νευτώνιο υγρό**;
5. Αμφότερες στερεές και υγρές φάσεις είναι **ομοιογενείς** και **ισότροπες**;
6. Οι θερμοφυσικές ιδιότητες του PCM και οι θερμικές ιδιότητες μόνωτικών υλικών εξαρτώνται από τις διακυμάνσεις της θερμοκρασίας;
7. Η πυκνότητα του PCM αλλάζει κατά τη μετάβασή του από στερεά σε υγρή φάση και αντίστροφα;
8. Το αδρανές αέριο αντιμετωπίζεται ως συμπιέσιμο ρευστό [278];
9. Η **μεταφορά θερμότητας μέσω ακτινοβολίας** μέσα στο δοχείο δεν λαμβάνεται υπόψην, όταν το PCM θερμαίνεται από τα πλευρικά τοιχώματα;
10. Τα τοιχώματα του δοχείου και τα μονωτικά υλικά μοντελοποιούνται είτε ως λεπτά τοιχώματα, λύνοντας μια 1Δ εξίσωση μεταφοράς θερμότητας μέσω αγωγής [278] είτε ως αδιαβατικά;
11. Η επίδραση **της επιφανειακής τάσης** μεταξύ των διαφορετικών φάσεων δεν λαμβάνεται υπόψην.

3.3 Επικύρωση μοντέλου (Στερεοποίηση/τήξη κεριού παραφίνης: Χαμηλές θερμοκρασίες)

Αρχικά, το μοντέλο CFD επικυρώνεται έναντι πειραματικών δεδομένων για τη διαδικασία στερεοποίησης/τήξης του κεριού παραφίνης, RT27, σε χαμηλές θερμοκρασίες, δηλαδή ~30 ºC, μέσα σε ένα σφαιρικό δοχείο ανοιχτό από την κορυφή. Τέτοια δεδομένα μαζί με τις κατάλληλες συνοριακές συνθήκες και συνθήκες λειτουργίας λαμβάνονται από την εργασία του Assis et al. [43], [282]. Κατά τη διαδικασία τήξης (στερεοποίησης), το δοχείο θερμαίνεται (ψύχεται) από τα τοιχώματά του, σχεδόν 10 ºC πάνω (20 ºC κάτω) από το σημερίο τήξης του. Κατά την επικύρωση του μοντέλου, διεξάγεται μια παραμετρική μελέτη σχετικά με την επίδραση της παραμέτρου A_{mush} στον ρυθμό στερεοποίησης/τήξης του PCM. Ένα σύνολο τιμών A_{mush} ίσο με [10^5, $5{\cdot}10^5$ and $2{\cdot}10^6$] και [10^5, 10^6 and 10^9] δοκιμάζεται κατά τη φάση της φόρτισης και εκφόρτισης, αντίστοιχα. Επιπλέον, η επίδραση της πυκνότητας του πλέγματος στα

αριθμητικά αποτελέσματα διερευνάται επίσης λαμβάνοντας ως αναφορά τη διαδικασία τήξης του PCM. Το επιλεγέν πλέγμα ακολουθεί τη μέθοδο αυτόματης τοπικής πύκνωσης δύο επιπέδων. Αυτό έχει ως αποτέλεσμα μέγιστο αριθμό κελιών ίσο με 11.133 και ελάχιστο μέγεθος κελιών ίσο με $1.07 \cdot 10^{-4}$ m.

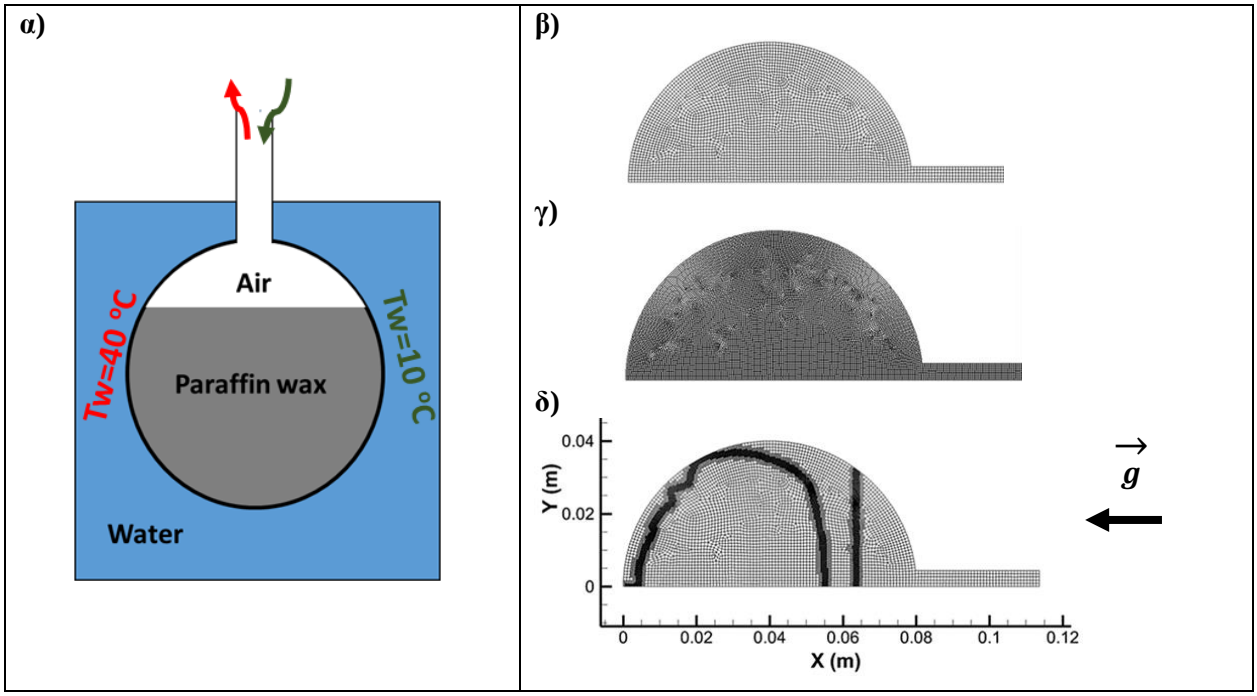

Εικόνα 4. α) 2Δ σχέδιο του δοχείου και διακριτοποίηση πεδίου με β) αραιό και γ) μεσαίο πλέγμα και δ) πλέγμα αυτόματης τοπικής πύκνωσης (2 επίπεδα πύκνωσης).

Το σφαιρικό δοχείο (**Εικόνα 4α**) είναι κατασκευασμένο από γυαλί και έχει εσωτερική διάμετρο ίση με 0,040 m. Αρχικά, το PCM γεμίζει το 85% του δοχείου (μελέτη τήξης) και το 96% του πεδίου (μελέτη στερεοποίησης). Για την επικύρωση του μοντέλου, χρησιμοποιήθηκε ένα αραιό πλέγμα 3.858 τετράπλευρων κελιών. Επιπρόσθετα, έγινε μελέτη ανεξαρτησίας πλέγματος συγκρίνοντας με ένα ενδιάμεσο και ένα πυκνό πλέγμα αποτελούμενων από 15,432 και 61,728 τετράπλευρα κελιά. Τέλος, για καλύτερη αναπαράσταση της διεπιφάνειας PCM-αερίου, αλλά και της διεπιφάνειας των δύο φάσεων του PCM, μία τεχνική αυτόματης πύκνωσης δύο επιπέδων (η οποία αναφέρεται ως 2Lev. ref.) χρησιμοποιείται, χρησιμοποιώντας κώδικες διαμορφωμένων από το χρήστη οι οποίοι βασίζονται στην εργασία του [94].

Η **Εικόνα 5α** συγκρίνει της χρονική μεταβολή του κλάσματος τήξης του μοντέλου CFD με τα αντίστοιχα πειραματικά και αριθμητικά αποτελέσματα των Assis et al. [43]. Το μοντέλο του Assis, το οποίο βασίζεται στη μέθοδο VOF με την προσέγγιση του πορώδους ενθαλπίας, χρησιμοποιεί πλέγμα 3,520 κελιών και σταθερό μέγεθος χρονικού βήματος ίσο με Δt=0.002 s. Η παράμετρος του κλάσματος τήξης που χρησιμοποιείται για τη σύγκριση υπολογίζεται ως ο λόγος μεταξύ της μάζας του υγρού PCM προς τη συνολική μάζα του PCM ($MFR = m_{liquid}/m_{PCM}$). Από το γράφημα αποδεικνύεται ότι για το μεγαλύτερο μέρος του χρόνου προσομοίωσης, τα αποτελέσματα του παρόντος μοντέλου συμπίπτουν με εκείνα του μοντέλου αναφοράς και είναι αρκετά κοντά στα πειραματικά δεδομένα. Μια μικρή απόκλιση περίπου ίση με 6 % μεταξύ των δύο μοντέλων, μπορεί να αποδοθεί κυρίως στον τρόπο προσδιορισμού του χρονικού βήματος. Στην παρούσα εργασία χρησιμοποιείται ένα μεταβλητό χρονικό βήμα με αριθμό courant ίσο με 0.2, σε αντίθεση με τη μέθοδο σταθερού χρονικού βήματος που υιοθετήθηκε στο μοντέλο των Assis et al. [43]. Επιπλέον, στην εργασία αναφοράς δεν υπάρχουν λεπτομέρειες σχετικά με τα σχήματα χωρικής και

χρονικής διακριτοποίησης και τη διατύπωση VOF (έμμεση ή ρητή), η επιλογή των οποίων μπορεί να επηρεάσει τα αριθμητικά αποτελέσματα.

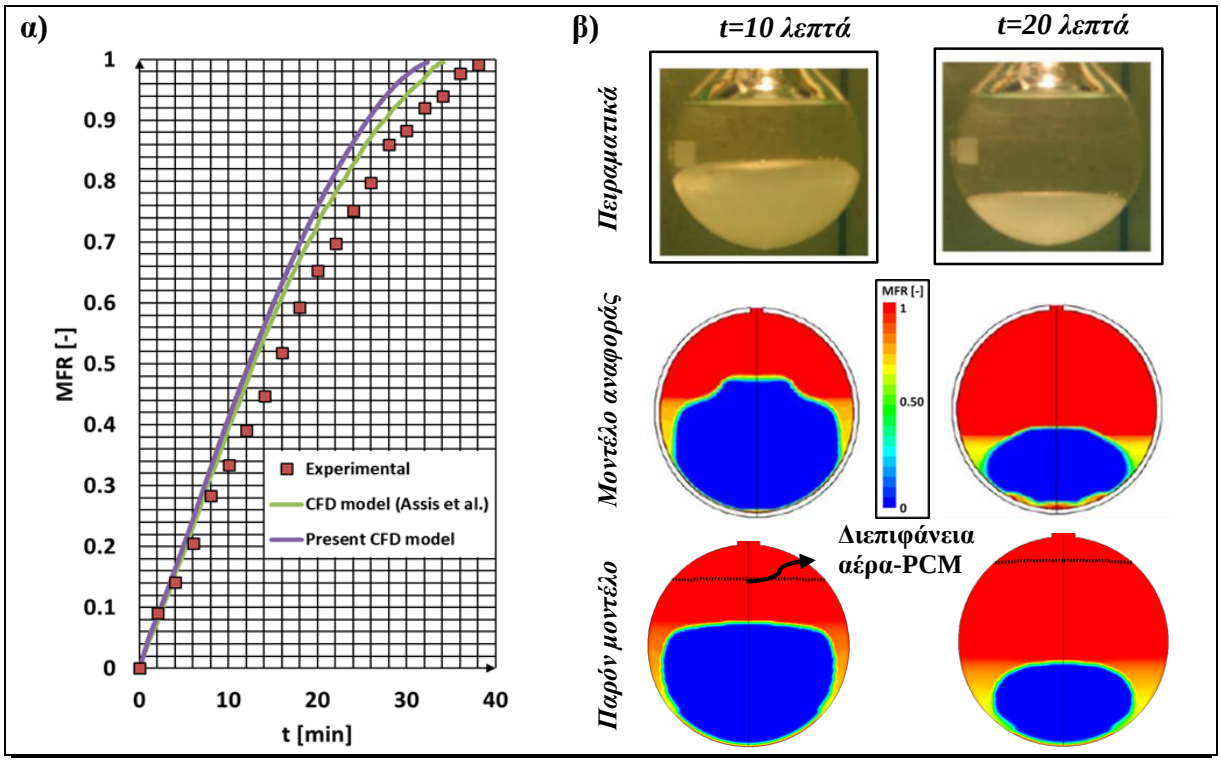

Εικόνα 5. α) χρονική εξέλιξη του κλάσματος τήγματος και β) contour κλάσματος τήγματος για *t*=10, 20 λεπτά (σύγκριση πειραματικών δεδομένων, του μοντέλου αναφοράς και του παρόντος μοντέλου).

Επιπρόσθετα, έχει πραγματοποιηθεί μία ποιοτική σύγκριση του παρόντος μοντέλου με τα πειραματικά και αριθμητικά αποτελέσματα των Assis et al. [43], όσον αφορά εποπτικές εικόνες του υγρού κλάσματος για δύο χρονικές στιγμές, t = 10 and 20 λεπτά. Όπως μπορεί να παρατηρηθεί από την **Εικόνα 5β**, ανάμεσα στο παρόν μοντέλο και το αντιστοιχο από το μοντέλο αναφοράς υπάρχουν παρόμοια ροικά φαινόμενα. Ωστόσο, με το τρέχον μοντέλο CFD, επιτυγχάνεται περιορισμένη αριθμητική διάχυση, ενώ τα μοτίβα του κλάσματος τήξης έχουν μεγαλύτερη ομοιότητα με τις πειραματικές απεικονίσεις των Assis et al. [43].

Από την **Εικόνα 6α** είναι προφανές ότι το μεσαίο, πυκνό και πλέγμα τοπικής πύκνωσης σχεδόν συμπίπτουν στα αριθμητικά τους αποτελέσματα, αποκαλύπτοντας ότι έχει επιτευχθεί ανεξαρτησία πλέγματος Από την άλλη πλευρά, το αραιό πλέγμα οδηγεί σε πιο αργή τήξη του PCM -σχεδόν δύο λεπτά - σε σύγκριση με τις υπόλοιπες περιπτώσεις που μελετήθηκαν. Επιπλέον, το δυναμικά μεταβαλλόμενο πλέγμα δίνει αποτελέσματα σχεδόν ίδιας ακρίβειας με το μεσαίο και το πυκνό πλέγμα, λόγω της αιχμηρής διεπιφάνειας υγρού-στερεού PCM που επιτυγχάνεται, όπως ακριβώς στο πυκνό πλέγμα, **Εικόνα 6β**.

Ο **Πίνακας 2** δίνει μια εικόνα του αριθμητικού κόστους που απαιτείται για να επιτευχθεί χρόνος προσομοίωσης 30 λεπτών για τις τέσσερις αναλύσεις πλέγματος που δοκιμάστηκαν, χρησιμοποιώντας λειτουργικό σύστημα 64-bit με εγκατεστημένη μνήμη RAM 16 GB και με το ίδιο σταθερό χρονικό βήμα ίσο με 0,002 s. Επιπλέον, παρουσιάζονται λεπτομέρειες σχετικά με τον αριθμό των υπολογιστικών κελιών και την ανάλυση πλέγματος, δηλαδή το ελάχιστο μέγεθος κελιών, για κάθε πλέγμα που χρησιμοποιήθηκε. Η περίπτωση 1 (αραιό πλέγμα) είναι η λιγότερο δαπανηρή υπολογιστικά, ενώ είναι αυτή που εισάγει τη μεγαλύτερη αριθμητική διάχυση. Από την άλλη πλευρά, η περίπτωση 3 (πυκνό πλέγμα) είναι η πιο ακριβής,

αλλά η πιο χρονοβόρα. Τέλος, η περίπτωση 4 (2 Levels. Ref.) απαιτεί σχετικά χαμηλό υπολογιστικό κόστος και είναι πολύ πιο ακριβής από την περίπτωση 1, όσον αφορά την αριθμητική διάχυση.

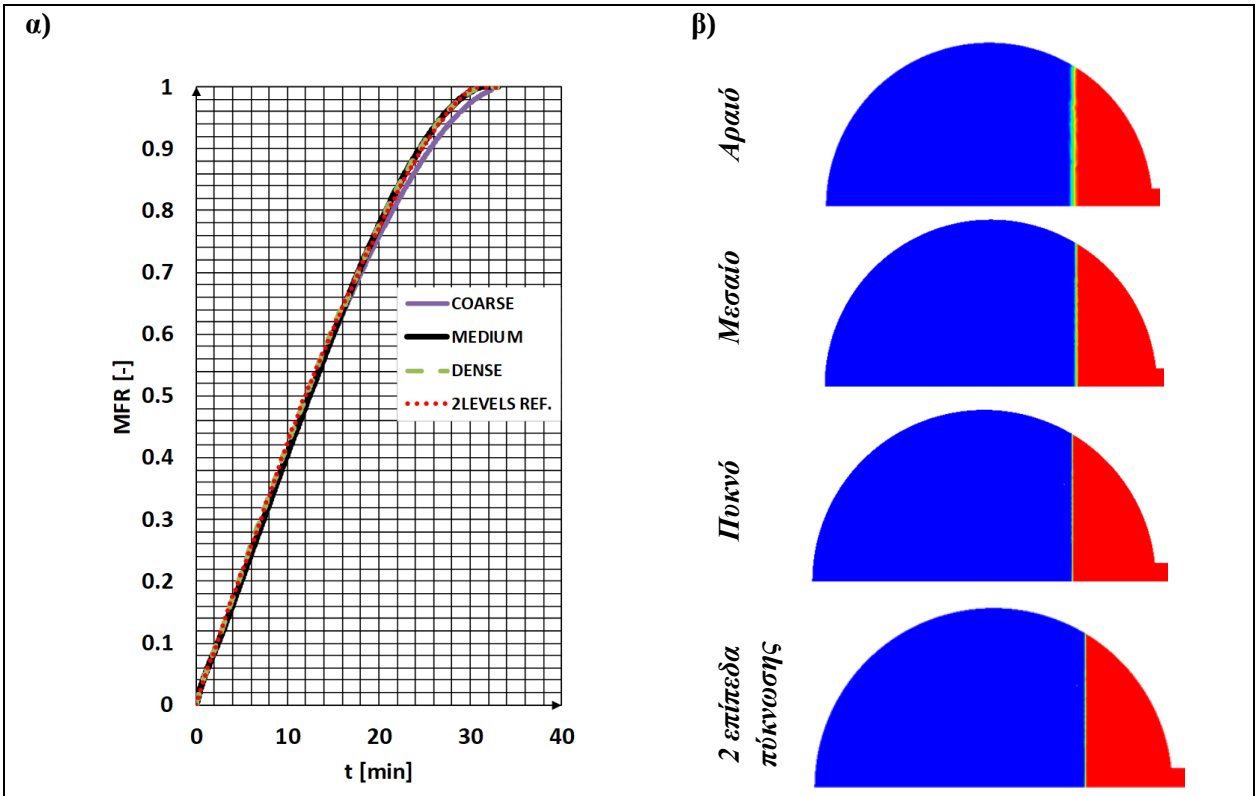

Εικόνα 6. Σύγκριση αραιού, μεσαίου και πυκνού σταθερού πλέγματος και του προσαρμοσμένου πλέγματος (2 επίπεδα βελτίωσης) για α) τις τιμές του κλάσματος τήγματος σε διαφορετικές χρονικές στιγμές και β) και των contour του κλάσματος αερίου-PCM σε t=0 λεπτά.

Λαμβάνοντας όλα υπόψη, το δυναμικά μεταβαλλόμενο πλέγμα (περίπτωση 4) θα πρέπει να προτιμηθεί έναντι των υπολοίπων, καθώς παρουσιάζει τα πλεονεκτήματα τόσο του μεσαίου όσο και του πυκνού σταθερού πλέγματος, όσον αφορά την αποτελεσματικότητα και την ακρίβεια, αντίστοιχα.

Πίνακας 2. Υπολογιστικό κόστος που απαιτείται για την προσομοίωση της τήξης κεριού παραφίνης (t=30 λεπτά χρόνος προσομοίωσης) για τις τέσσερις πυκνότητες πλέγματος που διερευνήθηκαν.

***** *Μεταβλητό από 5,664 (αρχή προσομοίωσης) έως 11,133 (μέγιστος αριθμός κατά τη διάρκεια προσομοίωσης)*

Περίπτωση	**Πλέγμα**	**Πραγματικών χρόνος (1 πυρήνας CPU) (μέρες)**	**Αριθμός κελιών**	**Ελάχιστο μέγεθος κελιού (m)**
1	Αραιό	2.55	3,858	$5.54 \cdot 10^{-4}$
2	Μεσαίο	12.5	15,432	$2.39 \cdot 10^{-4}$
3	Πυκνό	62.5	61,728	$1.07 \cdot 10^{-4}$
4	2 επίπεδα πύκνωσης	9.61	*	$1.07 \cdot 10^{-4}$

Η αριθμητική μελέτη έδειξε ότι η παράμετρος A_{mush} επηρεάζει σημαντικά τον ρυθμό τήξης του PCM. Μια τιμή A_{mush} ίση με $5 \cdot 10^5$, που αντιστοιχεί σε DAS=0.4 μm, δίνει τα πιο ακριβή αποτελέσματα για όσον αφορά τον ρυθμό τήξης του κεριού παραφίνης **(Εικόνα 7α)**. Επομένως, οι τιμές αυτής της παραμέτρου δεν θα πρέπει να επιλέγονται αυθαίρετα, καθώς η τιμή της εξαρτάται από την μορφολογία στερεού υλικού [283]. Αριθμητικά, η παρουσία δενδριτών στο στερεό PCM και επομένως η διαπερατότητα του PCM μοντελοποιούνται με έμμεσο τρόπο. Μία μείωση της παραμέτρου A_{mush}, η οποίο ισοδυναμεί με μεγαλύτερες

τιμές DAS και επομένως μεγαλύτερη διαπερατότητα του υλικού, οδηγεί στην αύξηση των ταχυτήτων στην «ενδιάμεση περιοχή», επιτρέποντας σημαντική κίνηση ροής στην συγκεκριμένη περιοχή. Αυτό με τη σειρά του επιταχύνει τη μεταφορά θερμότητας, μέσω συναγωγής, κοντά στην περιοχή ενδιαφέροντος.

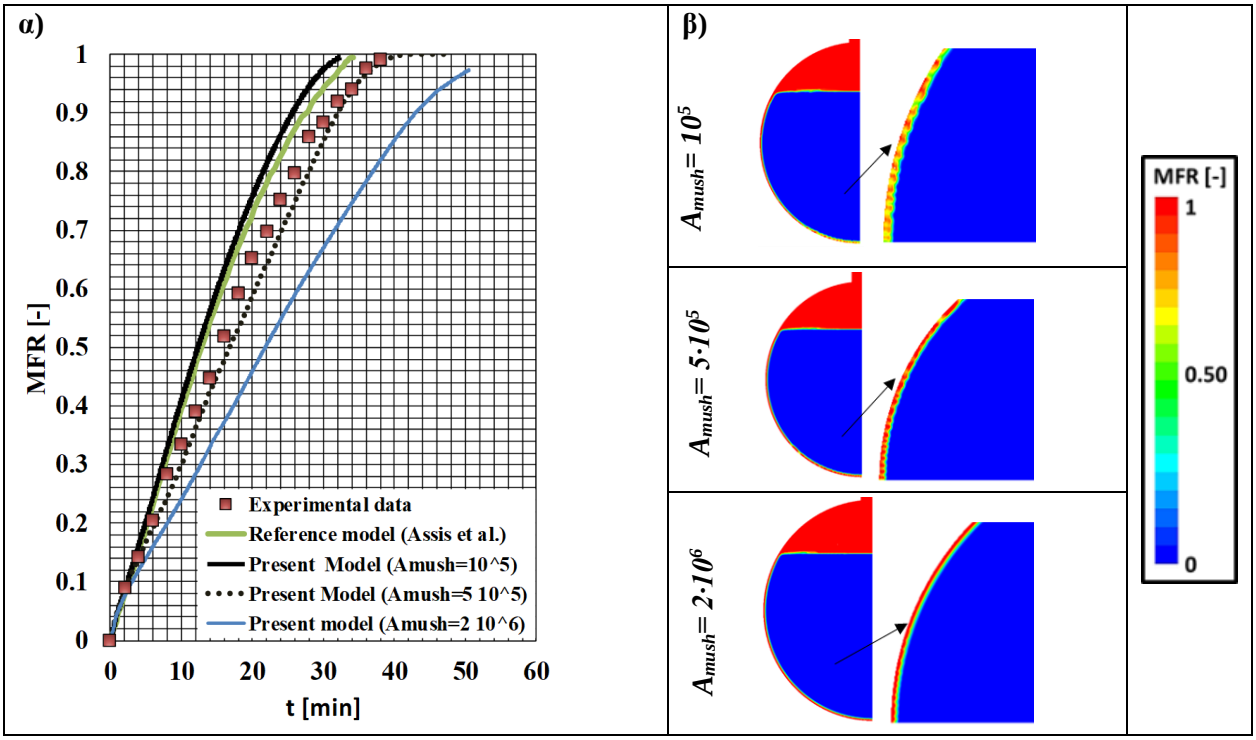

Εικόνα 7. α) Χρονική μεταβολή κλάσματος υγρού και β) contour υγρού κλάσματος για t= 1 λεπτό.

Όπως μπορεί να παρατηρηθεί στην **Εικόνα 7β**, η οπτικοποίηση «δομών» που μοιάζουν με δενδρίτες μπορεί να επιτευχθεί χονδρικά μέσω της δυναμικής πύκνωσης πλέγματος δύο επίπεδων (το μέγεθος κελιού στην περιοχή πύκνωσης είναι σχεδόν ίσο με 200 μm). Δεδομένου ότι το DAS για το A_{mush}=10^5 είναι περίπου 1 μm, αναμένεται ότι η αναπαράσταση των δενδριτών μπορεί να επιτευχθεί ρητά, εάν υιοθετηθεί μια αρκετά υψηλότερη ανάλυση τοπικού πλέγματος. Αυτό είναι ένα σημαντικό αποτέλεσμα, καθώς για πρώτη φορά προτείνεται ότι η προσέγγιση πορώδους ενθαλπίας σε συνδυασμό με μια αυτόματη πύκνωση πλέγματος μπορεί δυνητικά να αναπαράγει τη δενδριτική δομή.

Η **Εικόνα 8α** δείχνει αριθμητικά αποτελέσματα του κλάσματος τήξης του PCM ως συνάρτηση του χρόνου που λαμβάνεται για διαφορετικές τιμές της παραμέτρου A_{mush}. Οι τιμές αυτές συγκρίνονται με τις αντίστοιχες του μοντέλου των Assis et al. [282]. Όπως μπορεί να παρατηρηθεί, τα αριθμητικά αποτελέσματα του τρέχοντος μοντέλου συμφωνούν με το μοντέλο αναφοράς, εφόσον υψηλές τιμές του A_{mush} (~10^9) χρησιμοποιούνται. Πέρα από αυτό, για αυτήν την περίπτωση, επιτυγχάνεται μια περιορισμένη αριθμητική διάχυση, ενώ τα contour του κλάσματος τήξης έχουν μεγαλύτερη ομοιότητα με τις πειραματικές απεικονίσεις του Assis et al. [282], σε σχέση με τις περιπτώσεις για A_{mush}=10^5 και A_{mush}=10^6, **Εικόνα 8β**. Επομένως, για να αποφευχθεί η υπερβολική αριθμητική διάχυση, κατά τη φάση στερεοποίησης, συνιστώνται τέτοιες υψηλές τιμές.

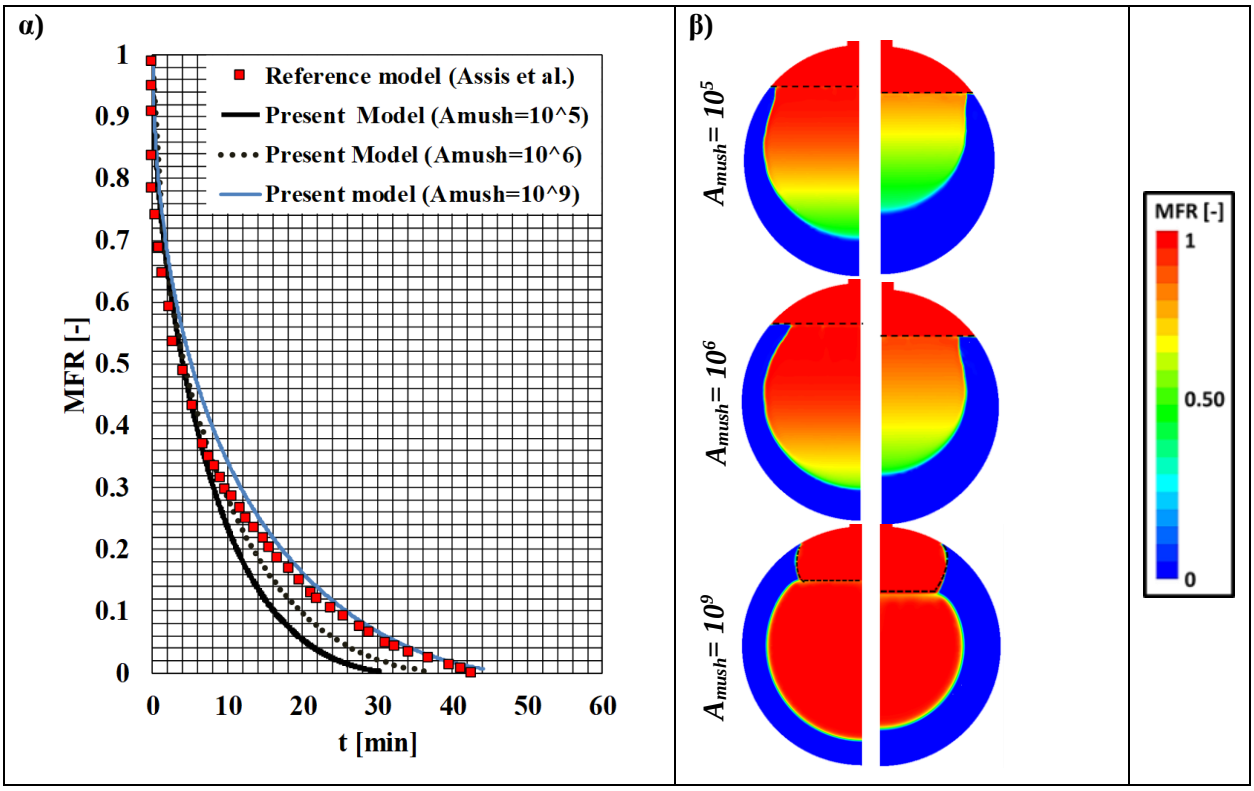

Εικόνα 8. α) χρονική μεταβολή του κλάσματος τήξης, β) contour του κλάσματος τήξης (*t*= 5, 10 λεπτά).

3.4 Επαλήθευση μοντέλου (Στερεοποίηση πυριτίου: πολύ υψηλές θερμοκρασίες)

Εν συνεχεία, το προηγμένο μοντέλο CFD επαληθεύεται έναντι άλλων μοντέλων για τη στερεοποίηση πυριτίου. Το δοχείο PCM που μελετήθηκε έχει σχήμα ανεστραμμένης αποκομμένης πυραμίδας (ITP), η οποία είναι σφραγισμένη στην κορυφή και λειτουργεί σε εξαιρετικά υψηλές θερμοκρασίες. Θα πρέπει να σημειωθεί ότι η επικύρωση με πειραματικά δεδομένα δεν είναι εφικτή, λόγω της έλλειψης πειραματικών δεδομένων σε υψηλές θερμοκρασίες. Επιπλέον, με τη μοντελοποίηση του καθαρού πυριτίου ως PCM λαμβάνονται υπόψη τα φαινόμενα διαστολής όγκου που συμβαίνουν κατά τη φάση στερεοποίησης του πυριτίου, τα οποία στη συνέχεια προκαλούν υψηλές τιμές πίεσης στο εσωτερικό του δοχείου και πιθανή ρηγμάτωση. Για λόγους ασφαλείας, και λόγω του γεγονότος ότι το δοχείο θα είναι σφραγισμένο, τοποθετείται αδρανές αέριο πάνω από το PCM για να ληφθεί υπόψη η διαστολή του PCM -ακόμη και για την περίπτωση κράματος πυριτίου-βορίου όπου αναμένεται μικρή διαστολή.

Στο παρόν υποκεφάλαιο, τα αποτελέσματα μιας απλουστευμένης έκδοσης του μοντέλου CFD που εφαρμόζεται επί του παρόντος στο Fluent, το οποίο δεν περιλαμβάνει τη διαστολή/συστολή του PCM και ονομάζεται μοντέλο Fluent1Phase συγκρίνονται με εκείνα που προκύπτουν από το αντίστοιχο απλουστευμένο μοντέλο που αναπτύχθηκε από [284] τον επιλύτη OpenFoam (meltFoam) [285] και ονομάζεται OpenFoam μοντέλο. Η σύγκριση μεταξύ των μοντέλων Fluent1Phase και OpenFoam πραγματοποιείται προκειμένου να αξιολογηθεί η εγκυρότητα του μοντέλου ενθαλπίας-πορώδους έναντι διαφορετικών επιλυτών, δηλαδή Fluent έναντι OpenFoam. Και τα δύο μοντέλα χρησιμοποιούν παρόμοιες ρυθμίσεις (πλέγμα, ιδιότητες PCM και συνθήκες λειτουργίας). Τέλος, εφαρμόζεται το προηγμένο μοντέλο CFD που αναπτύχθηκε στην παρούσα διατριβή (Fluent2Phase), και συγκρίνονται τα αποτελέσματα όλων των μοντέλων CFD, καθώς και με ένα 1Δ αναλυτικό μοντέλο που αναπτύχθηκε από τους Datas et al. [286],

όσον αφορά τα προφίλ θερμοκρασίας και την αδιάστατη διεπιφάνεια στερεού-υγρού PCM σε διαφορετικές χρονικές στιγμές.

Η γεωμετρία και το πλέγμα που χρησιμοποιούνται στα μοντέλα Fluent1Phase και Fluent2Phase παρουσιάζονται στην **Εικόνα 9α** και **β**. Και στα δύο μοντέλα, η ακτινοβολούμενη θερμότητα εξαρτάται από τη θερμοκρασία του εκπομπού, οποίος είναι στερεωμένος στο κάτω μέρος του δοχείου [286].

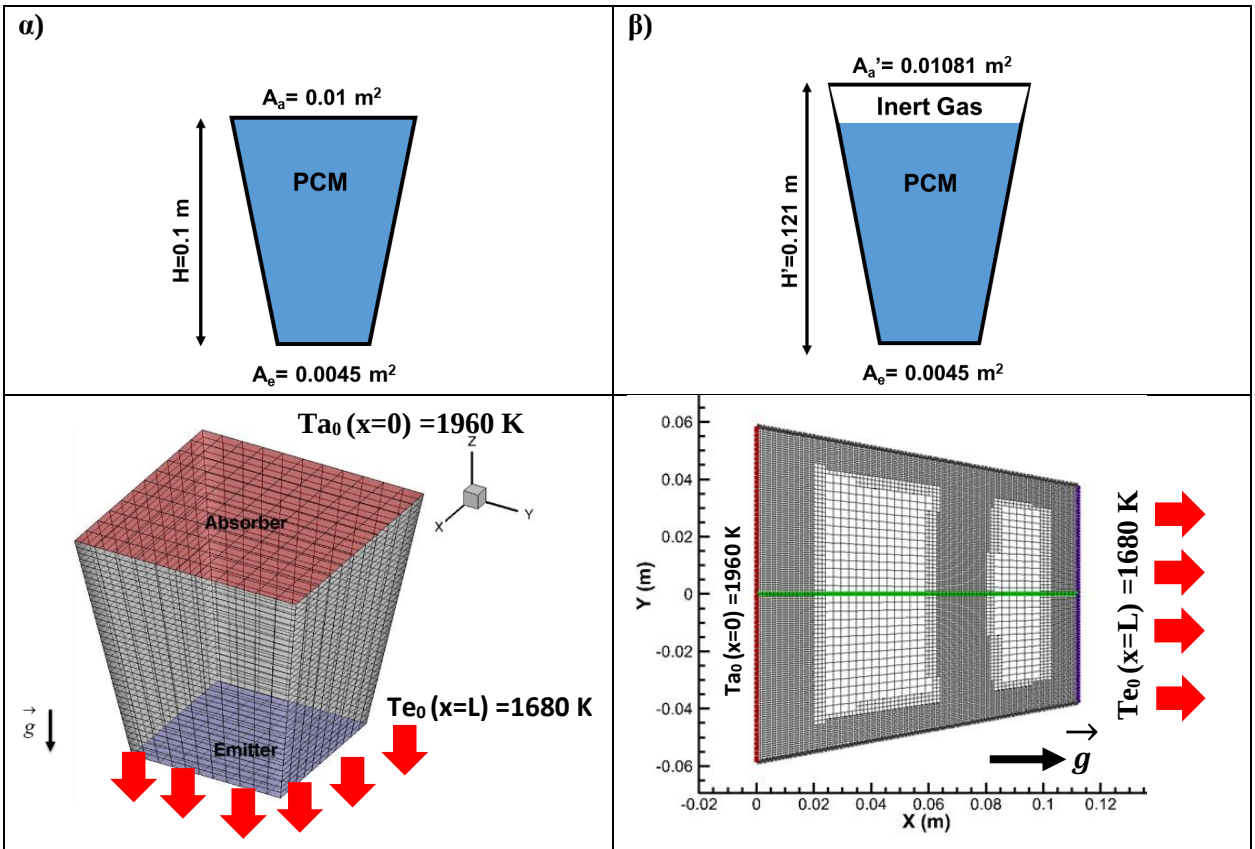

Εικόνα 9. Γεωμετρία και υπολογιστικό πλέγμα των μοντέλων α) Fluent1Phase (3Δ) και β) Fluent2Phase (αξονοσυμμετρικό). Μωβ: εκπομπός, πράσινο: άξονας, κόκκινο: απορροφητής, μαύρο: τοιχώματα.

Τέλος, το πάνω και τα πλευρικά τοιχώματα του δοχείου θεωρούνται αδιαβατικά κατά τη διαδικασία επαλήθευσης μοντέλου. Ορισμένες μικρές διαφορές εντοπίζονται μεταξύ των μοντέλων Fluent1Phase και Fluent2Phase όσον αφορά τη γεωμετρία και τη διάταξη πλέγματος. Πρώτα από όλα, στο μοντέλο Fluent1Phase το δοχείο περιέχει μόνο το PCM και έχει ύψος ίσο με 0,1 m, ενώ στο μοντέλο Fluent2Phase, το PCM γεμίζει το 85% του δοχείου και η υπόλοιπη περιοχή γεμίζει με αδρανές αέριο. Για το λόγο αυτό, στο τελευταίο μοντέλο το δοχείο επεκτείνεται σε ύψος 0,021 m για να περιέχει και το αδρανές αέριο. Τέλος, στο μοντέλο Fluent1Phase χρησιμοποιείται ένα ομοιόμορφο τρισδιάστατο πλέγμα 4,356 εξαεδρικών κελιών, όπως στο μοντέλο OpenFoam. Στο μοντέλο Fluent2Phase, το πρόβλημα επιλύεται ως αξονοσυμμετρικό και εφαρμόζεται η τοπική πύκνωση πλέγματος 2 επιπέδων, η οποία οδηγεί σε μέγιστο μέγεθος πλέγματος σχεδόν 7,000 κελιών. Επομένως, για μείωση του υπολογιστικού κόστους προτιμάται το αξονικό πρόβλημα έναντι του τρισδιάστατου για το συγκεκριμένο πρόβλημα μεταφοράς θερμότητας.

Οι συνοριακές συνθήκες που χρησιμοποιήθηκαν στα μοντέλα Fluent1Phase και Fluent2Phase παρουσιάζονται στο (**Πίνακας 3**). Η εξίσωση της ροής θερμότητας στην επιφάνεια του εκπομπού είναι 3ης

τάξης παρεμβολή σε ένα πιο περίπλοκο μοντέλο ακτινοβολίας που περιγράφει την ανταλλαγή ακτινοβολίας, μεταξύ μιας επιφάνειας εκπομπής και ενός φωτοβολταικού κελιού [27].

Πίνακας 3. Συνοριακές συνθήκες που χρησιμοποιούνται στα μοντέλα Fluent1Phase και Fluent2Phase.

	Συνοριακή συνθήκη	**Παράμετρος**	**Μονάδες**	**Τιμές**
Τοίχος	Τοίχος	Q	$W \cdot m^{-2}$	0
Απορροφητής	Τοίχος	Q	$W \cdot m^{-2}$	0
Εκπομπός	Τοίχος	Q	$W \cdot m^{-2}$	$Q_e\ (T)$

Οι θερμοφυσικές ιδιότητες PCM-αερίου ανακτώνται από τη βιβλιογραφία [287]. Στο μοντέλο Fluent2Phase, για αριθμητικούς λόγους, χρησιμοποιείται ένα διάστημα τήξης 1679-1681 K, προκειμένου να αποφευχθεί η απότομη μετάβαση των ιδιοτήτων του PCM μεταξύ των φάσεων στερεού-υγρού. Στην πραγματικότητα, στα καθαρά μέταλλα, όπως και στο καθαρό πυρίτιο, δεν υπάρχει "ενδιάμεση" ζώνη [288]. Επιπλέον, στο μοντέλο 1Phase η θερμική αγωγιμότητα του πυριτίου έχει μια απότομη μετάβαση στο σημείο τήξης του, ενώ στο μοντέλο 2Phase του Fluent υπάρχει μια γραμμική μεταβολή λόγω της παρουσίας της ενδιάμεσης περιοχής. Αρχικά, η θερμοκρασία τίθεται ίση με 1680 K στην επιφάνεια του εκπομπού και ίση με 1960 K στον απορροφητή. Για το θερμοκρασιακό προφίλ στο υπόλοιπο πεδίο χρησιμοποιείται γραμμική παρεμβολή αυτών των δύο τιμών. Το χρονικό βήμα στο Fluent1Phase μοντέλο είναι σταθερό ίσο με Δt=0.05 s και στο Fluent2Phase μεταβλητό (αριθμός Courant=0.2, μέγιστο χρονικό βήμα Δt=0.01 s).

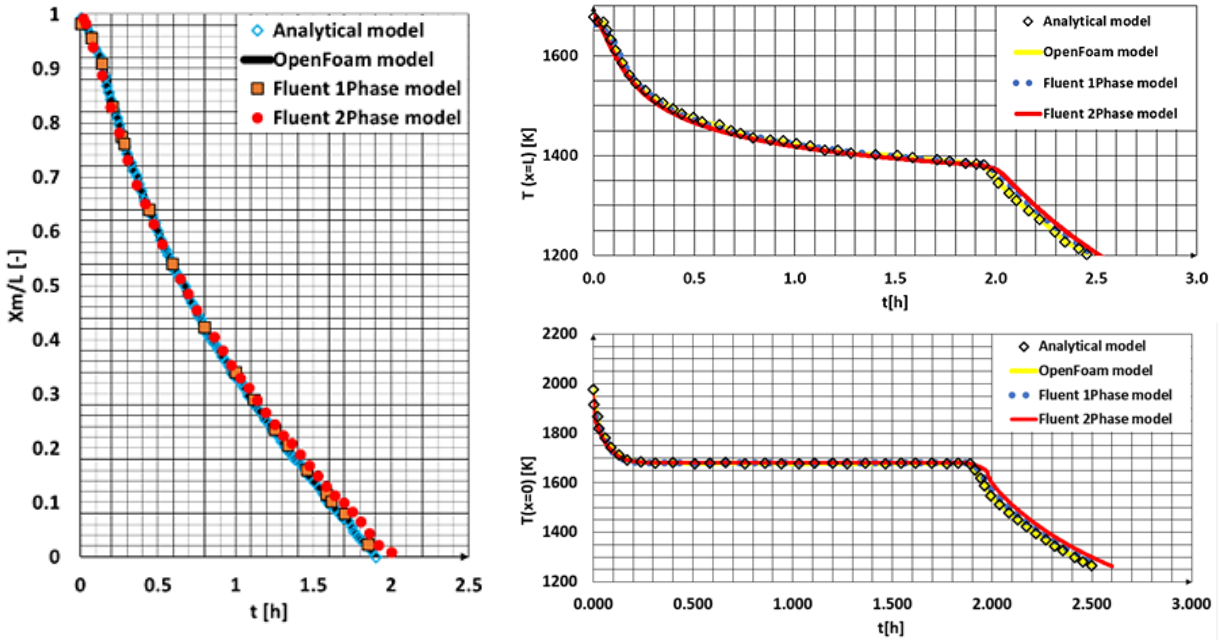

Εικόνα 10. Σύγκριση των τεσσάρων μοντέλων ως προς α) την αδιάστατη θέση της διεπιφάνειας στερεού-υγρού (X_m/L) και β) τη θερμοκρασία του PCM σε x=0 (άνω μέρος) και x=L (κάτω μέρος) ως συνάρτηση του χρόνου.

Η διαδικασία επαλήθευσης του μοντέλου απέδειξε την ακρίβεια του μοντέλου Fluent2Phase για την προσομοίωση συστημάτων LHTES που λειτουργούν σε εξαιρετικά υψηλές θερμοκρασίες. Πιο συγκεκριμένα, από την ανάλυση προέκυψε ότι για το μεγαλύτερο μέρος του χρόνου προσομοίωσης τα αποτελέσματα του προηγμένου μοντέλου Fluent2Phase πρακτικά συμπίπτουν με εκείνα των μοντέλων Fluent 1Phase, OpenFoam και 1Δ όσον αφορά τους ρυθμούς στερεοποίησης (**Εικόνα 10**). Μετά από

περίπου 2 ώρες χρόνου προσομοίωσης, τα αποτελέσματα θερμοκρασίας δείχνουν ότι η στερεοποίηση τερματίζεται και στη συνέχεια η θερμοκρασία μειώνεται γρήγορα. Μια μικρή απόκλιση μεταξύ των μοντέλων 1Phase και 2Phase ως προς τον συνολικό χρόνο στερεοποίησης, περίπου 4 %, οφείλεται στο ότι η διαδικασία στερεοποίησης στο μοντέλο 2Phase διαρκεί περισσότερο από ό,τι στο μοντέλο 1Phase, λόγω της διαστολής του PCM η οποία λαμβάνεται στο συγκεκριμένο μοντέλο. Αξίζει να σημειωθεί ότι με τα μοντέλα 1Δ και 1Phase δεν λαμβάνονται υπόψη τυχόν μεταβολές του όγκου του PCM και πιθανή επίδραση του σχηματισμού δενδριτών στη χρονική εξέλιξη του φαινομένου- η μεταβολή του όγκου του PCM κατά τη στερεοποίηση είναι περίπου 7%. Αντίθετα, το μοντέλο Fluent 2Phase προβλέπει τη διαδικασία στερεοποίησης του PCM με πιο ρεαλιστικό τρόπο, καθώς λαμβάνεται υπόψη η διαστολή του όγκου.

Συμπερασματικά, πολλές πτυχές του πραγματικού φαινομένου δεν λαμβάνονται υπόψην με τα μοντέλα 1Δ και Fluent1Phase. Από την άλλη πλευρά, το προηγμένο μοντέλο Fluent2Phase μπορεί να εφαρμοστεί για πιο περίπλοκα σχήματα δοχείων (π.χ. που περιλαμβάνουν σωλήνες), αλλά και για την πιο ρεαλιστική αναπαράσταση της διαδικασίας στερεοποίησης.

3.5 Παραμετρική μελέτη Α: Επίδραση μεγέθους/ σχήματος δοχείου

Στην παρούσα ενότητα αξιολογείται η επίδραση του σχήματος/μεγέθους δοχείου στον ρυθμό στερεοποίησης/τήξης του πυριτίου. Μελετόνται πέντε διαφορετικά σχήματα (**Εικόνα 11**), δηλαδή σφαίρα, κομμένη σφαίρα, κύλινδρος, κόλουρος κώνος και κύβος, με τον ίδιο όγκο (V_{vessel} = $3.75 \cdot 10^{-3}$ m^3) και επιφάνειας εκπομπού (A_{Em}=$2.25 \cdot 10^{-2}$ m^2) – η περιοχή του πυθμένα του δοχείου όπου γίνεται η εξαγωγή θερμότητας κατά την εκφόρτιση. Όλες οι υπό εξέταση γεωμετρίες δημιουργούνται στο ANSYS DesignModeller και είναι κλειστές στη κορυφή.

Η εφαρμοζόμενη μεθοδολογία πλέγματος ακολουθεί την τοπική μέθοδο αυτόματης πύκνωσης πλέγματος δύο επιπέδων. Χρησιμοποιούνται οι ίδες συνοριακές συνθήκες για τις πέντε γεωμετρίες κατά τη διάρκεια φόρτισης. Πιο συγκεκριμένα, τα πλευρικά τοιχώματα του δοχείου θερμαίνονται με ομοιόμορφη θερμοκρασία ίση με 1707 ºC. Ο εκπομπός είναι μονωμένος κατά την τήξη, καθώς η συσκευή βρίσκεται σε λειτουργία «φόρτισης». Αρχικά, το PCM καταλαμβάνει το 92% της περιοχής και υποψύχεται με θερμοκρασία 10 βαθμούς χαμηλότερη από το σημείο τήξης του PCM, i.e. 1413 ºC.

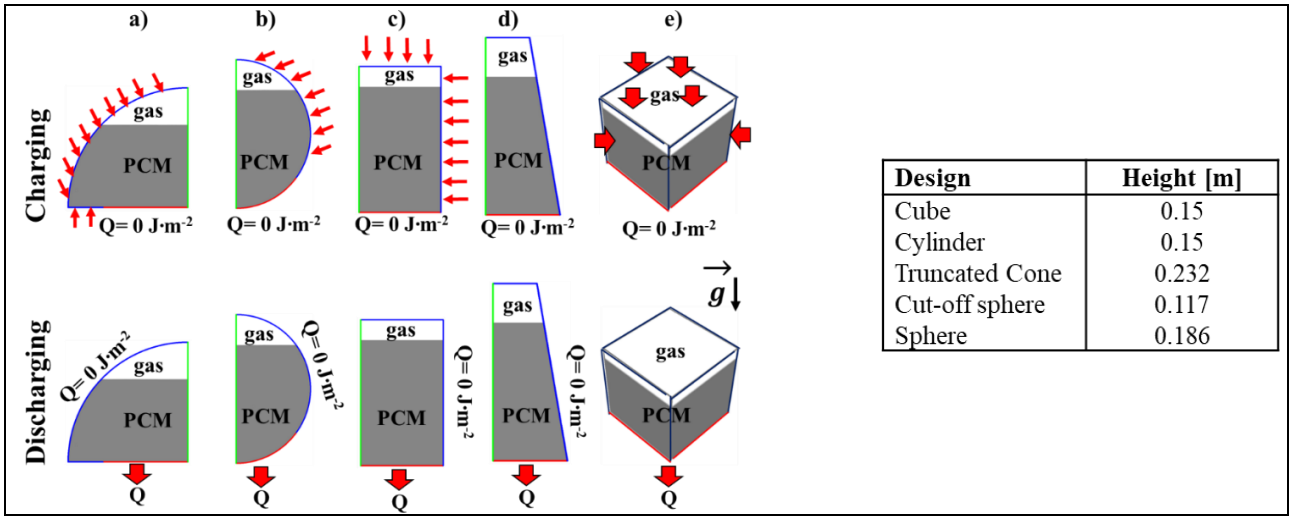

Design	Height [m]
Cube	0.15
Cylinder	0.15
Truncated Cone	0.232
Cut-off sphere	0.117
Sphere	0.186

Εικόνα 11. Φυσικά μοντέλα των μελετούμενων γεωμετριών: (α) μισή σφαίρα, (β) σφαίρα, (γ) κύλινδρος, (δ) κόλουρος κώνος και (ε) κύβος. Κόκκινο: εκπομπός, πράσινο: άξονας, μπλε: πλευρικά τοιχώματα.

Η διαδικασία στερεοποίησης του PCM προσομοιώνεται λίγο μετά τη φάση τήξης του. Σε αυτή την περίπτωση, η θερμότητα εκπέμπεται από το κάτω μέρος του δοχείου, καθιστώντας την κυρίαρχη κατεύθυνση μεταφοράς θερμότητας τον άξονα του δοχείου. Σε αυτή την επιφάνεια ορίζεται ομοιόμορφη θερμοκρασία ίση με 1097 ºC, ενώ στα πλευρικά τοιχώματα θεωρούνται μηδενικές απώλειες θερμότητας. Αρχικά, το λιωμένο PCM γεμίζει το 86.2 % της περιοχής, λόγω της συστολής του μετά την τήξη. Επιπλέον, ορίζεται σε ολόκληρη την περιοχή θερμοκρασία ίση με 5 βαθμούς μεγαλύτερη από το σημείο τήξης του PCM. Κατά την προσομοίωση και των δύο φάσεων (τήξη και στερεοποίηση) ορίζεται μεταβλητό χρονικό βήμα (αριθμός courant =0.2). Πληροφορίες σχετικά με τα σχήματα διακριτοποίησης και τις ιδιότητες αερίου-πυριτίου υπάρχουν στη [232].

Η **Εικόνα 12** απεικονίζει contours του υγρού κλάσματος πυριτίου για τις πέντε γεωμετρίες που εξετάστηκαν. Όπως μπορεί να παρατηρηθεί, μια σταδιακή τήξη του PCM συμβαίνει από τα πλευρικά τοιχώματα προς τον πυθμένα σε κάθε περίπτωση. Πιο συγκεκριμένα, στην αρχή της διαδικασίας τήξης, το στερεό πυρίτιο βρίσκεται σε άμεση επαφή με τα τοιχώματα του δοχείου. Κατά τη διάρκεια των πρώτων δευτερολέπτων της τήξης του PCM σε t=1 λεπτό, σχηματίζεται μια λεπτή υγρή περιοχή ομοιογενούς σχήματος -σχήμα παρόμοιο με αυτό των θερμαινόμενων πλευρικών τοιχωμάτων- γύρω από τη στερεά φάση. Αυτό το γεγονός αποδεικνύει ότι ο κυρίαρχος μηχανισμός μεταφοράς θερμότητας κατά τα αρχικά στάδια της διαδικασίας τήξης είναι η αγωγή. Αργότερα, καθώς η υγρή περιοχή μεγαλώνει με την πάροδο του χρόνου, η φυσική συναγωγή γίνεται έντονη, επηρεάζοντας το σχήμα τήξης του PCM.

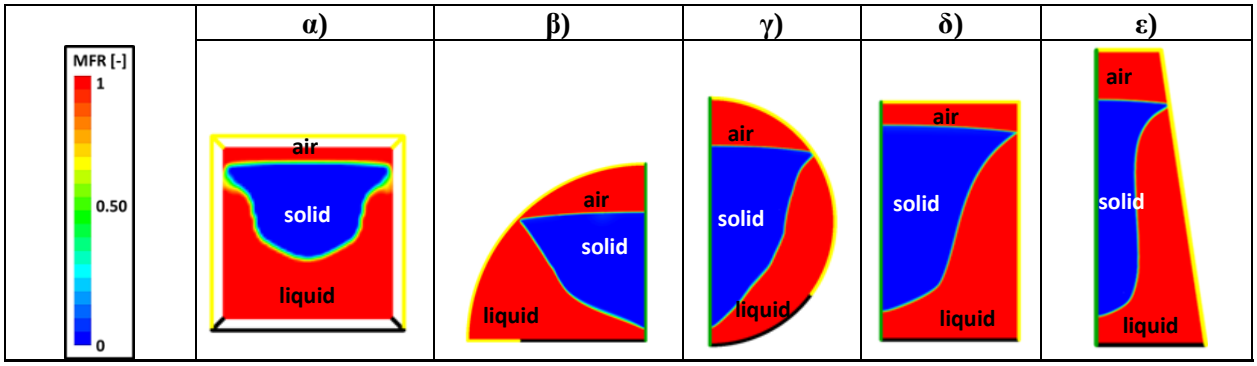

Εικόνα 12. Contour των κλασμάτων τήξης σε t=20 λεπτά για: α) κύβο, β) μισή σφαίρα, γ) σφαίρα, δ) κύλινδρο και ε) αποκομμένο κώνο (πράσινο: άξονας, κίτρινο: τοιχώματα και μαύρο: εκπομπός).

Η **Εικόνα 13α** παρουσιάζει τη χρονική εξέλιξη του κλάσματος τήξης για όλα τα σχήματα που εξετάσθηκαν. Μπορεί να συναχθεί ότι η διαδικασία τήξης είναι η πιο αργή στη σφαίρα (~40 λεπτά) και η πιο γρήγορη στον κύβο και τον ανεστραμμένο κώνο (~26-28 λεπτά). Στην πραγματικότητα, ο κύβος και ο κώνος είναι κατά 25 % και 21 % ταχύτεροι από τη σφαίρα, αντίστοιχα. Τονίζεται ότι το κυβικό σχήμα κατά τις διαδικασίες στερεοποίησης και αποθήκευσης αναμένεται να εμφανίσει τις υψηλότερες θερμικές απώλειες, καθώς έχει τη μεγαλύτερη επιφάνεια ανά μονάδα όγκου.

Η **Εικόνα 13β**, δείχνει τους ρυθμούς στερεοποίησης του πυριτίου για τις πέντε γεωμετρίες που μελετήθηκαν. Η διαδικασία στερεοποίησης είναι η πιο αργή στον κώνο (~280 λεπτά) και η πιο γρήγορη στη μισή σφαίρα (~ 140 λεπτά), λόγω του μεγαλύτερου ύψους του. Το ύψος του δοχείου παίζει σημαντικό ρόλο σε αυτό το πρόβλημα μεταφοράς θερμότητας, διότι η θερμότητα εξάγεται από τον πυθμένα του δοχείου, καθιστώντας κυρίαρχη κατεύθυνση της μεταφοράς θερμότητας τον άξονα του δοχείου. Στην πραγματικότητα, παρατηρείται μέγιστη διαφορά σχεδόν 50% στους χρόνους στερεοποίησης, μεταξύ της

μισής σφαίρας και του ανεστραμμένου κώνου - το ύψος του είναι σχεδόν δύο φορές υψηλότερο από εκείνο της αποκομμένης σφαίρας. Μεταξύ αυτών των δύο γεωμετριών, βρίσκονται ο κύβος, η σφαίρα και ο κύλινδρος, οι οποίες έχουν σχεδόν το ίδιο ύψος.

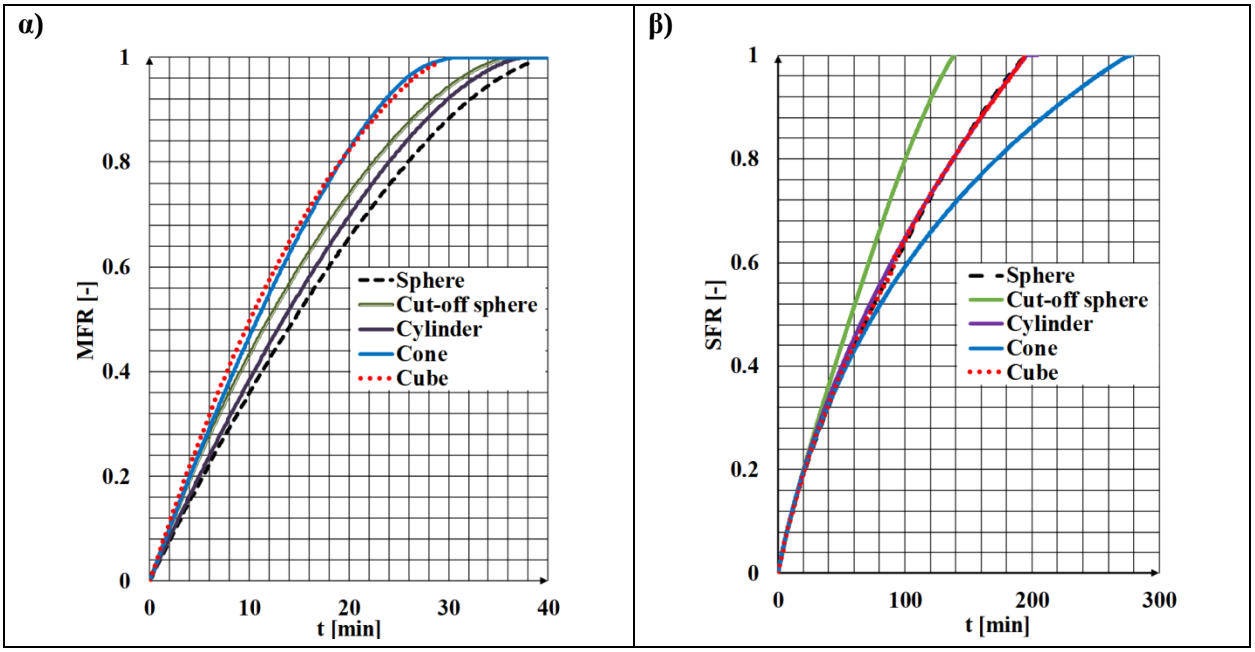

Εικόνα 13. Χρονική μεταβολή του α) κλάσματος τήξης και β) κλάσματος στερεοποίησης για τις διάφορες περιπτώσεις που εξετάσθηκαν.

Αναφέρονται επίσης ενδεικτικές τιμές των πλευρικών απωλειών θερμότητας κατά τη διάρκεια της περιόδου αποθήκευσης θερμικής ενέργειας των γεωμετριών που μελετήθηκαν. Σε όλες τις περιπτώσεις θεωρούνται συνθήκες θερμοκρασίας περιβάλλοντος, ενώ θεωρείται μόνωση μικρής θερμικής αντίστασης ≈0.002 m^2 K W^{-1}. Στην αρχή της προσομοίωσης t=0 s ορίζεται θερμοκρασία ίση με 2000 ^oC για όλες τις γεωμετρίες. Η κυρίαρχη παράμετρος που επηρεάζει τις θερμικές απώλειες του συστήματος κατά την περίοδο αποθήκευσης -για μια συγκεκριμένη μέθοδο μόνωσης- είναι ο λόγος εξωτερικής επιφάνειας προς όγκο. Επομένως, το σφαιρικό σχήμα, με τον μικρότερο λόγο επιφάνειας προς όγκο, είναι το πιο ευνοϊκό όσον αφορά τις απώλειες θερμότητας και ακολουθούν ο κύλινδρος και ο ανεστραμμένος κώνος. Ο κύβος είναι η δυσμενέστερη περίπτωση, καθώς έχει τον υψηλότερο πλευρικό λόγο επιφάνειας προς όγκο, με αποτέλεσμα τις υψηλότερες πλευρικές απώλειες θερμότητας, αντίστοιχα.

Πίνακας 4. Απώλειες θερμότητας κατά την περίοδο αποθήκευσης για τα μελετηθέντα σχήματα

Σχήμα	**Εξωτερική επιφάνεια (m^2)**	**Πλευρικές απώλειες* (kW)**	**Q_{loss} (kJ)***
Κύβος	0.135	~ 86.5	~ 5868
Κύλινδρος	0.1248	~ 80	~ 5517
Κόλουρος κώνος	0.1296	~ 84	~ 5720
Κομμένη σφαίρα	0.1296	~ 85	~ 5756
Σφαίρα	0.1088	~ 73	~ 4891

* Για t=60 δευτερόλεπτα μετά την έναρξη της προσομοίωσης.

Λαμβάνοντας όλα υπόψη, η μισή σφαίρα είναι το βέλτιστο σχήμα μεταξύ αυτών που δοκιμάστηκαν, όσον αφορά τις θερμικές απώλειες και τους ρυθμούς φόρτισης/εκφόρτισης, **Πίνακας 5**. Εκτός από αυτό, ένας τέτοιος σχεδιασμός εξαλείφει τις τάσεις καθώς ανακατευθύνει τη δύναμη βαρύτητας ή τις δυνάμεις

συμπίεσης, προς τα κάτω σε πολλαπλές κατευθύνσεις. Το πιο πλεονεκτικό, λαμβάνοντας υπόψη τις τάσεις και τις θερμικές απώλειες, αλλά όχι τόσο όσον αφορά τους ρυθμούς φόρτισης, είναι η σφαίρα. Και οι δύο γεωμετρίες θα ήταν ενδιαφέρον να κατασκευαστούν και να δοκιμαστούν σε ένα σύστημα P2H2P. Ωστόσο, η ενσωμάτωση του δοχείου αποθήκευσης σε ένα τέτοιο σύστημα μπορεί να είναι δύσκολη. Μια εναλλακτική επιλογή με ευκολότερη και πιο ευέλικτη κατασκευή για μια τέτοια εφαρμογή είναι ο ανεστραμμένος κώνος, ο οποίος οδηγεί σε υψηλά ποσοστά τήξης και μέτριες απώλειες θερμότητας. Τα ποσοστά στερεοποίησής του, αν και είναι τα χαμηλότερα σε σύγκριση με τα υπόλοιπα σχέδια, μπορούν να βελτιωθούν περαιτέρω με τη μεταβολή του λόγου κωνικότητας (λόγος κάτω προς άνω επιφάνεια).

Πίνακας 5. Ταξινόμηση των διαφόρων σχεδίων που δοκιμάστηκαν από το βέλτιστο προς το λιγότερο βέλτιστο όσον αφορά α) τη στερεοποίηση και β) το ρυθμό τήξης και γ) τις απώλειες θερμότητας κατά τη διάρκεια της περιόδου αποθήκευσης θερμικής ενέργειας.

Κριτήρια επιλογής	**Ρυθμός στερεοποίησης**	**Ρυθμός τήξης**	**Ελάχιστα Q_{loss} κατά την αποθήκευση**
	Μισή σφαίρα	Κύβος Κόλουρος κώνος	Σφαίρα
	Σφαίρα Κύλινδρος Κύβος		Κύλινδρος
		Μισή σφαίρα	Κόλουρος κώνος Μισή σφαίρα
		Κύλινδρος	
	Κόλουρος κώνος	Σφαίρα	Κύβος

3.6 Παραμετρική μελέτη Β: Μελέτη επίδρασης θερμικών απωλειών

Μετά τη μελέτη της επίδρασης του σχήματος του δοχείου στη διαδικασία στερεοποίησης/ τήξης του PCM, υπό την παραδοχή αδιαβατικών συνθηκών, το μοντέλο Fluent2Phase εφαρμόζεται για τη μελέτη με το πιο ρεαλιστικό σενάριο της συμπερίληψης απωλειών θερμότητας στο σχεδιασμό του ITC. Στο πλαίσιο αυτής της ανάλυσης, διερευνώνται διάφορες γεωμετρίες δοχείων, όγκοι και μονωτικά υλικά.

Όσον αφορά τη μόνωση του δοχείου, δοκιμάστηκαν δύο μέθοδοι. Στην πρώτη, χρησιμοποιείται μόνο στρώμα ινών γραφίτη - GFM (Περίπτωση 1Α, **Πίνακας 6**). Στη δεύτερη, χρησιμοποιείται GFM ως εσωτερικό στρώμα και πλάκα ατμίζοντος διοξειδίου του πυριτίου-FSB ως εξωτερικό στρώμα (Περιπτώσεις 2Α-4Α, **Πίνακας 6**). Τα δεδομένα σχετικά με τις θερμικές ιδιότητες των υλικών ανακτήθηκαν από [290]. Η γεωμετρία που χρησιμοποιήθηκε είναι ο ανεστραμμένος κώνος ITC με κωνικό λόγο (TR) - αναλογία επιφάνειας εκπομπού προς επιφάνεια απορροφητή - ίσο με 0.45 και όγκο αναφοράς V ίσο με $8{,}326 \cdot 10^{-4}$ m^3 (Περίπτωση 1Β, **Πίνακας 7**).

Πίνακας 6. Λίστα των περιπτώσεων που μελετήθηκαν όσον αφορά την επίδραση των μονωτικών στρωμάτων του δοχείου στις απώλειες θερμότητας του συστήματος.

* Θερμική αντίσταση των μονωτικών υλικών σε θερμοκρασία T=1680 K.

Περίπτωση	**# Μονωτικά στρώματα**	**b_{GFM} [m]**	**b_{FSB} [m]**	**$R_{th,total,1680}$* [$m^2 K \cdot W^{-1}$]**	**Φάση**
1Α	1	0.03	-	0.1179	φόρτιση/εκφόρτιση
2Α	**2**	0.03	0.06	1.88	φόρτιση/εκφόρτιση
3Α	2	0.06	0.09	2.88	εκφόρτιση
4Α	2	0.1	0.15	4.80	εκφόρτιση

Όσον αφορά τη γεωμετρία του δοχείου, έχουν διερευνηθεί οι ακόλουθες περιπτώσεις:

Α. Κατά τη φόρτιση/ εκφόρτιση του συστήματος, **Πίνακας 7**:

I. Διάφοροι όγκοι δοχείου *V* (Περίπτωση 1B), *V*/2 (2B) and *V*/4 (3B);

II. Διαφορετικά *TR* [*TR*=1 (Περίπτωση 5B-6B), 0.45 (1B), 0.225 (4B)], κρατώντας σταθερό τον όγκο του δοχείου ίσο με *V*.

Πίνακας 7. Περιπτώσεις που μελετήθηκαν όσον αφορά την επίδραση του σχήματος του δοχείου PCM στην απόδοση του συστήματος αποθήκευσης θερμότητας υπό τη μορφή λανθάνουσας θερμότητας.

Περίπτωση	V **[m^3]**	A_{em} **[m^2]**	A_{abs} **[m^2]**	A_{wall} **[m^2]**	H **[m]**	**Σχήμα**	**Φάση**
1B	0.0008326	0.0045	0.01081	0.03456	0.1121	ITC	φόρτιση/εκφόρτιση
2B	**0.0004163**	0.0045	0.01081	0.01813	0.0560	ITC	φόρτιση/εκφόρτιση
3B	**0.0002081**	0.0045	0.01081	0.01058	0.0280	ITC	φόρτιση/εκφόρτιση
4B	0.0008326	0.0045	**0.02054**	0.03130	0.0721	ITC	φόρτιση/εκφόρτιση
5B	0.0008326	0.0045	**0.0045**	**0.0440**	0.185	Κύλινδρος	φόρτιση/εκφόρτιση
6B	0.0008326	**0.01081**	0.01081	0.02839	0.077	Κύλινδρος	φόρτιση/εκφόρτιση

Β. Κατά της διάρκεια της αποθήκευσης: Μελέτη διαφόρων όγκων ITC (*V*, *V*/2, *V*/4, 2*V* and 4*V*). Σε αυτό το σύνολο περιπτώσεων που εξετάστηκαν **(Πίνακας 9**), χρησιμοποιήθηκε η μέθοδος μόνωσης δύο στρωμάτων (Περίπτωση 2A, **Πίνακας 6**).

Η γεωμετρία του δοχείου - όγκος *V* και λόγος *TR* ίσος με 0.45 - και το διακριτοποιημένο πεδίο που χρησιμοποιήθηκε κατά την παραμετρική μελέτη των μονωτικών στρωμάτων απεικονίζονται στην **Εικόνα 14α** και **Εικόνα 14β**, αντίστοιχα. Η γεωμετρία ITC τοποθετείται κάθετα. Στο κάτω μέρος της, ο εκπομπός του μετατροπέα TIPV είναι στερεωμένος, ερχόμενος σε άμεση επαφή με το λιωμένο πυρίτιο. Κατά την εκφόρτιση του συστήματος, η άνοδος του TIPV συνδέεται με το σύστημα και ενέργεια ακτινοβολείται από τον εκπομπό, προκαλώντας τη στερεοποίηση του PCM. Κατά τη διάρκεια της περιόδου φόρτισης ή αποθήκευσης η άνδος TIPV αποσυνδέεται από το σύστημα και ο εκπομπός σταματά να εκπέμπει θερμότητα. Άλλες επιφάνειες στο δοχείο περιλαμβάνουν πλευρικά και άνω τοιχώματα, που στην παρούσα ανάλυση ονομάζονται τοιχώματα και απορροφητής, αντίστοιχα.

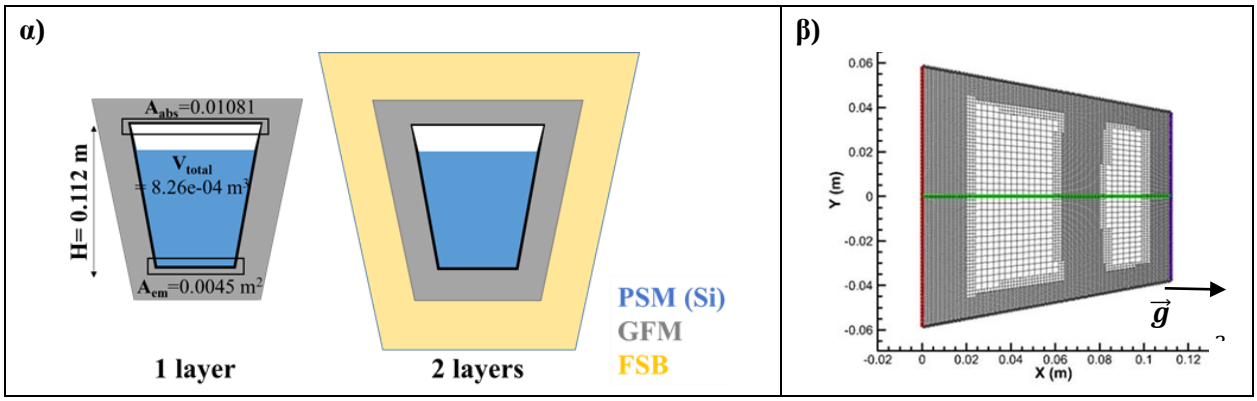

Εικόνα 14. α) Περιπτώσεις που εξετάστηκαν κατά την παραμετρική μελέτη των μονωτικών στρωμάτων και β) διακριτοποιημένη γεωμετρία (**μωβ**: εκπομπός, **πράσινο**: κεντρικός άξονας, **κόκκινο**: απορροφητής, **μαύρο**: τοιχώματα).

Διαδικασία στερεοποίησης/ τήξης

Ο **Πίνακας 8** παρουσιάζει οι οριακές συνθήκες που έχουν οριστεί κατά τη φόρτιση/εκφόρτιση του συστήματος. Οι θερμοφυσικές ιδιότητες PCM-αερίου ανακτώνται από το [232]. Κατά την εκφόρτιση του

συστήματος, η θερμοκρασία τίθεται αρχικά (t=0) ίση με 1680 K στην επιφάνεια του εκπομπού και ίση με 1960 K στον απορροφητή. Για το θερμοκρασιακό προφίλ στο υπόλοιπο πεδίο χρησιμοποιείται γραμμική παρεμβολή αυτών των δύο τιμών. Η διαδικασία τήξης του PCM προσομοιώνεται λίγο μετά τη φάση στερεοποίησής του. Αρχικά, το στερεό PCM γεμίζει το 92 % του δοχείου, για να αποφευχθούν τυχόν προβλήματα λόγω της διαστολής του μετά την τήξη. Στη φάση αυτή, η θερμοκρασία του PCM ορίζεται σε 140 βαθμούς χαμηλότερη από το σημείο τήξης του.

Πίνακας 8. Συνοριακές συνθήκες προβλήματος κατά τη φάση φόρτισης/ εκφόρτισης.

		Συνοριακή συνθήκη	Παράμετρος	Μονάδες	Τιμές
Εκφόρτιση	***Πλευρικά τοιχώματα/ Απορροφητής***	Τοίχος	T	K	300
			$R_{insulation}$	$m^2 K \cdot W^{-1}$	Μεταβλητό, (Table 27)
			b_{vessel}	m	0.01
			k_{vessel}	$W \cdot m^{-1} \cdot K^{-1}$	12.5
	Εκπομπός	Τοίχος	Q	$W \cdot m^{-2}$	Q_{em} (T), eq. (141)
Φόρτιση	***Εκπομπός/ Απορροφητής***	Τοίχος	T	K	300
			$R_{insulation}$	$m^2 K \cdot W^{-1}$	Μεταβλητό, (Table 27)
	Πλευρικά τοιχώματα	Τοίχος	T_{wall}	K	2000
			b_{vessel}	m	0.01
			k_{vessel}	$W \cdot m^{-1} \cdot K^{-1}$	12.5

Στην **Εικόνα 15**, απεικονίζονται τα contour του κλάσματος τήξης πυριτίου για τα διάφορα μονωτικά υλικά που δοκιμάστηκαν. Σε όλες τις περιπτώσεις παρατηρείται σταδιακή στερεοποίηση του PCM από τον πυθμένα προς την ανώτερη περιοχή του δοχείου, λόγω της έκλυσης θερμότητας από τον εκπομπό.

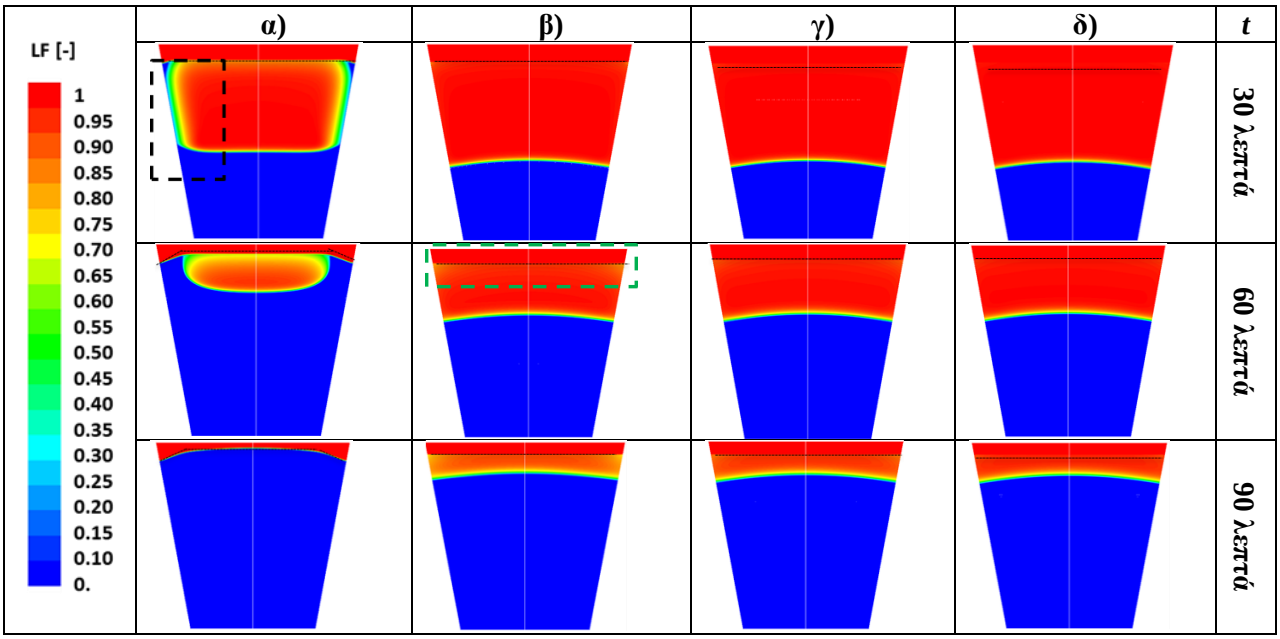

Εικόνα 15. Contour κλάσματος τήγματος για t=30, 60 and 90 λεπτά για τις περιπτώσεις α) 1A, β) 2A, γ) 3A, και δ) 4A (**κόκκινο**: αέριο-τήγμα PCM, **μπλε**: στερεό PCM, **διακεκομμένη μαύρη γραμμή**: διεπιφάνεια αερίου-PCM).

Σύμφωνα με την ανάλυση, για τις συγκεκριμένες συνθήκες λειτουργίας που εξετάστηκαν, απαιτείται μόνωση με συνολική μέση θερμική αντίσταση R_{th} τουλάχιστον ίση με 2 $m^2 \cdot K \cdot W^{-1}$ για να αποφευχθούν υψηλές θερμικές απώλειες. Σε κάθε άλλη περίπτωση, παρατηρήθηκε ότι οι απώλειες θερμότητας από τα

πλευρικά τοιχώματα είναι σημαντικά υψηλές, σχεδόν συγκρίσιμες με τη ροή θερμότητας που εξέρχεται από τον εκπομπό Q_{em} (από Q_{loss}/Q_{em}≈6.5 % για R≈2 $m^2 \cdot K \cdot W^{-1}$, έως Q_{loss}/Q_{em}≈65 % για R≈0.1 $m^2 \cdot K \cdot W^{-1}$). Σε αυτή την περίπτωση, σχηματίζεται μια διακριτή στερεή φάση κοντά στα πλευρικά τοιχώματα και μια λεπτή κρούστα στο ανώτερο τμήμα του PCM, κοντά στη διεπιφάνεια PCM-αδρανούς αερίου. Λόγω αυτών των σχηματισμών, υπάρχει μεγάλος κίνδυνος εγκλωβισμού υγρού PCM στο εσωτερικό του στερεού PCM που μπορεί δυνητικά να προκαλέσει υψηλές τιμές πίεσης στο εσωτερικό του δοχείου. Το φαινόμενο αυτό παρατηρείται 30 λεπτά μετά την έναρξη της διαδικασίας στερεοποίησης (**Εικόνα 15α**). Για περιπτώσεις όπου Q_{loss}<<Q_{em}, τέτοιου είδους σχηματισμοί δεν παρατηρούνται, αλλά μάλλον μια "κρούστα" στην διεπιφάνεια στερεού-υγρού η οποία σχηματίζεται μόνο κατά τα τελικά στάδια της στερεοποίησης του πυριτίου -σχεδόν 1 ώρα μετά την έναρξη της διαδικασίας στερεοποίησης (**Εικόνα 15β**, **γ** και **δ**).

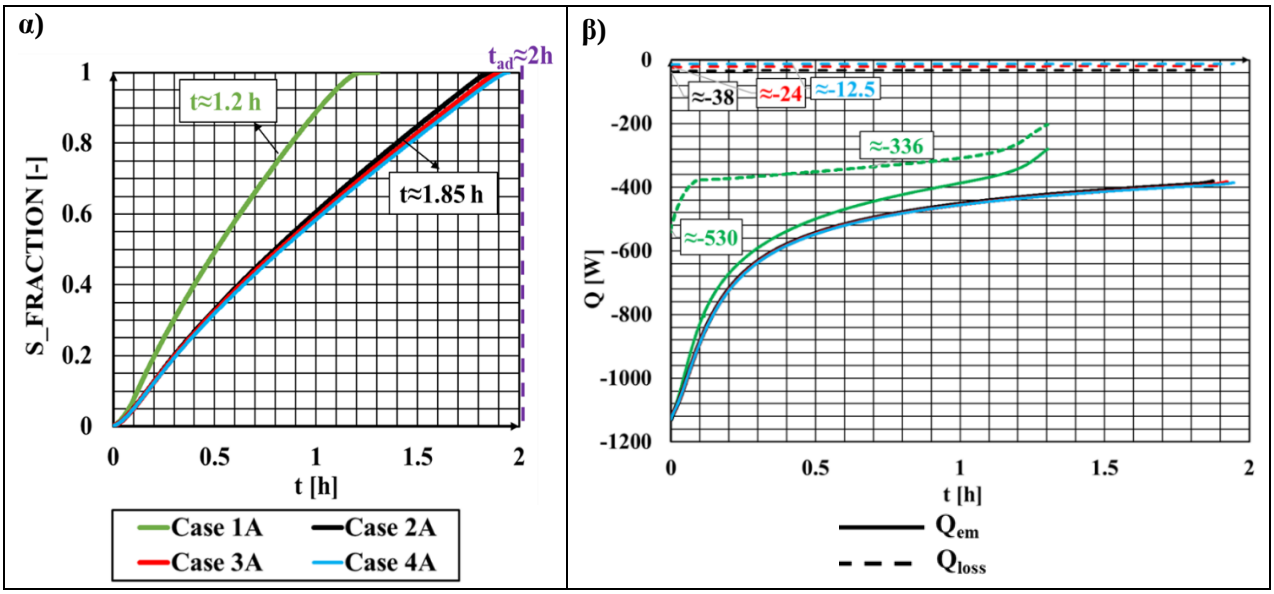

Εικόνα 16. α) Τιμές στερεού κλάσματος και β) απώλειες θερμότητας συναρτήσει του χρόνου για τα διάφορα μονωτικά στρώματα που δοκιμάστηκαν.

Τέλος, οι υψηλές πλευρικές απώλειες μπορούν να επηρεάσουν αρνητικά τη συνολική ισχύ εξόδου. Το γεγονός αυτό αποδεικνύεται στην περίπτωση 1Α, όπου η ισχύς εξόδου είναι χαμηλότερη από ό,τι στις υπόλοιπες περιπτώσεις που μελετήθηκαν. Επομένως, η συνολική θερμότητα που εκλύεται κατά την εκφόρτιση του συστήματος είναι σημαντικά χαμηλότερη στην περίπτωση 1Α από ό,τι στις περιπτώσεις 2Α-4Α (Q_{em}≈-2.3E+03 kJ για την1Α και Q_{em}~-3.5E+03 kJ για τις υπόλοιπες περιπτώσεις). Παρόλαυτα, η απώλεια θερμότητας μειώνεται σταδιακά, λόγω της μειούμενης διαφοράς θερμοκρασίας μεταξύ υλικού και περιβάλλοντος, καθώς το PCM στερεοποιείται, και λόγω των αυξανόμενων τιμών του R καθώς η θερμοκρασία πέφτει, **Εικόνα 16β**. Το γεγονός αυτό είναι πιο εμφανές για την περίπτωση 1Α.

Κατά τη διάρκεια της φόρτισης του συστήματος, κατάλληλη μόνωση πρέπει να εξασφαλίζει γρήγορους ρυθμούς τήξης, όπως αυτοί που επιτυγχάνονται σε αδιαβατικές συνθήκες, καθώς σε κάθε άλλη περίπτωση οι υπερβολικές απώλειες θερμότητας από τα πλευρικά τοιχώματα ενδέχεται να επιβραδύνουν τη διαδικασία τήξης. Κατά τη φάση αυτή, παρατηρήθηκε μικρή επίδραση στις θερμικές απώλειες του συστήματος για τιμές του R ίσες ή μεγαλύτερες από 0.1 $m^2 \cdot K \cdot W^{-1}$, καθώς η εισερχόμενη θερμότητα από τα πλευρικά τοιχώματα, Q_{wall}, είναι σημαντικά υψηλότερη από την Q_{loss}, **Εικόνα 17β**, διατηρώντας τους υψηλούς ρυθμούς φόρτισης που θα επιτυγχάνονταν υπό αδιαβατικές συνθήκες, **Εικόνα 17α**.

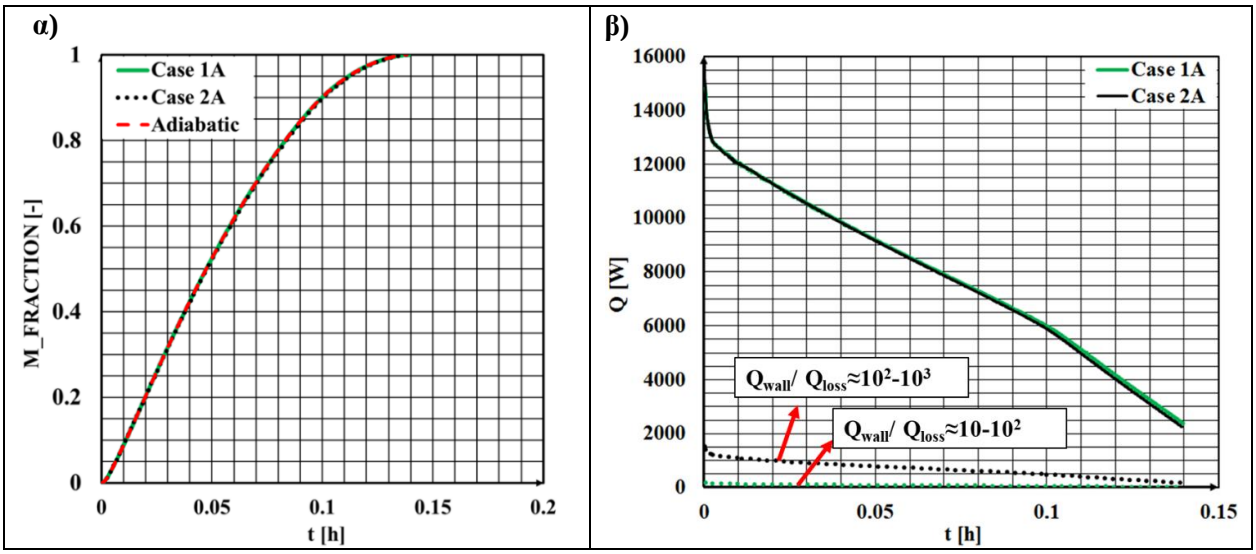

Εικόνα 17. α) Τιμές κλάσματος τήγματος και β) απώλειες θερμότητας συναρτήσει του χρόνου για τα διάφορα μονωτικά στρώματα που δοκιμάστηκαν.

Σύμφωνα με την ανάλυση η απόδοση του συστήματος κατά τη φάση φόρτισης/εκφόρτισης εξαρτάται σε μεγάλο βαθμό από τον όγκο του δοχείου, τον αριθμό *TR* και την επιφάνεια του εκπομπού. Πιο συγκεκριμένα, για γεωμετρίες ίδιου όγκου (περιπτώσεις 1B, 4B-6B), ο χρόνος στερεοποίησης αυξάνεται, όταν αυξάνεται αντίστοιχα το ύψος τους. Για το λόγο αυτό η περίπτωση 6B παρουσιάζει τον πιο γρήγορο χρόνο στερεοποίησης ($t_{discharge}$=0.72 ώρες), ενώ πιο αργή είναι η περίπτωση 5B ($t_{discharge}$=2.56 ώρες). Μέτριοι ρυθμοί στερεοποίησης παρατηρούνται στις περιπτώσεις 1B και 4B (ITC με *TR*=0.45 και 0.225). Συγκρίνοντας αυτές τις δύο, παρατηρείται ότι το ITC με *TR* ίσο με 0,225 (περίπτωση 4B) στερεοποιείται σχεδόν 17 % ταχύτερα από αυτό με *TR*=0.45.

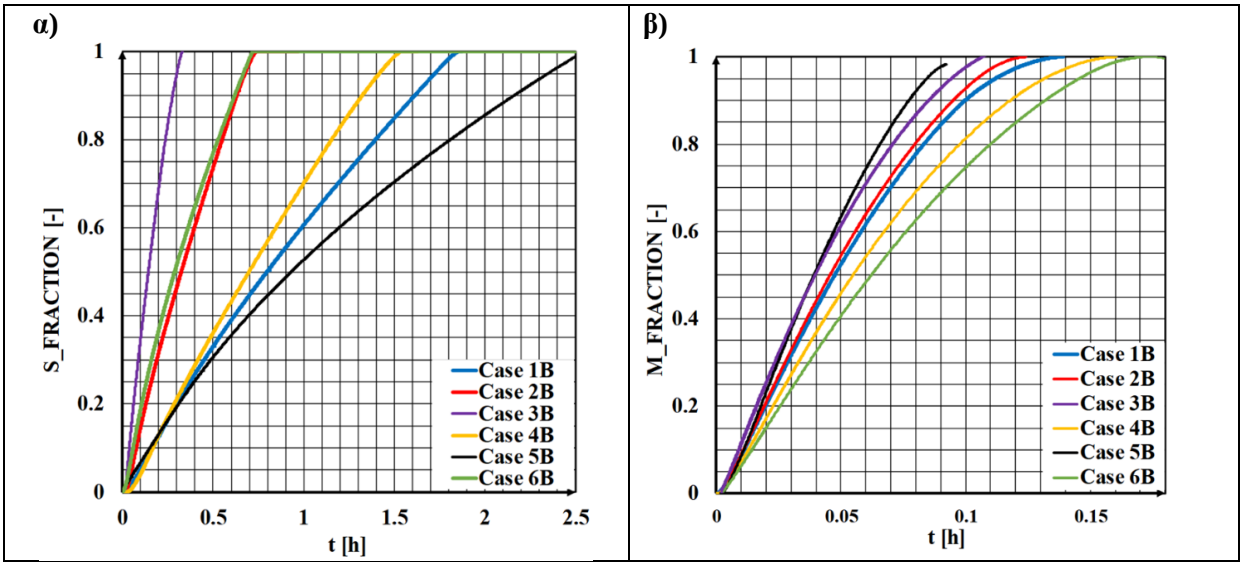

Εικόνα 18. Τιμές κλάσματος α) στερεού και β) υγρού για τις διάφορες γεωμετρίες που δοκιμάστηκαν.

Η αντίθετη τάση αναμένεται κατά την περίοδο τήξης του PCM, **Εικόνα 18β**, καθώς η θερμότητα σε αυτή την περίπτωση προέρχεται από τα πλευρικά τοιχώματα. Στην περίπτωση αυτή, για τον ίδιο όγκο δοχείου, όσο μεγαλύτερο είναι το ύψος και, επομένως, όσο μεγαλύτερη είναι η επιφάνεια του πλευρικού τοιχώματος, τόσο πιο γρήγορα λιώνει το PCM. Αυτός είναι ο λόγος για τον οποίο η περίπτωση 5B -

κύλινδρος με επιφάνεια πλευρικού τοιχώματος ίση με 0.044 m^2, σχεδόν 1.3 φορές μεγαλύτερη από την περίπτωση αναφοράς (περίπτωση 1Β) - λιώνει ταχύτερα από όλες τις περιπτώσεις που εξετάστηκαν. Από την άλλη πλευρά, ο βραδύτερος ρυθμός τήξης παρατηρείται στην περίπτωση 6Β, όπου το δοχείο έχει το μικρότερο θερμαινόμενο τοίχωμα, ίσο με 0,0284 m^2. Όσον αφορά τον λόγο κωνικότητας του ITC, το δοχείο με *TR*=0.45 τήκεται ταχύτερα, λόγω του μεγαλύτερου επιφανειακού τοιχώματός του σε σύγκριση με εκείνο με *TR*=0.225. Η αντιστάθμιση μεταξύ του ρυθμού φόρτισης και εκφόρτισης του συστήματος οδηγεί στο συμπέρασμα ότι ο ανεστραμμένος κώνος με λόγο κωνικότητας, μεταξύ 0.225-0.45 είναι η βέλτιστη λύση που μπορεί να κατασκευαστεί μεταξύ των γεωμετριών που δοκιμάστηκαν.

Περίοδος αποθήκευσης

Προκειμένου να μελετηθεί και να εκτιμηθεί πόσος χρόνος θα περάσει μέχρι το δοχείο να χάσει πλήρως την περιεχόμενη ενέργειά του υπό μορφή λανθάνουσας θερμότητας κατά τη διάρκεια της περιόδου αποθήκευσης, οι διάφορες περιπτώσεις που εξετάστηκαν, ορίστικαν αρχικά στους 2000 K. Θεωρήθηκε θερμοκρασία περιβάλλοντος 300 K, ενώ υπολογίστηκαν τόσο οι απώλειες θερμότητας μέσω συναγωγής όσο και οι απώλειες θερμότητας μέσω ακτινοβολίας προς το περιβάλλον. Για τις εξωτερικές επιφάνειες του συστήματος έχει οριστεί τιμή συντελεστή μεταφοράς θερμότητας συναγωγής ίση με 20 $W \cdot m^{-2} \cdot K^{-1}$ και συντελεστής ακτινοβολίας ίσος με 0.3.

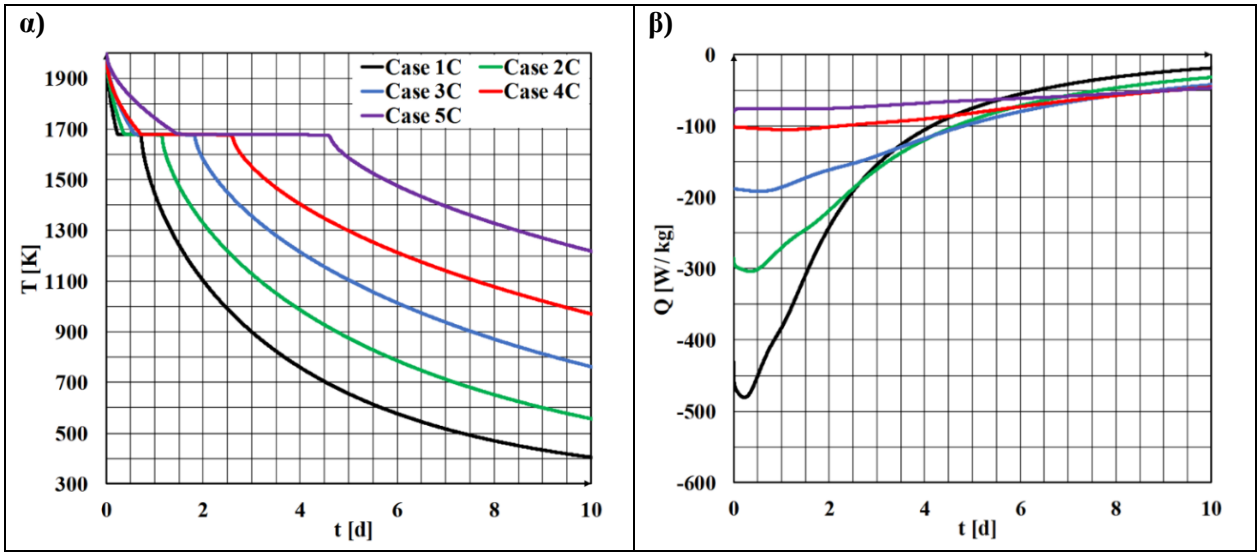

Εικόνα 19. α) μεταβολή της θερμοκρασίας και β) απώλειες θερμότητας ανά μονάδα μάζας του συστήματος κατά τη διάρκεια της φάσης αποθήκευσης.

Με βάση τα αποτελέσματα, το υπό διερεύνηση σύστημα μπορεί να διατηρήσει την αποθηκευμένη ενέργειά του με τη μορφή λανθάνουσας θερμότητας για σχεδόν δύο ημέρες τουλάχιστον εν μέρει. Ωστόσο, μέσα σε περίοδο αποθήκευσης μίας εβδομάδας το δοχείο χάνει σημαντικά ποσά της αποθηκευμένης ενέργειάς του και, έτσι, η θερμοκρασία του πέφτει στους 900 K. Μπορεί να επιτευχθεί μακροχρόνια αποθήκευση, αλλά με δοχεία μεγαλύτερης χωρητικότητας, π.χ. περίπτωση 5Γ. Επιπλέον, πρέπει να σημειωθεί ότι οι απώλειες θερμότητας του συστήματος ανά μάζα μειώνονται με την αύξηση του όγκου του δοχείου. Οι υψηλότερες τιμές εντοπίζονται για τις περιπτώσεις 1Γ και 2Γ - οι περιπτώσεις αυτές φαίνονται μη πρακτικές για αποθήκευση ακόμη και για μία ημέρα, δεδομένου ότι έχουν υψηλές πλευρικές απώλειες θερμότητας - υψηλότερες από 200 $W \cdot kg^{-1}$- εντός των δύο πρώτων ημερών αποθήκευσης.

Πίνακας 9. Χρόνος αποθήκευσης για κάθε δοχείο (ITC) πριν χάσει την περιεχόμενη λανθάνουσα θερμότητά του ($t_{discharge,\ latent}$).

Περίπτωση	V_{vessel} [m^3]	A_{vessel} [m^2]	V_{vessel}/A_{vessel} [m]	$V_{insulation}$ [m^3]	$R_{total,1680}^{*}$ [m^2 K·W^{-1}]	$t_{discharge,\ latent}$ [μέρες]
1Γ	0.0002081	0.02589	0.0080	0.00420	1.18	~0.7
2Γ	**0.0004163**	0.03344	0.0124	0.00839	1.49	~1.2
3Γ	**0.0008326**	0.04987	0.0167	0.01678	1.88	~1.8
4Γ	**0.0016652**	0.07917	0.02103	0.03356	2.37	~2.6
5Γ	**0.0033303**	0.12567	0.02650	0.06712	2.98	~4.6

3.7 Ανάλυση ευαισθησίας

Εν συντομία, παρουσιάζεται μια ανάλυση ευαισθησίας για τη λανθάνουσα θερμότητα τήξης, την ειδική θερμοχωρητικότητα, τη μεταβολή της διεπιφάνειας υγρού-στερεού και την επίδραση της θερμικής αγωγιμότητας στο χρόνο φόρτισης του συστήματος αποθήκευσης θερμότητας. Οι ιδιότητες αναφοράς του PCM αντιστοιχούν σε εκείνες του πυριτίου. Όσον αφορά τις δύο πρώτες παραμέτρους, παρατηρείται ότι με την αύξηση της λανθάνουσας θερμότητας με έναν παράγοντα επί δύο ο χρόνος φόρτισης του δοχείου αποθήκευσης θερμότητας αυξάνεται σχεδόν κατά 30 %. Το γεγονός αυτό καταδεικνύει την υψηλή επίδραση της λανθάνουσας θερμότητας του PCM στο χρόνο τήξης του. Αντίθετα, παρατηρείται μικρή επίδραση της ειδικής θερμοχωρητικότητας στα αριθμητικά αποτελέσματα. Μια αύξηση της ειδικής θερμότητας κατά σχεδόν 50 % οδηγεί σε μικρή αύξηση του χρόνου φόρτισης του δοχείου αποθήκευσης θερμότητας, δηλαδή 7 %. Παρατηρείται επίσης μια μικρή επίδραση του εύρους της "mushy" περιοχής στα αριθμητικά αποτελέσματα. Πιο συγκεκριμένα, η αύξηση του ΔT από 2 έως 20 K έχει ως αποτέλεσμα μια μεταβολή του χρόνου τήξης μικρότερη από 10 %.

Τέλος, η ανάλυση ευαισθησίας δείχνει μια μεγάλη επίδραση στο χρόνο φόρτισης με τη θερμική αγωγιμότητα *k*. Πιο συγκεκριμένα, μια περίπτωση μελέτης με k_s, k_l=20 W·m^{-2}·K^{-1} απαιτεί σχεδόν διπλάσιο χρόνο για να λιώσει το PCM σε σύγκριση με τις περιπτώσεις k_s,k_l=180 W·m^{-2}·K^{-1} και k_s=60,k_l=180 W·m^{-2}·K^{-1}. Επίσης παρατηρείται μία μείωση κατά 25 %, όταν το *k* αυξάνει από 20 W·m^{-2}·K^{-1}σε 60 W·m^{-2}·K^{-1} (66% αύξηση). Τέλος, ένα άλλο συμπέρασμα που εξάγεται είναι ότι κατά τη διάρκεια της διαδικασίας τήξης η θερμική αγωγιμότητα της υγρής φάσης του PCM επηρεάζει περισσότερο το χρόνο φόρτισης του από ό,τι η θερμική αγωγιμότητα της στερεάς φάσης, ιδίως μετά την έναρξη της τήξης.

ΚΕΦΑΛΑΙΟ 4 Μοντελοποίηση συστημάτων κοκκώδους ροής αποθήκευσης χημικής ενέργειας

4.1 Πρόλογος

Στόχος της παρούσας ενότητας είναι να παρουσιάσει την ανάπτυξη και την επικύρωση προηγμένων αριθμητικών μοντέλων, τα οποία μπορούν να χρησιμοποιηθούν για την προσομοίωση της υδροδυναμικής, των μηχανισμών μεταφοράς θερμότητας και των ρυθμών κινητικής αντίδρασης -εφόσον υπάρχουν- ενός συστήματος ρεστοποιημένης κλίνης αερίου-στερεού. Η κύρια προσέγγιση μοντελοποίησης κοκκώδους ροής βασίζεται στα μοντέλα κατά Euler-Euler TFM ή MFM για διφασική ή τριφασική ροή, αντίστοιχα, ενώ εφαρμόζεται με μια νέα έκδοση του μοντέλου οπισθέλκουσας ελαχιστοποίησης φάσεων (EMMS) που αναπτύχθηκε στο πλαίσιο της παρούσας Διατριβής. Επιπρόσθετα προσομοιώνονται όλοι οι μηχανισμοί μεταφοράς θερμότητας (συναγωγή, αγωγή και ακτινοβολία) σε συστήματα ρευστοποιημένων κλινών.

Τα μοντέλα που αναπτύχθηκαν κατασκευάστηκαν στην πλατφόρμα του ANSYS Fluent (v19.1 και v21.1) με τη χρήση δεδομένων λειτουργίας και οριακών συνθηκών μιας εγκατάστασης συζευγούς ζεύγους ενανθρακωτή-ασβεστοποιητή (DFB) 1 MW_{th} που βρίσκεται στο πανεπιστήμιο TUDA τόσο για την περίπτωση άμεσης καύσης καυσίμου μέσα στον ασβεστοποιητή όσο και για την περίπτωση έμμεσης πρόσδοσης θερμότητας (Indirectly heated calcium looping - IHCaL).

Η βασική ιδέα της τεχνολογίας του κύκλου ασβεστοποίησης-ενανθράκωσης (CaL) χρησιμοποιεί δύο διασυνδεδεμένους αντιδραστήρες ρευστοποιημένης κλίνης, συνήθως έναν ασβεστοποιητή φυσαλίδων και έναν ενανθρακωτή ρευστοποιημένης κλίνης κυκλοφορίας (**Εικόνα 20**). Η προσομοίωση της ρευστοποιημένης κλίνης γίνεται με τρισδιάστατο τρόπο για να αποτυπωθούν με μεγάλη ακρίβεια οι ετερογενείς σχηματισμοί (φυσαλίδες, συσσωματώματα σωματιδίων κ.λπ.) Ο κύκλος (CaL) μπορεί τελικά να χρησιμοποιηθεί τόσο για θερμοχημική αποθήκευση θερμότητας όσο και για δέσμευση διοξειδίου.

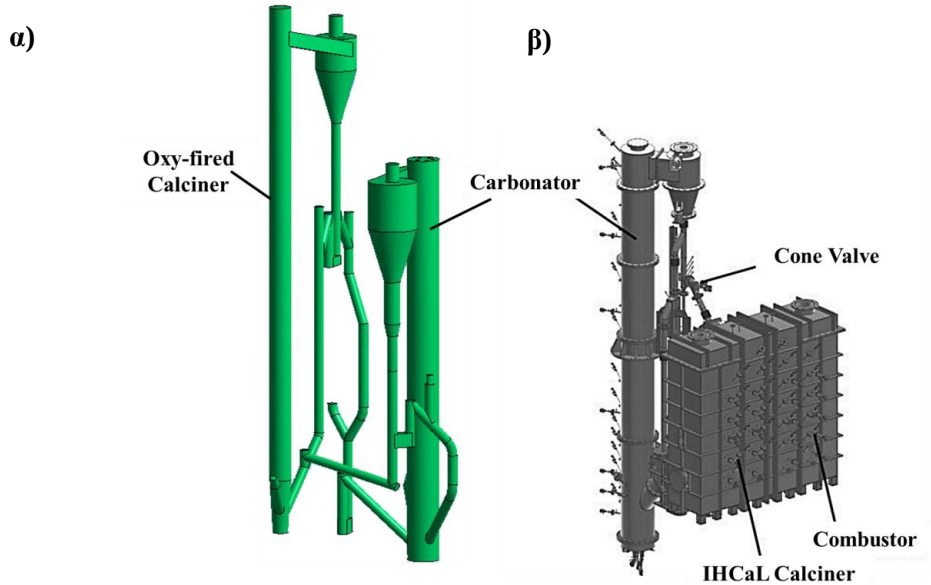

Εικόνα 20. Τρισδιάστατο σχήμα της εγκατάστασης 1 MW_{th} DFB με α) τον ασβεστοποιητή με καύση οξυγόνου και β) τον ασβεστοποιητή IHCaL [291].

4.2 Επικύρωση του μοντέλου EMMS (μονάδα ενανθράκωσης 1 MW_{th})

Το μοντέλο οπισθέλκουσας EMMS που αναπτύχθηκε στην παρούσα Διατριβή αποτελεί συνέχεια των ερευνητικών εργασιών που αναπτύχθηκαν από τους Nikolopoulos et al. [136] και Wang et al. [160]. Η διαφορά του μοντέλου που αναπτύχθηκε εδώ σε σχέση με τους [136] και [160] περιλαμβάνει τη χρήση ενός κώδικα σε FORTRAN ο οποίος μπορεί να τροποποιηθεί εύκολα ανάλογα με τα υπομοντέλα που χρειάζεται να συμπεριληφθούν στην εκάστοτε ανάλυση. Επιπλέον, χρησιμοποιήθηκε μια νέα συσχέτιση για την διάμετρο των συσσωμάτων σωματιδίων βασισμένη στην εργασία των Subarrao et al. [143], η οποία εισάγει για πρώτη φορά στην ανάλυση τη διάμετρο του αντιδραστήρα ως παράμετρο επίλυσης. Για να ελεγχθεί η εγκυρότητα του μοντέλου EMMS χρησιμοποιείται ο πιλοτικός αντιδραστήρας ενανθρακωτή 1 MW_{th} του TUDA, χρησιμοποιώντας σημεία λειτουργίας για σύγκριση και επικύρωση.

4.2.1 Αριθμητική μέθοδος

Στην παρούσα ενότητα παρουσιάζονται ορισμένες από τις κοινές παραδοχές που υιοθετήθηκαν:

- Τρισδιάστατη ροή με αριθμό Courant μικρότερο από 0.75 και 3Δ πεδίο;
- Πολυφασική μέθοδος: Μέθοδος κατά Euler-Euler – Μοντέλο δύο φάσεων (Two-fluid model);
- Οι δυνάμεις μεταξύ των σωματιδίων μοντελοποιούνται μέσω της θεωρίας KTGF;
- Χρήση ως μοντέλο οπισθέλκουσας το EMMS και σύγκρισή του με το μοντέλο του Gidaspow;
- Ισοθερμοκρασιακή στρωτή ροή με μέση θερμοκρασία 908 K και σταθερή μάζα σωματιδίων;
- Χρήση μοντέλου ενανθράκωσης σύμφωνα με τους Hawthorne et al.;

4.2.2 Γεωμετρία και αριθμητικό πλέγμα

Η **Εικόνα 21** απεικονίζει την πραγματική γεωμετρία του ενανθρακωτή, η οποία παρουσιάζεται λεπτομερώς στην εργασία του [294]. Το ύψος και η εσωτερική διάμετρος του κυρίως αντιδραστήρα – ο οποίος είναι ο μόνος που μοντελοποιείται στην παρούσα διατριβή- είναι 8.661 m και 0.59 m, αντίστοιχα. Εν συνεχεία, κατασκευάζεται ένα τρισδιάστατο υπολογιστικό πεδίο με δύο αναλύσεις πλέγματος, ένα αραιό και ένα πυκνό, που αποτελούνται από 31,207 and 285,369 εξαεδρικά κελιά και αντιστοιχούν σε έναν λόγο d_{cell}/d_p ίσο με 465.64 για το αραιό και 222.67 για το πυκνό πλέγμα.

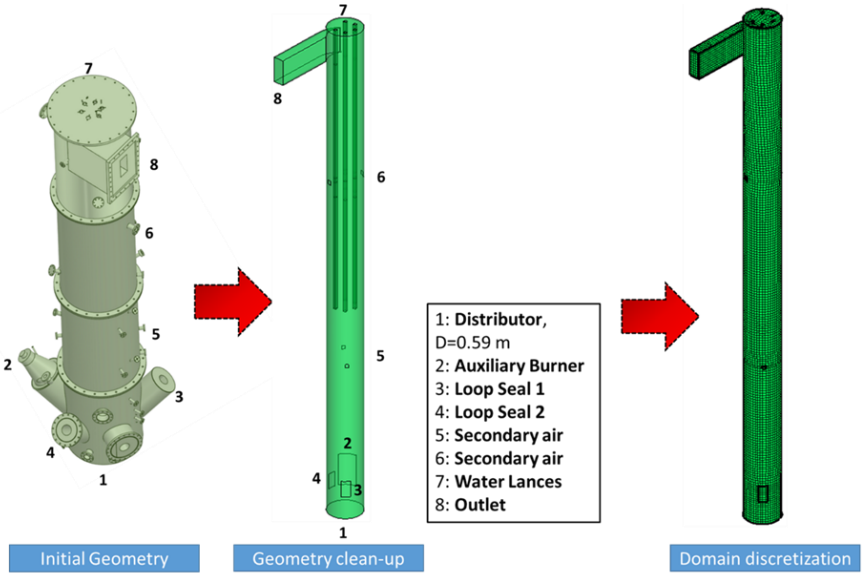

Εικόνα 21. Τρισδιάστατο σχήμα του ενανθρακωτή και διακριτοποιημένη γεωμετρία.

4.2.3 Συνοριακές συνθήκες και συνθήκες λειτουργίας

Οι συνοριακές συνθήκες του προβλήματος συνοψίζονται στο [174]. Αρχικά, η στερεά φάση είναι ομοιόμορφα κατανεμημένη σε όλο το τρισδιάστατο πεδίο με ε_s=0.067 που αντιστοιχεί σε μάζα στερεών ίση με 282 kg, όπως υποδεικνύουν τα πειραματικά δεδομένα. Η μέση διάμετρος των σωματιδίων είναι ίση με 91.39 μm και υπολογίζεται σύμφωνα με τη σχέση [52].

Πίνακας 10. Ιδιότητες της στερεής και αέριας φάσης.

Παράμετρος	**Τιμή**	**Παράμετρος**	**Τιμή**
ρ_s, kg·m^{-3}	1650	μ_g, kg m^{-1}s^{-1}	3.91085 ·10^{-5}
d_p, μm	91.39 (Geldart A)	ε_{mf}, (-)	0.55
U_g, m·s^{-1}	1.930375	ε_{max}, (-)	0.9997
U_{mf}, m·s^{-1}	2.9495 ·10^{-3}	$\varepsilon_{s,max}$, (-)	0.65
u_t, m·s^{-1}	0.175746	e_{ss}, (-)	0.9
ρ_g, kg·m^{-3}	0.389		

4.2.4 Αριθμητικό μοντέλο

Ο **Πίνακας 11** παρουσιάζει τις περιπτώσεις που μοντελοποιήθηκαν. Το χρονικό βήμα των υπολογισμών είναι ίσο με 10^{-4} δευτερόλεπτα για τις περιπτώσεις 2- 4, και 2·10^{-4} δευτερόλεπτα για την περίπτωση 1. Για την ακριβή πρόβλεψη του προφίλ πίεσης, ο συνολικός χρόνος προσομοίωσης είναι 20 δευτερόλεπτα, ενώ τα τελευταία 15 δευτερόλεπτα χρησιμοποιούνται για τον υπολογισμό χρονικά μέσων τιμών.

Πίνακας 11. Περιπτώσεις που προσομοιώθηκαν για την επικύρωση του μοντέλου.

Περίπτωση	**Πλέγμα**	**Μοντέλο οπισθέλκουσας**	**Specularity Coefficient**
Περίπτωση 1	Αραιό	Gidaspow	0.01
Περίπτωση 2	Αραιό	EMMS	0.01
Περίπτωση 3	Πυκνό	Gidaspow	0.01
Περίπτωση 4	Πυκνό	EMMS	0.01

4.2.5 Αποτελέσματα

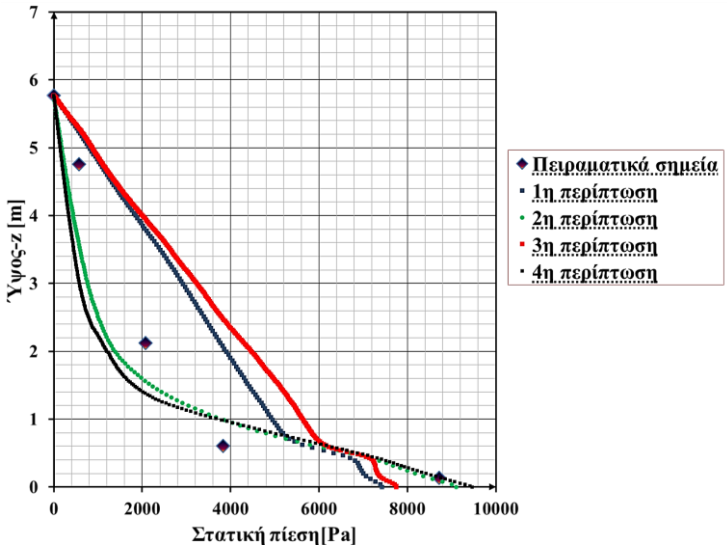

Εικόνα 22. Χρονικά μέση τιμή της πίεσης κατά μήκος του κεντρικού άξονα του αντιδραστήρα.

Με βάση τα αριθμητικά αποτελέσματα, το μοντέλο Gidaspow υπερεκτιμά τη στατική πίεση σχεδόν σε όλο το ύψος του ανυψωτήρα (**Εικόνα 22**). Το γεγονός αυτό έχει παρατηρηθεί και σε άλλες εργασίες [299]. Αντίθετα, το μοντέλο EMMS αναπαράγει αποτελέσματα σημαντικά υψηλότερης ακρίβειας, ιδίως στην περιοχή της πυκνής κλίνης. Οι αποκλίσεις από τα πειραματικά δεδομένα κοντά στο ύψος του 1m, σχετίζονται με το γεγονός ότι τα ανακυκλοφορούντα στερεά σωματίδια εισέρχονται στον αντιδραστήρα κοντά σε αυτό το ύψος και λόγω του ότι στην παρούσα μελέτη προσομοιώνεται μόνο ο κύριος αντιδραστήρας, δεν λαμβάνεται υπόψη τυχόν παλμική συμπεριφορά του συστήματος ανακυκλοφορίας. Όσον αφορά την επίδραση της πυκνότητας του πλέγματος, η απόκλιση της υπολογιζόμενης πτώσης πίεσης κατά μήκος του άξονα του αντιδραστήρα μεταξύ των αποτελεσμάτων των δύο πλεγμάτων που εξετάστηκαν για το μοντέλο EMMS είναι μικρότερη από 10%. Η υπολογιζόμενη εξάρτηση από το πλέγμα για το μοντέλο EMMS είναι περίπου 6,5 % (σφάλμα L2). Η τιμή αυτή θεωρείται αρκετά χαμηλή για αυτού του είδους τις προσομοιώσεις (σχεδόν ανεξάρτητη από το πλέγμα). Το ίδιο δεν παρατηρείται για την περίπτωση Gidaspow, όπου το υπολογισμένο σφάλμα της νόρμας L2 είναι περίπου 11 %.

Η **Εικόνα 23** απεικονίζει στιγμιότυπα του κλάσματος όγκου της στερεάς φάσης στο επίπεδο Y=0 και για ύψος αντιδραστήρα έως 3.5 μέτρα. Η πρόβλεψη σχηματισμού συσσωμάτων σωματιδίων είναι εμφανής για την περίπτωση του μοντέλου EMMS ακόμη και αν εφαρμοστεί το αραιό πλέγμα. Αντίθετα, το συμβατικό μοντέλο Gidaspow προκαλεί σημαντικά σφάλματα στην πρόβλεψη των ροικών φαινομένων. Τα στερεά σωματίδια κατανέμονται αρκετά ομοιόμορφα σε όλο το μήκος του αντιδραστήρα και δεν υπάρχει σαφής διάκριση μεταξύ της πυκνής κλίνης και της αραιής ροής στο πάνω μέρος του αντιδραστήρα. Επιπλέον, το ομογενές μοντέλο Gidaspow δίνει υψηλότερη τιμή ανακυκλοφορίας στερεών σωματιδίων, δηλαδή περίπου 182.89 $kg \cdot m^{-2} \cdot s^{-1}$, σε σύγκριση με το σχήμα EMMS που δίνει τιμή περίπου 25.6 $kg \cdot m^{-2} \cdot s^{-1}$. Η πρόβλεψη του μοντέλου Gidaspow φαίνεται μη ρεαλιστική, δεδομένου ότι οι υψηλοί ρυθμοί ανακυκλοφορίας είναι τυπικοί για ρευστοποιημένες κλίνες ανακυκλοφορίας υψηλής πυκνότητας [300].

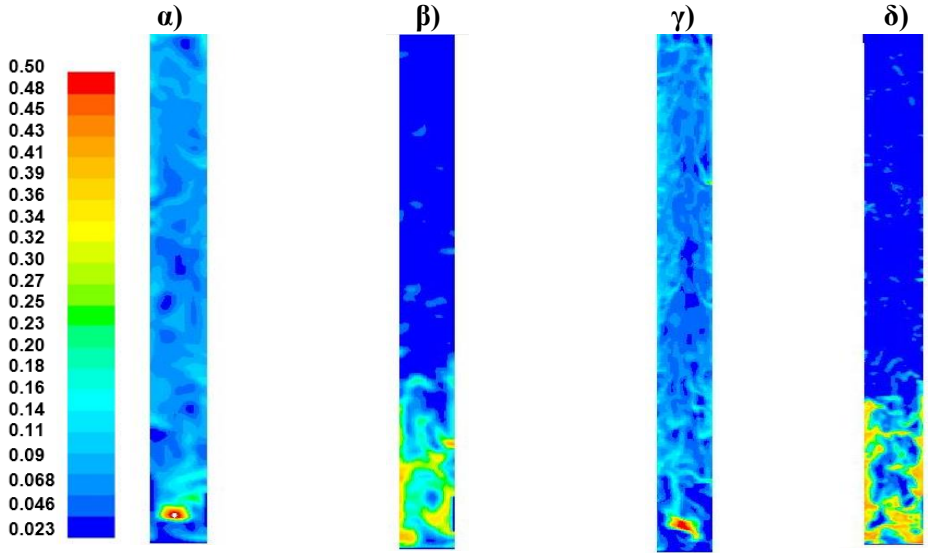

Εικόνα 23. Χρονικές στιγμές του κλάσματος όγκου στερεών σε t=20 δευτερόλεπτα μετά την αρχικοποίηση της περίπτωσης, σε επίπεδο Y=0 για: (α) Περίπτωση 1, (β) Περίπτωση 2, (γ) Περίπτωση 3 και (δ) Περίπτωση 4.

Τέλος, πραγματοποιήθηκαν πρόσθετες αριθμητικές δοκιμές για τη σύγκριση των τεσσάρων περιπτώσεων όσον αφορά το υπολογιστικό κόστος για την επίτευξη 20 δευτερολέπτων προσομοίωσης (**Πίνακας 12**). Τα αριθμητικά αποτελέσματα αποδεικνύουν ότι η περίπτωση 1 έχει το μικρότερο υπολογιστικό κόστος, αλλά

είναι η πιο ανακριβής. Η περίπτωση 2 απαιτεί σχετικά χαμηλό υπολογιστικό κόστος και είναι πολύ πιο ακριβής από τις περιπτώσεις 1 και 3. Συμπερασματικά, το αραιό πλέγμα των 31,207 αριθμητικών κελιών και το μοντέλο EMMS θεωρούνται ως ο καλύτερος συνδυασμός ακρίβειας και υπολογιστικού κόστους.

Πίνακας 12. Υπολογιστικό κόστος που απαιτείται για τις μελετηθείσες περιπτώσεις.

Περίπτωση	Πραγματικός χρόνος (1 CPU πυρήνας)
Περίπτωση 1	15.4 ώρες
Περίπτωση 2	23.15 ώρες
Περίπτωση 3	238.1 ώρες
Περίπτωση 4	333.35 ώρες

4.3 Βελτιστοποίηση του σχεδιασμού του αντιδραστήρα ενανθράκωσης

Στον κύκλο ασβεστοποίησης-ενανθράκωσης ο ενανθρακωτής είναι βασικό κομμάτι του όλου συστήματος. Ο βέλτιστος σχεδιασμός και λειτουργία του μπορούν να αυξήσουν σημαντικά την απόδοση της δέσμευσης του CO_2. Ο βέλτιστος σχεδιασμός του ενανθρακωτή θα πρέπει να επιτρέπει υψηλούς χρόνους παραμονής των στερεών σωματιδίων και καλή ανάμιξη αερίου-στερεού. Μια ιδέα, αρκετά εύκολη και ευέλικτη, είναι να εφοδιαστεί ο βασικός αντιδραστήρας του ενανθρακωτή (riser) με περισσότερες από μία γραμμές τροφοδοσίας του ασβέστου (sorbent staging design – SbS), μια ιδέα που έχει εισαχθεί σε λέβητες ρευστοποιημένης ανακυκλοφορίας [307], όπου τα στερεά καύσιμα εισάγονται στον λέβητα μέσω διαφόρων εισόδων. Μια άλλη εναλλακτική λύση είναι να τροποποιηθεί ο σχεδιασμός του πυθμένα της κλίνης του αντιδραστήρα και να εισαχθεί μια μεταβαλλόμενη διάμετρος (fat bottom design – FBD).

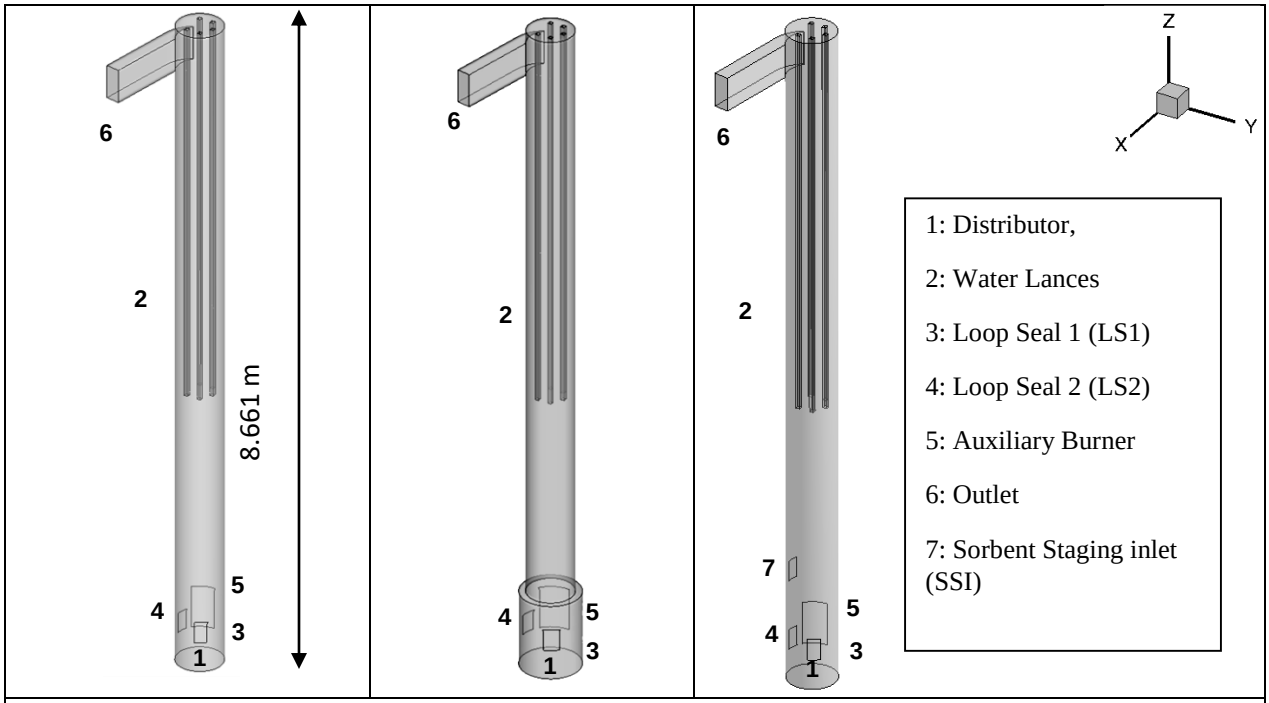

Εικόνα 24. Σχέδια των α) γεωμετρίας αναφοράς, β) γεωμετρίας μεταβλητού πυθμένα - FBD και γ) βαθμωτής εισαγωγής καυσίμου SbS/ SZD.

Στο πλαίσιο της διατριβής έχουν δοκιμαστεί και συγκριθεί πέντε διαφορετικές περιπτώσεις σχεδίων αντιδραστήρων ενανθράκωσης, όσον αφορά τα προφίλ στατικής πίεσης και την απόδοση δέσμευσης CO_2. Οι εν λόγω έννοιες περιλαμβάνουν μια σχεδίαση ανθρακοποιητή αναφοράς, με διάμετρο ίση με 590 mm,

και τέσσερις ιδέες μετασκευής του σχεδίου αναφοράς, δηλαδή κλίνη μεταβαλλόμενου πυθμένα - Fat Bottom Design (FBD) με δύο διαφορετικες μάζες στερεών, κλίνη με βαθμωτή εισαγωγή των στερεών σοματιδίων - Sorbent Staging Design (SbS) και κλίνη με εισαγωγή των στερεών σωματιδίων στην αραιή περιοχή - Sorbent in Splash Zone Design (SZD). Στην περίπτωση του FBD, η διάμετρος του αντιδραστήρα τροποποιείται και λαμβάνεται ίση με 0.759 μέτρα έως ένα ύψος 1 μέτρα από τον διανομέα, ενώ για ένα εύρος ύψους ίσο με [1, 8,661] μέτρα η διάμετρος του αντιδραστήρα παραμένει η ίδια με την αρχική γεωμετρία, δηλαδή 0.590 μέτρα. Στην SbS περίπτωση, 10% του αναγεννηθέντος υλικού που έρχεται από τον ασβεστοποιητή εισέρχεται στη μονάδα από ύψος ενός μέτρου πάνω από το σημείο εισόδου που ενώνει τις δύο μονάδες (ασβεστοποιητή-ενανθρακωτή) (staging inlet). Τέλος, στην περίπτωση SZD 100% του αναγεννηθέντος υλικού εισέρχεται στην μονάδα από το staging inlet. Για τις αριθμητικές προσομοιώσεις κατασκευάζεται αριθμητικό πλέγμα για κάθε περίπτωση με έναν λόγο d_{cell}/d_p ίσο με 465.64 [174]. Το χρονικό βήμα των υπολογισμών λαμβάνεται ίσο με 10^{-4} δευτερόλεπτα. Περισσότερες λεπτομέρειες για τις συνοριακές συνθήκες και τα μοντέλα που χρησιμοποιήθηκαν βρίσκονται στη [174].

Πίνακας 13. Συγκρινόμενες περιπτώσεις προσομοίωσης.

Αριθμός περίπτωσης	Περίπτωση	Μάζα στερεών	Αποδοση δέσμευσης
Περίπτωση 1	Σχέδιο αναφοράς (100%-0%)	282 κιλά	87.03 %
Περίπτωση 2	FBD-282	282 κιλά	90.36 %
Περίπτωση 3	FBD-340	340 κιλά	91.91 %
Περίπτωση 4	SbS (90% - 10%)	282 κιλά	89.64 %
Περίπτωση 5	SZD (0-100%)	282 κιλά	88.70 %

Τα αριθμητικά αποτελέσματα δείχνουν ότι σε όλες τις περιπτώσεις μετασκευής επιτυγχάνεται καλύτερη απόδοση δέσμευσης CO_2 σε σύγκριση με τον σχεδιασμό αναφοράς. Πιο συγκεκριμένα, η απόδοση δέσμευσης είναι ίση με 90.36% και 91.91%, για τις περιπτώσεις FBD-282 και FBD-340, αντίστοιχα (**Πίνακας 13**). Στην πρόταση σχεδιασμού SbS επιτυγχάνεται απόδοση δέσμευσης CO_2 ίση με 89.64%, ενώ η απόδοση είναι χαμηλότερη (88.70%) όταν το 100% της φάσης του προσροφητικού εγχέεται από την είσοδο της σταδιακής εισόδου του προσροφητικού. Συμπερασματικά, όσον αφορά την απόδοση δέσμευσης του διοξειδίου το άνθρακα, η περίπτωση FBD φαίνεται η πιο υποσχόμενη μεταξύ όλων, ωστόσο η ιδέα σχεδιασμού SbS είναι η πλέον προτιμώμενη λύση, επειδή μπορεί να εφαρμοστεί ευκολότερα στο σχέδιο αναφοράς.

4.4 Αξιολόγηση επέκτασης της κλίμακας του αντιδραστήρα προς 20 MW_{th}

Το επικυρωμένο μοντέλο CFD χρησιμοποιείται για την προσομοίωση ενός ανθρακοποιητή 20 MW_{th}, ο οποίος είναι μια αναβαθμισμένη μονάδα της μονάδας ανθρακοποιητή 1 MW_{th} [309]. Εκτός από τον αρχικό σχεδιασμό, δοκιμάστηκε επίσης η ιδέα της εισόδοου του ασβέστου από διάφορα ύψη (SbS), όπως είχε γίνει προηγουμένως για τη μονάδα 1 MW_{th} [310]. Σε αυτή την ιδέα, το 10 % του αναγεννημένου υλικού που προέρχεται από τη μονάδα ασβεστοποιητή διοχετεύεται από υψηλότερο ύψος από το πνευματικό σύστημα (loop seal) που που συνδέει τους δύο αντιδραστήρες.

4.4.1 Γεωμετρία/ υπολογιστικό πλέγμα και συνοριακές συνθήκες

Ο αντιδραστήρας της μονάδας των 20 MW_{th} έχει ύψος ίσο με 20 μέτρα και η διατομή του είναι τετράγωνη με διαστάσεις ίσες με 1.5x1.5 μέτρα. Η δεδομένη γεωμετρία, **Εικόνα 25α**, περιλαμβάνει τον διανομέα (distributor) από τον οποίο το καυσαέριο εισάγεται προς τα πάνω στη μονάδα, το τμήμα εξόδου και δύο τμήματα Loop Seal- το πρώτο (LS_recirculation) χρησιμοποιείται για την εσωτερική κυκλοφορία των

σωματιδίων του προσροφητικού υλικού στο εσωτερικό του ενανθρακωτή, ενώ το δεύτερο (LS_from_calciner) χρησιμεύει για τη μεταφορά του αναγεννημένου υλικού από τον ασβεστοποιητή στη μονάδα ενανθράκωσης. Επιπλέον, περιλαμβάνονται τα στάδια εισόδου (Stages) 1 και 2, τα οποία μπορούν δυνητικά να χρησιμοποιηθούν ως είσοδοι ροής μάζας των αναγεννημένων σωματιδίων του ροφητικού για την περίπτωση σχεδιασμού (SbS) [310]. Και τα δύο τοποθετούνται πάνω από το LS_from_calciner, με το πρώτο από αυτά, δηλαδή το Stage 1, να τοποθετείται στο ίδιο ύψος με το LS_recirculation. Το δεύτερο, τοποθετείται 1 m πάνω από το στάδιο 1.

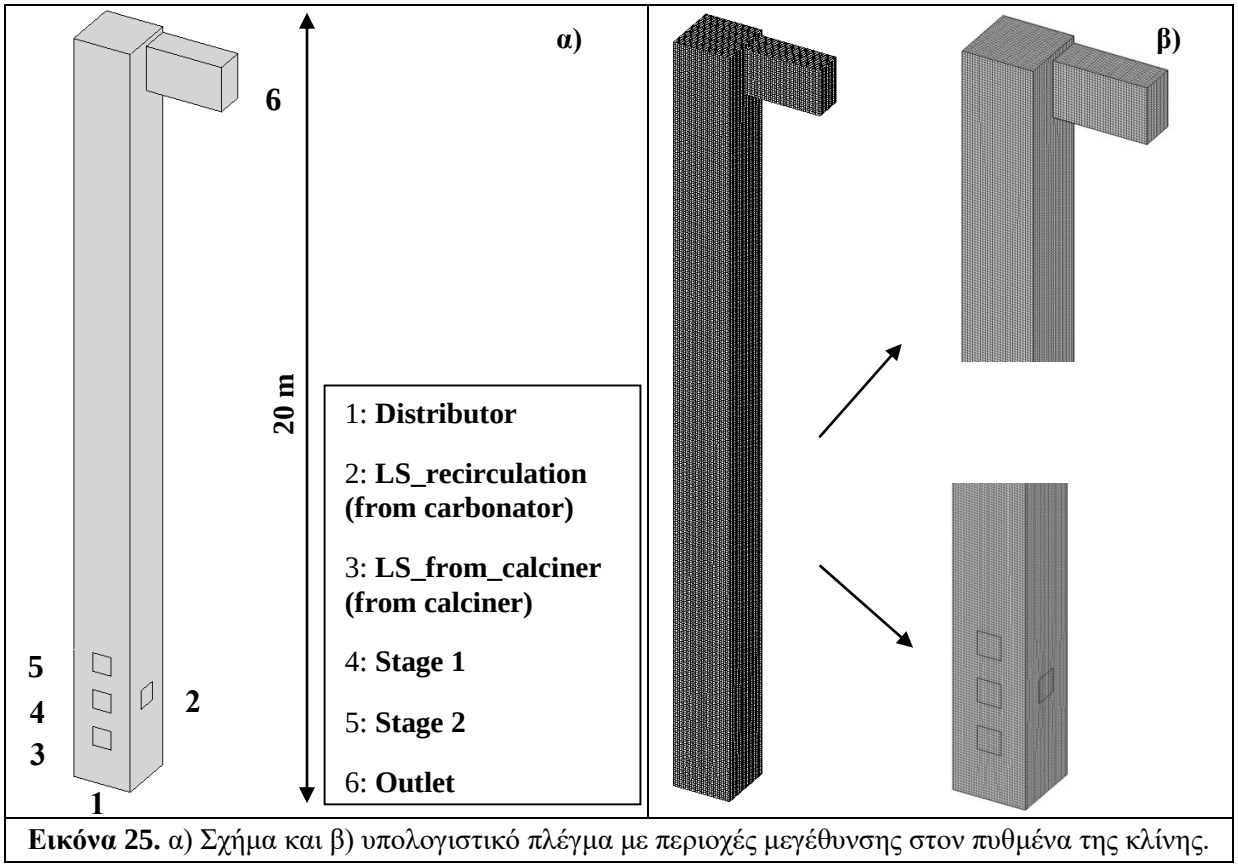

Εικόνα 25. α) Σχήμα και β) υπολογιστικό πλέγμα με περιοχές μεγέθυνσης στον πυθμένα της κλίνης.

Το τρισδιάστατο πλέγμα αποτελείται από 296,464 εξαεδρικά κελιά, που αντιστοιχούν σε έναν λόγο d_{cell}/d_p ίσο με 500.73. Η **Εικόνα 25β** απεικονίζει το τρισδιάστατο αραιό πλέγμα. Ο **Πίνακας 14** συνοψίζει τις φυσικές/χημικές ιδιότητες των δύο αλληλεπιδρώντων φάσεων (αέρια και στερεά φάση).

Πίνακας 14. Ιδιότητες στερεού-αερίου.

Παράμετρος	Τιμή	Μονάδες	Παράμετρος	Τιμή	Μονάδες
d_p	108.4327	μm	ε_{mf}	0.55	(-)
ρ_s	1923.276	$kg \cdot m^{-3}$	ε_{max}	0.9997	(-)
ρ_g	0.3567	$kg \cdot m^{-3}$	$\varepsilon_{s,max}$	0.65	(-)
μ_g	3.9515E-05	$kg \cdot m^{-1} \cdot s^{-1}$	e_{ss}	0.9	(-)

4.4.2 Προσομοιωμένες περιπτώσεις

Δύο σχέδια δοκιμάστηκαν για τη μονάδα 20 MW_{th}, τα οποία αντιστοιχούν σε δύο από τις περιπτώσεις που προσομοιώθηκαν για τη μονάδα ισχύος 1 MW_{th} [310]. Το πρώτο αντιστοιχεί στην περίπτωση σχεδιασμού

αναφοράς, κατά την οποία το αναγεννημένο υλικό που προέρχεται από τον ασβεστοποιητή διοχετεύεται αποκλειστικά μέσω του LS_from_calciner στον ανθρακοποιητή. Το δεύτερο είναι το SbS σχέδιο, κατά το οποίο το 10% του αναγεννημένου υλικού εγχέεται από υψηλότερο ύψος από το LS_from_calciner (από το στάδιο 2), ενώ το 90% αυτού εγχέεται μέσω του LS_from_calciner. Και στις δύο περιπτώσεις, η μάζα των στερεών είνα ίση με 2270 κιλά. Το χρονικό βήμα των υπολογισμών είναι ίσο με $5 \cdot 10^{-4}$ δευτερόλεπτα.

4.4.3 Αριθμητικά αποτελέσματα

Η **Εικόνα 26** απεικονίζει τον χρονικά μέσο όρο του κλάσματος όγκου στερεών στο επίπεδο X=0 για τις δύο περιπτώσεις που προσομοιώθηκαν. Όπως φαίνεται, η πυκνή ρευστοποιημένη κλίνη επεκτείνεται μέχρι ύψος περίπου 2.5 μέτρα, το οποίο είναι κοντά στο ύψος όπου είναι τοποθετημένο το LS_recirculation, το οποίο χρησιμεύει για την εσωτερική ανακυκλοφορία της μονάδας ενανθράκωσης, και 0.5 μέτρα περίπου προς τα πάνω από το στάδιο 2. Για το λόγο αυτό κοντά στην περιοχή αυτή επηρεάζεται σε μεγάλο βαθμό το πεδίο ταχύτητας, ενώ υπάρχει συσσώρευση στερεών σωματιδίων, γεγονός που επηρεάζει στη συνέχεια την απόδοση της δέσμευσης.

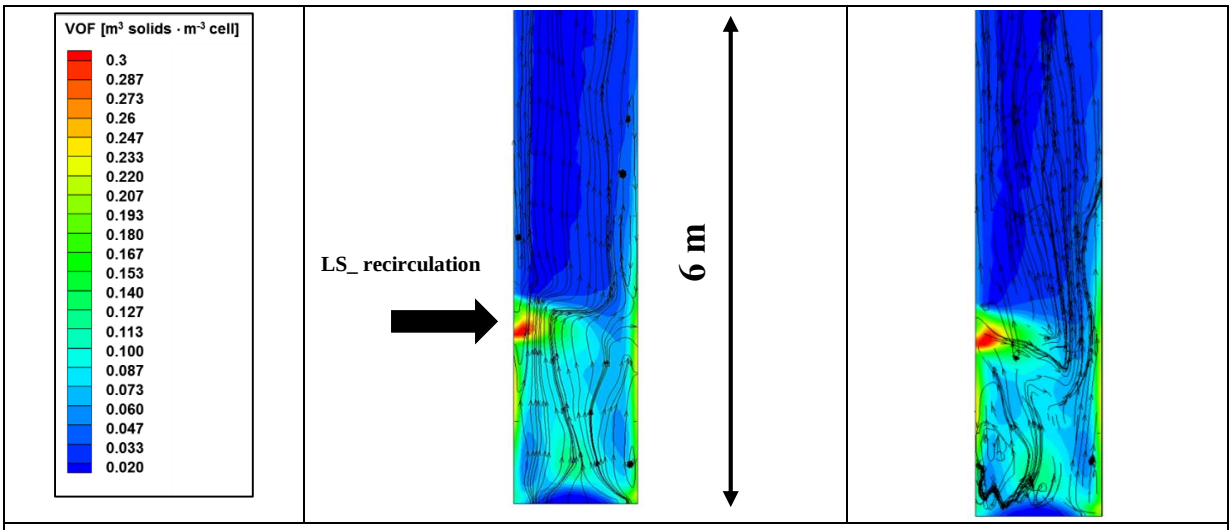

Εικόνα 26. Μέσο κλάσμα στερεού στον άξονα X=0 για τη α) Γεωμετρία αναφοράς και β) SbS.

Πίνακας 15. Απόδοση δέσμευσης CO_2 (1 MW_{th} και 20 MW_{th} μονάδες).

Μελετηθείσα περίπτωση	**Απόδοση δέσμευσης**
Σχέδιο αναφοράς (20 MW_{th})	86.95 %
SbS σχέδιο (20 MW_{th})	**87.13** %
Σχέδιο αναφοράς (1 MW_{th})	87.03 %
SbS σχέδιο (1 MW_{th})	89.64 %

Ο **Πίνακας 15** συνοψίζει τις αποδόσεις δέσμευσης CO_2 για τα δύο σχέδια που δοκιμάστηκαν τόσο στη μονάδα 1 MW_{th} όσο και στη μονάδα 20 MWth. Η έρευνα έδειξε μέχρι στιγμής ότι στην πιλοτική μονάδα 1 MW_{th} το SbS δίνει υψηλότερη απόδοση δέσμευσης CO_2 από τον σχεδιασμό αναφοράς. Ωστόσο, στην μονάδα ενανθράκωσης 20 MW_{th} η απόδοση δέσμευσης για το σχέδιο SbS είναι σχεδόν ίση -λιγότερο από 1% υψηλότερη- με το σχέδιο αναφοράς. Μια πιθανή εξήγηση γι' αυτό είναι ότι το στάδιο 2 είναι αρκετά κοντά στο LS_from_calciner. Συμπερασματικά, αυτή η ιδέα θα πρέπει να εξεταστεί περαιτέρω για τη μονάδα μεγάλης κλίμακας- ωστόσο, στη μονάδα 1 MW_{th} αποκαλύφθηκε ότι η ιδέα σχεδιασμού SbS φαίνεται να είναι πολύ ελπιδοφόρα όσον αφορά τη βελτιστοποίηση απόδοσης δέσμευσης CO_2.

4.5 Μοντέλο ασβεστοποιητή 1 MW_{th} με καύση οξυγόνου

4.5.1 Πρόλογος

Σκοπός της παρούσας εργασίας είναι η τρισδιάστατη προσομοίωση ενός ασβεστοποιητή πιλοτικής κλίμακας, μέρος της εγκατάστασης συζευγούς ζεύγους 1 MW_{th} που βρίσκεται στο TUDA. Η ενέργεια που απαιτείται για την ενδόθερμη αντίδραση παρέχεται από την καύση άνθρακα εντός του ίδιου αντιδραστήρα. Η ροή αερίου-προσροφητικού-καυσίμου προσομοιώνεται μέσω του Eulerian-Eulerian MFM. Λόγω της παρουσίας δύο στερεών φάσεων εφαρμόζεται μια τροποποιημένη έκδοση του μοντέλου KTFG [156] για πολυφασική ροή. Για τον υπολογισμό των συντελεστών συναλλαγής ορμής αερίου-προσροφητικού υλικού και αερίου-καυσίμου, χρησιμοποιούνται το προηγμένο μοντέλο EMMS και το ομογενές μοντέλο Gidaspow. Επιπλέον, το συμμετρικό μοντέλο Syamlal-Obrien χρησιμοποιείται για τον υπολογισμό του συντελεστή ανταλλαγής ορμής προσροφητικού υλικού-καυσίμου. Για την προσομοίωση των ετερογενών και ομογενών αντιδράσεων εφαρμόζονται ρυθμοί αντίδρασης που έχουν ανακτηθεί από τη βιβλιογραφία. Η επίδραση της τύρβης λαμβάνεται υπόψη με την εφαρμογή του μοντέλου *k-ε*. Ο ρυθμός αντίδρασης ενανθράκωσης προστίθεται επίσης, προκειμένου να εξεταστεί σε ποιο βαθμό λαμβάνει χώρα η αντίστροφη αντίδραση, όταν η θερμοκρασία στο εσωτερικό του αντιδραστήρα είναι κάτω από τις συνθήκες ενανθράκωσης. Η διάμετρος των στερεών σωματιδίων υπολογίζεται μέσω της διαμέτρου Sauter [52].

4.5.2 Γεωμετρία και πλέγμα

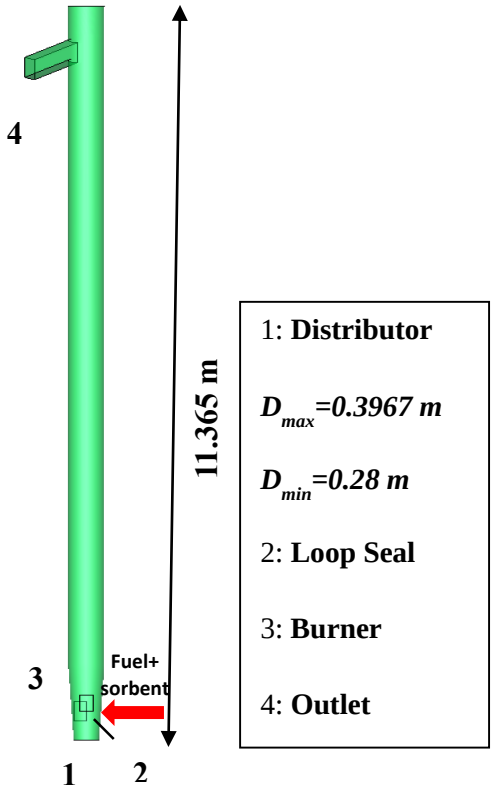

Εικόνα 27. 3Δ σχέδιο της μονάδας.

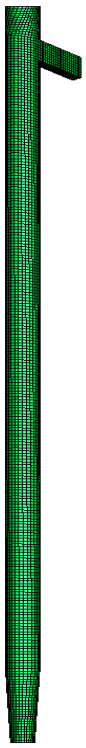

Εικόνα 28. 3Δ αραιό πλέγμα της μονάδας.

Το 3Δ υπολογιστικό πεδίο που αντιστοιχεί στην γεωμετρία του αντιδραστήρα απεικονίζεται στην **Εικόνα 27**. Το βασικό μέρος του αντιδραστήρα είναι ένας κυλινδρικός σωλήνας ύψους 11.365 μέτρων και μεταβλητούς εσωτερικής διαμέτρου από 0.28 m κοντά στον πυθμένα μέχρι 0.3967 μέτρα στο ύψος 1.14.

Από το ύψος αυτό και μετά η διάμετρος παραμένει σταθερή ίση με 0.3967 μέτρα. Το δομημένο αριθμητικό πλέγμα αποτελείται από 18,698 εξαεδρικά στοιχεία, με λόγο d_{cell}/d_p ίσο με 466.52 (**Εικόνα 28**).

4.5.3 Συνοριακές συνθήκες και συνθήκες λειτουργίας

Οι ροές αερίων/στερεών και άλλες οριακές συνθήκες του προβλήματος προσδιορίζονται πειραματικά από την TUDA [325]. Ο **Πίνακας 16** παρουσιάζει τις ιδιότητες των αέριων και στερεών φάσεων. Ακολουθήθηκε η παραδοχή ότι το μέγεθος των σωματιδίων του καυσίμου και του προσροφητικού δεν μεταβάλλεται με το χρόνο. Τέλος, η μάζα των σωματιδίων είναι ίση με 13.5 κιλά.

Πίνακας 16. Ιδιότητες στερεού-αερίου (Σωματίδια: **Geldart A**).

Παράμετρος	Τιμή	Μονάδες	Παράμετρος	Τιμή	Μονάδες
ρ_s	1650	$kg \cdot m^{-3}$	ε_{mf}	0.55	-
d_{ps}	91.39	μm	ε_{max}	0.9997	-
d_{pf}	34.67	μm	$\varepsilon_{s,max}$	0.65	-
ρ_g	0.3434	$kg \cdot m^{-3}$	e_{ss}	0.9	-
μ_g	$4.45 \cdot 10^{-5}$	$kg\ m^{-1}s^{-1}$			

4.5.4 Αποτελέσματα

Η **Εικόνα 29** απεικονίζει τη μέση χρονικά στατική πίεση κατά μήκος του άξονα του αντιδραστήρα σε σύγκριση με τα αντίστοιχα πειραματικά δεδομένα. Από το γράφημα συνάγεται ότι το προφίλ πίεσης προβλέπεται με μέτριο επίπεδο ακρίβειας. Με βάση προηγούμενες αριθμητικές μελέτες [133, 136, 174], κυρίως όσον αφορά την εγκυρότητα του μοντέλου EMMS, η παρούσα μελέτη δείχνει την καλύτερη εγκυρότητά του σε σχέση με το μοντέλο του Gidaspow, ακόμη και για πολύπλοκες αριθμητικές συνθήκες, όπου μια σειρά από πολλούς φυσικούς μηχανισμούς λαμβάνουν χώρα ταυτόχρονα, όπως στην περίπτωση ενός καυστήρα. Η μέγιστη απόκλιση από τα πειραματικά δεδομένα εντοπίζεται στην κάτω ζώνη του αντιδραστήρα, όπου το δεύτερο σημείο πίεσης είναι σχεδόν δύο φορές υψηλότερο από την πραγματική πίεση που υπολογίστηκε. Για τα υπόλοιπα σημεία, η συμφωνία του αριθμητικού μοντέλου με τα αντίστοιχα πειραματικά δεδομένα είναι καλύτερη- δικαιολογώντας έτσι ότι το προτεινόμενο μοντέλο EMMS, συμπεριφέρεται αρκετά καλά, ακόμη και υπό πολύπλοκες συνθήκες και υπό συνθήκες αραιούς πλέγματος.

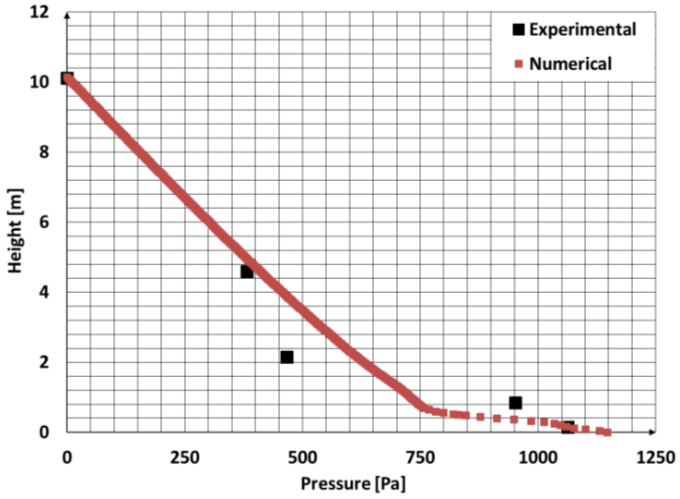

Εικόνα 29. Χρονικά μέση στατική πίεση στον άξονα του αντιδραστήρα για t_{aver} =15 δευτερόλεπτα.

Η **Εικόνα 30** απεικονίζονται contour των χρονικά μέσων κλασμάτων στερεού όγκου των φάσεων προσροφητικού και καυσίμου. Αξίζει να σημειωθεί ότι το σωματιδιακό φορτίο είναι σχετικά χαμηλό και το μέγεθος των σωματιδίων του καυσίμου είναι σχετικά μικρό, σε σχέση με μία τυπική μονάδα ρευστοποιημένης κλίνης ανακυκλοφορίας. Αυτές οι συνθήκες λειτουργίας ελαχιστοποιούν την αντίστροφη ροή των στερεών εντός της μονάδας, ενώ η παραγόμενη ιπτάμενη τέφρα λόγω της μικρής της κοκκωμετρίας δεν συλλέγεται αποδοτικά από τον κυκλώνα του ασβεστοποιητή, ώστε να επιστρέψει στον κύριο αντιδραστήρα. Αυτό έχει ως αποτέλεσμα, την ανακυκλοφορία αυτής της αδρανούς μάζας μεταξύ των δύο αντιδραστήρων του συζευγούς ζεύγους, γεγονός που πρέπει να αποφεύγεται. Ωστόσο, η ολίσθηση του άνθρακα στον ενανθρακωτή και η καύση εκεί ελαχιστοποιείται, λόγω του πολύ λεπτού μεγέθους των σωματιδίων του καυσίμου που ευνοεί την γρήγορη καύση του.

Όσον αφορά το θερμοκρασιακό προφίλ, τα αριθμητικά αποτελέσματα ακολουθούν σχεδόν την ίδια τάση με τα πειραματικά δεδομένα (**Εικόνα 31**). Μια μικρή υποεκτίμηση των αποτελεσμάτων του θερμοκρασιακού προφίλ αποδίδεται στο γεγονός ότι οι σταθερές ταχύτητας αντίδρασης που εφαρμόστηκαν στην παρούσα εργασία έχουν ανακτηθεί από τη βιβλιογραφία και ενδέχεται να μην περιγράφουν απόλυτα τη συμπεριφορά του συγκεκριμένου καυσίμου και του προσροφητικού υλικού που χρησιμοποιήθηκε στα πειράματα. Επιπλέον, η υπό πρόβλεψη θερμοκρασία αερίου μπορεί να διορθωθεί περαιτέρω με την εφαρμογή ακριβέστερων πολυωνυμικών συντελεστών για μια πιο ρεαλιστική εξάρτηση της ειδικής θερμοχωρητικότητας από τη θερμοκρασία [315], [316].

Άλλα συμπεράσματα που εξάγονται από την ανάλυση αυτή είναι ότι για ένα εύρος ύψους περίπου [0-0,9] μέτρα η θερμοκρασία του αερίου είναι μικρότερη από την απαιτούμενη για την ασβεστοποίηση. Για το λόγο αυτό, κοντά στην περιοχή αυτή, λαμβάνει χώρα η αντίστροφη αντίδραση, δηλαδή η ενανθράκωση. Το γεγονός αυτό, αποδίδεται στη ροή του πρωτεύοντος αέρα και του οξυγόνου που εισέρχεται στη μονάδα από τον πυθμένα του αντιδραστήρα, με θερμοκρασία ίση με 623.1 K, καθώς και στον δευτερεύοντα αέρα που προέρχεται από τα loop seal και τον βοηθητικό καυστήρα, με θερμοκρασία περίπου ίση με 300 K. Πάνω από το ύψος του τμήματος του καυστήρα, όπου το καύσιμο εισέρχεται στον αντιδραστήρα, η θερμοκρασία αυξάνεται γρήγορα στις συνθήκες ασβεστοποίησης.

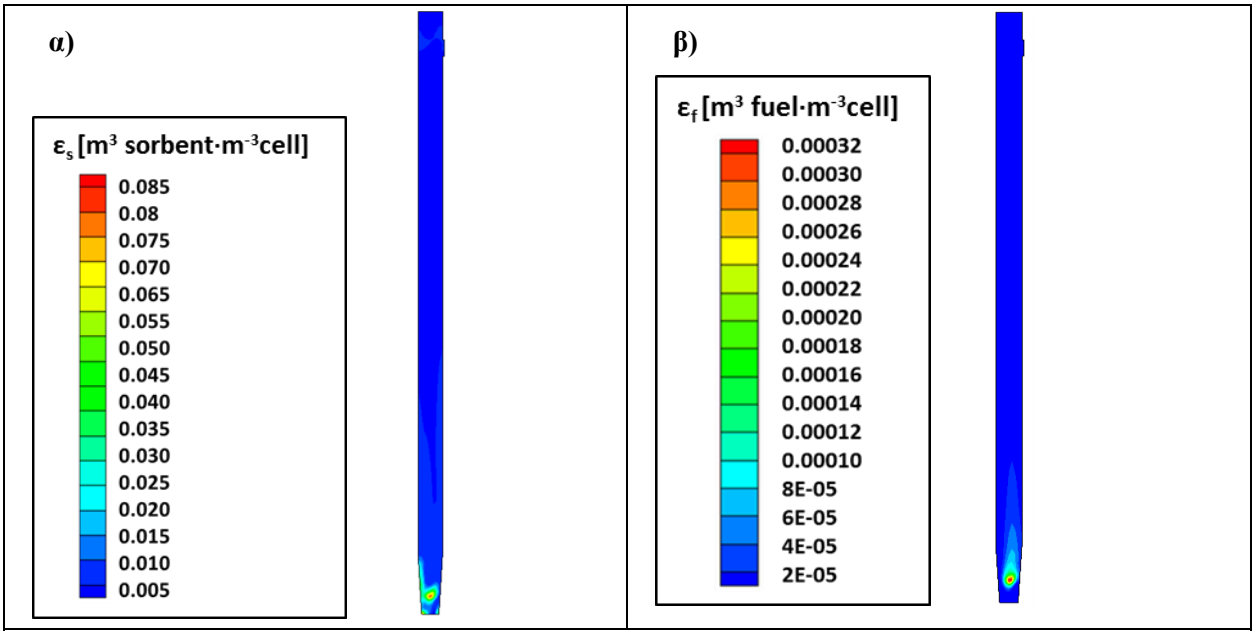

Εικόνα 30. Contour των μέσων χρονικών κλασμάτων όγκου του α) προσροφητικού και του β) καυσίμου σε ένα επίπεδο X=0 για μέσο χρόνο ίσο με t_{aver} =15 δευτερόλεπτα.

Ένα άλλο σημαντικό συμπέρασμα που εξάγεται είναι ότι τα στερεά σωματίδια του προσροφητικού υλικού κινούνται προς τα πάνω και δεν παρατηρείται ανάμιξη προς τα πίσω, εκτός από ένα ύψος περίπου ίσο με 0.4 μέτρα, όπου ορισμένα στερεά σωματίδια κινούνται προς τα κάτω (**Εικόνα 32**). Ωστόσο, στην περιοχή αυτή μέχρι ένα ύψος περίπου 1 μέτρου η θερμοκρασία είναι κάτω από τις συνθήκες ασβεστοποίησης και ευνοείται μόνο η αντίδραση ενανθράκωσης. Έτσι, με βάση τις τρέχουσες παραδοχές και συνοριακές συνθήκες του μοντέλου, τα σωματίδια του προσροφητικού υλικού που εισέρχονται στην περιοχή αυτή πιθανότατα δεν θα υποστούν πολλαπλούς κύκλους ενανθράκωσης-ασβεστοποίησης. Ωστόσο, δεδομένου ότι η εγκυρότητα του τρέχοντος μοντέλου θα πρέπει να εξεταστεί λεπτομερέστερα, όσον αφορά τις παραδοχές που ακολουθούνται, το επιχείρημα αυτό θα πρέπει να εξεταστεί περισσότερο στο μέλλον. Θα πρέπει να τονιστεί ότι μια πιθανή παγίδευση σωματιδίων του προσροφητικού υλικού σε περιοχές με πολλαπλούς κύκλους ενανθράκωσης-ασβεστοποίησης θα μπορούσε να μειώσει τη συνολική δραστικότητά του και θα πρέπει να εξεταστεί διεξοδικότερα σε μελλοντικές προσομοιώσεις.

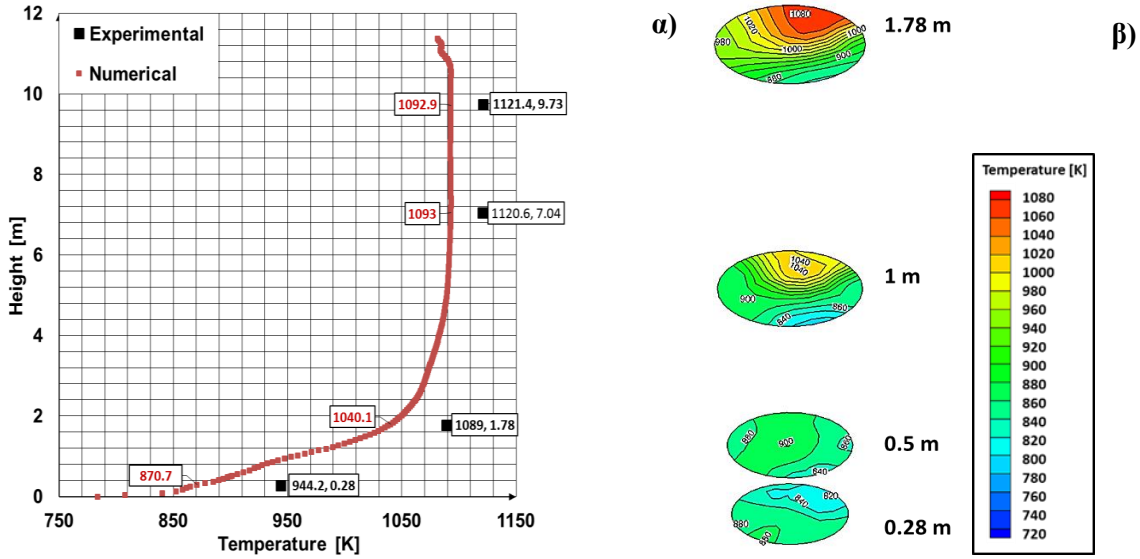

Εικόνα 31. α) Χρονικά μέση τιμή της θερμοκρασίας κατά μήκος του αντιδραστήρα. β) Contour των χρονικά μέσων τιμών της θερμοκρασίας σε διάφορα ύψη της μονάδας.

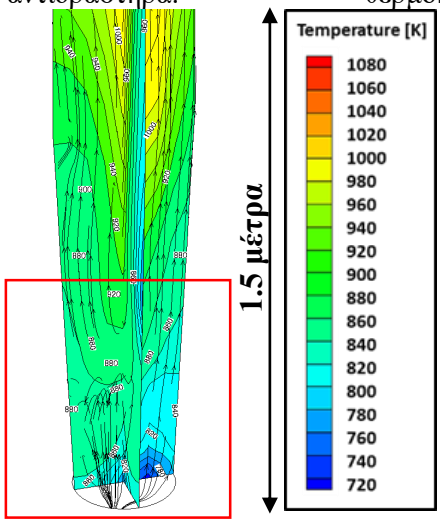

Εικόνα 32. Contour του προφίλ της μέσης θερμοκρασίας του αερίου με γραμμές ροής του ασβέστου για t_{aver} =15 δευτερόλεπτα.

Ο **Πίνακας 17** παρουσιάζει τις αριθμητικά υπολογισμένες συγκεντρώσεις CO_2, O_2 (σε ξηρή βάση) στην έξοδο του αντιδραστήρα, σταθμισμένες κατά μάζα και μέσο όρο χρόνου, σε σύγκριση με τα πειραματικά δεδομένα. Τα υψηλά σφάλματα των αριθμητικών μεταβλητών, μπορούν να αποδοθούν κυρίως στο γεγονός ότι το πολύπλοκο αριθμητικό μοντέλο που αναπτύχθηκε δεν έχει εξεταστεί εκτενώς από άποψη εγκυρότητας. Ένας λόγος μπορεί να είναι η πιθανή έλλειψη εγκυρότητας των συντελεστών μεταφοράς θερμότητας ή η αγνόηση τυχόν απωλειών θερμότητας από τα πλευρικά τοιχώματα του αντιδραστήρα. Οι ρυθμοί αντίδρασης -για τις ετερογενείς αντιδράσεις- που εφαρμόστηκαν προέρχονται από την ανοικτή βιβλιογραφία και επηρεάζουν, ως εκ τούτου, την ακρίβεια του μοντέλου, καθώς θα πρέπει να είναι για τα συγκεκριμένα στερά καύσιμα/προσροφητικά. Θα πρέπει να υπογραμμιστεί ωστόσο ότι το τρέχον μοντέλο είναι υψηλής πολυπλοκότητας και ότι άλλοι παράγοντες, όπως τα εφαρμοζόμενα μοντέλα οπισθέλκουσας, θα μπορούσαν ενδεχομένως να επηρεάσουν την αντίδραση των χημικών στοιχείων / ενώσεων.

Πίνακας 17. Μοριακά κλάσματα CO_2 και O_2 στην έξοδο του αντιδραστήρα.

Χημικό στοιχείο / ένωση	Αριθμητική τιμή	Πειραματική τιμή	Σχετικό σφάλμα
CO_2 στην έξοδο (για ξηρό καυσαέριο)			
	(38.55±6.79)%	(44.2±2.4)%	12.79%
O_2 στην έξοδο (για ξηρό καυσαέριο)			
	(4.11±3.722)%	(6±2.04)%	31.52%

4.6 Μοντελοποίηση ασβεστοποιητή 300 kW_{th} έμμεσης πρόσδοσης θερμότητας

4.6.1 Πρόλογος

Στην προηγούμενη υποενότητα, το μοντέλο EMMS επικυρώθηκε έναντι πειραμάτων, λαμβάνοντας ως σημείο αναφοράς μια μονάδα πιλοτικής κλίμακας, δηλαδή τον ανθρακοποιητή 1 MW_{th} που βρίσκεται στο TUDA. Επιπλέον, προσομοιώθηκε η αντίδραση ενανθράκωσης στο εσωτερικό ενός ενανθρακωτή 1 MW_{th} με καύση οξυγόνου και τα αποτελέσματα του κλάσματος μάζας CO_2 συμφωνούν με τα πειραματικά δεδομένα. Μετά την επικύρωση του μοντέλου EMMS και την επιτυχή αναπαράσταση της υδροδυναμικής ροής υπό ισοθερμικές συνθήκες στον ανθρακοποιητή, μαζί με την επιτυχή ανάπτυξη του μοντέλου αντίδρασης στον ασβεστοποιητή που τροφοδοτείται με οξυγόνο, σε αυτό την υποενότητα παρουσιάζεται η ανάπτυξη και επικύρωση του μοντέλου ενός έμμεσα θερμαινόμενου ασβεστοποιητή 300 kW_{th} που βρίσκεται στις εγκαταστάσεις του TUDA. Το μοντέλο αυτό, λαμβάνει υπόψη, εκτός από την υδροδυναμική της ροής, όλους τους μηχανισμούς μεταφοράς θερμότητας (αγωγή, συναγωγή, ακτινοβολία). Λαμβάνεται επίσης υπόψη η επίδραση της τύρβης, καθώς και η κινητική της αντίδρασης ασβεστοποίησης. Το τελικό προϊόν, το οποίο είναι ένα αποτελεσματικό και ακριβές μοντέλο CFD, μπορεί να αξιοποιηθεί περαιτέρω για τη μελέτη διαφόρων σεναρίων πολυφασικών ροών αερίου-στερεού.

Ο μελετώμενος ασβεστοποιητής αποτελεί μέρος του συστήματος IHCaL που απεικονίζεται στην **Εικόνα 20**, και λαμβάνει θερμότητα μέσω σωλήνων παροχής θερμότητας. Οι σωλήνες θερμότητας τοποθετούνται στο εσωτερικό του συστήματος με τη μορφή πεπλεγμένης οριζόντιας διάταξης (στο σχέδιο αναφοράς). Στο εσωτερικό των σωλήνων θερμότητας ρέει ένα εργαζόμενο ρευστό που είναι νατριούχο για ένα εύρος θερμοκρασιών λειτουργίας μεταξύ 890-950 ºC. Οι σωλήνες θερμότητας σχεδιάζονται για ικανότητα μεταφοράς θερμότητας περίπου 300 kW_{th} στους 950 °C [323].

4.6.2 Αριθμητική μέθοδος

Στην παρούσα ενότητα παρουσιάζονται ορισμένες από τις κοινές παραδοχές που υιοθετούνται για την μοντελοποίηση του συγκεκριμένου συστήματος:

- Χρονικά μεταβαλλόμενη ροή με αριθμό Courant μικρότερο από 0.75 με σχεδόν 2Δ πεδίο;
- Πολυφασική μέθοδος: Μέθοδος κατά Euler-Euler TFM δύο φάσεων (μία στερεά και μία αέρια);
- Χρήση του μοντέλου οπισθέλκουσας EMMS;
- Προσομοίωση όλων τον τρόπων μεταφοράς θερμότητας (αγωγή, συναγωγή και ακτινοβολία);
- Η ροή λαμβάνεται ως τυρβώδης;
- Μοντέλο ασβεστοποίησης βασιζόμενο στους Labiano et al. [324];
- Η μάζα των στερεών διατηρείται σταθερή ίση με 18 κιλά;
- Το ρευστό στο εσωτερικό των σωλήνων είναι νάτριο με μέση θερμοκρασία ίση με 895 ^{o}C.

4.6.3 Επικύρωση αριθμητικού μοντέλου

Η απλουστευμένη γεωμετρία του καυστήρα BFB απεικονίζεται στην **Εικόνα 33**. Μοντελοποιείται μόνο μία φέτα του τρισδιάστατου πεδίου, προκειμένου να μελετηθούν γρήγορα διάφορα σενάρια διάταξης των σωλήνων θερμότητας. Όσον αφορά το αριθμητικό πλέγμα, χρησιμοποιείται ένα καθαρό εξαεδρικό πλέγμα και δοκιμάζονται τρεις πυκνότητες πλέγματος ένα αραιό με 6600 κελιά, ένα μεσαίο με 28115 κελιά και ένα πυκνό με 224600 κελιά. Κάθε πυκνότητα πλέγματος αντιστοιχεί σε λόγο d_{cell}/d_p ίσο με ~220, ~110 και ~55, αντίστοιχα.

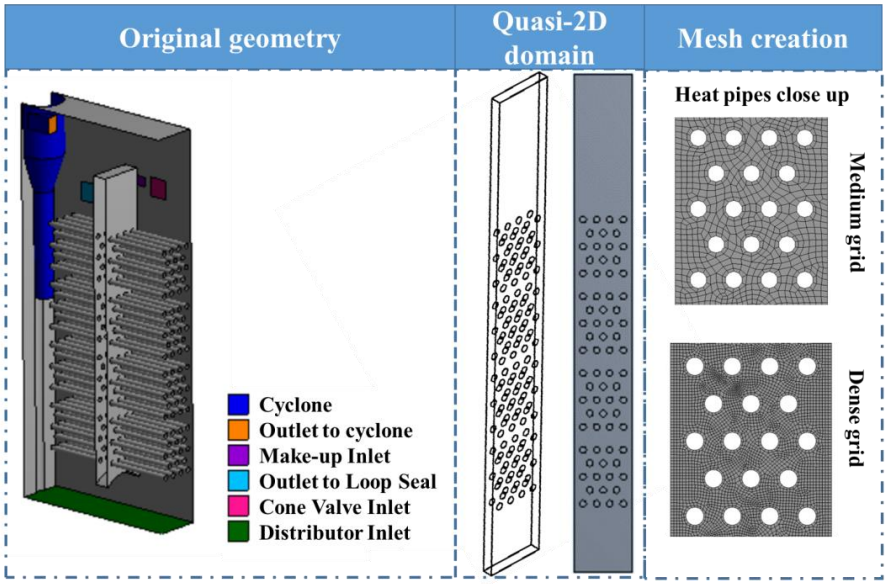

Εικόνα 33. Τρισδιάστατο σχήμα του αντιδραστήρα, σχεδόν 2Δ πεδίο και διακριτοποίηση πεδίου.

Ο **Πίνακας 18** συνοψίζει τις ιδιότητες αερίου-στερεού που χρησιμοποιήθηκαν στο μοντέλο. Οι θερμικές ιδιότητες του ασβέστου και ασβεστόλιθου λαμβάνονται από τους [325].

Πίνακας 18. Ιδιότητες στερεού-αερίου.

Παράμετρος	Μονάδες	Τιμή	Παράμετρος	Μονάδες	Τιμή
ρ_s	kg·m^{-3}	1657	U_0	m·s^{-1}	~0.16
d_p	μm	99	ρ_g	kg·m^{-3}	0.42
$k_{s,CaCo3}$	W·m^{-1}·K^{-1}	~2.259	μ_g	kg·m^{-1} ·s^{-1}	4.7·10^{-5}
$k_{s,CaO}$	W·m^{-1}·K^{-1}	~0.318			

Όσον αφορά τις εφαρμοζόμενες οριακές συνθήκες/συνθήκες λειτουργίας, πρέπει να σημειωθεί ότι αυτές αντιστοιχούν στον αρχικό πεδίο (όπως υποδεικνύουν από τα πειραματικά δεδομένα). Ο **Πίνακας 19** παραθέτει τις διαφορετικές τιμές των παραμέτρων εισόδου στο αρχικό και στο απλουστευμένο πεδίο.

Πίνακας 19. Συνοριακές συνθήκες και συνθήκες λειτουργίας (αρχικό και σχεδόν 2Δ πεδίο).

Παράμετρος	Αρχικό σχέδιο	Απλοποιημένη γεωμετρία*
Μάζα σωματιδίων [kg]	370	~18
Όγκος αντιδραστήρα [m^3]	0.724	0.036
Συνολική επιφάνεια σωλήνων θερμότητας [m^2]	6.45	0.375
Επιφάνεια πυθμένα αντιδραστήρα [m^2]	0.345	0.015
Πρωτεύον ρεύμα αέρα [kg/s]	0.0244	0.00106
Μάζα σωματιδίων από τον ενανθρακωτή [$kg \cdot s^{-1}$]	0.263	0.013
**** Οι τιμές υπολογίζονται με τον καθορισμό ενός συντελεστή προσαρμογής επί 20***		

Διάφορες περιπτώσεις προσομοιώθηκαν για να ελεγχθεί (i) η επίδραση του πλέγματος και (ii) η επίδραση του μοντέλου υπολογισμού του θερμικού οριακού στρώματος στις σωληνώσεις στα αποτελέσματα του αριθμητικού μοντέλου. Τα αριθμητικά αποτελέσματα δείχνουν ότι το μοντέλο CFD έχει καλή συμφωνία με τα πειραματικά αποτελέσματα όσον αφορά το κλάσμα μάζας CO_2 στην έξοδο του αντιδραστήρα. (**Πίνακας 20**). Όσον αφορά τη θερμότητα από τους σωλήνες θερμότητας, το αριθμητικό μοντέλο καταλήγει σε μια μικρή υπερεκτίμηση, γεγονός που μπορεί να αποδοθεί στις αβεβαιότητες που επιβάλλονται από το σύνολο των ιδιοτήτων των υλικών (π.χ. συντελεστής εκπομπής των σωλήνων θερμότητας). Επιπλέον, μπορεί να παρατηρηθεί ότι μπορεί να επιτευχθεί ανεξαρτησία δικτύου με μεσαία πυκνότητα πλέγματος. Έτσι, μπορεί να σημειωθεί ότι το μοντέλο με τη μεσαία πυκνότητα πλέγματος (d_{cell}/d_p ~110) δίνει αποτελέσματα αποδεκτής ακρίβειας και μπορεί να χρησιμοποιηθεί για την αριθμητική προσομοίωση διαφόρων σεναρίων (π.χ. βελτιστοποίηση διάταξης σωλήνων θερμότητας, μελέτη συνθηκών λειτουργίας κ.λπ.).

Πίνακας 20. Αποτελέματα του μοντέλου για διάφορες πυκνότητες πλέγματος (t_{aver}=10 δευτερόλεπτα).

	Πείραμα	**Αραιό πλέγμα**	**Σφάλμα (%)**	**Μεσαίο πλέγμα**	**Σφάλμα (%)**	**Πυκνό πλέγμα**	**Σφάλμα (%)**
CO_2 έξοδος ($kg \cdot kg^{-1}$)	0.32–0.33	~0.348	~5.45	~0.35	~6.00	~0.35	~6.00
Θερμότητα από τους σωλήνες θερμότητας ($kW \cdot m^{-2}$)	17.98-20.60	~21.67	5.23	~25.46	23.62	~24.79	20.4

Ένα άλλο συμπέρασμα που εξάγεται από την ανάλυση αυτή είναι ότι το μερίδιο της ροής θερμότητας ακτινοβολίας στο συνολικό ρυθμό μεταφοράς θερμότητας είναι 15 % έως 19 % για το χονδρό και το μεσαίο πλέγμα, αντίστοιχα. Το μεγαλύτερο μέρος της μεταφοράς θερμότητας, επομένως, προκύπτει από τον όρο συναγωγής. Αυτό είναι ένα αποτέλεσμα αρκετά ευσταθές που αποδείχθηκε επίσης τους [326], όπου προσομοιώθηκε ο πλήρης αντιδραστήρας και τα αποτελέσματα του ρυθμού μεταφοράς θερμότητας συγκρίθηκαν με θεωρητικά μοντέλα όπως αυτό των Kunii και Levenspiel [52].

4.6.4 Βελτιστοποίηση σχεδιασμού

Αυτή η υποενότητα παρουσιάζει τα αποτελέσματα της βελτιστοποίησης του σχεδιασμού της διάταξης των σωλήνων θερμότητας στο εσωτερικό του αντιδραστήρα, (i) μεταβάλλοντας την πλευρική τους απόσταση από 1.1d έως 2d και (ii) συγκρίνοντας τη διάταξη σε σειρά με την πεπλεγμένη διάταξη. Σε όλες τις

περιπτώσεις που μελετήθηκαν, ο ίδιος αριθμός (δηλ. 72) και η διάμετρος των σωλήνων θερμότητας έχει διατηρηθεί η ίδια καθώς και ο λόγος d_{cell}/d_p (~110) για να διατηρηθεί η ίδια πυκνότητα του πλέγματος.

Τα υδροδυναμικά αποτελέσματα αυτής της ανάλυσης δείχνουν ότι η διάταξη των σωλήνων θερμότητας δεν επηρεάζει σημαντικά τη συνολική πτώση πίεσης του συστήματος, **Εικόνα 34**. Μια μικρή διαφορά στη συνολική πτώση πίεσης, με την περίπτωση αναφοράς (πεπλεγμένη διάταξη 2d), μπορεί να εντοπιστεί για τη διάταξη σε σειρά στο ανώτερο τμήμα της ρευστοποιημένης κλίνης. Τοπικά παρατηρείται ότι στην περίπτωση της πεπλεγμένης διάταξης με τους σωλήνες θερμότητας να βρίσκονται σε κοντινή απόσταση 1.1 d, οι φυσαλίδες αερίου ρέουν στις πλευρές των σωλήνων κοντά στα πλευρικά τοιχώματα. Η καλή ανάμιξη αερίου-στερεών επιτυγχάνεται καλύτερα όταν προχωράμε σε μεγαλύτερες αποστάσεις των σωλήνων θερμότητας, όπως 2d, προωθώντας έτσι το συνολικό ρυθμό μεταφοράς θερμότητας.

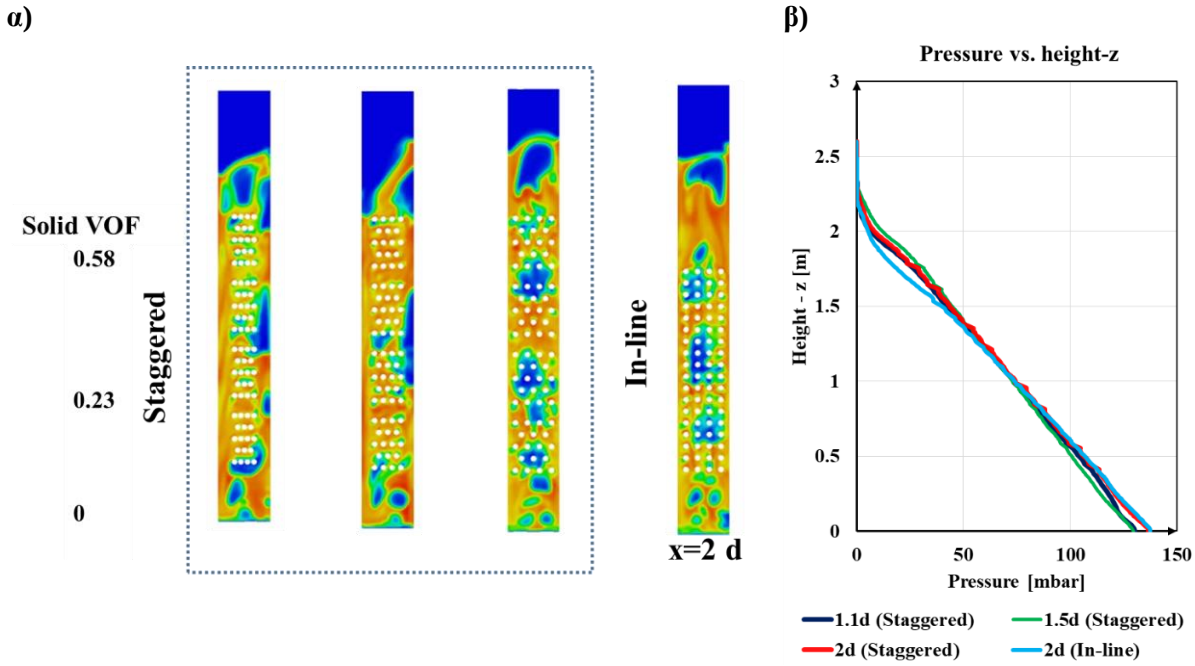

Εικόνα 34. α) Στιγμιαίο κλάσμα όγκου στερεών σε t=30 δευτερόλεπτα και β) μέσο προφίλ πίεσης (σύγκριση διαφορετικών πεπλεγμένων διατάξεων και πεπλεγμένης έναντι γραμμικής διάταξης).

Πίνακας 21. Αποτελέσματα διαφορετικών διατάξεων.

Αριθμός περίπτωσης	**Διάταξη**	**Συνολική μεταφορά θερμότητας Q [W]**	**Ακτινοβολία/ Συνολική μεταφορά θερμότητας %**	**CO_2 στην έξοδο ($kg \cdot kg^{-1}$)**
Περίπτωση 1	Πεπλεγμένη 1.1d	7943.29	~21.80	~ 0.328
Περίπτωση 2	Πεπλεγμένη 1.5d	9262.50	~22.01	~ 0.345
Περίπτωση 3	Πεπλεγμένη 2d	9544.82	~23.62	~ 0.35
Περίπτωση 4	Σε σειρά 2d	8929.34	~21.80	~ 0.34

ΚΕΦΑΛΑΙΟ 5 Μοντελοποίηση συστήματος αποθήκευσης αισθητής θερμότητας βιομηχανικής κλίμακας

5.1 Αριθμητική μέθοδος

Ο εναλλάκτης θερμότητας FBHE μεγάλης κλίμακας (INTREX™) που μελετήθηκε στην παρούσα υποενότητα, αναπτύχθηκε από την SFW. Σε αυτόν τον εναλλάκτη, τα θερμά στερεά που προέρχονται από τον κυκλώνα εισέρχονται στον κύριο θάλαμο HE μέσω του downcomer. Οι επιφάνειες μεταφοράς θερμότητας (δέσμες σωλήνων), όπου εισρέει ατμός ή νερό, βρίσκονται σε αυτόν τον θάλαμο και έρχονται σε επαφή με τα αιωρούμενα σωματίδια. Ο ρυθμός ροής των στερεών γύρω από τις δέσμες σωλήνων ελέγχεται με τον έλεγχο της ταχύτητας του αέρα ρευστοποίησης στο κάτω μέρος του θαλάμου. Εκτός από αυτό, ελέγχοντας τον ρυθμό ροής των στερεών μέσω του θαλάμου του υπερθερμαντήρα INTREX™, η απορρόφηση θερμότητας μπορεί να μεταβάλλεται δίνοντας λειτουργική ευελιξία για τον έλεγχο της θερμοκρασίας του κλιβάνου ή/και του ατμού υπερθέρμανσης. Τα ψυχθέντα στερεά επιστρέφουν στον κάτω κλίβανο μέσω του σωλήνα επιστροφής στερεών. Με εσωτερική ανακυκλοφορία στερεών, πρόσθετα υλικά θερμής κλίνης οδηγούνται από τον κλίβανο στον INTREX™ μέσω ανοιγμάτων στο πίσω μέρος/κοινό τοίχωμα του κλιβάνου. Τέλος, τυχόν περίσσεια στερεών σωματιδίων στο εσωτερικό του κύριου θαλάμου INTREXTM επιστρέφει στον κλίβανο μέσω ανοιγμάτων υπερχείλισης.

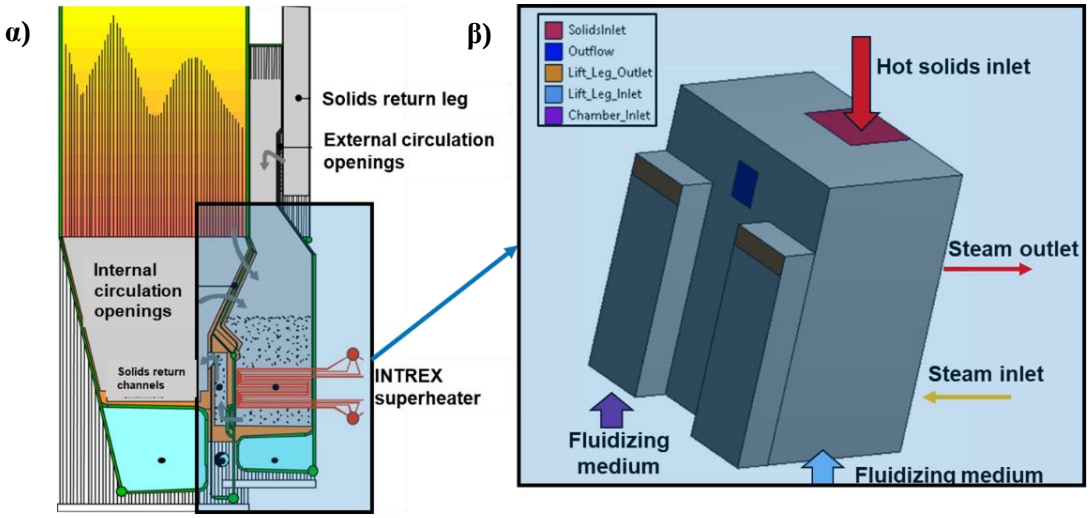

Εικόνα 35. α) Εναλλάκτης INTREX™, β) σχέδιο που χρησιμοποιήθηκε στο CFD μοντέλο.

Για να επιτευχθεί η ακριβής μοντελοποίηση του εναλλάκτη θερμότητας (INTREX™), αναπτύσσεται ένα τρισδιάστατο μοντέλο στην πλατφόρμα ANSYS Fluent v17.1. Το συγκεκριμένο μοντέλο προσομοιώνει ρητά τις δέσμες σωλήνων που περικλείονται στο εσωτερικό του θαλάμου του εναλλάκτη θερμότητας, σε αντίθεση με τα διαθέσιμα μοντέλα στην πρόσφατη βιβλιογραφία που προσομοιώνουν έμμεσα το τμήμα HE μέσω πορώδους μέσου. Το μοντέλο είναι παρόμοιο με εκείνο που χρησιμοποιήθηκε για τον ασβεστοποιητή φυσαλίδων 300kW_{th} που βρίσκεται στο TUDA, ωστόσο δεν λαμβάνει υπόψη την αντίδραση της ασβεστοποίησης, αλλά περιλαμβάνει επιπλέον ανάπτυξη κώδικα για τη μεταφορά θερμότητας στο

εσωτερικό των σωλήνων θερμότητας. Παρόλο που δεν υπάρχουν διαθέσιμα πειραματικά δεδομένα για την επικύρωση του μοντέλου, θεωρείται αρκετά αξιόπιστο και τα αποτελέσματα επαρκούς ακρίβειας.

Η μεταφορά θερμότητας από την ρευστοποιημένη κλίνη με φυσαλίδες στις οριζόντιες δέσμες σωλήνων περιλαμβάνει διάφορους μηχανισμούς. Πιο συγκεκριμένα, η θερμότητα μεταφέρεται από τη μάζα της κλίνης στα τοιχώματα των σωλήνων (i) μέσω συναγωγής των σωματιδίων και (ii) συναγωγής των αερίων (Α), μέσω αγωγής εντός του σωλήνα (Β) και μέσω συναγωγής στο εσωτερικό του σωλήνα (Γ). Η μεταφορά θερμότητας με ακτινοβολία από τις συστάδες και τη διασκορπισμένη φάση δεν περιλαμβάνεται σε αυτό το μοντέλο. Η εφαρμογή των μηχανισμών μεταφοράς θερμότητας Β και C περιλαμβάνεται στο μοντέλο CFD μέσω κατάλληλων UDFs στη γλώσσα προγραμματισμού C. Σε αυτόν τον αλγόριθμο σε κάθε επανάληψη, η συνολική μεταφορά θερμότητας σε Watt (συνολική Q) σε κάθε δέσμη σωλήνων ανακτάται από τον επιλύτη. Με βάση τις ιδιότητες του ατμού (c_p), τη ροή μάζας και τη θερμοκρασία εισόδου, μπορεί να εκτιμηθεί η θερμοκρασία εξόδου. Στη συνέχεια, η θερμοκρασία κατά μήκος των σωλήνων υπολογίζεται με βάση μια γραμμική παρεμβολή μεταξύ (θερμοκρασίας εισόδου) T_{in} και (θερμοκρασίας εξόδου) T_{out}. Η λύση συνεχίζεται μέχρι να επιτευχθεί ισορροπία. Η **Εικόνα 36** παρουσιάζει ένα σχηματικό διάγραμμα του αλγορίθμου του μοντέλου μεταφοράς θερμότητας που έχει αναπτυχθεί στην παρούσα διατριβή.

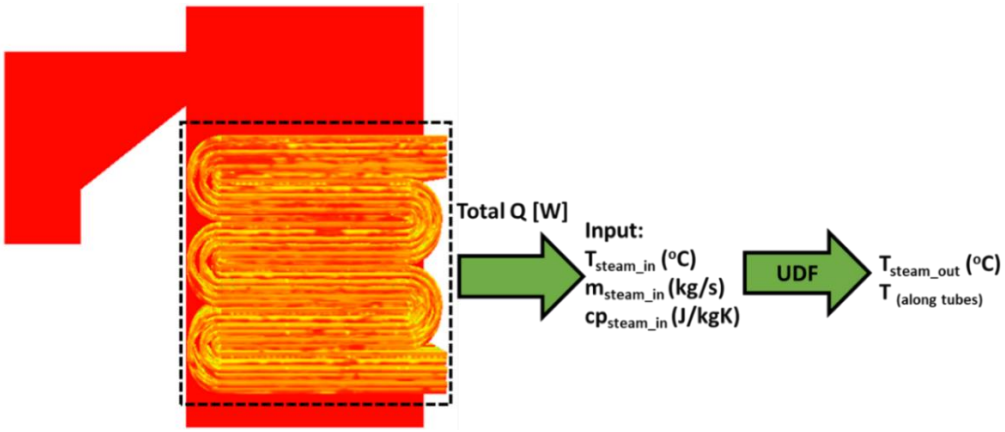

Εικόνα 36. Αλγόριθμος μοντέλου μεταφοράς θερμότητας, που εφαρμόζεται στην παρούσα διατριβή.

Η γεωμετρία CAD δημιουργείται στο ANSYS Design Modeler, **Εικόνα 37**. Οι σχεδιαστικές προδιαγραφές του μοντελοποιημένου ΗΕ είναι παρόμοιες με εκείνες του βιομηχανικού ΗΕ που παρουσιάζεται στο [63]. Ορισμένα δεδομένα σχεδιασμού και λειτουργίας δεν παρουσιάζονται στην παρούσα διατριβή λόγω εμπιστευτικών πληροφοριών για το μελετώμενο σύστημα. Ωστόσο, οι συγκεκριμένες λειτουργικές παράμετροι του εναλλάκτη θερμότητας (π.χ θερμοκρασία και παροχή του μέσου ρευστοποίησης, θερμοκρασία της κλίνης, πτώσης πίεσης, ιδιότητες του ατμού) είναι σύμφωνες με το τυπικό εύρος τιμών των λειτουργικών παραμέτρων για τους FBHE σε βιομηχανικούς λέβητες CFB.

Ένα τρισδιάστατο αριθμητικό πλέγμα αποτελούμενο από 3.7 εκατομμύρια εξαεδρικά στοιχεία κατασκευάζεται στο ANSYS (**Εικόνα 38)**. Λόγω της πολυπλοκότητας της γεωμετρίας και της παρουσίας δεσμίδων σωλήνων, χρησιμοποιείται η μέθοδος CutCell η οποία μετατρέπει ένα πλέγμα όγκου σε ένα κυρίως καρτεσιανό πλέγμα (δηλαδή το πλέγμα αποτελείται κυρίως από εξαεδρικά στοιχεία, με επιφάνειες που είναι ευθυγραμμισμένες με τους άξονες συντεταγμένων). Αυτό έχει μεγάλη σημασία για τη συγκεκριμένη γεωμετρική διαμόρφωση που αποτελείται από μια σειρά σωλήνων και απαιτείται ακριβής εκτίμηση του ρυθμού μεταφοράς θερμότητας.

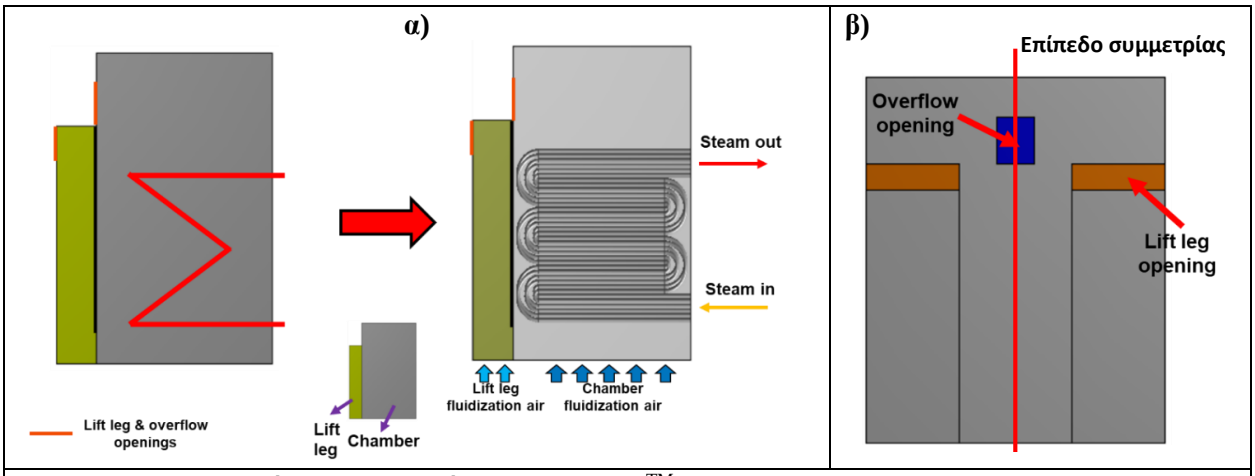

Εικόνα 37. Δημιουργία της γεωμετρίας του INTREX™ στο ANSYS DM.

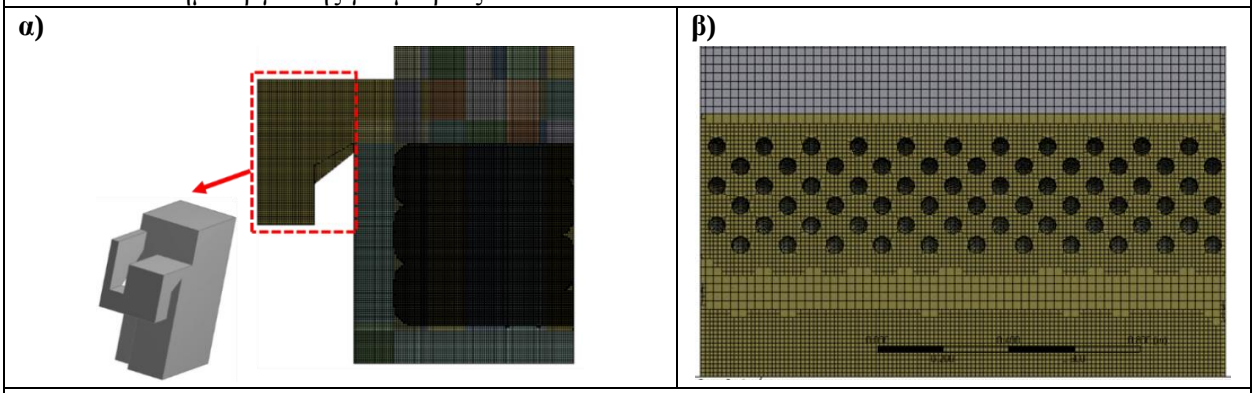

Εικόνα 38. Αριθμητικό πλέγμα (Cut cell μεθόδος): α) πλαινή και β) μπροστινή πλευρά.

5.2 Αποτελέσματα

Σύμφωνα με τα αριθμητικά αποτελέσματα μετά από περίπου 10 δευτερόλεπτα, η μάζα των στερεών ισορροπεί στα 9750 κιλά, τιμή που συμφωνεί με αυτή που λήφθηκε από τους βιομηχανικούς εταίρους. Ο μέσος όρος του χρόνου της ροής μάζας των στερεών σωματιδίων που εξέρχονται από το θάλαμο μέσω του τμήματος ανύψωσης και της υπερχείλισης είναι ίσος με περίπου 293.5 $kg \cdot s^{-1}$ και 3.35 $kg \cdot s^{-1}$, αντίστοιχα. Ο λόγος αυτών των δύο ροών είναι αρκετά ενδεικτικός για το ποσοστό των στερεών που εξέρχονται από τον BFB μέσω του τμήματος ανύψωσης και της υπερχείλισης.

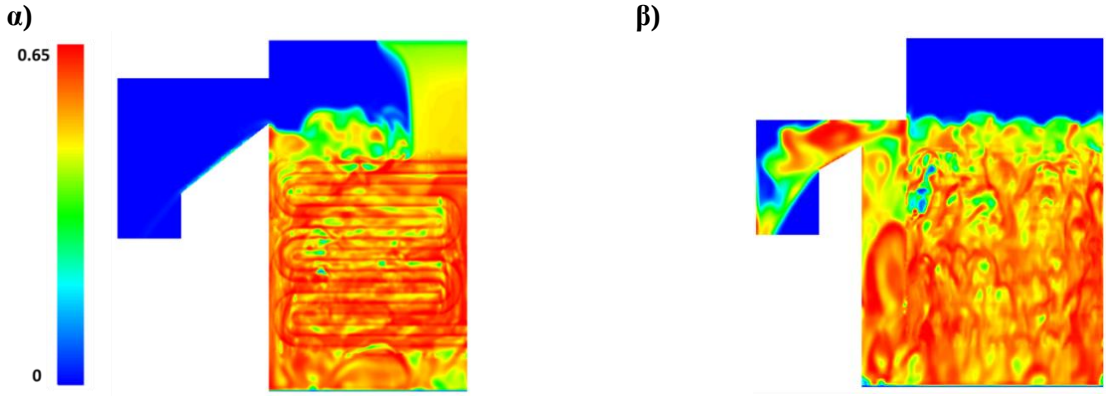

Εικόνα 39. Στιγμιαίο κλάσμα όγκου στερεών σε *t*=10 sec στο α) επίπεδο συμμετρίας (που βρίσκεται στο μέσο της υπερχείλισης) και στο) z=0.75 μέτρα (που βρίσκεται στο μέσο του τμήματος ανύψωσης).

Η **Εικόνα 39** παρουσιάζει το χωρικό προφίλ του στιγμιαίου κλάσματος όγκου των στερεών σωματιδίων σε *t*=10 δευτερόλεπτα σε ένα επίπεδο συμμετρίας και σε ένα επίπεδο σε *z*=0.75. Όπως μπορεί να παρατηρηθεί με τα μοντέλα που εφαρμόζονται σήμερα υπάρχει καλή αναπαράσταση των ροϊκών φαινομένων (σχηματισμός φυσαλίδων). Το ύψος της κλίνης είναι 3 μέτρα, το οποίο είναι υψηλότερο από το ύψος των τελευταίων περασμάτων των δεσμίδων των σωλήνων. Παρ' όλα αυτά, κοντά στο τελευταίο πέρασμα των δεσμίδων σωλήνων (έκτο πέρασμα) η ροή του ρευστού είναι πιο αραιή από ό,τι κοντά στον πυθμένα, γεγονός που μπορεί να επηρεάσει τον συντελεστή μεταφοράς θερμότητας στην περιοχή αυτή, **Εικόνα 40**.

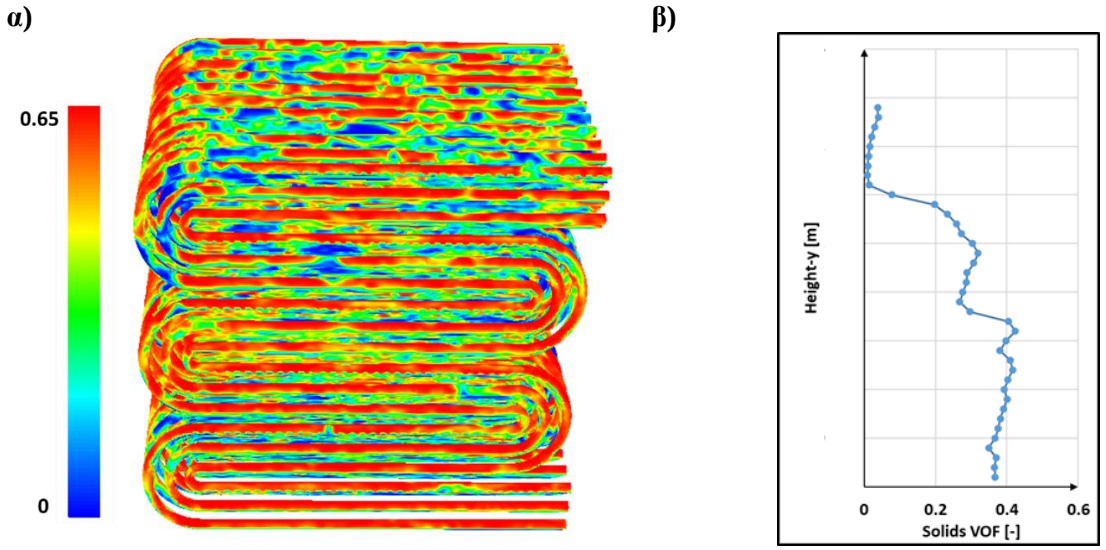

Εικόνα 40. Στιγμιαίο κλάσμα όγκου στερεών σε *t*=10 δευτερόλεπτα στις δέσμες σωλήνων.

ΚΕΦΑΛΑΙΟ 6 Αξιολόγηση καινοτόμων συστημάτων αποθήκευσης θερμικής ενέργειας

Στο Έκτο Κεφάλαιο παρουσιάστηκε μια σύνοψη των συστημάτων που μελετήθηκαν (FB-SHS, TCES-CaL και LHTES με βάση το Si) όσον αφορά τις γενικές πτυχές του σχεδιασμού (π.χ. ευελιξία σχεδιασμού, επίπεδο τεχνολογικής ωριμότητας, πλεονεκτήματα και μειονεκτήματα), το χρησιμοποιούμενο μέσο αποθήκευσης (χωρητικότητα αποθήκευσης, μέσο κόστος/κιλά, φιλικότητα προς το περιβάλλον). Επιπλέον, προσομοιώθηκαν δύο περιπτώσεις δοκιμών προκειμένου να οριστεί μια θεωρητική σύγκριση μεταξύ των διαφορετικών συστημάτων που μελετήθηκαν όσον αφορά τους ρυθμούς φόρτισης και τους συνολικούς χρόνους φόρτισης, όταν θερμαίνονται με διαφορετικές μεθόδους θέρμανσης (π.χ. θέρμανση μέσω σωλήνων θερμότητας με εργαζόμενο μέσο ατμό ή νάτριο ενός συστήματος ρευστοποιημένης κλίνης - FB για SHS ή TCES) ή όταν θερμαίνονται με την ίδια μέθοδο (π.χ. θέρμανση από τα πλευρικά τοιχώματα ενός LHTES και ενός FB-SHS θεωρώντας την ίδια θερμοκρασία τοιχώματος).

Κριτήριο	**Τύπος συστήματος αποθήκευσης (TES)**		
	1η επιλογή	**2η επιλογή**	**3η επιλογή**
Αποθηκευτική ικανότητα	Si-based LHTES	TCES-CaL	FB-SHS
Κόστος αποθηκευτικού μέσου	FB-SHS	TCES-CaL	Si-based LHTES
Όγκος συστήματος	Si-based LHTES	FB-SHS	TCES-CaL
Επίπεδο ωριμότητας (TRL)	FB-SHS	TCES-CaL	Si-based LHTES
Ευελιξία σχεδιασμού	Si-based LHTES	FB-SHS	TCES-CaL
Κόστος επένδυσης	Si-based LHTES	FB-SHS	TCES-CaL

Για τον ίδιο τύπο αποθηκευτικού μέσου και συστήματος (π.χ. κοκκώδες υλικό μέσα σε σύστημα ρευστοποιημένης κλίνης) η θέρμανση μέσω σωλήνων θερμότητας με νάτριο (στους ~900 ^{o}C) οδηγεί στους υψηλότερους ρυθμούς θέρμανσης σε σχέση με τις μεθόδους θέρμανσης μέσω σωλήνων θερμότητας με ατμό ή με απλούστερα συστήματα ρευστοποιημένης κλίνης, όπου το κοκκώδες υλικό θερμαίνεται απευθείας από ένα ρευστό μεταφοράς θερμότητας (π.χ. αέρα). Οι μέθοδοι SHS με TCES στον ίδιο αντιδραστήρα παρουσιάζουν παρόμοια συμπεριφορά όσον αφορά τους ρυθμούς φόρτισης, με την τελευταία να είναι ελαφρώς πιο αργή κοντά στους 900 ^{o}C, λόγω του γεγονότος ότι μέρος της εισερχόμενης θερμότητας χρησιμοποιείται για την αντίδραση ασβεστοποίησης. Η μέθοδος TCES παρουσιάζει το πλεονέκτημα της παραγωγής CaO που μπορεί να χρησιμοποιηθεί περαιτέρω για τη δέσμευση CO_2 μέσω του κύκλου ασβεστοποίησης-ενανθράκωσης, ωστόσο, το υλικό $CaO/CaCO_3$ υποφέρει από απώλεια αντιδραστικότητας μετά από μερικούς κύκλους (περίπου 20 κύκλους), απαιτώντας, επομένως, ένα νέο υλικό πλήρωσης.

Όσον αφορά τη σύγκριση της αποθήκευσης θερμότητας σε κοκκώδη υλικά με την αποθήκευση σε ένα σύστημα LHTES με υλικά αλλαγής φάσης, πρέπει να σημειωθεί ότι το FB-SHS παρουσιάζει υψηλότερους ρυθμούς φόρτισης από το σύστημα LHTES. Αρχικά, και τα δύο συστήματα έχουν παρόμοιους ρυθμούς φόταν βρίσκονται στη λειτουργία αποθήκευσης αισθητής θερμότητας (λόγω των παρόμοιων ειδικών θερμοχωρητικοτήτων των υλικών), αλλά όταν το PCM αρχίζει να λιώνει ο ρυθμός θέρμανσης του LHTES επιβραδύνεται μέχρι την πλήρη τήξη του PCM. Όσον αφορά το επίπεδο τεχνολογικής ωριμότητας (TRL), το FB-SHS αερίου-άμμου βρίσκεται σε υψηλότερο TRL από το LHTES με βάση το πυρίτιο, το οποίο βρίσκεται ακόμη σε εργαστηριακή κλίμακα και διάφορες πτυχές πρέπει να διερευνηθούν πριν

χρησιμοποιηθεί σε μεγάλη κλίμακα (π.χ. πιθανή ρωγμάτωση του μέσου αποθήκευσης, αντιδραστικότητα του PCM με την παρουσία ενός αέριου μέσου στο εσωτερικό του δοχείου, υπερβολικές πλευρικές απώλειες θερμότητας κ.λπ.) Από την άλλη πλευρά, το σύστημα LHTES με βάση το πυρίτιο παρουσιάζει μεγαλύτερες δυνατότητες όσον αφορά τη δυνατότητα αποθήκευσης, την ευελιξία σχεδιασμού και την οικονομική αποδοτικότητα (απαιτεί λιγότερο από το ήμισυ του όγκου ενός τυπικού συστήματος BFB για την αποθήκευση ενός αποθηκευτικού μέσου της ίδιας μάζας, χωρίς την ανάγκη πρόσθετων εξαρτημάτων που απαιτούνται στα συστήματα ρευστοποιημένης κλίνης, όπως κυκλώνες, στεγανοποιήσεις βρόχων κ.λπ.). Λόγω του συμπαγούς σχεδιασμού του, το σύστημα LHTES αναμένεται να απαιτήσει το μικρότερο κόστος επένδυσης σε σχέση με τα συστήματα TES κοκκώδους ροής.

Συνολικά, όλα τα συστήματα TES που μελετήθηκαν στην παρούσα διατριβή παρουσιάζουν αρκετά πλεονεκτήματα και φαίνονται πολλά υποσχόμενα για την αποθήκευση θερμικής ενέργειας σε υψηλές θερμοκρασίες. Η επιλογή τους για θερμική αποθήκευση χρήζει περαιτέρω διερεύνησης με ένα εργαλείο λήψης αποφάσεων που θα πρέπει να παρέχει μια πολυκριτηριακή ανάλυση που θα καλύπτει τόσο τεχνικές όσο και μη τεχνικές (περιβαλλοντικές, κοινωνικές, οικονομικές) πτυχές για μια στοχευμένη εφαρμογή. Τα αριθμητικά μοντέλα που αναπτύχθηκαν στη συγκεκριμένη διατριβή, μπορούν να αξιοποιηθούν στο μέλλον για να παρέχουν διάφορες τεχνικές παραμέτρους ενδιαφέροντος για τους διάφορους τύπους τεχνολογιών. Τέτοιες παράμετροι, όπως οι ρυθμοί φόρτισης/εκφόρτισης, η χωρητικότητα αποθήκευσης, η αποδοτικότητα αποθήκευσης και ο χρόνος φόρτισης μπορούν να χρησιμοποιηθούν ως δεδομένα εισόδου για ένα τέτοιο εργαλείο λήψης αποφάσεων. Τα αποτελέσματα του μοντέλου CFD μπορούν επίσης να τροφοδοτήσουν άλλους τύπους μοντέλων μειωμένης τάξης (π.χ. μοντέλα διεργασιών) για να βελτιώσουν την ακρίβεια των προβλέψεών τους, ή μπορούν να συνδυαστούν με μοντέλα τάσεων-παραμορφώσεων (2D/3D κατανομή πίεσης/θερμοκρασίας) για να επαληθεύσουν εάν μπορεί να εμφανιστεί πιθανή αστοχία των μελετώμενων συστημάτων.

ΚΕΦΑΛΑΙΟ 7 Συμπεράσματα – προτάσεις για μελλοντική εργασία

7.1 Βασικα συμπεράσματα

Στην παρούσα διατριβή, αναπτύχθηκαν προηγμένα μοντέλα υπολογιστικής ρευστοδυναμικής, για να διερευνήσουν διάφορες καινοτόμες ιδέες πολυφασικής ροής που στοχεύουν κυρίως σε εφαρμογές αποθήκευσης ενέργειας. Στο πλαίσιο αυτό, αναπτύχθηκε μια σειρά μοντέλων στην πλατφόρμα ANSYS Fluent™ για την ακριβή και αποτελεσματική προσομοίωση των διαφόρων εφαρμογών.

Στο **Κεφάλαιο 3**, μελετήθηκε η στερεοποίηση/τήξη πυριτίου σε εξαιρετικά υψηλές θερμοκρασίες (~1410-2000 ^{o}C) στο εσωτερικό ενός συστήματος LHTES καλύπτοντας διάφορες πτυχές σχεδιασμού και λειτουργίας. Από αριθμητική άποψη, αναδείχθηκε η υπεροχή της τοπικής πύκνωσης πλέγματος έναντι σταθερών πλεγμάτων, από άποψη αποτελεσματικότητας (μείωση χρόνου προσομοίωσης κατά 85 %) και ακρίβειας. Δεύτερον, αναδείχθηκε η ισχυρή επίδραση της παραμέτρου της ενδιάμεσης περιοχής στον ρυθμό τήξης. Τέλος, αποκαλύφθηκε ότι με τη μέθοδο πορώδους ενθαλπίας, η επίπλευση/βύθιση του στερεού PCM μέσα στη λιωμένη φάση του αναπαρίσταται έμμεσα μέσω της κίνησης του υγρού, η οποία ανάλογα με την ανοδική ή καθοδική της κίνηση διαμορφώνει αντίστοιχα το σχήμα του μετώπου τήξης. Από πλευράς σχεδιασμού, το κυβικό σχήμα δοχείου οδηγεί στον υψηλότερο ρυθμό τήξης, περίπου 25 % υψηλότερο από αυτόν που επιτυγχάνεται με ένα σφαιρικό, λόγω της μεγαλύτερης θερμαινόμενης επιφάνειας. Από την άλλη πλευρά, το σφαιρικό σχήμα αναμένεται να έχει τις χαμηλότερες πλευρικές θερμικές απώλειες και θερμικές τάσεις κατά την περίοδο στερεοποίησης και αποθήκευσης, αλλά δεν αποτελεί πρακτική λύση για να ενσωματωθεί σε μια συμπαγή συσκευή μετατροπής θερμότητας σε ηλεκτρική ενέργεια. Η πιο πρακτική λύση όσον αφορά τους ρυθμούς τήξης, τις θερμικές απώλειες και την ευελιξία σχεδιασμού είναι ο αποκομμένος κώνος.

Ως περαιτέρω βήμα, αξιολογήθηκε η απόδοση του συστήματος κατά τη διάρκεια της περιόδου φόρτισης/εκφόρτισης και αποθήκευσης λαμβάνοντας υπόψη το φαινόμενο των θερμικών απωλειών. Από την αριθμητική ανάλυση προέκυψε ότι η παράμετρος *TR* και το ύψος του δοχείου έχουν χαμηλή έως μέτρια επίδραση στις θερμικές απώλειες του συστήματος, εφόσον εφαρμόζεται επαρκής μόνωση στα τοιχώματα του συστήματος, δηλαδή για R_{th} >2 $m^2 \cdot K \cdot W^{-1}$. Οι συνολικές απώλειες κατά τη φάση στερεοποίησης του PCM είναι ίσες με ~223 kJ και ~158.2 kJ για τον κώνο με λόγο κωνικότητας ίσο με 0.45 και 0.225, αντίστοιχα. Κατά τη διάρκεια της φόρτισης, παρατηρήθηκε μια μικρή επίδραση του *TR* στις απώλειες του συστήματος. Όσον αφορά τους ρυθμούς φόρτισης/εκφόρτισης, όταν αυξάνεται ο λόγος κωνικότητας του δοχείου, τότε αυξάνεται ο χρόνος στερεοποίησης, αντίστοιχα, ενώ η αντίθετη τάση παρατηρείται κατά τη φάση της φόρτισης. Μια γεωμετρία με τον ίδιο όγκο, αλλά χαμηλότερο *TR* (0.225), στερεοποιείται ταχύτερα από εκείνη με *TR*=0.45. Ο χρόνος στερεοποίησης στην πρώτη περίπτωση είναι σχεδόν 17 % χαμηλότερος από ό,τι στη δεύτερη περίπτωση. Η αντιστάθμιση μεταξύ των ρυθμών φόρτισης και εκφόρτισης του συστήματος οδηγεί στο συμπέρασμα ότι ο αποκομμένος κώνος με *TR*, μεταξύ 0.225-0.45 είναι η βέλτιστη λύση που μπορεί να κατασκευαστεί μεταξύ των γεωμετριών που δοκιμάστηκαν. Τέλος, ο όγκος του δοχείου επηρεάζει σημαντικά τη συνολική ικανότητα αποθήκευσης ενέργειας- το συγκεκριμένο δοχείο μπορεί να χρησιμοποιηθεί για αποθήκευση έως και δύο ημέρες, πριν χάσει την ενέργεια που περιέχει με τη μορφή λανθάνουσας θερμότητας. Συνοψίζοντας, η κατασκευή ενός αποδοτικού συστήματος αποθήκευσης θερμότητας συμπεριλαμβάνει ένα δοχείο με μικρό μήκος, χαμηλό λόγο πλευρικής επιφάνειας προς όγκο, κατάλληλη μέθοδο μόνωσης (R≈2 $m^2 \cdot K \cdot W^{-1}$) και λόγο κωνικότητας μεταξύ 0.225-0.45.

Τέλος, παρουσιάστηκε μια ανάλυση ευαισθησίας σχετικά με την επίδραση των ιδιοτήτων του πυριτίου στο χρόνο φόρτισης του συστήματος αποθήκευσης ενέργειας. Τα αποτελέσματα αποκάλυψαν ότι με τον διπλασιασμό της λανθάνουσας θερμότητας ο χρόνος φόρτισης του συστήματος αυξάνεται σχεδόν κατά 30 %. Αντίθετα, η αύξηση της ειδικής θερμοχωρητικότητας κατά σχεδόν 50 % οδηγεί σε μικρή αύξηση του χρόνου φόρτισης κατά 7 %. Παρατηρήθηκε επίσης μια μικρή επίδραση του εύρους της ενδιάμεσης ζώνης στα αριθμητικά αποτελέσματα. Πιο συγκεκριμένα, η αύξηση του ΔT από 2 έως 20 K οδηγεί σε μεταβολή του χρόνου τήξης μικρότερη από 10 %. Τέλος, η ανάλυση ευαισθησίας έδειξε μεγάλη επίδραση στο χρόνο φόρτισης με τη θερμική αγωγιμότητα k. Πιο συγκεκριμένα, μια περίπτωση μελέτης με k_s, k_l=20 $W \cdot m^{-2} \cdot K^{-1}$ απαιτεί σχεδόν διπλάσιο χρόνο για το υλικό να λιώσει σε σχέση με τις περιπτώσεις k_s, k_l=180 $W \cdot m^{-2} \cdot K^{-1}$ και k_s=60, k_l=180 $W \cdot m^{-2} \cdot K^{-1}$. Τέλος, παρατηρείται μία μείωση της τάξεως του 25 %, όταν το k αυξάνει από 20 $W \cdot m^{-2} \cdot K^{-1}$ σε 60 $W \cdot m^{-2} \cdot K^{-1}$ (66% αύξηση).

Το **Κεφάλαιο 4** περιγράφει τις δραστηριότητες προσομοίωσης για έναν ενανθρακωτή CFB πιλοτικής κλίμακας 1 MW_{th}, ο οποίος βρίσκεται στις εγκαταστάσεις της TUDA. Τα αριθμητικά αποτελέσματα του μοντέλου CFD που αναπτύχθηκε συγκρίθηκαν και αξιολογήθηκαν σε σχέση με τα διαθέσιμα πειραματικά δεδομένα για i) την κατανομή της αξονικής πίεσης κατά μήκος του αντιδραστήρα και ii) τη συγκέντρωση διοξειδίου του άνθρακα στην έξοδο του ενανθρακωτή. Τα αναπαραγόμενα πρότυπα ροής σε διάφορες τομές του αντιδραστήρα έχουν επίσης αξιολογηθεί και διασταυρωθεί με βάση πειραματικές παρατηρήσεις. Ουσιαστικά, η συγκεκριμένη πιλοτική μονάδα χρησιμοποιήθηκε ως σημείο αναφοράς για την επικύρωση του μοντέλου EMMS για τις συνθήκες λειτουργίας μιας τυπικής ρευστοποιημένης κλίνης ανακυκλοφορίας. Χωρίς απώλεια γενικότητας, το μοντέλο που αναπτύχθηκε μπορεί να χρησιμοποιηθεί για την προσομοίωση αντιδραστήρων CFB που λειτουργούν με ή χωρίς οποιαδήποτε χημική αντίδραση σε διάφορες κλίμακες (από εργαστηριακή έως βιομηχανική κλίμακα). Επισημαίνεται η προστιθέμενη αξία της επικύρωσης των αναπτυχθέντων μοντέλων με πειραματικά δεδομένα που βασίζονται σε μονάδες πιλοτικής κλίμακας.

Πιο συγκεκριμένα, η διαδικασία προσομοίωσης του ενανθρακωτή αποκάλυψε ότι το προηγμένο μοντέλο EMMS σε συνδυασμό με την προσέγγιση TFM αναπαρήγαγε αποτελέσματα υψηλότερης ακρίβειας, σε σύγκριση με το αντίστοιχο ομογενές μοντέλο του Gidaspow. Επιπλέον, σε αντίθεση με το μοντέλο Gidaspow με το μοντέλο EMMS επιτυγχάνεται μια σχετικά χαμηλή εξάρτηση από το πλέγμα (επίπεδο σφάλματος της τάξεως του 6.5 %). Το γεγονός αυτό μπορεί να ενισχύσει την εφαρμογή ενός τέτοιου μοντέλου για αντιδραστήρες βιομηχανικής κλίμακας με σχετικά αραιό πλέγμα μέχρι d_{cell}/d_p~500. Όσον αφορά την κινητική της αντίδρασης, ο ρυθμός αντίδρασης των Hawthorne et al. δίνει αποτελέσματα υψηλής ακρίβειας για τη συγκέντρωση CO_2 με σχετικό σφάλμα 7.22 %, ενώ η παραδοχή ομοιογενών συνθηκών σε κάθε υπολογιστικό κελί για τον υπολογισμό του ρυθμού αντίδρασης ενανθράκωσης μπορεί να περιορίσει την ακρίβεια του μοντέλου. Αυτό δείχνει για άλλη μια φορά τη σημασία της αναπαραγωγής των ετερογενών σχηματισμών με υψηλό επίπεδο ακρίβειας, με την εφαρμογή ενός κατάλληλου μοντέλου οπισθέλκουσας, όπως το μοντέλο EMMS που χρησιμοποιήθηκε στην παρούσα διατριβή.

Συμπληρωματικά με την ανάπτυξη και την επικύρωση του μοντέλου TFM-EMMS γίνεται η βελτιστοποίηση του σχεδιασμού του ενανθρακωτή. Όλες οι περιπτώσεις δοκιμών που προσομοιώθηκαν είναι ιδέες μετασκευής του αρχικού αντιδραστήρα ενανθράκωσης 1 MW_{th} που είναι εγκατεστημένος στο TUDA. Τα σχέδια μετασκευής είναι ένας σχεδιασμός αλλαγής μεγέθους του πυθμένα του αντιδραστήρα (FBD) με δύο διαφορετικές περιεκτικότητες στερεών, δηλ. 282 κιλά (τιμή αναφοράς) και 340 κιλά, ένας σχεδιασμός σταδιακής έγχυσης του προσροφητικού υλικού (SbS) και ένας σχεδιασμός προσροφητικού υλικού στην αραιή περιοχή πάνω από την πυκνή κλίνη (SZD). Τα αριθμητικά αποτελέσματα έδειξαν ότι με όλες τις περιπτώσεις μετασκευής επιτυγχάνεται καλύτερη απόδοση δέσμευσης CO_2 σε σύγκριση με το

σχέδιο αναφοράς. Η υψηλότερη δέσμευση επιτυγχάνεται με το σχέδιο FBD- στις περιπτώσεις FBD-282 κιλά και FBD-340 κιλά η απόδοση δέσμευσης είναι ίση με 90.36 % και 91.91 %, αντίστοιχα. Στις περιπτώσεις SbS και SZD η απόδοση δέσμευσης είναι 89.94 % και 88.7 %, τιμές υψηλότερες από το σχέδιο αναφοράς (87.03 %), κυρίως επειδή επιτυγχάνεται καλύτερη ανάμιξη στο κατώτερο τμήμα του αντιδραστήρα. Ο σχεδιασμός SbS είναι η πιο ελκυστική λύση, διότι εκτός από την υψηλότερη απόδοση δέσμευσης που επιτυγχάνεται σε σχέση με το σχέδιο αναφοράς, μπορεί να εξεταστεί ευκολότερα ως ιδέα μετασκευής.

Όσον αφορά την τριφασική ροή ("αέριο-προσροφητικό-καύσιμο") στο εσωτερικό του ασβεστοποιητή πιλοτικής κλίμακας 1 MW_{th}, τα αποτελέσματα της προσομοίωσης δείχνουν ότι το εφαρμοζόμενο μοντέλο CFD είναι μέτριας ακρίβειας, ιδίως όσον αφορά τις προβλεπόμενες τιμές O_2 (με σφάλμα σχεδόν 31 %) και σχετικά καλής ακρίβειας όσον αφορά τις τιμές CO_2 (με σφάλμα περίπου 12 %). Οι αριθμητικές προβλέψεις μπορούν να βελτιωθούν περαιτέρω εάν στο μέλλον χρησιμοποιηθούν πιο ρεαλιστικές κινητικές παράμετροι για το συγκεκριμένο προσροφητικό υλικό και το καύσιμο που μοντελοποιούνται. Όσον αφορά την ασβεστοποίηση του ανθρακικού ασβεστίου, τα αποτελέσματα δείχνουν ότι η αντίδραση λαμβάνει χώρα σε ύψη πάνω από την περιοχή όπου καίγεται το καύσιμο. Για τα χαμηλότερα ύψη, δηλαδή κοντά στο κάτω μέρος της κλίνης και μέχρι ύψος 4 μέτρων ευνοείται η επαναανθράκωση του παραγόμενου οξειδίου του ασβεστίου λόγω των χαμηλών τιμών θερμοκρασίας, κυρίως λόγω του ψυχρού ρεύματος αερίου που εισέρχεται στον αντιδραστήρα από το τμήμα του πυθμένα και του βοηθητικού καυστήρα. Τέλος, από τα ρεύματα ταχύτητας συνάγεται ότι παρατηρείται μικρή ανάμιξη της φάσης του προσροφητικού υλικού μόνο μέχρι το ύψος 0.4, όπου λαμβάνει χώρα μόνο ενανθράκωση, γεγονός που δείχνει ότι δεν υπάρχει τάση εγκλωβισμού των στερεών σωματιδίων σε πολλαπλούς κύκλους ενανθράκωσης-ασβεστοποίησης. Ωστόσο, υπό συγκεκριμένες συνθήκες λειτουργίας/σχεδιασμούς αντιδραστήρων τα σωματίδια του προσροφητικού μπορεί να παγιδευτούν σε περιοχές όπου ευνοούνται παράλληλα οι αντιδράσεις ενανθράκωσης και ασβεστοποίησης, γεγονός που τελικά θα μειώσει τη συνολική δραστικότητα του προσροφητικού.

Μετά την επικύρωση του μοντέλου ασβεστοποίησης στον ασβεστοποιητή 1MW_{th} ο οποίος θερμαίνεται μέσω ενδογενούς κάυσης στερεού καυσίμου, εφαρμόζεται ένα τρισδιάστατο μοντέλο για την προσομοίωση ενός έμμεσα θερμαινόμενου ασβεστοποιητή 300 kW_{th}, ο οποίος απορροφά θερμότητα από σωλήνες θερμότητας με νάτριο ως εργαζόμενο μέσο. Το χρησιμοποιούμενο μοντέλο περιλαμβάνει την προσέγγιση προσομοίωσης TFM-KTGF-EMMS για την προσομοίωση της διφασικής ροής (αέριο-προσροφητικό) στο εσωτερικό του ασβεστοποιητή, καθώς και την επίδραση της τύρβης στη συνολική διαδικασία μεταφοράς θερμότητας και την υδροδυναμική της ροής. Μια προσθήκη αυτού του μοντέλου, είναι η συμπερίληψη της μεταφοράς θερμότητας με ακτινοβολία από τους σωλήνες θερμότητας προς την κλίνη φυσαλίδων και στο εσωτερικό του αντιδραστήρα. Χρησιμοποιήθηκε επίσης ένα σχεδόν 2D πεδίο για την επιτάχυνση της αριθμητικής προσομοίωσης και τη διευκόλυνση της ανάλυσης ευαισθησίας/πολλαπλών παραμέτρων λόγω του μεγάλου υπολογιστικού πλέγματος που απαιτείται για την αποτύπωση της απαιτητικής γεωμετρίας του έμμεσα θερμαινόμενου καυστήρα. Η επικύρωση του χρησιμοποιούμενου μοντέλου έναντι πειραματικών δεδομένων έγινε με την επίτευξη καλής ακρίβειας πρόβλεψης του κλάσματος μάζας CO_2 (σχετικό σφάλμα ~6.00 %) στην έξοδο του αντιδραστήρα και μέτριας ακρίβειας πρόβλεψης του συνολικού ρυθμού μεταφοράς θερμότητας από τους σωλήνες προς την κλίνη (σχετικό σφάλμα ~23.00 %). Μια ανάλυση ευαισθησίας αποκάλυψε ότι το μοντέλο *k-ε* με ενισχυμένη μοντέλο για τον υπολογισμό του θερμικού οριακού στρώματος στα τοιχώματα μπορεί να οδηγήσει σε μια σχεδόν ανεξάρτητη από το πλέγμα λύση για d_{cell}/d_p~110. Μια παραμετρική μελέτη σχετικά με την επίδραση της διάταξης των σωλήνων θερμότητας στο συνολικό ρυθμό μεταφοράς θερμότητας αποκάλυψε ότι τόσο ο πλευρικός διάκενος μεταξύ των σωλήνων όσο και η διάταξη των σωλήνων θερμότητας (κλιμακωτοί έναντι σε σειρά) επηρεάζουν το

συνολικό ρυθμό μεταφοράς θερμότητας. Γενικά, η χρήση μιας πλευρικής απόστασης μεταξύ των σωλήνων θερμότητας στο εύρος 1.5-2 d είναι μια καλή επιλογή για ενισχυμένη μεταφορά θερμότητας, ενώ η κλιμακωτή διάταξη οδηγεί σε υψηλότερο ρυθμό μεταφοράς θερμότητας (κατά 7 % μεγαλύτερο) από τη διάταξη σε σειρά. Το μοντέλο που αναπτύχθηκε είναι αποτελεσματικό και ακριβές και μπορεί να βοηθήσει στη μελέτη παρόμοιων συστημάτων TCES/SHS κοκκώδους ροής.
Στο **Πέμπτο Κεφάλαιο**, το τρισδιάστατο μοντέλο που βασίζεται στο μοντέλο TFM χρησιμοποιήθηκε για την προσομοίωση ενός εναλλάκτη θερμότητας BFB ενός βιομηχανικού λέβητα CFB. Το μοντέλο χρησιμοποιήθηκε για τη μοντελοποίηση της διαδικασίας μεταφοράς θερμότητας από τη κλίνη φυσσαλίδων προς τις σωλήνες με ατμό ως εργαζόμενο μέσο. Ο ΗΕ χρησιμεύει ως υπερθερμαντήρας, αλλά μπορεί να χρησιμοποιηθεί και ως εσωτερικό σύστημα αποθήκευσης ενέργειας. Με βάση τα αποτελέσματα, η υδροδυναμική της ροής αναπαρίσταται με αποδεκτή ακρίβεια. Στο πλαίσιο αυτό, μπορεί να εφαρμοστεί η χρήση της μεθόδου πλέγματος Cutcell για την κατασκευή του απαιτητικού υπολογιστικού πλέγματος. Με τη χρήση του μοντέλου μεταφοράς θερμότητας που κατασκευάστηκε στην παρούσα διδακτορική διατριβή ο συνολικός ρυθμός μεταφοράς θερμότητας είναι ίσος με 2.7 MW_{th}. Τα αποτελέσματα αυτού του μοντέλου, που αφορούν κυρίως την υδροδυναμική της ροής, μπορούν να τροφοδοτήσουν θεωρητικά μοντέλα προκειμένου να πραγματοποιηθεί ανάλυση ευαισθησίας της επίδρασης διαφόρων παραμέτρων στον συνολικό συντελεστή μεταφοράς θερμότητας εξοικονομώντας υπολογιστικό χρόνο.

Τέλος, στο **Έκτο Κεφάλαιο** παρουσιάζεται μια σύνοψη των συστημάτων που μελετήθηκαν όσον αφορά το σχεδιασμό τους, το χρησιμοποιούμενο μέσο αποθήκευσης και τις δυνατότητες φόρτισης. Συνολικά, όλα τα συστήματα TES που μελετήθηκαν στην παρούσα διατριβή, παρουσιάζουν αρκετά πλεονεκτήματα και φαίνονται πολλά υποσχόμενα για την αποθήκευση θερμικής ενέργειας σε υψηλές θερμοκρασίες (> 800-900 ^oC) και μπορούν να επιλεγούν ανάλογα με τη στοχευμένη εφαρμογή. Τέτοια συστήματα θα συμβάλουν στην απελευθέρωση υψηλότερων ενεργειακών πυκνοτήτων και αποδόσεων αποθήκευσης σε σχέση με τα σύγχρονα συστήματα που βασίζονται σε στήλες άλατος. Η βελτιστοποίηση τέτοιων συστημάτων όσον αφορά το σχεδιασμό και τη λειτουργία μπορεί επίσης να επιτευχθεί με την αξιοποίηση των προηγμένων αριθμητικών εργαλείων που παρουσιάζονται στην παρούσα διατριβή. Τέλος, τα αποτελέσματα του μοντέλου μπορούν να τροφοδοτήσουν μοντέλα διεργασιών για την ενίσχυση της ακρίβειας των προβλέψεών τους, μπορούν να συνδυαστούν με μοντέλα τάσεων-παραμορφώσεων για να επαληθεύσουν εάν μπορεί να εμφανιστεί πιθανή θραύση των μελετώμενων συστημάτων ή ακόμη και να τροφοδοτήσουν προηγμένα εργαλεία πολυκριτηριακής ανάλυσης για τη λήψη αποφάσεων.

7.2 Καινοτόμα στοιχεία

Στην παρούσα διατριβή, έχουν επιτευχθεί αρκετές αριθμητικές καινοτομίες. Όσον αφορά τα συστήματα κοκκώδους ροής τα καινοτόμα στοιχεία περιλαμβάνουν:

- Στο μοντέλο MFM/TFM έχει ενσωματωθεί μια βελτιωμένη έκδοση του μοντέλου EMMS για τους συντελεστές οπισθέλκουσας, με χρήση διαδικασίας παρεμβολής. Σε αυτή τη νέα έκδοση του μοντέλου EMMS, προτάθηκε μια νέα συσχέτιση για την πρόβλεψη του μεγέθους συσσωματωμάτων των σωματιδίων σε συνάρτηση με το μέγεθος του αντιδραστήρα.
- Το αναπτυχθέν μοντέλο προσομοιώνει την υδροδυναμική της ροής στο εσωτερικό των συστημάτων πολυφασικής ροής, αλλά και την κινητική των αντιδράσεων και την εξέλιξη της μεταφοράς θερμότητας.
- Έχουν μελετηθεί διάφορες εφαρμογές (με αντίδραση και χωρίς) και έχει επιτευχθεί επικύρωση των μοντέλων με βάση πειραματικά δεδομένα από πιλοτικές μονάδες (σε κλίμακα 300 kW_{th}-1 MW_{th}).

- Όσον αφορά την αντίδραση ενανθράκωσης, εφαρμόστηκε μια συσχέτιση του ρυθμού αντίδρασης που αντλήθηκε από τη βιβλιογραφία. Διερευνήθηκε η ισχυρή εξάρτηση του ρυθμού αντίδρασης - και συνακολούθως της δέσμευσης του διοξειδίου του άνθρακα- από την υδροδυναμική της ροής.
- Όσον αφορά τον αντιδραστήρα ασβεστοποίησης, εφαρμόστηκαν μοντέλα CFD τόσο για συνθήκες καύσης με οξυγόνο όσο και για συνθήκες έμμεσης θέρμανσης. Το μοντέλο του έμμεσα θερμαινόμενου καυστήρα μπορεί επίσης να εφαρμοστεί στο μέλλον για καυστήρες που θερμαίνονται με ηλιακή ενέργεια.
- Μια σημαντική πτυχή που μοντελοποιήθηκε για τον ασβεστοποιητή είναι η επαναανθράκωση του ασβέστη, όταν η θερμοκρασία στο εσωτερικό του αντιδραστήρα ευνοεί μια τέτοια αντίδραση.
- Στον έμμεσα θερμαινόμενο ασβεστοποιητή, η μεταφορά θερμότητας μέσω ακτινοβολίας έχει συμπεριληφθεί στο μοντέλο, ενώ έχει εκτιμηθεί η επίδραση της τύρβης.

Οι καινοτομίες που αφορούν το LHTES είναι οι εξής:

- ✓ Αναπτύχθηκε ένα αξονοσυμμετρικό μοντέλο CFD για την προσομοίωση της διαδικασίας στερεοποίησης/ τήξης των PCM που καλύπτει ένα ευρύ φάσμα τιμών θερμοκρασίας.
- ✓ Το μοντέλο συνδυάζει τα πλεονεκτήματα i) της μεθόδου ενθαλπίας- πορώδους σταθερού πλέγματος που μοντελοποιεί έμμεσα τη διεπιφάνεια στερεού/υγρού PCM, ii) της μεθόδου VOF που μοντελοποιεί τη ροή αερίου-PCM και iii) μιας τεχνικής τοπικής πύκνωσης πλέγματος.
- ✓ Το μοντέλο που αναπτύχθηκε λαμβάνει υπόψη τη συστολή/διαστολή του PCM κατά τη διαδικασία στερεοποίησης/ τήξης για ένα πιο ρεαλιστικό πεδίο ροής (που συνήθως παραλείπεται σε παρόμοια μοντέλα CFD στη βιβλιογραφία), τη μεταβολή των θερμο-φυσικών ιδιοτήτων από την υγρή στη στερεά φάση και αντίστροφα και τις πλευρικές απώλειες θερμότητας του δοχείου.
- ✓ Το μοντέλο CFD μπορεί να μοντελοποιήσει έμμεσα τους δενδριτικούς σχηματισμούς σε ένα PCM.

7.3 Προτάσεις για μελλοντική εργασία

Μελλοντικές αριθμητικές βελτιώσεις, παίρνοντας ως βάση την παρούσα διατριβή, περιλαμβάνουν:

- Ανάπτυξη μοντέλων CFD για την προσομοίωση νέων ρευστοποιημένων κάψουλων PCM που συνδυάζουν τα πλεονεκτήματα τόσο του κοκκώδους υλικού όσο και των PCM.
- Εφαρμογή μοντέλων τεχνητής νοημοσύνης για την αναβάθμιση κλίμακας των μελετώμενων συστημάτων ρευστοποιημένης κλίνης.
- Επέκταση της αριθμητικής εργασίας με το EMMS σε άλλες συνθήκες λειτουργίας (π.χ. πολύ αραιές ροές) ή για ροές που περιλαμβάνουν πάνω από δύο στερεές φάσεις.
- Ανάπτυξη ενός μοντέλου μεταφοράς θερμότητας και σύζευξη με το μοντέλο EMMs.
- Ανάπτυξη υβριδικών αριθμητικών μοντέλων για την προσομοίωση των ρευστοποιημένων κλινών, εκτός από το σύγχρονο μοντέλο Eulerian-Eulerian TFM (π.χ. το υβριδικό μοντέλο DDPM).
- Ρητή προσομοίωση του σχηματισμού δενδριτών σε συστήματα LHTES.
- Ρητή προσομοίωση του φαινομένου της επίπλευσης/βύθισης του PCM, λαμβάνοντας υπόψη την κίνηση των στερεών στο εσωτερικό του συστήματος LHTES.
- Συμπερίληψη του φαινομένου της επιφανειακής τάσης μεταξύ του αδρανούς αερίου και του PCM στο εσωτερικό του συστήματος LHTES.
- Συμπερίληψη των φαινομένων ακτινοβολίας και επικύρωση με πειραματικές μετρήσεις για εξαιρετικά υψηλές θερμοκρασίες στο εσωτερικό του PCM.
- Ενδελεχής μελέτη της πιθανής αντίδρασης του PCM με οποιοδήποτε αέριο στην κορυφή.

References

1. IEA, *Annual change in CO2 emissions from energy combustion and industrial processes, 1900-2021*. Paris.
2. IEA, *Coal 2021 - Analysis and forecast to 2024.* 2021.
3. IEA, *Global Energy Review 2021 - Assessing the effects of economic recoveries on global energy demand and CO2 emissions in 2021.* 2021.
4. IEA. *Fuels and technologies: Coal*. Available from: https://www.iea.org/fuels-and-technologies/coal.
5. IEA, *Renewables share of power generation in the Net Zero Scenario, 2010-2030.*
6. IEA, *Renewables.* 2022.
7. Council, W.E., *World Energy Resources* 2016.
8. Zhang, P., F. Ma, and X. Xiao, *Thermal energy storage and retrieval characteristics of a molten-salt latent heat thermal energy storage system.* Applied Energy, 2016. **173**: p. 255-271.
9. Agency, P.N.E.A., *Trends in global CO2 emmissions*. 2015.
10. IEA, *Grid-Scale Storage*. 2022: Paris.
11. Romaní, J., et al., *Evaluation of energy density as performance indicator for thermal energy storage at material and system levels.* Applied Energy, 2019. **235**: p. 954-962.
12. Mabrouk, R., et al., *Sensible and Latent Heat Thermal Energy Storage. .* Encyclopedia, 2023.
13. Dincer, I. and M.A. Ezan, *Heat Storage: A Unique Solution for Energy Systems*. 2018, Cham, Switzerland: Springer.
14. Gil, A., et al., *State of the art on high temperature thermal energy storage for power generation. Part 1—Concepts, materials and modellization.* Renewable and Sustainable Energy Reviews, 2010. **14**(1): p. 31-55.
15. Pointner, H. and W.-D. Steinmann, *Experimental demonstration of an active latent heat storage concept.* Applied Energy, 2016. **168**: p. 661-671.
16. Dutil, Y., et al., *A review on phase-change materials: Mathematical modeling and simulations.* Renewable and Sustainable Energy Reviews, 2011. **15**(1): p. 112-130.
17. Tomizawa, Y., et al., *Experimental and numerical study on phase change material (PCM) for thermal management of mobile devices.* Applied Thermal Engineering, 2016. **98**: p. 320-329.
18. Lizana, J., et al., *Advances in thermal energy storage materials and their applications towards zero energy buildings: A critical review.* Applied Energy, 2017. **203**: p. 219-239.
19. Umair, M.M., et al., *Novel strategies and supporting materials applied to shape-stabilize organic phase change materials for thermal energy storage–A review.* Applied Energy, 2019. **235**: p. 846-873.
20. Alva, G., et al., *Synthesis and characterization of microencapsulated myristic acid–palmitic acid eutectic mixture as phase change material for thermal energy storage.* Applied Energy, 2017. **203**: p. 677-685.
21. Pereira da Cunha, J. and P. Eames, *Thermal energy storage for low and medium temperature applications using phase change materials – A review.* Applied Energy, 2016. **177**: p. 227-238.
22. Liu, M., W. Saman, and F. Bruno, *Review on storage materials and thermal performance enhancement techniques for high temperature phase change thermal storage systems.* Renewable and Sustainable Energy Reviews, 2012. **16**(4): p. 2118-2132.
23. Mehling, H. and L.F. Cabeza, *Heat and cold storage with PCM*. 2008: Springer.
24. Tao, Y.B. and Y.L. He, *Numerical study on thermal energy storage performance of phase change material under non-steady-state inlet boundary.* Applied Energy, 2011. **88**(11): p. 4172-4179.

25. Ding, W., et al., *Molten chloride salts for next generation concentrated solar power plants: Mitigation strategies against corrosion of structural materials.* Solar Energy Materials and Solar Cells, 2019. **193**: p. 298-313.
26. Robinson, A., *Ultra-high temperature thermal energy storage. part 1: concepts.* Journal of Energy Storage, 2017. **13**: p. 277-286.
27. Datas, A., et al., *Ultra high temperature latent heat energy storage and thermophotovoltaic energy conversion.* Energy, 2016. **107**: p. 542-549.
28. Reid, M.R., D.B. Scharfe, and R.N. Webb, *Computational evaluation of a latent heat energy storage system.* Solar Energy, 2013. **95**: p. 99-105.
29. Chan, W., et al., *Modeling low-bandgap thermophotovoltaic diodes for high-efficiency portable power generators.* Solar Energy Materials and Solar Cells, 2010. **94**(3): p. 509-514.
30. Datas, A., et al., *Electric energy storage system.*
31. Viskanta, R., *Phase-Change heat transfer*, in *Solar heat storage: Latent heat material, Volume I*. 1983. p. 153-222.
32. Wang, Z., et al., *Aluminum and silicon based phase change materials for high capacity thermal energy storage.* Applied Thermal Engineering, 2015. **89**: p. 204-208.
33. Dhaidan, N.S. and J.M. Khodadadi, *Melting and convection of phase change materials in different shape containers: A review.* Renewable and Sustainable Energy Reviews, 2015. **43**: p. 449-477.
34. Hu, Y. and M. Shi, *Close-contact melting in a spherical enclosure.* Science in China Series E: Technological Sciences, 1998. **41**(1): p. 82-87.
35. Khodadadi, J.M. and Y. Zhang, *Effects of buoyancy-driven convection on melting within spherical containers.* International Journal of Heat and Mass Transfer, 2001. **44**(8): p. 1605-1618.
36. Moore, F.E. and Y. Bayazitoglu, *Melting Within a Spherical Enclosure.* Journal of Heat Transfer, 1982. **104**(1): p. 19-23.
37. Zhao, W., et al., *Heat transfer analysis of encapsulated phase change material for thermal energy storage.* International Journal of Heat and Mass Transfer, 2013. **63**: p. 323-335.
38. Yap, Y.F., et al., *Numerical modeling of three-phase flow with phase change using the level-set method.* International Journal of Heat and Mass Transfer, 2017. **115**: p. 730-740.
39. Vu, T.V., et al., *Numerical investigations of solidification around a circular cylinder under forced convection.* Journal of Mechanical Science and Technology, 2016. **30**(11): p. 5019-5028.
40. Voller, V.R. and C. Prakash, *A fixed grid numerical modelling methodology for convection-diffusion mushy region phase-change problems.* International Journal of Heat and Mass Transfer, 1987. **30**(8): p. 1709-1719.
41. Pourakabar, A. and A.A. Rabienataj Darzi, *Enhancement of phase change rate of PCM in cylindrical thermal energy storage.* Applied Thermal Engineering, 2019. **150**: p. 132-142.
42. Diao, Y.H., et al., *Numerical investigation of the thermal performance enhancement of latent heat thermal energy storage using longitudinal rectangular fins and flat micro-heat pipe arrays.* Applied Energy, 2019. **233-234**: p. 894-905.
43. Assis, E., et al., *Numerical and experimental study of melting in a spherical shell.* International Journal of Heat and Mass Transfer, 2007. **50**(9): p. 1790-1804.
44. Lamberg, P., R. Lehtiniemi, and A.-M. Henell, *Numerical and experimental investigation of melting and freezing processes in phase change material storage.* International Journal of Thermal Sciences, 2004. **43**(3): p. 277-287.
45. Sattari, H., et al., *CFD simulation of melting process of phase change materials (PCMs) in a spherical capsule.* International Journal of Refrigeration, 2017. **73**: p. 209-218.

46. Tan, F.L., et al., *Experimental and computational study of constrained melting of phase change materials (PCM) inside a spherical capsule.* International Journal of Heat and Mass Transfer, 2009. **52**(15): p. 3464-3472.
47. Archibold, A.R., et al., *The melting process of storage materials with relatively high phase change temperatures in partially filled spherical shells.* Applied Energy, 2014. **116**: p. 243-252.
48. Elmozughi, A.F., et al., *Encapsulated phase change material for high temperature thermal energy storage – Heat transfer analysis.* International Journal of Heat and Mass Transfer, 2014. **78**: p. 1135-1144.
49. Pirasaci, T., et al., *Dynamics of phase change in a vertical PCM capsule in the presence of radiation at high temperatures.* Applied Energy, 2017. **206**: p. 498-506.
50. Wei, G., et al., *Selection principles and thermophysical properties of high temperature phase change materials for thermal energy storage: A review.* Renewable and Sustainable Energy Reviews, 2018. **81**: p. 1771-1786.
51. Kunii, D., *Chemical Reaction Engineering and Research and development of gas solid systems.* Chemical Engineering Science, 1980. **35**(9): p. 1887-1911.
52. Kunii, D. and O. Levenspiel, *Fluidization Engineering (2nd Ed.)*. 1991: Boston: Butterworth-Heinemann.
53. Alonso, E. and M. Romero, *Review of experimental investigation on directly irradiated particles solar reactors.* Renewable and Sustainable Energy Reviews, 2015. **41**: p. 53-67.
54. Ho, C.K., *A review of high-temperature particle receivers for concentrating solar power.* Applied Thermal Engineering, 2016. **109**: p. 958-969.
55. Nie, F., et al., *Solid particle solar receivers in the next-generation concentrated solar power plant.* EcoMat, 2022. **4**(5): p. e12207.
56. Tan, T. and Y. Chen, *Review of study on solid particle solar receivers.* Renewable and Sustainable Energy Reviews, 2010. **14**(1): p. 265-276.
57. Flamant, G., et al., *Dense suspension of solid particles as a new heat transfer fluid for concentrated solar thermal plants: On-sun proof of concept.* Chemical Engineering Science, 2013. **102**: p. 567-576.
58. Zhang, M., et al., *Heat transfer characteristics of fluidized bed heat exchanger in a 300MW CFB boiler.* Powder Technology, 2012. **222**: p. 1-7.
59. Junfu LYU, H.Y., Wen LING, Li NIE, Guangxi YUE, Ruixin LI, Ying CHEN, Shilong WANG, *Development of a supercritical and an ultra-supercritical circulating fluidized bed boiler.* Front. Energy, 2019. **13**(1): p. 114-119.
60. Sun, S., et al., *Investigation on heat exchange feasibility of internal solids circulation for an ultra-supercritical CFB boiler.* Powder Technology, 2018. **339**: p. 223-231.
61. Zhu, Q., *Developments in circulating fluidised bed combustion*, in *IEA Clean Coal Centre*. 2013.
62. Stefanitsis, D., et al., *Simulation of a CFB Boiler Integrated With a Thermal Energy Storage System During Transient Operation.* Frontiers in Energy Research, 2020. **8**.
63. Blaszczuk, A. and S. Jagodzik, *Investigation of Heat Transfer in a Large-Scale External Heat Exchanger with Horizontal Smooth Tube Bundle.* Energies, 2022. **14**(17).
64. Wang, Q., et al., *Development of a new external heat exchanger for a circulating fluidized bed boiler.* Chemical Engineering and Processing: Process Intensification, 2003. **42**(4): p. 327-335.
65. Kim, S.W., et al., *Heat transfer and bubble characteristics in a fluidized bed with immersed horizontal tube bundle.* International Journal of Heat and Mass Transfer, 2003. **46**(3): p. 399-409.
66. Mickley, H.S. and D.F. Fairbanks, *Mechanism of heat transfer to fluidized beds.* AIChE Journal, 1955. **1**(3): p. 374-384.
67. Charitos, A., et al., *Validation of a carbonator model for the ca-looping postcombustion CO 2 capture process.* 21st International conference on fluidized bed combustion, 2012. **1**: p. 311-8.

68. Bailera, M., et al., *Modelling calcium looping at industrial scale for energy storage in concentrating solar power plants.* Energy, 2021. **225**: p. 120306.
69. Shimizu, T., et al., *A Twin Fluid-Bed Reactor for Removal of CO2 from Combustion Processes.* Chemical Engineering Research and Design, 1999. **77**(1): p. 62-68.
70. Ylätalo, J., et al., *Modeling of the oxy-combustion calciner in the post-combustion calcium looping process.* Fuel, 2013. **113**: p. 770-779.
71. Reitz, M., et al., *Design and operation of a 300kWth indirectly heated carbonate looping pilot plant.* International Journal of Greenhouse Gas Control, 2016. **54**: p. 272-281.
72. Hodgson, P., et al., *Direct Separation Calcination Technology for Carbon Capture: Demonstrating a Low Cost Solution for the Lime and Cement Industries in the LEILAC Project*. 2018.
73. Martínez, I., et al., *Conceptual design of a three fluidised beds combustion system capturing CO2 with CaO.* International Journal of Greenhouse Gas Control, 2011. **5**(3): p. 498-504.
74. Tregambi, C., et al., *110th Anniversary: Calcium Looping Coupled with Concentrated Solar Power for Carbon Capture and Thermochemical Energy Storage.* Industrial & Engineering Chemistry Research, 2019. **58**(47): p. 21262-21272.
75. Atsonios, K., et al., *Calcium looping process simulation based on an advanced thermodynamic model combined with CFD analysis.* Fuel, 2015. **153**: p. 370-381.
76. Greco-Coppi, M., et al., *Efficient CO2 capture from lime production by an indirectly heated carbonate looping process.* International Journal of Greenhouse Gas Control, 2021. **112**: p. 103430.
77. Dieter, H., A.R. Bidwe, and G. Scheffknecht, *Pilot plant experience with calcium looping*, in *Calcium and Chemical Looping Technology for Power Generation and Carbon Dioxide (CO_2) Capture*. 2015, Woodhead Publishing. p. 171-194.
78. Alonso, M., et al., *Carbon dioxide capture from combustion flue gases with a calcium oxide chemical loop. Experimental results and process development.* International Journal of Greenhouse Gas Control, 2010. **4**(2): p. 167-173.
79. Lu, D.Y., R.W. Hughes, and E.J. Anthony, *Ca-based sorbent looping combustion for CO_2 capture in pilot-scale dual fluidized beds.* Fuel Processing Technology, 2008. **89**(12): p. 1386-1395.
80. Charitos, A., et al., *Parametric investigation of the calcium looping process for CO_2 capture in a 10 kWth dual fluidized bed.* International Journal of Greenhouse Gas Control, 2010. **4**(5): p. 776-784.
81. Charitos, A., et al., *Experimental Validation of the Calcium Looping CO_2 Capture Process with Two Circulating Fluidized Bed Carbonator Reactors.* Industrial & Engineering Chemistry Research, 2011. **50**(16): p. 9685-9695.
82. Arias, B., et al., *Demonstration of steady state CO_2 capture in a 1.7 MWth calcium looping pilot.* International Journal of Greenhouse Gas Control, 2013. **18**: p. 237-245.
83. Plotz, S., et al., *First carbonate looping experiments with a 1 mwth test facility consisting of two interconnected CFBs*, in *21st international conference on fluidized bed combustion*. 2012: Naples, Italy. p. 421-428.
84. Dieter, H., et al., *Development of the calcium looping CO_2 capture technology from lab to pilot scale at IFK, University of Stuttgart.* Fuel, 2014. **127**: p. 23-37.
85. Rodríguez, N., M. Alonso, and J.C. Abanades, *Experimental investigation of a circulating fluidized-bed reactor to capture CO_2 with CaO.* AIChE Journal, 2011. **57**(5): p. 1356-1366.
86. Gale, J., et al., *10th International Conference on Greenhouse Gas Control Technologies. Postcombustion CO_2 capture with CaO. Status of the technology and next steps towards large scale demonstration.* Energy Procedia, 2011. **4**: p. 852-859.
87. Peng, Q., et al., *Design of new molten salt thermal energy storage material for solar thermal power plant.* Applied Energy, 2013. **112**: p. 682-689.

88. Kyaw, K., H. Matsuda, and M. Hasatani, *Applicability of Carbonation/Decarbonation Reactions to High-Temperature Thermal Energy Storage and Temperature Upgrading.* JOURNAL OF CHEMICAL ENGINEERING OF JAPAN, 1996. **29**(1): p. 119-125.
89. Chacartegui, R., et al., *Thermochemical energy storage of concentrated solar power by integration of the calcium looping process and a CO2 power cycle.* Applied Energy, 2016. **173**: p. 589-605.
90. Wentworth, W.E. and E. Chen, *Simple thermal decomposition reactions for storage of solar thermal energy.* Solar Energy, 1976. **18**(3): p. 205-214.
91. J.M.;, V. and S. Medina, *Limestone calcination under calcium-looping conditions for CO2 capture and thermochemical energy storage in the presence of H2O: An in situ XRD analysis.* Physical Chemistry Chemical Physics, 2017. **19**(11): p. 7587 - 7596.
92. Da, Y., et al., *Calcium-based composites for direct solar-thermal conversion and thermochemical energy storage.* Chemical Engineering Journal, 2020. **382**: p. 122815.
93. Chacartegui, R., C. Ortiz, and A. Carro, *SOlar Calcium-looping integRAtion for Thermo-Chemical Energy Storage - Deliverable D9.8*. 2019.
94. Malgarinos, I., N. Nikolopoulos, and M. Gavaises, *Coupling a local adaptive grid refinement technique with an interface sharpening scheme for the simulation of two-phase flow and free-surface flows using VOF methodology.* Journal of Computational Physics, 2015. **300**: p. 732-753.
95. Nikolopoulos, N., et al., *Single droplet impacts onto deposited drops. Numerical analysis and comparison.* 2010. **20**(11): p. 935-953.
96. Nikolopoulos, N., A. Theodorakakos, and G. Bergeles, *A numerical investigation of the evaporation process of a liquid droplet impinging onto a hot substrate.* International Journal of Heat and Mass Transfer, 2007. **50**(1): p. 303-319.
97. Strotos, G., et al. *Performance of VOF methodology in predicting the deformation and breakup of impulsively accelerated droplets*. in *Proc., 13th Triennial Int. Conf. on Liquid Atomization and Spray Systems*. 2015.
98. Malgarinos, I., et al., *VOF simulations of the contact angle dynamics during the drop spreading: Standard models and a new wetting force model.* Advances in Colloid and Interface Science, 2014. **212**: p. 1-20.
99. Knowlton, T.M., *10 - Fluidized bed reactor design and scale-up*, in *Fluidized Bed Technologies for Near-Zero Emission Combustion and Gasification*, F. Scala, Editor. 2013, Woodhead Publishing. p. 481-523.
100. Zhou, Q. and J. Wang, *Coarse grid simulation of heterogeneous gas–solid flow in a CFB riser with EMMS drag model: Effect of inputting drag correlations.* Powder Technology, 2014. **253**(0): p. 486-495.
101. Xie, N., F. Battaglia, and S. Pannala, *Effects of using two- versus three-dimensional computational modeling of fluidized beds: Part I, hydrodynamics.* Powder Technology, 2008. **182**(1): p. 1-13.
102. Yang, N., et al., *CFD simulation of concurrent-up gas–solid flow in circulating fluidized beds with structure-dependent drag coefficient.* Chemical Engineering Journal, 2003. **96**(1–3): p. 71-80.
103. Li, T., J.-F. Dietiker, and L. Shadle, *Comparison of full-loop and riser-only simulations for a pilot-scale circulating fluidized bed riser.* Chemical Engineering Science, 2014. **120**(0): p. 10-21.
104. Chen, Y.-M., *Recent advances in FCC technology.* Powder Technology, 2006. **163**(1–2): p. 2-8.
105. Wang, Q., et al., *Application of CPFD method in the simulation of a circulating fluidized bed with a loop seal, part I—Determination of modeling parameters.* Powder Technology, 2014. **253**(0): p. 814-821.

106. Chu, K., W., B. Wang, and A. Yu. *Discrete Particle Simulation of the Gas-Solid Flow in a Circulating Fluidized Bed*. in *12th International Conferenceon Fluidization-New Horizons in Fluidization Engineering*. 2007. Vancouver, Canada.
107. Zhang, N., et al., *Virtual experimentation through 3D full-loop simulation of a circulating fluidized bed.* Particuology, 2008. **6**(6): p. 529-539.
108. Zhang, N., et al., *3D CFD simulation of hydrodynamics of a 150 MWe circulating fluidized bed boiler.* Chemical Engineering Journal, 2010. **162**(2): p. 821-828.
109. Nikolopoulos, A., et al., *High-resolution 3-D full-loop simulation of a CFB carbonator cold model.* Chemical Engineering Science, 2013. **90**(0): p. 137-150.
110. Zeneli, M., et al. *High-resolution 3-D full - loop simulation of a CFB carbonator cold model*. in *CCT 2013*. 2013. Thessaloniki.
111. Ding, J. and D. Gidaspow, *A bubbling fluidization model using kinetic theory of granular flow.* AIChE Journal, 1990. **36**(4): p. 523-538.
112. Gidaspow, D., *Multiphase flow and fluidization: Continuum and kinetic theory descriptions with applications*. New York: Academic Press. 1994, USA.
113. Tsuji, Y., T. Tanaka, and T. Ishida, *Lagrangian numerical simulation of plug flow of cohesionless particles in a horizontal pipe.* Powder Technology, 1992. **71**(3): p. 239-250.
114. Zeneli, M., et al., *Numerical Simulation of a Slugging FB Gasifier Hydrodynamics, Using DDPM, DEM and TFM approaches*, in *CFB-11 Conference*. 2014: Beijing, China.
115. Chen, X. and J. Wang, *A comparison of two-fluid model, dense discrete particle model and CFD-DEM method for modeling impinging gas–solid flows.* Powder Technology, 2014. **254**(0): p. 94-102.
116. Andrews, M.J. and P.J. O'Rourke, *The multiphase particle-in-cell (MP-PIC) method for dense particulate flows.* International Journal of Multiphase Flow, 1996. **22**(2): p. 379-402.
117. O'Rourke, P.J. and D.M. Snider, *Inclusion of collisional return-to-isotropy in the MP-PIC method.* Chemical Engineering Science, 2012. **80**(0): p. 39-54.
118. Li, F., et al., *MP-PIC simulation of CFB riser with EMMS-based drag model.* Chemical Engineering Science, 2012. **82**(0): p. 104-113.
119. Sundaresan, S. *Reflections on Mathematical Models and Simulation of Gas-Particle Flows*. in *10th International Conference on Circulating Fluidized Beds and Fluidization Technology - CFB-10*. 2011.
120. Wen, C.-Y. and Y.H. Yu. , *Mechanics of Fluidization.* Chem. Eng. Prog. Symp. Series 62, 1966: p. 100-111.
121. Syamlal, M. and T. O'brien, *Computer simulation of bubbles in a fluidized bed.* AIChE Symp. Ser, 1989. **85**(27): p. 22-31.
122. Wang, J., W. Ge, and J. Li, *Eulerian simulation of heterogeneous gas-solid flows in CFB risers: EMMS-based sub-grid scale model with a revised cluster description.* Chemical Engineering Science, 2008. **63**(6): p. 1553-1571.
123. Hartge, E.U., et al., *CFD-simulation of a circulating fluidized bed riser.* Particuology, 2009. **7**(4): p. 283-296.
124. Senior, R.C. and C. Brereton, *Modelling of circulating fluidised-bed solids flow and distribution.* Chemical Engineering Science, 1992. **47**(2): p. 281-296.
125. Zhou, Q. and J. Wang, *CFD study of mixing and segregation in CFB risers: Extension of EMMS drag model to binary gas–solid flow.* Chemical Engineering Science, 2015. **122**(0): p. 637-651.
126. Lu, B., W. Wang, and J. Li, *Searching for a mesh-independent sub-grid model for CFD simulation of gas–solid riser flows.* Chemical Engineering Science, 2009. **64**(15): p. 3437-3447.

127. Cloete, S., S.T. Johansen, and S. Amini, *Grid independence behaviour of fluidized bed reactor simulations using the Two Fluid Model: Effect of particle size.* Powder Technology, 2015. **269**: p. 153-165.
128. Igci, Y., et al., *Filtered two-fluid models for fluidized gas-particle suspensions.* AIChE Journal, 2008. **54**(6): p. 1431-1448.
129. Parmentier, J.-F., O. Simonin, and O. Delsart, *A functional subgrid drift velocity model for filtered drag prediction in dense fluidized bed.* AIChE Journal, 2012. **58**(4): p. 1084-1098.
130. Schneiderbauer, S., S. Puttinger, and S. Pirker, *Comparative analysis of subgrid drag modifications for dense gas-particle flows in bubbling fluidized beds.* AIChE Journal, 2013. **59**(11): p. 4077-4099.
131. Wang, J., M.A. van der Hoef, and J.A.M. Kuipers, *Coarse grid simulation of bed expansion characteristics of industrial-scale gas–solid bubbling fluidized beds.* Chemical Engineering Science, 2010. **65**(6): p. 2125-2131.
132. Li, J. and M. Kwauk, *Particle-Fluid Two-Phase Flow: The Energy-Minimization Multi-Scale Method* 1994.
133. Wang, X.-y., et al., *The simulation and experimental validation on gas-solid two phase flow in the riser of a dense fluidized bed.* Journal of Thermal Science, 2009. **18**(2): p. 137-141.
134. Hong, K., et al., *Extending the bubble-based EMMS model to CFB riser simulations.* Powder Technology, 2014. **266**(0): p. 424-432.
135. Shi, Z., W. Wang, and J. Li, *A bubble-based EMMS model for gas–solid bubbling fluidization.* Chemical Engineering Science, 2011. **66**(22): p. 5541-5555.
136. Nikolopoulos, A., et al., *An advanced EMMS scheme for the prediction of drag coefficient under a 1.2 MWth CFBC isothermal flow-Part I: Numerical formulation.* Chemical Engineering Science, 2010. **65**(13): p. 4080-4088.
137. Harris, A.T., J.F. Davidson, and R.B. Thorpe, *The prediction of particle cluster properties in the near wall region of a vertical riser (200157).* Powder Technology, 2002. **127**(2): p. 128-143.
138. Gu, W.K. and J.C. Chen, *A model for solid concentration in circulating fluidized beds*, in *Fluidization IX. Engineering Foundation*, K.T.M.E. Fan L.S., Editor. 1998: Durago, Colorado. p. 501-508.
139. Zou, B., et al., *Cluster structure in a circulating fluidized bed.* Powder Technology, 1994. **78**(2): p. 173-178.
140. Chavan, V.V. and R.A. Mashelkar, *Advances in transport processes*. v. 1 ed. 1980.
141. Shah, M.T., et al., *Hydrodynamics of an FCC riser using energy minimization multiscale drag model.* Chemical Engineering Journal, 2011. **168**(2): p. 812-821.
142. Hong, K., et al., *An EMMS-based multi-fluid model (EFM) for heterogeneous gas–solid riser flows: Part I. Formulation of structure-dependent conservation equations.* Chemical Engineering Science, 2012. **75**(0): p. 376-389.
143. Subbarao, D., *A model for cluster size in risers.* Powder Technology, 2010. **199**(1): p. 48-54.
144. García-Labiano, F., et al., *Calcination of calcium-based sorbents at pressure in a broad range of CO2 concentrations.* Chemical Engineering Science, 2002. **57**(13): p. 2381-2393.
145. Stanmore, B.R. and P. Gilot, *Review—calcination and carbonation of limestone during thermal cycling for CO2 sequestration.* Fuel Processing Technology, 2005. **86**(16): p. 1707-1743.
146. Huang, J.-M. and K.E. Daugherty, *Inhibition of the calcination of calcium carbonate.* Thermochimica Acta, 1988. **130**: p. 173-176.
147. Martínez, I., et al., *Kinetics of Calcination of Partially Carbonated Particles in a Ca-Looping System for CO2 Capture.* Energy & Fuels, 2012. **26**(2): p. 1432-1440.

148. Silcox, G.D., J.C. Kramlich, and D.W. Pershing, *Mathematical model for the flash calcination of dispersed CaCO3 and Ca(OH)2 particles.* Industrial and Engineering Chemistry Research, 1989. **28**(2): p. 155-160.
149. Lun, C.K.K., et al., *Kinetic theories for granular flow: inelastic particles in Couette flow and slightly inelastic particles in a general flowfield.* Journal of Fluid Mechanics, 1984. **140**: p. 223-256.
150. Gidaspow, D., R. Bezburuah, and J. Ding, *Hydrodynamics of Circulating Fluidized Beds: Kinetic Theory Approach*. 1991: United States. Department of Energy.
151. Syamlal, M., W. Rogers, and O.B.T. J., *MFIX Documentation: Volume 1, Theory Guide.* National Technical Information Service, Springfield, VA, 1993.
152. Gidaspow, D., R. Bezburuah, and J. Ding, *Hydrodynamics of circulating fluidized beds: Kinetic theory approach*. 1991. Medium: ED; Size: Pages: (8 p).
153. Johnson, P., C. and R. Jackson., *Frictional–collisional constitutive relations for granular materials, with application to plane shearing.* Journal of Fluid Mechanics, 1987. **176**: p. 67-93.
154. Arastoopour, H., *Numerical simulation and experimental analysis of gas/solid flow systems: 1999 Fluor-Daniel Plenary lecture.* Powder Technology, 2001. **119**(2–3): p. 59-67.
155. Mathiesen, V., T. Solberg, and B.H. Hjertager, *Predictions of gas/particle flow with an Eulerian model including a realistic particle size distribution.* Powder Technology, 2000. **112**(1–2): p. 34-45.
156. Nikolopoulos, A., et al. *PSD incorporation in full - loop CFD modeling of CFBs* in *21st international conference on Fluidized Bed Combustion*. 2012. Naples, Italy.
157. Ergun, S., *Fluid flow through packed columns.* Chemical Engineering Progress, 1952. **48**: p. 89–94.
158. Li, J. and M. Kwauk, *Exploring complex systems in chemical engineering - The multi-scale methodology.* Chemical Engineering Science, 2003. **58**: p. 521-535.
159. Wang, X.-Q., C. Yap, and A.S. Mujumdar, *A parametric study of phase change material (PCM)-based heat sinks.* International Journal of Thermal Sciences, 2008. **47**(8): p. 1055-1068.
160. Wang, W. and J. Li, *Simulation of gas–solid two-phase flow by a multi-scale CFD approach—of the EMMS model to the sub-grid level.* Chemical Engineering Science, 2007. **62**(1–2): p. 208-231.
161. Naren, P.R., A.M. Lali, and V.V. Ranade, *Evaluating EMMS Model for Simulating High Solid Flux Risers.* Chemical Engineering Research and Design, 2007. **85**(8): p. 1188-1202.
162. Soong, C., K. Tuzla, and J. Chen, *Experimental determination of cluster size and velocity in circulating fluidized bed.* Fluidization VIII, Engineering Foundation, New York, 1995: p. 219-227.
163. Yan, A., et al. *The interdependence of micro and macro flow structures under a high-flux flow*. in *Proceedings of the Seventh International Circulating Fluidized Beds Conference* 2002. Ottawa: Canadian Society for Chemical Engineering.
164. Manyele, S.V., J.H. Pärssinen, and J.X. Zhu, *Characterizing particle aggregates in a high-density and high-flux CFB riser.* Chemical Engineering Journal, 2002. **88**(1–3): p. 151-161.
165. Liu, X., *Aggregation and Lateral Transfer Behaviour of Particles in Gas–Solid Fluidized Beds.* Institute of Process Engineering, Chinese Academy of Science, Beijing, PR China, 2005.
166. Sharma, A.K., et al., *Parametric effects of particle size and gas velocity on cluster characteristics in fast fluidized beds.* Powder Technology, 2000. **111**(1–2): p. 114-122.
167. Tuzla, K., et al., *Transient dynamics of solid concentration in downer fluidized bed.* Powder Technology, 1998. **100**(2–3): p. 166-172.
168. Yang, N., Wang, W., Ge, W., Li, J., *Analysis of flow structure and calculation of drag coefficient for concurrent-up gas–solid flow.* Chinese Journal of Chemical Engineering, 2003. **1**(11): p. 79–84.

169. Yang, N., et al., *Simulation of Heterogeneous Structure in a Circulating Fluidized-Bed Riser by Combining the Two-Fluid Model with the EMMS Approach.* Industrial & Engineering Chemistry Research, 2004. **43**(18): p. 5548-5561.
170. Syamlal, M., *The particle-particle drag term in a multiparticle model of fluidization*, in *Other Information: Portions of this document are illegible in microfiche products. Original copy available until stock is exhausted*. 1987. p. Medium: X; Size: Pages: 25.
171. Charitos, A., et al., *Parametric investigation of the calcium looping process for CO2 capture in a 10kWth dual fluidized bed.* International Journal of Greenhouse Gas Control, 2010. **4**(5): p. 776-784.
172. Hawthorne, C., et al. *Design of a dual fluidized bed system for the post-combustion removal of CO using CaO. Part I. CFB carbonator model*. in *9th International Conference on Circulating Fluidized Beds*. 2008. Hamburg,Germany.
173. Abanades, J.C., et al., *Capture of CO2 from combustion gases in a fluidized bed of CaO.* AIChE J, 2004. **50**: p. 1614-22.
174. Zeneli, M., et al., *Application of an advanced coupled EMMS-TFM model to a pilot scale CFB carbonator.* Chemical Engineering Science, 2015. **138**: p. 482-498.
175. Kuo, K.K.Y., *Principles of Combustion*, ed. John Wiley & Sons. 1986, New York.
176. Nikolopoulos, A., et al., *A decoupled approach for NOx–N2O 3-D CFD modeling in CFB plants.* Fuel, 2014. **115**: p. 401-415.
177. Álvarez, L., et al., *Oxy-coal combustion in an entrained flow reactor: Application of specific char and volatile combustion and radiation models for oxy-firing conditions.* Energy, 2013. **62**: p. 255-268.
178. Tognotti, L., J.P. Longwell, and A.F. Sarofim, *The products of the high temperature oxidation of a single char particle in an electrodynamic balance.* Symposium (International) on Combustion, 1991. **23**(1): p. 1207-1213.
179. Nikolopoulos, N., et al., *Numerical investigation of the oxy-fuel combustion in large scale boilers adopting the ECO-Scrub technology.* Fuel, 2011. **90**(1): p. 198-214.
180. Rajan, R., R. Krishnan, and C.Y. Wen, *Simulation of fluidized bed coal combustors*. 1979, West Virginia University.
181. Syamlal, M. and L.A. Bissett, *METC Gasifier Advanced Simulation (MGAS) model*. 1992. p. Medium: X; Size: Pages: (91 p).
182. Syamlal, M., W. Rogers, and T.J. O'Brien, *MFIX Documentation Theory Guide.* 1993.
183. Gunn, D.J., *Transfer of heat or mass to particles in fixed and fluidised beds.* International Journal of Heat and Mass Transfer, 1978. **21**(4): p. 467-476.
184. Wen, C.Y., et al., *User's Manual for Computer Simulation and Design of the Moving Bed Coal Gasifier: Final Report, Task Order*. 1982: Technical Information Center, U.S. Department of Energy.
185. Desai, P.R. and C.Y. Wen, *Computer modeling of the Morgantown Energy Research Center's fixed bed gasifier. [Theory and development]*. 1978, ; West Virginia Univ., Morgantown (USA). Dept. of Chemical Engineering. p. Medium: ED; Size: Pages: 136.
186. Magnussen, B.F. and B.H. Hjertager, *On mathematical modeling of turbulent combustion with special emphasis on soot formation and combustion.* Symposium (International) on Combustion, 1977. **16**(1): p. 719-729.
187. Drosatos, P., et al., *Numerical investigation of firing concepts for a flexible Greek lignite-fired power plant.* Fuel Processing Technology, 2016. **142**: p. 370-395.
188. Migliavacca, G., et al., *A general mathematical model of solid fuels pyrolysis.* Energy, 2005. **30**(8): p. 1453-1468.

189. Cheng, P., *Two-dimensional radiating gas flow by a moment method.* AIAA Journal, 1964. **2**(9): p. 1662-1664.
190. Ray, M.S., *Thermal Radiation Heat Transfer, 3rd edn, by R. Siegel and J.R. Howell, Hemisphere Publishing Corporation, USA (1992). 1072 pages. ISBN 0-89116-271-2.* Developments in Chemical Engineering and Mineral Processing, 1994. **2**(2-3): p. 190-190.
191. Modest, M.F. and S. Mazumder, *Section 11.7* in *Radiative Heat Transfer*. 2022.
192. Eriksson, M. and M.R. Golriz, *Radiation heat transfer in circulating fluidized bed combustors.* International Journal of Thermal Sciences, 2005. **44**(4): p. 399-409.
193. Gutfinger, C. and N. Abuaf, *Heat Transfer in Fluidized Beds*. 1974. p. 167-218.
194. Agyenim, F., et al., *A review of materials, heat transfer and phase change problem formulation for latent heat thermal energy storage systems (LHTESS).* Renewable and Sustainable Energy Reviews, 2010. **14**(2): p. 615-628.
195. König-Haagen, A., et al., *A comprehensive benchmark of fixed-grid methods for the modeling of melting.* International Journal of Thermal Sciences, 2017. **118**: p. 69-103.
196. Kroeger, P.G. and S. Ostrach, *The solution of a two-dimensional freezing problem including convection effects in the liquid region.* International Journal of Heat and Mass Transfer, 1974. **17**(10): p. 1191-1207.
197. Dincer, I., *Thermal Energy Storage: Systems and Applications*. 2011: Wiley.
198. Alam, T.E., et al., *Macroencapsulation and characterization of phase change materials for latent heat thermal energy storage systems.* Applied Energy, 2015. **154**: p. 92-101.
199. Yu, S., X. Wang, and D. Wu, *Microencapsulation of n-octadecane phase change material with calcium carbonate shell for enhancement of thermal conductivity and serving durability: Synthesis, microstructure, and performance evaluation.* Applied Energy, 2014. **114**: p. 632-643.
200. Hawlader, M.N.A., M.S. Uddin, and M.M. Khin, *Microencapsulated PCM thermal-energy storage system.* Applied Energy, 2003. **74**(1): p. 195-202.
201. Tumirah, K., et al., *Nano-encapsulated organic phase change material based on copolymer nanocomposites for thermal energy storage.* Energy, 2014. **66**: p. 881-890.
202. Zeneli, M., et al., *Numerical simulation of a silicon-based latent heat thermal energy storage system operating at ultra-high temperatures.* Applied Energy, 2019. **242**: p. 837-853.
203. Gupta, S.C., *The Classical Stefan Problem: Basic Concepts, Modelling and Analysis with Quasi-Analytical Solutions and Methods*. 2017: Elsevier Science.
204. Crank, J., *Free and Moving Boundary Problems*. 1987: Clarendon Press.
205. Morgan, K., *A numerical analysis of freezing and melting with convection.* Computer Methods in Applied Mechanics and Engineering, 1981. **28**(3): p. 275-284.
206. Jany, P. and A. Bejan, *Scaling theory of melting with natural convection in an enclosure.* International Journal of Heat and Mass Transfer, 1988. **31**(6): p. 1221-1235.
207. Evans, K.J., D.A. Knoll, and M. Pernice, *Development of a 2-D algorithm to simulate convection and phase transition efficiently.* Journal of Computational Physics, 2006. **219**(1): p. 404-417.
208. Vidalain, G., L. Gosselin, and M. Lacroix, *An enhanced thermal conduction model for the prediction of convection dominated solid–liquid phase change.* International Journal of Heat and Mass Transfer, 2009. **52**(7): p. 1753-1760.
209. Wang, S., A. Faghri, and T.L. Bergman, *A comprehensive numerical model for melting with natural convection.* International Journal of Heat and Mass Transfer, 2010. **53**(9): p. 1986-2000.
210. Gau, C. and R. Viskanta, *Melting and Solidification of a Pure Metal on a Vertical Wall.* Journal of Heat Transfer, 1986. **108**(1): p. 174-181.
211. Muhammad, M.D. and O. Badr, *Performance of a finned, latent-heat storage system for high temperature applications.* Applied Thermal Engineering, 2017. **116**: p. 799-810.

212. Fornarelli, F., et al., *Numerical simulation of a complete charging-discharging phase of a shell and tube thermal energy storage with phase change material.* Energy Procedia, 2017. **126**: p. 501-508.
213. Bagheri, G.h., M. Mehrabian, and K. Hooman, *Numerical study of the transient behaviour of a thermal storage module containing phase-change material.* Proceedings of the Institution of Mechanical Engineers Part A Journal of Power and Energy, 2010. **224**.
214. Verma, P., Varun, and S.K. Singal, *Review of mathematical modeling on latent heat thermal energy storage systems using phase-change material.* Renewable and Sustainable Energy Reviews, 2008. **12**(4): p. 999-1031.
215. Sharma, A., et al., *Review on thermal energy storage with phase change materials and applications.* Renewable and Sustainable Energy Reviews, 2009. **13**(2): p. 318-345.
216. Kasibhatla, R.R., A. König-Haagen, and D. Brüggemann, *Numerical Modelling of Wetting Phenomena During Melting of PCM.* Procedia Engineering, 2016. **157**: p. 139-147.
217. Brackbill, J.U., D.B. Kothe, and C. Zemach, *A continuum method for modeling surface tension.* Journal of Computational Physics, 1992. **100**(2): p. 335-354.
218. Zeneli, M., et al., *Study of heat losses during charge, discharge and storage period of a LHTES system operating at ultra-high temperatures*, in *ECOS Conference*. 2019: Wroclaw, Poland.
219. Assis, E., G. Ziskind, and R. Letan, *Numerical and Experimental Study of Solidification in a Spherical Shell.* Journal of Heat Transfer-transactions of The Asme - J HEAT TRANSFER, 2009. **131**.
220. Hosseinizadeh, S.F., et al., *Unconstrained melting inside a sphere.* International Journal of Thermal Sciences, 2013. **63**: p. 55-64.
221. Shmueli, H., G. Ziskind, and R. Letan, *Melting in a vertical cylindrical tube: Numerical investigation and comparison with experiments.* International Journal of Heat and Mass Transfer, 2010. **53**(19): p. 4082-4091.
222. Bareiss, M. and H. Beer, *An analytical solution of the heat transfer process during melting of an unfixed solid phase change material inside a horizontal tube.* International Journal of Heat and Mass Transfer, 1984. **27**(5): p. 739-746.
223. Sparrow, E.M. and J.A. Broadbent, *Inward Melting in a Vertical Tube Which Allows Free Expansion of the Phase-Change Medium.* Journal of Heat Transfer, 1982. **104**(2): p. 309-315.
224. Jones, B.J., et al., *Experimental and numerical study of melting in a cylinder.* International Journal of Heat and Mass Transfer, 2006. **49**(15): p. 2724-2738.
225. Darzi, A.R., M. Farhadi, and K. Sedighi, *Numerical study of melting inside concentric and eccentric horizontal annulus.* Applied Mathematical Modelling, 2012. **36**(9): p. 4080-4086.
226. Lacroix, M., *Numerical simulation of a shell-and-tube latent heat thermal energy storage unit.* Solar Energy, 1993. **50**(4): p. 357-367.
227. Rösler, F. and D. Brüggemann, *Shell-and-tube type latent heat thermal energy storage: numerical analysis and comparison with experiments.* Heat and Mass Transfer, 2011. **47**(8): p. 1027.
228. Gong, Z.-X. and A.S. Mujumdar, *Finite-element analysis of cyclic heat transfer in a shell-and-tube latent heat energy storage exchanger.* Applied Thermal Engineering, 1997. **17**(6): p. 583-591.
229. Brent, A.D., V.R. Voller, and K.J. Reid, *Enthalpy porosity technique for modelling convection-diffusion phase change: Application to the melting of a pure metal.* Numerical Heat Transfer, 1988. **13**(3): p. 297-318.
230. Pal, D. and Y.K. Joshi, *Melting in a side heated tall enclosure by a uniformly dissipating heat source.* International Journal of Heat and Mass Transfer, 2001. **44**(2): p. 375-387.
231. Sharma, R.K., et al., *Numerical study for enhancement of solidification of phase change materials using trapezoidal cavity.* Powder Technology, 2014. **268**: p. 38-47.

232. Datas, A., et al., *Molten silicon storage of concentrated solar power with integrated thermophotovoltaic energy conversion.* AIP Conference Proceedings, 2018. **2033**(1): p. 090005.
233. Hua, J. and D. Mortensen, *A front tracking method for simulation of two-phase interfacial flows on adaptive unstructured meshes for complex geometries.* International Journal of Multiphase Flow, 2019. **119**: p. 166-179.
234. Unverdi, S.O. and G. Tryggvason, *A front-tracking method for viscous, incompressible, multi-fluid flows.* Journal of Computational Physics, 1992. **100**(1): p. 25-37.
235. Juric, D. and G. Tryggvason, *A Front-Tracking Method for Dendritic Solidification.* Journal of Computational Physics, 1996. **123**(1): p. 127-148.
236. Marshall, G., *A Front Tracking Method for One-Dimensional Moving Boundary Problems.* SIAM Journal on Scientific and Statistical Computing, 1986. **7**(1): p. 252-263.
237. Meyer, G.H., *The numerical solution of Stefan problems with front-tracking and smoothing methods.* Applied Mathematics and Computation, 1978. **4**(4): p. 283-306.
238. Meyer, G.H., *Direct and iterative one-dimensional front tracking methods for the two-dimensional stefan problem.* Numerical Heat Transfer, 1978. **1**: p. 351-364.
239. Vu, T.V., et al., *Numerical investigations of drop solidification on a cold plate in the presence of volume change.* International Journal of Multiphase Flow, 2015. **76**: p. 73-85.
240. Bonnerot, R. and P. Jamet, *A conservative finite element method for one-dimensional stefan problems with appearing and disappearing phases.* Journal of Computational Physics, 1981. **41**(2): p. 357-388.
241. Zhao, P. and J.C. Heinrich, *Front-Tracking Finite Element Method for Dendritic Solidification.* Journal of Computational Physics, 2001. **173**(2): p. 765-796.
242. Patankar, S.V., *Numerical Heat Transfer and Fluid Flow*. 1980: Hemisphere Publishing Corporation.
243. Gloth, O., et al., *A front tracking method on unstructured grids.* Computers & Fluids, 2003. **32**: p. 547-570.
244. Jo, J.C., W.K. Shin, and C.Y. Choi, *Multidimensional phase change problems by the dual-reciprocity boundary-element method.* Numerical Heat Transfer, Part B: Fundamentals, 1999. **36**(1): p. 95-113.
245. Partridge, P.W. and C.A. Brebbia, *Dual Reciprocity Boundary Element Method*. 2012: Springer Netherlands.
246. DeLima-Silva, W. and L.C. Wrobel, *A front-tracking BEM formulation for one-phase solidification/melting problems.* Engineering Analysis with Boundary Elements, 1995. **16**(2): p. 171-182.
247. Brattkus, K. and D.I. Meiron, *Numerical Simulations of Unsteady Crystal Growth.* SIAM Journal on Applied Mathematics, 1992. **52**(5): p. 1303-1320.
248. Wrobel, L.C. and C.A. Brebbia, *The dual reciprocity boundary element formulation for nonlinear diffusion problems.* Computer Methods in Applied Mechanics and Engineering, 1987. **65**(2): p. 147-164.
249. Dehghan, M. and M. Najafi, *Numerical solution of a non-classical two-phase Stefan problem via radial basis function (RBF) collocation methods.* Engineering Analysis with Boundary Elements, 2016. **72**: p. 111-127.
250. Vrankar, L., et al. *Solving one-dimensional phase change problems with moving grid method and mesh free radial basis functions*. in *Proceedings of the International Conference Nuclear Energy for New Europe 2006*. 2006. Slovenia: Nuclear Society of Slovenia.
251. Rønquist, E.M. and A.T. Patera, *A Legendre spectral element method for the Stefan problem.* International Journal for Numerical Methods in Engineering, 1987. **24**(12): p. 2273-2299.

252. C.R, S. and V. V.R, *ON THE ENTHALPY METHOD.* International Journal of Numerical Methods for Heat & Fluid Flow, 1993. **3**(3): p. 233-244.
253. Nestler, B., D. Danilov, and P. Galenko, *Crystal growth of pure substances: Phase-field simulations in comparison with analytical and experimental results.* Journal of Computational Physics, 2005. **207**(1): p. 221-239.
254. Song, J.-H., et al., *Phase field simulations of coupled microstructure solidification problems via the strong form particle difference method.* International Journal of Mechanics and Materials in Design, 2018. **14**(4): p. 491-509.
255. Rabienataj Darzi, A.A., M. Jourabian, and M. Farhadi, *Melting and solidification of PCM enhanced by radial conductive fins and nanoparticles in cylindrical annulus.* Energy Conversion and Management, 2016. **118**: p. 253-263.
256. Chen, S., et al., *A Simple Level Set Method for Solving Stefan Problems.* Journal of Computational Physics, 1997. **135**(1): p. 8-29.
257. Papac, J., F. Gibou, and C. Ratsch, *Efficient symmetric discretization for the Poisson, heat and Stefan-type problems with Robin boundary conditions.* Journal of Computational Physics, 2010. **229**(3): p. 875-889.
258. Udaykumar, H.S., R. Mittal, and W. Shyy, *Computation of Solid–Liquid Phase Fronts in the Sharp Interface Limit on Fixed Grids.* Journal of Computational Physics, 1999. **153**(2): p. 535-574.
259. Shyy, W., H.S. Udaykumar, and S.J. Liang, *An interface tracking method applied to morphological evolution during phase change.* International Journal of Heat and Mass Transfer, 1993. **36**(7): p. 1833-1844.
260. Vincent, S., et al., *Penalty and Eulerian–Lagrangian VOF methods for impact and solidification of metal droplets plasma spray process.* Computers & Fluids, 2015. **113**: p. 32-41.
261. Raessi, M. and J. Mostaghimi, *Three-Dimensional Modelling of Density Variation Due to Phase Change in Complex Free Surface Flows.* Numerical Heat Transfer, Part B: Fundamentals, 2005. **47**(6): p. 507-531.
262. Ghoneim, A.Y., *A smoothed particle hydrodynamics-phase field method with radial basis functions and moving least squares for meshfree simulation of dendritic solidification.* Applied Mathematical Modelling, 2020. **77**: p. 1704-1741.
263. Shaikh, J., A. Sharma, and R. Bhardwaj, *On sharp-interface level-set method for heat and/or mass transfer induced Stefan problem.* International Journal of Heat and Mass Transfer, 2016. **96**: p. 458-473.
264. Voller, V.R., M. Cross, and N.C. Markatos, *An enthalpy method for convection/diffusion phase change.* International Journal for Numerical Methods in Engineering, 1987. **24**(1): p. 271-284.
265. Miranda Fuentes, J., et al., *Melting with convection and radiation in a participating phase change material.* Applied Energy, 2013. **109**: p. 454-461.
266. Tan, F.L. and S.C. Fok. *Thermal Management of Mobile Phone using Phase Change Material*. in *2007 9th Electronics Packaging Technology Conference*. 2007.
267. Yang, B., et al., *Microstructural evolution within mushy zone during paraffin's melting and solidification.* International Journal of Heat and Mass Transfer, 2019. **141**: p. 769-778.
268. Poirier, D.R. and S. Ganesan, *Permeabilities for flow of interdendritic liquid in equiaxial structures.* Materials Science and Engineering: A, 1992. **157**(1): p. 113-123.
269. Kovačević, I., A. Poredoš, and B. Šarler, *SOLVING THE STEFAN PROBLEM WITH THE RADIAL BASIS FUNCTION COLLOCATION MEHOD.* Numerical Heat Transfer, Part B: Fundamentals, 2003. **44**(6): p. 575-599.
270. Kosec, G. and B. Sarler, *Solution of Phase Change Problems by Collocation with Local Pressure Correction.* CMES. Computer Modeling in Engineering & Sciences, 2009. **47**.

271. Souayfane, F., P.H. Biwole, and F. Fardoun, *Melting of a phase change material in presence of natural convection and radiation: A simplified model.* Applied Thermal Engineering, 2018. **130**: p. 660-671.
272. Gowreesunker, B.L., et al., *Experimental and numerical investigations of the optical and thermal aspects of a PCM-glazed unit.* Energy and Buildings, 2013. **61**: p. 239-249.
273. Hou, T.Y., J.S. Lowengrub, and M.J. Shelley, *Boundary Integral Methods for Multicomponent Fluids and Multiphase Materials.* Journal of Computational Physics, 2001. **169**(2): p. 302-362.
274. Tan, F.L., *Constrained and unconstrained melting inside a sphere.* International Communications in Heat and Mass Transfer, 2008. **35**(4): p. 466-475.
275. Datas, A. *Hybrid thermionic-photovoltaic converter*. 2016. **108**.
276. Xiao, G., et al., *Thermodynamic assessment of solar photon-enhanced thermionic conversion.* Applied Energy, 2018. **223**: p. 134-145.
277. Datas, A., et al., *Ultra-high temperature energy storage and conversion: A review of the AMADEUS project results.* AIP Conference Proceedings, 2020. **2303**(1): p. 190008.
278. *ANSYS Fluent 17.1 Theory Guide.* 2016.
279. Hirt, C.W. and B.D. Nichols, *Volume of fluid (VOF) method for the dynamics of free boundaries.* Journal of Computational Physics, 1981. **39**(1): p. 201-225.
280. Worster, M.G., *Natural convection in a mushy layer.* Journal of Fluid Mechanics, 2006. **224**: p. 335-359.
281. *Fluent, ANSYS FLUENT Release 17.0 User Manual.* 2016.
282. Assis, E., G. Ziskind, and R. Letan, *Numerical and Experimental Study of Solidification in a Spherical Shell.* Journal of Heat Transfer, 2008. **131**(2): p. 024502-024502-5.
283. Hemanth, J., *Effect of cooling rate on dendrite arm spacing (DAS), eutectic cell count (ECC) and ultimate tensile strength (UTS) of austempered chilled ductile iron.* Materials & Design, 1999. **21**(1): p. 1-8.
284. Veeraragavan, A., L. Montgomery, and A. Datas, *Night time performance of a storage integrated solar thermophotovoltaic (SISTPV) system.* Solar Energy, 2014. **108**: p. 377-389.
285. Pawlak–Kruczek, H., et al., *Drying of Lignite of Various Origins in a Pilot Scale Toroidal Fluidized Bed Dryer using Low Quality Heat.* Energies, 2019. **12**(7): p. 1191.
286. Datas, A., D.L. Chubb, and A. Veeraragavan, *Steady state analysis of a storage integrated solar thermophotovoltaic (SISTPV) system.* Solar Energy, 2013. **96**: p. 33-45.
287. Basu, S., *Crystalline Silicon - Properties and Uses*. 2011: Web of Sciences.
288. Reardon, A.C., *Metallurgy for the Non-Metallurgist, Second Edition*. ASM International. 2011.
289. Xie, G., et al., *The influence of Marangoni effect on the growth quality of multi-crystalline silicon during the vacuum directional solidification process.* Materials Science in Semiconductor Processing, 2019. **91**: p. 124-132.
290. Lang, S., et al., *Thermal insulation of an ultra-high temperature thermal energy store for concentrated solar power.* AIP Conference Proceedings, 2018. **2033**(1): p. 090020.
291. Hofmann, C., et al., *Pilot Testing of the Indirectly Heated Carbonate Looping Process for Cement and Lime Plants*, in *16th International Conference on Greenhouse Gas Control Technologies GHGT-16*. 2022: Lyon, France.
292. Nikolopoulos, A., et al., *Introducing an Artificial Neural Network Energy Minimization Multi-Scale drag scheme for fluidized particles.* Chemical Engineering Science, 2020. **229**: p. 116013.
293. Benyahia, S., M. Syamlal, and T.J. O'Brien, *Study of the ability of multiphase continuum models to predict core-annulus flow.* AIChE Journal, 2007. **53**(10): p. 2549-2568.
294. Ströhle, J., et al., *Carbonate looping experiments in a 1 MWth pilot plant and model validation.* Fuel 127, 2014: p. 13–22.

295. Wang, J. and Y. Liu, *EMMS-based Eulerian simulation on the hydrodynamics of a bubbling fluidized bed with FCC particles.* Powder Technology, 2010. **197**(3): p. 241-246.
296. Nikolopoulos, A., et al. *PSD incorporation in full - loop CFD modeling of CFBs* in *21st international conference on Fluidized Bed Combustion*. 2012. Naples, Italy.
297. Fluent, *Theory Guide.* 2014.
298. Wang, X., et al., *3D full-loop simulation and experimental verification of gas–solid flow hydrodynamics in a dense circulating fluidized bed.* Particuology, 2014. **16**(0): p. 218-226.
299. Lu, B., et al., *Extending EMMS-based models to CFB boiler applications.* Particuology, 2012. **10**(6): p. 663-671.
300. Grace, J. and H. Bi, *Circulating Fluidized Beds*, in *Handbook of Fluidization and Fluid-Particle Systems.*, W.-C. Yang, Editor. 2003. p. 485-544.
301. Duelli, G., et al., *Analysis of the calcium looping system behavior by implementing simple reactor and attrition models at a 10 kWth dual fluidized bed facility under continuous operation.* Fuel, 2016. **169**: p. 79-86.
302. Grasa, G.S., et al., *Reactivity of highly cycled particles of CaO in a carbonation/calcination loop.* Chemical Engineering Journal, 2008. **137**(3): p. 561-567.
303. Coppola, A., et al., *Fluidized bed calcium looping: The effect of SO2 on sorbent attrition and CO2 capture capacity.* Chemical Engineering Journal, 2012. **207–208**: p. 445-449.
304. Coppola, A., et al., *Reactivation by water hydration of the CO2 capture capacity of a calcium looping sorbent.* Fuel, 2014. **127**: p. 109-115.
305. Hawthorne, C., et al., *CO2 capture with CaO in a 200 kWth dual fluidized bed pilot plant.* Energy Procedia, 2011. **4**: p. 441-448.
306. Dieter, H., et al. *High Temperature CO2 Capture with CaO in a 200 kWth Dual Fluidized Bed Pilot Facility*. in *2nd ICEPE - Efficient Carbon Capture for Coal Power Plants*. 2011. Frankfurt am Main, Germany.
307. Zhu, Q., *Developments in circulating fluidised bed combustion*. 2013.
308. Levenspiel, O., *Chemical reaction engineering*. 1999, New York: Jonh Wiley & Sons. 660.
309. Nikolopoulos, A., et al., *Deliverable D2.5: Results of 3D two-fluid model.* 2016.
310. *Deliverable D2.6: Evaluation of concepts for improved design.* 2016.
311. Nikolopoulos, A., et al., *An advanced EMMS scheme for the prediction of drag coefficient under a 1.2 MWth CFBC isothermal flow—Part II: Numerical implementation.* Chemical Engineering Science, 2010. **65**(13): p. 4089-4099.
312. Diego, M.E., et al., *Experimental testing of a sorbent reactivation process in La Pereda 1.7 MWth calcium looping pilot plant.* International Journal of Greenhouse Gas Control, 2016. **50**: p. 14-22.
313. Grasa, G., et al., *Determination of CaO Carbonation Kinetics under Recarbonation Conditions.* Energy & Fuels, 2014. **28**(6): p. 4033-4042.
314. N., T., *Particle Size Distribution in CFD Simulation of Gas-Particle Flows*, in *Aalto University*. 2012.
315. Pandey, K.M., D.H. Das, and B. Acharya, *Effects of Variation of Specific Heat on Temperature in Gaseous Combustion with Fluent Software.* International Journal of Environmental Science and Development: IJESD, 2010. **419**(422).
316. Zahirovic, S., R. Scharler, and I. Obernberger, *Advanced CFD modelling of pulverised biomass combustion.* 2004.
317. Chang, J., et al., *CFD modeling of particle–particle heat transfer in dense gas-solid fluidized beds of binary mixture.* Powder Technology, 2012. **217**: p. 50-60.
318. Behjat, Y., S. Shahhosseini, and S.H. Hashemabadi, *CFD modeling of hydrodynamic and heat transfer in fluidized bed reactors.* International Communications in Heat and Mass Transfer, 2008. **35**(3): p. 357-368.

319. Lathouwers, D. and J. Bellan, *Modeling of dense gas–solid reactive mixtures applied to biomass pyrolysis in a fluidized bed.* International Journal of Multiphase Flow, 2001. **27**(12): p. 2155-2187.
320. Biteau, H., et al., *Calculation Methods for the Heat Release Rate of Materials of Unknown Composition.* 2008.
321. Kremer, J., et al., *Continuous CO2 Capture in a 1-MWth Carbonate Looping Pilot Plant.* Chemical Engineering & Technology, 2013. **36**(9): p. 1518-1524.
322. Reitz, M., et al., *Design and Erection of a 300 kWth Indirectly Heated Carbonate Looping Test Facility.* Energy Procedia, 2014. **63**: p. 2170-2177.
323. *Carbon capture by means o indirectly heated cabonate looping process - Final report.* 2014.
324. Zeneli, M., et al., *Simulation of the reacting flow within a pilot scale calciner by means of a three phase TFM model.* Fuel Processing Technology, 2017. **162**: p. 105-125.
325. instruments, T. *Materials Thermal Properties Database*. Available from: https://thermtest.com/thermal-resources/materials-database.
326. Kanellis, G., Zeneli M., Nikolopoulos, N.,, Hofmann, C., Ströhle, J., Karellas, S., Konttinen, J., , *CFD modelling of an indirectly heated calciner reactor, utilized for CO2 capture, in an Eulerian framework*, in *FBC24*. 2022: Gothenburg, Sweden
327. Korolev, V.N. and N.I. Syromyatnikov, *Hydrodynamics of a fluidized bed in the intertube space of staggered and in-line tube bundles.* Journal of engineering physics, 1980. **38**: p. 514-519.
328. Subbarao, D. and P. Basu, *A model for heat transfer in circulating fluidized beds.* International Journal of Heat and Mass Transfer, 1986. **29**(3): p. 487-489.
329. Fernández, A.G., et al., *Mainstreaming commercial CSP systems: A technology review.* Renewable Energy, 2019. **140**: p. 152-176.
330. Perez Lopez, I., et al., *On-sun operation of a 150kWth pilot solar receiver using dense particle suspension as heat transfer fluid.* Solar Energy, 2016. **137**: p. 463-476.
331. Fantini, M., et al., *Calcium Looping technology demonstration in industrial environment: the CLEANKER project and status of the CLEANKER pilot plant* in *75° National ATI Congress*. 2020.
332. Calix, *LEILAC2 Demonstration Plant's Preliminary Front End Engineering Design (Pre-FEED) Report*. 2021.
333. *Socratces Project EU*. Available from: https://socratces.eu.
334. Zhang, G., et al., *Study on the influence of glass encapsulating on the hygroscopicity of high temperature phase change heat storage materials.* IOP Conference Series: Earth and Environmental Science, 2020. **474**: p. 052094.
335. *Silicon price rises boost European producers.*
336. Statista, *Average silicon prices in the United States from 2017 to 2021, by type.*
337. Kang, Q., et al., *Particles in a circulation loop for solar energy capture and storage.* Particuology, 2019. **43**: p. 149-156.
338. INTRATEC. *Calcium Carbonate Prices*. Available from: https://www.intratec.us/chemical-markets/calcium-carbonate-price.
339. Charitos, A., et al., *Hydrodynamic analysis of a 10kWth Calcium Looping Dual Fluidized Bed for post-combustion CO2 capture.* Powder Technology, 2010. **200**(3): p. 117-127.
340. Saxena, S.C., *Heat Transfer between Immersed Surfaces and Gas-Fluidized Beds*, in *Advances in Heat Transfer*, J.P. Hartnett and T.F. Irvine, Editors. 1989, Elsevier. p. 97-190.
341. Ozkaynak, T.F. and J.C. Chen, *Emulsion phase residence time and its use in heat transfer models in fluidized beds.* AIChE Journal, 1980. **26**(4): p. 544-550.
342. Yusuf, R., M.C. Melaaen, and V. Mathiesen, *Convective Heat and Mass Transfer Modeling in Gas-Fluidized Beds.* Chemical Engineering & Technology, 2005. **28**(1): p. 13-24.

343. Blaszczuk, A. and S. Jagodzik, *Heat transfer characteristic in an external heat exchanger with horizontal tube bundle.* International Journal of Heat and Mass Transfer, 2020. **149**: p. 119253.
344. Grewal, N., *Heat Transfer Between Tubes and Gas-Solid Fluid Beds.* Department of Mechanical Engineering, University of North Dakota: Grand Forks, ND, USA, 1984.
345. Basu, P., *Combustion and gasification in fluidized beds*. 2006: CRC press.
346. WebBook, N.C. *Thermophysical Properties of Fluid Systems*. Available from: https://webbook.nist.gov/chemistry/fluid/.

Appendix

Simplified model to simulate heat transfer inside a FB system

To assess the effect of radiation on the total HTCs, a mechanistic heat transfer model based on the packet renewal theory proposed by Mickley and Fairbanks [66] with additional equations from Kunii and Levenspiel and Subbarao and Basu is used as a reference to compare results with the CFD model.

In the dense part of the BFB (bottom bed), the horizontal tube bundle remain in the emulsion phase. In this case, the average bed-to-tube heat transfer coefficient, h_{bottom} is expressed as a summation of three components: packet particles convection h_e, gas convection hg and thermal radiation h_r:

Table 61. Basic theoretical model equations**.**

Equation	Description
$h_{bottom} = h_g\delta_b + h_e(1-\delta_b)+h_r$	Overall HTC at the bottom of the BFB
$h_e = \frac{2}{\sqrt{\pi}}\sqrt{k_e c_{pe}\rho_e}\frac{1}{\sqrt{t_e}}$	Convective HTC from emulsion phase to the tube bundle in the bottom section [66]
$h_r = \frac{5.67\times10^{-8}(T_s^4 - T_w^4)}{(1/e_s + 1/e_w)(T_s - T_w)}$	Radiative HTC
$h_g = 0.009\times\left(\frac{k_g}{d_p}\right)\times(Ar)^{0.5}\times Pr^{0.33}$	HTC of the gas in the bubbles [22]
Dimensionless numbers	
$Fr = \frac{d_p g}{U_{mf}^2(U_g/U_{mf} - A)^2}$	Dimensionless Froude number used to indicate the effect of gravity on fluid motion
$Ar = \frac{\rho_g d_p^3(\rho_p - \rho_g)g}{\mu_g^2}$	Dimensionless Archimedes number is the ratio of gravitational forces to viscous forces

The correlations used to determine physical properties of emulsion phase are mostly based on the mechanistic model of Subbarao and Basu [328] and are as follows:

Voidage of emulsion phase, ε_e, at the vicinity of the tubes is [340]:

$$\varepsilon_e = 1 - \frac{(1-\varepsilon_{mf})\left[0.7293 + 0.5139(^{d_p}/_{d_{t,HP}})\right]}{1 + (^{d_p}/_{d_{t,HP}})} \quad 144)$$

, where $d_{t,HP}$ in this case in the cylinder/tube diameter.

Emulsion packet density, ρ_e [341], [328]

$$\rho_e = (1-\varepsilon_e)\rho_s \quad (145)$$

Emulsion heat capacity, c_e [342]:

$$c_{pe} = (1-\varepsilon_e)c_{ps} + \varepsilon_e c_{pg} \quad (146)$$

The last term in this equation can be omitted during calculation.

Emulsion thermal conductivity, k_e [52]

$$k_e = \varepsilon_e k_g + (1-\varepsilon_e)k_s \left[\frac{1}{\varphi_b\left({}^{k_s}/_{k_g}\right) + 2/3}\right] \quad (147)$$

, where φ_b is the ratio of an equivalent thickness of gas film referring to particle diameter, [-] and can be taken by the following graph (**Figure 111**):

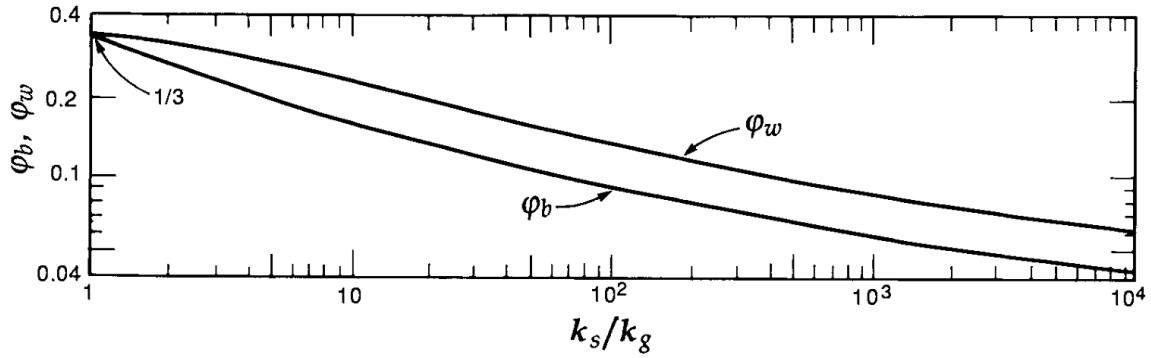

Figure 111. Ratio of effective thickness of gas film around a contact point to particle diameter: φ_b, for contact between adjacent particles, φ_w for contact between particle and surface [52].

The emulsion contact time t_e [-] with the heat transfer surface is defined as:

$$t_e = 1.20[Fr]^{0.3}\left(\frac{d_p}{d_{t,HP}}\right) \quad (148)$$

A is a dimensionless number defined as:

$$A = 1 - \frac{A_t}{A_b} \quad (149)$$

, where A_b is the bed cross-sectional area and A_t is the total surface area of the tubes taken as:

$$A_t = d_{t,HP}\, l_{t,HP}\, n \quad (150)$$

, where $l_{t,HP}$ is the tubes length and n the number of tubes.

The bubble fraction, δ_b, can be determined as [343]:

$$\delta_e = 0.19[Fr]^{-0.23} \quad (151)$$

For the calculation of the radiative heat transfer coefficient, the following properties are used:

Effective emissivity of bed particles, e_b [344]

$$e_b = (1 + e_p)/2 \quad 152)$$

, where e_p is the emissivity of particles.

Effective bed temperature, T_{eb} [345]:

$$T_{eb} = 0.85T_b \quad 153)$$

Wall (metal) temperature, T_W [345]:

$$T_w = T_{medium} + \Delta T_w \quad 154)$$

, where ΔT_w is the temperature difference between the internal and external temperatures of the tube surface and T_{medium} is the heat transfer medium average temperature.

Gas thermo-physical properties

The different gas medium thermo-physical properties are calculated based on NIST WebBook [346].

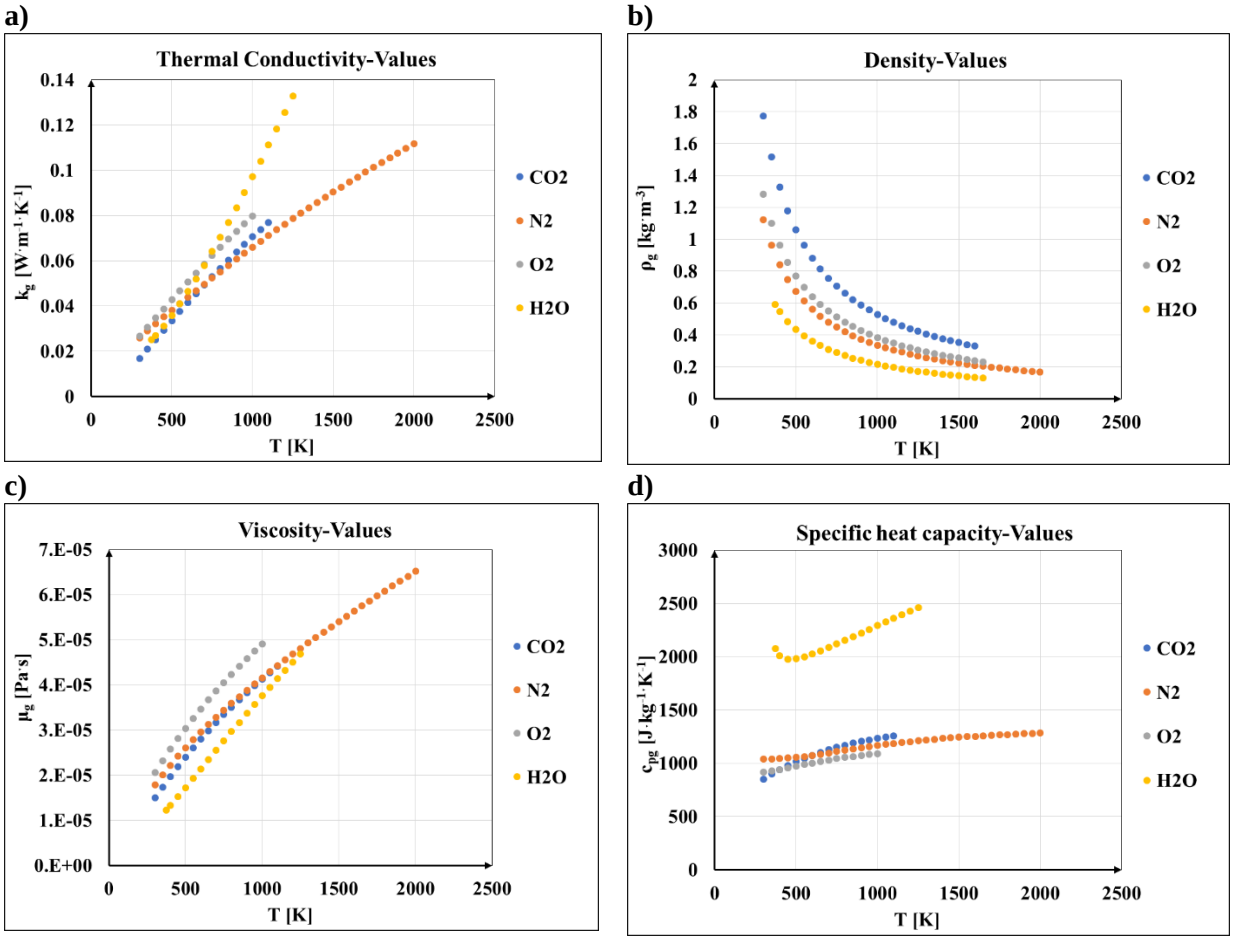

Figure 112. Thermo-physical properties of several species setup in the CFD model (a) thermal conductivity, (b) density, (c) viscosity, and, (d) specific heat capacity.

Gas thermo-physical properties setup in oxy-fired calciner

Table 62. Specific heat capacity coefficients setup in the oxy-fired calciner model.

Specie	***Method***	c_p **(J·kg^{-1}·K^{-1})**						
		Piecewise-polynomial: $c_p(T) = a_0 + a_1T_1 + a_2T_2^2 + a_3T_3^3 + a_4T_4^4 + a_5T_5^5 + a_6T_6^6$ Polynomial law: for $T_{min,1} \leq T < T_{max,1}$ $c_p(T) = a_0 + a_1T_1 + a_2T_2^2 + a_3T_3^3 + a_4T_4^4 + a_5T_5^5 + a_6T_6^6$ for $T_{min,2} \leq T < T_{max,2}$ $c_p(T) = b_0 + b_1T_1 + b_2T_2^2 + b_3T_3^3 + b_4T_4^4 + b_5T_5^5 + b_6T_6^6$						
		a_0	***a_1***	***a_2***	***a_3***	***a_4***	***a_5***	***a_6***
Vol(g)	CST	1500	0	0	0	0	0	0
O_2	PL	876.3	0.1228	5.583e-04	-1.202e-06	1.147e-09	-5.124e-13	8.566e-17
N_2	PL	1027	0.02162	1.486e-04	-4.484e-08	0	0	0
CO	PP	*$T_{min,1}$=300 K, $T_{max,1}$= 1000 K*						
		968.3898	0.44879	-1.1522e-03	1.65688e-06	-7.346e-10	0	0
CO_2	PL	535.4	1.279	-5.468e-04	-2.382e-07	1.892e-10	0	0
H_2O(v)	PL	1938	-1.181	3.644e-03	-2.863e-06	7.596e-10	0	0
H_2O(l)	CST	4182	0	0	0	0	0	0
Ash/char	PP	*$T_{min,1}$=273 K, $T_{max,1}$= 1000 K*						
		-464.1782	4.97117	-3.8992e-03	1.48294e-06	-2.886e-10	0	0
Vol(f)	PP	*$T_{min,1}$=300 K, $T_{max,1}$=1000 K*						
		-403.5847	9.05734	-1.4425e-02	1.58052e-05	-6.343e-09	0	0
		$T_{min,1}$=300 K, $T_{max,1}$= 1000 K						
CaO	PP	251.1235	2.69093	-4.2066e-03	3.0414e-06	-8.181e-10	0	0
		$T_{min,1}$= 300 K, $T_{max,1}$= 1000 K						
$CaCO_3$	PP	-147.0097	5.14113	-7.33e-03	3.83712e-06	-2.482e-10	0	0
		b_0	***b_1***	***b_2***	***b_3***	***b_4***	***b_5***	***b_6***
CO	PP	*$T_{min,2}$= 1000 K, $T_{max,2}$= 5000 K*						
		897.9305	0.42823	-1.6714e-04	3.02344e-08	-2.051e-12	0	0
Ash/char	PP	*$T_{min,2}$= 1000 K, $T_{max,2}$= 5000 K*						
		1031.521	1.15055	-4.629e-04	8.9357e-08	-6.372e-12	0	0
Vol(f)	PP	*$T_{min,2}$= 1000 K, $T_{max,2}$= 5000 K*						
		-872.4671	5.30547	-2.0083e-04	3.51665e-07	-2.334e-11	0	0
CaO	PP	*$T_{min,2}$= 1000 K, $T_{max,2}$= 3200 K*						
		838.5397	0.15071	-3.7921e-05	8.08248e-09	-6.313e-13	0	0
$CaCO_3$	PP	*$T_{min,2}$= 1000 K, $T_{max,2}$= 1200 K*						
		1199.445	-0.1161	1.69741e-04	0	0	0	0

Indirectly heated-calciner additional graphs

Turbulence effect investigation

The following graphs present the time evolution of the heat transfer at the heat pipes for the different turbulence models tested.